frontiers | Research Topics

Challenges associated with identifying preclinical animal models for the development of immune-based therapies

Edited by
Rajan P. Adhikari, Rajat Varma, Silke Paust and An Coosemans

Published in
Frontiers in Immunology

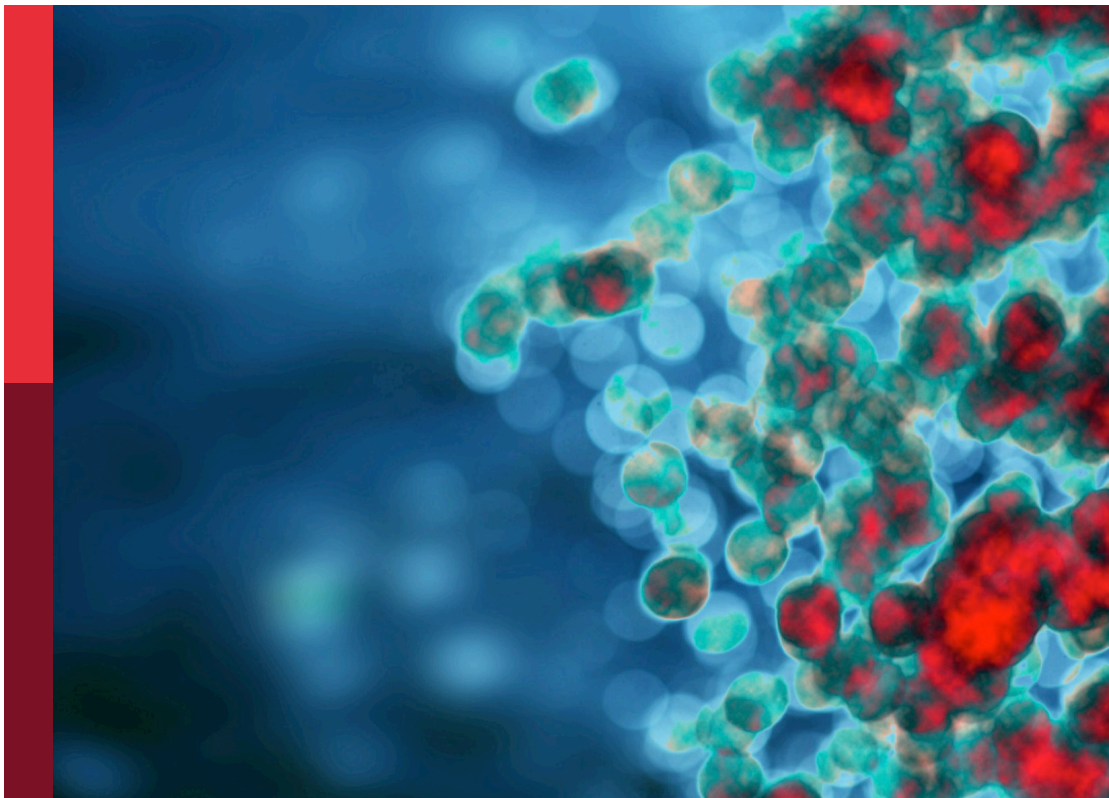

FRONTIERS EBOOK COPYRIGHT STATEMENT

The copyright in the text of individual articles in this ebook is the property of their respective authors or their respective institutions or funders. The copyright in graphics and images within each article may be subject to copyright of other parties. In both cases this is subject to a license granted to Frontiers.

The compilation of articles constituting this ebook is the property of Frontiers.

Each article within this ebook, and the ebook itself, are published under the most recent version of the Creative Commons CC-BY licence. The version current at the date of publication of this ebook is CC-BY 4.0. If the CC-BY licence is updated, the licence granted by Frontiers is automatically updated to the new version.

When exercising any right under the CC-BY licence, Frontiers must be attributed as the original publisher of the article or ebook, as applicable.

Authors have the responsibility of ensuring that any graphics or other materials which are the property of others may be included in the CC-BY licence, but this should be checked before relying on the CC-BY licence to reproduce those materials. Any copyright notices relating to those materials must be complied with.

Copyright and source acknowledgement notices may not be removed and must be displayed in any copy, derivative work or partial copy which includes the elements in question.

All copyright, and all rights therein, are protected by national and international copyright laws. The above represents a summary only. For further information please read Frontiers' Conditions for Website Use and Copyright Statement, and the applicable CC-BY licence.

ISSN 1664-8714
ISBN 978-2-8325-5211-7
DOI 10.3389/978-2-8325-5211-7

About Frontiers

Frontiers is more than just an open access publisher of scholarly articles: it is a pioneering approach to the world of academia, radically improving the way scholarly research is managed. The grand vision of Frontiers is a world where all people have an equal opportunity to seek, share and generate knowledge. Frontiers provides immediate and permanent online open access to all its publications, but this alone is not enough to realize our grand goals.

Frontiers journal series

The Frontiers journal series is a multi-tier and interdisciplinary set of open-access, online journals, promising a paradigm shift from the current review, selection and dissemination processes in academic publishing. All Frontiers journals are driven by researchers for researchers; therefore, they constitute a service to the scholarly community. At the same time, the *Frontiers journal series* operates on a revolutionary invention, the tiered publishing system, initially addressing specific communities of scholars, and gradually climbing up to broader public understanding, thus serving the interests of the lay society, too.

Dedication to quality

Each Frontiers article is a landmark of the highest quality, thanks to genuinely collaborative interactions between authors and review editors, who include some of the world's best academicians. Research must be certified by peers before entering a stream of knowledge that may eventually reach the public - and shape society; therefore, Frontiers only applies the most rigorous and unbiased reviews. Frontiers revolutionizes research publishing by freely delivering the most outstanding research, evaluated with no bias from both the academic and social point of view. By applying the most advanced information technologies, Frontiers is catapulting scholarly publishing into a new generation.

What are Frontiers Research Topics?

Frontiers Research Topics are very popular trademarks of the *Frontiers journals series*: they are collections of at least ten articles, all centered on a particular subject. With their unique mix of varied contributions from Original Research to Review Articles, Frontiers Research Topics unify the most influential researchers, the latest key findings and historical advances in a hot research area.

Find out more on how to host your own Frontiers Research Topic or contribute to one as an author by contacting the Frontiers editorial office: frontiersin.org/about/contact

Challenges associated with identifying preclinical animal models for the development of immune-based therapies

Topic editors
Rajan P. Adhikari — AbVacc Inc, United States
Rajat Varma — AstraZeneca, United States
Silke Paust — Jackson Laboratory for Genomic Medicine, United States
An Coosemans — KU Leuven, Belgium

Citation
Adhikari, R. P., Varma, R., Paust, S., Coosemans, A., eds. (2024). *Challenges associated with identifying preclinical animal models for the development of immune-based therapies*. Lausanne: Frontiers Media SA.
doi: 10.3389/978-2-8325-5211-7

Dr. Rajat Varma works at AztraZenica and is the Director of Oncology Research (Nextgen IO).

Dr. Rajan Adhikari works at BioTherapeutics Inc. and is the Associate Director of Bacterial Therapeutics.

Table of contents

frontiers | Frontiers in Immunology

TYPE Editorial
PUBLISHED 28 March 2024
DOI 10.3389/fimmu.2024.1404085

Check for updates

OPEN ACCESS

EDITED AND REVIEWED BY
Peter Brossart,
University of Bonn, Germany

*CORRESPONDENCE
An Coosemans
an.coosemans@kuleuven.be

RECEIVED 20 March 2024
ACCEPTED 25 March 2024
PUBLISHED 28 March 2024

CITATION
Jamil K, Sherchand SP, Adhikari RP and Coosemans A (2024) Editorial: Challenges associated with identifying preclinical animal models for the development of immune-based therapies.
Front. Immunol. 15:1404085.
doi: 10.3389/fimmu.2024.1404085

COPYRIGHT
© 2024 Jamil, Sherchand, Adhikari and Coosemans. This is an open-access article distributed under the terms of the Creative Commons Attribution License (CC BY). The use, distribution or reproduction in other forums is permitted, provided the original author(s) and the copyright owner(s) are credited and that the original publication in this journal is cited, in accordance with accepted academic practice. No use, distribution or reproduction is permitted which does not comply with these terms.

Editorial: Challenges associated with identifying preclinical animal models for the development of immune-based therapies

Kainat Jamil[1], Shardulendra P. Sherchand[2], Rajan P. Adhikari[2] and An Coosemans[1*]

[1]Department of Oncology, Laboratory of Tumor Immunology and Immunotherapy, Katholieke Universiteit (KU) Leuven, Leuven, Belgium, [2]Bacteriological Immunotherapy, AbVacc Inc., Rockville, MD, United States

KEYWORDS

animal, preclinical (*in vivo*) studies, immunotherapy, immune-based therapeutics, editorial

Editorial on the Research Topic
Challenges associated with identifying preclinical animal models for the development of immune-based therapies

Immunotherapy holds great potential as a cornerstone of cancer treatment due to effective clinical outcomes. Ongoing research aims to enhance its efficacy and overcome its associated pitfalls through preclinical research in animal models. However, identifying a suitable preclinical animal model, to mimic the intricate network of biological mechanisms in humans, is challenging (Chen et al.). The same holds true for autoimmune diseases, like rheumatoid arthritis (RA), inflammatory bowel disease (IBD), collagen-induced arthritis (CIA), Crohn's disease, systemic lupus erythematosus (SLE), reactive arthritis, type I diabetes, juvenile arthritis and sclerosis. Findings from pre-clinical animal models have the potential to be extrapolated to humans, but the question is if a single animal model can help us find answers to different autoimmune diseases induced by the intricate interplay between host, microbes, and autoimmune response.

This was perfectly underscored by the publications of Berckmans et al. and Sitnikova et al. Both researchers demonstrated that the choice of the preclinical model is crucial to accurately reflect the clinical situation and draw meaningful conclusions from preclinical therapy testing. Given the fact that it is of utmost importance that these models have an intact immune system, also age and realistic location of the tumor (orthotopic models) are needed. Sitnikova et al. investigated how aging can impact the immune profile and tumor progression through their experimental research in 60-72 weeks-old mice models. They observed reduced naïve T cell populations and fewer intratumoral CD8 T cell versus T regulatory (CD8/Treg) cell fractions in aged mice compared to young mice. On average, since cancer is mostly diagnosed in older people, the authors recommend to extend preclinical research in aged mice to predict accurately the treatment response. Furthermore, Giardino Torchia and Moody developed a framework called DIAL, to characterize the testing of cell therapies in mice. The DIAL model evaluates the current

preclinical evidence at four levels (Distribution, Infiltration, Accumulation, and Longevity) and highlights which preclinical models could answer the research question (= on gene-modified lymphocyte therapy development) best.

In addition, it is important to consider the distinct time points during tumor progression to evaluate the immune profile in preclinical models. Shields et al. provided a comprehensive overview of the MC38 colorectal cancer preclinical model utilized in investigating T cells during tumor progression to understand the immune-resistance mechanisms. The authors underscored the importance of time-point selection in elucidating the disparities in early-stage and late-stage tumor microenvironments (TME). They demonstrated that the early-stage tumors displayed primitive TME, lacking clinically relevant immune-resistance mechanisms. In contrast, the late-stage MC38 tumor model depicted a mature and developed TME like human TME, characterized by T cell exhaustion, T cell exclusions, and desmoplasia.

Zhou et al. reviewed the advancements achieved with human tumor models in mice and rats. They compared different mice models (induced, spontaneous, transgenic, transplantable, patient-derived xenografts (PDX), and humanized mice models) and explored the development processes along with the advantages and disadvantages. The success rate of implanting human cells in mice has been constantly low, from the earliest nude mice and progressing to the later severe combined immunodeficiency (SCID) and nonobese diabetic/severe combined immunodeficiency (NOD/SCID) mice. All humanized mice models lack one or more immune cells, limiting the human immune system reconstruction in animal models. The recent humanized-hematopoietic stem cells (Hu-HSCs) model with less graft-versus-host disease (GvHD) is expected to be used for long-term research, however, it is still lacking human cytokines and stem cells.

Jia et al. went for another approach. They demonstrated that Syrian hamsters exhibit characteristics like humans in terms of their anatomy, physiology, and pathology and can act as the preferred emerging tumor model to develop immunotherapies. They further reported that human granulocyte-macrophage colony-stimulating factor (GM-CSF), human interleukin (IL)-21 and IL-12 are immunologically active in this tumor model. However, the absence of specialized immune reagents poses a challenge in conducting thorough investigations. Initiatives are ongoing to address these limitations by establishing repositories of Syrian hamster tumor cell lines, designing transgenic hamster models, and producing research reagents to precisely evaluate immune functionalities.

Similarly, Xu et al. focused on establishing an orthotopic tumor model in C57BL/6 mice to better understand the immune biology of and validate new therapeutic targets for anaplastic thyroid cancer. The research group compared the original B6129SF1/J hybrid mice model with the adapted model by molecular characterization of the tumor and immune cell populations. They observed upregulation of both pro-inflammatory cells (cytotoxic T cells, helper T cells, pro-inflammatory M1-macrophages) and immune suppressive cells (myeloid-derived suppressor cells), along with enhanced proliferative characteristics of cancer cells. However, the *in vitro* and *in vivo* results were contradictory regarding tumor growth. Therefore, further research in this new model is warranted before it can be further used.

Differences between anatomy, histology, and sites of prostatitis in men and rodents are reviewed by He et al. Inflammation pertaining to prostatitis could be acute, chronic, due to a pathogen infection or non-infectious immune-related. For all these subtypes, various preclinical models exist, e.g., non-bacterial prostatitis models arise from hormonal disorders, stress, urinal reflux, nervous dysfunction chemicals, immune mediations diet, and lactations. Readouts for animal models of prostatitis could be changes in behavior, body weight, pathology of the prostate, biochemical results, and measurements of urodynamics. This study highlights the complexity to study prostatitis and it underscores the importance of using multiple animal models to study the disease.

Karmele et al. reviewed single-cell RNA-sequencing (scRNA-seq) similarities and differences between human and animal IBD. There is a complex interaction between immune, microbiological, stromal and epithelial cells. In this study, they also summarized common pre-clinical models of IBD with various mechanisms and their advantages over other models. Chronic inflammation of intestinal cells can be induced chemically, by genetically knocking out IL10, antibody-mediated, via bacterial infections or spontaneously. Destruction of intestinal cells can be generated chemically and genetically by trinitrobenzene sulfonic acids, oxazolone and IL10 knockouts. Spontaneous colitis models can be developed by the production of TNFα, IL23, and Th1 driven immune response in AKR mice, who spontaneously develop lymphatic leukemia. Interestingly, infection of murine intestinal epithelial cells with *Citrobacter rodentium* and *Helicobacter hepaticus* can activate cytokine production and induce inflammation which serves as a good pre-clinical model for studying IBD (1).

Likewise, Kim et al. identified RA-associated beneficial microbial species; out of 36 isolates they found *Peptoniphilus gorbachii* to have major significance. Their results showed that *P. gorbachii* alleviated CIA in mice by improving intestinal homeostasis and immune regulations. Their novel findings in CIA mice were confirmed by low serum antibody levels against *P. gorbachii* in patients with worse disease outcomes.

Another successful use of animal models is the mechanically ventilated rabbit model of hyperdynamic septic shock. Nguyen et al. showed that passive immunization with neutralizing alpha-hemolysin, biocomponent leukocidins, and clumping factor A has protective efficacy against *Staphylococcus aureus* mediated acute septic shock in the mechanically ventilated rabbit model. In this model, authors measured cardiac output (CO), stroke volume (SV), and systemic vascular resistance (SVR). Mean arterial pressure (MAP) decline, increased SVR, reduced SV, increased CO, and reduced left ventricular ejection volume could be measured in this rabbit model. These parameters mimicked the clinical hallmarks of septic shock triggered by *S. aureus* in patients.

Besides the relevance of a clinical representative immune biology mimicked in the preclinical models, the evaluation of treatments is of course the true reason why we perform

preclinical experiments. Berckmans et al. also demonstrated that the timing of the treatments and their order will influence the survival of the mice and that this is (most of the time) not considered when designing preclinical and clinical trials. Kametani et al. evaluated liposome-encapsulated anti-programmed death ligand 1 antibody-conjugated progesterone in humanized peripheral blood mononuclear cells (Hu-PBMCs) breast cancer mice models. The authors noticed that GvHD and short survival periods can affect the evaluation of long-term immune response. Therefore, additional research is required. Gao et al. evaluated the effects of transdermal formestane anti-breast cream using a rat model. They induced mammary carcinoma in female Sprague-Dawley rats using dimethylbenz(a)anthracene administrations. Results demonstrated downregulation of extracellular matrix-related genes, increased immune cell infiltration in tumors, and negative effects on cell growth. The study suggests that formestane can potentially modulate the tumor microenvironment and immune response in breast cancer leading to improved outcomes. Kyuuma et al. developed nanobodies (ozoralizumab) against TNFα that lack the Fc portion of IgG, abrogating immune complex-induced inflammation in an RA model of mice compared to adalimumab (a TNFα inhibitor).

Animal models are very important surrogates for humans to measure pharmacodynamics, toxicity, immunogenicity, biomarkers, and allergic reactions to therapeutics. However, efficacy data generated by animal models are hard to reproduce in humans. The enormous repertoire of preclinical models already available and the continuous creation of newer models should provide us in the future with dedicated models to answer specific research questions. Nevertheless, some parts are still understudied/underrepresented, like for example the response of the nervous system. Humans are a highly developed intellectual entity, and it is understandable that our neuronal response to host and pathogen interaction is different than other animal models which are severely understudied. It is of utmost importance to consider different aspects of a preclinical animal model for evaluating the efficacy of immune-based therapies to translate into better clinical outcomes.

Author contributions

KJ: Writing – original draft, Writing – review & editing. SS: Writing – original draft, Writing – review & editing. RA: Writing – original draft, Writing – review & editing. AC: Writing – original draft, Writing – review & editing.

Conflict of interest

Authors SS and RA were employed by the company AbVacc Inc.

The remaining authors declare that the research was conducted in the absence of any commercial or financial relationships that could be construed as a potential conflict of interest.

The author(s) declared that they were an editorial board member of Frontiers, at the time of submission. This had no impact on the peer review process and the final decision.

Publisher's note

All claims expressed in this article are solely those of the authors and do not necessarily represent those of their affiliated organizations, or those of the publisher, the editors and the reviewers. Any product that may be evaluated in this article, or claim that may be made by its manufacturer, is not guaranteed or endorsed by the publisher.

Reference

1. Ho YT, Shimbo T, Wijaya E, Kitayama T, Takaki S, Ikegami K, et al. Longitudinal single-cell transcriptomics reveals a role for serpina3n-mediated resolution of inflammation in a mouse colitis model. *Cell Mol Gastroenterol Hepatol.* (2021) 12:547–66. doi: 10.1016/j.jcmgh.2021.04.004

frontiers | Frontiers in Immunology

TYPE Review
PUBLISHED 19 October 2022
DOI 10.3389/fimmu.2022.1007579

Check for updates

OPEN ACCESS

EDITED BY
Silke Paust,
The Scripps Research Institute,
United States

REVIEWED BY
Marcus O. Muench,
Vitalant Research Institute,
United States
Thomas Tsutomu Murooka,
University of Manitoba, Canada

*CORRESPONDENCE
Hua-feng Liu
liuhf@gdmu.edu.cn
Qingjun Pan
pqj@gdmu.edu.cn

†These authors have contributed equally to this work

SPECIALTY SECTION
This article was submitted to Cancer Immunity and Immunotherapy, a section of the journal Frontiers in Immunology

RECEIVED 23 August 2022
ACCEPTED 07 October 2022
PUBLISHED 19 October 2022

CITATION
Chen J, Liao S, Xiao Z, Pan Q, Wang X, Shen K, Wang S, Yang L, Guo F, Liu H-f and Pan Q (2022) The development and improvement of immunodeficient mice and humanized immune system mouse models. *Front. Immunol.* 13:1007579. doi: 10.3389/fimmu.2022.1007579

COPYRIGHT
© 2022 Chen, Liao, Xiao, Pan, Wang, Shen, Wang, Yang, Guo, Liu and Pan. This is an open-access article distributed under the terms of the Creative Commons Attribution License (CC BY). The use, distribution or reproduction in other forums is permitted, provided the original author(s) and the copyright owner(s) are credited and that the original publication in this journal is cited, in accordance with accepted academic practice. No use, distribution or reproduction is permitted which does not comply with these terms.

The development and improvement of immunodeficient mice and humanized immune system mouse models

Jiaxuan Chen†, Shuzhen Liao†, Zengzhi Xiao, Quanren Pan, Xi Wang, Kangyuan Shen, Shuting Wang, Lawei Yang, Fengbiao Guo, Hua-feng Liu* and Qingjun Pan*

Guangdong Provincial Key Laboratory of Autophagy and Major Chronic Non-communicable Diseases, Affiliated Hospital of Guangdong Medical University, Zhanjiang, China

Animal models play an indispensable role in the study of human diseases. However, animal models of different diseases do not fully mimic the complex internal environment of humans. Immunodeficient mice are deficient in certain genes and do not express these or show reduced expression in some of their cells, facilitating the establishment of humanized mice and simulation of the human environment *in vivo*. Here, we summarize the developments in immunodeficient mice, from the initial nude mice lacking T lymphocytes to NOD/SCID rg^{null} mice lacking T, B, and NK cell populations. We describe existing humanized immune system mouse models based on immunodeficient mice in which human cells or tissues have been transplanted to establish a human immune system, including humanized-peripheral blood mononuclear cells (Hu-PBMCs), humanized hematopoietic stem cells (Hu-HSCs), and humanized bone marrow, liver, thymus (Hu-BLT) mouse models. The different methods for their development involve varying levels of complexity and humanization. Humanized mice are widely used in the study of various diseases to provide a transitional stage for clinical research. However, several challenges persist, including improving the efficiency of reconstructing the human B cell immune response, extending lifespan, improving the survival rate of mice to extend the observation period, and improving the development of standardized commercialized models and as well as their use. Overall, there are many opportunities and challenges in the development of humanized immune system mouse models which can provide novel strategies for understanding the mechanisms and treatments of human disease.

KEYWORDS

immunodeficient mouse, humanized immune system mouse, nude mouse, NOD mouse, NOD/SCID mouse

Immunodeficient mice

The development of immunodeficient mice occurred in four main stages. The first stage included nude mice that are simply deficient in T lymphocytes owing to abnormal thymus development (1). However, the application of nude mice in many diseases remains limited because of their low relative degree of immunodeficiency. The second stage included mice with severe combined immunodeficiency (SCID), carrying a mutation of the *Prkdc* gene (2, 3). SCID mice are deficient in T and B lymphocytes, but retain natural killer (NK) cells and show "leakage" (4). The SCID mutation was then introduced into non-obese diabetic (NOD) mice with NK cell defects to obtain NOD/SCID mice (5), forming the third stage of immunodeficient mice. However, these mice exhibit a high frequency of spontaneous thymic lymphoma and short life cycles, as well as partial NK cell activity. Therefore, their application as a humanized animal model has remained limited (5). To improve this situation, the fourth stage of immunodeficient mice, NOD/SCID rg^{null} mice, was developed by knocking out the IL-2 receptor gamma chain (IL-2 rg); these knock-out mice had a higher rate of human-cell implantation without leakage or spontaneous thymomas, and are currently the gold standard immunodeficient mouse model (6). The characteristics of different immunodeficient mice are summarized in Figure 1.

Nude mice

Nude mice are the earliest immunodeficient mouse model, first reported by Flanagan in 1966 (1). Owing to an allele mutation on chromosome 11, a resultant defect in the *Foxn1* gene prevents normal thymus development (7), thereby leading to a mature T lymphocyte deficiency. The main immunoglobulin in these mice is IgM (8), with little or no IgA. As such, they do not show a rejection reaction to allogeneic tissue (9). The commonly used strains include BALB/c-nu, Swiss-nu, NC-nu, and NIH-nu, all of which are widely used in the study of immune diseases and tumors (10). However, as they still retain B cells and NK cells, they cannot completely accept human immune cell engraftment, and so cannot be used as an ideal humanized mouse model (11).

SCID mice

In 1983, researchers found CB-17 inbred mice that carried a recessive mutation of a single gene on chromosome 16, which led to the abnormal recombination enzyme activity of the sequence encoding the mouse lymphocyte antigen receptor gene VDJ, due to which immunoglobulin, T, and B lymphocyte receptors could not be synthesized effectively (3). This mutation obstructs the repair and recombination of T and B cell receptors and seriously affects the differentiation and maturation of these cells, resulting in the lack of mature T and B cells and low immunoglobulin levels in the peripheral blood or lymphoid organs of SCID mice (2). However, the NK cells and macrophages in SCID mice function normally (12, 13). Furthermore, "leakage" was observed (4, 14, 15), meaning that 2 to 23 percent of the mice showed recovery of T and B lymphocytes with increasing age (16). As SCID mice are highly sensitive to radiation, Rag^{null} mice were generated by the knockout of recombinant activated genes Rag1 (15) or Rag2 (17) to reduce their radiosensitivity. Rag1 and Rag2 induce V(D)J rearrangement of TCR and immunoglobulin genes by producing DNA double-strand breaks. Homozygous mutations in these genes result in the inability to produce mature T and B cells and produce the same SCID-like phenotype (18). Similar to the SCID mutation, mice with the Rag mutations lack mature T and B lymphocytes. Contrastingly, this mutation does not repair spontaneously. Nevertheless, these mice also allow limited human cell and tissue engraftment because of highly active NK cells (19–21).

NOD/SCID mice

In 1980, researchers obtained nonobese diabetic (NOD) mice *via* inbreeding and selective breeding, with pathological characteristics and changes similar to those in human diabetes (22). NOD mice have defects in their innate immune system, with low NK cells and macrophage activity, and an absence of circulating complement. Introducing the SCID mutation into the genetic background of NOD mice was hypothesized to result in NOD/SCID mice with simultaneously defective adaptive and innate immunity (23). Indeed, researchers successfully introduced the SCID mutation into NOD mice in 1995. The resulting NOD/SCID mice showed functional loss of T and B lymphocytes and other immune cells, as well as defective NK cell function, resulting in a higher degree of immune deficiency than in the previously noted mouse models (5). Human B cell reconstruction in nude mice and SCID mice was poor. In one study, NOD/SCID mice injected with 1×10^5 human $CD34^+$ cells showed that humanized B cells from different organs showed different stages of maturation, with immature IgM^-IgD^- $CD24^{hi}$ $CD38^{hi}$ B cells predominating in the bone marrow and mature $CD5^+$ IgM^+ IgD^+ $CD24^{int}$ $CD38^{int}$ $CD19^+$ B cells predominating in the spleen and peripheral blood.

Compared with SCID mice, human tumors and immune cells had better survival status in NOD/SCID mice (23). The NOD/SCID mice had the following characteristics (1): low NK cell levels, with significantly reduced killing function; (2) complement C5 deficiency, resulting in inhibition of

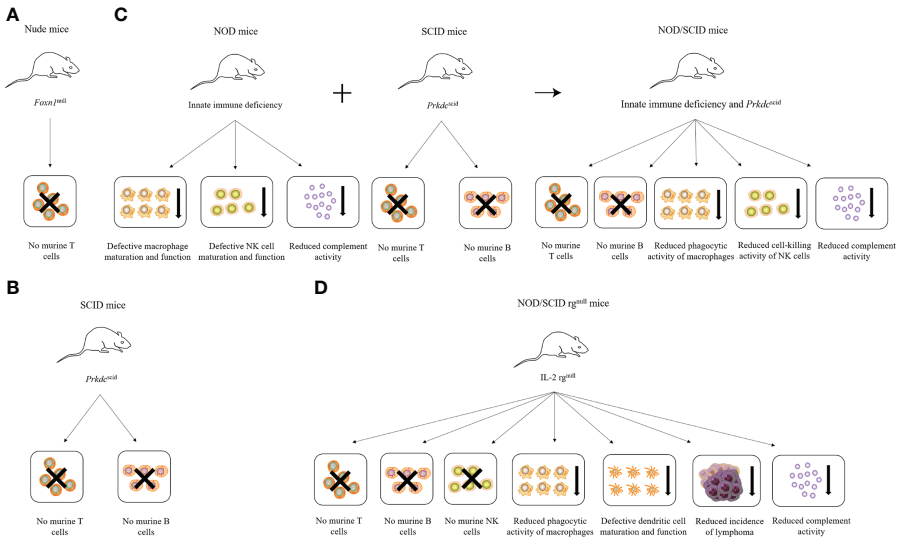

FIGURE 1
Characteristics of different immunodeficient mice. **(A)** Nude mice lack T cells due to *Foxn1* mutation. **(B)** SCID mice lack T and B cells due to *Prkdc* mutation. **(C)** NOD mice combined with SCID mice produce NOD/SCID mice, which lack T and B cells and have reduced phagocytic activity of macrophages, the cell-killing activity of NK cells, and complement activity. **(D)** NOD/SCID rg^{null} mice lack T, B, and NK cells and have reduced phagocytic activity of macrophages and complement activity, defective dendritic cell maturation and function, and reduced incidence of lymphoma due to the loss of the IL-2 receptor γ chain.

complement activation;(3) defective IL-1 secretion in lipopolysaccharide-induced macrophages. These characteristics enabled the generation and survival of human cells and grafts in NOD/SCID mice at higher levels. However, this model remained unsuitable, owing to certain defects, including radiosensitivity, which only allows a small radiation dose. T and B cell leakage also occurred in older mice, and their average life span was only 8 months. Furthermore, the NOD gene mutation in NOD/SCID mice increased the probability of spontaneous thymic lymphoma, resulting in a short life cycle of such mice along with partial NK cell activity, limiting its application as a humanized animal model (5).

NOD/SCID mice are not as commonly used to generate humanized mice because they require a higher dose of HSCs for efficient engraftment, compared with more deficient mouse strains like NOD/SCID rg^{null} mice and they developed thymic lymphomas shortening their lifespan. Despite these disadvantages, the model is still in use because of its unique characteristics. For example, it has been shown that NOD/SCID mice better support the development of human gut-associated lymphoid tissue (GALT) structures due to the presence of the common gamma chain. Therefore, when more robust human GALT structures are needed, NOD/SCID BLT mice may be preferred (24). One study also showed enhanced human cell reconstitution in the GALT of BLT mice. This study, using HIV infection of humanized mice (BLT) as a model of heterosexual transmission, demonstrated that blocking lymphocyte egress from lymph nodes prevented viremia and infection of the gut (25).In addition, NOD/SCID mice transplanted with HSCs are specifically used to generate mice that possess human myeloid and B cells but are devoid of human T cells following the transplant to study certain aspects of EBV and HIV infection (26, 27).

NOD/SCID rg^{null} mice

The IL-2 receptor gamma chain, also known as the common cytokine receptor gamma chain, is a key component of high-affinity receptors for cytokines such as IL-2, IL-4, IL-7, IL-9, IL-15, and IL-21. The development and maturation of T and B lymphocytes and NK cells require the participation of some of these cytokines. The loss of the IL-2 receptor gamma chain hinders the development of T and B lymphocytes as well as NK cells and severely weakens the innate and adaptive immune systems of mice (28). When IL-2 rg^{null} was combined with SCID, $Rag1^{null}$, or $Rag2^{null}$ mutations, the resulting NOD/Shi-SCID IL-2^{null} (NOG) (29), NOD/LtSz-SCID IL-2^{null} (NSG) (30), and NOD-$Rag1^{null}$ IL-2 rg^{null} (NRG) (31) mice were deficient in T and B lymphocytes as well as NK cells (13). These mice completely lost the ability to mount an adaptive immune response and showed serious defects in the innate immune system; which are the main requirements for immunodeficient mice for the construction of humanized mouse models (6).

NOD/SCID rg^{null} mice can be divided into NOG and NSG mice according to the mutation of the IL-2 receptor gamma chain. The major difference between the NSG and NOG strains is that the IL-2 rg targeted mutation used to develop the NSG strain is a complete null so that no IL-2 rg is expressed, effectively hindering cytokine binding, whereas the IL-2 rg mutation in the NOG strain produces a protein that is expressed and will bind cytokines but cannot transduce the signal (32). NOG and NSG mice were found to be the best models for human cell and tissue transplantation, with a higher transplantation success rate than either SCID or NOD/SCID mice (33, 34). Another important advantage of NOG and NSG mice is the absence of leakage and spontaneous thymomas, which may also be related to the lack of active IL-2 rg. Moreover, several immunodeficient mouse strains, such as NSGB2m and NSG-SGM3, have been derived by gene modification based on NSG mice. These mice are more advantageous in xenotransplantation (35, 36). One study comparing the implantation rate of human cells in the peripheral tissues of NSG mice with that in NOD/SCID mice showed a significantly higher implantation rate of human cells in NSG and NOG mice than in NOD/SCID mice. In addition, the implantation rate of human cells in the bone marrow of NSG mice was higher than that in the other strains, especially in females (37). Therefore, NSG mice are good candidates for generating humanized immune system mouse models. Another study examined the recovery of the immune system in humanized mice after the transplantation of human hematopoietic stem cells in NSG mice. The results showed that T, B cells, monocytes, macrophages, and neutrophils were developed to normal human levels in these mice. Moreover, the phagocytic ability of monocytes and macrophages, and the secretion ability of inflammatory factors under TLR4 stimulation also developed to normal human levels (38).

Signal regulatory protein α (SIRPα) is a transmembrane protein that contains three Ig-like domains within the extracellular region. SIRPα is expressed in macrophages, myeloid cells, and neurons, and interacts with its ligand CD47 *via* respective IgV-like domains, where the NOD strain has specific polymorphism. CD47 is a member of the immunoglobulin (Ig) superfamily that is ubiquitously expressed in hematopoietic as well as non-hematopoietic cells. The cytoplasmic region of SIRPα has immunoreceptor tyrosine-based inhibitory motifs (ITIMs), and the cell surface binding of CD47 with SIRPα on macrophages provokes inhibitory signals *via* phosphorylation of ITIM of SIRPα (39), preventing their phagocytic activity (40–42). A recent study showed that transgenic expression of mouse CD47 into the CD34^{+}CD38^{-} human fetal liver cells significantly enhanced the human cell engraftment into BALB-RG mice (43). Based on these results, it is assumed that the binding of NOD-SIRPα with human CD47 produces signals for mouse macrophages not to engulf human HSCs, presumably making the strain permissive for human HSC engraftment (44). The important question was whether the NOD-specific highly efficient human cell engraftment *in vivo* could be explained solely by the NOD-SIRPα polymorphism. In one study, Yamauchi et al. established a C57BL/6-Rag2^{null}IL-2rg^{null} (C57BL/6-RG) line harboring the NOD-type SIRPα. The results clearly show that the replacement of the C57BL/6-type SIRPα with the NOD-type SIRPα is sufficient for the C57BL/6-RG strain to be endowed with the xenotransplantation capability at least equal to NOD-RG mice. Thus, they successfully segregated the genetic abnormality responsible for efficient human cell engraftment from multiple genetic abnormalities in the NOD strain (45). The simplified humanized mouse system established by the new C57BL/6-Rag2^{null}IL-2rg^{null}NOD-SIRPα (BRGS) strain should be very useful to improve xenotransplantation strategies in studies on human cell biology. In one study, Di Santo et al. induced the expression of thymic-stromal-cell-derived lymphopoietin (TSLP) in a BALB/c Rag2$^{-/-}$IL-2rg$^{-/-}$SIRPα^{NOD} (BRGS) human immune system (HIS) mouse model. The resulting BRGST HIS mice developed a full array of LNs with compartmentalized human B and T cells. Compared with BRGS HIS mice, BRGST HIS mice have a larger thymus, more mature B cells, and abundant IL-21-producing follicular helper T (TFH) cells, and show enhanced antigen-specific responses. Peripheral human B cells in HIS mice retain an immature, transitional phenotype with elevated expression of CD24 and CD38. In BRGS and BRGST HIS mice, they observed this predominant population of CD24^{hi}CD38^{hi} immature B cells in the bone marrow, liver, and spleen. In contrast, mature CD24^{lo}CD38^{lo} cells were the dominant human B cell subset in LNs of BRGST mice. Although they did not observe notable differences in these different B cell subsets between the two models, the total numbers of mature CD24^{lo}CD38^{lo} B cells in LNs were significantly increased in BRGST HIS mice compared with those in BRGS mice (46).

Humanized mouse models constructed by engrafting peripheral blood mononuclear cells have mainly revealed the presence of human T cells (47, 48). However, in stem cell transplant models, B-cell reconstitution is efficient with T-cell engraftment lagging (49). Although both HSC-infused newborn and adult mice were highly reconstituted with human B cells, the development of B cells was arrested in an early stage and did not suffice for reconstitution of human immunoglobulins (natural antibodies) in serum, other than IgM (50). Impairment of human T and B cell function in HSC reconstituted IL-2 rg^{null} genetic stocks has been attributed to the lack of expression of human leukocyte antigens (HLA) in the mouse thymus since HLA molecules are required for the development of human T cells that in turn, are essential for stimulation of B cells towards immunoglobulin class switching and antibody secretion (51, 52). In one study, Danner et al. generated NOD.Rag1KO.IL2RγcKO mice expressing HLA-DR4 molecules under the I-E^{d} promoter infused as adults with HLA-DR-matched human hematopoietic stem cells generating a new strain of NOD.Rag1KO.IL2RγcKO mice expressing HLA-

DR*0401 molecules (DRAG mice). The presence of these HLA-DR4-IE transgenes allows irradiated DRAG mice to be engrafted with HLA-DR-matched hematopoietic stem cells; resulting in humanized T-cell and B-cell populations. The HLA-DR4 expressing mice reconstituted serum levels (natural antibodies) of human IgM, IgG (all four subclasses), IgA, and IgE comparable to humans, and elicited high titers of specific human IgG antibodies upon tetanus toxoid vaccination (53). In another study, Ito et al. generated transgenic mice with HLA-DRA-IEα and HLA-DRB1*0401-IEβ chimeric genes. The HLA-DRA-IEα/HLA-DRB1*0401-IEβ molecules rescued the development of $CD4^+$ T cells in major histocompatibility complex (MHC) class II-deficient mice, but T cells expressing Vβ5, Vβ11, and Vβ12 were specifically deleted (54).

These various types of mice are suitable for constructing various humanized mouse models for studying tumors, hematological diseases, infectious diseases, immune diseases, and metabolic diseases (29).

Development of humanized immune system mice

Humanized immune system mice can be divided into three groups according to the method used for immune system reconstruction: humanized-peripheral blood mononuclear cells (Hu-PBMCs) or humanized-peripheral blood lymphocytes (Hu-PBLs), humanized hematopoietic stem cells (Hu-HSCs) and humanized bone marrow, liver, thymus (Hu-BLT) mouse models. The different construction methods and characteristics of humanized mice are shown in Figure 2 and Table 1.

Hu-PBMCs/PBLs mouse model

In this model, human peripheral blood mononuclear cells (PBMCs) or peripheral blood lymphocytes (PBLs) are transplanted into mice *via* a caudal vein or peritoneal injection (48, 55, 56). In general, 50–80% of human $CD45^+$ cells can be detected in the blood and spleen of mice. Human $CD3^+$ T cells are usually detected in the first week after transplantation, forming an ideal model for studying mature effector T cells (57). Small numbers of B cells, myeloid cells, and other immune cells are also detected in these mice (57, 58). In this model, human memory B cells can produce antibodies after antigen stimulation, but cannot produce a primary immune response. Human immune cells can survive for several weeks after transplantation and are effective to some extent. They can be efficiently infected with HIV, HBV, EBV, HSV, HCMV, KSHV, etc., and play an important role in allogeneic immune response and viral immunity studies (59–65). In the early stage of establishing the humanized mouse model, human peripheral blood mononuclear cells or peripheral blood lymphocytes were injected into nude mice. Since nude mice are only deficient in T lymphocytes, they cannot completely accept human PBMCs or PBLs, resulting in immune rejection (2). In later work, PBLs were directly transplanted into SCID mice to construct a humanized PBLs-SCID mouse model. In this model, a multi-lineage humanized immune system can be obtained, and long-term reconstruction can be maintained. However, the main problem with this model is the fatal graft-versus-host disease (GVHD) caused by the MHC mismatch between human T cells and mouse immune cells (35, 66). GVHD symptoms usually appear 4–6 weeks after injection of human PBMCs, with a short observation window of limited use (58, 67). However, this window can be prolonged and ameliorated by using NSG (NOD/SCID IL-2Rγ $C^{-/-}$) or RG (BALB/C $Rag2^{-/-}$ IL-2R γ $C^{-/-}$) mice with deletion of the MHC-I or II genes (68). The Hu-PBLs model is the simplest and most economical humanized mouse model because of the easy availability of human PBLs. However, it also has several shortcomings, such as the low and unstable level of human lymphocyte reconstruction, lack of a normal lymphoid tissue structure and a follicular germinal structure in the spleen, EBV-associated lymphoproliferative disease after massive injection of human cells, and xenograft rejection.

Hu-HSCs mouse model

In this model, the immunodeficient mice were irradiated with a sublethal dose to destroy the hematopoietic function of the autologous bone marrow in mice; human $CD34^+$ hematopoietic stem cells (HSCs) were then transplanted into these immunodeficient mice through the vein or femoral artery (HSCs *via* intrahepatic injection as pups and *via* tail vein injection as adults) (69–71). Human HSCs in mice (such as NOG, NSG, etc.) developed into T cells, B cells, and NK cells, and formed bone marrow sources of inhibitory myeloid-derived suppressor cells (MDSCs), and other immune cells (72). The number of human $CD45^+$ T cells usually reaches 25–60% in peripheral blood at 4 weeks after implantation (72). As these immune cells develop from transplanted HSCs and are tolerant to the mouse host, GVHD usually does not occur. The stable period can be as long as 10–12 weeks (73), allowing the study of HIV (74), EBV (75), other infection models, and hematopoietic system development. HSCs can be obtained from bone marrow, umbilical cord blood, or peripheral blood after mobilization using granulocyte colony-stimulating factor (G-CSF) (76). In the early stage of developing this model, human $CD34^+$ hematopoietic stem cells were transplanted into NOD/SCID mice, which could reconstruct lymphocyte proliferation, but the resulting T cells were dysplastic. NSG, RG, or NOG (NOD/Shi-SCID IL-2Rγ $C^{-/-}$) mice now allow better implantation of human cells (77, 78).

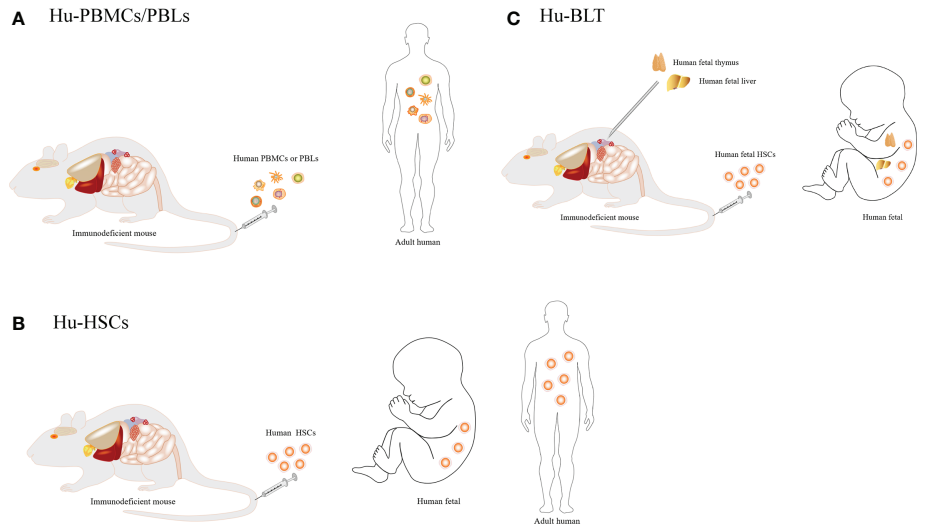

FIGURE 2
Different construction methods of humanized mice. **(A)** Injection of human peripheral blood mononuclear cells or lymphocytes. **(B)** Injection of human CD34$^+$ hematopoietic stem cells. **(C)** Co-transplantation of human fetal thymus and fetal liver into the renal capsule of mice, involving injection of hematopoietic stem cells from the fetal liver or bone marrow of the same individual into mice.

Hu-BLT mouse model

The precursor of this model was the SCID-hu mouse model, which involved surgical implantation with a human fetal thymus and liver under the renal capsule of SCID mice (79, 80). However, this model had obvious shortcomings, such as a low level of human cell reconstruction, unstable development of human T cells, and short survival time (81). Human fetal thymus was also transplanted into SCID-hu mice; and although human T cells developed in the thymus, the level of humanized development was low and unstable. However, when human HSCs were transferred into the hu-HSCs mouse model, a large number of B cells and myeloid cells were generated, but human T cells were completely lacking. In one study, the advantages of SCID-hu mice and Hu-HSCs mice were combined. Human fetal thymus and fetal liver tissue blocks were transplanted from

TABLE 1 Different construction methods and characteristics of humanized mice.

Models	Construction methods	Advantages	Disadvantages
Hu-PBMCs/PBLs	Injection of human peripheral blood mononuclear cells or lymphocytes	1 Sample is easy to obtain and the transplantation method is simple 2 Efficient and stable transplantation of T cells	1 Lack of B, NK, and other immune cells 2 Possible induction of GVHD 3 The massive injection of human cells results in EBV-associated lymphoproliferative disease
Hu-HSCs	Injection of human CD34$^+$ hematopoietic stem cells	1 Multiple line of hematopoietic cell development, including T, B, myeloid, and NK cells 2 Less GVHD	1 Limited sample sources 2 Lack of T cells (NOD/SCID mice)
Hu-BLT	Co-transplantation of human fetal thymus and fetal liver into the renal capsule of mice, involving injection of hematopoietic stem cells from the fetal liver or bone marrow of the same individual into mice	1 Better T, B, myeloid, and NK cell development 2 Can produce the human mucosal immune system and secondary lymphoid tissue and mount an adaptive immune response 3 Human T cells are educated on human MHC (HLA-restricted) in the human thymic organoid	1 Limited sample sources 2 Possible induction of GVHD

Hu-PBMCs/PBLs, humanized-peripheral blood mononuclear cells/peripheral blood lymphocytes; Hu-HSCs, humanized hematopoietic stem cells; Hu-BLT, humanized bone marrow, liver, thymus; GVHD, graft-versus-host disease.

NOD/SCID mice irradiated with a sublethal dose under the renal capsule, and $CD34^+$ HSCs were isolated from the homologous fetal liver by tail vein injection to construct Hu-BLT mice (82). The major difference between the BLT and the SCID-hu mouse model is the additional reconstruction of hematopoietic stem cells from the same fetal liver in the BLT model. The complete range of T cells, B cells, NK cells, DCs, monocytes, macrophages, and other human immune cells can be found in Hu-BLT mice *in vivo*. Furthermore, they can produce a human adaptive immune response, thereby constituting the most effective mouse model of human immune system reconstruction (83).

The Hu-BLT mouse model (NOD/SCID mice) also shows a human mucosal immune system, and secondary lymphoid tissue, and mounts adaptive human immune responses, such as the production of IgM, IgG, and other immunoglobulins. Therefore, the immune response of humanized BLT mice to implanted exogenous tissues or cells is more similar to the natural response of the human body. NOD/SCID mice were used in the early BLT model, whereas NSG, NOG, or RG mice are used in the improved model (82, 84). The use of human grafts can result in the production of more T cells, B cells, macrophages, NK cells, and DCs. In one study, the generation of humanized BLT mice by the co-transplantation of human fetal thymus and liver tissues and $CD34^+$ fetal liver cells into NOD/SCID rg^{null} mice allows for the long-term reconstitution of a functional human immune system, with human T cells, B cells, dendritic cells, and monocytes/macrophages repopulating mouse tissues (85). As T cells in human thymus tissue have a high affinity for the MHC of mice, the Hu-BLT model may exhibit a graft-versus-host reaction after 20 weeks of implantation. Humanized mice constructed in the TKO-BLT model, (Rag2, IL-2YC, and CD47 triple gene knockout) did not develop GVHD at 45 weeks, and showed a better effect than the existing BLT mouse model (86).

BLT humanized mice are now widely used for studying tumors, immunology, infectious diseases, regenerative medicine, stem cell therapy, and other research areas (87–89). BLT mice have made a lot of contributions to the study of HIV infection. Using HIV vaginal infection of humanized mice as a model of heterosexual transmission, Deruaz et al. demonstrate that blocking the ability of leukocytes to respond to chemoattractants prevented HIV from leaving the female genital tract (25). In one interesting study, intravital microscopy was used to observe changes in humanized mice after the intervention. Usmani et al. show by intravital microscopy in humanized mice that perturbation of the actin cytoskeleton *via* the lentiviral protein Nef, and not changes to chemokine receptor expression or function, is the dominant cause of dysregulated infected T cell motility in lymphoid tissue by preventing stable cellular polarization required for fast migration (90). Smith et al. have developed a method to quickly propagate established BLT mice by the secondary transfer of bone marrow cells and human thymus implants from BLT mice into NSG recipient mice. In this way, they were able to expand one primary BLT mouse into a colony of 4–5 propagated BLT mice in 6–8 weeks. These propagated BLT mice reconstituted human immune cells, including T cells, at levels comparable to those of their primary BLT donor mouse. They also faithfully inherited the human immune cell genetic traits from their donor BLT mouse, such as the HLA-A2 haplotype that is of special interest for studying HLA-A2-restricted human T cell immunotherapies. This method provides an opportunity to overcome a critical hurdle to utilizing the BLT humanized mouse model and enables its more widespread use as a valuable preclinical research tool (91). Vatakis et al. used the BLT humanized mouse as a stem cell-based gene therapy tumor model. They use genetically modified human HSCs to construct the thymus/liver implant followed by injection of transduced autologous human HSCs. This approach results in the generation of genetically modified lineages. After the intervention, the regression of the tumor was observed by positron emission tomography (PET) (92). In conclusion, the BLT mouse model has many advantages in human disease research, but its complex construction process needs to be further optimized.

The improvement of humanized immune system mouse models

The humanized mouse models can be further improved by irradiation or chemical pre-treatment, deletion of mouse autoimmune cells, injection of human cytokines, construction of viral vectors, high-pressure injection of gene expression plasmids, and construction of genetically engineered mice. The methods for improving humanized immune system mouse models are summarized in Table 2.

Irradiation or chemical pretreatment

Immunodeficient mice could be irradiated or pretreated with chemical reagents to provide more "space" for humanized construction. One study compared the efficiency of transplantation and found that human immune cells could survive better in NOD/SCID mice when 2–3 Gy pre-radiation was performed before injection of human HSCs (93). Furthermore, a single dose (35 mg/kg) of Busilvex can achieve the same transplantation effect as 3.5 Gy irradiation (66). Therefore, these pretreatments may result in increased concentrations of growth factors and chemoattractants and reserve a certain amount of space for the development of human HSCs and immune cells in immunodeficient mice.

Depletion of auto-immune cells in mice

The innate immunity of immunodeficient mice limits the regeneration of human immune cells. Mouse NK cells can be depleted by using CD122 or IL-2R antibodies (94). Another

TABLE 2 Improvement of humanized immune system mouse models.

Treatment	Results	Reference
Irradiation and chemical reagents	Busilvex (35 mg/kg) → Mouse immune system ↓	(66)
	Irradiation (2–3 Gy) → Mouse immune system ↓	(93)
Knock out of mouse autoimmune cells	Anti-asialo GM1 antibody → Mouse NK cells ↓	(29)
	CD122 antibody → Mouse NK cells ↓	(94)
	IL-2R antibody → Mouse NK cells ↓	(94)
	Cl2MDP → Mouse macrophages ↓	(94)
Injection of human cytokines	Human G-CSF → Human dendritic cells, monocytes, and neutrophils ↑	(38)
	Human IL-7 → Multi-lineage human cell differentiation	(95)
	Human SCF, IL-3, GMCSF, TPO → Human myeloid cells and lymphocytes ↑	(96)
	Human FLT3L → Human dendritic cells ↑	(97)
Construction of viral vectors	Adenoviral vectors overexpress human IL-15 → Human NK cells ↑	(98)
	Lentiviral vectors overexpress human IL-7 → Human T cells and B cells ↑	(99)
Injection of gene expression plasmids	Human IL-15 and Flt3l gene expression plasmid → Human NK cells ↑	(100)
Genetic engineering	Human M-CSF gene knock-in → Human monocytes and macrophages ↑	(41)
	Human M-CSF, IL-3, GM-CSF, TPO gene knock-in →Humanized myeloid and NK cells ↑	(101)
	Human SIRPαand TPO gene knock-in → Human hematopoietic engraftment levels ↑	(102)
	Human TPO gene knock-in → Multi-lineage human immune cells and platelets ↑	(103)
	Human SIRPα gene knock-in → Phagocytosis of macrophages ↓	(104)
	Human SCF, GM-CSF, and IL-3 gene knock-in → Human myeloid cells ↑	(105)
	Human SF, IL-3, and GM-CSF gene knock-in → Humanized myeloid cells ↑	(106)
	Human SCF and KITL gene knock-in → Humanized myeloid cells ↑	(106)
	Human M-CSF, IL-3, GM-CSF, TPO, SIRPα gene knock-in → Human myeloid and NK cells ↑	(107)
	Human M-CSF, IL-3, SIRPα, TPO, GM-CSF, and IL-6 gene knock-in →More susceptible to SARS-CoV-2 infection	(108)

"↑/↓" in humanized immune system mouse models represent an increase or decrease respectively compared with non-intervention control.

approach to deplete NK activity is the use of anti-asialo GM1 antibody injection before HSC transfer (29). Liposome-encapsulated dichloroethylene diphosphonate (Cl_2MDP) can deplete mouse macrophages and facilitate better reconstruction of the human immune system (94, 109). Therefore, when a particular cell type needs to be focused, specific elimination of antibodies may be a good choice.

Injection of human cytokines

With the development of immunodeficient mice and the improvement of reconstitution levels, the role of cytokines has attracted wide attention. In one study, a significant increase in neutrophils, monocytes, and DCs was obtained by injecting human G-CSF into NOG mice (38). Injection of human IL-7 into NOG mouse models was found to promote multi-lineage cell differentiation, achieving a reconstruction effect equivalent to that obtained with umbilical cord blood stem cells (95). In NOD/SCID mice injected with human SCF, IL-3, GMCSF, and TPO for two weeks, the development and differentiation of lymphocytes and myeloid cells were significantly improved (96). Furthermore, in NOD/SCID mice injected with human FLT3L, the number and function of DCs were significantly increased after four weeks (97). In summary, cytokines can greatly promote the construction of humanized mice. Further studies should focus on finding more suitable cytokines for the construction of humanized mice.

Construction of viral vectors

With advances in molecular biology, viral vectors have become a common tool, which can transfer the required genetic material into cells, to achieve the effect of foreign gene expression. In one study, injection of human IL-15 or overexpression of human IL-15 using adenoviral vectors was found to promote NK cell development and maturation (98). Lentiviral vectors carrying the human IL-7 gene have been used to overexpress human IL-7 in $Rag2^{-/-}$ γ $C^{-/-}$ mice; the serum level of human IL-7 was maintained at a high level during the observation period of up to six months in these mice. Il-7 overexpression significantly increased the proportion of T and B cells in peripheral blood, but had little effect on the overall immune reconstitution and did not affect the differentiation of T cell subsets (99).

Injection of gene expression plasmids

The high-pressure injection is a common technique for gene overexpression *in vivo*. A study on humanized mice generated *via* high-pressure injection of IL-15 and Flt3l expression vector found that the reconstruction of NK cells was significantly increased. Furthermore, these NK cells showed normal expression of activated receptors and inhibitory receptors, which could be induced to cause liver damage and could kill target cells *in vitro*, demonstrating that the reconstructed NK cells were functional (100).

Genetic engineering

Mouse models genetically engineered from immunodeficient mice are more stable. Mice repopulated with human hematopoietic cells are a powerful tool for the study of human T and B cells *in vivo*. However, existing humanized mouse models are unable to support the development of human innate immune cells, including myeloid cells and NK cells. In one study, Rongvaux et al. describe a mouse strain, called MI(S)TRG, in which human versions of four genes (human M-CSF, IL-3, GM-CSF, and TPO) encoding cytokines important for innate immune cell development are knocked into their respective mouse loci. The human cytokines support the development and function of monocytes/macrophages and natural killer cells derived from human fetal liver or adult $CD34^+$ progenitor cells injected into the mice. Human macrophages infiltrated a human tumor xenograft in MI(S)TRG mice in a manner resembling that observed in tumors obtained from human patients (101).

Human $CD34^+$ hematopoietic stem and progenitor cells (HSPCs) can reconstitute a human hemato-lymphoid system when transplanted into immunodeficient mice. Although fetal liver-derived and cord blood-derived $CD34^+$ cells lead to high engraftment levels, engraftment of mobilized, adult donor-derived $CD34^+$ cells has remained poor. Saito et al. generated so-called MSTRG and MISTRG humanized mice on a $Rag2^{-/-}$IL-$2rg^{-/-}$ background carrying a transgene for human SIRPα and human homologs of the cytokine macrophage colony-stimulating factor, TPO, with or without IL-3 and granulocyte-macrophage colony-stimulating factor under murine promoters. They transplanted mobilized peripheral blood (PB) $CD34^+$ cells in sublethally irradiated newborn and adult recipients. Human hematopoietic engraftment levels were significantly higher in bone marrow (BM), spleen, and PB in newborn transplanted MSTRG/MISTRG recipients as compared with non-obese diabetic/severe combined immunodeficient IL-$2rg^{-/-}$ or human SIRPα-transgenic $Rag2^{-/-}$ IL-$2rg^{-/-}$ recipients. Furthermore, newborn transplanted MSTRG/MISTRG mice supported higher engraftment levels of human phenotypically defined HSPCs in BM, T cells in the thymus, and myeloid cells in non-hematopoietic organs such as liver, lung, colon, and skin, approximating the levels in the human system. Similar results were obtained in adult recipient mice (102).

In addition, in one study, human TPO knock-in mice were constructed using $Rag2^{-/-}\gamma C^{-/-}$ mice, resulting in an increased level of humanized reconstruction, multi-lineage immune cell development and differentiation, and increased platelet counts (103). SIRPα inhibits the phagocytosis of macrophages physiologically (110) and plays an important role in the maintenance of hematopoietic stem cells, red blood cells, and platelets (101). In one study, the phagocytic activity of macrophages was significantly inhibited by knock-in human SIRPα in $Rag2^{-/-}$ γ $C^{-/-}$ mice (104). In another study, the expression of human monocytes and macrophages in bone marrow, spleen, peripheral blood, lung, liver, and the abdominal cavity was significantly increased by knock-in of human M-CSF into $Rag2^{-/-}$ γ $C^{-/-}$ mice and their migration, phagocytosis, and activation were enhanced (41). Human SCF, GM-CSF, and IL-3 have also been expressed in NSG mice using transgenic technology, to form NSG-SGM3 mice. The reconstruction level of myeloid cells, especially dendritic cells, is significantly improved in these mice (105). In addition, NSG-3GS mice were also constructed by knock-in of human SF, IL-3, and GM-CSF into NSG mice. Humanized myeloid cells were significantly increased in these mice (106). Similarly, myeloid cells were significantly increased by the knock-in of human SCF and KITL in NSG mice (106). On this basis, a study was conducted integrating human M-CSF, IL-3/GM-CSF, TPO, and SIRPα in $Rag2^{-/-}\gamma C^{-/-}$ mice which promoted the increase of human myeloid and NK cells (107).

Humanized mice are also irreplaceable in COVID-19 research. Severe COVID-19 is characterized by persistent lung inflammation, inflammatory cytokine production (111–113), viral RNA, and sustained interferon (IFN) response all of which are recapitulated and required for pathology in the SARS-CoV-2 infected MISTRG6-hACE2 humanized mouse model (based on the $Rag2^{-/-}$ $IL2rg^{-/-}$129xBalb/c background supplemented with genes for human M-CSF, IL-3, SIRPα, TPO, GM-CSF, and IL-6 knocked into their respective mouse loci) of COVID-19 with a human immune system (108). In this study, Sefik et al. show that SARS-CoV-2 infection and replication in lung-resident human macrophages is a critical driver of the disease (108). In summary, the genetic engineering of humanized mice plays a unique role in modeling and studying specific diseases.

Conclusions and future prospects

To the present day, immunodeficient mice have undergone development from Nude mice to SCID, NOD/SCID, and NOD/SCID rg^{null} mice, and their immunity level has gradually increased. To better simulate human diseases, researchers have constructed the human immune system in immunodeficient mice, and the humanized immune system mouse model provides a powerful tool for studying human diseases. However, there are still many limitations of the various humanized mouse models, and further improvements are needed to truly recapitulate the human immune system. One major hurdle is the scarcity of sources of human cells and tissues, in particular, those obtained from fetal samples carry ethical restrictions. One possible solution to this is induced pluripotent stem cell (iPSC) technology, which enables the use of patient-specific iPSCs allowing a renewable source of autologous cells without immune rejection. The second obstacle is that in humanized mice, secondary lymphoid structures are either missing or disorganized, curtailing essential humoral responses, resulting in impairments for both class switching

and affinity maturation post-immunization. To overcome this, lymphoid tissue inducer cells should be introduced without affecting IL2rg receptors. Alternatively, immunodeficient mice can be engrafted with both fetal liver and cells that support fetal liver cell growth from the same clinical donor and supplemented with cytokines, to ensure that the differentiation and maturation of HSCs can take place to improve functional immune cells including macrophages, follicular DC, and T helper cell reconstitution. The third obstacle is that an absence of essential human cytokines hinders optimal HSC engraftment, differentiation, and maturation of functional immune cells. To tackle this issue, mouse models can be hydrodynamically boosted with plasmids encoding cytokines. Despite this improvement, the binding of human cytokines may be hindered by residual mouse cytokines or may induce mouse cells to proliferate and displace the engraftment of human cells due to the cross-reactivity between human and mouse cytokines. Eliminating this problem would require the absolute depletion of murine cells or the introduction of high-affinity human-specific cytokines and growth factors. The fourth hurdle is that human cell engraftment is being negatively affected by mouse cells (red blood cells and innate immune cells) that were not completely depleted during the construction of immunodeficient mice. To improve this, additional gene knock-outs could be added to current strains of immunodeficient mice to further reduce mouse red blood cells, granulocytes, and macrophage functions. However, because of the low human erythrocyte engraftment, excessive reduction of mouse red blood cells might result in anemic mice which have short lifespans, are weak, and are not suitable for experiments. A long-term solution would be to optimize and increase the engraftment rate of human red blood cells in humanized mice so that all traces of mouse red blood cells can be removed. The fifth is the irreproducibility of mouse studies when donors are different for each "batch" of mice. This may be the most important and challenging task for the development of humanized mouse models. Indeed, there is a significant lack of evaluation criteria for donors including clinical data of patients in different disease states and the quantity and quality of their donated specific immune cells. For humanized mouse models, various systemic characteristics are still needed to comment on the development of a successful model. In summary, despite great progress and advances, there are still many limitations to the various humanized mouse models, and further improvements are needed to truly recapitulate the human immune system.

Author contributions

JC and SL wrote the manuscript. ZX and QRP designed the figures. XW, KS, and SW designed the tables. LY, FG, H-FL, and QJP revised the manuscript. All authors contributed to the article and approved the submitted version.

Funding

This study was supported by the National Natural Science Foundation of China (no.82070757, 81471530), the Department of established positions for the Zhujiang Scholar from Guangdong Medical University, and Guangdong Basic and Applied Basic Research Foundation (no.2019A1515012203).

Conflict of interest

The authors declare that the research was conducted in the absence of any commercial or financial relationships that could be construed as a potential conflict of interest.

Publisher's note

All claims expressed in this article are solely those of the authors and do not necessarily represent those of their affiliated organizations, or those of the publisher, the editors and the reviewers. Any product that may be evaluated in this article, or claim that may be made by its manufacturer, is not guaranteed or endorsed by the publisher.

References

1. Flanagan SP. 'Nude', a new hairless gene with pleiotropic effects in the mouse. *Genetical Res* (1966) 8:295–309. doi: 10.1017/s0016672300010168

2. Blunt T, Finnie NJ, Taccioli GE, Smith GC, Demengeot J, Gottlieb TM, et al. Defective DNA-dependent protein kinase activity is linked to V(D)J recombination and DNA repair defects associated with the murine scid mutation. *Cell* (1995) 80:813–23. doi: 10.1016/0092-8674(95)90360-7

3. Bosma GC, Custer RP, Bosma MJ. A severe combined immunodeficiency mutation in the mouse. *Nature* (1983) 301:527–30. doi: 10.1038/301527a0

4. Priestley A, Beamish HJ, Gell D, Amatucci AG, Muhlmann-Diaz MC, Singleton BK, et al. Molecular and biochemical characterisation of DNA-dependent protein kinase-defective rodent mutant irs-20. *Nucleic Acids Res* (1998) 26:1965–73. doi: 10.1093/nar/26.8.1965

5. Shultz LD, Schweitzer PA, Christianson SW, Gott B, Schweitzer IB, Tennent B, et al. Multiple defects in innate and adaptive immunologic function in NOD/LtSz-scid mice. *J Immunol (Baltimore Md. 1950)* (1995) 154:180–91.

6. Katano I, Ito R, Kamisako T, Eto T, Ogura T, Kawai K, et al. NOD-Rag2null IL-2Rγnull mice: an alternative to NOG mice for generation of humanized mice. *Exp Anim* (2014) 63:321–30. doi: 10.1538/expanim.63.321

7. Pantelouris EM, Hair J. Thymus dysgenesis in nude (nu nu) mice. *J embryol Exp morphol* (1970) 24:615–23. doi: 10.1242/dev.24.3.615

8. Tani N, Kuchiba K, Osada T, Watanabe Y, Umemoto T. Effect of T-cell deficiency on the formation of periapical lesions in mice: histological comparison between periapical lesion formation in BALB/c and BALB/c nu/nu mice. *J endodontics* (1995) 21:195–9. doi: 10.1016/s0099-2399(06)80565-0

9. Morikawa K, Walker SM, Nakajima M, Pathak S, Jessup JM, Fidler IJ. Influence of organ environment on the growth, selection, and metastasis of human colon carcinoma cells in nude mice. *Cancer Res* (1988) 48:6863–71.

10. Velasquez LG, Galuppo MK, Rezende ED, Brandão WN, Peron JP, Uliana SR, et al. Distinct courses of infection with leishmania (L.) amazonensis are observed in BALB/c, BALB/c nude and C57BL/6 mice. *Parasitology* (2016) 143:692–703. doi: 10.1017/s003118201600024x

11. Ganick DJ, Sarnwick RD, Shahidi NT, Manning DD. Inability of intravenously injected monocellular suspensions of human bone marrow to establish in the nude mouse. *Int Arch Allergy Appl Immunol* (1980) 62:330–3. doi: 10.1159/000232530

12. Zhang B, Duan Z, Zhao Y. Mouse models with human immunity and their application in biomedical research. *J Cell Mol Med* (2009) 13:1043–58. doi: 10.1111/j.1582-4934.2008.00347.x

13. Shultz LD, Ishikawa F, Greiner DL. Humanized mice in translational biomedical research. *Nat Rev Immunol* (2007) 7:118–30. doi: 10.1038/nri2017

14. Greiner DL, Hesselton RA, Shultz LD. SCID mouse models of human stem cell engraftment. *Stem Cells (Dayton Ohio)* (1998) 16:166–77. doi: 10.1002/stem.160166

15. Mombaerts P, Iacomini J, Johnson RS, Herrup K, Tonegawa S, Papaioannou VE. RAG-1-deficient mice have no mature b and T lymphocytes. *Cell* (1992) 68:869–77. doi: 10.1016/0092-8674(92)90030-g

16. Bosma GC, Fried M, Custer RP, Carroll A, Gibson DM, Bosma MJ. Evidence of functional lymphocytes in some (leaky) scid mice. *J Exp Med* (1988) 167:1016–33. doi: 10.1084/jem.167.3.1016

17. Shinkai Y, Rathbun G, Lam KP, Oltz EM, Stewart V, Mendelsohn M, et al. RAG-2-deficient mice lack mature lymphocytes owing to inability to initiate V(D)J rearrangement. *Cell* (1992) 68:855–67. doi: 10.1016/0092-8674(92)90029-c

18. Shultz LD, Banuelos S, Lyons B, Samuels R, Burzenski L, Gott B, et al. NOD/LtSz-Rag1nullPfpnull mice: a new model system with increased levels of human peripheral leukocyte and hematopoietic stem-cell engraftment. *Transplantation* (2003) 76:1036–42. doi: 10.1097/01.Tp.0000083041.44829.2c

19. Walsh NC, Kenney LL, Jangalwe S, Aryee KE, Greiner DL, Brehm MA, et al. Humanized mouse models of clinical disease. *Annu Rev Pathol* (2017) 12:187–215. doi: 10.1146/annurev-pathol-052016-100332

20. Chambers BJ, Ljunggren HG. Unique features of NK cell development during ontogeny revealed in studies of RAG-1-deficient mice. *Immunol Cell Biol* (2010) 88:105–6. doi: 10.1038/icb.2009.103

21. Andrews DM, Smyth MJ. A potential role for RAG-1 in NK cell development revealed by analysis of NK cells during ontogeny. *Immunol Cell Biol* (2010) 88:107–16. doi: 10.1038/icb.2009.94

22. Makino S, Kunimoto K, Muraoka Y, Mizushima Y, Katagiri K, Tochino Y. Breeding of a non-obese, diabetic strain of mice. *Jikken dobutsu. Exp Anim* (1980) 29:1–13. doi: 10.1538/expanim1978.29.1_1

23. Hesselton RM, Greiner DL, Mordes JP, Rajan TV, Sullivan JL, Shultz LD. High levels of human peripheral blood mononuclear cell engraftment and enhanced susceptibility to human immunodeficiency virus type 1 infection in NOD/LtSz-scid/scid mice. *J Infect Dis* (1995) 172:974–82. doi: 10.1093/infdis/172.4.974

24. Wahl A, Victor Garcia J. The use of BLT humanized mice to investigate the immune reconstitution of the gastrointestinal tract. *J Immunol Methods* (2014) 410:28–33. doi: 10.1016/j.jim.2014.06.009

25. Deruaz M, Murooka TT, Ji S, Gavin MA, Vrbanac VD, Lieberman J, et al. Chemoattractant-mediated leukocyte trafficking enables HIV dissemination from the genital mucosa. *JCI Insight* (2017) 2:e88533. doi: 10.1172/jci.insight.88533

26. Islas-Ohlmayer M, Padgett-Thomas A, Domiati-Saad R, Melkus MW, Cravens PD, Martin MP, et al. Experimental infection of NOD/SCID mice reconstituted with human CD34+ cells with Epstein-Barr virus. *J Virol* (2004) 78 (24):13891–900. doi: 10.1128/jvi.78.24.13891-13900.2004

27. Miyoshi H, Smith KA, Mosier DE, Verma IM, Torbett BE. Transduction of human CD34+ cells that mediate long-term engraftment of NOD/SCID mice by HIV vectors. *Sci (New York N.Y.)* (1999) 283:682–6. doi: 10.1126/science.283.5402.682

28. Takahashi T, Katano I, Ito R, Goto M, Abe H, Mizuno S, et al. Enhanced antibody responses in a novel NOG transgenic mouse with restored lymph node organogenesis. *Front Immunol* (2017) 8:2017. doi: 10.3389/fimmu.2017.02017

29. Ito M, Hiramatsu H, Kobayashi K, Suzue K, Kawahata M, Hioki K, et al. NOD/SCID/gamma(c)(null) mouse: an excellent recipient mouse model for engraftment of human cells. *Blood* (2002) 100:3175–82. doi: 10.1182/blood-2001-12-0207

30. Shultz LD, Lyons BL, Burzenski LM, Gott B, Chen X, Chaleff S, et al. Human lymphoid and myeloid cell development in NOD/LtSz-scid IL2R gamma null mice engrafted with mobilized human hemopoietic stem cells. *J Immunol (Baltimore Md. 1950)* (2005) 174:6477–89. doi: 10.4049/jimmunol.174.10.6477

31. Pearson T, Shultz LD, Miller D, King M, Laning J, Fodor W, et al. Non-obese diabetic-recombination activating gene-1 (NOD-Rag1 null) interleukin (IL)-2 receptor common gamma chain (IL2r gamma null) null mice: a radioresistant model for human lymphohaematopoietic engraftment. *Clin Exp Immunol* (2008) 154:270–84. doi: 10.1111/j.1365-2249.2008.03753.x

32. Brooks DG, Kitchen SG, Kitchen CM, Scripture-Adams DD, Zack JA. Generation of HIV latency during thymopoiesis. *Nat Med* (2001) 7:459–64. doi: 10.1038/86531

33. Brehm MA, Cuthbert A, Yang C, Miller DM, DiIorio P, Laning J, et al. Parameters for establishing humanized mouse models to study human immunity: analysis of human hematopoietic stem cell engraftment in three immunodeficient strains of mice bearing the IL2rgamma(null) mutation. *Clin Immunol (Orlando Fla.)* (2010) 135:84–98. doi: 10.1016/j.clim.2009.12.008

34. Machida K, Suemizu H, Kawai K, Ishikawa T, Sawada R, Ohnishi Y, et al. Higher susceptibility of NOG mice to xenotransplanted tumors. *J toxicol Sci* (2009) 34:123–7. doi: 10.2131/jts.34.123

35. King MA, Covassin L, Brehm MA, Racki W, Pearson T, Leif J, et al. Human peripheral blood leucocyte non-obese diabetic-severe combined immunodeficiency interleukin-2 receptor gamma chain gene mouse model of xenogeneic graft-versus-host-like disease and the role of host major histocompatibility complex. *Clin Exp Immunol* (2009) 157:104–18. doi: 10.1111/j.1365-2249.2009.03933.x

36. Wunderlich M, Chou FS, Link KA, Mizukawa B, Perry RL, Carroll M, et al. AML xenograft efficiency is significantly improved in NOD/SCID-IL2RG mice constitutively expressing human SCF, GM-CSF and IL-3. *Leukemia* (2010) 24:1785–8. doi: 10.1038/leu.2010.158

37. Zhang L, Meissner E, Chen J, Su L. Current humanized mouse models for studying human immunology and HIV-1 immuno-pathogenesis. *Sci China. Life Sci* (2010) 53:195–203. doi: 10.1007/s11427-010-0059-7

38. Tanaka S, Saito Y, Kunisawa J, Kurashima Y, Wake T, Suzuki N, et al. Development of mature and functional human myeloid subsets in hematopoietic stem cell-engrafted NOD/SCID/IL2rγKO mice. *J Immunol (Baltimore Md. 1950)* (2012) 188:6145–55. doi: 10.4049/jimmunol.1103660

39. Oshima K, Ruhul Amin AR, Suzuki A, Hamaguchi M, Matsuda S. SHPS-1, a multifunctional transmembrane glycoprotein. *FEBS Lett* (2002) 519:1–7. doi: 10.1016/s0014-5793(02)02703-5

40. Barclay AN, Brown MH. The SIRP family of receptors and immune regulation. *Nat Rev Immunol* (2006) 6:457–64. doi: 10.1038/nri1859

41. Matozaki T, Murata Y, Okazawa H, Ohnishi H. Functions and molecular mechanisms of the CD47-SIRPalpha signalling pathway. *Trends Cell Biol* (2009) 19:72–80. doi: 10.1016/j.tcb.2008.12.001

42. Tsai RK, Discher DE. Inhibition of "self" engulfment through deactivation of myosin-II at the phagocytic synapse between human cells. *J Cell Biol* (2008) 180:989–1003. doi: 10.1083/jcb.200708043

43. Legrand N, Huntington ND, Nagasawa M, Bakker AQ, Schotte R, Strick-Marchand H, et al. Functional CD47/signal regulatory protein alpha (SIRP(alpha)) interaction is required for optimal human T- and natural killer- (NK) cell homeostasis *in vivo*. *Proc Natl Acad Sci United States America* (2011) 108:13224–9. doi: 10.1073/pnas.1101398108

44. Takenaka K, Prasolava TK, Wang JC, Mortin-Toth SM, Khalouei S, Gan OI, et al. Polymorphism in sirpa modulates engraftment of human hematopoietic stem cells. *Nat Immunol* (2007) 8(12):1313–23. doi: 10.1038/ni1527

45. Yamauchi T, Takenaka K, Urata S, Shima T, Kikushige Y, Tokuyama T, et al. Polymorphic sirpa is the genetic determinant for NOD-based mouse lines to achieve efficient human cell engraftment. *Blood* (2013) 121:1316–25. doi: 10.1182/blood-2012-06-440354

46. Li Y, Masse-Ranson G, Garcia Z, Bruel T, Kök A, Strick-Marchand H, et al. A human immune system mouse model with robust lymph node development. *Nat Methods* (2018) 15:623–30. doi: 10.1038/s41592-018-0071-6

47. Andrade D, Redecha PB, Vukelic M, Qing X, Perino G, Salmon JE, et al. Engraftment of peripheral blood mononuclear cells from systemic lupus erythematosus and antiphospholipid syndrome patient donors into BALB-RAG-2-/- IL-2Rγ-/- mice: a promising model for studying human disease. *Arthritis rheumatism* (2011) 63:2764–73. doi: 10.1002/art.30424

48. Chen J, Liao S, Zhou H, Yang L, Guo F, Chen S, et al. Humanized mouse models of systemic lupus erythematosus: Opportunities and challenges. *Front Immunol* (2021) 12:816956. doi: 10.3389/fimmu.2021.816956

49. Akkina R. Humanized mice for studying human immune responses and generating human monoclonal antibodies. *Microbiol Spectr* (2014) 2(2):0003–2012. doi: 10.1128/microbiolspec.AID-0003-2012

50. Watanabe Y, Takahashi T, Okajima A, Shiokawa M, Ishii N, Katano I, et al. The analysis of the functions of human b and T cells in humanized NOD/shi-scid/gammac(null) (NOG) mice (hu-HSC NOG mice). *Int Immunol* (2009) 21:843–58. doi: 10.1093/intimm/dxp050

51. Takahama Y, Nitta T, Mat Ripen A, Nitta S, Murata S, Tanaka K. Role of thymic cortex-specific self-peptides in positive selection of T cells. *Semin Immunol* (2010) 22:287–93. doi: 10.1016/j.smim.2010.04.012

52. Fairfax KA, Kallies A, Nutt SL, Tarlinton DM. Plasma cell development: from b-cell subsets to long-term survival niches. *Semin Immunol* (2008) 20:49–58. doi: 10.1016/j.smim.2007.12.002

53. Danner R, Chaudhari SN, Rosenberger J, Surls J, Richie TL, Brumeanu TD, et al. Expression of HLA class II molecules in humanized NOD.Rag1KO.IL2RgcKO mice is critical for development and function of human T and b cells. *PloS One* (2011) 6:e19826. doi: 10.1371/journal.pone.0019826

54. Ito K, Bian HJ, Molina M, Han J, Magram J, Saar E, et al. HLA-DR4-IE chimeric class II transgenic, murine class II-deficient mice are susceptible to experimental allergic encephalomyelitis. *J Exp Med* (1996) 183:2635–44. doi: 10.1084/jem.183.6.2635

55. Yue X, Petersen F, Shu Y, Kasper B, Magatsin JDT, Ahmadi M, et al. Transfer of PBMC from SSc patients induces autoantibodies and systemic inflammation in Rag2-/-/IL2rg-/- mice. *Front Immunol* (2021) 12:677970. doi: 10.3389/fimmu.2021.677970

56. Ehx G, Somja J, Warnatz HJ, Ritacco C, Hannon M, Delens L, et al. Xenogeneic graft-Versus-Host disease in humanized NSG and NSG-HLA-A2/HHD mice. *Front Immunol* (2018) 9:1943. doi: 10.3389/fimmu.2018.01943

57. Lin S, Huang G, Cheng L, Li Z, Xiao Y, Deng Q, et al. Establishment of peripheral blood mononuclear cell-derived humanized lung cancer mouse models for studying efficacy of PD-L1/PD-1 targeted immunotherapy. *mAbs* (2018) 10:1301–11. doi: 10.1080/19420862.2018.1518948

58. Koo GC, Hasan A, O'Reilly RJ. Use of humanized severe combined immunodeficient mice for human vaccine development. *Expert Rev Vaccines* (2009) 8:113–20. doi: 10.1586/14760584.8.1.113

59. Racki WJ, Covassin L, Brehm M, Pino S, Ignotz R, Dunn R, et al. NOD-scid IL2rgamma(null) mouse model of human skin transplantation and allograft rejection. *Transplantation* (2010) 89:527–36. doi: 10.1097/TP.0b013e3181c90242

60. Kumar P, Ban HS, Kim SS, Wu H, Pearson T, Greiner DL, et al. T Cell-specific siRNA delivery suppresses HIV-1 infection in humanized mice. *Cell* (2008) 134:577–86. doi: 10.1016/j.cell.2008.06.034

61. Kremsdorf D, Strick-Marchand H. Modeling hepatitis virus infections and treatment strategies in humanized mice. *Curr Opin Virol* (2017) 25:119–25. doi: 10.1016/j.coviro.2017.07.029

62. Cui X, Snapper CM. Epstein Barr Virus: Development of vaccines and immune cell therapy for EBV-associated diseases. *Front Immunol* (2021) 12:734471. doi: 10.3389/fimmu.2021.734471

63. Jaggi U, Wang S, Tormanen K, Matundan H, Ljubimov AV, Ghiasi H. Role of herpes simplex virus type 1 (HSV-1) glycoprotein K (gK) pathogenic CD8(+) T cells in exacerbation of eye disease. *Front Immunol* (2018) 9:2895. doi: 10.3389/fimmu.2018.02895

64. Crawford LB, Streblow DN, Hakki M, Nelson JA, Caposio P. Humanized mouse models of human cytomegalovirus infection. *Curr Opin Virol* (2015) 13:86–92. doi: 10.1016/j.coviro.2015.06.006

65. Fujiwara S. Animal models of human gammaherpesvirus infections. *Adv Exp Med Biol* (2018) 1045:413–36. doi: 10.1007/978-981-10-7230-7_19

66. Nervi B, Rettig MP, Ritchey JK, Wang HL, Bauer G, Walker J, et al. Factors affecting human T cell engraftment, trafficking, and associated xenogeneic graft-vs-host disease in NOD/SCID beta2mnull mice. *Exp Hematol* (2007) 35:1823–38. doi: 10.1016/j.exphem.2007.06.007

67. De La Rochere P, Guil-Luna S, Decaudin D, Azar G, Sidhu SS, Piaggio E. Humanized mice for the study of immuno-oncology. *Trends Immunol* (2018) 39:748–63. doi: 10.1016/j.it.2018.07.001

68. Brehm MA, Kenney LL, Wiles MV, Low BE, Tisch RM, Burzenski L, et al. Lack of acute xenogeneic graft- versus-host disease, but retention of T-cell function following engraftment of human peripheral blood mononuclear cells in NSG mice deficient in MHC class I and II expression. *FASEB J* (2019) 33:3137–51. doi: 10.1096/fj.201800636R

69. Billerbeck E, Mommersteeg MC, Shlomai A, Xiao JW, Andrus L, Bhatta A, et al. Humanized mice efficiently engrafted with fetal hepatoblasts and syngeneic immune cells develop human monocytes and NK cells. *J Hepatol* (2016) 65:334–43. doi: 10.1016/j.jhep.2016.04.022

70. Cao B, Zhang Z, Grassinger J, Williams B, Heazlewood CK, Churches QI, et al. Therapeutic targeting and rapid mobilization of endosteal HSC using a small molecule integrin antagonist. *Nat Commun* (2016) 7:11007. doi: 10.1038/ncomms11007

71. Abarrategi A, Foster K, Hamilton A, Mian SA, Passaro D, Gribben J, et al. Versatile humanized niche model enables study of normal and malignant human hematopoiesis. *J Clin Invest* (2017) 127:543–8. doi: 10.1172/jci89364

72. Rongvaux A, Takizawa H, Strowig T, Willinger T, Eynon EE, Flavell RA, et al. Human hemato-lymphoid system mice: current use and future potential for medicine. *Annu Rev Immunol* (2013) 31:635–74. doi: 10.1146/annurev-immunol-032712-095921

73. Kim SS, Kumar P, Ye C, Shankar P. Humanized mice for studying human leukocyte integrins *in vivo*. *Methods Mol Biol (Clifton N.J.)* (2012) 757:509–21. doi: 10.1007/978-1-61779-166-6_30

74. Su H, Cheng Y, Sravanam S, Mathews S, Gorantla S, Poluektova LY, et al. Immune activations and viral tissue compartmentalization during progressive HIV-1 infection of humanized mice. *Front Immunol* (2019) 10:340. doi: 10.3389/fimmu.2019.00340

75. Worni-Schudel IM, Clark AG, Chien T, Hwang KK, Chen BJ, Foster MH. Recovery of a human natural antibody against the noncollagenous-1 domain of type IV collagen using humanized models. *J Trans Med* (2015) 13:185. doi: 10.1186/s12967-015-0539-4

76. Lepus CM, Gibson TF, Gerber SA, Kawikova I, Szczepanik M, Hossain J, et al. Comparison of human fetal liver, umbilical cord blood, and adult blood hematopoietic stem cell engraftment in NOD-scid/gammac-/-, balb/c-Rag1-/-gammac-/- and C.B-17-scid/bg immunodeficient mice. *Hum Immunol* (2009) 70:790–802. doi: 10.1016/j.humimm.2009.06.005

77. Berges BK, Rowan MR. The utility of the new generation of humanized mice to study HIV-1 infection: transmission, prevention, pathogenesis, and treatment. *Retrovirology* (2011) 8:65. doi: 10.1186/1742-4690-8-65

78. Shultz LD, Brehm MA, Bavari S, Greiner DL. Humanized mice as a preclinical tool for infectious disease and biomedical research. *Ann New York Acad Sci* (2011) 1245:50–4. doi: 10.1111/j.1749-6632.2011.06310.x

79. McCune JM. Development and applications of the SCID-hu mouse model. *Semin Immunol* (1996) 8:187–96. doi: 10.1006/smim.1996.0024

80. McCune JM, Namikawa R, Kaneshima H, Shultz LD, Lieberman M, Weissman IL. The SCID-hu mouse: murine model for the analysis of human hematolymphoid differentiation and function. *Sci (New York N.Y.)* (1988) 241:1632–9. doi: 10.1126/science.241.4873.1632

81. Jamieson BD, Zack JA. Murine models for HIV disease. *AIDS (London England)* (1999) 13:S5–11.

82. Lan P, Tonomura N, Shimizu A, Wang S, Yang YG. Reconstitution of a functional human immune system in immunodeficient mice through combined human fetal thymus/liver and CD34+ cell transplantation. *Blood* (2006) 108:487–92. doi: 10.1182/blood-2005-11-4388

83. Wege AK, Melkus MW, Denton PW, Estes JD, Garcia JV. Functional and phenotypic characterization of the humanized BLT mouse model. *Curr topics Microbiol Immunol* (2008) 324:149–65. doi: 10.1007/978-3-540-75647-7_10

84. Stoddart CA, Maidji E, Galkina SA, Kosikova G, Rivera JM, Moreno ME, et al. Superior human leukocyte reconstitution and susceptibility to vaginal HIV transmission in humanized NOD-scid IL-2Rγ(-/-) (NSG) BLT mice. *Virology* (2011) 417:154–60. doi: 10.1016/j.virol.2011.05.013

85. Brainard DM, Seung E, Frahm N, Cariappa A, Bailey CC, Hart WK, et al. Induction of robust cellular and humoral virus-specific adaptive immune responses in human immunodeficiency virus-infected humanized BLT mice. *J Virol* (2009) 83:7305–21. doi: 10.1128/jvi.02207-08

86. Lavender KJ, Pace C, Sutter K, Messer RJ, Pouncey DL, Cummins NW, et al. An advanced BLT-humanized mouse model for extended HIV-1 cure studies. *AIDS (London England)* (2018) 32:1–10. doi: 10.1097/qad.0000000000001674

87. Bonte S, Snauwaert S, Vanhee S, Dolens AC, Taghon T, Vandekerckhove B, et al. Humanized mice to study human T cell development. *Methods Mol Biol (Clifton N.J.)* (2016) 1323:253–72. doi: 10.1007/978-1-4939-2809-5_21

88. Bournazos S, DiLillo DJ, Ravetch JV. Humanized mice to study FcγR function. *Curr topics Microbiol Immunol* (2014) 382:237–48. doi: 10.1007/978-3-319-07911-0_11

89. Brehm MA, Jouvet N, Greiner DL, Shultz LD. Humanized mice for the study of infectious diseases. *Curr Opin Immunol* (2013) 25:428–35. doi: 10.1016/j.coi.2013.05.012

90. Usmani SM, Murooka TT, Deruaz M, Koh WH, Sharaf RR, Di Pilato M, et al. HIV-1 balances the fitness costs and benefits of disrupting the host cell actin cytoskeleton early after mucosal transmission. *Cell Host Microbe* (2019) 25:73–86.e75. doi: 10.1016/j.chom.2018.12.008

91. Smith DJ, Lin LJ, Moon H, Pham AT, Wang X, Liu S, et al. Propagating humanized BLT mice for the study of human immunology and immunotherapy. *Stem Cells Dev* (2016) 25:1863–73. doi: 10.1089/scd.2016.0193

92. Vatakis DN, Bristol GC, Kim SG, Levin B, Liu W, Radu CG, et al. Using the BLT humanized mouse as a stem cell based gene therapy tumor model. *J visualized experiments* (2012) 18(70):e4181. doi: 10.3791/4181

93. Tournoy KG, Depraetere S, Pauwels RA, Leroux-Roels GG. Mouse strain and conditioning regimen determine survival and function of human leucocytes in immunodeficient mice. *Clin Exp Immunol* (2000) 119:231–9. doi: 10.1046/j.1365-2249.2000.01099.x

94. Santini SM, Rizza P, Logozzi MA, Sestili P, Gherardi G, Lande R, et al. The SCID mouse reaction to human peripheral blood mononuclear leukocyte engraftment. neutrophil recruitment induced expression of a wide spectrum of murine cytokines and mouse leukopoiesis, including thymic differentiation. *Transplantation* (1995) 60:1306–14. doi: 10.1097/00007890-199512000-00020

95. André MC, Erbacher A, Gille C, Schmauke V, Goecke B, Hohberger A, et al. Long-term human CD34+ stem cell-engrafted nonobese diabetic/SCID/IL-2R gamma(null) mice show impaired CD8+ T cell maintenance and a functional arrest of immature NK cells. *J Immunol (Baltimore Md. 1950)* (2010) 185:2710–20. doi: 10.4049/jimmunol.1000583

96. Cashman JD, Eaves CJ. Human growth factor-enhanced regeneration of transplantable human hematopoietic stem cells in nonobese diabetic/severe combined immunodeficient mice. *Blood* (1999) 93:481–7. doi: 10.1182/blood.V93.2.481

97. Ding Y, Wilkinson A, Idris A, Fancke B, O'Keeffe M, Khalil D, et al. FLT3-ligand treatment of humanized mice results in the generation of large numbers of CD141+ and CD1c+ dendritic cells *in vivo*. *J Immunol (Baltimore Md. 1950)* (2014) 192:1982–9. doi: 10.4049/jimmunol.1302391

98. Pek EA, Chan T, Reid S, Ashkar AA. Characterization and IL-15 dependence of NK cells in humanized mice. *Immunobiology* (2011) 216:218–24. doi: 10.1016/j.imbio.2010.04.008

99. O'Connell RM, Balazs AB, Rao DS, Kivork C, Yang L, Baltimore D. Lentiviral vector delivery of human interleukin-7 (hIL-7) to human immune system (HIS) mice expands T lymphocyte populations. *PloS One* (2010) 5: e12009. doi: 10.1371/journal.pone.0012009

100. Chen Q, Khoury M, Chen J. Expression of human cytokines dramatically improves reconstitution of specific human-blood lineage cells in humanized mice. *Proc Natl Acad Sci United States America* (2009) 106:21783–8. doi: 10.1073/pnas.0912274106

101. Rongvaux A, Willinger T, Martinek J, Strowig T, Gearty SV, Teichmann LL, et al. Development and function of human innate immune cells in a humanized mouse model. *Nat Biotechnol* (2014) 32:364–72. doi: 10.1038/nbt.2858

102. Saito Y, Ellegast JM, Rafiei A, Song Y, Kull D, Heikenwalder M, et al. Peripheral blood CD34(+) cells efficiently engraft human cytokine knock-in mice. *Blood* (2016) 128:1829–33. doi: 10.1182/blood-2015-10-676452

103. Ito R, Takahashi T, Katano I, Kawai K, Kamisako T, Ogura T, et al. Establishment of a human allergy model using human IL-3/GM-CSF-transgenic NOG mice. *J Immunol (Baltimore Md. 1950)* (2013) 191:2890–9. doi: 10.4049/jimmunol.1203543

104. Rongvaux A, Willinger T, Takizawa H, Rathinam C, Auerbach W, Murphy AJ, et al. Human thrombopoietin knock-in mice efficiently support human hematopoiesis *in vivo*. *Proc Natl Acad Sci United States America* (2011) 108:2378–83. doi: 10.1073/pnas.1019524108

105. Billerbeck E, Barry WT, Mu K, Dorner M, Rice CM, Ploss A. Development of human CD4+FoxP3+ regulatory T cells in human stem cell factor-, granulocyte-macrophage colony-stimulating factor-, and interleukin-3-expressing NOD-SCID IL2Rγ(null) humanized mice. *Blood* (2011) 117:3076–86. doi: 10.1182/blood-2010-08-301507

106. Miller PH, Cheung AM, Beer PA, Knapp DJ, Dhillon K, Rabu G, et al. Enhanced normal short-term human myelopoiesis in mice engineered to express human-specific myeloid growth factors. *Blood* (2013) 121:e1–4. doi: 10.1182/blood-2012-09-456566

107. Sherr CJ, Rettenmier CW, Roussel MF. Macrophage colony-stimulating factor, CSF-1, and its proto-oncogene-encoded receptor. *Cold Spring Harbor Symp quantitative Biol* (1988) 53:521–30. doi: 10.1101/sqb.1988.053.01.060

108. Sefik E, Qu R, Junqueira C, Kaffe E, Mirza H, Zhao J, et al. Inflammasome activation in infected macrophages drives COVID-19 pathology. *Nature* (2022) 606:585–93. doi: 10.1038/s41586-022-04802-1

109. Giuliani AL, Wiener E, Lee MJ, Brown IN, Berti G, Wickramasinghe SN. Changes in murine bone marrow macrophages and erythroid burst-forming cells following the intravenous injection of liposome-encapsulated dichloromethylene diphosphonate (Cl2MDP). *Eur J haematol* (2001) 66:221–9. doi: 10.1034/j.1600-0609.2001.066004221.x

110. Barclay AN, Van den Berg TK. The interaction between signal regulatory protein alpha (SIRPα) and CD47: structure, function, and therapeutic target. *Annu Rev Immunol* (2014) 32:25–50. doi: 10.1146/annurev-immunol-032713-120142

111. Vandenberg O, Martiny D, Rochas O, van Belkum A, Kozlakidis Z. Considerations for diagnostic COVID-19 tests. *Nat Rev Microbiol* (2021) 19:171–83. doi: 10.1038/s41579-020-00461-z

112. Chen Y, Klein SL, Garibaldi BT, Li H, Wu C, Osevala NM, et al. Aging in COVID-19: Vulnerability, immunity and intervention. *Ageing Res Rev* (2021) 65:101205. doi: 10.1016/j.arr.2020.101205

113. Taleghani N, Taghipour F. Diagnosis of COVID-19 for controlling the pandemic: A review of the state-of-the-art. *Biosensors bioelectronics* (2021) 174:112830. doi: 10.1016/j.bios.2020.112830

frontiers | Frontiers in Immunology

TYPE Review
PUBLISHED 27 February 2023
DOI 10.3389/fimmu.2023.1126969

Check for updates

OPEN ACCESS

EDITED BY
An Coosemans,
KU Leuven, Belgium

REVIEWED BY
Tibor Bakacs,
Alfred Renyi Institute of Mathematics, Hungary
Jinxin Miao,
Henan University of Traditional Chinese Medicine, China

*CORRESPONDENCE
Yaohe Wang
yaohe.wang@qmul.ac.uk
Pengju Wang
wangpengju@zzu.edu.cn

SPECIALTY SECTION
This article was submitted to Cancer Immunity and Immunotherapy, a section of the journal Frontiers in Immunology

RECEIVED 18 December 2022
ACCEPTED 09 February 2023
PUBLISHED 27 February 2023

CITATION
Jia Y, Wang Y, Dunmall LSC, Lemoine NR, Wang P and Wang Y (2023) Syrian hamster as an ideal animal model for evaluation of cancer immunotherapy.
Front. Immunol. 14:1126969.
doi: 10.3389/fimmu.2023.1126969

COPYRIGHT
© 2023 Jia, Wang, Dunmall, Lemoine, Wang and Wang. This is an open-access article distributed under the terms of the Creative Commons Attribution License (CC BY). The use, distribution or reproduction in other forums is permitted, provided the original author(s) and the copyright owner(s) are credited and that the original publication in this journal is cited, in accordance with accepted academic practice. No use, distribution or reproduction is permitted which does not comply with these terms.

Syrian hamster as an ideal animal model for evaluation of cancer immunotherapy

Yangyang Jia[1], Yanru Wang[1], Louisa S Chard Dunmall[2], Nicholas R. Lemoine[1,2], Pengju Wang[1]* and Yaohe Wang[1,2]*

[1]State Key Laboratory of Esophageal Cancer Prevention & Treatment, School of Basic Medical Sciences, Academy of Medical Sciences, Zhengzhou University, Zhengzhou, China, [2]Centre for Cancer Biomarkers & Biotherapeutics, Barts Cancer Institute, Queen Mary University of London, London, United Kingdom

Cancer immunotherapy (CIT) has emerged as an exciting new pillar of cancer treatment. Although benefits have been achieved in individual patients, the overall response rate is still not satisfactory. To address this, an ideal preclinical animal model for evaluating CIT is urgently needed. Syrian hamsters present similar features to humans with regard to their anatomy, physiology, and pathology. Notably, the histological features and pathological progression of tumors and the complexity of the tumor microenvironment are equivalent to the human scenario. This article reviews the current tumor models in Syrian hamster and the latest progress in their application to development of tumor treatments including immune checkpoint inhibitors, cytokines, adoptive cell therapy, cancer vaccines, and oncolytic viruses. This progress strongly advocates Syrian hamster as an ideal animal model for development and assessment of CIT for human cancer treatments. Additionally, the challenges of the Syrian hamster as an animal model for CIT are also discussed.

KEYWORDS

Syrian hamster, tumor model, cancer immunotherapy, immune checkpoint inhibitor, cytokine, adoptive cell therapy, cancer vaccine, oncolytic virus

1 Introduction

With increasing incidence and mortality, cancer is a major public health problem worldwide and is a major obstacle to increasing life expectancy (1, 2). Cancer immunotherapy (CIT) works by stimulating or re-invigorating the body's immune system to directly attack cancer cells (3). In recent years, the number of approved CIT drugs has increased dramatically and it has become a mainstay cancer therapy alongside traditional therapeutic options. Despite the widespread application of CIT in human cancers, only a minority of patients benefit from these therapies (4). Therefore, there is an urgent need for an ideal animal model that can accurately reflect the complexity of the immunosuppressive human tumor microenvironment to predict the immune response and

efficacy of immunotherapy, promoting the development of CIT and reducing the failure rate of clinical trials.

Syrian hamster (Mesocricetus auratus) belongs to the Cricitinae family of hamsters and is commonly known as the golden hamster. These animals originated in Syria and are naturally found in the arid, temperate southeast Europe and Asia Minor (5). Syrian hamsters currently used as laboratory animals originated from a litter captured in 1930 (5, 6). There is mounting evidence that the Syrian hamster is highly similar to humans in anatomy, physiology, and pathology (7–9). Their similarity is especially valuable in terms of the similarity of pathophysiology, *i.e* the occurrence, development, symptoms, pathology, and outcomes of disease (10). Syrian hamsters have a short reproductive cycle, are docile, and are easy to raise and handle (8, 11).

It has been reported that the human granulocyte-macrophage colony-stimulating factor (GM-CSF) is immunologically functional in hamsters (12) and recently we reported that human interleukin (IL)-12 was biologically active towards the immune cells of Syrian hamsters (13). The human cytokines IL-21 and IL-2 have also demonstrated immunological activity in hamsters (14, 15). The Syrian hamster macrophage migration inhibitory factor (MIF) is structurally and functionally similar to humans and significantly enhanced tumor growth and promoted tumor-associated angiogenesis in Syrian hamster tumor models (16). An animal model with an intact and functional immune system is indispensable for the development and characterization of cancer immunotherapy efficacy and potential toxicities, therefore, the Syrian hamster is the preferred animal model in many fields of medical research. In this review, we discuss the current landscape of the Syrian hamster tumor models, the promises and challenges of the Syrian hamster as a model for evaluating cancer immunotherapy.

2 Syrian hamster tumor models

2.1 Syngeneic tumor models

Syngeneic tumor models are the most used preclinical models for evaluating cancer immunotherapy and refer to the transplantation of *in vitro* cultured tumor cell lines into immunocompetent animals (Figure 1A), typically including subcutaneous, intraperitoneal disseminated and orthotopic tumor models. In recent years, Syrian hamsters have been widely used in preclinical research as tumor models. The Syrian hamster model can better simulate the development of human cancer and reproduce the genomic heterogeneity of human cancer and the complexity of its microenvironment (8, 17).

It has been reported that the hamster peritoneal omentum-associated lymphoid tissue is anatomically equivalent to the human milky spots, which are mainly composed of macrophages and are closely related to the spread of cancer cells (18, 19) The Syrian hamster cheek pouch lacks an intact lymphatic drainage pathway and is considered immune privileged, which supports the long-term survival of transplanted foreign tissue without immunological rejection (5). It was previously reported that human myofibrosarcoma (MFS-l) and melanoticmelanoma (ME-l) transplanted into the cheek pouch of Syrian hamsters were fully sensitive to colchicine stimulation throughout growth and that this sensitivity persisted after multiple

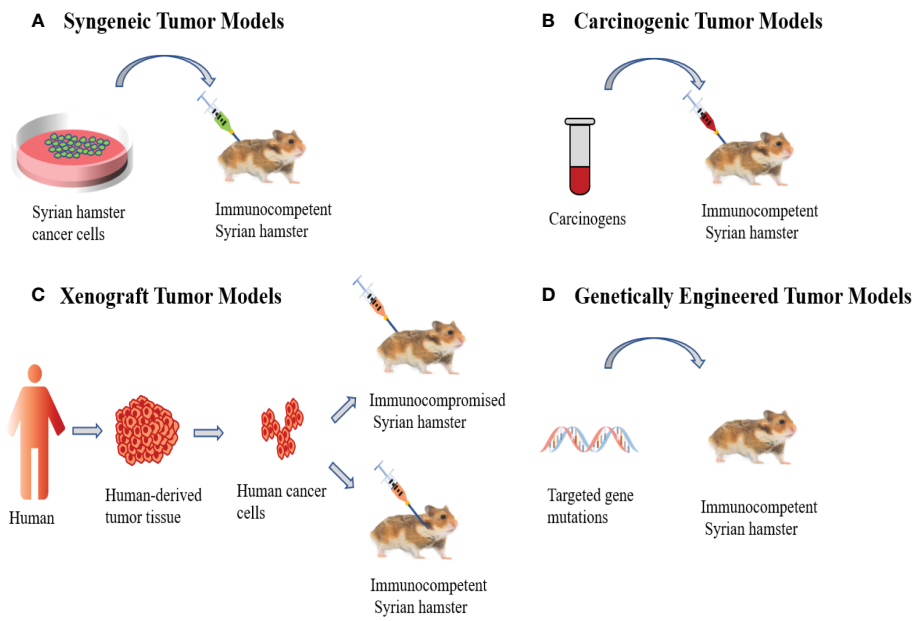

FIGURE 1
Syrian Hamster Tumor Models. **(A)** Syngeneic tumor models involve the transplantation of *in vitro* cultured Syrian hamster cancer cells into immunocompetent Syrian hamsters. **(B)** Carcinogenic tumor models are induced by carcinogens, which allows tumors to undergo *de novo* formation. **(C)** Human xenograft tumor models utilize human cancer cells to inject into immunocompromised Syrian hamsters or the cheek pouches of immunocompetent Syrian hamsters. **(D)** Genetically engineered models are the application of genetic engineering techniques to modify hamster genes to induce cancer development.

consecutive transplants, thus providing support for the hamster-human tumor system as a tool to evaluate human antitumor agents (20). The Syrian hamster pancreatic cancer cell line HaP-T1 has been established and exhibits tumorigenicity on syngeneic Syrian hamsters, and histologically showed obvious epithelial characteristics similar to human pancreatic cancer. Further studies have shown that hamster N-terminal Sonic hedgehog (SHH) is 99% identical to human, while N-SHH promotes desmoplasia in human pancreatic cancer (21, 22). Researchers have also established the Syrian hamster pancreatic carcinoma cell line SHPC6, which when injected into peritoneal cavity, forms disseminated tumor nodules and nodules attached to the pancreas, faithfully simulating patients with advanced pancreatic cancer metastasis (23). Additionally, the syngeneic Syrian hamster glioma orthotopic model showed hypercellularity and necrotic areas, consistent with the characteristics of human glioma (24). At present, the Syrian hamster syngeneic tumor models used for research include pancreatic cancer (25–27), oral cancer (28), gallbladder cancer (29), glioma (24), kidney cancer (23, 30), liver cancer (23), lung cancer (23) and breast cancer (31). However, the challenge with all syngeneic tumor models is that they cannot reflect the multi-stage process of carcinogenesis due to the direct engraftment of malignant cells, therefore, these models are not suitable for the evaluation of the application of anti-tumor immunotherapy in the early stages of tumorigenesis (32).

2.2 Carcinogenic tumor models

Oncogenic tumor models are primarily caused by carcinogens (Figure 1B). The instability of the genome allows tumors to undergo *de novo* formation in the microenvironment. This produces great genomic complexity and accurately reflects the occurrence and development of tumors in humans (33). It has been reported that N-nitroso-bis(2-oxopropyl) amine (BOP) can induce pancreatic ductal adenocarcinoma in Syrian hamsters and its histology, morphology, biology, pathology, and genetics are similar to humans. For example, its development from ductal cells, local invasion, distant metastasis, cachexia, and point mutations in the *K-ras* gene (34–37). In addition, studies have shown that the Syrian hamster cholangiocarcinoma model induced by the combination of Clonorchis Sinensis infection and dimethyl nitrosamine resulted in chronic inflammation, bile duct injury and atypical bile duct hyperplasia, with progression to cholangiocarcinoma, histopathologically similar to human liver fluke infection-associated cholangiocarcinoma (38–40). The chemically induced Syrian hamster cheek pouch carcinogenesis model can accurately reflect a series of common processes seen in human oral precancerous lesions and carcinogenesis, including mutations and expression changes of oncogenes and tumor suppressor genes. Histologically, the cells showed varying degrees of atypia and differentiation, similar to those seen in human squamous cell carcinoma (41–46). Researchers used 9,10-dimethyl-1,2-benzthracene (DMBA) to induce the formation of cheek pocket squamous cell carcinoma in Syrian hamsters and established the Syrian hamster cheek pocket squamous cell carcinoma cell line. Subsequently, the cell lines were transplanted into the subcutaneous and cheek pouch of hamsters and treated with the oncolytic adenovirus HAdV5 exhibiting significant antitumor effects (28). In addition, it has been reported that chemical carcinogens could induce lung cancer in Syrian hamsters (47–52), and the N-nitrosobis (2-oxopropyl) amine (BOP) induced Syrian hamster lung cancer model faithfully mimics human small cell and non-small cell lung cancer (NSCLC) (47, 51, 52). Histopathologically, it shows a subtype of adenocarcinoma, which is very similar to the type of adenocarcinoma of human non-small cell lung cancer (NSCLC), and the common feature with human lung cancer is that tumor tissues overexpress cyclooxygenase-2 (COX-2) and nuclear factor kappa B (NF-kappaB), which are important factors in the pathogenesis of lung cancer (44). Compared with mice and rats, the streptozotocin-induced Syrian hamster hepatocellular carcinoma tumor model has the advantage of high incidence and short latency, making it an ideal animal model for assessing hepatocarcinogenesis (53). Researchers have also used N-methyl-N-nitrosourea (MNU) to induce hamster breast cancer, and histopathological analysis showed that this animal model resembled human high-grade poorly differentiated breast adenocarcinoma. At the same time, they established the first immortalization of a Syrian hamster breast cancer cell line HMAM5, with a high tumorigenic rate in female hamsters (31). Additional carcinogen-induced cancers in Syrian hamsters include kidney cancer (51, 54, 55), cholangiocellular tumors (52), endometrial adenocarcinoma (56) and laryngeal cancer (57).

2.3 Xenograft tumor models

Human xenograft tumor models are established by transplantation of human-derived tumor cell lines or tumor tissues into immunocompromised Syrian hamsters (Figure 1C). Recently, we created a new pancreatic cancer xenograft model using *IL2RG* gene knockout Syrian hamsters (named ZZU001) with IL-2, IL-4, IL-7, IL-9, IL-15, and IL- 21 receptor function deficiencies, resulting in a significantly decrease in T lymphocyte activity and non-functional B and NK cells, producing a severely immunocompromised state (8, 11). Subcutaneous and orthotopic transplantation of a panel of human pancreatic cancer (PC) cell lines into ZZU001 Syrian hamsters and immunodeficient mice demonstrated that only in ZZU001 did multi-organ metastases similar to those seen in human pancreatic cancer develop. PC tissue from Syrian hamsters exhibited desmoplastic reactions in both stromal and epithelial-to-mesenchymal transition phenotypes, whereas PC tissues from immunodeficient mice did not show this feature. In addition, we transplanted an established human esophageal cancer (EC) cell line (SBRC-EC01) into immunodeficient ZZU001 Syrian hamsters, resulting in a subcutaneous tumor with a pathological structure similar to the primary tumor, but SBRC-EC01 has no tumorigenicity in B-NDG mice and BALB/c nude mice. This suggests the Syrian hamster is a very valuable animal model for studying treatment responses in human PC and EC (8).

Most commonly, human tumor models are established by subcutaneous inoculation of human tumor cells into immunodeficient mice, however, in these models, the histological features of the primary tumor are not reflected (17) The cheek pouches of hamsters possess immune-privileged sites that allow human tumor transplantation to form a distinctive xenograft tumor model. Sakakibara et al. (58) showed that when human malignant tumor tissue-derived cell lines were transplanted into the cheek pouches of Syrian hamsters, the histology of these tumors was consistent with the primary tumor. This was not reflected when the same model was established in mice (59). In addition, serial transplantation of human lymphomas in neonatal hamsters has also been reported, a model that may be a practical system for the study of immunotherapeutic agents, however, no similar reports have been reported in neonatal mice (60, 61). The establishment of human osteosarcoma model in newborn Syrian hamsters has also been reported (62). In conclusion, although xenograft mouse models have become common models for evaluating tumor progression and the efficacy of cancer drugs, they do not faithfully reflect human tumor progression. However, the immune-deficient Syrian hamster model ZZU001 can be used to better simulate human tumors and show the histological and pathological characteristics of human tumors.

2.4 Genetically engineered tumor models

Genetically engineered models involve the application of genetic engineering techniques to modify hamster genes to induce cancer development (Figure 1D). Currently, hamster transgenic models mainly include *KCNQ1* knockout, *TP53* knockout and *IL2RG* knockout as discussed above (8, 63, 64). *KCNQ1* is a gene encoding a potassium channel that is widely expressed in human and rodent tissues, and *KCNQ1* functions as a tumor suppressor gene in the gastrointestinal tract of both humans and mice (65). Li et al. created the first genetically engineered *KCNQ1* knockout hamster cancer model by CRISPR/Cas9 genetic engineering technology, and the homozygous *KCNQ1* knockout hamsters showed severe physical discomfort response at day 70. 85.7% of the hamsters had visible cancers at necropsy, including T-cell lymphoma, plasma cell tumors, hemangiosarcomas, and suspected myeloid leukemia, and developed multi-organ infiltrates (63). In addition, Miao et al. used CRISPR/Cas9 genetic engineering technology to generate *TP53* knockout hamsters. In *TP53* homozygous mutant hamsters, lymphomas, hemangiosarcomas, and myeloid leukemias were the predominant types of cancer developed, while *TP53* heterozygous hamsters mainly developed lymphomas (64). Of note, in contrast with *TP53* homozygous KO mice, hamsters developed carcinomas in several epithelial tissues that were not observed in *TP53* KO mice. *TP53*-deficient acute myeloid leukemia (AML) in human is highly malignant, has a low response rate to chemotherapy, and has a mediate overall survival of only 5-10 months (66), so there is an urgent need for effective animal models to develop new treatments. Most importantly, *TP53*-deficient hamsters can develop acute myelogenous leukemia, however, *TP53*-deficient mice generally do not develop acute myelogenous leukemia (64). Thus, hamsters can be used to evaluate new therapeutic modalities for *TP53*-deficient acute myeloid leukemia. Recently, Miao et al. established a novel *SHARPIN* knockout (KO) Syrian hamster using the CRISPR/Cas9 system, and eosinophil infiltration in esophagus and other organs was observed in S*HARPIN* KO transgenic hamsters, which may represent early symptoms of human eosinophilic esophagitis (EoE). Therefore, it is expected that *SHARPIN* KO transgenic hamsters will encapsulate the syndrome of human autoinflammatory diseases (67).

3 Cancer immunotherapy in the Syrian hamster model

Cancer Immunotherapy (CIT) was the breakthrough of the year 2013 (68). More than a dozen immunotherapies have been approved for cancer treatment to date, however, there are many more immunotherapies in preclinical trials and there is an urgent need for suitable preclinical models to effectively assess their suitability. CIT methods currently evaluated in Syrian hamsters include immune checkpoint inhibitors (14, 69), cytokines (13, 70–72), adoptive cell therapy (15, 60, 73), cancer vaccines (19, 74) and oncolytic viruses (14, 26, 29, 75). A summary of Syrian hamster models used for evaluation of CIT is presented in Table 1.

3.1 Immune checkpoint inhibitors

Immune checkpoint inhibitors (ICI) are by far the most thoroughly studied and clinically advanced form of immunotherapy. PD-1/PD-L1 and CTLA-4 are the two most common immune checkpoint inhibitor targets and several ICI drugs have been approved by the FDA for cancer treatment. Although ICI produces more durable responses than conventional chemoradiation, response rates remain low in many cancers (3, 96), a situation that may be improved by the application of more suitable animal models during pre-clinical testing of these agents.

It has been reported that in a Syrian hamster PC subcutaneous tumor model, αPD-1 (anti-mouse) combined with oncolytic adenovirus (AdV) co-expressing IL-12, GM-CSF, and RLX (Relaxin), which can inhibit the synthesis of extracellular matrix (ECM) and degrade the overexpressed ECM in tumor tissue, to allow full dispersion of the therapeutics,exhibited stronger tumor inhibition compared with the αPD-1 group (69). In the Syrian hamster orthotopic PC model, αPD-1 combined with oncolytic AdV significantly inhibited the growth of primary and metastatic tumors without ascites formation, whereas the αPD-1 group exhibits extensive tumor metastasis and ascites formation. Further studies showed that application of oncolytic Ad/IL12/GM-RLX enhanced penetration of α-PD1 into tumor tissues, and enhanced T cell activation and infiltration into tumors (69). Both the Syrian hamster orthotopic and intraperitoneal dissemination models can faithfully mimic the characteristics of human PC and like human PC, the Syrian hamster PC models are insensitive to ICI. However, combination therapy sensitized PC to αPD-1 treatment and enhanced antitumor effects.

TABLE 1 The Syrian Hamster Models in Cancer Immunotherapy.

Cancer models	Cell lines	Reagents	Immunotherapy approach	Refs
Pancreatic cancer	HPD-1NR, HaK	Oncolytic adenovirus, Vaccinia virus	Oncolytic virus therapy	(9)
	HPD1NR, SHPC6, Hap-T1	Ad-TD-nsIL-12	Cytokine, Oncolytic virus therapy	(13)
	SHPC6	VVLΔTK-STCΔN1L-IL21	Cytokine, Oncolytic virus therapy	(14)
	HPD-1NR	Ad5	Oncolytic virus therapy	(76)
	PGHAM-1	Dendritic cell (DC)	Therapeutic Cancer Vaccine	(19)
	SHPC6	INGN 007	Oncolytic virus therapy	(23)
	HP-1	RGD-ΔE3-ADP-ham-IFN	Cytokine, Oncolytic virus therapy	(25)
	HaP-T1	Ad-OSM, NDV-OSM	Oncolytic virus therapy	(26)
	PGHAM-1	AdCV-hamIFN	Cytokine, Oncolytic virus therapy	(27)
	HapT1	Ad5-D24, Tumor-infiltrating lymphocytes (TILs)	Oncolytic virus therapy, Adoptive Cell Therapy	(60)
	HaP-T1	oAd/IL12/GM-RLX αPD-1	Cytokine, Oncolytic virus therapy, Immune Checkpoint Inhibitor	(69)
	Hap-T1	vvdd-tdTomato-hGMCSF	Oncolytic virus therapy, Cytokine	(70)
	HapT1	Ad5/3-E2F-d24-hIL2, rhIL-2, TIL therapy	Cytokine, Oncolytic virus therapy, Adoptive Cell Therapy	(73)
	HapT1	Ad5/3-E2F-d24-hTNF-α-IRES-hIL-2 (TILT-123), Tumor-infiltrating lymphocytes (TILs)	Cytokine, Oncolytic virus therapy, Adoptive Cell Therapy	(15)
	HPD1NR	Dendritic cell (DC)	Therapeutic Cancer Vaccine	(74)
	HaK, PC1	VRX-007	Oncolytic virus therapy	(77)
	HP-1	VCN-01	Oncolytic virus therapy	(78)
	HP-1	VCN-11	Oncolytic virus therapy	(79)
	SHPC6	VRX-007	Oncolytic virus therapy	(80)
	HaP-T1, HP-1, H2T	Ad-WTLuc	Oncolytic virus therapy	(81)
	HaP-T1	AxE1CAUP	Oncolytic virus therapy	(82)
	HaP-T1, H2T	Human adenovirus	Oncolytic virus therapy	(83)
	H2T	Ad-DHscIL12	Cytokine, Oncolytic virus therapy	(84)
	HapT1	Ad5/3-E2F-d24-vIL2	Cytokine, Oncolytic virus therapy	(85)
	HapT1, HapT1 AIM2-/-	Ad5/3-d24-E2F-hTNFa-IRES-hIL2	Cytokine, Oncolytic virus therapy	(86)
	HaP-T1	Ad-IL12G Virus-loaded monocytes	Cytokine, Oncolytic virus therapy	(87)
Human Esophageal Squamous Cell Carcinoma	SBRC-EC01	Ad-TD-nsIL12	Cytokine, Oncolytic virus therapy	(17)
Glioblastoma	HamGSC-1, HamGSC-2	Delta-24-RGD	Oncolytic virus therapy	(24)

(Continued)

TABLE 1 Continued

Cancer models	Cell lines	Reagents	Immunotherapy approach	Refs
Cheek pouch SCC tumor	HPT11, HPT12	lp11w/Δ55K	Oncolytic virus therapy	(28)
Head and neck cancer	HCPC1	VVΔTKΔN1L-hIL12	Cytokine, Oncolytic virus therapy	(88)
Gallbladder cancer	G207	KIGB-5	Oncolytic virus therapy	(29, 89)
Renal cancer	HaK	KD3-IFN	Cytokine, Oncolytic virus therapy	(30)
	HaK	vvdd-tdTomato-hGMCSF	Cytokine, Oncolytic virus therapy	(70)
	HaK	VRX-007	Oncolytic virus therapy	(80, 90, 91)
	HaK	VRX-007, Ad5	Oncolytic virus therapy	(92)
	HaK	INGN 007	Oncolytic virus therapy	(93)
Lymphosarcoma	TBD 932	IFN-α	Cytokine	(71, 72)
Leiomyosarcoma	DDT1 MF-2	VRX-007	Oncolytic virus therapy	(77)
	DDT1-MF2	Ad5/3-D24-GMCSF	Cytokine, Oncolytic virus therapy	(94, 95)

3.2 Cytokines

Cytokines were the first type of immunotherapy to be used in the clinic and have a history of over 40 years of clinical use. IFNα and IL-2 have been approved for the treatment of malignant tumors (97, 98). Cytokines are key mediators of cell-to-cell communication in the tumor microenvironment (TME) and dysregulation of cytokine expression is present in all human cancers (99). Cytokine therapy refers to the direct stimulation of immune cell growth and activity by injected cytokines. Former commonly used cytokines treatments involved mono-therapeutic use of interferons, interleukins, or granulocyte-macrophage colony-stimulating factor (GM-CSF) (3). However, studies have shown that, except for a few cancers, such as melanoma and renal cell carcinoma, single cytokine therapy in clinical trials is not satisfactory (99) and testing of multiple agents in suitable pre-clinical models is necessary for future application of cytokine therapy.

Interestingly, it appears that the similarities between hamster and human disease pathology extend to the immune system and many human cytokines are functional in the Syrian hamster. Parviainen et al. (70) reported that human GM-CSF has immunological functions in immunocompetent Syrian hamsters. In the Syrian hamster PC model, oncolytic Vaccinia virus expressing human GM-CSF can enhance specific anti-tumor immune responses by recruitment and activation of natural killer cells, monocytes, and granulocytes to enhance the anti-tumor effect. However, human GM-CSF is not functional in mice. We reported that human IL-12 stimulated the proliferation of hamster, but not murine peripheral blood mononuclear cells and induced the expression of interferon-γ and tumor necrosis factor-alpha. At the same time, we constructed an oncolytic AdV expressing non-secreting IL-12 to achieve local low-dose release of IL-12, solving the problems of short half-life and high systemic toxicity associated with IL-12. Using the Syrian hamster PC peritoneal dissemination model and orthotopic tumor models, we demonstrated a good anti-tumor effect and prolonged survival with no toxic side effects observed (13). We also demonstrated that the oncolytic Vaccinia virus (VV) expressing human IL-21 prolongs survival in an intraperitoneal dissemination hamster model of pancreatic cancer (14). Joao Manuel Santos et al. (73) demonstrated that oncolytic AdV expressing human IL-2 achieved the local release of IL-2 in hamster pancreatic cancer, improved the efficacy of adoptive cell therapy, and significantly enhanced the infiltration of $CD8^+$ T cells into the tumor microenvironment, while avoiding systemic toxicity caused by a intravenous delivery of IL-2. In addition, it was reported that human IFN-α is also immunologically functional in hamsters and prolongs survival in a hamster lymphosarcoma model (71, 72). Thus, many human cytokines are biologically active in Syrian hamsters, suggesting this model as a highly suitable immunocompetent model for direct assessment of the role of human cytokines in antitumor activity. This model will also provide robust toxicity information regarding the side-effects of cytokine treatment that can only be determined in mice by use of the murine cytokine counterparts.

3.3 Adoptive cell therapy

Adoptive cell therapy (ACT) mainly utilizes tumor-infiltrating lymphocyte (TIL)-derived T cells or genetically engineered T cells to express tumor-recognition receptors, resulting in durable anti-tumor responses (100). TIL-based ACT relies on (i) non-myeloablative lymphoid exhaustion, (ii) tumor-specific T cells isolated from tumor tissues, expanded *in vitro*, and injected into the host, and (iii) IL-2 administration after TIL infusion (100). Currently, TIL therapy has a durable antitumor effect in melanoma patients (101), but to make TIL therapy widely available, many

researchers have improved the efficacy and safety of ACT through combination therapy strategies.

Mikko Siurala et al. (60) reported for the first time that tumor-infiltrating lymphocytes (TILs) from Syrian hamsters combined with oncolytic AdV enhanced tumor cell killing ability *in vitro*, and oncolytic adenovirus enhanced the efficacy of TIL therapy. However, systemic administration of high doses of IL-2 can lead to severe systemic toxicity and even death (73). It has been reported that using ACT to treat hamster PC, the local high-dose release of IL-2 achieved by co-treatment with Ad5/3-E2F-d24-hIL2 avoided toxicity associated with systemic administration. More interestingly, Ad5/3-E2F-d24-hIL2 increased $CD8^+$ T cells in the tumor microenvironment compared with systemic IL-2 administration. Therefore, Syrian hamster models have demonstrated that in ACT therapy, local release of IL-2 can effectively replace systemic administration and reduce toxicity associated with this form of therapy (73). The Syrian hamster is crucial for this modelling as they not only have immune responses that are reflective of the human scenario and support human IL-2 functions, but critically hamster models are supportive of AdV replication, a feature not shared by murine models. The first step in ACT therapy is host lymphoid depletion, but this can lead to severe cytopenia, systemic inflammatory responses, and damage to vital organs (15, 100). In order to overcome this problem, João Manuel Santos et al. (15) used a hamster PC model to demonstrate that oncolytic AdV armed with human IL-2 and human tumor necrosis factor alpha (TNF-α) could achieve antitumor effects without lymphoid depletion. Indeed, compared with lymphoid depletion, hamsters receiving oncolytic adenovirus and TILs had a significantly longer survival time and repeated AdVtreatment resulted in durable antitumor effects. The mechanism for this is postulated as dependent on AdV-induced upregulation of major histocompatibility complex (MHC) class II in draining lymph nodes, which effectively stimulates $CD4^+$ T cells. These data suggest that the Syrian hamster provides a reliable preclinical animal model for ACT, accurately modeling the toxicity of treatments with human cytokines and that they are critical models for evaluating the ACT combination with oncolytic AdV therapy. Data obtained from Syrian hamster models provide more relevant and reliable evidence for the clinical translation of this therapeutic strategy.

3.4 Therapeutic cancer vaccines

Therapeutic cancer vaccines are designed to induce tumor regression and eradicate cancer cells by boosting a patient's immune response and developing durable antitumor memory immune responses (102). Dendritic cells (DCs) are the most functional antigen-presenting cells (APCs) in the body and play a key role in coordinating the innate and adaptive immune responses against the tumor (103). In 2010, the first therapeutic cancer vaccine (SiPuleucel-T) was approved by the FDA, which improved overall survival for patients with refractory prostate cancer (104, 105).

To understand the potential for a DC vaccine in hamster PC, Akiyama et al. (74) reported that hamster bone marrow (BM)-derived DC (BM-DC) stimulated with hamster tumor cell lysate had an obvious anti-tumor effect on hamster subcutaneous PC. Further studies showed that tumor lysate-pulsed hamster DC could enhance activity of tumor-specific cytotoxic T lymphocytes (CTL). Akiyama et al. (19) also reported that in the hamster PC intraperitoneal dissemination tumor model, tumor lysate-treated DCs significantly inhibited the growth of orthotopic tumor cells and the formation of ascites. Further studies showed that the antitumor effect of tumor lysate-pulsed DCs was mainly due to the activation and expansion of tumor-specific CTLs. Given the lack of success in development of successful therapeutic cancer vaccines to date, the Syrian hamster tumor model should be considered for the development and testing of these regimes as it can better demonstrate the complexity of human cancer and thus has many advantages over mouse models.

3.5 Oncolytic virus therapy

Oncolytic viral therapy is a promising strategy for CIT. Naturally tumor-tropic viruses, or viruses genetically modified for tumor tropism are used to generate anti-tumor activity. The mechanisms by with oncolytic viruses achieve this are (i) selective replication in and killing of tumor cells, (ii) release of tumor-related antigens to induce a systemic anti-tumor immune response, and (iii) induction of potent anti-tumor immune responses *via* infiltration and activation of innate and adaptive immune cells (106). While the prospects for oncolytic viral therapy are positive, with 4 licensed treatments to date, animal models to evaluate these vectors have significant limitations. Oncolytic AdV was the first approved oncolytic virus, licensed in 2005 in China for treatment of refractory head and neck cancer. Since then, AdV has been intensively studied as an oncolytic agent as their genome and biology are well understood, safe, and easily manipulated. However, replication of AdV is species-selective and immunocompetent mouse models are not supportive of AdV replication. Therefore, the evaluation of oncolytic AdV vectors is often performed in immunodeficient mice with human xenograft tumors that do support virus replication. This limits the useful information that is produced through *in vivo* experimentation, as these models cannot adequately assess the safety of viral vectors and their role in host immune responses. Furthermore, as human AdV replicates poorly in normal and tumor tissues of mice, off target effects are difficult to determine (19, 77, 107).

The Syrian hamster is both immunocompetent and allows human AdV replication in normal and tumor tissues, and many research papers have detailed the usefulness of Syrian hamster models for investigation on oncolytic AdV (9, 13, 23–26, 28, 76–80, 82, 84–87, 90–95, 108–111). Phillips et al. (24) established the first immunocompetent Syrian hamster glioma model that is oncolytic AdV replication-permissive, which is novel platform for studying the interactions between the host immune system, tumors, and oncolytic adenoviral therapy. Further studies showed that T-cell infiltration in the tumor microenvironment was significantly increased after treatment with the oncolytic AdV Delta-24-RGD and significant prolongation of survival was achieved compared to

the control group (24). Moreover, it was reported that in the Syrian hamster xenograft human esophageal tumor model, AdV-TD-nsIL12 showed strong anti-tumor effects and inhibited tumor cell proliferation and reduced microvascular density in tumor tissue (17). In addition to its advantages for testing oncolytic AdV, the immune response elicited following VV virus infection in Syrian hamsters has been shown to be partly mediated by natural killer cells in a similar manner to human infection, and this phenomenon is not seen in mice (112), suggesting the Syrian hamster as a suitable model for assessing the immune competence of the oncolytic VV (8, 9, 14, 70, 83, 88). The immune-competent Syrian hamster has also been used to evaluate oncolytic Herpes Simplex Virus (HSV) (29, 89), Reovirus (75), and Newcastle disease virus (NDV) (26), thus providing reliable preclinical studies for the development of oncolytic virus drugs. Nakano et al. (29) demonstrated that the antitumor ability of HSV G207 in athymic-free mice was significantly lower than that in immunocompetent Syrian hamsters, indicating that T-cell-mediated immune response played an important role in the local and systemic anti-tumor effects of G207. This demonstrates the necessity of using animal models with intact immune responses to evaluate oncolytic virus therapy. Interestingly, a novel therapeutic regime to eradicate established tumors by sequential use of two different oncolytic viruses was demonstrated in immunocompetent Syrian hamster PC (HPD-1NR) and kidney cancer (HaK) models (9). Sequential administration of low-dose oncolytic adenovirus and Vaccinia virus exhibited stronger antitumor effects compared to the reverse combination or single agent therapy. Further studies showed that AdV-VV treatment increased tumor-infiltrating lymphocytes and induced a higher tumor-specific immune response (9). Therefore, the immunocompetent Syrian hamster is an appropriate animal model to evaluate the combined treatment strategy of oncolytic AdV and VV as well as other oncolytic viruses.

4 Conclusions and prospects

The number of cancer immunotherapy drugs approved by the FDA has been increasing and cancer immunotherapy is an exciting new paradigm in cancer therapy. An ideal preclinical animal model is urgently needed to evaluate cancer immunotherapy. The US Food and Drug Administration indicates a suitable model is similar to humans in disease onset, progression, symptoms, pathology, and pathophysiology. The Syrian hamster complies with this requirement and immunocompetent hosts can accurately mimic the human scenario in terms of immune responses to disease states and pathogens. Indeed, we and others have recently reported its relevance over mouse models for modelling of SARS-CoV2 infection and disease (113). The Syrian hamster tumor model is more representative of the occurrence and development of human tumors and faithfully recapitulates the complexity of the tumor microenvironment (23, 41). Many human cytokines, including GM-CSF, IL-21, and IL-12, have immunological functions in the hamster (13, 14, 70) and this model is also favored for the examination of species-selective oncolytic viruses such as AdV, which replicate poorly in immunocompetent mice (88).

Challenges do remain with the use of the Syrian hamster model. For example, there are fewer syngeneic tumor cell lines and genetically engineered cancer models available compared with mice and a lack of specific immune reagents can hamper in-depth investigation of immune responses and cytokine changes in the TME after CIT. Moreover, there is currently no humanized Syrian hamster model. We and others are working hard to overcome these constraints, building banks of Syrian hamster tumor cell lines, transgenic hamster models, and developing research reagents to assess immune functions accurately. Thus, we believe that soon, the Syrian hamster will become a widely-used preclinical animal model that accurately simulates various human disease states. This will allow a more accelerated, refined analysis of CIT that can be confidently applied to clinical practice in a more timely manner.

Author contributions

Conceptualization, YJ and YHW. Writing, original draft preparation, YJ and YRW. Writing, review and editing, NL, LD and YHW. Supervision, YHW and PW. Project administration, YHW. Funding acquisition, YHW and PW. All authors contributed to the article and approved the submitted version.

Funding

This project was supported by the National Natural Science Foundation of China (81872486), the National Key R&D program of China (2019YFC1316101), the Natural Science Foundation of Henan Province for Excellent Young Scholars (202300410360) and the UK Medical Research Council (MR/V006053/1) to LD and YHW.

Conflict of interest

The authors declare that the research was conducted in the absence of any commercial or financial relationships that could be construed as a potential conflict of interest.

Publisher's note

All claims expressed in this article are solely those of the authors and do not necessarily represent those of their affiliated organizations, or those of the publisher, the editors and the reviewers. Any product that may be evaluated in this article, or claim that may be made by its manufacturer, is not guaranteed or endorsed by the publisher.

References

1. Siegel RL, Miller KD, Fuchs HE, Jemal A. Cancer statistics, 2021. *CA: Cancer J Clin* (2021) 71(1):7–33. doi: 10.3322/caac.21654

2. Sung H, Ferlay J, Siegel RL, Laversanne M, Soerjomataram I, Jemal A, et al. Global cancer statistics 2020: Globocan estimates of incidence and mortality worldwide for 36 cancers in 185 countries. *CA: Cancer J Clin* (2021) 71(3):209–49. doi: 10.3322/caac.21660

3. Riley RS, June CH, Langer R, Mitchell MJ. Delivery technologies for cancer immunotherapy. *Nat Rev Drug Discovery* (2019) 18(3):175–96. doi: 10.1038/s41573-018-0006-z

4. Hegde PS, Chen DS. Top 10 challenges in cancer immunotherapy. *Immunity* (2020) 52(1):17–35. doi: 10.1016/j.immuni.2019.12.011

5. Miedel EL, Hankenson FC. *Biology and diseases of hamsters: Laboratory animal medicine*. (2015), 209–45. doi: 10.1016/B978-0-12-409527-4.00005-5

6. Mohr U. The Syrian golden hamster as a model in cancer research. *Prog Exp tumor Res* (1979) 24:245–52. doi: 10.1159/000402101

7. Miao J, Ying B, Li R, Tollefson AE, Spencer JF, Wold WSM, et al. Characterization of an n-terminal non-core domain of Rag1 gene disrupted Syrian hamster model generated by crispr Cas9. *Viruses* (2018) 10(5):243. doi: 10.3390/v10050243

8. Miao JX, Wang JY, Li HZ, Guo HR, Dunmall LSC, Zhang ZX, et al. Promising xenograft animal model recapitulating the features of human pancreatic cancer. *World J Gastroenterol* (2020) 26(32):4802–16. doi: 10.3748/wjg.v26.i32.4802

9. Tysome JR, Li X, Wang S, Wang P, Gao D, Du P, et al. A novel therapeutic regimen to eradicate established solid tumors with an effective induction of tumor-specific immunity. *Clin Cancer Res an Off J Am Assoc Cancer Res* (2012) 18(24):6679–89. doi: 10.1158/1078-0432.Ccr-12-0979

10. Warner BM, Safronetz D, Kobinger GP. Syrian Hamsters as a small animal model for emerging infectious diseases: Advances in immunologic methods. *Adv Exp Med Biol* (2017) 972:87–101. doi: 10.1007/5584_2016_135

11. Li R, Ying B, Liu Y, Spencer JF, Miao J, Tollefson AE, et al. Generation and characterization of an I L2rg knockout Syrian hamster model for xscid and hadv-C6 infection in immunocompromised patients. *Dis Models Mech* (2020) 13(8): dmm044602. doi: 10.1242/dmm.044602

12. Cho SA, Park JH, Seok SH, Juhn JH, Kim SJ, Ji HJ, et al. Effect of granulocyte macrophage-colony stimulating factor (Gm-csf) on 5-Fu-Induced ulcerative mucositis in hamster buccal pouches. *Exp toxicologic Pathol Off J Gesellschaft fur Toxikologische Pathologie* (2006) 57(4):321–8. doi: 10.1016/j.etp.2005.09.006

13. Wang P, Li X, Wang J, Gao D, Li Y, Li H, et al. Re-designing interleukin-12 to enhance its safety and potential as an anti-tumor immunotherapeutic agent. *Nat Commun* (2017) 8(1):1395. doi: 10.1038/s41467-017-01385-8

14. Marelli G, Chard Dunmall LS, Yuan M, Di Gioia C, Miao J, Cheng Z, et al. A systemically deliverable vaccinia virus with increased capacity for intertumoral and intratumoral spread effectively treats pancreatic cancer. *J immunotherapy Cancer* (2021) 9(1):e001624. doi: 10.1136/jitc-2020-001624

15. Santos JM, Cervera-Carrascon V, Havunen R, Zafar S, Siurala M, Sorsa S, et al. Adenovirus coding for interleukin-2 and tumor necrosis factor alpha replaces lymphodepleting chemotherapy in adoptive T cell therapy. *Mol Ther J Am Soc Gene Ther* (2018) 26(9):2243–54. doi: 10.1016/j.ymthe.2018.06.001

16. Suresh V, Sundaram R, Dash P, Sabat SC, Mohapatra D, Mohanty S, et al. Macrophage migration inhibitory factor of Syrian golden hamster shares structural and functional similarity with human counterpart and promotes pancreatic cancer. *Sci Rep* (2019) 9(1):15507. doi: 10.1038/s41598-019-51947-7

17. Zhang Z, Zhang C, Miao J, Wang Z, Wang Z, Cheng Z, et al. A tumor-targeted replicating oncolytic adenovirus ad-Td-Nsil12 as a promising therapeutic agent for human esophageal squamous cell carcinoma. *Cells* (2020) 9(11):2438. doi: 10.3390/cells9112438

18. Shimotsuma M, Shields JW, Simpson-Morgan MW, Sakuyama A, Shirasu M, Hagiwara A, et al. Morpho-physiological function and role of omental milky spots as omentum-associated lymphoid tissue (Oalt) in the peritoneal cavity. *Lymphology* (1993) 26(2):90–101.

19. Takigawa Y, Akiyama Y, Maruyama K, Sugiyama K, Uchida E, Kosuge T, et al. Antitumor effect induced by dendritic cell (Dc)-based immunotherapy against peritoneal dissemination of the hamster pancreatic cancer. *Cancer Lett* (2004) 215 (2):179–86. doi: 10.1016/j.canlet.2004.07.007

20. Cardinalli G, Cardinali G, Handler AH. Effect of colchicine on human tumours transplanted in cheek pouch of Syrian hamster. *Nature* (1964) 203:90–2. doi: 10.1038/203090b0

21. Saito S, Nishimura N, Kubota Y, Yamazaki K, Shibuya T, Sasaki H. Establishment and characterization of a cultured cell line derived from nitrosamine-induced pancreatic ductal adenocarcinoma in Syrian golden hamsters. *Gastroenterologia Japonica* (1988) 23(2):183–94. doi: 10.1007/bf02799031

22. Suklabaidya S, Das B, Ali SA, Jain S, Swaminathan S, Mohanty AK, et al. Characterization and use of Hapt1-derived homologous tumors as a preclinical model to evaluate therapeutic efficacy of drugs against pancreatic tumor desmoplasia. *Oncotarget* (2016) 7(27):41825–42. doi: 10.18632/oncotarget.9729

23. Spencer JF, Sagartz JE, Wold WS, Toth K. New pancreatic carcinoma model for studying oncolytic adenoviruses in the permissive Syrian hamster. *Cancer Gene Ther* (2009) 16(12):912–22. doi: 10.1038/cgt.2009.36

24. Phillips LM, Li S, Gumin J, Daou M, Ledbetter D, Yang J, et al. An immune-competent, replication-permissive Syrian hamster glioma model for evaluating delta-24-Rgd oncolytic adenovirus. *Neuro-oncology* (2021) 23(11):1911–21. doi: 10.1093/neuonc/noab128

25. LaRocca CJ, Han J, Gavrikova T, Armstrong L, Oliveira AR, Shanley R, et al. Oncolytic adenovirus expressing interferon alpha in a syngeneic Syrian hamster model for the treatment of pancreatic cancer. *Surgery* (2015) 157(5):888–98. doi: 10.1016/j.surg.2015.01.006

26. Nistal-Villan E, Bunuales M, Poutou J, Gonzalez-Aparicio M, Bravo-Perez C, Quetglas JI, et al. Enhanced therapeutic effect using sequential administration of antigenically distinct oncolytic viruses expressing oncostatin m in a Syrian hamster orthotopic pancreatic cancer model. *Mol Cancer* (2015) 14:210. doi: 10.1186/s12943-015-0479-x

27. Hara H, Kobayashi A, Yoshida K, Ohashi M, Ohnami S, Uchida E, et al. Local interferon-alpha gene therapy elicits systemic immunity in a syngeneic pancreatic cancer model in hamster. *Cancer Sci* (2007) 98(3):455–63. doi: 10.1111/j.1349-7006.2007.00408.x

28. Vijayalingam S, Kuppusamy M, Subramanian T, Strebeck FF, West CL, Varvares M, et al. Evaluation of apoptogenic adenovirus type 5 oncolytic vectors in a Syrian hamster head and neck cancer model. *Cancer Gene Ther* (2014) 21(6):228–37. doi: 10.1038/cgt.2014.22

29. Nakano K, Todo T, Chijiiwa K, Tanaka M. Therapeutic efficacy of G207, a conditionally replicating herpes simplex virus type 1 mutant, for gallbladder carcinoma in immunocompetent hamsters. *Mol Ther J Am Soc Gene Ther* (2001) 3(4):431–7. doi: 10.1006/mthe.2001.0303

30. Shashkova EV, Spencer JF, Wold WS, Doronin K. Targeting interferon-alpha increases antitumor efficacy and reduces hepatotoxicity of E1a-mutated spread-enhanced oncolytic adenovirus. *Mol Ther J Am Soc Gene Ther* (2007) 15(3):598–607. doi: 10.1038/sj.mt.6300064

31. Coburn MA, Brueggemann S, Bhatia S, Cheng B, Li BD, Li XL, et al. Establishment of a mammary carcinoma cell line from Syrian hamsters treated with n-Methyl-N-Nitrosourea. *Cancer Lett* (2011) 312(1):82–90. doi: 10.1016/j.canlet.2011.08.003

32. Greenberg NM, DeMayo F, Finegold MJ, Medina D, Tilley WD, Aspinall JO, et al. Prostate cancer in a transgenic mouse. *Proc Natl Acad Sci United States America* (1995) 92(8):3439–43. doi: 10.1073/pnas.92.8.3439

33. Hanahan D, Weinberg RA. Hallmarks of cancer: The next generation. *Cell* (2011) 144(5):646–74. doi: 10.1016/j.cell.2011.02.013

34. Pour P, Krüger FW, Althoff J, Cardesa A, Mohr U. Cancer of the pancreas induced in the Syrian golden hamster. *Am J Pathol* (1974) 76(2):349–58.

35. Li J, Qin D, Knobloch TJ, Tsai MD, Weghorst CM, Melvin WS, et al. Expression and characterization of Syrian golden hamster P16, a homologue of human tumor suppressor P16 Ink4a. *Biochem Biophys Res Commun* (2003) 304(2):241–7. doi: 10.1016/s0006-291x(03)00577-1

36. Tsutsumi M, Kondoh S, Noguchi O, Horiguchi K, Kobayashi E, Okita S, et al. K-Ras gene mutation in early ductal lesions induced in a rapid production model for pancreatic carcinomas in Syrian hamsters. *Japanese J Cancer Res Gann* (1993) 84 (11):1101–5. doi: 10.1111/j.1349-7006.1993.tb02807.x

37. Takahashi M, Hori M, Mutoh M, Wakabayashi K, Nakagama H. Experimental animal models of pancreatic carcinogenesis for prevention studies and their relevance to human disease. *Cancers* (2011) 3(1):582–602. doi: 10.3390/cancers3010582

38. Lee JH, Rim HJ, Sell S. Heterogeneity of the "Oval-cell" response in the hamster liver during cholangiocarcinogenesis following clonorchis sinensis infection and dimethylnitrosamine treatment. *J Hepatol* (1997) 26(6):1313–23. doi: 10.1016/s0168-8278(97)80467-9

39. Pinlaor S, Hiraku Y, Ma N, Yongvanit P, Semba R, Oikawa S, et al. Mechanism of no-mediated oxidative and nitrative DNA damage in hamsters infected with opisthorchis viverrini: A model of inflammation-mediated carcinogenesis. *Nitric Oxide Biol Chem* (2004) 11(2):175–83. doi: 10.1016/j.niox.2004.08.004

40. Yoon BI, Kim YH, Yi JY, Kang MS, Jang JJ, Joo KH, et al. Expression of thioredoxin during progression of hamster and human cholangiocarcinoma. *Cancer Sci* (2010) 101(1):281–8. doi: 10.1111/j.1349-7006.2009.01353.x

41. Vairaktaris E, Spyridonidou S, Papakosta V, Vylliotis A, Lazaris A, Perrea D, et al. The hamster model of sequential oral oncogenesis. *Oral Oncol* (2008) 44 (4):315–24. doi: 10.1016/j.oraloncology.2007.08.015

42. Gimenez-Conti IB, Slaga TJ. The hamster cheek pouch carcinogenesis model. *J Cell Biochem Supplement* (1993) 17f:83–90. doi: 10.1002/jcb.240531012

43. Chang KW, Sarraj S, Lin SC, Tsai PI, Solt D. P53 expression, P53 and ha-ras mutation and telomerase activation during nitrosamine-mediated hamster pouch carcinogenesis. *Carcinogenesis* (2000) 21(7):1441–51. doi: 10.1093/carcin/21.7.1441

44. Sumida T, Hamakawa H, Sogawa K, Bao Y, Zen H, Sugita A, et al. Telomerase activation and cell proliferation during 7,12-Dimethylbenz[a]Anthracene-Induced hamster cheek pouch carcinogenesis. *Mol carcinogenesis* (1999) 25(3):164–8. doi: 10.1002/(sici)1098-2744(199907)25:3<164::aid-mc2>3.0.co;2-5

45. Chen YK, Huse SS, Lin LM. Differential expression of P53, P63 and P73 protein and mrna for dmba-induced hamster buccal-pouch squamous-cell carcinomas. *Int J Exp Pathol* (2004) 85(2):97–104. doi: 10.1111/j.0959-9673.2004.0374.x

46. Monti-Hughes A, Aromando RF, Pérez MA, Schwint AE, Itoiz ME. The hamster cheek pouch model for field cancerization studies. *Periodontology 2000* (2015) 67 (1):292–311. doi: 10.1111/prd.12066

47. Vegeler RC, Yip-Schneider MT, Ralstin M, Wu H, Crooks PA, Neelakantan S, et al. Effect of celecoxib and novel agent lc-1 in a hamster model of lung cancer. *J Surg Res* (2007) 143(1):169–76. doi: 10.1016/j.jss.2007.08.007

48. Schuller HM, Becker KL, Witschi HP. An animal model for neuroendocrine lung cancer. *Carcinogenesis* (1988) 9(2):293–6. doi: 10.1093/carcin/9.2.293

49. Ishinishi N, Yamamoto A, Hisanaga A, Inamasu T. Tumorigenicity of arsenic trioxide to the lung in Syrian golden hamsters by intermittent instillations. *Cancer Lett* (1983) 21(2):141–7. doi: 10.1016/0304-3835(83)90200-8

50. Rehm S, Takahashi M, Ward JM, Singh G, Katyal SL, Henneman JR. Immunohistochemical demonstration of Clara cell antigen in lung tumors of bronchiolar origin induced by n-nitrosodiethylamine in Syrian golden hamsters. *Am J Pathol* (1989) 134(1):79–87.

51. Furukawa F, Nishikawa A, Imazawa T, Kasahara K, Takahashi M. Enhancing effects of quinacrine on development of hepatopancreatic lesions in n-Nitrosobis(2-Oxopropyl)Amine-Initiated hamsters. *Japanese J Cancer Res Gann* (1998) 89(2):131–6. doi: 10.1111/j.1349-7006.1998.tb00540.x

52. Son HY, Nishikawa A, Furukawa F, Lee IS, Ikeda T, Miyauchi M, et al. Modifying effects of 4-phenylbutyl isothiocyanate on n-Nitrosobis(2-Oxopropyl) Amine-Induced tumorigenesis in hamsters. *Cancer Lett* (2000) 160(2):141–7. doi: 10.1016/s0304-3835(00)00570-x

53. Bell RHJr., Hye RJ, Miyai K. Streptozotocin-induced liver tumors in the Syrian hamster. *Carcinogenesis* (1984) 5(10):1235–8. doi: 10.1093/carcin/5.10.1235

54. Li JJ, Gonzalez A, Banerjee S, Banerjee SK, Li SA. Estrogen carcinogenesis in the hamster kidney: Role of cytotoxicity and cell proliferation. *Environ Health Perspect* (1993) 101 Suppl 5(Suppl 5):259–64. doi: 10.1289/ehp.93101s5259

55. Zurawa-Janicka D, Kobiela J, Stefaniak T, Wozniak A, Narkiewicz J, Wozniak M, et al. Changes in expression of serine proteases Htra1 and Htra2 during estrogen-induced oxidative stress and nephrocarcinogenesis in Male Syrian hamster. *Acta Biochim Polonica* (2008) 55(1):9–19. doi: 10.18388/abp.2008_3123

56. Leavitt WW, Evans RW, Hendry WJ3rd. Etiology of des-induced uterine tumors in the Syrian hamster. *Adv Exp Med Biol* (1981) 138:63–86. doi: 10.1007/978-1-4615-7192-6_4

57. Homburger F, Bernfeld P. Cigarette smoke-induced laryngeal cancer: A model for bronchogenic carcinoma in humans. *New Engl J Med* (1979) 300(15):862. doi: 10.1056/nejm197904123001517

58. Sakakibara K, Oota K. Heterotransplantation of cell lines derived from human malignant neoplasms into golden hamsters treated with antithymocyte serum. *Japanese J Exp Med* (1975) 45(6):501–14.

59. Wold WS, Toth K. Chapter three–Syrian hamster as an animal model to study oncolytic adenoviruses and to evaluate the efficacy of antiviral compounds. *Adv Cancer Res* (2012) 115:69–92. doi: 10.1016/b978-0-12-398342-8.00003-3

60. Siurala M, Vähä-Koskela M, Havunen R, Tähtinen S, Bramante S, Parviainen S, et al. Syngeneic Syrian hamster tumors feature tumor-infiltrating lymphocytes allowing adoptive cell therapy enhanced by oncolytic adenovirus in a replication permissive setting. *Oncoimmunology* (2016) 5(5):e1136046. doi: 10.1080/2162402x.2015.1136046

61. Adams RA, Flowers A, Sundeen R, Merk LP. Chemotherapy and immunotherapy of three human lymphomas serially transplantable in the neonatal Syrian hamster. *Cancer* (1972) 29(2):524–33. doi: 10.1002/1097-0142(197202)29:2<524::aid-cncr2820290244>3.0.co;2-s

62. Singh I, Tsang KY, Blakemore WS. A model for human osteosarcoma in hamsters. *Clin orthopaedics related Res* (1979) 144):305–10. doi: 10.1097/00003086-197910000-00053

63. Li R, Miao J, Tabaran AF, O'Sullivan MG, Anderson KJ, Scott PM, et al. A novel cancer syndrome caused by Kcnq1-deficiency in the golden Syrian hamster. *J carcinogenesis* (2018) 17:6. doi: 10.4103/jcar.JCar_5_18

64. Miao J, Li R, Wettere AJV, Guo H, Tabaran AF, O'Sullivan MG, et al. Cancer spectrum in Tp53-deficient golden Syrian hamsters: A new model for Li-fraumeni syndrome. *J carcinogenesis* (2021) 20:18. doi: 10.4103/jcar.jcar_18_21

65. Wang Z, Cormier RT. Golden Syrian hamster models for cancer research. *Cells* (2022) 11(15):2395. doi: 10.3390/cells11152395

66. Daver NG, Maiti A, Kadia TM, Vyas P, Majeti R, Wei AH, et al. Tp53-mutated myelodysplastic syndrome and acute myeloid leukemia: Biology, current therapy, and future directions. *Cancer Discovery* (2022) 12(11):2516–29. doi: 10.1158/2159-8290.Cd-22-0332

67. Miao J, Lan T, Guo H, Wang J, Zhang G, Wang Z, et al. Characterization of sharpin knockout Syrian hamsters developed using Crispr/Cas9 system. *Anim Models Exp Med* (2022). doi: 10.1002/ame2.12265

68. Couzin-Frankel J. Breakthrough of the year 2013. *Cancer Immunother Sci (New York NY)* (2013) 342(6165):1432–3. doi: 10.1126/science.342.6165.1432

69. Jung BK, Ko HY, Kang H, Hong J, Ahn HM, Na Y, et al. Relaxin-expressing oncolytic adenovirus induces remodeling of physical and immunological aspects of cold tumor to potentiate pd-1 blockade. *J immunotherapy Cancer* (2020) 8(2):e000763. doi: 10.1136/jitc-2020-000763

70. Parviainen S, Ahonen M, Diaconu I, Kipar A, Siurala M, Vähä-Koskela M, et al. Gmcsf-armed vaccinia virus induces an antitumor immune response. *Int J Cancer* (2015) 136(5):1065–72. doi: 10.1002/ijc.29068

71. Altrock BW, Fagin KD, Hockman HR, Fish EN, Goldstein L, Chang D, et al. Antiviral and antitumor effects of a human interferon analog, ifn-alpha con 1, assessed in hamsters. *J Interferon Res* (1986) 6(4):405–15. doi: 10.1089/jir.1986.6.405

72. Lee SH, Chiu H, Renton KW, Stebbing N. Modulation by a human interferon of antitumor effects of cyclophosphamide against a lymphosarcoma in hamsters. *Biochem Pharmacol* (1984) 33(21):3439–43. doi: 10.1016/0006-2952(84)90117-5

73. Santos JM, Havunen R, Siurala M, Cervera-Carrascon V, Tähtinen S, Sorsa S, et al. Adenoviral production of interleukin-2 at the tumor site removes the need for systemic postconditioning in adoptive cell therapy. *Int J Cancer* (2017) 141(7):1458–68. doi: 10.1002/ijc.30839

74. Akiyama Y, Maruyama K, Nara N, Hojo T, Cheng JY, Mori T, et al. Antitumor effects induced by dendritic cell-based immunotherapy against established pancreatic cancer in hamsters. *Cancer Lett* (2002) 184(1):37–47. doi: 10.1016/s0304-3835(02)00189-1

75. Himeno Y, Etoh T, Matsumoto T, Ohta M, Nishizono A, Kitano S. Efficacy of oncolytic reovirus against liver metastasis from pancreatic cancer in immunocompetent models. *Int J Oncol* (2005) 27(4):901–6. doi: 10.3892/ijo.27.4.901

76. Li X, Wang P, Li H, Du X, Liu M, Huang Q, et al. The efficacy of oncolytic adenovirus is mediated by T-cell responses against virus and tumor in Syrian hamster model. *Clin Cancer Res an Off J Am Assoc Cancer Res* (2017) 23(1):239–49. doi: 10.1158/1078-0432.Ccr-16-0477

77. Thomas MA, Spencer JF, La Regina MC, Dhar D, Tollefson AE, Toth K, et al. Syrian Hamster as a permissive immunocompetent animal model for the study of oncolytic adenovirus vectors. *Cancer Res* (2006) 66(3):1270–6. doi: 10.1158/0008-5472.Can-05-3497

78. Bazan-Peregrino M, Garcia-Carbonero R, Laquente B, Álvarez R, Mato-Berciano A, Gimenez-Alejandre M, et al. Vcn-01 disrupts pancreatic cancer stroma and exerts antitumor effects. *J immunotherapy Cancer* (2021) 9(11):e003254. doi: 10.1136/jitc-2021-003254

79. Mato-Berciano A, Morgado S, Maliandi MV, Farrera-Sal M, Gimenez-Alejandre M, Ginestà MM, et al. Oncolytic adenovirus with hyaluronidase activity that evades neutralizing antibodies: Vcn-11. *J Controlled release Off J Controlled Release Soc* (2021) 332:517–28. doi: 10.1016/j.jconrel.2021.02.035

80. Young BA, Spencer JF, Ying B, Toth K, Wold WS. The effects of radiation on antitumor efficacy of an oncolytic adenovirus vector in the Syrian hamster model. *Cancer Gene Ther* (2013) 20(9):531–7. doi: 10.1038/cgt.2013.50

81. Bortolanza S, Bunuales M, Alzuguren P, Lamas O, Aldabe R, Prieto J, et al. Deletion of the E3-6.7k/Gp19k region reduces the persistence of wild-type adenovirus in a permissive tumor model in Syrian hamsters. *Cancer Gene Ther* (2009) 16(9):703–12. doi: 10.1038/cgt.2009.12

82. Hasegawa N, Abei M, Yokoyama KK, Fukuda K, Seo E, Kawashima R, et al. Cyclophosphamide enhances antitumor efficacy of oncolytic adenovirus expressing uracil phosphoribosyltransferase (Uprt) in immunocompetent Syrian hamsters. *Int J Cancer* (2013) 133(6):1479–88. doi: 10.1002/ijc.28132

83. Bortolanza S, Alzuguren P, Buñuales M, Qian C, Prieto J, Hernandez-Alcoceba R. Human adenovirus replicates in immunocompetent models of pancreatic cancer in Syrian hamsters. *Hum Gene Ther* (2007) 18(8):681–90. doi: 10.1089/hum.2007.017

84. Bortolanza S, Bunuales M, Otano I, Gonzalez-Aseguinolaza G, Ortiz-de-Solorzano C, Perez D, et al. Treatment of pancreatic cancer with an oncolytic adenovirus expressing interleukin-12 in Syrian hamsters. *Mol Ther J Am Soc Gene Ther* (2009) 17(4):614–22. doi: 10.1038/mt.2009.9

85. Quixabeira DCA, Zafar S, Santos JM, Cervera-Carrascon V, Havunen R, Kudling TV, et al. Oncolytic adenovirus coding for a variant interleukin 2 (Vil-2) cytokine re-programs the tumor microenvironment and confers enhanced tumor control. *Front Immunol* (2021) 12:674400. doi: 10.3389/fimmu.2021.674400

86. Heiniö C, Havunen R, Santos J, de Lint K, Cervera-Carrascon V, Kanerva A, et al. Tnfa and Il2 encoding oncolytic adenovirus activates pathogen and danger-associated immunological signaling. *Cells* (2020) 9(4):798. doi: 10.3390/cells9040798

87. Bunuales M, Garcia-Aragoncillo E, Casado R, Quetglas JI, Hervas-Stubbs S, Bortolanza S, et al. Evaluation of monocytes as carriers for armed oncolytic adenoviruses in murine and Syrian hamster models of cancer. *Hum Gene Ther* (2012) 23(12):1258–68. doi: 10.1089/hum.2012.043

88. Ahmed J, Chard LS, Yuan M, Wang J, Howells A, Li Y, et al. A new oncolytic V accinia virus augments antitumor immune responses to prevent tumor recurrence and metastasis after surgery. *J immunotherapy Cancer* (2020) 8(1):e000415. doi: 10.1136/jitc-2019-000415

89. Nakano K, Todo T, Zhao G, Yamaguchi K, Kuroki S, Cohen JB, et al. Enhanced efficacy of conditionally replicating herpes simplex virus (G207) combined with 5-fluorouracil and surgical resection in peritoneal cancer dissemination models. *J Gene Med* (2005) 7(5):638–48. doi: 10.1002/jgm.700

90. Young BA, Spencer JF, Ying B, Tollefson AE, Toth K, Wold WS. The role of cyclophosphamide in enhancing antitumor efficacy of an adenovirus oncolytic vector in subcutaneous Syrian hamster tumors. *Cancer Gene Ther* (2013) 20(9):521–30. doi: 10.1038/cgt.2013.49

91. Dhar D, Toth K, Wold WS. Cycles of transient high-dose cyclophosphamide administration and intratumoral oncolytic adenovirus vector injection for long-term tumor suppression in Syrian hamsters. *Cancer Gene Ther* (2014) 21(4):171–8. doi: 10.1038/cgt.2014.13

92. Thomas MA, Spencer JF, Toth K, Sagartz JE, Phillips NJ, Wold WS. Immunosuppression enhances oncolytic adenovirus replication and antitumor efficacy in the Syrian hamster model. *Mol Ther J Am Soc Gene Ther* (2008) 16 (10):1665–73. doi: 10.1038/mt.2008.162

93. Dhar D, Spencer JF, Toth K, Wold WS. Effect of preexisting immunity on oncolytic adenovirus vector ingn 007 antitumor efficacy in immunocompetent and immunosuppressed Syrian hamsters. *J Virol* (2009) 83(5):2130–9. doi: 10.1128/jvi.02127-08

94. Siurala M, Bramante S, Vassilev L, Hirvinen M, Parviainen S, Tähtinen S, et al. Oncolytic adenovirus and doxorubicin-based chemotherapy results in synergistic antitumor activity against soft-tissue sarcoma. *Int J Cancer* (2015) 136(4):945–54. doi: 10.1002/ijc.29048

95. Bramante S, Koski A, Kipar A, Diaconu I, Liikanen I, Hemminki O, et al. Serotype chimeric oncolytic adenovirus coding for gm-csf for treatment of sarcoma in rodents and humans. *Int J Cancer* (2014) 135(3):720–30. doi: 10.1002/ijc.28696

96. He X, Xu C. Immune checkpoint signaling and cancer immunotherapy. *Cell Res* (2020) 30(8):660–9. doi: 10.1038/s41422-020-0343-4

97. Quesada JR, Hersh EM, Manning J, Reuben J, Keating M, Schnipper E, et al. Treatment of hairy cell leukemia with recombinant alpha-interferon. *Blood* (1986) 68 (2):493–7. doi: 10.1182/blood.V68.2.493.493

98. Rosenberg SA. Il-2: The first effective immunotherapy for human cancer. *J Immunol (Baltimore Md 1950)* (2014) 192(12):5451–8. doi: 10.4049/jimmunol.1490019

99. Propper DJ, Balkwill FR. Harnessing cytokines and chemokines for cancer therapy. *Nat Rev Clin Oncol* (2022) 19(4):237–53. doi: 10.1038/s41571-021-00588-9

100. Met Ö, Jensen KM, Chamberlain CA, Donia M, Svane IM. Principles of adoptive T cell therapy in cancer. *Semin immunopathology* (2019) 41(1):49–58. doi: 10.1007/s00281-018-0703-z

101. Rosenberg SA, Restifo NP. Adoptive cell transfer as personalized immunotherapy for human cancer. *Sci (New York NY)* (2015) 348(6230):62–8. doi: 10.1126/science.aaa4967

102. Saxena M, van der Burg SH, Melief CJM, Bhardwaj N. Therapeutic cancer vaccines. *Nat Rev Cancer* (2021) 21(6):360–78. doi: 10.1038/s41568-021-00346-0

103. Sabado RL, Balan S, Bhardwaj N. Dendritic cell-based immunotherapy. *Cell Res* (2017) 27(1):74–95. doi: 10.1038/cr.2016.157

104. Cheever MA, Higano CS. Provenge (Sipuleucel-T) in prostate cancer: The first fda-approved therapeutic cancer vaccine. *Clin Cancer Res an Off J Am Assoc Cancer Res* (2011) 17(11):3520–6. doi: 10.1158/1078-0432.Ccr-10-3126

105. Kantoff PW, Higano CS, Shore ND, Berger ER, Small EJ, Penson DF, et al. Sipuleucel-T immunotherapy for castration-resistant prostate cancer. *New Engl J Med* (2010) 363(5):411–22. doi: 10.1056/NEJMoa1001294

106. Kaufman HL, Kohlhapp FJ, Zloza A. Oncolytic viruses: A new class of immunotherapy drugs. *Nat Rev Drug Discovery* (2015) 14(9):642–62. doi: 10.1038/nrd4663

107. Thomas MA, Spencer JF, Wold WS. Use of the Syrian hamster as an animal model for oncolytic adenovirus vectors. *Methods Mol Med* (2007) 130:169–83. doi: 10.1385/1-59745-166-5:169

108. Puig-Saus C, Laborda E, Rodríguez-García A, Cascalló M, Moreno R, Alemany R. The combination of I-leader truncation and gemcitabine improves oncolytic adenovirus efficacy in an immunocompetent model. *Cancer Gene Ther* (2014) 21 (2):68–73. doi: 10.1038/cgt.2013.85

109. Thaci B, Ahmed AU, Ulasov IV, Tobias AL, Han Y, Aboody KS, et al. Pharmacokinetic study of neural stem cell-based cell carrier for oncolytic virotherapy: Targeted delivery of the therapeutic payload in an orthotopic brain tumor model. *Cancer Gene Ther* (2012) 19(6):431–42. doi: 10.1038/cgt.2012.21

110. Kim KH, Ryan MJ, Estep JE, Miniard BM, Rudge TL, Peggins JO, et al. A new generation of serotype chimeric infectivity-enhanced conditionally replicative adenovirals: The safety profile of Ad5/3-Δ24 in advance of a phase I clinical trial in ovarian cancer patients. *Hum Gene Ther* (2011) 22(7):821–8. doi: 10.1089/hum.2010.180

111. Poutou J, Bunuales M, Gonzalez-Aparicio M, Garcia-Aragoncillo E, Quetglas JI, Casado R, et al. Safety and antitumor effect of oncolytic and helper-dependent adenoviruses expressing interleukin-12 variants in a hamster pancreatic cancer model. *Gene Ther* (2015) 22(9):696–706. doi: 10.1038/gt.2015.45

112. Nelles MJ, Duncan WR, Streilein JW. Immune response to acute virus infection in the Syrian hamster. ii. studies on the identity of virus-induced cytotoxic effector cells. *J Immunol (Baltimore Md 1950)* (1981) 126(1):214–8. doi: 10.4049/jimmunol.126.1.214

113. Muñoz-Fontela C, Dowling WE, Funnell SGP, Gsell PS, Riveros-Balta AX, Albrecht RA, et al. Animal models for covid-19. *Nature* (2020) 586(7830):509–15. doi: 10.1038/s41586-020-2787-6

frontiers | Frontiers in Immunology

TYPE Original Research
PUBLISHED 03 March 2023
DOI 10.3389/fimmu.2023.1107848

Check for updates

OPEN ACCESS

EDITED BY
An Coosemans,
KU Leuven, Belgium

REVIEWED BY
Eduardo Huarte,
PTC Therapeutics, United States
Sushil Kumar,
Oregon Health and Science University,
United States

*CORRESPONDENCE
Alba Matas-Céspedes
alba.matas@astrazeneca.com
Richard Stebbings
richard.stebbings@astrazeneca.com

SPECIALTY SECTION
This article was submitted to
Cancer Immunity
and Immunotherapy,
a section of the journal
Frontiers in Immunology

RECEIVED 25 November 2022
ACCEPTED 21 February 2023
PUBLISHED 03 March 2023

CITATION
Matas-Céspedes A, Lapointe J-M,
Elder MJ, Browne GJ, Dovedi SJ,
de Haan L, Maguire S and Stebbings R
(2023) Characterization of a novel potency
endpoint for the evaluation of immune
checkpoint blockade in humanized mice.
Front. Immunol. 14:1107848.
doi: 10.3389/fimmu.2023.1107848

COPYRIGHT
© 2023 Matas-Céspedes, Lapointe, Elder,
Browne, Dovedi, de Haan, Maguire and
Stebbings. This is an open-access article
distributed under the terms of the Creative
Commons Attribution License (CC BY). The
use, distribution or reproduction in other
forums is permitted, provided the original
author(s) and the copyright owner(s) are
credited and that the original publication in
this journal is cited, in accordance with
accepted academic practice. No use,
distribution or reproduction is permitted
which does not comply with these terms.

Characterization of a novel potency endpoint for the evaluation of immune checkpoint blockade in humanized mice

Alba Matas-Céspedes[1]*, Jean-Martin Lapointe[1], Matthew J. Elder[2], Gareth J. Browne[3], Simon J. Dovedi[2], Lolke de Haan[1], Shaun Maguire[1] and Richard Stebbings[1]*

[1]Clinical Pharmacology and Safety Sciences, R&D, AstraZeneca, Cambridge, United Kingdom, [2]Early Oncology, R&D, AstraZeneca, Cambridge, United Kingdom, [3]Antibody Discovery and Protein Engineering, R&D , AstraZeneca, Cambridge, United Kingdom

Introduction: Humanized mice are emerging as valuable models to experimentally evaluate the impact of different immunotherapeutics on the human immune system. These immunodeficient mice are engrafted with human cells or tissues, that then mimic the human immune system, offering an alternative and potentially more predictive preclinical model. Immunodeficient NSG mice engrafted with human CD34+ cord blood stem cells develop human T cells educated against murine MHC. However, autoimmune graft versus host disease (GvHD), mediated by T cells, typically develops 1 year post engraftment.

Methods: Here, we have used the development of GvHD in NSG mice, using donors with HLA alleles predisposed to autoimmunity (psoriasis) to weight in favor of GvHD, as an endpoint to evaluate the relative potency of monoclonal and BiSpecific antibodies targeting PD-1 and CTLA-4 to break immune tolerance.

Results: We found that treatment with either a combination of anti-PD-1 & anti-CTLA-4 mAbs or a quadrivalent anti-PD-1/CTLA-4 BiSpecific (MEDI8500), had enhanced potency compared to treatment with anti-PD-1 or anti-CTLA-4 monotherapies, increasing T cell activity both *in vitro* and *in vivo*. This resulted in accelerated development of GvHD and shorter survival of the humanized mice in these treatment groups commensurate with their on target activity.

Discussion: Our findings demonstrate the potential of humanized mouse models for preclinical evaluation of different immunotherapies and combinations, using acceleration of GvHD development as a surrogate of aggravated antigenic T-cell response against host.

KEYWORDS

humanized mice, immune checkpoint inhibitors, immunotherapy, preclinical safety assessment, GvHD

Introduction

Immunotherapy has emerged in recent years as a novel approach for treatment of cancer through modulation of the patient's immune system. Antibodies targeting immune checkpoint inhibitors such as programmed cell death-1 (PD-1) its ligand (PD-L1), or cytotoxic T-lymphocyte-associated antigen 4 (CTLA-4) have greatly contributed to advances in cancer treatment in diverse tumour types (1–4). Regulation of immune responses through PD-1 and CTLA-4 is mediated by non-redundant mechanisms (5). While both are negative signals for T cell activation, CTLA-4 is expressed exclusively on T cells and regulates the amount of CD28 co-stimulatory signalling a T cell receives during both activation and also at later stages of differentiation (5, 6). By contrast PD-1 is more broadly expressed and regulates T cells at later stages of immune activation in peripheral tissues or at the tumour site (5). Though recent evidence points to an overlap in the PD-1 and CTLA-4 pathways, given the novel finding that CD80, a ligand for CTLA-4, can dimerise in *cis* with PD-L1 (7). Hence, combined blockade of both immune checkpoints could lead to additive or synergistic effects and improve the response rate to these therapies compared to their use as monotherapies. In this line, clinical data demonstrates the impact of combined therapy with increases in overall survival observed in patients with different solid tumours (8–10).

Syngeneic mouse models are relevant for the study of immunotherapies as they consist of immunocompetent mice engrafted with tumour tissues derived from the same genetic background and can help to understand the immune response after immunotherapy treatment. However, a number of limitations complicate the translational value of these models for humans (11). First, mouse cancer cell lines are limited and do not carry many of the relevant mutations associated with clinical disease. Second, surrogate antibodies, which are functionally equivalent to the therapeutic antibody candidate but binding to the target ortholog expressed in mice, are sometimes difficult to be generated and usually have affinities and binding domains that may not closely resemble the biology of the candidate drug, rendering the data of limited use to understand the pharmacology of the drug on the immune system (11, 12).

Immunodeficient mice engrafted with a functional human immune system are emerging as useful models to evaluate some human immune responses in different pre-clinical scenarios, however they have a number of caveats given their incomplete human immune reconstitution (13–16). The most common immunocompromised strain of mice used for humanization is the NOD-*scid IL2*Rγ^{null} (NSG) (17, 18). These mice can be engrafted with either PBMCs (13) or human haematopoietic stem cells (HSCs), isolated from umbilical cord blood (UCB) (19), bone marrow (BM) (20) or foetal liver (21). This latter model leads to the generation of a diverse repertoire of human immune cells in the mice, including B, T, NK cells, monocytes and dendritic cells, and humanization is improved if newborn mice are used instead of adult mice (22). It typically takes 16 weeks to obtain stable human cell engraftment in mice, and they can survive for more than one year without developing T cells-mediated graft-*versus*-host disease (GvHD). In these humanized mice, injected stem cells are educated against the murine major histocompatibility complex (MHC) during their differentiation into T cells, making them tolerant to the mouse environment, compared to the PBMC model (13), with higher thresholds for their activation (23, 24). The use of human HSCs cells with certain human leucocyte antigen (HLA) types associated with development of autoimmune disorders such as psoriasis or rheumatoid arthritis has been previously reported to accelerate the development of GvHD in this model (25, 26).

In this study, we first compared the *in vitro* biological functionality of different immune checkpoint inhibitors: anti-PD-1 monoclonal antibody (mAb), anti-CTLA-4 mAb, a combination of anti-PD-1 & anti-CTLA-4 mAbs and MEDI8500 that is bivalent for both targets (27) but has reduced affinity to the CTLA-4 receptor. For *in vivo* comparisons, we used UCB-derived CD34$^+$ HSCs from donors with HLA alleles predisposed to psoriasis to humanize newborn NSG mice, in order to accelerate development of GvHD, as previously described (25, 26). In these mice we compared the ability of anti-PD-1 and anti-CTLA-4 mAbs as single agents, in combination, and MEDI8500 to break tolerance to the mouse environment, using the development of GvHD lesions as a surrogate to evaluate aggravated antigenic T cell response and as an endpoint to determine relative potency. We demonstrate that both the combination of anti-PD-1 & anti-CTLA-4 mAbs and MEDI8500, show enhanced potency compared to anti-PD-1 or anti-CTLA-4 monotherapy both *in vitro* and *in vivo*. This study provides further evidence for the utility of humanized mice for the evaluation of comparative potency of different immunotherapeutics and combinations.

Materials and methods

Antibodies

Anti-PD-1 LO115 is a fully human IgG1 mAb with an affinity for human PD-1 of K_D = 0.81nM. Anti-CTLA-4 TM is a fully human IgG1 mAb with an affinity for human CTLA-4 of K_D = 0.42nM. Anti-PD-1/CTLA-4 BiS 5 (MEDI8500) is a bivalent BiSpecific antibody where the Fab domains are specific for PD-1, and where the scFv domains are specific for CTLA-4 and are tethered to the CH3 domain. In the BiSpecific format the affinity for human PD-1 is K_D = 1.23nM and human CTLA-4 is K_D = 1.22nM (Supplementary Figure 1). All antibodies were generated by AstraZeneca.

PD-1 reporter assay

CHO K1 OKT3-CD14 (low) hB7H1 (high) cl 2 cells (expressing anti-CD3 and PD-L1) were seeded at 0.6 × 10^4 cells in RPMI1640

GlutaMAX™ medium (Gibco, Paisley, UK) supplemented with 10% FBS, in 384-well tissue culture-treated plates and incubated for 18 hours at 37°C. Supernatants were removed and fresh culture medium added with 1.5×10^4 Jurkat NFAT Luc2 PD1 clone 3L-B9 cells (expressing PD-1 and possessing NFAT promoter driven luciferase expression) supplemented with 2.31 nM anti-CD28 antibody (BD Biosciences, Oxford, UK). Single agents anti-PD-1 and anti-CTLA-4 were added to this co-culture in a 3-fold dose titration from 0.005 nM to 300 nM. MEDI8500 was added in a 3-fold dose titration from 0.016 nM to 1000 nM. Co-cultures were incubated for 5 hours and 40 minutes at 37°C followed by 20 minutes at room temperature. Steady-Glo Buffer (Promega, Southampton, UK) was added to tissue culture wells for 10 minutes to lyse cells and luminescence was detected using the using the ultra-sensitive luminescence settings on an Envision spectrophotometer (Perkin Elmer, Seer Green, UK).

CTLA-4 reporter assay

2×10^4 Raji cells (expressing CD80 and CD86) and 8×10^4 Jurkat CTLA4 IL2 luc2 cells (expressing CTLA-4 and possessing IL-2 promoter driven luciferase expression) were seeded in RPMI1640 GlutaMAX™ medium supplemented with 10% FBS and 1% non-essential amino acids), in 96-well tissue culture-treated plates supplemented with 2.5 µg/mL anti-CD3 (eBioscience, UK). Single agents anti-PD-1 and anti-CTLA-4 were added to this co-culture in a 3-fold dose titration from 0.008 nM to 500 nM. MEDI8500 was added in a 3-fold dose titration from 0.160 nM to 1111 nM. Co-cultures were incubated for 6 hours at 37°C. Steady-Glo Buffer was added to tissue culture wells for 10 minutes to lyse cells and luminescence was detected using the ultra-sensitive luminescence settings on an Envision spectrophotometer.

Human anti-CD3/SEB assay

Human PBMCs were isolated and re-suspended in assay medium, RPMI1640 GlutaMAX™ medium supplemented with 10% FBS and 1% penicillin-streptomycin and a total of 2×10^5 PBMCs/well were added in triplicates to a 96-well flat-bottomed tissue culture-treated plate, pre-coated for 2 hours at 37°C with 0.5 µg/mL mouse anti-human CD3 antibody (Invitrogen, Paisley, UK), then Staphylococcal enterotoxin B (SEB) (Sigma-Aldrich, St. Louis, MO, USA) was added to a final concentration of 100 ng/mL. Next, anti-PD-1, anti-CTLA-4, MEDI8500, or a combination of anti-PD-1 + anti-CTLA-4 monotherapies were added in a 4-fold dose titration from 400 nM. Cell cultures were incubated at 37°C with 5% CO_2 for 3 days, supernatants were harvested, and IL-2 secretion was evaluated by ELISA (R&D Systems, Minneapolis, MN, USA).

TABLE 1 HLA profile for each donor.

Donor	2315	2340	5263	5437	5443	5445	5468
HLA-A	A*03:02	A*23:01	A*02:01	A*01:03	A*02:01	A*02:01	A*01:01
	A*24:02	A*30:04	A*26:01	A*33:03	A*30:01	A*02:01	A*68:01
HLA-B	B*51:01	B*44:03	B*27:05	B*13:02	B*13:02	B*07:02	B*18:01
	B*57:01	B*53:01	B*35:01	B*39:24	B*13:02	B*35:01	B*35:02
HLA-C	C*04:01	C*06:02	C*02:02	C*06:02	C*06:02	C*04:01	C*04:01
	C*06:02	C*07:01	C*04:01	C*07:01	C*06:02	C*07:02	C*07:01
HLA-DRB	DRB1*04:01	DRB1*07:01	DRB1*04:04	DRB1*11:02	DRB1*07:01	DRB1*11:01	DRB1*08:01
	DRB1*07:01	DRB1*13:04	DRB1*12:01	DRB1*12:01	DRB1*07:01	DRB1*13:05	DRB1*13:01
	DRB4*01:03	DRB3*02:02	DRB3*02:02	DRB3*02:02	DRB4*01:03	DRB3*02:02	DRB3*01:01
	DRB4*01:03N	DRB4*01:01	DRB4*01:03	DRB3*02:02	DRB4*01:03	DRB3*02:02	Blank
HLA-DQ	DQB1*03:01	DQB1*02:02	DQB1*03:01	DQB1*03:01	DQB1*02:02	DQB1*03:01	DQB1*04:02
	DQB1*03:03	DQB1*03:01	DQB1*03:02	DQB1*05:01	DQB1*02:02	DQB1*03:01	DQB1*06:03
	DQA1*02:01	DQA1*02:01	DQA1*03:01	DQA1*01:04	DQA1*02:01	DQA1*05:05	DQA1*01:03
	DQA1*03:03	DQA1*05:05	DQA1*05:05	DQA1*05:05	DQA1*02:01	DQA1*05:05	DQA1*04:01
HLA-DP	DPB1*04:01G	DPB1*13:01G	DPB1*04:01G	DPB1*01:01G	DPB1*04:01G	DPB1*02:01G	DPB1*02:01G
	DPB1*04:01G	DPB1*17:01G	DPB1*04:01G	DPB1*04:02G	DPB1*20:01G	DPB1*09:01G	DPB1*04:01G
	DPA1*01:03	DPA1*02:01	DPA1*01:03	DPA1*02:02	DPA1*01:03	DPA1*01:03	DPA1*01:03
	DPA1*01:03	DPA1*02:01	DPA1*01:03	DPA1*03:01	DPA1*01:03	DPA1*02:01	DPA1*01:03

The * symbol is a separator used in HLA nomenclature to separate gene and allele group.

Mice

Human CD34^{+} haematopoietic stem cell-engrafted NSG™ females (huNSG) were purchased from The Jackson Laboratory (Sacramento, CA, USA) with specific HLA types predisposed to autoimmunity (Table 1). Mice were housed in individually ventilated cages under SPF conditions and used at~19 weeks of age. Animals were checked daily for morbidity and mortality. At the time of routine monitoring, the animals were checked for any effects of treatments on normal behaviour such as mobility, visual estimation of food and water consumption, body weight gain/loss, eye/hair matting and any other abnormal observations. All study procedures were conducted following an approved IACUC protocol and Crown Bioscience San Diego Standard Operating Procedures.

In vivo study design

Two different *in vivo* studies were run using the same design. Before grouping and treatment all animals were weighed. The grouping was performed by using StudyDirector™ software (Studylog Systems, Inc. CA, USA). One optimal randomization design (generated by Matched distribution) that showed minimal group to group variation was selected for group allocation. Animals within a single HLA cohort were evenly distributed throughout the groups. Randomization was based on body weight and donor HLA type. Prior to dosing, cheek bleeds were collected from each animal for flow cytometry to detect the baseline immune cell population prior to treatment.

The data presented is a compilation of two different studies. There were 5 treatment groups in total: vehicle (n = 35), anti-PD-1 (n = 15), anti-CTLA-4 (n = 15), combination of anti-PD-1 + anti-CTLA-4 (n = 20) and MEDI8500 (n = 35). Mice received 3 mg/kg of the corresponding single agent or MEDI8500, or a combination of 3mg/kg + 3 mg/kg in the anti-PD-1 + anti-CTLA-4 combination group subcutaneously every 3 days, followed by termination on day 46 (Supplementary Figure 2). Body weight and clinical observations were made 3 times a week. Signs and clinical observations of GvHD were established as follows: Grade 0 = Normal; Grade 1 (mild) = 5-10% weight loss, mildly decreased activity, hunching only at rest and/or mild ruffling; Grade 2 (moderate) = 10-20% weight loss, moderately decreased activity, hunching only at rest and/or moderate alopecia; Grade 3 (severe) = >20% weight loss, stationary until stimulated, impaired movement and/or severe ruffling.

Animals were terminated for humane reasons if body weight loss was > 20% over a period of 72 hours. Upon termination, blood was collected for plasma processing and flow cytometric analysis. Lungs, liver and half of the spleen were collected for histology and immunohistochemistry. The other half of the spleen was processed for flow cytometric analysis. For any animals found dead, tissues were not taken for analysis.

Histopathology and immunohistochemistry

Samples of liver, lung and spleen were fixed in 10% neutral-buffered formalin, and processed to paraffin blocks using routine methods. Previous observations (unpublished) had shown that these organs were the most consistently and strongly affected in animals that developed GvHD. Tissues were sectioned at 4 µm thickness and stained with hematoxylin and eosin (H&E), or with immunohistochemistry using a rabbit monoclonal antibody specific for human CD45 (D9M81, Cell Signaling Technology, Leiden, The Netherlands) at a 0.05 µg/mL dilution, on an automated Leica Bond-RX immunostainer (Leica Biosystems, Wetzlar, Germany), using DAB as a chromogen. This antibody was demonstrated not to cross-react with mouse CD45 in wild-type mouse lymphoid tissues (unpublished observations).

For histopathology evaluation, H&E stained sections were examined by a board-certified veterinary pathologist with experience in mouse pathology, and evaluated for inflammatory/immune changes. Changes that were considered by the pathologist to be a consequence of GvHD (rather than background/incidental changes) were characterised and scored for severity on a subjective scale of 1 to 4, depending on the extent of the change thoughout the tissue. A total GvHD score (0-12) was calculated by adding the lesion scores from each tissue (if more than one change was observed per tissue, only the highest lesion score was used for that tissue).

For immunohistochemistry evaluation, sections stained for huCD45 were digitally scanned at 20x magnification, using an Aperio scanner (Leica Biosystems). The extent of huCD45 cell infiltration in the tissues was quantified using Halo image analysis software (Indica Labs, Albuquerque, NM, USA). Briefly, the tissue region of interest (ROI) was annotated by the pathologist, targeting the maximal amount of tissue, but excluding large tissue artifacts (debris, folds, etc…) and extraneous tissue. Positive huCD45 staining was quantified, using the Halo Area Quantification algorithm (v.2.1.3), adapted to the staining characteristics of the study. An area-based detection was considered more representative than cell-based quantification, because the intensity of huCD45 staining and the tendency of huCD45-positive cells to form dense clusters made single-cell recognition difficult. The huCD45-positive area was reported as percentage of total tissue area (excluding clear spaces).

Flow cytometry

Flow cytometric analysis was conducted on whole blood from cheek bleeds prior to dosing, and also on blood and spleen from all mice taken at termination, except for those found dead. Upon collection of blood samples, red blood cells (RBC) were lysed first with 1x RBC Lysis Buffer (Invitrogen, Waltham, MA, USA), followed by mouse Fc blocking with TruStain FcX™ (anti-mouse

CD16/32, BioLegend, San Diego, CA, USA) and human Fc blocking with Human TruStain FcX™ (BioLegend) prior to the staining. The spleens were smashed through PBS pre-wet 70-µM cell strainers, followed by RBC lysis and Fc blocking before staining. Single cells were stained with the following anti-human antibodies obtained from BioLegend: CD45 (clone 2D1), CD3 (clone HIT3a), CD8 (clone SK1), CD4 (clone RPA-T4), CD154 (CD40L) (clone 24-31) and CD134 (OX40) (clone Ber-ACT35). Stained samples were run on a BD LSRFortessa™ flow cytometer (BD Biosciences, San Jose, CA, USA). Data were analysed with the Kaluza Analysis Software (Beckman Coulter, Brea, CA, USA). Human cells were phenotyped following the gating strategy presented in Supplementary Figure 3.

Statistical analysis

Data analysis was conducted using GraphPad Prism 8 (GraphPad Software, San Diego, CA, USA). Survival curves were represented with Kaplan-Meier plots and statistical differences calculated using the Mantel-Cox test. A Mixed-effects analysis followed by Sidak's multiple comparisons test was used to evaluate statistical differences between pre-treatment and post-treatment groups. A one-way ANOVA followed by Tukey's multiple comparison was used to evaluate statistical differences between treatment and control groups. Differences in incidence of histologic GvHD lesions between groups were evaluated with chi-square tests.

Results

In vitro functionality of monoclonal antibodies and MEDI8500 targeting PD-1 and CTLA-4

We performed two separate reporter assays to evaluate the *in vitro* potency of the different antibodies blocking both pathways: PD-1/PD-L1 and CTLA-4/CD80&86. In the PD-1 reporter assay, we observed that the potency for human PD-1 reporter blockade of anti-PD-1 mAb as single agent (EC50 = 0.92 nM) was similar to

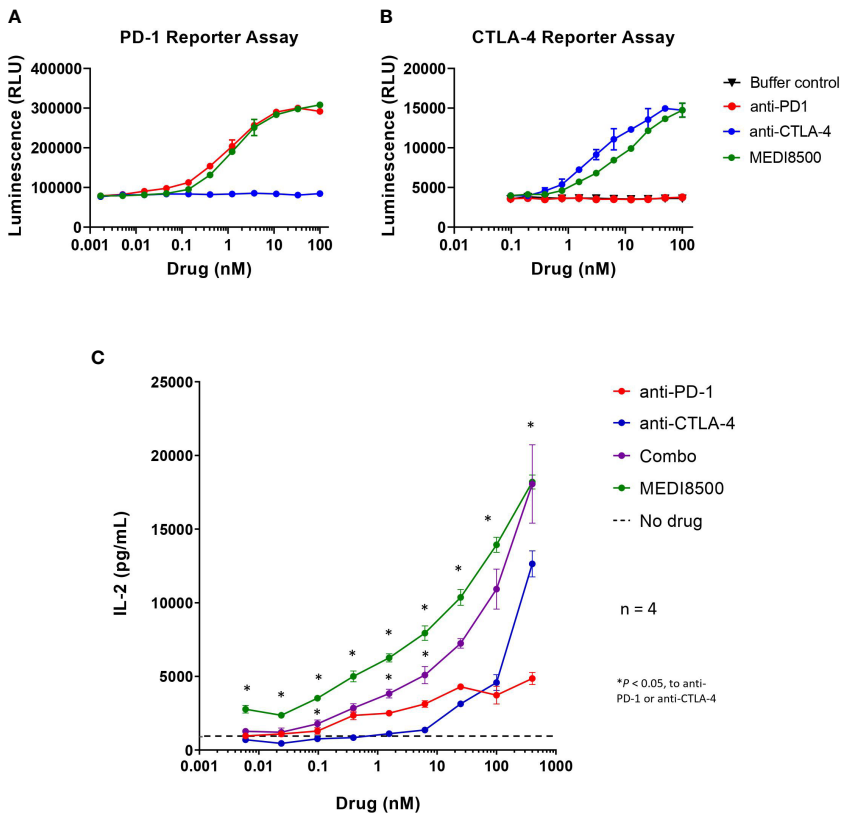

FIGURE 1
Increased *in vitro* potency with antibody combination and MEDI8500 compared to monotherapies **(A)** Bioluminescence levels in a PD-1/PD-L1 blockade bioassay after 5 hours and 40 minutes of incubation with increasing doses (3-fold) of either anti-PD-1, anti-CTLA-4 or MEDI8500. **(B)** Bioluminescence levels in a CTLA-4 blockade bioassay after 6 hours of incubation with increasing doses (3-fold) of either anti-PD-1, anti-CTLA-4 or MEDI8500. Data are represented as Mean ± SD of duplicates in each point. **(C)** Levels of IL-2 secretion by human PBMCs after 72h of *in vitro* treatment with increasing doses (4-fold) of either anti-PD-1, anti-CTLA-4, combination of anti-PD-1 + anti-CTLA-4 or MEDI8500, on an anti-huCD3 + SEB stimulation assay. Data are represented as Mean ± SEM for 4 independent donors. A two-way ANOVA followed by Tukey's multiple comparison was used to evaluate statistical differences between antibody combination or MEDI8500 and single agents at each concentration; statistically significant differences are noted when $*P < 0.05$.

10.3389/fimmu.2023.1107848

that of MEDI8500 (EC50 = 1.30 nM) (Figure 1A). In the CTLA-4 reporter assay, the potency for human CTLA-4 receptor blockade of anti-CTLA-4 mAb as single agent (EC50 = 3.57 nM) was~ 4-fold higher compared to that of MEDI8500 (EC50 = 12.61 nM) (Figure 1B).

Moreover, treatment of primary PBMCs with MEDI8500 significantly increased the levels of IL-2 secreted by PBMCs at all concentrations after 72 hours, compared to the respective single agents (Figure 1C). Similarly, the combination of anti-PD-1 + anti-CTLA-4 mAbs significantly raised the levels of IL-2 secreted at different concentrations compared to the single agents, but to a lesser extent than MEDI8500. No significant differences were observed in the level of IL-2 secretion between MEDI8500 and combination treatment (Figure 1C).

In vivo functionality of monoclonal antibodies and MEDI8500 targeting PD-1 and CTLA-4

Acceleration of GvHD in huNSG mice after immunotherapy treatment was used as an endpoint to evaluate the relative potency of monoclonal & BiSpecific antibodies targeting PD-1 and CTLA-4. Most animals treated with the single agents did not develop symptoms of GvHD (Grade 0) or had mild signs of rough coats and hunching (Grade 0-1) between day 24-46, and the majority survived until the end of the study (12 out of 15 in the anti-PD-1 mAb group and 14 out of 15 in the anti-CTLA-4 mAb group). However, survival was significantly decreased in the anti-PD-1 group compared to vehicle (Figure 2A). In the mice that received the anti-PD-1 + anti-CTLA-4 combination significantly reduced survival was noted compared to the control group, and when compared to the anti-PD-1 or anti-CTLA-4 single agent groups (Figure 2A), with some animals terminated as soon as 11 days after the start of treatment due to the onset of Grade 3 adverse signs, including moderate rough coats and hunching, in addition to weight loss (Supplementary Figure 4), and just 6 out of 20 mice (30%) surviving until the end of the study with mild (Grade 0-1) or moderate (Grade 2) symptoms of GvHD. Similarly, mice in the MEDI8500 group showed a significantly decreased survival compared to the control animals, and animals receiving anti-PD-1 or anti-CTLA-4 as single agents, with mice terminated from day 19 onwards due to development of Grade 3 GvHD phenotype, including moderate rough coats, hunching and emaciation. Just 11 out of 35 mice (31%) survived until the end of the study with mild (Grade 0-1) or moderate (Grade 2) symptoms of GvHD. There was no significant difference in survival between the antibody combination and MEDI8500 groups.

We observed differences in survival rate after treatment between some of the donor HLA types in both the antibody combination (Figure 2B) and MEDI8500 group (Figure 2C). Mice reconstituted with cells from donor 5443 showed a significant reduction in overall survival after treatment with either the antibody combination or

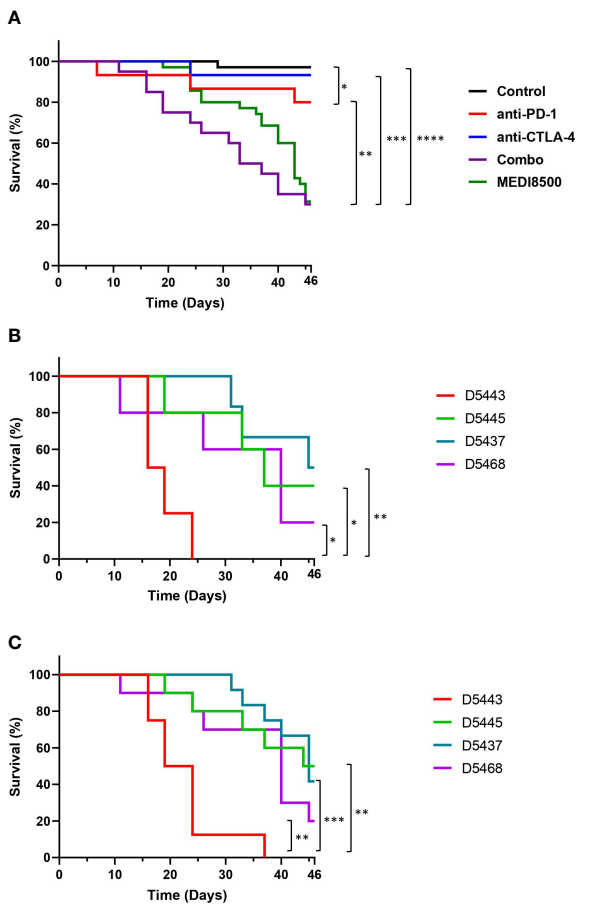

FIGURE 2
Acceleration of GvHD with antibody combination and MEDI8500 compared to monotherapies **(A)** Kaplan-Meier plot showing overall survival in the different groups of treatment. The control (n=35) and MEDI8500 (n=35) groups include data from two independent experiments, while the data for the anti-PD-1 (n=15), anti-CTLA-4 (n=15) and antibody combination (n=20) groups are from a single experiment. **(B)** Survival curves in the antibody combination group depending on the HLA type of the donor. Each donor showed was used to reconstitute 4-6 mice per treatment group. **(C)** Survival curves in MEDI8500 group depending on the HLA type of the donor. Each donor showed was used to reconstitute 4-6 mice per treatment group. The Mantel-cox test was used to assess statistical differences between groups; $^{*}P < 0.05$, $^{**}P < 0.01$, $^{***}P < 0.001$, $^{****}P < 0.0001$.

MEDI8500, with all mice terminated due to adverse GvHD signs Grade 3 between days 16-24 after the start of treatment in the antibody combination group (Figure 2B) or after 16-37 days in MEDI8500 group (Figure 2C). Donor 5443 was unusual, in that this donor was homozygous for a total of 7 out of 9 HLA alleles: HLA-B, HLA-C, HLA-DRB1, DRB4, DQA1, DQB1 and DPA1, with specific HLA alleles more predisposed to autoimmunity (Table 1). By contrast, the other donors were more heterozygous, with at most 4 homozygous alleles, and mice reconstituted with stem cells from more heterozygous donors survived significantly longer with both treatment regimens (Figures 2B, C).

10.3389/fimmu.2023.1107848

Expansion of T cells in humanized mice after administration of PD-1 and CTLA-4 targeting antibodies

Analysis of the percentage of huCD3$^+$ T cell population in dissociated spleen at termination revealed significant T cell expansion in the antibody combination (> 60%) and MEDI8500 (> 55%) groups compared to the control group (~ 20%) and the single agent groups (~ 30%) (Figure 3A). Similarly, the percentages of huCD4$^+$ and huCD8$^+$ T cells were significantly increased solely in the antibody combination and MEDI8500 groups (huCD4$^+$ > 35%; huCD8$^+$ ~ 18%) compared to the control (~ 10%) and single agent groups (Figures 3B, C).

Likewise, a significant increase on the percentage of huCD3$^+$ T cell population was found in blood at termination in the different groups after treatment compared to the pre-treatment levels (Supplementary Figure 5A). This rise in huCD3$^+$ T cells corresponded with a significant increase of circulating huCD4$^+$ and huCD8$^+$ T cells in the antibody combination and MEDI8500 groups after treatment (huCD4$^+$ > 50%; huCD8$^+$ > 20%), when compared to the control and anti-PD-1 groups (Supplementary Figures 5B, C). The percentage of huCD4$^+$ T cells was also significantly higher in the anti-CTLA-4 single agent group (> 35%) after treatment (Supplementary Figure 5B), but not the percentage of huCD8$^+$ T cells (Supplementary Figure 5C).

Activation of T cells in humanized mice after administration of PD-1 and CTLA-4 targeting antibodies

We evaluated the expression levels of different activation markers on human T cells circulating in blood in the different groups of mice at sacrifice. We observed that T cells from mice from the antibody combination and MEDI8500 groups showed a significantly increased percentage of OX40$^+$ (~ 13% and~ 11%, respectively) and CD40L$^+$ (~ 18% and~ 14%) huCD4$^+$ T cells compared to the control group (Figure 4). Similarly, we found a significant increase of huCD8$^+$ T cells expressing these markers in the antibody combination and MEDI8500 groups (OX40$^+$~ 4% and~ 3%, respectively; CD40L$^+$~ 4% and~ 3%, respectively) when compared to control, but the extent of increase in the percentage of cells expressing these markers was lower on huCD8+ T cells than on huCD4$^+$ T cells (Figure 4).

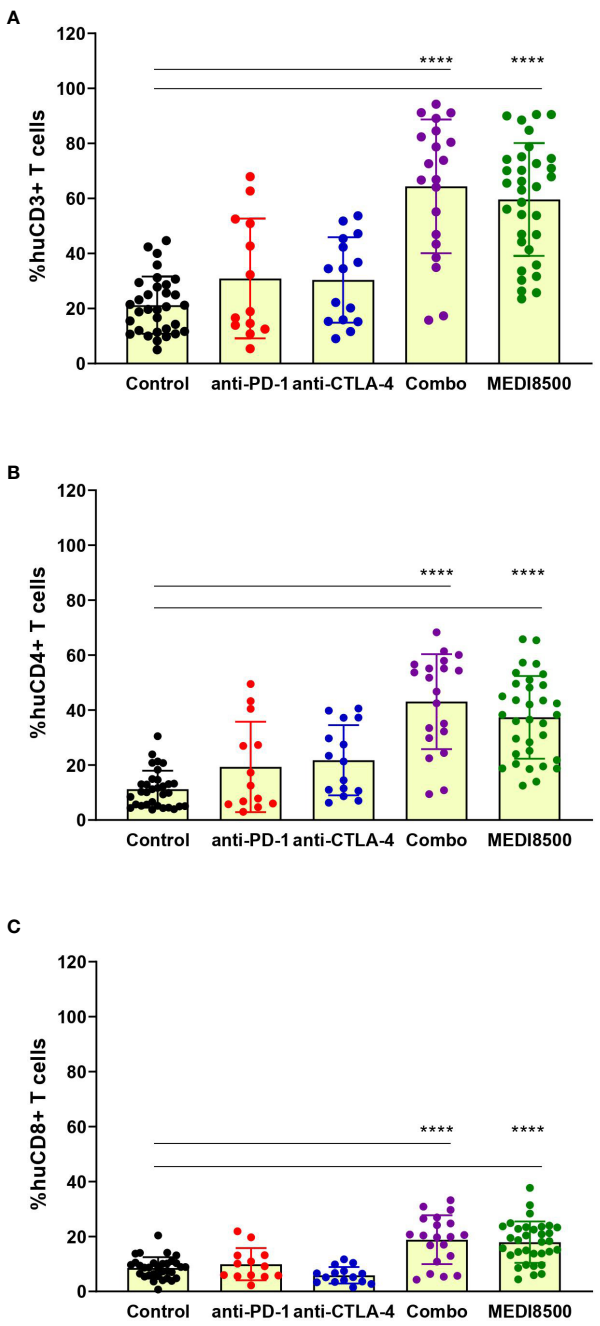

FIGURE 3
Significant expansion of T cells with antibody combination and MEDI8500 compared to monotherapies. Flow cytometry analysis of the percentages of **(A)** huCD3$^+$ T cells, **(B)** huCD4$^+$ T cells and **(C)** huCD8$^+$ T cells in spleen of mice at sacrifice. Data are represented as percentage within huCD45$^+$ population for each individual mouse and as Mean ± SD of all mice in each treatment group. Mice numbers are the same as in Figure 2A. A one-way ANOVA followed by Tukey's multiple comparison was used to evaluate statistical differences between treatment and control groups; ****$P < 0.0001$.

Highest incidence of GvHD lesions after antibody combination or MEDI8500 in humanized mice

Sections of liver, lung and spleen stained with H&E were examined to detect inflammatory changes consistent with GvHD (Figure 5). In the liver (Figure 5A), inflammatory changes consisted mostly of infiltration of the portal spaces by immune cells, predominantly lymphocytes but frequently accompanied by macrophages. This infiltrate often breached the portal limiting plate to extend into the lobular parenchyma, and was occasionally associated with the presence of single necrotic hepatocytes within

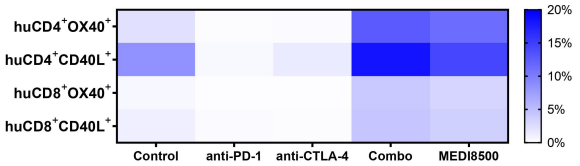

FIGURE 4
Significant activation of T cells with antibody combination and MEDI8500 compared to monotherapies. Percentage of huCD4$^+$ and huCD8$^+$ T cells expressing T cell activation markers in terminal blood of mice in the different groups of treatment. Data were analysed by flow cytometry and represented as mean of all mice in each treatment group. Mice numbers are the same as in Figure 2A. A Mixed-effects analysis followed by Dunnett's multiple comparisons test was used to evaluate statistical differences between control and treated groups. A significant difference (***$P < 0.001$) was noted in the antibody combination and MEDI8500 groups compared to the control group in the percentage of huCD4$^+$OX40$^+$ T cells, huCD8$^+$OX40$^+$ T cells and huCD8$^+$CD40L$^+$ T cells. *$P < 0.05$ was noted in the antibody combination and MEDI8500 groups compared to the control group in the percentage of huCD4$^+$CD40L$^+$ T cells.

the infiltrate. This immune infiltrate was also occasionally observed perivascularly, around centrolobular veins, as well as in random foci in the lobular parenchyma. In the more severe cases the immune infiltrate was very abundant, with miliary foci throughout the tissue. In some cases the infiltrate had a distinctly granulomatous component, with prominent macrophages and multinucleated giant cells.

In the lung (Figure 5A), the observed inflammatory changes consisted predominantly of perivascular immune cell infiltrates around small and medium sized vessels, sometimes associated with leukocyte margination in the vascular lumen and focal intimal immune cell infiltration. The immune cells were predominantly lymphocytes, with the macrophage component observed in the liver not as prominent in the lung lesion. The alveolar parenchyma around the vessels with perivascular infiltrates often contained small foci of interstitial immune cell infiltration. In the more severe cases, the perivascular infiltrates formed thick cuffs, with the intima markedly thickened by immune cells, and the surrounding parenchyma showing significant interstitial infiltration.

In the spleen (Figure 5A), the changes were variable. Expansion of the periarteriolar white pulp areas by a dense population of immune cells, mostly lymphocytes, was frequently observed, but in some cases significant numbers of macrophages were also present. Another frequently observed change was infiltration of the red pulp area with small nodules of macrophages and occasional multinucleate giant cells; in more severe cases this infiltration became almost diffuse throughout the red pulp, significantly expanding the spleen, and associated with areas of necrosis. Often, a significant and variable degree of extra-medullary hematopoiesis (EMH) was observed. This is a common observation in mouse spleen, and this was not interpreted as associated with GvHD. However, individual variability in EMH likely had a confounding effect on relative huCD45$^+$ area measurements.

The incidence of mice with GvHD lesions in at least one tissue and the severity score of GvHD lesions per group are shown in Figure 5B. The incidence of histologic lesions was clearly higher than the incidence of pre-mortem clinical signs. Overall, there were more frequent GvHD lesions in the anti-PD-1 and anti-CTLA-4 groups than in the vehicle group, and more frequent lesions in the antibody combination and MEDI8500 groups than in the vehicle and monotherapy groups. A similar pattern was noted in the total lesion severity scores, with the antibody combination and MEDI8500 groups showing higher mean scores than the monotherapy groups, and the latter groups showing higher severity scores than the vehicle group. This overall pattern was preserved when animals without lesions were excluded. This indicates that, when present, lesions tended to be more severe in the antibody combination and MEDI8500 groups than in the monotherapy and vehicle groups. In the monotherapy groups, when present, lesions were more severe in the anti-PD-1 group than in the vehicle group, but there was no statistically significant difference in lesion severity between the CTLA-4 group and vehicle. Finally, there were no differences in lesion incidence or overall severity between the antibody combination and MEDI8500 groups. Potential effect of donors on the incidence and severity of GvHD lesions was difficult to reliably assess, because of the small number of animals per donor within each treatment group, and the individual variability in GvHD lesion scores.

Immunohistochemical staining of liver, lung and spleen section with a huCD45-specific antibody was carried out in an attempt to quantify GvHD-linked immune cell infiltration, and compare these results to histopathologic evaluation (Figure 5C and Supplementary Figure 6). Significant increases in huCD45 staining were noted in the livers of some treatment groups, mainly the antibody combination and MEDI8500 groups which showed significantly higher huCD45 infiltration than the vehicle and monotherapy groups. In the lung, the anti-CTLA-4, antibody combination and MEDI8500 groups showed higher huCD45 staining than the vehicle group, with MEDI8500 group showing the most marked increase in huCD45 staining. These results tended to mirror the results from the GvHD lesion scores, although GvHD lesion scores tended to show more statistically significant differences between groups than huCD45 staining (Supplementary Table 1). In the spleen, some differences in huCD45 staining were noted between groups, but these did not correlate with GvHD lesion severity, and therefore huCD45 staining was not helpful in quantifying GvHD lesions in the spleen (Supplementary Figure 6).

Discussion

In this study we have analysed the *in vitro* functionality of the immune checkpoint inhibitors anti-PD-1 and anti-CTLA-4 antibodies as either single agents or in combination, along with MEDI8500, which is an anti-PD-1/CTLA-4 BiSpecific antibody. PD-1 and CTLA-4 are immune checkpoint inhibitors that provide negative signals for T cell activation after interaction with their

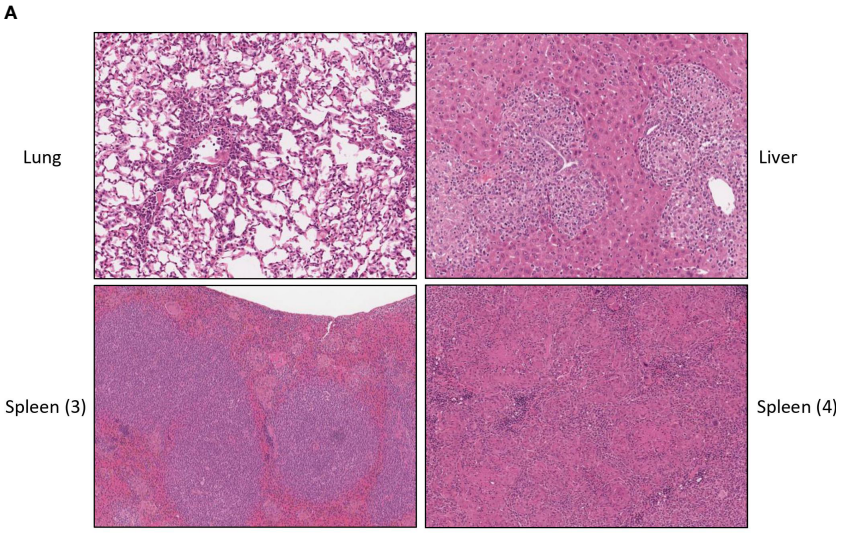

B

	GvHD lesion score					GvHD incidence	
	Liver (0-4)	Lung (0-4)	Spleen (0-4)	Total (0-12) (all mice)	Total (0-12) (affected mice)	affected/ total	%
Vehicle	0.1 ± 0.3	0.3 ± 0.5	0.2 ± 0.6	0.7 ± 1.1	2.0 ± 1.1	11/34	32.4
anti-PD-1	1.2 ± 1.4[a]	1.2 ± 1.2[a]	1.1 ± 1.3	3.5 ± 3.7[a]	5.2 ± 3.1[a]	8/13	61.5
anti-CTLA-4	1.1 ± 1.1[a]	1.4 ± 1.2[a]	1.2 ± 0.9[a]	3.7 ± 2.9[a]	3.9 ± 2.4	12/15	80
anti-PD-1+CTLA-4 combo	2.6 ± 0.9[b]	1.8 ± 1.2[a]	2.1 ± 1.4[a]	6.5 ± 2.8[b]	6.5 ± 2.8[b]	20/20	100
MEDI8500	2.4 ± 1.2[b]	2.2 ± 1.1[c]	2.4 ± 1.3[b]	7.0 ± 2.5[b]	7.0 ± 2.5[d]	33/33	100

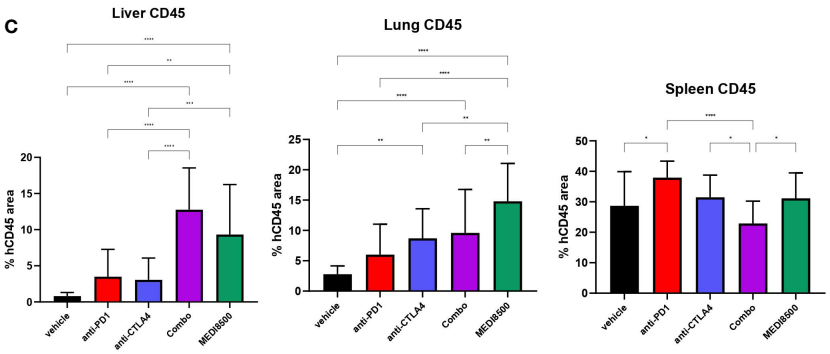

FIGURE 5
Greater GvHD lesion score with antibody combination and MEDI8500 compared to monotherapies. **(A)** Representative images of GvHD lesions in tissues: (1) lung, with vascular intimal, perivascular and interstitial lymphocytic infiltration (20x magnification) (2) Liver, with portal infiltration with lymphocytes and macrophages extending to the lobular parenchyma (20x magnification) (3) spleen, with expansion of white pulp by lymphocytes, and small macrophage nodules in the red pulp (10x magnification) (4) spleen, with diffuse granulomatous infiltration with coalescing macrophage nodules (12x magnification) **(B)** Histopathologic scoring of GvHD lesions, shown as mean ± SD per treatment group. Total score is sum of liver, lung and spleen scores. Mean total scores are calculated either for the whole group (including animals without any lesions), or excluding the animals without lesions. [a] significant difference (*$P < 0.05$) with vehicle, [b] significant difference (*$P < 0.05$) with vehicle, anti-PD-1 and anti-CTLA-4, [c] significant difference (*$P < 0.05$) with vehicle and anti-PD-1, [d] significant difference (*$P < 0.05$) with vehicle and anti-CTLA-4 **(C)** huCD45 positive cell infiltration in liver, lung and spleen, expressed as proportion of total tissue area. **P<0.01, ***P<0.001, ****P<0.0001.

ligands, helping to maintain immune tolerance (5). In the clinic, when anti-PD-1 and anti-CTLA-4 mAbs are administered as monotherapy, patients who respond can have significantly increased survival. However, only a proportion of patients respond to these monotherapies (28), hence there was rationale for combining PD-1 and CTLA-4 inhibitors, as it could lead to synergistic increases in T cell activation and patient response rate (28). The combination of anti-PD-1 and anti-CTLA-4 mAbs has shown improved responses in the clinic and a sustained survival benefit, compared to those in the monotherapy groups (8–10, 29–31), and is approved for different types of solid cancers (32). However these combinations can lead to an increase in immune related adverse events. Development of an anti-PD-1/CTLA-4 BiSpecific antibody is a novel approach aiming to release the full potential of the combination into a single molecule. MEDI8500 has a similar potency against human PD-1 as the anti-PD-1 mAb, but it

has a lower affinity for the CTLA-4 receptor and a 4-fold lower potency than the anti-CTLA-4 mAb. The first-in-class anti-PD-1/CTLA-4 bispecific to be recently approved for the treatment of advanced cervical cancer has been Cadonilimab (33), which is a quadrivalent bispecific with similar format to MEDI8500. Similarly, MEDI5752, which is a monovalent anti-PD-1/CTLA-4 BiSpecific (34), is currently under evaluation in patients and durable responses have been seen across diverse tumour types (35–37). In this line, our *in vitro* data demonstrate that both the anti-PD-1 and anti-CTLA-4 combination and MEDI8500 induced increased activity on primary immune cells compared to the single agents treatment.

We next evaluated the *in vivo* potency of anti-PD-1 and anti-CTLA-4 mAbs as monotherapies, combination and MEDI8500 in non tumour-bearing humanized mice, using GvHD development as a potential predictor of toxicity and potency of these immunotherapies and combinations. Our model used mice reconstituted with CD34$^+$ HSCs cells derived from donors with HLA alleles predisposed to autoimmune disorders. The use of HLA donors predisposed to autoimmunity has previously been described for studies of the pathogenesis of GvHD (25, 26). For our purposes, use of such donors was designed to increase the incidence of GvHD after treatment with immunotherapies and potentially shorten the study duration. However, for other study purposes these HLA type donors should be avoided in order to lengthen the survival of the humanized mice.

As expected, we observed a significantly lower survival rate due to accelerated development of GvHD in the checkpoint inhibitor treated groups compared to the controls, consistent with enhanced immune activation in humanized mice treated with these agents. The anti-PD-1 + anti-CTLA-4 combination and MEDI8500 groups showed lower survival, and accelerated onset of clinical GvHD compared to vehicle and to the single agents anti-PD-1 and anti-CTLA-4, and generally higher GvHD lesion levels compared to the single agent treated mice.

Certain HLA types are more likely to be susceptible to autoimmune disorders, viral infections or development of cancer (26, 38). Patients with autoimmune disorders treated with immune checkpoint inhibitors may show aggravation of their disease, more severely when given in combination (39). In our study, there was evidence of an effect of the donor HLA type on the onset and severity of GvHD reactions. Specifically, mice reconstituted with cells from one homozygous HLA type donor (D5443) appeared to have lower survival rate and acceleration of GvHD development compared with mice reconstituted with HLA donors with higher heterozygosity, in response to anti-PD-1 + anti-CTLA-4 combination and MEDI8500.

Flow cytometric analysis of circulating human lymphocyte profiles in the mice revealed a significant increase in the percentage of huCD3$^+$ T cells in all groups, including the controls. This increase in controls was likely due to a baseline immune activation associated with incipient development of GvHD, as was seen histologically in several of the control animals. The choice of human cell donors predisposed to autoimmunity would be expected to lead to quicker development of GvHD reactions even in the absence of immune stimulatory drugs, and therefore this should be carefully considered when interpreting data from this model; effect of administered drugs should be interpreted in light of the baseline immune activation present. This was the case in this study, where we saw a significant increase in the percentage of huCD3$^+$, huCD4$^+$ and huCD8$^+$ T cells in groups treated with either the anti-PD-1 + anti-CTLA-4 combination or MEDI8500, compared to the control or anti-PD-1 or anti-CTLA-4 monotherapy groups. PD-1 and CTLA-4 act at different stages of T cell activation, thus, combined blockade of both immune checkpoint inhibitors has synergistic effects on T cell activation and proliferation, as aforementioned (28). The increase in percentage of circulating human lymphocytes has been reported previously after treatment of humanized mice with either anti-PD-1 or anti-CTLA-4 mAbs (40, 41), and it likely reflects an increased production of these cells as a response to induction of GvHD reactions in various tissues by PD-1 and CTLA-4 blockade. Furthermore, it was also associated with an increase in T cell activation. We used 2 different cell markers associated with T cell activation: OX40, which is not constitutively expressed on resting naïve T cells and expressed after 24 to 72 hours following activation (42); and CD40L, which is predominantly expressed by activated huCD4$^+$ T cells shortly after T cell activation (43). We observed a significant increase in activated T cells in terminal blood with antibody combination and MEDI8500 treatments, compared to vehicle and monotherapy groups.

Histologic evaluation of liver, lung and spleen confirmed the presence of GvHD type lesions in these mice. This evaluation not only revealed lesions in mice culled prematurely due to adverse clinical signs, but also in mice that survived until the end of the study. However mice that were culled prematurely showed more severe lesions, an increased GvHD score and greater influx of huCD45+ based on IHC analysis.

Although some of the control group animals had GvHD lesions, these were mild, and not associated with adverse clinical signs or body weight loss (Supplementary Figure 4). This early development of GvHD was likely related to the use of donors predisposed to autoimmunity, and there was some evidence for donor-related differences in the incidence of lesions. The presence of such lesions underscores the need for careful study design when using such a model, with a need to use multiple donors and distribute donors evenly throughout the treatment groups to avoid confounding effects of variable degrees of donor predisposition to GvHD.

The histopathological lesions observed in these mice were consistent with those previously reported for humanized mice (14, 44) and with some of the changes reported for chronic human GvHD (45, 46), although overall the mouse lesions tended to be less variable than the fairly broad spectrum of changes reported in humans. This is not surprising, considering the consistent and well-controlled methodology, limited genetic variability of the host mice, and use of a limited pool of donors in this model compared to the myriad possible variations in the human population. One frequent feature of the mouse lesions was

the presence of a significant, often abundant, macrophage component within the immune cell infiltrate of the liver or spleen; in some cases macrophages were the dominant immune population, forming granulomatous nodular infiltrates. This has also been previously reported in this model (14), but it is unclear why this cell population becomes stimulated to this extent, and why it is prominent in some mice and not others. There did not appear to be an association of this observation with specific treatments or donors.

In order to be able to compare different treatments based on histopathology, we evaluated the incidence of GvHD lesions per group, and developed a semi-quantitative histopathologic scoring system based on lesion severity. Both incidence and severity showed clear differences between groups, with the severity score providing more granularity to the analysis, and better differentiation between groups. When considering the total severity score (combined scores for the liver, lung and spleen), significant differences were evident between the anti-PD-1 or anti-CTLA-4 monotherapy groups and the control group, as well as between the antibody combination or MEDI8500 groups and the monotherapy and vehicle groups. This confirmed the additive immune-stimulatory activity of anti-PD-1 and and-CTLA-4, when combined as single agents or as a BiSpecific. We could not detect clear differences in activity between the antibody combination and MEDI8500 treatment.

Immunohistochemical staining for huCD45 was applied to the liver, lung and spleen, with image analysis quantitation of positive cells, in an effort to develop a quantitative tool for GvHD evaluation. This proved a useful way to obtain more quantitative and objective data on human immune cell infiltration in liver and lung, with huCD45 positivity generally mirrorring the GvHD lesion scores; however it proved to be somewhat less sensitive than histopathologic evaluation in identifying the early, milder lesions. This is most likely because immune cell infiltration in GvHD lesions must attain a threshold in order to be detectable above of the normal baseline level of huCD45 cells in tissues, which are either circulating through the vasculature or resident tissue immune cells. In line with this notion, liver and lung huCD45 staining in the antibody combination and MEDI8500 groups, which had higher lesion severity scores, clearly was significantly increased when compared to controls and monotherapy groups, whilst huCD45 staining in monotherapy groups were generally not high enough to show statistically significant differences from controls, despite presence of mild histopathologic lesions. In the spleen, huCD45 staining did not consistently detect GvHD lesions. This was likely due to the fact that human cells administered to these mice would be expected to home in to normal lymphoid tissue sites like the spleen, and therefore a large proportion of cells within the spleen of reconstituted mice would normally be huCD45^{+} in the absence of any GvHD reaction.

In summary, evaluation of mice with a humanized immune system showed it was a useful model for comparing the *in vivo* potency and safety profile of PD-1 and CTLA-4 based immuno-oncology therapeutics. Analysis of blood and tissue responses provided quantitative and semi-quantitative data with sufficient granularity to differentiate the potency of different treatment modalities. Induction of GvHD in these mice was a consistent endpoint for demonstration of immunotherapeutic potency. This aggravated antigenic T-cell response against host due to checkpoint blockade is a surrogate of the antigenic T-cell response that can be potent in targeting cancer cells or any other foreign antigens. Histopathologic evaluation of liver, lung and spleen was the most sensitive indicator of GvHD, compared to huCD45 IHC or clinical observations. Administration of anti-PD-1 or anti-CTLA-4 as single agents induced a significant degree of immune stimulation, but significantly less than a combination of the two or MEDI8500. However, the results in the monotherapy groups do not completely correlate with the safety profile of anti-CTLA-4 mAbs in the clinic, where these therapies have much more severe immune mediated adverse reactions than anti-PD-1 mAbs when given as monotherapies (47). Taken together, the use of humanized mice may be a useful platform to evaluate the function of human immunotherapies, where no other preclinical models exist. These models may also provide information on the potential for immune related adverse reactions with immunotherapies combination, but like all animal models, this model has limitations which must be understood and improved upon to increase their translational predictivity to the clinical situation.

Data availability statement

The original contributions presented in the study are included in the article/Supplementary Material. Further inquiries can be directed to the corresponding authors.

Ethics statement

The animal study was reviewed and approved by AstraZeneca ethics review.

Author contributions

RS, SM and LH contributed to conception and design of the *in vivo* study. J-ML performed the histology evaluation. ME and GB performed the *in vitro* experiments. SD surpevised the *in vitro* experiments and project development. AM-C performed data analysis and interpretation. AM-C wrote the first draft of the manuscript. J-ML and RS wrote sections of the manuscript. All authors contributed to manuscript revision, read, and approved the submitted version.

Funding

The authors declare that this study received funding from AstraZeneca. The funder was not involved in the study design, collection, analysis, interpretation of data, the writing of this article, or the decision to submit it for publication.

Acknowledgments

We thank Dr Ann E. Lin, Dr Dan Duan, Ian Hines-Ike, Eunmi Hwang and their technical team at CrownBio in San Diego (USA) for running the *in vivo* studies, collecting and analysing data and generating the study reports.

Conflict of interest

AM-C, J-ML, ME, GB, SD, LH, SM, and RS report being AstraZeneca employees during the conduct of the submitted work. LH is currently an employee at ADC therapeutics.

Publisher's note

All claims expressed in this article are solely those of the authors and do not necessarily represent those of their affiliated organizations, or those of the publisher, the editors and the reviewers. Any product that may be evaluated in this article, or claim that may be made by its manufacturer, is not guaranteed or endorsed by the publisher.

Supplementary material

The Supplementary Material for this article can be found online at: https://www.frontiersin.org/articles/10.3389/fimmu.2023.1107848/full#supplementary-material

References

1. Duffy AG, Ulahannan SV, Makorova-Rusher O, Rahma O, Wedemeyer H, Pratt D, et al. Tremelimumab in combination with ablation in patients with advanced hepatocellular carcinoma. *J Hepatol* (2017) 66:545–51. doi: 10.1016/j.jhep.2016.10.029

2. Sahni S, Valecha G, Sahni A. Role of anti-PD-1 antibodies in advanced melanoma: The era of immunotherapy. *Cureus* (2018) 10:e3700–0. doi: 10.7759/cureus.3700

3. Sharma P, Sohn J, Shin SJ, Oh DY, Keam B, Lee HJ, et al. Efficacy and tolerability of tremelimumab in locally advanced or metastatic urothelial carcinoma patients who have failed first-line platinum-based chemotherapy. *Clin Cancer Res* (2020) 26:61–70. doi: 10.1158/1078-0432.CCR-19-1635

4. Bockorny B, Semenisty V, Macarulla T, Borazanci E, Wolpin BM, Stemmer SM, et al. BL-8040, a CXCR4 antagonist, in combination with pembrolizumab and chemotherapy for pancreatic cancer: the COMBAT trial. *Nat Med* (2020) 26:878–85. doi: 10.1038/s41591-020-0880-x

5. Pardoll DM. The blockade of immune checkpoints in cancer immunotherapy. *Nat Rev Cancer* (2012) 12:252–64. doi: 10.1038/nrc3239

6. Friese C, Harbst K, Borch TH, Westergaard MCW, Pedersen M, Kverneland A, et al. CTLA-4 blockade boosts the expansion of tumor-reactive CD8+ tumor-infiltrating lymphocytes in ovarian cancer. *Sci Rep* (2020) 10:3914. doi: 10.1038/s41598-020-60738-4

7. Zhao Y, Lee CK, Lin C-H, Gassen RB, Xu X, Huang Z, et al. PD-L1:CD80 cis-heterodimer triggers the Co-stimulatory receptor CD28 while repressing the inhibitory PD-1 and CTLA-4 pathways. *Immunity* (2019) 51:1059–73.e9. doi: 10.1016/j.immuni.2019.11.003

8. Motzer RJ, Tannir NM, McDermott DF, Arén Frontera O, Melichar B, Choueiri TK, et al. Nivolumab plus ipilimumab versus sunitinib in advanced renal-cell carcinoma. *N Engl J Med* (2018) 378:1277–90. doi: 10.1056/NEJMoa1712126

9. Larkin J, Chiarion-Sileni V, Gonzalez R, Grob J-J, Rutkowski P, Lao CD, et al. Five-year survival with combined nivolumab and ipilimumab in advanced melanoma. *N Engl J Med* (2019) 381:1535–46. doi: 10.1056/NEJMoa1910836

10. Hellmann MD, Paz-Ares L, Bernabe Caro R, Zurawski B, Kim S-W, Carcereny Costa E, et al. Nivolumab plus ipilimumab in advanced non–Small-Cell lung cancer. *N Engl J Med* (2019) 381:2020–31. doi: 10.1056/NEJMoa1910231

11. Mosely SIS, Prime JE, Sainson RCA, Koopmann J-O, Wang DYQ, Greenawalt DM, et al. Rational selection of syngeneic preclinical tumor models for immunotherapeutic drug discovery. *Cancer Immunol Res* (2017) 5:29–41. doi: 10.1158/2326-6066.CIR-16-0114

12. Bareham B, Georgakopoulos N, Matas-Céspedes A, Curran M, Saeb-Parsy K. Modeling human tumor-immune environments *in vivo* for the preclinical assessment of immunotherapies. *Cancer Immunol Immunother* (2021) 70:2737–50. doi: 10.1007/s00262-021-02897-5

13. Matas-Céspedes A, Brown L, Mahbubani KT, Bareham B, Higgins J, Curran M, et al. Use of human splenocytes in an innovative humanised mouse model for prediction of immunotherapy-induced cytokine release syndrome. *Clin Transl Immunol* (2020) 9:e1202. doi: 10.1002/cti2.1202

14. Curran M, Mairesse M, Matas-Céspedes A, Bareham B, Pellegrini G, Liaunardy A, et al. Recent advancements and applications of human immune system mice in preclinical immuno-oncology. *Toxicol Pathol* (2020) 48:302–16. doi: 10.1177/0192623319886304

15. De La Rochere P, Guil-Luna S, Decaudin D, Azar G, Sidhu SS, Piaggio E. Humanized mice for the study of immuno-oncology. *Trends Immunol* (2018) 39:748–63. doi: 10.1016/j.it.2018.07.001

16. Pearson T, Greiner DL, Shultz LD. Creation of "Humanized" mice to study human immunity. *Curr Protoc Immunol* (2008) 81:15.21.1–15.21.21. doi: 10.1002/0471142735.im1521s81

17. Ito M, Hiramatsu H, Kobayashi K, Suzue K, Kawahata M, Hioki K, et al. NOD/SCID/γnull mouse: an excellent recipient mouse model for engraftment of human cells. *Blood* (2002) 100:3175 LP – 3182. doi: 10.1182/blood-2001-12-0207

18. Shultz LD, Lyons BL, Burzenski LM, Gott B, Chen X, Chaleff S, et al. Human lymphoid and myeloid cell development in NOD/LtSz-scid IL2Rγnull mice engrafted with mobilized human hemopoietic stem cells. *J Immunol* (2005) 174:6477 LP – 6489. doi: 10.4049/jimmunol.174.10.6477

19. Pflumio F, Izac B, Katz A, Shultz LD, Vainchenker W, Coulombel L. Phenotype and function of human hematopoietic cells engrafting immune- deficient CB17-severe combined immunodeficiency mice and nonobese diabetic-severe combined immunodeficiency mice after transplantation of human cord blood mononuclear cells. *Blood* (1996) 88:3731–40. doi: 10.1182/blood.V88.10.3731.bloodjournal88103731

20. Lapidot T, Pflumio F, Doedens M, Murdoch B, Williams DE, Dick JE. Cytokine stimulation of multilineage hematopoiesis from immature human cells engrafted in SCID mice. *Sci (80-)* (1992) 255:1137 LP – 1141. doi: 10.1126/science.1372131

21. Holyoake TL, Nicolini FE, Eaves CJ. Functional differences between transplantable human hematopoietic stem cells from fetal liver, cord blood, and adult marrow. *Exp Hematol* (1999) 27:1418–27. doi: 10.1016/S0301-472X(99)00078-8

22. Brehm MA, Cuthbert A, Yang C, Miller DM, DiIorio P, Laning J, et al. Parameters for establishing humanized mouse models to study human immunity: analysis of human hematopoietic stem cell engraftment in three immunodeficient strains of mice bearing the IL2rgamma(null) mutation. *Clin Immunol* (2010) 135:84–98. doi: 10.1016/j.clim.2009.12.008

23. André MC, Erbacher A, Gille C, Schmauke V, Goecke B, Hohberger A, et al. Long-term human CD34+ stem cell-engrafted nonobese Diabetic/SCID/IL-2Rγnull mice show impaired CD8+ T cell maintenance and a functional arrest of immature NK cells. *J Immunol* (2010) 185:2710 LP – 2720. doi: 10.4049/jimmunol.1000583

24. Lee JY, Han A-R, Lee DR. T Lymphocyte development and activation in humanized mouse model. *Dev Reprod* (2019) 23:79–92. doi: 10.12717/DR.2019.23.2.079

25. Greenblatt MB, Vrbanac V, Tivey T, Tsang K, Tager AM, Aliprantis AO. Graft versus host disease in the bone marrow, liver and thymus humanized mouse model. *PLoS One* (2012) 7:e44664. doi: 10.1371/journal.pone.0044664

26. Sonntag K, Eckert F, Welker C, Müller H, Müller F, Zips D, et al. Chronic graft-versus-host-disease in CD34+-humanized NSG mice is associated with human susceptibility HLA haplotypes for autoimmune disease. *J Autoimmun* (2015) 62:55–66. doi: 10.1016/j.jaut.2015.06.006

27. Manikwar P, Mulagapati SHR, Kasturirangan S, Moez K, Rainey GJ, Lobo B. Characterization of a novel bispecific antibody with improved conformational and chemical stability. *J Pharm Sci* (2020) 109:220–32. doi: 10.1016/j.xphs.2019.06.025

28. Rotte A, Jin JY, Lemaire V. Mechanistic overview of immune checkpoints to support the rational design of their combinations in cancer immunotherapy. *Ann Oncol* (2018) 29:71–83. doi: 10.1093/annonc/mdx686

29. Overman MJ, Lonardi S, Wong KYM, Lenz HJ, Gelsomino F, Aglietta M, et al. Durable clinical benefit with nivolumab plus ipilimumab in DNA mismatch repair-deficient/microsatellite instability-high metastatic colorectal cancer. *J Clin Oncol* (2018) 36:773–9. doi: 10.1200/JCO.2017.76.9901

30. Hellmann MD, Ciuleanu T-E, Pluzanski A, Lee JS, Otterson GA, Audigier-Valette C, et al. Nivolumab plus ipilimumab in lung cancer with a high tumor mutational burden. *N Engl J Med* (2018) 378:2093–104. doi: 10.1056/NEJMoa1801946

31. Hodi FS, Chiarion-Sileni V, Gonzalez R, Grob JJ, Rutkowski P, Cowey CL, et al. Nivolumab plus ipilimumab or nivolumab alone versus ipilimumab alone in advanced melanoma (CheckMate 067): 4-year outcomes of a multicentre, randomised, phase 3 trial. *Lancet Oncol* (2018) 19:1480–92. doi: 10.1016/S1470-2045(18)30700-9

32. Lee JB, Kim HR, Ha S-J. Immune checkpoint inhibitors in 10 years: Contribution of basic research and clinical application in cancer immunotherapy. *Immune Netw* (2022) 22(1):e2. doi: 10.4110/in.2022.22.e2

33. Keam SJ. Cadonilimab: First approval. *Drugs* (2022) 82:1333–9. doi: 10.1007/s40265-022-01761-9

34. Dovedi SJ, Elder MJ, Yang C, Sitnikova SI, Irving L, Hansen A, et al. Design and efficacy of a monovalent bispecific PD-1/CTLA4 antibody that enhances CTLA4 blockade on PD-1+ activated T cells. *Cancer Discovery* (2021) 11:1100–17. doi: 10.1158/2159-8290.CD-20-1445

35. Albiges L, Medina Rodriguez L, Kim S-W, Im S-A, Carcereny E, Rha SY, et al. Safety and clinical activity of MEDI5752, a PD-1/CTLA-4 bispecific checkpoint inhibitor, as monotherapy in patients (pts) with advanced renal cell carcinoma (RCC): Preliminary results from an FTIH trial. *J Clin Oncol* (2022) 40:107. doi: 10.1200/JCO.2022.40.16_suppl.107

36. MEDI5752 suppresses two immune checkpoints. *Cancer Discovery* (2022) 12:1402. doi: 10.1158/2159-8290.CD-NB2022-0030

37. Tran B, Voskoboynik M, Kim S-W, Lemech C, Carcereny E, Rha SY, et al. Abstract CT016: MEDI5752, a novel PD-1/CTLA-4 bispecific checkpoint inhibitor for advanced solid tumors: First-in-human study. *Cancer Res* (2022) 82:CT016–6. doi: 10.1158/1538-7445.AM2022-CT016

38. Crux NB, Elahi S. Human leukocyte antigen (HLA) and immune regulation: How do classical and non-classical HLA alleles modulate immune response to human immunodeficiency virus and hepatitis c virus infections? *Front Immunol* (2017) 8:1–26. doi: 10.3389/fimmu.2017.00832

39. Kennedy LC, Bhatia S, Thompson JA, Grivas P. Preexisting autoimmune disease: Implications for immune checkpoint inhibitor therapy in solid tumors. *JNCCN J Natl Compr Cancer Netw* (2019) 17:750–7. doi: 10.6004/jnccn.2019.7310

40. Al-Khami AA, Youssef S, Abdiche Y, Nguyen H, Chou J, Kimberlin CR, et al. Pharmacologic properties and preclinical activity of sasanlimab, a high-affinity engineered anti-human PD-1 antibody. *Mol Cancer Ther* (2020) 19:2105–16. doi: 10.1158/1535-7163.MCT-20-0093

41. Gao C, Gardner D, Theobalds M-C, Hitchcock S, Deutsch H, Amuzie C, et al. Cytotoxic T lymphocyte antigen-4 regulates development of xenogenic graft versus host disease in mice *via* modulation of host immune responses induced by changes in human T cell engraftment and gene expression. *Clin Exp Immunol* (2021) 206:422–38. doi: 10.1111/cei.13659

42. Croft M. Co-Stimulatory members of the TNFR family: Keys to effective T-cell immunity? *Nat Rev Immunol* (2003) 3:609–20. doi: 10.1038/nri1148

43. Elmetwali T, Salman A, Wei W, Hussain SA, Young LS, Palmer DH. CD40L membrane retention enhances the immunostimulatory effects of CD40 ligation. *Sci Rep* (2020) 10:1–15. doi: 10.1038/s41598-019-57293-y

44. Lockridge JL, Zhou Y, Becker YA, Ma S, Kenney SC, Hematti P, et al. Mice engrafted with human fetal thymic tissue and hematopoietic stem cells develop pathology resembling chronic graft-versus-host disease. *Biol Blood marrow Transplant J Am Soc Blood Marrow Transplant* (2013) 19:1310–22. doi: 10.1016/j.bbmt.2013.06.007

45. Quaglia A, Duarte R, Patch D, Ngianga-Bakwin K, Dhillon AP. Histopathology of graft versus host disease of the liver. *Histopathology* (2007) 50:727–38. doi: 10.1111/j.1365-2559.2007.02679.x

46. Khurshid I, Anderson LC. Non-infectious pulmonary complications after bone marrow transplantation. *Postgrad Med J* (2002) 78:257–62. doi: 10.1136/pmj.78.919.257

47. Karimi A, Alilou S, Mirzaei HR. Adverse events following administration of anti-CTLA4 antibody ipilimumab. *Front Oncol* (2021) 11:624780. doi: 10.3389/fonc.2021.624780

frontiers | Frontiers in Immunology

TYPE Review
PUBLISHED 10 March 2023
DOI 10.3389/fimmu.2023.1095388

Check for updates

OPEN ACCESS

EDITED BY
Rajat Varma,
AstraZeneca, United States

REVIEWED BY
Michael W. Melkus,
Texas Tech University Health Science Center Amarillo, United States
Virginia Brancato,
Italian Institute of Technology (IIT), Italy

*CORRESPONDENCE
Jie Lei
leijiemd@163.com
Yanlu Xiong
xiong21@fmmu.edu.cn
Tao Jiang
jiangtaochest@163.com

†These authors have contributed equally to this work

SPECIALTY SECTION
This article was submitted to Cancer Immunity and Immunotherapy, a section of the journal Frontiers in Immunology

RECEIVED 11 November 2022
ACCEPTED 20 February 2023
PUBLISHED 10 March 2023

CITATION
Zhou Y, Xia J, Xu S, She T, Zhang Y, Sun Y, Wen M, Jiang T, Xiong Y and Lei J (2023) Experimental mouse models for translational human cancer research. *Front. Immunol.* 14:1095388. doi: 10.3389/fimmu.2023.1095388

COPYRIGHT
© 2023 Zhou, Xia, Xu, She, Zhang, Sun, Wen, Jiang, Xiong and Lei. This is an open-access article distributed under the terms of the Creative Commons Attribution License (CC BY). The use, distribution or reproduction in other forums is permitted, provided the original author(s) and the copyright owner(s) are credited and that the original publication in this journal is cited, in accordance with accepted academic practice. No use, distribution or reproduction is permitted which does not comply with these terms.

Experimental mouse models for translational human cancer research

Yinxi Zhou†, Jinghua Xia†, Shuonan Xu†, Tao She†, Yanning Zhang, Ying Sun, Miaomiao Wen, Tao Jiang*, Yanlu Xiong* and Jie Lei*

Department of Thoracic Surgery, The Second Affiliated Hospital, Air Force Medicel University, Xi'an, China

The development and growth of tumors remains an important and ongoing threat to human life around the world. While advanced therapeutic strategies such as immune checkpoint therapy and CAR-T have achieved astonishing progress in the treatment of both solid and hematological malignancies, the malignant initiation and progression of cancer remains a controversial issue, and further research is urgently required. The experimental animal model not only has great advantages in simulating the occurrence, development, and malignant transformation mechanisms of tumors, but also can be used to evaluate the therapeutic effects of a diverse array of clinical interventions, gradually becoming an indispensable method for cancer research. In this paper, we have reviewed recent research progress in relation to mouse and rat models, focusing on spontaneous, induced, transgenic, and transplantable tumor models, to help guide the future study of malignant mechanisms and tumor prevention.

KEYWORDS

tumor, immune microenvironment, animal model, spontaneity, induced, transgene, PDX, immunodeficiency

1 Introduction

According to the World Health Organization, there were 19.3 million new cancer cases worldwide in 2020, resulting in nearly 10 million related deaths (1). Furthermore, with the acceleration in population growth and social aging, the global cancer burden will continue to increase. It is estimated that by 2040, the number of newly diagnosed cancer patients will reach 28.4 million per year, an increase of 47% when compared with 2020 (2). Recently, new therapeutic strategies, such as immunotherapies and targeted therapies, have significantly improved the survival rates of tumor patients when compared with traditional therapies; however, there are fewer sensitive and beneficial people, and the problem of drug resistance is almost inevitable (3). Therefore, in-depth exploration of the occurrence and development mechanisms of cancer and the improvement of diagnosis and treatment strategies are of critical global importance, and consequently, this is a major focus of academic research.

Animal tumor models are valuable for experimental analysis as the animal tumors can have similar characteristics to human tumors. We can study the occurrence and development of tumors by observing animal tumor models, and study the effect of genes on tumorigenesis and development by knocking out or knocking in a certain gene, and we can also establish PDX models for drug screening and preclinical trials. Furthermore, this experimental strategy is also advantageous as these experiments are low cost, the animals have short life cycles, and it can help to avoid human experiments. Thus, the use of animal models is extremely valuable for tumor research (4). At present, based on the causes of tumor formation, we divide the animal model into four categories: spontaneous, induced, transgenic, and transplant. Among them, the spontaneous tumor model, the induced tumor model, and the transgenic model belong to the primary tumor of animals, and the transplantable tumor models include allogeneic transplantation and xenogeneic transplantation; the most used transplantable tumor model is human tumor xenografts in immunodeficient mice. Compared with non-mammals, mammals have a higher degree of similarity to humans, especially mice and rats, and the short reproduction cycle of mice greatly improves the efficiency of these experiments. The mouse genome sequencing project was completed in 2002, and it revealed that 99% of human genes exist in mice; gene homology is as high as 78.5% (5). Consequently, mice are the most commonly used animals in tumor research. This paper introduces the research progress that has been made with various human tumor models in mice and rats, and analyzes their development processes, advantages and disadvantages, applications, and future development prospects.

2 Animal models for spontaneous tumors

Spontaneous animal tumor models are utilized to investigate tumors that occur naturally in experimental animals without any conscious artificial intervention, and this occurrence type and incidence vary greatly with different species and strains of experimental animal (Figure 1). The advantage of the spontaneous animal tumor model is that the process of tumor formation is similar to that of human tumors, and the long period of tumor occurrence and development can be treated comprehensively with the intervention of many factors, and the role of genetic factors in tumorigenesis can be observed. However, the disadvantage of the spontaneous animal tumor model is that the experimental cycle is long, many experimental animals are required, and the cost is high; in addition, the spontaneous tumors of animals are often heterogeneous and there are individual growth differences, making it difficult to obtain a large number of tumor-bearing animals with uniform growth at the same time.

2.1 Breast tumors

The incidence and mortality of breast cancer worldwide are increasing and have surpassed lung cancer in 2020 to become the most predominant cancer in the world (1). Mice have a high incidence of breast cancer (6). The occurrence of breast tumors in mice is affected by many factors, including factors such as viruses, hormones, heredity, and feed (7). Mouse mammary tumor virus (MMTV) is the most common cause of breast cancer, which causes breast cancer and lymphoma in mice mainly by insertion mutations and clone amplification in the genome; therefore, mice carrying MMTV have a higher incidence of breast tumors (8). C3H/He mice were inbred by Strong after crossing Bagg albino female mice with a high incidence of the breast tumor strain DBA male mice in 1920. C3H/He female mice carried MMTV, and the average incidence of spontaneous breast tumors reached 99% at an average of 7.2 months, but the average age of tumorigenesis in the virgin mice was approximately 2 months older than that in postpartum mice (9). DD mice also carry MMTV, and the incidence of breast tumors is 84% at the age of 7–8 months (9). BALB/c and other mouse strains do not carry MMTV, and the incidence of breast tumors is low; in 1932, the 26th generation of mice bred by MacDowell from Bagg albino mice through inbred lines was named BALB/c mice, and the incidence of breast cancer in the BALB/c mice was only 20% at 16–17 months (9), and the incidence of breast tumors in C57BR, C57BL, AKR, and other mice without MMTV was lower (10). However, some strains of mice without MMTV had a high incidence of breast tumors, such as the A mice, SHN mice, and TA2 mice; A mice were inbred by Strong after inbreeding with the offspring of the local albino mice and Bagg albino mice in 1921, which is a highly spontaneous breast tumor strain, but the A mice do not carry MMTV, and Strain A female mice had an average breast tumor incidence of 40% at the age of 12.4 months (9). SHN mice were bred by Nagasawa et al. on the basis of the Swiss albino mice, and the incidence of breast tumors in female SHN mice was 97.2% at an average age of 6.6 months, and 88.3% in virgin female SHN mice at 8.7 months (10). In addition, the inbred strain TA2 mice bred by Sun et al. also had a high incidence of spontaneous breast cancer, and pathological analysis showed that the breast cancer cells of the TA2 mice were triple-negative. The incidence of

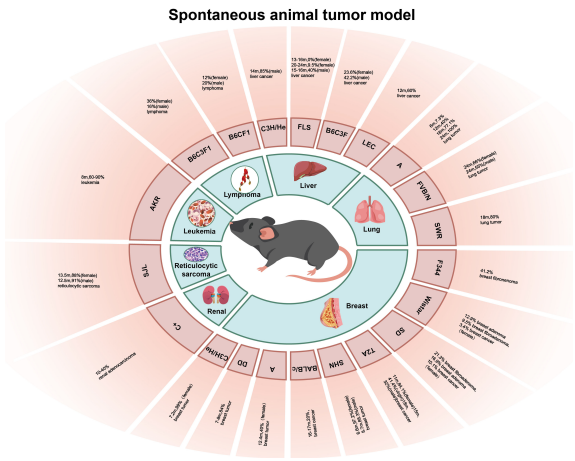

FIGURE 1
The incidence of various spontaneous tumors in different strains of mice (rat).

spontaneous breast cancer reached 84.1% after 11 months in the TA2 mice, 41.4% in the virgin TA2 mice at 15 months, and 32% in the male TA2 mice at 18 months (11). Wistar, SD, F344, and other rat strains also had a high incidence of breast cancer; Wistar rats were bred by the Wistar Institute of the United States in 1907, and SD rats were bred by Wistar rats in 1925. The incidences of breast fibroadenoma, breast adenoma, and breast cancer in female SD rats were 21.3%, 16.9%, and 10.1%, respectively, while those in female Wistar rats were 12.9%, 9.5%, and 3.4%, respectively (12). F344 rats were inbred and established by Dunning in subline 344 of the Fischer strain, and the incidence of breast fibroadenoma in the F344 rats was 41.2% (13).

2.2 Lung tumors

Lung cancer is one of the most common cancers and the leading cause of cancer-related death worldwide, with an estimated 2 million new cases and 1.76 million deaths annually (14). The histopathological subtypes of lung cancer include non-small cell lung cancer (NSCLC) and small cell lung cancer (SCLC), which can be further divided into adenocarcinoma and squamous cell carcinoma (SCC) (15). The incidence of spontaneous lung tumors in mice is high, and the pathological types are mainly adenoma and adenocarcinoma, depending on the mouse strain. A mice and SWR mice have a higher incidence of lung tumors, followed by BALB/C mice, CBA mice, and C3H mice, which have a lower incidence of lung tumors, and the lowest incidence of lung tumors was observed in DBA and C57BL/6 mice (16). A mice are a high spontaneous lung tumor strain, and lung tumors can be detected at 3–4 weeks of age. The incidence of lung tumor was 7.3% (6/83) at 6 months of age, 40.0% (71/178) at 12 months of age, 77.1% (105/136) at 18 months, and almost 100% at 24 months (17). SWR mice were bred by Lynch et al. in 1926 using Swedish mice for inbreeding. The spontaneous rate of lung tumors in SWR mice over 18 months was 80%, and the incidence of lung tumors in mice whose parents had spontaneous lung tumors was higher than that in mice whose parents had lung tumors alone, while the incidence of lung tumors in mice whose parents had no lung tumors was lower (18), suggesting a role for genetic factors in tumorigenesis. Although the incidence of lung tumors in SWR mice is high, the long culture period limits the use of this strain in lung tumor research. FVB/N mice were established in the 1970s, and they have a high spontaneous lung tumor rate. The mean incidence of lung tumors in male and female mice at 24 months was 55% and 66%, respectively, and the fertilized egg of FVB/N mice has a large and significant pronucleus and is easy to be microinjected with DNA. Consequently, FVB/N mice have been widely used as animal tumor models (19).

2.3 Liver tumors

Primary liver cancer is the fourth leading cause of cancer death worldwide, and its incidence is increasing every year. Histologically, it can be divided into hepatocellular carcinoma (HCC) and intrahepatic cholangiocarcinoma (20). Spontaneous liver tumors in mice often originate from hepatocytes, cholangiocarcinoma is rare, and sarcomas are even rarer. The incidence of liver tumors is different in different strains of mice, but the incidence in male mice is usually higher than that in female mice (21). Male C3H/He mice are a highly spontaneous liver tumor strain, and Heston et al. found that the incidence of liver cancer in 14-month-old male C3H/He mice could reach 85% (9). In Japanese FLS mice, inbred mice with non-obese spontaneous fatty liver developed a fatty liver shortly after being fed a normal diet, but were not visibly obese; multiple white protruding nodules appeared in the liver of mice over 12 months of age, and were histologically diagnosed as hepatocytic adenoma and HCC. The incidence of HCC in male mice was 40% at an average of 15–16 months, and that in female Japanese FLS mice was 0% (0/36) at 13–16 months and 9.5% (4/42) at 20–24 months (22). B6C3F1 mice are the first generation of female C57BL/6 and male C3H hybridizations, and the incidence of liver tumor was 42.2% in male B6C3F1 mice and 23.6% in female B6C3F1 mice (13). LEC rats are inbred mutant rats established by Joseph A. Long and Herbert M.E. Vans of the University of California, USA. Approximately 40% of LEC rats develop acute posthepatitic death 3–4 months after birth and approximately 60% of rats experience chronic hepatitis and develop HCC a year later (23, 24). Some studies have pointed out that the cause of spontaneous hepatitis and HCC in LEC rats is the excessive accumulation of copper in the liver, which produces a large amount of ROS hydroxyl radicals, followed by oxidative stress, which is similar to the development of HCC in humans. Therefore, LEC rats have been widely used in HCC models (25).

2.4 Other tumors

In 1958, Claude et al. described an animal model of renal adenocarcinoma in C+ mice. The incidence of renal adenocarcinoma in C+ mice was between 10% and 40%, and the incidence of tumors increased with age (26). The AKR mouse is a new strain established by further inbreeding of AK mice by the Rockefeller Institute in 1936; AKR mice are born with carcinogenic RNA virus, the incidence of leukemia after 8 months is approximately 60%–90%, and that of 18-month-old mice can be as high as 90% (27). The incidence of reticulocytic sarcoma in the SJL mice was high, and the incidence of reticulocytic sarcoma in 13.5-month-old female and 12.5-month-old male mice was 88% and 91%, respectively (28). Dragani et al. established hybrid mice (C57BL/6J × C3Hf) F1 (B6C3F1) and (C57BL/6J × BALB/c) F1 (B6CF1); the incidence of lymphoma in male B6C3F1 and B6CF1 mice was 16% and 20%, respectively, and that in female B6C3F1 and B6CF1 mice was 36% and 12%, respectively (21).

3 Animal models of induced tumor

The induced tumor model refers to the use of exogenous carcinogens to cause changes in the cellular genetic characteristics, resulting in the abnormal growth of active cells and the formation of

tumors (Figure 2). Induction methods include physical, chemical, and biological methods, of which the chemical methods are the most extensive and effective for the induction (Table 1), and have the advantages of easy application, short experimental time, and high reproducibility (45). However, the disadvantage is a high animal mortality rate, and the time, location, and number of lesions are not uniform among individuals.

3.1 Urethan

Urethan was originally used as a herbicide and was later found to inhibit cell division and, thus, utilized as a chemotherapeutic drug for leukemia (46). Urethan is structurally one of the simplest carcinogens; it is soluble in both water and lipids and was the first water-soluble carcinogen to be discovered (47). The biological effects of urethan depend on the direct inhibition of nucleic acid synthesis, especially of the pyrimidine bases, and an apparent antagonism between urea and pyrimidines also exists (47). In the 1950s, a study on a model of lung tumors induced by urethan as a carcinogen found that 100% of highly sensitive mice could induce lung tumors (48). Mice are highly sensitive to urethan, especially newborn mice, and studies have shown that the rate of clearance of the urethan in newborn mice is 1/10 of that in adult mice, and 0.5 mg/g urethan can be metabolized in adult mice within 8 h, while the same dose takes 72 h in newborn mice (49). Strain A mice have highly spontaneous lung tumor development; while >75% of mice can develop lung tumors at 18 months, 75% of A mice can develop lung tumors at 6 months after a single injection of 1,000 mg/kg urethan (29). For BALB/c mice, Koohdani et al. injected 600 mg/kg intraperitoneally with urea three times every 2 days and the incidence of lung tumors in the BALB/c mice reached 70% at 20 weeks (7/10) (30). In 1962, De Benedictis et al. induced lung tumors in Swiss mice, and the parental female mice were administered 30 mg of urea 1, 3, and 5 days after delivery; the results showed that the incidence of lung tumors in the offspring was 52% and 78% at 3 months and 7 months, respectively, and another group of offspring received a single subcutaneous injection of 2 mg in the interscapular area within 24 h after birth, and the incidence of lung tumor was 100% in 3 months (31). However, the C57BL/6 mice commonly used in genetic engineering have high resistance to lung tumors induced by urethan, and consequently, multiple injections of urethan are required to overcome their genetic resistance and induce lung cancer. C57BL/6J mice were intraperitoneally injected with 1,000 mg/kg once a week for 10 weeks, and the results showed that the incidence of lung tumors in C57BL/6J mice was close to 100% at 30 weeks (32).

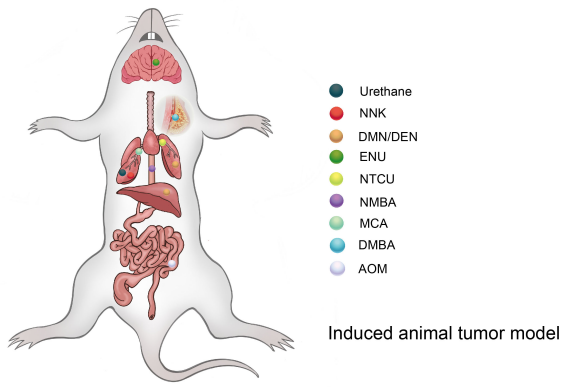

FIGURE 2
Different types of compounds can induce tumors in different organs of mice (rat).

3.2 NNK

NNK, also known as (methylnitrosamine)-1-(3-pyridine)-1-butanone, is one of the main chemical carcinogens in cigarette smoke (50), and it can effectively induce lung cancer in mice, rats, and hamsters (51). The α-hydroxylation of NNK catalyzed by a cytochrome 450 scan easily binds to DNA and forms DNA adducts, causing gene mutations that lead to tumor development (33, 52). Belinsky et al. showed that in 6-week-old A/J mice, a single intraperitoneal injection of 100 mg/kg NNK resulted in the development of hyperplasia along the alveolar septum after 14 weeks, and the frequency of lung adenomas in A/J mice at 34–42 weeks resulted in a significant increase to 50% (53). In another independent study, 7-week-old female A/J mice were given intraperitoneal injections of NNK 3 μmol weekly for 8 weeks, and 100% of the mice developed lung adenomas after 26 weeks (34). NNK can also induce lung cancer in offspring, as Anderson et al. gave 100 mg/kg NNK doses to female A/J mice on days 14, 16, and 18 of their pregnancies, and it was found that lung tumors occurred in 12 of the 66 offspring and 13 of the 14 female mice (54). The effects of NNK on young mice were also studied in Swiss mice. Mice were given 50 mg/kg NNK i.p. on postnatal days 1, 4, 7, 10, and 14, and the incidence of lung tumors was 57% in male mice and 37% in female mice at 13–15 months (35).

3.3 DMN/DEN

Dimethylnitrosamines (DMN) and diethylnitrosamines (DEN) are nitrosamines, which can induce various tumors in mice and rats, but predominantly liver and lung tumors. Nitrosamines are activated by CYP450 enzymes *in vivo* and converted into a strong alkylating agent, forming adducts in the DNA (active chemicals and cellular macromolecules form stable complexes through covalent bonds), resulting in carcinogenicity (55). Kohda et al. confirmed the mutagenicity of nitrosamines by treating Chinese hamster V79 cells with nitrosamines (56). After DEN exposure, A/J mice developed lung adenocarcinoma, 82% of which possessed KRAS mutations (57). FVB/N mice also have a high incidence of lung cancer, as Zsolt injected 15 μg/g DEN intraperitoneally into 15-day-old FVB/N mice, and the incidence of lung cancer (papillary cancer) was 72% (28/39) after 12 months. Interestingly, there were no mutations in the Kras and EGFR genes (36). In a study by Chen et al., C57BL/6 male mice were intragastrically administered 0.014% DEN for 6

TABLE 1 Construction method of animal tumor model induced by chemical drugs.

Chemical	Species	Injection	Dose	Type of tumor	Incidence	Reference
Urethan	A mice	i.p.	1,000 mg/kg, single injection	Lung tumor	6 months: 75%	(29)
	BALB/c mice	i.p.	600 mg/kg, three times every 2 days	Lung tumor	20 weeks: 70%	(30)
	Swiss mice (newborn)	Breast-feeding	Parental female mice were administered 30 mg in 1, 3, and 5 days after delivery	Lung tumor	3 months: 52%; 7 months: 78%	(31)
	Swiss mice (newborn)	i.h.	2 mg, single injection	Lung tumor	3 months: 100%	(31)
	C57BL/6J mice	i.p.	1,000 mg/kg, once a week for 10 weeks	Lung tumor	30 weeks: 100%	(32)
NNK	A/J mice	i.p.	100 mg/kg, single injection	Lung adenomas	34–42 weeks: 50%	(33)
	A/J mice	i.p.	3 μmol weekly for 8 weeks	Lung adenomas	26 weeks: 100%	(34)
	Swiss mice (newborn)	i.p.	50 mg/kg, on postnatal days 1, 4, 7, 10, and 14	Lung tumor	13–15 months: 57% (male), 37% (female)	(35)
DEN	FVB/N mice (15-day-old)	i.p.	15 μg/g, single injection	Lung cancer (papillary cancer)	12 months: 72%	(36)
	C57BL/6 mice (male)	i.g.	0.014% DEN for 6 days a week	Hepatocellular carcinoma	11–15 weeks: 100%	(37)
DEN+ CCl4	B6C3F1/J mice(male)	i.p. (CCl4) i.v. (DEN)	1 mg/kg DEN, 40.2 ml/kg CCL4 every week from week 8 to 14	Liver adenoma/liver cancer	22 weeks: 100% (liver adenoma), 50% (liver cancer)	(38)
ENU	SD rats (offspring)	i.v. (pregnant rats)	50 mg/kg, on day 20 of their pregnancy	Nervous system tumor	1 year: 100%	(39)
NTCU	SWR/J mice	Skin smear	25-μl drop of 0.04 M, twice a week for 8 months	Lung squamous cell carcinoma	8 months: 100%	(40)
	NIH Swiss mice	Skin smear	25-μl drop of 0.04 M, twice a week for 8 months	Lung squamous cell carcinoma	8 months: 83%	(40)
	A/J mice	Skin smear	25-μl drop of 0.04 M, twice a week for 8 months	Lung squamous cell carcinoma	8 months: 75%	(40)
	FVB/J mice	Skin smear	25-μl drop of 0.04 M, twice a week for 8 months	Lung squamous cell carcinoma	8 months: 44%	(40)
	BALB/cJ mice	Skin smear	25-μl drop of 0.04 M, twice a week for 8 months	Lung squamous cell carcinoma	8 months: 38%	(40)
DMBA	SD rats	i.g.	80 mg/kg, gavaged once	Breast cancer	12 weeks: 100%	(41)
NMBA	SD rats	i.h.	0.5 mg/kg, three times a week for 5 weeks or once a week for 15 weeks	Esophageal tumors	20 weeks: 100%	(42)
MCA	BC3Fl mice	Tracheal drip	0.5 mg, 6 times a week	Respiratory tract squamous cell carcinoma	10–28 weeks: 86%	(43)
	DBA/2 mice	Tracheal drip	0.5 mg, 6 times a week	Respiratory tract squamous cell carcinoma	7 months: 6%	(43)
AOM	A/J or FVB/N mice	i.p.	10 mg/kg, once a week for 6 weeks	Colon tumors	30 weeks: 80%–100%	(44)

days a week and given normal drinking water on the 7th day for 15 weeks, and 100% of these mice developed fibrosis (3–6 weeks), cirrhosis (7–10 weeks), and HCC (11–15 weeks) at 3–15 weeks (37). The incidence of liver tumors caused by the combination of DEN and CCl4 was significantly higher than that of DEN or CCl4 alone. Uehara et al. used 14-day-old B6C3F1/J male mice and administered 1 mg/kg DEN intravenously, and 40.2 ml/kg CCL4 was injected intraperitoneally every week from weeks 8 to 14. The incidence of liver adenoma and liver cancer was 40% and 20% at 17 weeks, and the incidence of liver adenoma and liver cancer was 100% and 50% at 22 weeks (38). In 1974, Cardesa et al. divided 8-week-old Swiss mice into two groups: subcutaneous injection of

DMN or DEN 8 mg/kg; the results showed that the incidence of tumors in mice was 79% (31/39) and 87% (34/39), and the incidence of lung tumors was 67% and 61%, respectively. Lung tumors in the two groups were mainly adenocarcinoma, adenoma, and atypical adenomatoid hyperplasia (58).

3.4 ENU

Acetylnitrosourea (ENU) is a strong mutagenic agent that can cause rapid oncogenic genetic mutations in mice (59). Raju et al. reported that SD rats were administered a single intravenous injection of ENU (50 mg/kg) on day 20 of their pregnancy, and almost 100% of the offspring had central and peripheral nervous system tumors at 1 year of age (39).

3.5 NTCU

N-nitroso-tris-chloroethylurea (NTCU) is a nitrosoalkylurea compound, which has been shown to induce lung SCC in mice. Wang et al. treated eight different strains of female mice by smearing NTCU on the skin to establish a model. In their study, the back skin of 7-week-old mice was scraped, and they were injected with NTCU 25-μl drop of 0.04 M, twice a week, with a 3-day interval; 8 months later, five strains of the mice had successfully induced lung SCC *in situ* or lung SCC [the induction rates were as follows: SWR/J, 100% (3/3); NIH Swiss, 83% (10/12); A/J, 75% (6/8); FVB/J, 44% (4/9); and BALB/cJ, 38% (3/8)]. The other strains (AKR/J, 129/svJ, and C57BL/6J) failed to develop the carcinomas, and histological and pathological analysis showed that mouse SCC induced by NTCU had the same pathological process as human SCC, which is "normal-proliferative-metaplastic-abnormal-SCC" (40, 60).

3.6 DMBA

Dimethylbenzanthracene (DMBA) is frequently used as a model for polycyclic aromatic hydrocarbon (PAH)-induced mammary tumorigenesis because of its potent carcinogenic and immunosuppressive activities (61). Female SD rats at the age of 7 weeks were diluted with 80 mg/kg DMBA in 0.5 ml of corn oil and gavaged once, and after 12 weeks, animal models of breast cancer lesions could be established in all rats (41).

3.7 NMBA

Methyl benzylnitrosamine (NMBA) is also an important carcinogenic compound that is classified as a nitrosamine. NMBA is currently the most effective inducer of rat esophageal tumors, as they can be induced in 15 weeks or less (62). SD rats were given 0.5 mg/kg NMBA three times a week for 5 weeks or once a week for 15 weeks, and the esophageal tumor incidence was 100% at 20 weeks (42).

3.8 MCA

Methylcholanthracene (MCA) is a potent carcinogen that is often used to induce the transformation of cultured cells, and it was found that repeated intratracheal injection of MCA into BC3Fl [(C57BL×C3H)F1] and DBA/2 mice could induce respiratory tract SCC, and the induced SCC had obvious infiltration and metastasis (43). BC3F1 mice were injected with 0.5 mg of MCA six times a week, and the incidence of respiratory tract SCC was 86% at 10–28 weeks. In contrast, DBA/2 mice that received intratracheal injections of 0.5 mg of MCA four times a week resulted in 6% incidence of SCC of the respiratory tract at 7 months (43).

3.9 AOM

Azomethane (AOM) is a chemical reagent that can promote base mismatch and cause cancer through the alkylation of DNA, which is often used in colonic carcinogenicity (63); 10 mg/kg AOM was injected intraperitoneally into A/J or FVB/N mice once a week for 6 weeks, and resulted in 80%–100% of mice having spontaneous colon tumors within 30 weeks (44).

3.10 Fattening diet

Nonalcoholic fatty liver disease (NAFLD) is a condition characterized by the excessive accumulation of fat in the liver without chronic alcohol intake; it is estimated that the global prevalence rate is approximately 24% (64). NAFLD and nonalcoholic steatohepatitis (NASH) are the liver manifestations of metabolic syndrome, and some patients with NAFLD develop into NASH with associated inflammation and fibrosis, which can progress to HCC (64). Asgharpour et al. successively established a model by following a fattening diet (high fructose-glucose solution and high-fat, high-carbohydrate diet—42% calorie fat and 0.1% cholesterol) in 8- to 12-week-old male mice; 89% of the mice developed HCC at 32–52 weeks, and each mouse had three or more tumor foci (65).

3.11 Ionizing radiation

Moderate to high doses of radiation are well-established causes of cancer (66), and ionizing radiation such as x-rays, α-rays, β-rays, and γ-rays can break through genetic material and cause DNA fracture damage and gene mutations (67). Some studies have shown that irradiated mice may develop a series of malignant tumors, including sarcomas, and single high-dose radiation significantly increases the incidence of tumors when compared with fractionated radiation (68). Edmondson et al. locally irradiated the right hindlimb of C3Hf/Kam and C57BL/6J mice with a high dose (10–70 Gy) or a fractionated dose (40–80 Gy, 2 Gy per day, five times a week, for 4–8 weeks), and after 800 days, 210 tumors were induced in 788 mice. The observed tumors were primarily sarcoma (n = 201), and the occurrence frequency of cancer was low (n = 9). The

incidence of tumor after single irradiation was 36.1%, and that of graded irradiation was only16.4% (68).

4 Transgenic models

In recent years, increasing evidence has shown that gene mutation is an important cause of tumorigenesis, and targeted therapies for driving genes have achieved good results in tumor patients with a specific genetic background, but the problem of drug resistance still restricts the further benefits (3). Understanding the mechanism of driving mutations in tumorigenesis and development is thus crucial. Due to the high similarity between mouse and human protein coding genes, transgenic mice have been used to study the effects of gene mutations on tumorigenesis and development since the mid-1980s (5) (Table 2). The advantages of transgenic animal tumor models are that they have great advantages in studying tumorigenesis mechanisms and tumor immune escape. However, the establishment process of transgenic animal models is long, the feeding costs are high, and it is difficult to obtain a large number of experimental animals, which hinders rapid and high-throughput research (76).

4.1 KRAS

Approximately 30% of human tumors carry ras gene mutations, and the ras gene family includes Kras, Nras, and Hras. Kras is the most commonly mutated gene in the lung, colon, and pancreatic tumors (77), with a mutation rate of approximately 70%–90% in pancreatic cancer, 50% in colon cancer, 25%–50% in lung cancer (69), and 15%–25% in lung adenocarcinoma (78, 79). Point mutations (including G12D, G12V, G12C, G13D, AMP, and G12R) are the most common Kras mutations (70). Under normal circumstances, the activation and inactivation of Kras are finely regulated, as wild-type Kras is temporarily activated by tyrosine kinases such as active epidermal growth factor receptor (EGFR). Activated Kras can motivate downstream signaling networks to execute diverse bioactivities, and Kras is then rapidly inactivated (80). Mutant Kras proteins are uncontrollable, as they can be continuously activated in the absence of an EGFR activation signal, inducing uncontrolled cell proliferation and malignant invasion (80). Most mutations in lung cancer models are Kras dependent; Kras mutations are found in 90% of spontaneous and chemically induced lung tumors in mice, and genetically engineered Kras mice have been widely used in lung cancer research, which is very similar to the genetic and pathophysiological characteristics of human lung cancer (45, 81, 82). Johnson et al. constructed a new type of mouse with a potential KrasG12D allele (KrasLA), and mice carrying these mutations easily formed a variety of tumor types, predominantly lung tumors, and 100% of mice developed numerous kinds of lung tumors at an early stage (68). However, KrasLA mice were found to die of respiratory failure caused by lung lesions at a very young age, and the incidence of other tumors is difficult to predict, which restricts the application of this model (69). Kras gene mutations account for 6% and 18% of diffuse-type and intestinal-type gastric cancers, respectively (83). Brembeck et al. established Kras transgenic mice under the control of the cytokeratin 19 (K19) promoter; parietal cell decrease and mucous neck cell proliferation were found in 3- to 6-month-old mice (84). In pancreatic cancer, the Kras mutation occurs in the early stages of tumorigenesis and accounts for approximately 90% of pancreatic ductal adenocarcinomas; it is often combined with other classical mutations (PTEN, etc.) to induce pancreatic cancer, which will be mentioned in the following article (85).

4.2 TP53

Somatic mutations in the tumor protein P53 (TP53) gene are the most common changes in human cancers (86). The incidence of TP53 mutations in ovarian, esophageal, colorectal, head, neck, laryngeal, and lung cancers is 38%–50%, and the mutation rate is approximately 5% in primary leukemia, sarcoma, testicular cancer, malignant melanoma, and cervical cancer, and it is more common in advanced or invasive cancer subtypes (71). Most TP53 mutations are missense mutations, followed by truncated mutations, intra-frame mutations, and synonymous and uncoded mutations, which are mainly concentrated in known hot spots (the most common sites are 157, 158, 179, 245, 248, 249, and 273) (72). Normally,TP53

TABLE 2 The type of tumor caused by gene mutation.

Gene mutations	Type	Tumor	Common mutation sites	References
KRAS	Proto-oncogene	Pancreatic cancer (70%–90%), colon cancer (50%), lung cancer (25%–50%)	G12D, G12V, G12C, G13D, AMP, G12R	(69, 70)
TP53	Tumor suppressor gene	Esophageal, colorectal, head, neck, laryngeal, and lung cancers	157, 158, 179, 245, 248, 249, 273	(71, 72)
PTEN	Tumor suppressor gene	Breast cancer (12%), thyroid cancer (1%), endometrial cancer (2.6%), renal cell cancer (1.6%), colon cancer (5%), and malignant melanoma (2%)		(73)
EGFR	Proto-oncogene	Glioblastoma, non-small-cell lung cancer, breast cancer, pediatric gliomas, medulloblastomas, and ovarian cancer	Exon 19 deletion, exon 21 point mutation, exon 18 point mutation, and exon 20 insertion	(74, 75)

functions by activating or inhibiting the transcription of numerous critical genes in diverse bioactivities, including cell cycle arrest, DNA repair, metabolism, senescence, and apoptosis (86). Trp53 (TP53 is called Trp53 in mice) knockout mice are common transgenic animal models that formulate spontaneous tumors at the age of 6 months (including breast cancer, sarcoma, brain tumor, and adrenocortical carcinoma) (87). Compared with homozygous mice, mice with the Trp53 allele heterozygotes had later spontaneous tumors; the most common tumor type in homozygotes was malignant lymphoma, and the main heterozygotes were osteosarcoma and soft tissue sarcoma (88). In C57BL/6 or 129/Sv mice, the Trp53 deletion preferentially induces sarcoma and lymphoma, and the incidence of breast cancer has gradually increased from 21.4%-46.2% in the fourth generation after backcrossing with BALB/c mice for many generations (89). It has been reported that the incidence of gastric invasive adenocarcinoma in Trp53$^{-/-}$ mice is significantly higher than that in WT mice (90). Ralph et al. established a mouse model of neuroendocrine lung tumors by conditionally inactivating Rb1 and Trp53 in mouse lung epithelial cells, and its morphology and immunophenotype were significantly similar to those of SCLC (91). However, increasing evidence shows that the TP53 gene still has antitumor effects after the loss of these classical activities (92). Using a mutant mouse model of p53-3KR (K120R, K161R, and K162R), researchers found that Trp53 can still inhibit cancer initiation, mainly by regulating cell metabolism, despite losing the antitumor effect of inducing cell cycle arrest, apoptosis, and senescence (93).

4.3 PTEN

Pten (phosphatase and tensin homolog deleted on chromosome ten) is a classical tumor suppressor gene with a mutation rate of approximately 12% in breast cancer, 1% in thyroid cancer, 2.6% in endometrial cancer, 1.6% in renal cell cancer, 5% in colon cancer, and 2% in malignant melanoma (73). The PTEN deletion was also reported in 15% of poorly differentiated serous ovarian cancers (94), and Pten mutations were also found in 20% of endometrioid ovarian cancers (95); approximately 53% of patients with primary bladder cancer showed a decrease or deletion of the Pten protein in the cytoplasm or nucleus of their tumor cells (96). The tumor inhibitory activity of PTEN depends to a large extent on its phosphatase activity, which regulates the activity of many important cellular pathways, such as PI3K/AKT; thus, it can regulate many cell processes, including proliferation, survival, energy metabolism, cell structure, and movement (97). The current transgenic model of Pten is widely used in the study of tumorigenesis mechanisms; however, half of the Pten knockout mice died within 1 year after birth, and the rest developed a variety of tumors, including lung, breast, thyroid, endometrial, and prostate cancer, and T-cell lymphoma (98). AlbCrePten (flox/flox) mice established by Horie et al. using the Cre-loxP system showed hepatocyte specific knockouts of Pten, and AlbCrePten (flox/flox) mice showed huge liver hypertrophy and steatohepatitis, as well as triglyceride accumulation similar to human nonalcoholic steatohepatitis (NASH); at 78 weeks of age, all AlbCrePten (flox/flox) mice had liver adenomas, and 66% of AlbCrePten (flox/flox) mice had HCC (99). Yanagi et al. specifically knocked out the Pten gene in bronchiolar alveolar epithelial cells of mice under the control of doxycycline to establish SOPten (flox/flox) mice, of which 90% of the SOPten (flox/flox) offspring mice died of hypoxia shortly after birth (100). Ninety weeks later, all SOPten (flox/flox) mice born showed significant visible lung tumors: 13 tumors were adenocarcinoma and 1 tumor was SCC, as determined by histological examination (100). Russo et al. found that the Pten deletion increases cell migration, invasion, and upregulation of WNT4, which is a key regulator of Müllerian duct development during embryogenesis (101). Tsuruta et al. used the Cre-loxP system to specifically knock out the Pten gene in the urine epithelium of mice to obtain FPten (flox/flox) mice; histologically, the urine epithelium cells of the mice showed enlargement of the nucleus and cell volume, and ultimately, approximately 10% of FPten (flox/flox) mice spontaneously developed into pedicled papillary transitional cell carcinoma (TCC) (96).

4.4 EGFR

Epidermal growth factor receptor (EGFR) is a member of the HER family, which includes HER1 (erbB1, EGFR), HER2 (erbB2, NEU), HER3 (erbB3), and HER4 (erbB4) (102). Studies have shown that there is high or abnormal expression of EGFR in many solid tumors, which is related to tumor cell proliferation, angiogenesis, invasion, metastasis, and inhibition of apoptosis (103). In a study using EGFR knockout mice, the types of cells most affected by the EGFR deletion were epithelial cells and glial cells, while the types of cells overexpressing EGFR in the human tumors were epithelial cells and glial cells (104, 105). A large number of EGFR mRNA deletions have been observed in a number of neoplasms, first in glioblastoma, but recently in non-small-cell lung cancer, breast cancer, pediatric gliomas, medulloblastomas, and ovarian cancer (74). There are four main types of EGFR mutations: exon 19 deletion, exon 21 point mutation, exon 18 point mutation, and exon 20 insertion (75). The most common EGFR mutations are the exon 19 deletion mutations (19DEL) and exon 21 mutations (21L858R), followed by exon 18 G719X, exon 20 S768I, exon 21 L861Q mutation, and T790M mutation in exon 20, which are associated with acquired drug resistance in the first and second generations of EGFR-TKIs (75). EGFR knockout mice were stunted and died at different developmental stages (implantation, second trimester, or early postpartum), and mainly characterized by epithelial cell defects (including skin, lung, gastrointestinal tract, teeth, and eyelid defects), impaired intestinal proliferation, reduced stem cell area, and mucosal structure disorder (105). In order to study the role of activated EGFR mutations in lung cancer, Ohashi et al. established transgenic mice carrying EGFR mutations (five nucleotides encoding five amino acids were deleted, which was equivalent to the EGFRdelEN746-A750 mutation found in lung cancer patients) specifically in type II alveolar epithelial cells through its specific SP-C promoter and found that 9 of 47 newborn mice were positive for

EGFR gene mutations, 3 mice of the positive type developed lung adenocarcinoma, only 1 mouse carrying lung adenocarcinoma could reproduce, and all of its offspring developed lung tumors after 7 weeks (106). Ohashi et al. also used EGFR-mutated mouse models to study the evolution of lung adenocarcinoma. Transgenic mice were killed at different time points for pathological examination; atypical adenomatoid hyperplasia (AAH) appeared at 3–4 weeks, diffuse bronchiolo-alveolar carcinoma (BAC) appeared at 4–5 weeks, adenocarcinoma with solid features was observed at 7 weeks, and multiple tumor nodules were observed on the lung surface (106). Ohashi et al. used a similar method to construct transgenic mice expressing EGFRL858R in type II alveolar epithelial cells; 8 mice had L858R deletion mutations in 27 newborn mice, and 2 mice with the positive mutation developed multifocal adenocarcinomas at 7 weeks. All the offspring of these two mice had BAC at 4–5 weeks and adenocarcinomas at 7 weeks (107).

4.5 Combined mutations

Tumors are often caused by multiple gene mutations, the most common of which is the activation of oncogenes and inactivation of tumor suppressor genes (108). Kras and TP53 are common combined gene mutations in human cancer, and KP mice with both Kras and Trp53 mutations are the most classic transgenic model; all KP mice developed primary lung tumors. Six weeks after the lung lesions of mice developed from atypical adenomatous hyperplasia to lung adenomas, the tumors of these mice showed a high degree of nuclear atypia, causing interstitial connective tissue hyperplasia, invasiveness, and metastasis (109). Kras mutations were found in 95% of pancreatic ductal adenocarcinomas. KPC mice were triple mutants with aKras$^{LSL\text{-}G12D}$, p53^{LoxP}, and Pdx1-CreER for tamoxifen-inducible pancreatic ductal adenocarcinoma. Pancreatic ductal metaplasia and pancreatic intraepithelial neoplasia occurred in KPC mice at 8–10 weeks, and invasive pancreatic ductal adenocarcinoma occurred at 14–16 weeks, and metastasized to the liver, lung, and peritoneum (110). Combined mutations of Kras and Pten are also common in human cancers, and the Ptf1a$^{Cre\text{-}ERTM}$, Kras$^{LSL\text{-}G12D}$, and Pten^{flox}, tamoxifen-inducible triple mutant strain (KPP) may be useful as a model for pancreatic adenocarcinoma (PDA)-induced cachexia-a wasting syndrome characterized by the pronounced loss of skeletal and cardiac muscle and adipose tissues (111). Mutation activation of BRAF is the earliest and most common genetic change in human melanoma; mice specifically expressing BRAF(V600E) showed benign melanocyte proliferation, but did not develop melanoma after 15–20 months, and BRAF(V600E) expression combined with PTEN gene silencing could induce malignant melanoma and metastasis to lymph nodes and lungs (112). The Rb1 deletion, TP53 deletion, and Myc amplification are all common mutations in SCLC (113). RPM mice carried three gene mutations: Rb1$^{fl/fl}$, Trp53$^{fl/fl}$, and Myc$^{LSL/LSL}$; 100% of these mice developed SCLC after 6–8 weeks (113). It is worth noting that these common classical gene mutations are often combined with new gene mutations to study the function of these new genes in carcinogenesis.

5 Transplantable animal tumor models

Human tumor generated mouse models are established by transplanting human tumor cells and/or tissues of research interest into recipient animals (almost always possessing immune function deficiencies) (Figure 3). The advantage is that most types of human tumors can establish transplantable tumor models in immunodeficient animals, and under the same inoculation conditions, the growth rate of animals is the same, the difference in tumor formation rate is small, and the inoculation tumor formation rate is high. The disadvantage is that the recipient host animal needs to be in an immunodeficient state requiring special housing in an aseptic environment, which is expensive to maintain. Furthermore, not all cell types of human tumors can be successfully established in rodent models and the stroma of the human tumor tissue obtained may contain the components of the recipient animals. It is worth noting that the key to developing an optimal transplanted tumor model lies in the immune status of the host (immunodeficiency state) and the composition of the graft (containing important or all components of the tumor).

5.1 Immunodeficient mice

The immune status of the host has undergone many improvements, which is the key to the development of a successful transplant tumor model. Transplantable tumors are divided into allogeneic transplantation and xenogeneic transplantation, and the most used is the xenotransplantation of human tumors. Due to the existence of immune rejection, wild mice cannot be used for xenotransplantation of human tumor. However, human tumors can be implanted in immunodeficient mice, and the tumors can maintain the histological, immunological, and biological characteristics of original tumors. Nude mice were first identified by Grist in 1962, and they were called nude mice as they are hairless. Flanagan found that nude mice lack thymus and T lymphocytes, and thus, they lacked T cell-mediated immune responses and could be used as recipients for human tumor xenotransplantation (114). However, because nude mice still have B cells and NK, they are not suitable for use as hosts for lymphoma and leukemia, which limits the extensive application of nude mice in relation to transplanted tumors. Severe combined immunodeficiency (SCID) mice were first reported by Bosma in 1983 (115). SCID mice are more severely immunodeficient than nude mice, and the mutant genes of the SCID mice were identified in 1996. The maturation defects of B lymphocytes and T lymphocytes in SCID mice were caused by a point mutation in the Prkdc (protein kinase, DNA-activated, catalytic subunit) gene, which causes the affected lymphocytes to die prior to maturation or be cleared by the macrophages, granulocytes, and NK cells in the body (116, 117). However, it is usually difficult to establish a successful model for lymphoma and metastatic tumors in SCID mice because of leakage (some SCID mice will restore the function of some T and B lymphocytes with age) (118). In addition, NK cells

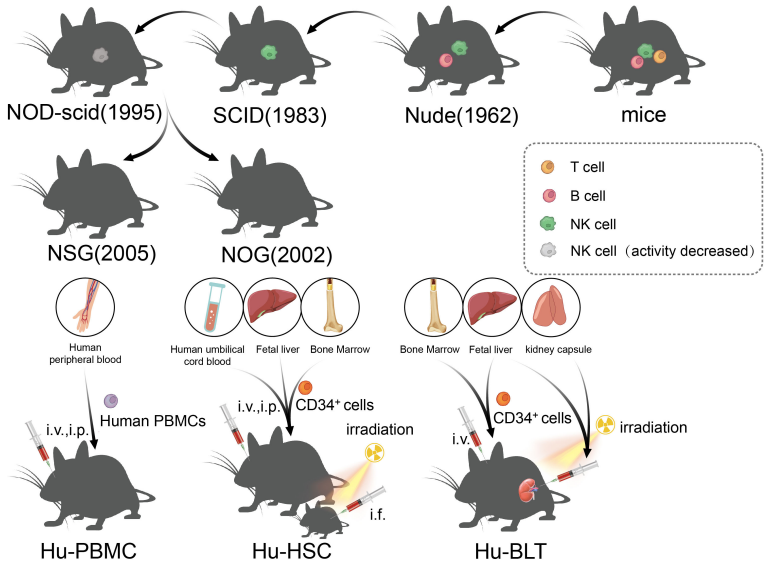

FIGURE 3
The development of immunodeficient mice and the construction method of the humanized mice model.

and other innate immunoreactive substances in SCID mice were present at high levels, which limits the success rate of transplantation, such as human hematopoietic stem cell (HSC) transplantation (119). Subsequently, the establishment of NOD/SCID mice ushered in a new breakthrough in transplanted animal tumors, which are a type of spontaneous type 1 diabetic mice, caused by T lymphocytes infiltrating and destroying islets, as well as complement loss and impaired function of NK, macrophages, and dendritic cells (120, 121). NOD/SCID mice were established through the hybridization of NOD and SCID mice, and NOD/SCID mice will not develop type 1 diabetes, as they lack an adaptive immune system and the loss of effector T cells; moreover, due to extensive defects in innate and adaptive immunity (low activity of NK cells and loss of T- and B-cell function), NOD/SCID mice have become a stable and excellent animal model for human HSCs and human solid tumor transplantation (122). At the beginning of the 21st century, scientists introduced IL-2Ry mutations on the basis of NOD/SCID mice, resulting in NSG and NOG mice, which, in addition to being the mice with the highest degree of immunodeficiency at present, could also be used to construct humanized immune system mice to study the antitumor effects of chimeric antigen receptor T-cell immunotherapy (CAR-T) and immune checkpoint inhibitors (ICIs) (123), and will be discussed in detail later.

5.2 PDX

Transplant components have also been the focus of transplantable tumor model research in recent years, and in the past, we transplanted tumor cell lines into animals, which are simpler and easier to use, but the defects cannot be ignored: first, this tumor model cannot fully represent the unique characteristics of each cancer patient; furthermore, this model cannot reconstruct the remaining non-tumor cell components in the tumor tissues, which plays an important role in tumorigenesis and development. Consequently, the patient-derived xenotransplantation (PDX) model has been actively generated and applied, and the PDX model can directly implant cancerous tissues from the patient's tumor into immunodeficient mice, thus preserving both the cell–cell interaction and the tumor microenvironment (124). The PDX model retains the characteristics of the primary patient tumor, including the gene expression profile and drug response, and offers great advantages for drug screening, biomarker development, and the evaluation of therapeutic effects (125). The PDX model usually takes approximately 6 months to 2 years to establish, and the success rate varies (10%–90%), depending on the tumor source and disease characteristics (125). Specifically, invasive, recurrent, and the transplantation rates tend to be higher for highly metastatic tumors (126). Gastrointestinal tumors (such as colon and pancreatic cancers) have higher transplantation success rates than other cancers, and the transplantation rate in breast cancer is low (127). The success rates of the PDX model is as follows: colon cancer [63.5% (54/85) in nude mice and 87% (74/85) in NOD/SCID mice] (128, 129), pancreatic cancer [61% (42/69) in nude mice and 67% (8/12) in SCID mice] (130, 131), and breast cancer [12.5% (25/200) in nude mice and 27% (13/49) in NOD/SCID mice] (132, 133).

Animal models also play an important role in drug development and screening. In the past, the average success rate of translating animal research into human clinical trials was approximately 8%, and <5% of antineoplastic drugs were approved to enter the market (134, 135). Although the accuracy of the PDX model on drug efficacy and drug resistance was up to 90% (136), the traditional PDX model takes a long time to construct; owing to this, it cannot quickly reflect the drug sensitivity of patients and cannot meet clinical needs. China Lidi Biological has developed a new rapid PDX drug sensitivity detection technique (OncoVee ®MiniPDX) for screening clinically related

programs of cancer, which uses patient-derived tumor cells arranged in hollow fiber capsules after 7 days of subcutaneous culture. The active morphology and pharmacokinetics of the tumor cells in MiniPDX capsules were evaluated systematically, and the morphological and histopathological characteristics of the tumor cells in MiniPDX capsules were consistent with those of the PDX model and primary tumor (137).

5.3 Humanized mice model

Recently, ICI and CAR-T have enabled new breakthroughs in the treatment of tumors (138, 139). Although PDX, which depends on immunodeficient mice, has been widely used in the research of tumor immunity and the development of new therapies, the lack of models for the human immune system and tumor immune microenvironment limits the study of immune mechanisms and transformation of immunotherapy to a great extent. The humanized mouse model is a mouse model that reconstructs the human immune system by implanting human hematopoietic cells, lymphocytes, or tissues into immunodeficient mice, which can effectively reconstruct the human immune system and better simulate the characteristics of human immunity (140). From the earliest nude mice to the later SCID and NOD/SCID mice, the success rate of human cell implantation has been low either due to the existence of innate immunity or because of high sensitivity to radiation and the limited life cycle. Owing to this, all these models limited the application of immune system-humanized mice in practical research to some extent. In NOG mice, mature T/B cells and NK cells are lacking, complement activity is decreased, and the function of macrophages and dendritic cells is impaired; therefore, NOG mice are an ideal model for human immune cell transplantation (141). Subsequently, the IL-2 receptor γ mutation was further developed. NSG mice had a complete IL-2 receptor γ chain-invalid allele, similar to NOG mice, with a loss of T/B and NK cells, lack of complement activity, and defects in macrophages and dendritic cells (142). In addition, other highly immunodeficient mice, such as BRG and BRGS mice, have been established as humanized mouse models that lack T/B cells and NK cells (143). Although NOG and NSG mice are very useful humanized models, they still lack the ability to reconstruct myeloid and NK cells, and a new generation of super immunodeficiency models HuNOG-EXL and HuNSG-SGM3 have been developed, which can express some growth factors to promote myeloid regeneration (142, 144). According to the method of human immune system reconstruction, the humanized mouse model can be divided into three categories: Hu-PBMCs (humanized-peripheral blood mononuclear cells), Hu-HSCs (humanized-hematopoietic stem cells), and Hu-BLTs (humanized-bone marrow, liver, thymus) (145). The Hu-PBMC model is a simple and economical humanized mouse model in which mature lymphocytes from peripheral blood mononuclear cells (PBMCs) are injected into immunodeficient host mice through intraperitoneal (i.p.) or intravenous (i.v.) injection (145). This method was first described in CB17-SCID mice in 1988 and has been widely used to study the human immune response in autoimmunity and infectious diseases (117). However, graft-versus-host disease (GvHD) occurs in the Hu-PBMC model in 2–3 weeks, and the survival time is short (146). At present, this model is often used to study the activation of human effector T cells and to evaluate immunosuppressive drugs; in the Hu-HSC mouse model, human $CD34^+$ HSCs from human umbilical cord blood, adult bone marrow, or fetal liver were injected into adult mice (intravenous or intrafemoral) or newborn mice (intracardiac or intrahepatic) (147, 148), and sublethal irradiation of host mice is needed to eliminate HSC and promote the transfer of human HSC (145). Fetal liver and umbilical cord blood are the most commonly used sources of human $CD34^+$ HSCs, which are easier to colonize in immunodeficient mice than that in adult HSCs. Although this method can produce a variety of HSCs in adult mice, the number of T cells produced is small and the model does not possess functional immune cells (149). In newborn mice (less than 4 weeks old), good human cell transplantation can be obtained, and T cells, B cells, macrophages, NK cells, and DCs can be produced (150). At present, it is believed that the Hu-HSC model can establish the human innate immune system and lymphocytes, with little or no occurrence of GvHD, which can be used for long-term research; however, owing to the species differences between humans and mice, there is a lack of human cytokines in mice, and the development of human stem cells in mice is limited (149). The method of establishing Hu-BLT is to transplant human fetal liver and thymus tissue into the renal capsule of adult immunodeficient recipient mice after sublethal irradiation, and at the same time, fetal liver or bone marrow-derived $CD34^+$ HSCs from the same individual is injected intravenously (i.v.) into recipient mice (151). The Hu-BLT model is often used to study adaptive immune responses, such as HIV infection. However, the incidence of GvHD in the Hu-BLT model is higher than that in other $CD34^+$ HSC transplantation models (145), and complex and precise surgical procedures are required, thus limiting the application of the Hu-BLT model in the research and development of tumor immune drugs.

6 Prospects

The use of animal models to develop human healthcare can be traced back to the 6th century BC (152). During this time, there have been significant developments in biotechnology and animal models that have contributed to the development of mechanisms of disease and drug discovery. Since the establishment of the earliest spontaneous animal tumor model, we have obtained a great deal of information about tumor generation and progression. However, we have gradually eliminated this method because of its randomness, high cost, and long cycle of tumorigenesis. Then, we used chemical drugs to induce tumors in mice to establish tumor models and study the carcinogenic effect of a certain factor. In fact, induced tumor is the most widely used method for establishing animal tumor models at present, due to the low technical requirements and cost, most of the laboratories can perform this biotechnique. With the development of the transgenic animal model and the PDX model, we have made great progress in understanding specific gene function, building animal models of human diseases, and evaluating the safety and effectiveness of new drugs, and it is hopeful that it will be a bright light for the study of animal tumor models in the future.

However, they still have significant limitations in modeling human cancer, which is mainly reflected in the immune microenvironment and tumor microenvironment, or the more subtle differences caused by species-specific differences. Although we have developed the PDX model and humanized model to reduce these differences, it is urgent that we develop and establish more effective animal tumor models to facilitate more detailed investigation of the tumor development process.

Author contributions

All authors contributed to the article and approved the submitted version.

Funding

This study was funded by the National Natural Science Foundation of China (82002421), the Young Talent Program of Tangdu Hospital, Health Research Fund of Shaanxi Province (2021B004), and the Discipline Innovation Development Plan Project of Tangdu Hospital (2021LCYJ005).

Conflict of interest

The authors declare that the research was conducted in the absence of any commercial or financial relationships that could be construed as a potential conflict of interest.

Publisher's note

All claims expressed in this article are solely those of the authors and do not necessarily represent those of their affiliated organizations, or those of the publisher, the editors and the reviewers. Any product that may be evaluated in this article, or claim that may be made by its manufacturer, is not guaranteed or endorsed by the publisher.

References

1. Sung H, Ferlay J, Siegel RL, Laversanne M, Soerjomataram I, Jemal A, et al. Global cancer statistics 2020: GLOBOCAN estimates of incidence and mortality worldwide for 36 cancers in 185 countries. *CA Cancer J Clin* (2021) 71(3):209–49. doi: 10.3322/caac.21660

2. Sengupta R, Zaidi SK. AACR cancer progress report 2021: Discovery science driving clinical breakthroughs. *Clin Cancer Res* (2021) 27(21):5757–9. doi: 10.1158/1078-0432.CCR-21-3367

3. Aldea M, Andre F, Marabelle A, Dogan S, Barlesi F, Soria JC. Overcoming resistance to tumor-targeted and immune-targeted therapies. *Cancer Discovery* (2021) 11(4):874–99. doi: 10.1158/2159-8290.CD-20-1638

4. Robinson NB, Krieger K, Khan FM, Huffman W, Chang M, Naik A, et al. The current state of animal models in research: A review. *Int J Surg* (2019) 72:9–13. doi: 10.1016/j.ijsu.2019.10.015

5. Mouse Genome Sequencing Consortium, Waterston RH, Lindblad-Toh K, Birney E, Rogers J, Abril JF, et al. Initial sequencing and comparative analysis of the mouse genome. *Nature* (2002) 420(6915):520–62. doi: 10.1038/nature01262

6. Zeng L, Li W, Chen CS. Breast cancer animal models and applications. *Zool Res* (2020) 41(5):477–94. doi: 10.24272/j.issn.2095-8137.2020.095

7. Holland JF, Pogo BG. Mouse mammary tumor virus-like viral infection and human breast cancer. *Clin Cancer Res* (2004) 10(17):5647–9. doi: 10.1158/1078-0432.CCR-04-1234

8. Parisi F, Freer G, Mazzanti CM, Pistello M, Poli A. Mouse mammary tumor virus (MMTV) and MMTV-like viruses: An in-depth look at a controversial issue. *Viruses* (2022) 14(5):977. doi: 10.3390/v14050977

9. Heston WE, Vlahakis G. Mammary tumors, plaques, and hyperplastic alveolar nodules in various combinations of mouse inbred strains and the different lines of the mammary tumor virus. *Int J Cancer* (1971) 7(1):141–8. doi: 10.1002/ijc.2910070116

10. Nagasawa H, Yanai R, Taniguchi H, Tokuzen R, Nakahara W. Two-way selection of a stock of Swiss albino mice for mammary tumorigenesis: establishment of two new strains (SHN and SLN). *J Natl Cancer Inst* (1976) 57(2):425–30. doi: 10.1093/jnci/57.2.425

11. Sun B, Zhang S, Zhang D, Li Y, Zhao X, Luo Y, et al. Identification of metastasis-related proteins and their clinical relevance to triple-negative human breast cancer. *Clin Cancer Res* (2008) 14(21):7050–9. doi: 10.1158/1078-0432.CCR-08-0520

12. He YN, Zhang SC, Zhang HM. [Pathologic changes of spontaneous tumors in sprague-dawley and wistar rats]. *Zhonghua Bing Li Xue Za Zhi* (2017) 46(4):249–54. doi: 10.3760/cma.j.issn.0529-5807.2017.04.007

13. Haseman JK, Hailey JR, Morris RW. Spontaneous neoplasm incidences in Fischer 344 rats and B6C3F1 mice in two-year carcinogenicity studies: a national toxicology program update. *Toxicol Pathol* (1998) 26(3):428–41. doi: 10.1177/019262339802600318

14. Thai AA, Solomon BJ, Sequist LV, Gainor JF, Heist RS. Lung cancer. *Lancet* (2021) 398(10299):535–54. doi: 10.1016/S0140-6736(21)00312-3

15. Bade BC, Dela Cruz CS. Lung cancer 2020: Epidemiology, etiology, and prevention. *Clin Chest Med* (2020) 41(1):1–24. doi: 10.1016/j.ccm.2019.10.001

16. Tuveson DA, Jacks T. Modeling human lung cancer in mice: similarities and shortcomings. *Oncogene* (1999) 18(38):5318–24. doi: 10.1038/sj.onc.1203107

17. Shimkin MB, Stoner GD. Lung tumors in mice: application to carcinogenesis bioassay. *Adv Cancer Res* (1975) 21:1–58. doi: 10.1016/S0065-230X(08)60970-7

18. Lynch CJ. Studies on the relation between tumor susceptibility and heredity : Iii. spontaneous tumors of the lung in mice. *J Exp Med* (1926) 43(3):339–55. doi: 10.1084/jem.43.3.339

19. Mahler JF, Stokes W, Mann PC, Takaoka M, Maronpot RR. Spontaneous lesions in aging FVB/N mice. *Toxicol Pathol* (1996) 24(6):710–6. doi: 10.1177/019262339602400606

20. Dasgupta P, Henshaw C, Youlden DR, Clark PJ, Aitken JF, Baade PD. Global trends in incidence rates of primary adult liver cancers: A systematic review and meta-analysis. *Front Oncol* (2020) 10:171. doi: 10.3389/fonc.2020.00171

21. Dragani TA, Sozzi G, Della Porta G. Spontaneous and urethan-induced tumor incidence in B6C3F1 versus B6CF1 mice. *Tumori* (1984) 70(6):485–90. doi: 10.1177/030089168407000603

22. Soga M, Kishimoto Y, Kawamura Y, Inagaki S, Makino S, Saibara T. Spontaneous development of hepatocellular carcinomas in the FLS mice with hereditary fatty liver. *Cancer Lett* (2003) 196(1):43–8. doi: 10.1016/S0304-3835(03)00213-1

23. Yoshida MC, Masuda R, Sasaki M, Takeichi N, Kobayashi H, Dempo K, et al. New mutation causing hereditary hepatitis in the laboratory rat. *J Hered* (1987) 78(6):361–5. doi: 10.1093/oxfordjournals.jhered.a110416

24. Li Y, Togashi Y, Sato S, Emoto T, Kang JH, Takeichi N, et al. Spontaneous hepatic copper accumulation in long-Evans cinnamon rats with hereditary hepatitis. a model of wilson's disease. *J Clin Invest* (1991) 87(5):1858–61. doi: 10.1172/JCI115208

25. Marquez A, Villa-Trevino S, Gueraud F. The LEC rat: a useful model for studying liver carcinogenesis related to oxidative stress and inflammation. *Redox Rep* (2007) 12(1):35–9. doi: 10.1179/135100007X162220

26. Claude A. [Morphology and organization of nuclear constituents in a case of renal carcinoma in the mouse]. *C R Seances Soc Biol Fil* (1961) 252:4186–8.

27. Kawashima K, Ikeda H, Hartley JW, Stockert E, Rowe WP, Old LJ. Changes in expression of murine leukemia virus antigens and production of xenotropic virus in the late preleukemic period in AKR mice. *Proc Natl Acad Sci USA* (1976) 73(12):4680–4. doi: 10.1073/pnas.73.12.4680

28. Owens MH, Bonavida B. Immune functions characteristic of SJL/J mice and their association with age and spontaneous reticulum cell sarcoma. *Cancer Res* (1976) 36(3):1077–83.

29. Cowen PN. Some studies on the action of urethane on mice. *Br J Cancer* (1947) 1(4):401–5. doi: 10.1038/bjc.1947.39

30. Koohdani F, Sasani F, Mohammad K, Mehdipour P. Comparison of ki-67 antigen expression and K-ras mutation in lung tumours induced by urethane in mice. *Singapore Med J* (2009) 50(7):729–33.

31. De Benedictis G, Maiorano G, Chiecobianchi L, Fiore-Donati L. Lung carcinogenesis by urethane in newborn, suckling, and adult Swiss mice. *Br J Cancer* (1962) 16:686–9. doi: 10.1038/bjc.1962.78

32. Sozio F, Schioppa T, Sozzani S, Del Prete A. Urethane-induced lung carcinogenesis. *Methods Cell Biol* (2021) 163:45–57. doi: 10.1016/bs.mcb.2020.09.005

33. Hecht SS, Carmella SG, Kenney PM, Low SH, Arakawa K, Yu MC. Effects of cruciferous vegetable consumption on urinary metabolites of the tobacco-specific lung carcinogen 4-(methylnitrosamino)-1-(3-pyridyl)-1-butanone in singapore chinese. *Cancer Epidemiol Biomarkers Prev* (2004) 13(6):997–1004. doi: 10.1158/1055-9965.997.13.6

34. Hecht SS, Isaacs S, Trushin N. Lung tumor induction in A/J mice by the tobacco smoke carcinogens 4-(methylnitrosamino)-1-(3-pyridyl)-1-butanone and benzo[a] pyrene: a potentially useful model for evaluation of chemopreventive agents. *Carcinogenesis* (1994) 15(12):2721–5. doi: 10.1093/carcin/15.12.2721

35. Anderson LM, Hecht SS, Kovatch RM, Amin S, Hoffmann D, Rice JM. Tumorigenicity of the tobacco-specific carcinogen 4-(methyl-nitrosamino)-1-(3-pyridyl)-1-butanone in infant mice. *Cancer Lett* (1991) 58(3):177–81. doi: 10.1016/0304-3835(91)90097-2

36. Mervai Z, Egedi K, Kovalszky I, Baghy K. Diethylnitrosamine induces lung adenocarcinoma in FVB/N mouse. *BMC Cancer* (2018) 18(1):157. doi: 10.1186/s12885-018-4068-4

37. Chen Q, You X, Yang W, Jiang S, Lai J, Zhang H, et al. Survival of endogenous hepatic stem/progenitor cells in liver tissues during liver cirrhosis. *Life Sci* (2020) 241:117121. doi: 10.1016/j.lfs.2019.117121

38. Uehara T, Ainslie GR, Kutanzi K, Pogribny IP, Muskhelishvili L, Izawa T, et al. Molecular mechanisms of fibrosis-associated promotion of liver carcinogenesis. *Toxicol Sci* (2013) 132(1):53–63. doi: 10.1093/toxsci/kfs342

39. Raju NR, Yaeger MJ, Okazaki DL, Lovell K, Koestner A. Immunohistochemical characterization of rat central and peripheral nerve tumors induced by ethylnitrosourea. *Toxicol Pathol* (1990) 18(1Pt 1):18–23. doi: 10.1177/019262339001800103

40. Wang Y, Zhang Z, Yan Y, Lemon WJ, LaRegina M, Morrison C, et al. A chemically induced model for squamous cell carcinoma of the lung in mice: histopathology and strain susceptibility. *Cancer Res* (2004) 64(5):1647–54. doi: 10.1158/0008-5472.CAN-03-3273

41. Karnam KC, Ellutla M, Bodduluru LN, Kasala ER, Uppulapu SK, Kalyankumarraju M, et al. Preventive effect of berberine against DMBA-induced breast cancer in female sprague dawley rats. *BioMed Pharmacother* (2017) 92:207–14. doi: 10.1016/j.biopha.2017.05.069

42. Aisner J. *Comprehensive textbook of thoracic oncology*. Williams & Wilkins (1996).

43. Nettesheim P, Hammons AS. Induction of squamous cell carcinoma in the respiratory tract of mice. *J Natl Cancer Inst* (1971) 47(3):697–701.

44. Neufert C, Becker C, Neurath MF. An inducible mouse model of colon carcinogenesis for the analysis of sporadic and inflammation-driven tumor progression. *Nat Protoc* (2007) 2(8):1998–2004. doi: 10.1038/nprot.2007.279

45. Malyla V, Paudel KR, Shukla SD, Donovan C, Wadhwa R, Pickles S, et al. Recent advances in experimental animal models of lung cancer. *Future Med Chem* (2020) 12(7):567–70. doi: 10.4155/fmc-2019-0338

46. Field KJ, Lang CM. Hazards of urethane (ethyl carbamate): a review of the literature. *Lab Anim* (1988) 22(3):255–62. doi: 10.1258/002367788780746331

47. Mirvish SS. The carcinogenic action and metabolism of urethan and n-hydroxyurethan. *Adv Cancer Res* (1968) 11:1–42. doi: 10.1016/s0065-230x(08)60386-3

48. Malkinson AM, Beer DS. Major effect on susceptibility to urethan-induced pulmonary adenoma by a single gene in BALB/cBy mice. *J Natl Cancer Inst* (1983) 70(5):931–6.

49. Mirvish SS. The metabolism of n-hydroxyurethane in relation to its carcinogenic action: conversion into urethane and an n-hydroxyurethane glucuronide. *Biochim Biophys Acta* (1966) 117(1):1–12. doi: 10.1016/0304-4165(66)90146-2

50. Liu Y, Yin T, Feng Y, Cona MM, Huang G, Liu J, et al. Mammalian models of chemically induced primary malignancies exploitable for imaging-based preclinical theragnostic research. *Quant Imaging Med Surg* (2015) 5(5):708–29. doi: 10.3978/j.issn.2223-4292.2015.06.01

51. Ge GZ, Xu TR, Chen C. Tobacco carcinogen NNK-induced lung cancer animal models and associated carcinogenic mechanisms. *Acta Biochim Biophys Sin (Shanghai)* (2015) 47(7):477–87. doi: 10.1093/abbs/gmv041

52. Kiyohara C, Yoshimasu K, Takayama K, Nakanishi Y. NQO1, MPO, and the risk of lung cancer: a HuGE review. *Genet Med* (2005) 7(7):463–78. doi: 10.1097/01.gim.0000177530.55043.c1

53. Belinsky SA, Devereux TR, Foley JF, Maronpot RR, Anderson MW. Role of the alveolar type II cell in the development and progression of pulmonary tumors induced by 4-(methylnitrosamino)-1-(3-pyridyl)-1-butanone in the A/J mouse. *Cancer Res* (1992) 52(11):3164–73.

54. Anderson LM, Hecht SS, Dixon DE, Dove LF, Kovatch RM, Amin S, et al. Evaluation of the transplacental tumorigenicity of the tobacco-specific carcinogen 4-(methylnitrosamino)-1-(3-pyridyl)-1-butanone in mice. *Cancer Res* (1989) 49(14):3770–5.

55. Verna L, Whysner J, Williams GM. N-nitrosodiethylamine mechanistic data and risk assessment: bioactivation, DNA-adduct formation, mutagenicity, and tumor initiation. *Pharmacol Ther* (1996) 71(1-2):57–81. doi: 10.1016/0163-7258(96)00062-9

56. Huang Kohda K, Anjo T, Mochizuki M, Kawazoe Y, Okada M. Mutagenicity of alpha-acetoxy derivatives of n-methyl-N-benzylnitrosamine and N,N-dibenzylnitrosamine in V79 cells: A comparison between methylating and benzylating mutagens. *Gan* (1982) 73(4):517–21.

57. You M, Wang Y, Lineen AM, Gunning WT, Stoner GD, Anderson MW. Mutagenesis of the K-ras protooncogene in mouse lung tumors induced by n-ethyl-N-nitrosourea or n-nitrosodiethylamine. *Carcinogenesis* (1992) 13(9):1583–6. doi: 10.1093/carcin/13.9.1583

58. Cardesa A, Pour P, Althoff J, Mohr U. Comparative studies of neoplastic response to a single dose of nitroso compounds. 4. the effect of dimethyl- and diethyl-nitrosamine in Swiss mice. *Z Krebsforsch Klin Onkol Cancer Res Clin Oncol* (1974) 81(3-4):229–33. doi: 10.1007/BF00305023

59. Salinger AP, Justice MJ. Mouse mutagenesis using n-Ethyl-N-Nitrosourea (ENU). *CSH Protoc* (2008) 2008:pdb prot4985. doi: 10.1101/pdb.prot4985

60. Wang Y, Zhang Z, Garbow JR, Rowland DJ, Lubet RA, Sit D, et al. Chemoprevention of lung squamous cell carcinoma in mice by a mixture of Chinese herbs. *Cancer Prev Res (Phila)* (2009) 2(7):634–40. doi: 10.1158/1940-6207.CAPR-09-0052

61. Jung KJ, Wallig MA, Singletary KW. Purple grape juice inhibits 7,12-dimethylbenz[a]anthracene (DMBA)-induced rat mammary tumorigenesis and in vivo DMBA-DNA adduct formation. *Cancer Lett* (2006) 233(2):279–88. doi: 10.1016/j.canlet.2005.03.020

62. Beer DG, Stoner GD. Clinical models of chemoprevention for the esophagus. *Hematol Oncol Clin North Am* (1998) 12(5):1055–77. doi: 10.1016/S0889-8588(05)70041-1

63. Papanikolaou A, Shank RC, Delker DA, Povey A, Cooper DP, Rosenberg DW. Initial levels of azoxymethane-induced DNA methyl adducts are not predictive of tumor susceptibility in inbred mice. *Toxicol Appl Pharmacol* (1998) 150(1):196–203. doi: 10.1006/taap.1998.8393

64. Younossi Z, Anstee QM, Marietti M, Hardy T, Henry L, Eslam M, et al. Global burden of NAFLD and NASH: Trends, predictions, risk factors and prevention. *Nat Rev Gastroenterol Hepatol* (2018) 15(1):11–20. doi: 10.1038/nrgastro.2017.109

65. Asgharpour A, Cazanave SC, Pacana T, Seneshaw M, Vincent R, Banini BA, et al. A diet-induced animal model of non-alcoholic fatty liver disease and hepatocellular cancer. *J Hepatol* (2016) 65(3):579–88. doi: 10.1016/j.jhep.2016.05.005

66. Abalo KD, Rage E, Leuraud K, Richardson DB, Le Pointe HD, Laurier D, et al. Early life ionizing radiation exposure and cancer risks: systematic review and meta-analysis. *Pediatr Radiol* (2021) 51(1):45–56. doi: 10.1007/s00247-020-04803-0

67. Morgan C. Ionizing radiation study. *Science* (1979) 206(4420):769. doi: 10.1126/science.493980

68. Edmondson EF, Hunter NR, Weil MM, Mason KA. Tumor induction in mice after localized single- or fractionated-dose irradiation: Differences in tumor histotype and genetic susceptibility based on dose scheduling. *Int J Radiat Oncol Biol Phys* (2015) 92(4):829–36. doi: 10.1016/j.ijrobp.2015.03.002

69. Johnson L, Mercer K, Greenbaum D, Bronson RT, Crowley D, Tuveson DA, et al. Somatic activation of the K-ras oncogene causes early onset lung cancer in mice. *Nature* (2001) 410(6832):1111–6. doi: 10.1038/35074129

70. Hofmann MH, Gerlach D, Misale S, Petronczki M, Kraut N. Expanding the reach of precision oncology by drugging all KRAS mutants. *Cancer Discov* (2022) 12(4):924–37. doi: 10.1158/2159-8290.CD-21-1331

71. Petitjean A, Mathe E, Kato S, Ishioka C, Tavtigian SV, Hainaut P, et al. Impact of mutant p53 functional properties on TP53 mutation patterns and tumor phenotype: lessons from recent developments in the IARC TP53 database. *Hum Mutat* (2007) 28(6):622–9. doi: 10.1002/humu.20495

72. Saleh MM, Scheffler M, Merkelbach-Bruse S, Scheel AH, Ulmer B, Wolf J, et al. Comprehensive analysis of TP53 and KEAP1 mutations and their impact on survival in localized- and advanced-stage NSCLC. *J Thorac Oncol* (2022) 17(1):76–88. doi: 10.1016/j.jtho.2021.08.764

73. Ngeow J, Eng C. PTEN in hereditary and sporadic cancer. *Cold Spring Harb Perspect Med* (2020) 10(4):a036087. doi: 10.1101/cshperspect.a036087

74. Voldborg BR, Damstrup L, Spang-Thomsen M, Poulsen HS. Epidermal growth factor receptor (EGFR) and EGFR mutations, function and possible role in clinical trials. *Ann Oncol* (1997) 8(12):1197–206. doi: 10.1023/A:1008209720526

75. Santos EDS, Nogueira KAB, Fernandes LCC, Martins JRP, Reis AVF, Neto JBV, et al. EGFR targeting for cancer therapy: Pharmacology and immunoconjugates with drugs and nanoparticles. *Int J Pharm* (2021) 592:120082. doi: 10.1016/j.ijpharm.2020.120082

76. Sharpless NE, Depinho RA. The mighty mouse: genetically engineered mouse models in cancer drug development. *Nat Rev Drug Discov* (2006) 5(9):741–54. doi: 10.1038/nrd2110

77. Prior IA, Hood FE, Hartley JL. The frequency of ras mutations in cancer. *Cancer Res* (2020) 80(14):2969–74. doi: 10.1158/0008-5472.CAN-19-3682

78. Riely GJ, Kris MG, Rosenbaum D, Marks J, Li A, Chitale DA, et al. Frequency and distinctive spectrum of KRAS mutations in never smokers with lung adenocarcinoma. *Clin Cancer Res* (2008) 14(18):5731–4. doi: 10.1158/1078-0432.CCR-08-0646

79. Brose MS, Volpe P, Feldman M, Kumar M, Rishi I, Gerrero R, et al. BRAF and RAS mutations in human lung cancer and melanoma. *Cancer Res* (2002) 62(23):6997–7000.

80. Reck M, Carbone DP, Garassino M, Barlesi F. Targeting KRAS in non-small-cell lung cancer: recent progress and new approaches. *Ann Oncol* (2021) 32(9):1101–10. doi: 10.1016/j.annonc.2021.06.001

81. Prior IA, Lewis PD, Mattos C. A comprehensive survey of ras mutations in cancer. *Cancer Res* (2012) 72(10):2457–67. doi: 10.1158/0008-5472.CAN-11-2612

82. Malkinson AM. Molecular comparison of human and mouse pulmonary adenocarcinomas. *Exp Lung Res* (1998) 24(4):541–55. doi: 10.3109/01902149809087385

83. Ushijima T, Sasako M. Focus on gastric cancer. *Cancer Cell* (2004) 5(2):121–5. doi: 10.1016/S1535-6108(04)00033-9

84. Brembeck FH, Moffett J, Wang TC, Rustgi AK. The keratin 19 promoter is potent for cell-specific targeting of genes in transgenic mice. *Gastroenterology* (2001) 120(7):1720–8. doi: 10.1053/gast.2001.24846

85. Mann KM, Ying H, Juan J, Jenkins NA, Copeland NG. KRAS-related proteins in pancreatic cancer. *Pharmacol Ther* (2016) 168:29–42. doi: 10.1016/j.pharmthera.2016.09.003

86. Levine AJ. Spontaneous and inherited TP53 genetic alterations. *Oncogene* (2021) 40(41):5975–83. doi: 10.1038/s41388-021-01991-3

87. Donehower LA, Harvey M, Slagle BL, McArthur MJ, Montgomery CA Jr, Butel JS, et al. Mice deficient for p53 are developmentally normal but susceptible to spontaneous tumours. *Nature* (1992) 356(6366):215–21. doi: 10.1038/356215a0

88. Harvey M, McArthur MJ, Montgomery CA Jr, Butel JS, Bradley A, Donehower LA. Spontaneous and carcinogen-induced tumorigenesis in p53-deficient mice. *Nat Genet* (1993) 5(3):225–9. doi: 10.1038/ng1193-225

89. Machida Y, Sudo Y, Uchiya N, Imai T. Increased susceptibility to mammary carcinogenesis and an opposite trend in endometrium in Trp53 heterozygous knockout female mice by backcrossing the BALB/c strain onto the background C3H strain. *J Toxicol Pathol* (2019) 32(3):197–203. doi: 10.1293/tox.2018-0057

90. Ohgaki H, Fukuda M, Tohma Y, Huang H, Stoica G, Tatematsu M, et al. Effect of intragastric application of n-methylnitrosourea in p53 knockout mice. *Mol Carcinog* (2000) 28(2):97–101. doi: 10.1002/1098-2744(200006)28:2<97::AID-MC5>3.0.CO;2-O

91. Meuwissen R, Linn SC, Linnoila RI, Zevenhoven J, Mooi WJ, Berns A. Induction of small cell lung cancer by somatic inactivation of both Trp53 and Rb1 in a conditional mouse model. *Cancer Cell* (2003) 4(3):181–9. doi: 10.1016/S1535-6108(03)00220-4

92. Liu Y, Gu W. The complexity of p53-mediated metabolic regulation in tumor suppression. *Semin Cancer Biol* (2021) 85:4–32. doi: 10.1016/j.semcancer.2021.03.010

93. Li T, Kon N, Jiang L, Tan M, Ludwig T, Zhao Y, et al. Tumor suppression in the absence of p53-mediated cell-cycle arrest, apoptosis, and senescence. *Cell* (2012) 149(6):1269–83. doi: 10.1016/j.cell.2012.04.026

94. Hanrahan AJ, Schultz N, Westfal ML, Sakr RA, Giri DD, Scarperi S, et al. Genomic complexity and AKT dependence in serous ovarian cancer. *Cancer Discovery* (2012) 2(1):56–67. doi: 10.1158/2159-8290.CD-11-0170

95. Cho KR. Ovarian cancer update: lessons from morphology, molecules, and mice. *Arch Pathol Lab Med* (2009) 133(11):1775–81. doi: 10.5858/133.11.1775

96. Tsuruta H, Kishimoto H, Sasaki T, Horie Y, Natsui M, Shibata Y, et al. Hyperplasia and carcinomas in pten-deficient mice and reduced PTEN protein in human bladder cancer patients. *Cancer Res* (2006) 66(17):8389–96. doi: 10.1158/0008-5472.CAN-05-4627

97. Worby CA, Dixon JE. Pten. *Annu Rev Biochem* (2014) 83:641–69. doi: 10.1146/annurev-biochem-082411-113907

98. Di Cristofano A, Kotsi P, Peng YF, Cordon-Cardo C, Elkon KB, Pandolfi PP. Impaired fas response and autoimmunity in pten+/- mice. *Science* (1999) 285(5436):2122–5. doi: 10.1126/science.285.5436.2122

99. Horie Y, Suzuki A, Kataoka E, Sasaki T, Hamada K, Sasaki J, et al. Hepatocyte-specific pten deficiency results in steatohepatitis and hepatocellular carcinomas. *J Clin Invest* (2004) 113(12):1774–83. doi: 10.1172/JCI20513

100. Yanagi S, Kishimoto H, Kawahara K, Sasaki T, Sasaki M, Nishio M, et al. Pten controls lung morphogenesis, bronchioalveolar stem cells, and onset of lung adenocarcinomas in mice. *J Clin Invest* (2007) 117(10):2929–40. doi: 10.1172/JCI31854

101. Russo A, Czarnecki AA, Dean M, Modi DA, Lantvit DD, Hardy L, et al. PTEN loss in the fallopian tube induces hyperplasia and ovarian tumor formation. *Oncogene* (2018) 37(15):1976–90. doi: 10.1038/s41388-017-0097-8

102. Schlessinger J. Ligand-induced, receptor-mediated dimerization and activation of EGF receptor. *Cell* (2002) 110(6):669–72. doi: 10.1016/S0092-8674(02)00966-2

103. Kumar R, George B, Campbell MR, Verma N, Paul AM, Melo-Alvim C, et al. HER family in cancer progression: From discovery to 2020 and beyond. *Adv Cancer Res* (2020) 147:109–60. doi: 10.1016/bs.acr.2020.04.001

104. Sibilia M, Kroismayr R, Lichtenberger BM, Natarajan A, Hecking M, Holcmann M. The epidermal growth factor receptor: from development to tumorigenesis. *Differentiation* (2007) 75(9):770–87. doi: 10.1111/j.1432-0436.2007.00238.x

105. Sibilia M, Wagner EF. Strain-dependent epithelial defects in mice lacking the EGF receptor. *Science* (1995) 269(5221):234–8. doi: 10.1126/science.7618085

106. Ohashi K, Rai K, Fujiwara Y, Osawa M, Hirano S, Takata K, et al. Induction of lung adenocarcinoma in transgenic mice expressing activated EGFR driven by the SP-c promoter. *Cancer Sci* (2008) 99(9):1747–53. doi: 10.1111/j.1349-7006.2008.00875.x

107. Ohashi K, Takigawa N, Osawa M, Ichihara E, Takeda H, Kubo T, et al. Chemopreventive effects of gefitinib on nonsmoking-related lung tumorigenesis in activating epidermal growth factor receptor transgenic mice. *Cancer Res* (2009) 69(17):7088–95. doi: 10.1158/0008-5472.CAN-08-4205

108. Iranzo J, Martincorena I, Koonin EV. Cancer-mutation network and the number and specificity of driver mutations. *Proc Natl Acad Sci USA* (2018) 115(26):E6010–9. doi: 10.1073/pnas.1803155115

109. Jackson EL, Olive KP, Tuveson DA, Bronson R, Crowley D, Brown M, et al. The differential effects of mutant p53 alleles on advanced murine lung cancer. *Cancer Res* (2005) 65(22):10280–8. doi: 10.1158/0008-5472.CAN-05-2193

110. Maddipati R, Stanger BZ. Pancreatic cancer metastases harbor evidence of polyclonality. *Cancer Discovery* (2015) 5(10):1086–97. doi: 10.1158/2159-8290.CD-15-0120

111. Talbert EE, Cuitiño MC, Ladner KJ, Rajasekerea PV, Siebert M, Shakya R, et al. Modeling human cancer-induced cachexia. *Cell Rep* (2019) 28(6):1612–1622.e4. doi: 10.1016/j.celrep.2019.07.016

112. Dankort D, Curley DP, Cartlidge RA, Nelson B, Karnezis AN, Damsky WE Jr, et al. Braf(V600E) cooperates with pten loss to induce metastatic melanoma. *Nat Genet* (2009) 41(5):544–52. doi: 10.1038/ng.356

113. Mollaoglu G, Guthrie MR, Böhm S, Brägelmann J, Can I, Ballieu PM, et al. MYC drives progression of small cell lung cancer to a variant neuroendocrine subtype with vulnerability to aurora kinase inhibition. *Cancer Cell* (2017) 31(2):270–85. doi: 10.1016/j.ccell.2016.12.005

114. Flanagan SP. 'Nude', a new hairless gene with pleiotropic effects in the mouse. *Genet Res* (1966) 8(3):295–309. doi: 10.1017/s0016672300010168

115. Bosma GC, Custer RP, Bosma MJ. A severe combined immunodeficiency mutation in the mouse. *Nature* (1983) 301(5900):527–30. doi: 10.1038/301527a0

116. McCune JM, Namikawa R, Kaneshima H, Shultz LD, Lieberman M, Weissman IL. The SCID-hu mouse: murine model for the analysis of human hematolymphoid differentiation and function. *Science* (1988) 241(4873):1632–9. doi: 10.1126/science.241.4873.1632

117. Mosier DE, Gulizia RJ, Baird SM, Wilson DB. Transfer of a functional human immune system to mice with severe combined immunodeficiency. *Nature* (1988) 335(6187):256–9. doi: 10.1038/335256a0

118. Shigematsu T, Wolf RE, Granger DN. T-Lymphocytes modulate the microvascular and inflammatory responses to intestinal ischemia-reperfusion. *Microcirculation* (2002) 9(2):99–109. doi: 10.1080/mic.9.2.99.109

119. Miao M, Masengere H, Yu G, Shan F. Reevaluation of NOD/SCID mice as NK cell-deficient models. *BioMed Res Int 2021* (2021) p:8851986. doi: 10.1155/2021/8851986

120. Makino S, Kunimoto K, Muraoka Y, Mizushima Y, Katagiri K, Tochino Y. Breeding of a non-obese, diabetic strain of mice. *Jikken Dobutsu* (1980) 29(1):1–13. doi: 10.1538/expanim1978.29.1_1

121. Kikutani H, Makino S. The murine autoimmune diabetes model: NOD and related strains. *Adv Immunol* (1992) 51:285–322. doi: 10.1016/S0065-2776(08)60490-3

122. Shultz LD, Schweitzer PA, Christianson SW, Gott B, Schweitzer IB, Tennent B, et al. Multiple defects in innate and adaptive immunologic function in NOD/LtSz-scid mice. *J Immunol* (1995) 154(1):180–91. doi: 10.4049/jimmunol.154.1.180

123. Shultz LD, Ishikawa F, Greiner DL. Humanized mice in translational biomedical research. *Nat Rev Immunol* (2007) 7(2):118–30. doi: 10.1038/nri2017

124. Jung J, Seol HS, Chang S. The generation and application of patient-derived xenograft model for cancer research. *Cancer Res Treat* (2018) 50(1):1–10. doi: 10.4143/crt.2017.307

125. Okada S, Vaeteewoottacharn K, Kariya R. Application of highly immunocompromised mice for the establishment of patient-derived xenograft (PDX) models. *Cells* (2019) 8(8):889. doi: 10.3390/cells8080889

126. Collins AT, Lang SH. A systematic review of the validity of patient derived xenograft (PDX) models: the implications for translational research and personalised medicine. *PeerJ* (2018) 6:e5981. doi: 10.7717/peerj.5981

127. Murayama T, Gotoh N. Patient-derived xenograft models of breast cancer and their application. *Cells* (2019) 8(6):621. doi: 10.3390/cells8060621

128. Julien S, Merino-Trigo A, Lacroix L, Pocard M, Goéré D, Mariani P, et al. Characterization of a large panel of patient-derived tumor xenografts representing the clinical heterogeneity of human colorectal cancer. *Clin Cancer Res* (2012) 18(19):5314–28. doi: 10.1158/1078-0432.CCR-12-0372

129. Bertotti A, Migliardi G, Galimi F, Sassi F, Torti D, Isella C, et al. A molecularly annotated platform of patient-derived xenografts ("xenopatients") identifies HER2 as an effective therapeutic target in cetuximab-resistant colorectal cancer. *Cancer Discov* (2011) 1(6):508–23. doi: 10.1158/2159-8290.CD-11-0109

130. Mattie M, Christensen A, Chang MS, Yeh W, Said S, Shostak Y, et al. Molecular characterization of patient-derived human pancreatic tumor xenograft models for preclinical and translational development of cancer therapeutics. *Neoplasia* (2013) 15(10):1138–50. doi: 10.1593/neo.13922

131. Garrido-Laguna I, Uson M, Rajeshkumar NV, Tan AC, de Oliveira E, Karikari C, et al. Tumor engraftment in nude mice and enrichment in stroma- related gene pathways predict poor survival and resistance to gemcitabine in patients with pancreatic cancer. *Clin Cancer Res* (2011) 17(17):5793–800. doi: 10.1158/1078-0432.CCR-11-0341

132. Marangoni E, Vincent-Salomon A, Auger N, Degeorges A, Assayag F, de Cremoux P, et al. A new model of patient tumor-derived breast cancer xenografts for preclinical assays. *Clin Cancer Res* (2007) 13(13):3989–98. doi: 10.1158/1078-0432.CCR-07-0078

133. DeRose YS, Wang G, Lin YC, Bernard PS, Buys SS, Ebbert MT, et al. Tumor grafts derived from women with breastcancer authentically reflect tumor pathology, growth, metastasis and disease outcomes. *Nat Med* (2011) 17(11):1514–20. doi: 10.1038/nm.2454

134. Mak IW, Evaniew N, Ghert M. Lost in translation: animal models and clinical trials in cancer treatment. *Am J Transl Res* (2014) 6(2):114–8.

135. DiMasi JA, Reichert JM, Feldman L, Malins A. Clinical approval success rates for investigational cancer drugs. *Clin Pharmacol Ther* (2013) 94(3):329–35. doi: 10.1038/clpt.2013.117

136. Tentler JJ, Tan AC, Weekes CD, Jimeno A, Leong S, Pitts TM, et al. Patient-derived tumour xenografts as models for oncology drug development. *Nat Rev Clin Oncol* (2012) 9(6):338–50. doi: 10.1038/nrclinonc.2012.61

137. Zhang F, Wang W, Long Y, Liu H, Cheng J, Guo L, et al. Characterization of drug responses of mini patient-derived xenografts in mice for predicting cancer patient clinical therapeutic response. *Cancer Commun (Lond)* (2018) 38(1):60. doi: 10.1186/s40880-018-0329-5

138. Portuguese AJ, Tykodi SS, Blosser CD, Gooley TA, Thompson JA, Hall ET. Immune checkpoint inhibitor use in solid organ transplant recipients: A systematic review. *J Natl Compr Canc Netw* (2022) 20(4):406–416.e11. doi: 10.6004/jnccn.2022.7009

139. Huang R, Li X, He Y, Zhu W, Gao L, Liu Y, et al. Recent advances in CAR-T cell engineering. *J Hematol Oncol* (2020) 13(1):86. doi: 10.1186/s13045-020-00910-5

140. Shultz LD, Brehm MA, Garcia-Martinez JV, Greiner DL. Humanized mice for immune system investigation: progress, promise and challenges. *Nat Rev Immunol* (2012) 12(11):786–98. doi: 10.1038/nri3311

141. Ito M, Hiramatsu H, Kobayashi K, Suzue K, Kawahata M, Hioki K, et al. NOD/SCID/gamma(c)(null) mouse: an excellent recipient mouse model for engraftment of human cells. *Blood* (2002) 100(9):3175–82. doi: 10.1182/blood-2001-12-0207

142. Shultz LD, Lyons BL, Burzenski LM, Gott B, Chen X, Chaleff S, et al. Human lymphoid and myeloid cell development in NOD/LtSz-scid IL2R gamma null mice engrafted with mobilized human hemopoietic stem cells. *J Immunol* (2005) 174(10):6477–89. doi: 10.4049/jimmunol.174.10.6477

143. Legrand N, Huntington ND, Nagasawa M, Bakker AQ, Schotte R, Strick-Marchand H, et al. Functional CD47/signal regulatory protein alpha (SIRP(alpha)) interaction is required for optimal human T- and natural killer- (NK) cell homeostasis in vivo. *Proc Natl Acad Sci USA* (2011) 108(32):13224–9. doi: 10.1073/pnas.1101398108

144. Jangalwe S, Shultz LD, Mathew A, Brehm MA. Improved b cell development in humanized NOD-scid IL2Rgamma(null) mice transgenically expressing human stem cell factor, granulocyte-macrophage colony-stimulating factor and interleukin-3. *Immun Inflamm Dis* (2016) 4(4):427–40. doi: 10.1002/iid3.124

145. De La Rochere P, Guil-Luna S, Decaudin D, Azar G, Sidhu SS, Piaggio E. Humanized mice for the study of immuno-oncology. *Trends Immunol* (2018) 39(9):748–63. doi: 10.1016/j.it.2018.07.001

146. King MA, Covassin L, Brehm MA, Racki W, Pearson T, Leif J, et al. Human peripheral blood leucocyte non-obese diabetic-severe combined immunodeficiency interleukin-2 receptor gamma chain gene mouse model of xenogeneic graft-versus-host-like disease and the role of host major histocompatibility complex. *Clin Exp Immunol* (2009) 157(1):104–18. doi: 10.1111/j.1365-2249.2009.03933.x

147. Traggiai E, Chicha L, Mazzucchelli L, Bronz L, Piffaretti JC, Lanzavecchia A, et al. Development of a human adaptive immune system in cord blood cell-transplanted mice. *Science* (2004) 304(5667):104–7. doi: 10.1126/science.1093933

148. Holyoake TL, Nicolini FE, Eaves CJ. Functional differences between transplantable human hematopoietic stem cells from fetal liver, cord blood, and adult marrow. *Exp Hematol* (1999) 27(9):1418–27. doi: 10.1016/S0301-472X(99)00078-8

149. Watanabe Y, Takahashi T, Okajima A, Shiokawa M, Ishii N, Katano I, et al. The analysis of the functions of human b and T cells in humanized NOD/shi-scid/gammac(null) (NOG) mice (hu-HSC NOG mice). *Int Immunol* (2009) 21(7):843–58. doi: 10.1093/intimm/dxp050

150. Brehm MA, Bortell R, Diiorio P, Leif J, Laning J, Cuthbert A, et al. Human immune system development and rejection of human islet allografts in spontaneously diabetic NOD-Rag1null IL2rgammanull Ins2Akita mice. *Diabetes* (2010) 59(9):2265–70. doi: 10.2337/db10-0323

151. Xia J, Hu Z, Yoshihara S, Li Y, Jin CH, Tan S, et al. Modeling human leukemia immunotherapy in humanized mice. *EBioMedicine* (2016) 10:101–8. doi: 10.1016/j.ebiom.2016.06.028

152. Ericsson AC, Crim MJ, Franklin CL. A brief history of animal modeling. *Mo Med* (2013) 110(3):201–5.

frontiers | Frontiers in Immunology

TYPE Original Research
PUBLISHED 28 March 2023
DOI 10.3389/fimmu.2023.1041525

Check for updates

OPEN ACCESS

EDITED BY
An Coosemans,
KU Leuven, Belgium

REVIEWED BY
Weinan Guo,
Fourth Military Medical University, China
Taobo Hu,
Peking University People's Hospital, China
Guan-Jun Yang,
Ningbo University, China

*CORRESPONDENCE
Yao Luo
luoyao@scu.edu.cn
Wenguang Fu
fuwg@swmu.edu.cn

†These authors have contributed equally to this work and share first authorship

SPECIALTY SECTION
This article was submitted to Cancer Immunity and Immunotherapy, a section of the journal Frontiers in Immunology

RECEIVED 11 September 2022
ACCEPTED 08 March 2023
PUBLISHED 28 March 2023

CITATION
Gao L, Zhu L, Shen C, Hou X, Chen Y, Zou L, Qiang H, Teichmann AT, Fu W and Luo Y (2023) The transdermal cream of Formestane anti-breast cancer by controlling PI3K-Akt pathway and the tumor immune microenvironment. *Front. Immunol.* 14:1041525. doi: 10.3389/fimmu.2023.1041525

COPYRIGHT
© 2023 Gao, Zhu, Shen, Hou, Chen, Zou, Qiang, Teichmann, Fu and Luo. This is an open-access article distributed under the terms of the Creative Commons Attribution License (CC BY). The use, distribution or reproduction in other forums is permitted, provided the original author(s) and the copyright owner(s) are credited and that the original publication in this journal is cited, in accordance with accepted academic practice. No use, distribution or reproduction is permitted which does not comply with these terms.

The transdermal cream of Formestane anti-breast cancer by controlling PI3K-Akt pathway and the tumor immune microenvironment

Lanyang Gao[1†], Lei Zhu[2†], Chen Shen[2], Xiaoming Hou[2], Youyou Chen[1], Linglin Zou[1], Huiyan Qiang[1], Alexander T. Teichmann[3], Wenguang Fu[1*] and Yao Luo[2*]

[1]Academician (Expert) Workstation of Sichuan Province, The Affiliated Hospital of Southwest Medical University, Southwest Medical University, Luzhou, China, [2]West China Hospital, Sichuan University, Chengdu, China, [3]Sichuan Provincial Center for Gynaecology and Breast Disease, The Affiliated Hospital of Southwest Medical University, Southwest Medical University, Luzhou, China

Background: Treatment of ER^+ breast cancer with intramuscular formulation of Formestane (4-OHA) shrinks the tumor within weeks. Since the tedious way of intramuscular administration and side effects are not suited for adjuvant treatment, Formestane was withdrawn from the market. A new transdermal formulation of 4-OHA cream may overcome the defects and retain the effect of shrinking the breast cancer tumor. However, the effects of 4-OHA cream on breast cancer need further confirmatory studies.

Methods: In this work, *in vivo*, the influence of 4-OHA cream on breast cancer was evaluated using the mode of 7,12-dimethylbenz(a)anthracene (DMBA) induced rat mammary cancer. We explored the common molecule mechanisms of action of 4-OHA cream and its injection formulation on breast cancer through RNA- sequencing-based transcriptome analysis and several biochemical experiments.

Results: The results showed that the cream substantially reduced the entire quantity, size, and volum of tumors in DMBA-treated rats consistent with 4-OHA injection, and indicated that there were comprehensive signals involved in 4-OHA antitumor activity, such as ECM-receptor interaction, focal adhesion, PI3K-Akt signaling pathway, and proteoglycans in cancer. In addition, we observed that both 4-OHA formulations could enhance immune infiltration, especially $CD8^+$ T cells, B cells, natural killer cells, and macrophages infiltration, in the DMBA-induced mammary tumor tissues. The antitumor effects of 4-OHA partly depended on these immune cells.

Conclusion: 4-OHA cream could inhibit breast cancer growth as its injection formulation and may provide a new way for neoadjuvant treatment of ER^+ breast cancer.

KEYWORDS

Formestane cream, DMBA-induced mammary cancer, PI3K-Akt signaling pathway, tumor immune microenvironment, RNA transcriptome sequencing

1 Introduction

More than 50% of breast cancers are estrogen receptor alpha (ERα)-positive and their development and growth depend on estrogens (1, 2). Consequently, the major treatment strategy is deprivation of estradiol (E2). In postmenopausal women, estrogen deprivation is achieved by inhibiting aromatase, which is a key enzyme of estrogen synthesis from adrenal precursor molecules (3). 4-hydroxyandrostenedione (4-OHA), named Formestane, is the first specific steroidal aromatase inhibitor (AI) in clinical use (4). Its intramuscular depot preparation (Lentaron®Depot) is administered at a single dose of 250 mg/patient/application once every 2 weeks. High serum concentrations of the aromatase inhibitor (AI) are aimed at taking the desired action in the tumor, and exploring whether it would lead to systemic side effects by both reducing the systemic estrogen levels and inhibiting the autocrine production of estrogens. Unfortunately, because the tedious way of administration and side effects are not suited for adjuvant treatment, Lentaron was withdrawn from the market. Nevertheless, clinical trials have found that 4-OHA could be still effective when the tumor showed a relapse in spite of thoroughly removing the E2 by nonsteroidal AIs (5–7). This clinical effect must be due to a mechanism independent from the deprivation of E2. To reuse the clinical benefits of 4-OHA on mammary carcinoma and overcome its disadvantages, Heinrich Wieland and his colleagues developed a new formulation of 4-OHA cream which could be topically applied to the mammary gland and then penetrate through the skin and concentrate in the fatty tissue (8). The cream was clinically evaluated by Savetherapeutics®, a Germany-based biotech company. Four studies were conducted, in which resorption, tolerability, and efficacy of the topically applied formestane were shown. However, these promising results need further confirmatory studies to finally achieve market authorization for the transdermal formestane cream.

Brodie et al. had previously shown that 4-OHA markedly shrank dimethylbenz(a)anthracene (DMBA)-induced mammary carcinoma in rats (9). DMBA-induced tumors of rats were the most widely used *in vivo* model of breast cancer (3, 10–12). Therefore, in the study reported here, we also used this model to evaluate the effects of 4-OHA cream on breast cancer (Figure 1A). In addition, the effects of 4-OHA on the immune microenvironment in rats' breast cancer model were assessed as well. Moreover, we clarified the underlying mechanisms of 4-OHA action on breast cancer (Figure 1B). This study is the first report to identify the global gene expression profile and the intra-tumor immune landscape of DMBA-induced mammary tumor after treatment with 4-OHA.

2 Materials and methods

2.1 Animal

Female Sprague-Dawley (SD) rats were supplied by Chengdu dashuo experimental animal Co. Ltd. Rats are housed at five per cage under a regimen of 14 h of light and 10 h of darkness (lights on

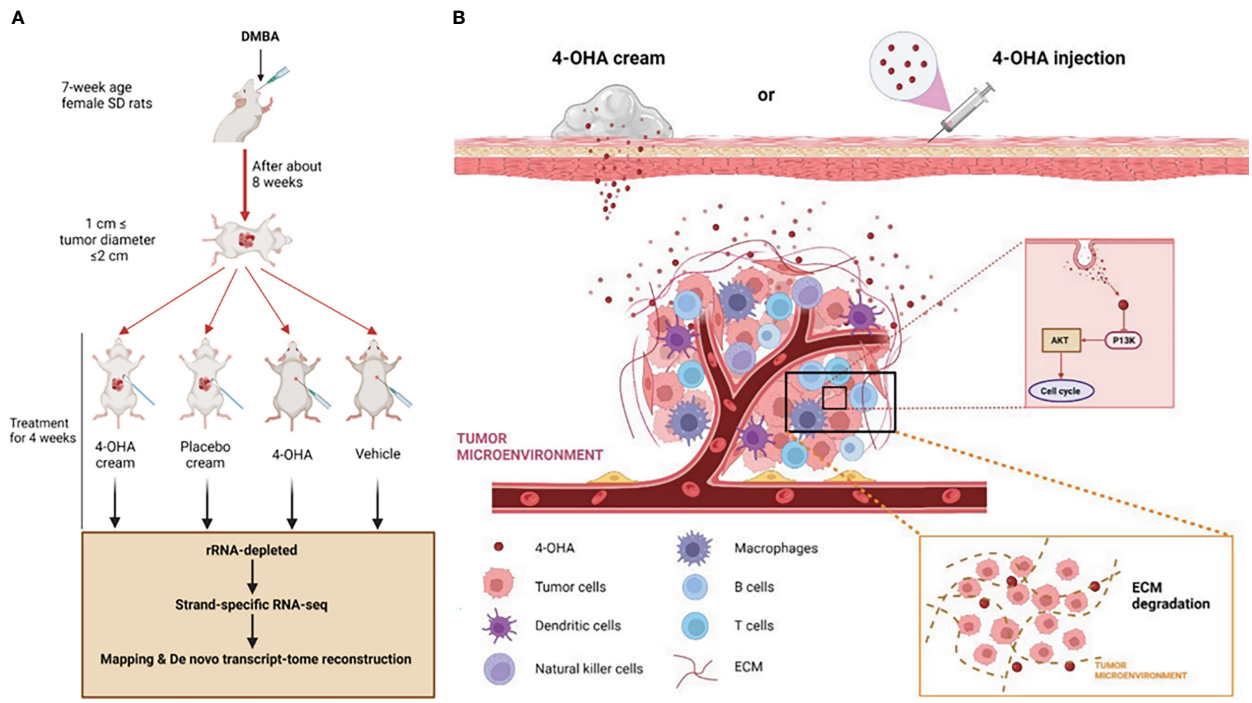

FIGURE 1
Study design and mechanism of 4-OHA cream anti-breast cancer. Study design. Mammary tumors were initiated with DMBA at PND 49, and when the first tumor per rat reached a size of 1.5 cm in diameter but less than 2 cm, 4-OHA was given to the rats as indicated in the Materials and Methods. **(A)** Tumors responding to 4-OHA were harvested for RNA-seq. **(B)** The mechanism of action of 4-OHA cream.

at 05:00 a.m.). Animals received rat chow and water *ad libitum*. The animal experiments were performed under the 'Guideline for Care and Use of Experimental Animals' and were approved by the Institutional Review Board (or Ethics Committee) of The Affiliated Hospital of Southwest Medical University, Southwest Medical University (protocol code 201903-37 and date of approval 2019-03-05).

2.2 Mammary tumor model

Six-week-old female SD rats, weighing approximately 150 g, were used in this study. Mammary carcinomas were induced by two oral administrations of DMBA (Sigma Chemical Co.) at a total dose of 20 mg/body at 6 and 7 weeks of age. Starting 40 days after DMBA treatment, animals were examined weekly by palpation; the rats with at least one tumor reaching 1.5 cm in diameter were placed sequentially into experimental groups (10 rats/test group). The body weights of the rats were also measured weekly. Animals with no tumors were discarded 150 days after DMBA treatment. The two perpendicular tumor axes were measured with calipers twice a week. Tumor volume was calculated by the formula $d^2 \times D/2$, where d is the minimal and D is the maximal diameter.

2.3 Drug and treatment schedule

4-OHA (Sigma Chemical Co.) was dissolved in benzyl alcohol and diluted in peanut oil when given subcutaneously (s.c.) (defined as 4-OHA injection) or made into cream as the formulation of the patent (US 20030092693A1) (designate as 4-OHA cream). Rats were then divided into four groups of 10 animals each. Rats in group A received 1 ml/kg of peanut oil as subcutaneous vehicle daily; rats of group B were applied transdermally with 1 ml of placebo cream twice daily; rats in group C were treated subcutaneously with 1 ml/kg of oil suspension of 4-OHA (50 mg/kg/day) twice daily; group D was administered transdermally with 1 ml of 2.5% 4-OHA cream twice daily. All treatments were maintained for 4 weeks. The doses chosen for testing the antitumor effect of 4-OHA in this study were based on Brodie's previous studies (13) and the patent of 4-OHA ointment. Tumor growth was expressed as a percent value to the initial tumor volume, measured on the first day of treatment and taken as 100%. At the end of the treatment period, the rats were euthanized with cervical dislocation; tumors were removed and measured. The tissues were removed from fat and necrotic areas, weighed, and stored at -80° or placed in 10% buffered formalin solution until assayed.

2.4 UPLC analysis of 4-OHA in cream chemical components

4-OHA cream 10 mg was ultrasonically extracted with 10 ml acetonitrile for 20 min following matrix impurity removal with saturated sodium chloride. The extract was evenly distributed to a 10 ml volumetric flask and the volume was adjusted to 10 ml with methanol to obtain a 1 mg/ml sample solution. After filtration with a 0.22 μm filter membrane, sample injection was determined. UPLC was then used to analyze the sample solution to quantify the content of 4-OHA. The samples were subjected to UPLC analysis on a C18 column (2.1 mm i.d × 100 mm length, 1.6 μm) by a single injection of 5 μl detected at 278 nm; isometric mobile phase: Water (A); Acetonitrile (B) = 50:50; column temperature: 30°C; flow rate: 0.3 ml/min. 4-OHA was identified by their characteristic absorption spectra and their typical retention time corresponding to its standards. The concentration of 4-OHA in cream was determined using a four-level calibration curve based on a concentration series at 10, 20, 30, and 40 μg/ml. The calibration curve showed good linearity (correlation coefficients >0.999).

2.5 Cell viability

Cell viability was evaluated by MTT assay. Briefly, MCF-7 and ZR-75-1 cells were seeded in a 96-well culture plate (1000 cells/well). After 24 h, cells were treated by 4-OHA at a dose of 1 μM or left untreated in a 5% CO_2 incubator for the indicated time. The incubation time and the concentrations of compounds were used based on previous studies (14). At the end of incubation, 10 μl of 5 mg/ml MTT solution was added to each well. After a 3-h incubation, 100 μl DMSO was added to dissolve the resultant purple formazan crystals. The absorbance was measured at 570 nm on a Thermo Scientific Varioskan Flash Multimode Reader.

2.6 Colony formation assay

About 2×10^3 breast cancer cells were seeded in six-well plates and exposed to 1 μM 4-OHA in a 5% CO_2 incubator. After 7 days, cells were fixed with 4% polyoxymethylene and stained with crystal violet. The images for colony formation were recorded by a high-resolution scanner.

2.7 Cell cycle

The cell cycle was measured by flow cytometry assays. Breast cancer cells (2×10^5 cells/well) were plated in a 6-well plate and treated with DMSO, or 4-OHA (1 μM) for 72 h. For cell cycle analysis, cells were harvested with trypsin without EDTA to obtain single-cell suspensions and then washed once with ice-cold 1× PBS. After that, cells were fixed overnight in 70% ice-cold ethanol. The fixed cells were washed once with ice-cold 1× PBS, stained with PI solution (50 mg/ml PI, 0.1% NP-40, 0.1% sodium citrate, 0.1% Triton X-100), and then analyzed on a FACS Calibur (BD Biosciences).

2.8 RT-PCR and qRT-PCR

Total RNAs were isolated from DMBA-induced tumor tissues of rats or cells using TRIzol reagent (Life Technologies). cDNAs were synthesized by M-MLV reverse transcriptase (Life

Technologies) as the manufacturer's instructions, followed by real-time PCR using SYBR Green mix. Oligonucleotide sequences are listed in Supplementary Table 1, 2.

2.9 Western Blot Analysis

Total proteins were extracted in RIPA buffer (25 mM Tris·HCl, pH 7.6, 150 mM NaCl, 1% Nonidet P-40, 1% sodium deoxycholate, 0.1% SDS, 1× phosphotase inhibitor and protease inhibitor cocktail. The resultant proteins in the supernatants were stored at -80°C or directly subjected to SDS-PAGE. Proteins were resolved on SDS-PAGE gels and transferred onto PVDF membranes. The membrane was blocked for 1 h at room temperature in 5% non-fat dry milk or bovine serum albumin (BSA) in TBST buffer (20 mM Tris-HCl, pH 7.5,150 mM NaCl, and 0.1% NP-40), then incubated with the primary antibody at 4°C overnight, washed, and incubated with horseradish peroxidase-conjugated secondary antibody for 1 h. The signals were detected using ECL reagents (Life Technologies). The antibodies used are shown in Supplementary Table 3.

2.10 Immunohistochemistry and immunofluorescence

Tumor tissues obtained from the rat bearing DMBA-induced mammary carcinoma were subjected to immunohistological analysis. Immunohistochemistry was performed as previously described (15). The tissue sections were blocked by goat serum and incubated with primary antibody (1:200) and then incubated with biotinylated secondary antibody (1:200). Finally, the ImageJ software was used to analyze the data. For IF, sections were incubated with rat anti-mouse CD8, CD19, and CD56/CD16 antibodies, followed by staining with goat anti-rat (Abcam, ab150088) antibodies. DAPI (Invitrogen) was added to counterstain the nuclei. Finally, images were acquired by a slice section scanner (Pannoramic DESK) scanning microscope system and analyzed using the CaseViewer software. The antibodies used are shown in Supplementary Table 3.

2.11 Flow cytometry analysis

Single-cell suspensions were prepared from tumor tissue homogenates. Contaminated red blood cells were hemolyzed using ammonium chloride solution (IMGENEX). The resulting single-cell suspensions were incubated with the Abs for 30 minutes on ice. Isotype-matched control Igs were used to detect the nonspecific binding of Ig in the samples. The stained cells were analyzed on a CytoFLEX S system (Beckman Coulter, Brea, CA), and the obtained data were analyzed using the FlowJo_v10 software.

2.12 Subacute toxicity assessment

The safety of 4-OHA cream *in vivo* was evaluated by serum biochemical analysis, H&E staining. Briefly, following topical administration of 4-OHA cream or placebo cream in SD rats, the peripheral blood samples were collected using heparin and centrifuged for serum biochemical analysis. The tissue samples were simultaneously excised and fixed in 10% buffered formalin. The ALT, AST, TBIL, ALB, BUN, and total protein analyses in serum were performed using blood chemistry assay kits (BioAssay Systems). The tissue samples were embedded in paraffin, then cut into 5-μm-thick paraffin sections and subsequently placed on a glass slide. The slides were stained with H&E. Finally, images were acquired by a slice section scanner (Pannoramic DESK).

2.13 RNA Transcriptome sequencing

RNAs 3 μg were used to generate a sequencing library using NEBNext Ultra™ RNA Library Prep Kit for Illumina (New England BioLabs) as the manufacturer's instructions. Then PCR was performed with Phusion High-Fidelity DNA polymerase, Universal PCR primers, and Index (X) Primer, and the resultant PCR products were purified (AMPure XP system) and library quality was assessed on the Agilent Bioanalyzer 2100 system. The clustering of the index-coded samples was performed on a cBot Cluster Generation System using TruSeq PE Cluster Kit v3-cBot-HS (Illumia) according to the manufacturer's recommendations. After cluster generation, the library preparations were sequenced on an Illumina Hiseq 2500 platform.

2.14 Statistical analysis

The data are presented as the mean ± SD of at least three independent experiments. Statistical analysis among groups was conducted using the two-tailed Student's *t*-test and one-way analysis of variance on GraphPad Prism (GraphPad Software). The *p*-values <0.05 were considered statistically significant and marked with an asterisk (*, $p < 0.05$; **, $p < 0.01$; ***, $p < 0.001$).

3 Results

3.1 Effects of 4-OHA cream on breast cancer

Previous studies had shown that 4-OHA given s.c. to rats markedly shrank DMBA-induced mammary carcinoma (9, 16). To investigate whether 4-OHA cream had a similar effect to 4-OHA injection on breast cancer, we established a model of DMBA-induced mammary carcinoma in SD rats, developed the 4-OHA cream based on the formulation of patent, and assessed the antitumor efficacy of 4-OHA cream (Figure 2 and Supplementary Figure 1).

Starting 60 days after DMBA treatment, mammary tumors were successfully induced as shown in Supplementary Figures 1A–C. Neoplasias occur with a frequency of >90% (data not shown). DMBA-induced mammary cancer had been proved to be estrogen and progesterone receptor positive (9). Similarly, our

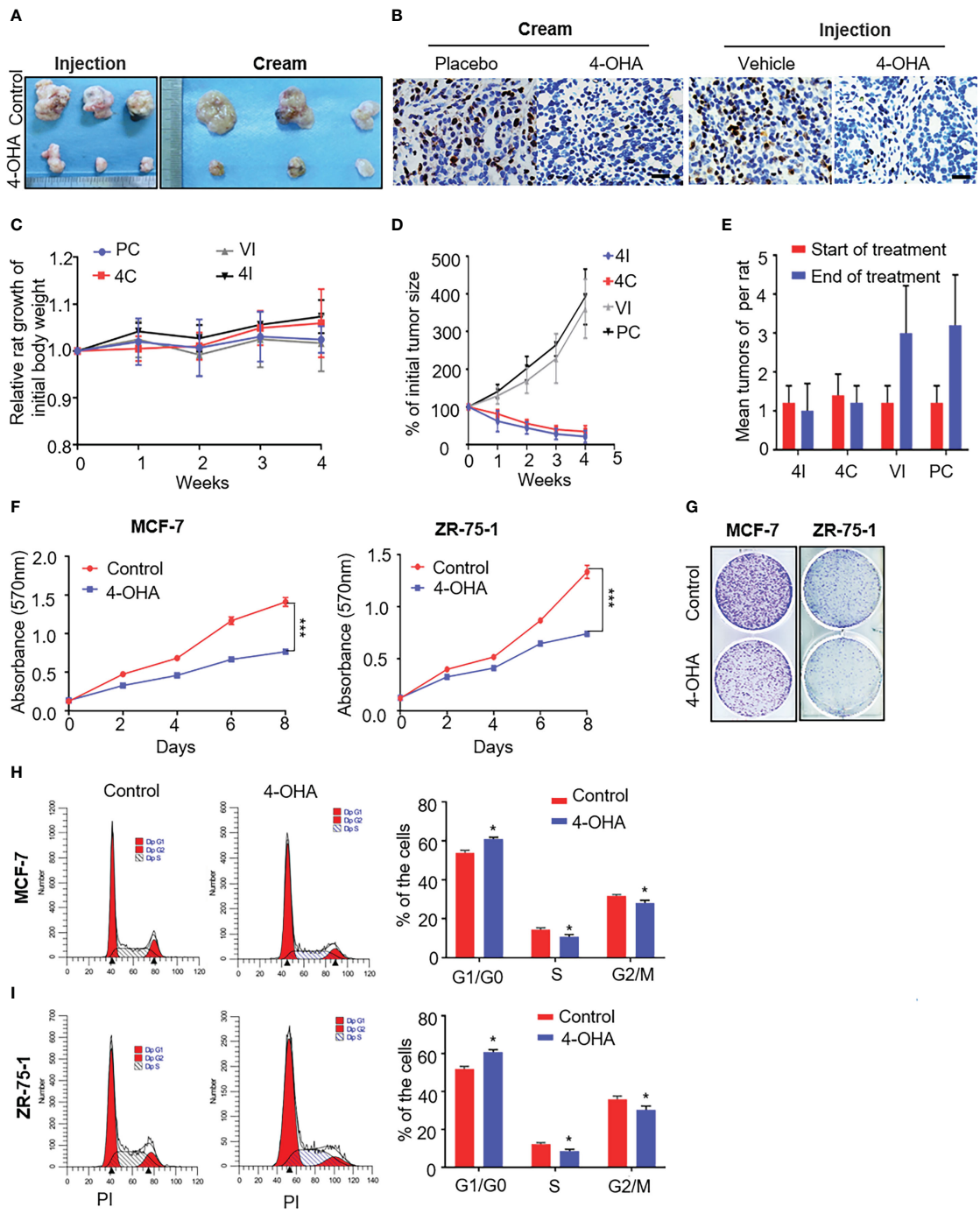

FIGURE 2
The effects of 4-OHA cream on breast cancer growth. At an age of 50–54 days, female Sprague-Dawley rats were dosed intragastrically with 20 mg DMBA. Animals were selected for experiments when at least one tumor per rat had reached a diameter of 1.5 cm but less than 2 cm. The skin covering the tumor was shaved and the animals were divided into four groups. In 4-OHA and placebo cream groups, tumors were treated by direct application of the cream. **(A–E)** Tumors in the 4-OHA injection group were treated with twice-daily s.c. injections of 1 ml/kg of 4-OHA (50 mg/kg/day), and control animals received injections of the 4-OHA-suspending vehicle (peanut oil) at the same time. **(A)** Representative images of the tumors. **(B)** Expression of the proliferation marker Ki67 in tumor tissues was measured by immunohistochemistry. Scale bar, 20 µm. **(C)** Rat weight evolution during the experiment. The values are expressed as the mean. **(D)** Tumor growth curve. Average number of tumor nodules before and after treatment. **(E)** The data represent six sets of independent experiments and are shown as the means ± SD. *$p < 0.05$ vs. control group. The effects of 4-OHA on the growth of the cells. **(F–I)** Cells were cultured in 10% PRF-CT with E2 1 nM for 3 days before the experiment.
(F, G) Cells were seeded in 96-well or six-well plates and 24 h later they were exposed to 1 µM of 4-OHA for 8 days. MTT **(F)** and Colony formation **(G)** assay were performed. Analysis of the cell cycle of MCF-7 **(H)** and ZR-75-1 **(I)** by flow cytometry as described in the Materials and Methods. Data represent a mean ± SEM of three independent experiments, each in triplicate; bars, SEM. *$p \leq 0.05$ vs. control. control. PC, Placebo cream; 4C, 4-OHA cream; VI, vehicle; 4I, 4-OHA injection.

immunohistochemical results showed to be ER- and PR-positive in DMBA-induced tumors (Supplementary Figure 1C). Then, we used this model to repeat Brodie's results that 4-OHA at a dose of 50 mg/kg per day could diminish tumors by more than half. Likewise, the 4-OHA cream caused a significant regression of tumors (Figures 2A, D, and Supplementary Figure 1D). Immunohistochemical results showed that the proliferation marker Ki67 was reduced by 4-OHA cream or injection as compared with control (Figure 2B). The average number of tumor was 1.25 ± 0.15 tumors per rat at the beginning of the treatment for all groups. Values of 3.0 ± 1.2, 3.2 ± 1.3, 1.0 ± 0.7, and 1.2 ± 0.4 were found after 28 days of treatment with vehicle, placebo cream, 4-OHA injection, and 4-OHA cream, respectively. Both 4-OHA dosage forms significantly decreased the number of new tumors at the end of the experiment compared to their respective control (Figure 2E). The weight of rats in drug groups increased slightly after 4 weeks of treatment (Figure 2C). Subsequently, to confirm that the antitumor effects of the cream derived from the compound of 4-OHA, we performed UPLC to detect the concentration of active ingredients in the cream. The main peak of the cream was identical to the peak of a single compound of 4-OHA (Supplementary Figure 2A). Then, according to the calibration curve, the 4-OHA content of the cream was determined to be 2.5%–2.7% (Supplementary Figure 2B). In consequence, these findings indicated that 4-OHA cream worked in tumors as 4-OHA injection.

Additionally, as shown in Figures 2F, G, 4-OHA inhibited the proliferation of MCF-7 and ZR-75-1 cells at a dose of 1 μM. This antiproliferative action of 4-OHA correlated well with the results of the cell-cycle analysis in breast cancer cells. 4-OHA significantly arrested the cell cycle, increasing the portion of MCF-7 and ZR-75-1 cells in the G1 phase and decreasing the portion in the S phase (Figures 2H, I), which further demonstrated that the compound of 4-OHA we used worked. In summary, the above results supported the notion that 4-OHA could work in breast cancer through transdermal absorption.

3.2 Safety evaluation of 4-OHA cream

In vivo, pathological studies in SD rats were performed to evaluate 4-OHA cream safety. The female SD rats were topically applied with placebo cream, 4-OHA cream, or without treatment. Because 1 g/kg was the efficacious dose of 4-OHA cream to suppress DMBA-induced tumor growth in rats (14), the high dose of 10 g/kg was used to evaluate 4-OHA cream toxicity. The serum biochemistry data showed that 4-OHA cream had no hematological or liver toxicity (Figure 3B). The H&E staining indicated that there were no obvious necrotic cells or tissues in the major organs, including heart, liver, spleen, lung, and kidney (Figure 3A). Moreover, the side effects (vomiting, diarrhea, and significant decrease in rat body weight) were not observed in rats (data not shown). Thus, 4-OHA cream at a 10 g/kg dose was safe.

3.3 RNA-Seq gene expression profiling in DMBA-induced tumor treated with 4-OHA cream

To understand the molecular mechanism of action of 4-OHA cream anti-breast cancer, we used high-throughput sequencing technology to determine the differentially expressed genes (DEGs) in the experimental vs. control group. As shown in Figures 4A, B, 4-OHA cream caused 378 up-regulated genes (normalized FPKM of experimental group ≥40) and 220 down-regulated genes (normalized FPKM of control ≥40) compared to its control by ≥2-fold (i.e. average |log2 (fold-change)| ≥2). 4-OHA injection vs. vehicle had 201 up-regulated genes and 135 down-regulated genes. Hierarchical clustering based on differentially expressed RNA transcripts (Figure 4A) revealed clear clustering of 4-OHA-treated DMBA-induced tumors from the control. Venn diagram showed that 102 up-regulated genes and 69 down-regulated genes were shared by 4-OHA cream and injection (Figure 4B), and the remaining DEGs were unique to each individual.

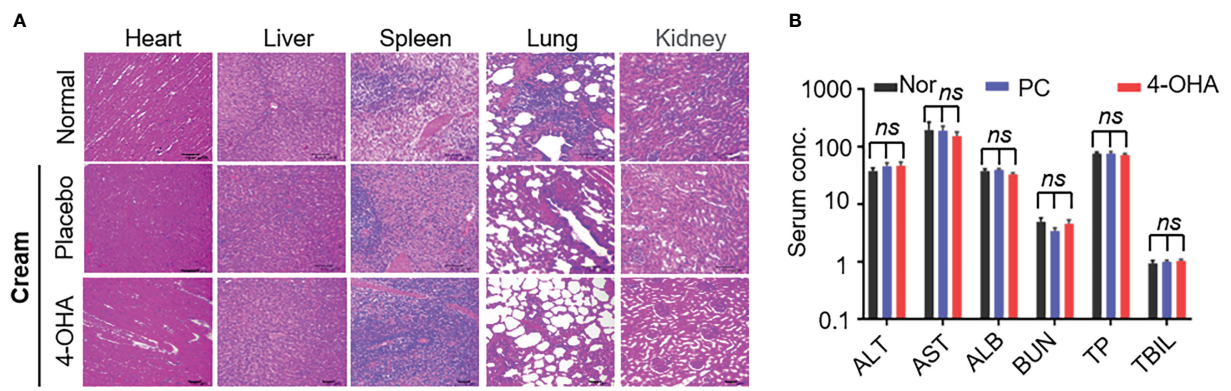

FIGURE 3
Safety evaluation of 4-OHA. Seven-week-old female SD rats were topically applied with cream at a dose of 10 g/kg. **(A)** H&E staining of main organs in SD rats after treatment with placebo or 4-OHA cream, or without treatment. **(B)** Serum biochemical parameters, including ALT, AST, TBIL, ALB, BUN, and TP, in rats treated with or without cream. Nor, normal; PC, placebo cream; 4-OHA, 4-OHA cream. There is no significance between the group of placebo cream or 4-OHA cream and normal group. $p > 0.05$, *ns*. ns means no significant difference.

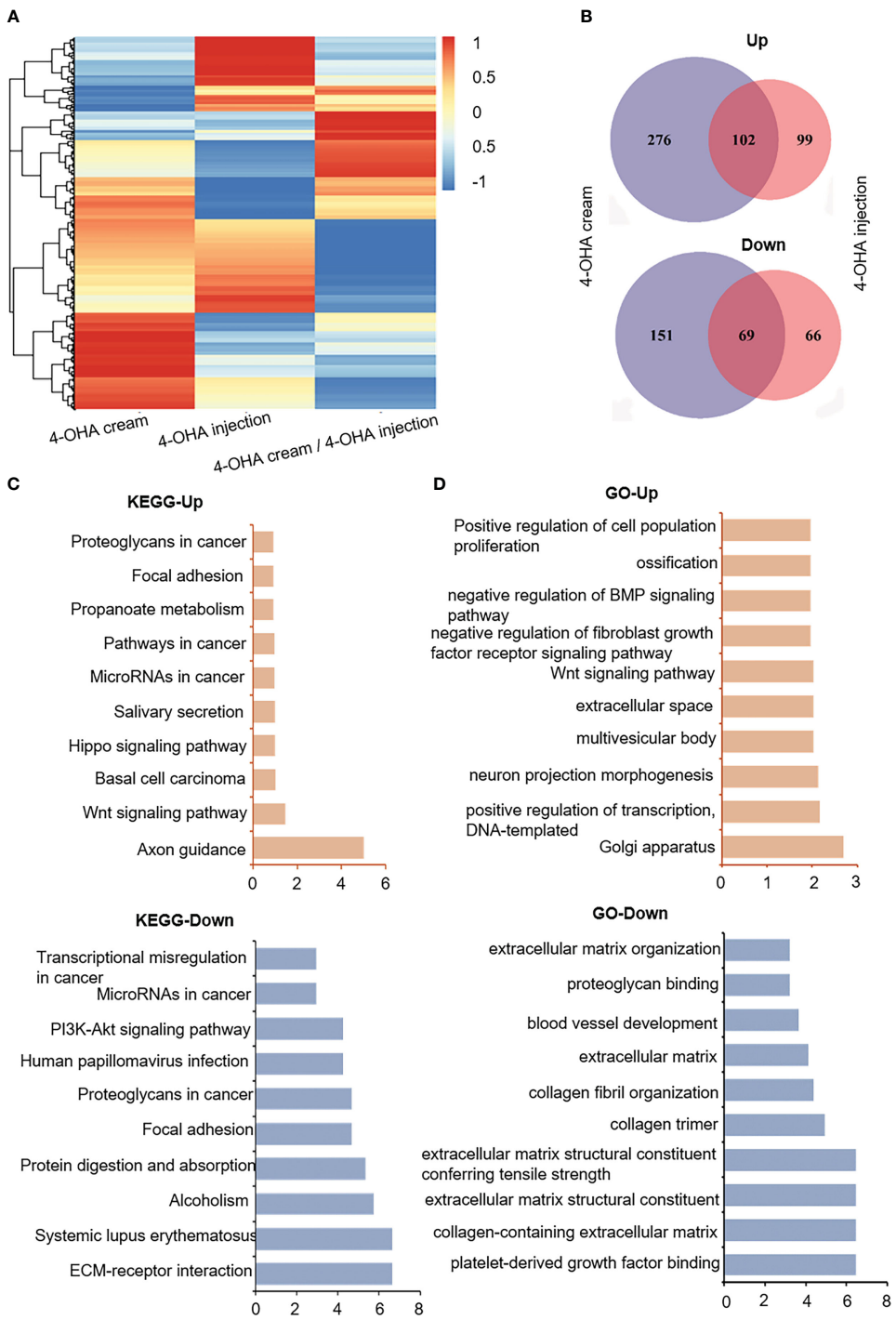

FIGURE 4
RNA-seq gene expression analysis of DMBA-induced mammary tumors treated with or without 4-OHA. **(A)** Heatmap of detected genes differentially expressed in the control and experimental group. **(B)** Venn diagram of 4-OHA-induced up-regulated or down-regulated DEGs in DMBA-induced tumors treated by 4-OHA cream or 4-OHA injection formulation. Kyoto Encyclopedia of Genes and Genomes (KEGG) **(C)** and Gene Ontology (GO) term **(D)** analysis of common differentially expressed genes between 4-OHA cream and 4-OHA injection group.

To further explore the biological implications of the common DEGs, the Kyoto Encyclopedia of Genes and Genomes (KEGG) pathway enrichment analysis and Gene Ontology (GO) term analysis were performed with these common DEGs, and the results were shown in Figures 4C, D. For KEGG term analysis, it demonstrated that 4-OHA cream as its injection had significant effects on ECM-receptor interaction, focal adhesion, PI3K-Akt signaling pathway, and axon guidance (Figure 4C). In the GO term analysis, as expected, DEGs were mainly related to extracellular matrix (ECM) structural components (Figure 4D), which have been reported to be associated with PI3K-Akt signaling pathway and tumor proliferation (17).

3.4 The effects of 4-OHA on extracellular matrix and PI3K-Akt signaling pathway

It is well known that 4-OHA is an aromatase inhibitor that can block estrogen biosynthesis (18). Estrogen activity can modulate components of the ECM in the tumor microenvironment, upregulating transcripts of *COL1A1*, and several matricellular proteins such as *TNC*, *FN1*, and *POSTN* (19). As shown in Figure 5A, both 4-OHA treatment methods downregulated transcripts of ECM-related genes in DMBA-induce tumors, such as *Col1a1*, *Tnc*, *Fn1*, and *Itga5*. Meanwhile, the expression levels of these genes in MCF-7 and ZR-75-1 cells were downregulated by 4-OHA at a dose of 1 μM, which suggested that 4-OHA could cause an extracellular matrix remodeling of ER+ breast cancer cells.

Multiple studies have demonstrated remodeling ECM was accompanied by alteration of signals activation in tumor, including focal adhesion kinase, MAP kinases, and the PI3K-AKT cascade (19–21). In this study, our results suggested that 4-OHA could inactivate the PI3K-Akt signaling pathway (Figure 4C), which was further confirmed by immunoblotting and immunohistochemistry assays. The results showed that phosphorylated Akt, but not Akt, was significantly reduced by 4-OHA treatment *in vivo* and *in vitro* (Figures 5C, D, G; Supplementary Figures 3A, B). In addition, Akt overexpression in MCF-7 cells can counteract the ability of 4-OHA inhibiting breast cancer growth (Figures 5H–J; Supplementary Figure 3C).

It is well known that cell cycle transitions are regulated by the PI3K-Akt signaling pathway. To confirm the expression levels of cell cycle-related genes and proteins that decreased with the reduction of PI3K-Akt signaling, qRT-PCR and immunoblotting were carried out following 4-OHA treatment. As shown in Figures 5B–G, the expression levels of cell-cycle-related genes significantly decreased, while the expression of cyclin kinase inhibitor P27Kip1 was significantly upregulated by 4-OHA. In tumor tissues, the variation of CyclinD1 and P27Kip1 were further verified by immunohistochemistry again (Figure 5D).

Above all, results suggested that 4-OHA arrested the cell cycle of breast cancer cells by reduction of PI3K-Akt signaling caused.

3.5 4-OHA antitumor growth by upregulating tumor suppressors

As shown in Figure 4C, both 4-OHA formulations had a significant impact on axon guidance in mammary tumors. The expression levels of *Lrrc4* and *Sema3b* in axon guidance were significant upregulation *in vivo* and *in vitro* (Figures 5A, E). Another two tumor suppressor genes *Btg1* and *Nbl1* were also significantly upregulated following 4-OHA treatment (Figures 5A, E).

3.6 4-OHA enhanced the infiltration of immune cells into tumor tissues

It is reported that ECM degradation could improve the infiltration of immune cells into tumor tissues and achieve strong immune response to antitumor immunity (22). As mentioned above, both 4-OHA formulations reduced the components of ECM. To verify whether 4-OHA promoted immune infiltration in DMBA-induced mammary tumors, we performed the CIBERSORT algorithm to calculate the relative proportion of immune cells in tumor tissues treated with/without 4-OHA (Figure 6A). The results showed that the proportion of naive B cells, resting NK cells, and naïve $CD8^+$ T cells dramatically increased. In contrast, the proportion of M2 macrophages and activated DCs were reduced in both 4-OHA formulations groups as compared with controls. Additionally, several types of immune cells exhibited statistically significant differences between the 4-OHA injection group and the 4-OHA cream group, including activated $CD8^+$ T cells, immature DCs, and Th17 cells. They increased in the 4-OHA injection group alone. Furthermore, the expression levels of interferon-signaling genes (e.g., *Stat1, Stat3*) were up-regulated after 4-OHA treatment (Figure 6B), while the immunosuppressive cytokine genes *Vegfa* in the 4-OHA cream and injection group displayed 2.04- and 1.39-fold downregulation, respectively (Figure 6B).

To verify the results of bioinformatic analysis, we further conducted the immunofluorescence analysis to evaluate the distribution patterns of $CD8^+$ T cells, $CD19^+$ B cells, and NK cells in tumors treated with 4-OHA or not. Representative tumor sections stained for the CD8, CD19, or CD16/CD56 antibody labeled with dye, and cell nucleus labeled with DAPI are shown in Figure 6C. Both formulations of 4-OHA resulted in significantly increasing numbers of tumor-infiltrating $CD8^+$ T cells, $CD19^+$ B cells, and NK cells as compared with their respective control (Figure 6D). The results of flow cytometry analysis also confirmed that $CD8^+$ T cells and NK cells play a role in 4-OHA against breast cancer growth (Figures 6E, F).

The above results indicated that 4-OHA could significantly promote the infiltration of immune cells into DMBA-induced mammary tumors, but with some differences between the two formulations, such as there were more active $CD8^+$ T cells, immature DCs, and Th17 cells in the 4-OHA injection group than in the 4-OHA cream group.

4 Discussion

Previously, the potent aromatase inactivator (= suicide inhibitor) 4-OHA was developed by Ciba and Novartis, respectively, as intramuscular depot injection preparation (Lentaron®Depot) for treatment of the postmenopausal patients with advanced breast cancer. The medication proved to be very effective and showed high systemic tolerability but was hampered by local tolerability problems, which also did not allow increasing the dosing for higher efficacy. These aspects and the availability of new potent oral aromatase inhibitors led to the strategic decision to stop the marketing of Lentaron®Depot by Novartis. However, clinical studies had shown that 4-OHA still worked, when the nonsteroidal AIs failed, which led to a desire to exploit this compound again.

In the late 90s of the last century, researchers at Freiburg postulated that a topical formulation of steroidal aromatase

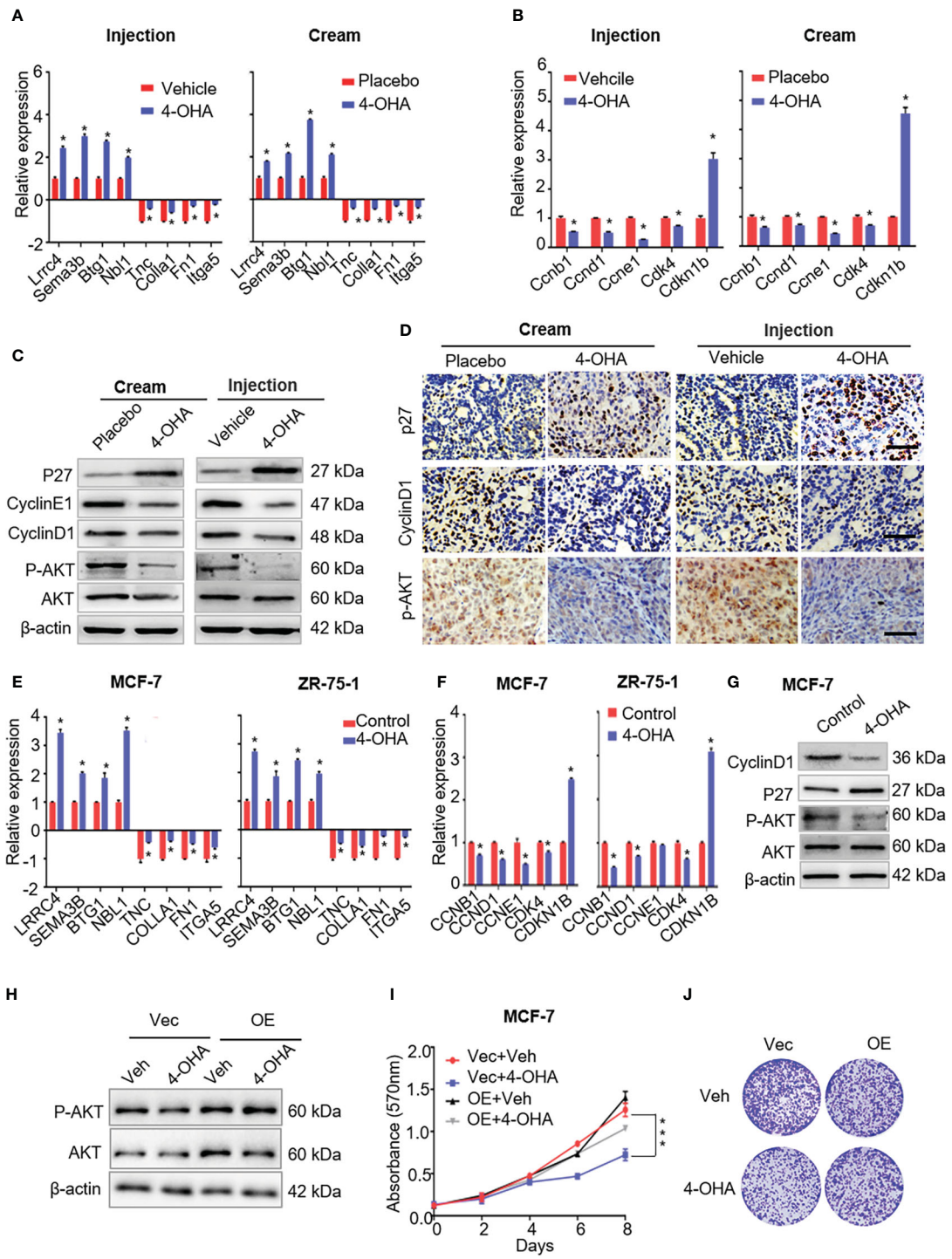

FIGURE 5
The effects of 4-OHA on extracellular matrix, cell cycle, and PI3K-Akt signaling pathways related genes or proteins. **(A)** The qRT-PCR was carried out to validate indicated DEGs in both 4-OHA cream and 4-OHA injection groups. **(B)** Representative levels of cell cycle-related genes by qRT-PCR. The key protein levels of the cell cycle and the PI3K-Akt signaling pathways were analyzed by western blotting **(C)** and immunohistochemistry **(D)** after 4-OHA treatment in DMBA-induced breast cancer tumors. Scale bar, 50 μm. **(E–G)** The expression levels of cell cycle, PI3K-Akt signaling pathways related genes, and tumor suppressors by qRT-PCR and western blotting in MCF-7 and ZR-75-A cells exposed to 1 μM of 4-OHA for 72 h. **(H–J)** Following Akt overexpression in MCF-7 cells, MTT **(I)** and Colony formation **(J)** assay were performed. The protein expression of Akt and P-AkT were analyzed by western blotting **(H)**. Vec, Vector; OE, overexpression; Veh, Vehicle. Data are represented as the mean ± SEM of three independent experiments, each in triplicate; bars, SEM. ***$p \leq 0.001$, *$p \leq 0.05$ vs. control.

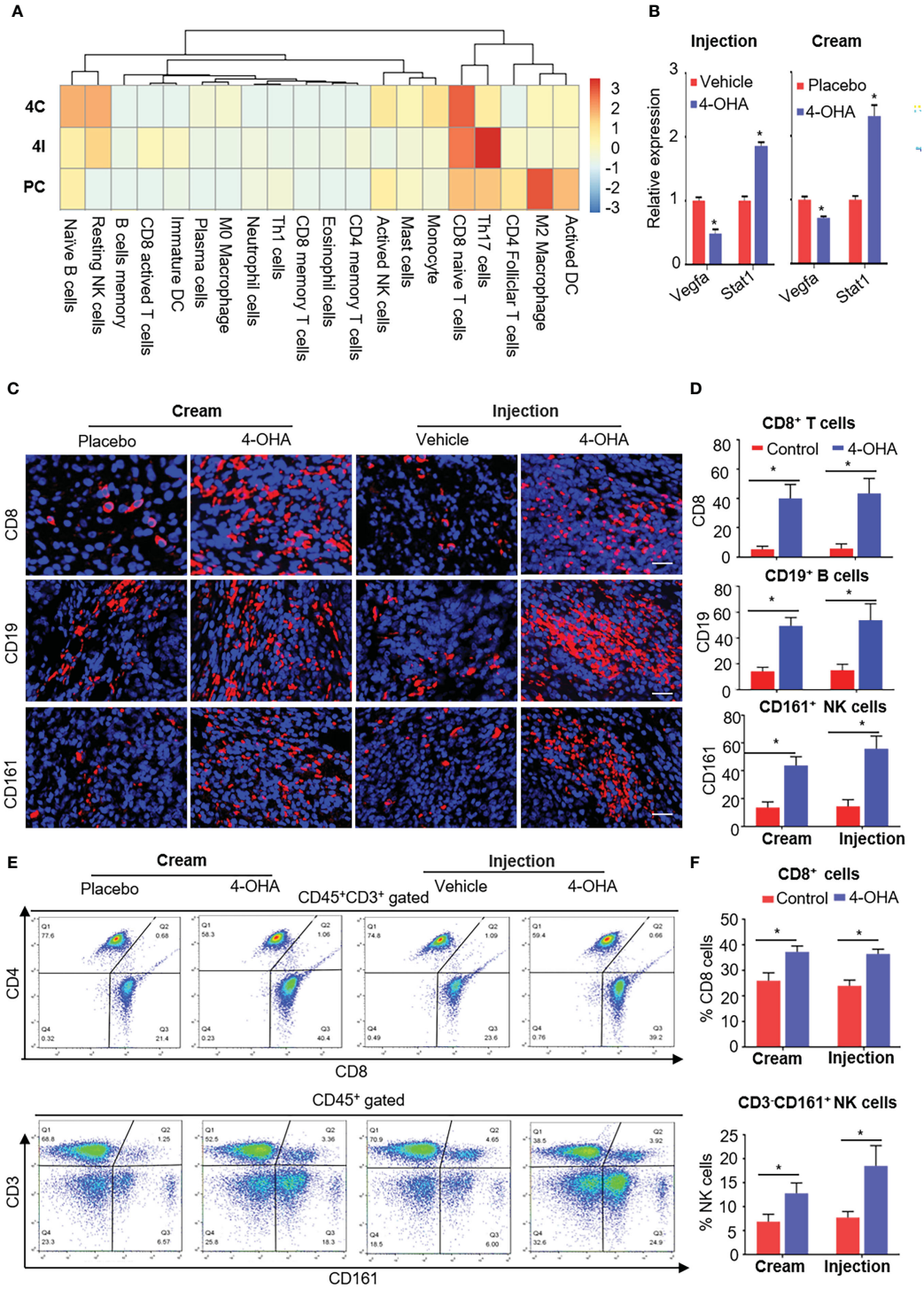

FIGURE 6
4-OHA treatment remodeled the tumor immune microenvironment. Female SD rats with at least one tumor reaching a size of 1.5 cm in diameter received vehicle peanut oil, placebo cream, 4-OHA cream, or 4-OHA injection for 4 weeks, as indicated in the Materials and Methods. **(A)** Heatmap of relative infiltrations of immune-cell populations in tumor tissues. **(B)** Expression levels of immune-related genes. **(C)** Representative images of tumors stained for CD8, CD19, or CD16/CD56. DAPI (nuclei) was also shown with each antibody. Scale bar, 20 μm. **(D)** Percentage of CD8, CD19, or CD161 positive cells. Counts were quantified from five representative high-powered fields from each sample. **(E, F)** Flow cytometric analysis of the number of CD45+CD3+CD8+ and CD3- CD161+ NK cells in the tumor tissues. E shows an exemplary gating, F gives an overview of the results versus WT. Data are represented as the mean ± SEM. bars, SEM. *$p \leq 0.05$ vs. control. PC, Placebo cream; 4C, 4-OHA cream; VI, vehicle; 4I, 4-OHA injection.

inactivators would be of benefit and could overcome the limitations (local intolerance at higher concentrations) of intramuscular formulation of Lentaron®. The novel concept to treat breast cancer with a topical formulation of formestane is based on two rationales: (i) Formestane is by chemical nature a steroid like molecule; this molecule is known to be well resorbed *via* the skin. Estrogen-containing creams are used for a variety of diseases, such as estrogen patches for the treatment of certain menopausal conditions. As Formestane differs only by minor modification from estrogen it should be applied by the transdermal route. (ii) It is well described that breast cancer tissue itself can produce its estrogen by expressing the necessary quantities of the aromatase enzyme. Thus, exposure of the tumor to an aromatase inhibitor *via* topical transdermal application should allow achieving significant inhibitory levels in the tumor being eventually higher than *via* the systemic route. However, so far no literature reported the effects of these new formulations of aromatase inhibitors on breast cancer and their mechanism of action.

In the present study, we developed 4-OHA cream and compared its effect on DMBA-induced mammary tumors with that of 4-OHA subcutaneous injection. Moreover, we used high-throughput sequencing technology to explore the molecular mechanism of action of this cream anti-breast cancer.

Brodie had proved that 4-OHA could reduce ovarian estrogen production and cause regression of carcinogen (DMBA)-induced mammary tumors (9). As shown in Figure 2A, we got the same results as Brodie's when 4-OHA was subcutaneously injected in rats at a dose of 50 mg/kg per day. Of course, this antitumor effect was not due to 4-OHA toxicity, because the toxicity assessment assay showed that 4-OHA cream at the dose was safe (Figures 3A, B). The cream absorbed directly *via* the skin might cause a locally high concentration of 4-OHA in the tumor, which efficiently and directly reduced estrogen biosynthesis in tumors and led to an inhibition of tumor growth. Furthermore, analysis of the cell cycles by flow cytometry clearly showed an arrest of breast cancer cells in the G1/G0 phase (Figures 2H, I), indicating that the 4-OHA antiproliferative effect on breast cancer cells was due to the cell cycle retardation.

Next, through high-throughput sequencing, we identified the differential expression genes (DEGs) after 4-OHA treatment the DMBA-induced tumors for 28 days. DEGs were primarily associated with extracellular matrix (ECM) ECM-receptor interaction, focal adhesion, PI3K-Akt signaling pathway, axon guidance, and tumor suppressors. Literature reported that estradiol (E2) could increase ECM remodeling, accompanied by upregulating transcripts for *COL1A1*, and several matricellular proteins, including TNC, FN1, and POSTN (19). 4-OHA as a well-known aromatase inhibitor could efficiently reduce estrogen biosynthesis in tumor tissues, which might cause a reduction of ECM remodeling in the tumor microenvironment. As shown in Figures 5A, E, 4-OHA decreased the components of ECM in breast cancer cells by downregulating the expression levels of ECM-related genes, such as *Col1a1*, *Tnc*, *Fn1*, and *Itga5*. Moreover, these ECM-related genes play a role in the PI3K-Akt signaling pathway (20, 23, 24). The reduction of phosphorylated AKT, a key protein of the pathway, was determined by Western blot and immunohistochemistry (Figures 5C, D, G). These findings indicated that 4-OHA could reduce the PI3K-Akt signaling. And then, the reduction of the PI3K-Akt signaling downregulated the cell cycle-related gene or protein expression (Figures 5B, C, F, G), which resulted in the arrest of breast cancer cells in the G1/G0 phase. In addition, the downregulation of ECM-related genes might influence breast cancer metastasis, which would be the topic of future research.

Furthermore, 4-OHA significantly up-regulated the expression levels of tumor suppressors, such as *Lrrc4*, *Sema3b*, *Btg1*, and *Nbl1*. Of these tumor suppressors, *Btg1* had higher expressed levels in the 4-OHA treatment group than the control group (4-OHA cream 798.8 vs. control 297.8; 4-OHA injection 888.1 vs. 328). *BTG1* belongs to the BTG/Tob families, had been proved to inhibit various cancer cells growth, and expresses primarily in the G0/G1 phase transition, with levels decreasing as cells enter S phase (25). Literature also reported that overexpression of *BTG*1 decreased the levels of phosphorylated CDC2, cyclin B1, cyclin D1, and cyclin E1 in the MCF-7 cells (26). As for the two tumor suppressors *Lrrc4* and *Sema3b*, they were rich in the axon guidance signaling pathway. *LRRC4* could arrest the cell cycle in late G1 phase by upregulating the level of cell cycle inhibitory molecules and downregulating the expression of cell cycle regulatory proteins (27–29). Sema3b inhibited axonal extension and exerted an antitumor effect on lung and ovarian cancer cells *in vitro* (30). *Nbl1* also had a work on preventing cells from entering the final stage (G1/S) (31). Therefore, the upregulation of the four tumor suppressors partly accounted for the antitumor activity of 4-OHA cream.

Moreover, increasing evidence indicates that small-molecule inhibitors can remodel the tumor immune microenvironment and improve immune-mediated tumor destruction (32–34). It was reported that the dense ECM blocks the infiltration of immune cells into tumor tissue, limiting the antitumor effect of immunotherapy (35, 36). On the other hand, the degradation of tumor ECM can promote the infiltrations of immune cells into tumors (22). Given these views, 4-OHA also could reduce the components of breast cancer ECM, such as collagens, integrins, and fibronectins (Figure 4 and Figure 5). Hence, 4-OHA increased the number of infiltrated immune cells in DMBA-induced tumors, including naive B cells, resting NK cells, and naïve $CD8^+$ T cells, but reduced that of M2 Macrophage and DC Active (Figure 6A). Immunofluorescence analysis confirmed the proportion of $CD8^+$ T cells, NK cells, and B cells increased in DMBA-induced tumor tissues after treatment with 4-OHA or not (Figures 6C, D). The antitumor role of NK cells and cytotoxic T cells has long been well-documented. However, the role of B cells is still controversial in tumor immune microenvironment. Recently, literature reported that tumor-infiltrated B-cells were significantly associated with improved survival in breast cancer patients (37–39). In contrast, M2 macrophages support tumor growth and progression through hypoxia and the secretion of cytokines (e.g. IL-4). Although according to the results of bioinformatic analysis, the 4-OHA treatment decreased the proportion of activated DCs; facilitated the infiltration of naive B cells, resting NK cells, and naïve $CD8^+$ T cells into tumor tissue; and did not activate these three immune

cells, qRT-PCR results showed that the expression levels of interferon-signaling genes (e.g., *Stat1*) and immunosuppressive cytokine genes (e.g., *Vegfa*) were up- and down-regulated in response to 4-OHA treatments, respectively (Figure 6B). This result indicated that 4-OHA could induce a proinflammatory immune response in the tumor microenvironment. Taken together, we concluded that 4-OHA treatment promoted recruitment of lymphocyte in tumor tissue to regulate tumor growth. From this perspective, 4-OHA inducing the lymphocyte infiltration is a promising strategy to convert poorly infiltrated breast cancer from a 'cold' tumor to a 'hot' tumor.

Additionally, in 4-OHA injection group tumor tissues, there were more active $CD8^+$ T cells, immature DCs, and Th17 cells than in 4-OHA cream group tumor tissues, which suggested that there were other mechanisms of action of 4-OHA injection formulation on DMBA-induced of tumors. 4-OHA injection agents might reach multiple organs of rats through the blood circulation system and have complex metabolic pathways and metabolites, which might produce different drug effects in the body of rats, and then promoted the infiltration of more types of immune cells. Whereas, the 4-OHA cream directly infiltrated into the tumor lesion by penetrating the skin without passing through the liver and other organs, which caused a relatively simple metabolic pathway and simpler drug effects.

Moreover, the morphologic changes of 4-OHA cream entering the body might lead to different effects of drugs remodeling the immune environment from 4-OHA injection. This will be the topic of future research.

5 Conclusions

This study showed that 4-OHA cream could penetrate the skin and play a role in antitumor action as intramuscular depot preparation (Lentaron®Depot). Further, we preliminarily elucidated the molecular mechanism of 4-OHA against breast cancer. The results suggested that Formestane was being reintroduced as a cream for breast cancer therapy. Importantly, the results of the study gives us a way out for new use of old drugs straddling another therapeutic niche, such as atypical immunotherapy like this study.

Data availability statement

The data presented in the study are deposited in the NCBI databases repository, accession number PRJNA945180. https://www.ncbi.nlm.nih.gov/bioproject/PRJNA945180.

Ethics statement

The animal study protocol was approved by the Institutional Review Board (or Ethics Committee) of The Affiliated Hospital of Southwest Medical University, Southwest Medical University (protocol code 201903-37 and date of approval 2019-03-05).

Author contributions

All authors participated in the design, interpretation of the studies, analysis of the data, and review of the manuscript. YL, LG, and WF conceived and designed the whole project and wrote the manuscript. LG and LeZ performed the data analyses. LG, YL, XH, and LeZ interpreted the data and partook in the discussion. CS, YC, LiZ, HQ, and AT revised the final version of the manuscript. All authors contributed to the article and approved the submitted version.

Funding

This research was funded by the Science and technology Strategic cooperation Project of Southwest Medical University of Luzhou People's Government (No. 2019LZXNYDJ08, 2019LZXNYDJ19), and supported by the National Natural Science Foundation of China (No. 82003262), China Postdoctoral Science Foundation (No. 2019TQ0221, 2019M663517), and Post-Doctor Research Project, West China Hospital, Sichuan University (No. 2019HXBH059, No. 2020HXBH052).

Acknowledgments

Partial cell lines, partial reagents, and partial antibodies used for experiments were gifted from Doctor Tao Wang, Master Jiayi Xu, Doctor Yi Li (West China Hospital, Sichuan University).

Conflict of interest

The authors declare that the research was conducted in the absence of any commercial or financial relationships that could be construed as a potential conflict of interest.

Publisher's note

All claims expressed in this article are solely those of the authors and do not necessarily represent those of their affiliated organizations, or those of the publisher, the editors and the reviewers. Any product that may be evaluated in this article, or claim that may be made by its manufacturer, is not guaranteed or endorsed by the publisher.

Supplementary material

The Supplementary Material for this article can be found online at: https://www.frontiersin.org/articles/10.3389/fimmu.2023.1041525/full#supplementary-material

References

1. Murase K, Yanai A, Saito M, Imamura M, Miyagawa Y, Takatsuka Y, et al. Biological characteristics of luminal subtypes in pre- and postmenopausal estrogen receptor-positive and Her2-negative breast cancers. *Breast Cancer* (2014) 21(1):52–7. doi: 10.1007/s12282-012-0348-z

2. Carey LA, Perou CM, Livasy CA, Dressler LG, Cowan D, Conway K, et al. Race, breast cancer subtypes, and survival in the Carolina breast cancer study. *JAMA* (2006) 295(21):2492–502. doi: 10.1001/jama.295.21.2492

3. Riemsma R, Forbes CA, Kessels A, Lykopoulos K, Amonkar MM, Rea DW, et al. Systematic review of aromatase inhibitors in the first-line treatment for hormone sensitive advanced or metastatic breast cancer. *Breast Cancer Res Treat* (2010) 123 (1):9–24. doi: 10.1007/s10549-010-0974-0

4. Coombes RC, Goss P, Dowsett M, Gazet JC, Brodie A. 4-hydroxyandrostenedione in treatment of postmenopausal patients with advanced breast cancer. *Lancet* (1984) 2 (8414):1237–9. doi: 10.1016/s0140-6736(84)92795-8

5. Carlini P, Frassoldati A, De Marco S, Casali A, Ruggeri EM, Nardi M, et al. Formestane, a steroidal aromatase inhibitor after failure of non-steroidal aromatase inhibitors (Anastrozole and letrozole): Is a clinical benefit still achievable? *Ann Oncol Off J Eur Soc Med Oncol* (2001) 12(11):1539–43. doi: 10.1023/a:1013180214359

6. Carlini P, Ferretti G, Di Cosimo S, Colella E, Tonachella R, Romiti A, et al. Is there a benefit by the sequence anastrozole-formestane for postmenopausal metastatic breast cancer women? *J Steroid Biochem Mol Biol* (2003) 86(1):107–9. doi: 10.1016/s0960-0760(03)00249-8

7. Carlini P, Michelotti A, Ferretti G, Ricci S, Giannarelli D, Pellegrini M, et al. Clinical evaluation of the use of exemestane as further hormonal therapy after nonsteroidal aromatase inhibitors in postmenopausal metastatic breast cancer patients. *Cancer Invest* (2007) 25(2):102–5. doi: 10.1080/07357900701224789

8. Schmidt A, Wieland H. Medicament for Preveting and/or Treating a Mammary Carcinoma, Containing a Sterodal Aromatase Inhibitor [P], US 20030092693A1. (2003).

9. Zhou JL, Brodie A. The effect of aromatase inhibitor 4-hydroxyandrostenedione on steroid receptors in hormone-dependent tissues of the rat. *J Steroid Biochem Mol Biol* (1995) 52(1):71–6. doi: 10.1016/0960-0760(94)00145-c

10. Shagufta AI. Tamoxifen a pioneering drug: An update on the therapeutic potential of tamoxifen derivatives. *Eur J medicinal Chem* (2018) 143:515–31. doi: 10.1016/j.ejmech.2017.11.056

11. Dhillon S. Everolimus in combination with exemestane: A review of its use in the treatment of patients with postmenopausal hormone receptor-positive, Her2-negative advanced breast cancer. *Drugs* (2013) 73(5):475–85. doi: 10.1007/s40265-013-0034-2

12. Dauvois S, Labrie F. Androstenedione and androst-5-Ene-3 Beta,17 beta-diol stimulate dmba-induced rat mammary tumors–role of aromatase. *Breast Cancer Res Treat* (1989) 13(1):61–9. doi: 10.1007/BF01806551

13. Brodie AM, Garrett WM, Hendrickson JR, Tsai-Morris CH. Effects of aromatase inhibitor 4-hydroxyandrostenedione and other compounds in the 7, 12-Dimethylbenz(a) Anthracene-Induced breast carcinoma model. *Cancer Res* (1982) 42(8 Suppl):3360s–4s. doi: 10.1016/0304-3835(82)90136-7

14. Gao L, Bao Z, Deng H, Li X, Li J, Rong Z, et al. The beneficial androgenic action of steroidal aromatase inactivators in estrogen-dependent breast cancer after failure of nonsteroidal drugs. *Cell Death Dis* (2019) 10(7):494. doi: 10.1038/s41419-019-1724-9

15. Gao L, Zhu D, Wang Q, Bao Z, Yin S, Qiang H, et al. Proteome analysis of Usp7 substrates revealed its role in melanoma through Pi3k/Akt/Foxo and ampk pathways. *Front Oncol* (2021) 11:650165. doi: 10.3389/fonc.2021.650165

16. Brodie AM, Marsh D, Brodie HJ. Aromatase inhibitors–iv. regression of hormone-dependent, mammary tumors in the rat with 4-Acetoxy-4-Androstene-3,17-Dione. *J Steroid Biochem* (1979) 10(4):423–9. doi: 10.1016/0022-4731(79)90330-3

17. Li Z, Li X, Chen C, Chan MTV, Wu WKK, Shen J. Melatonin inhibits nucleus pulposus (Np) cell proliferation and extracellular matrix (Ecm) remodeling *Via* the melatonin membrane receptors mediated Pi3k-akt pathway. *J Pineal Res* (2017) 63 (3):1–10. doi: 10.1111/jpi.12435

18. Wing LY, Garrett WM, Brodie AM. Effects of aromatase inhibitors, aminoglutethimide, and 4-hydroxyandrostenedione on cyclic rats and rats with 7,12-Dimethylbenz(a)Anthracene-Induced mammary tumors. *Cancer Res* (1985) 45(6):2425–8. doi: 10.1016/0304-3835(85)90059-X

19. Jallow F, O'Leary KA, Rugowski DE, Guerrero JF, Ponik SM, Schuler LA. Dynamic interactions between the extracellular matrix and estrogen activity in progression of er+ breast cancer. *Oncogene* (2019) 38(43):6913–25. doi: 10.1038/s41388-019-0941-0

20. Shea MP, O'Leary KA, Wegner KA, Vezina CM, Schuler LA. High collagen density augments mtor-dependent cancer stem cells in eralpha+ mammary carcinomas, and increases mtor-independent lung metastases. *Cancer Lett* (2018) 433:1–9. doi: 10.1016/j.canlet.2018.06.025

21. Zanconato F, Cordenonsi M, Piccolo S. Yap/Taz at the roots of cancer. *Cancer Cell* (2016) 29(6):783–803. doi: 10.1016/j.ccell.2016.05.005

22. Chen Z, Pan H, Luo Y, Yin T, Zhang B, Liao J, et al. Nanoengineered car-T biohybrids for solid tumor immunotherapy with microenvironment photothermal-remodeling strategy. *Small* (2021) 17(14):e2007494. doi: 10.1002/smll.202007494

23. Keely PJ. Mechanisms by which the extracellular matrix and integrin signaling act to regulate the switch between tumor suppression and tumor promotion. *J mammary gland Biol neoplasia* (2011) 16(3):205–19. doi: 10.1007/s10911-011-9226-0

24. Barcus CE, O'Leary KA, Brockman JL, Rugowski DE, Liu Y, Garcia N, et al. Elevated collagen-I augments tumor progressive signals, intravasation and metastasis of prolactin-induced estrogen receptor alpha positive mammary tumor cells. *Breast Cancer Res BCR* (2017) 19(1):9. doi: 10.1186/s13058-017-0801-1

25. Corjay MH, Kearney MA, Munzer DA, Diamond SM, Stoltenborg JK. Antiproliferative gene Btg1 is highly expressed in apoptotic cells in macrophage-rich areas of advanced lesions in Watanabe heritable hyperlipidemic rabbit and human. *Lab investigation; J Tech Methods Pathol* (1998) 78(7):847–58. doi: 10.1007/s001090050255

26. Zhu R, Zou ST, Wan JM, Li W, Li XL, Zhu W. Btg1 inhibits breast cancer cell growth through induction of cell cycle arrest and apoptosis. *Oncol Rep* (2013) 30 (5):2137–44. doi: 10.3892/or.2013.2697

27. Li P, Xu G, Li G, Wu M. Function and mechanism of tumor suppressor gene Lrrc4/Ngl-2. *Mol Cancer* (2014) 13:266. doi: 10.1186/1476-4598-13-266

28. Wu M, Huang C, Gan K, Huang H, Chen Q, Ouyang J, et al. Lrrc4, a putative tumor suppressor gene, requires a functional leucine-rich repeat cassette domain to inhibit proliferation of glioma cells in vitro by modulating the extracellular signal-regulated Kinase/Protein kinase B/Nuclear factor-kappab pathway. *Mol Biol Cell* (2006) 17(8):3534–42. doi: 10.1091/mbc.e05-11-1082

29. Zhang QH, Wu MH, Wang LL, Cao L, Tang K, Peng C, et al. Profiling of differentially expressed genes in Lrrc4 overexpressed glioblastoma cells by cdna array. *Acta Biochim Biophys Sin* (2005) 37(10):680–7. doi: 10.1111/j.1745-7270.2005.00100.x

30. Castro-Rivera E, Ran S, Thorpe P, Minna JD. Semaphorin 3b (Sema3b) induces apoptosis in lung and breast cancer, whereas Vegf165 antagonizes this effect. *Proc Natl Acad Sci United States America* (2004) 101(31):11432–7. doi: 10.1073/pnas.0403969101

31. Ozaki T, Nakamura Y, Enomoto H, Hirose M, Sakiyama S. Overexpression of Dan gene product in normal rat fibroblasts causes a retardation of the entry into the s phase. *Cancer Res* (1995) 55(4):895–900. doi: 10.1002/1097-0142(19950215)75:4<1051::AID-CNCR2820750423>3.0.CO

32. Sanlorenzo M, Vujic I, Moy A, Quaglino P, Fierro MT, Gammaitoni L, et al. Synergy of molecular targeted approaches and immunotherapy in melanoma: Preclinical basis and clinical perspectives. *Expert Opin Biol Ther* (2015) 15(10):1491–500. doi: 10.1517/14712598.2015.1069272

33. Yang G-J, Wang W, Mok SWF, Wu C, Law BYK, Miao X-M, et al. Selective inhibition of lysine-specific demethylase 5a (Kdm5a) using a Rhodium(Iii) complex for triple-negative breast cancer therapy. *Angew Chem Int Ed Engl* (2018) 57(40):13091–5. doi: 10.1002/anie.201807305

34. Cheng S-S, Qu Y-Q, Wu J, Yang G-J, Liu H, Wang W, et al. Inhibition of the Cdk9-cyclin T1 protein-protein interaction as a new approach against triple-negative breast cancer. *Acta Pharm Sin B* (2022) 12(3):1390–405. doi: 10.1016/j.apsb.2021.10.024

35. Overchuk M, Zheng G. Overcoming obstacles in the tumor microenvironment: Recent advancements in nanoparticle delivery for cancer theranostics. *Biomaterials* (2018) 156:217–37. doi: 10.1016/j.biomaterials.2017.10.024

36. Zhou Q, Dong C, Fan W, Jiang H, Xiang J, Qiu N, et al. Tumor extravasation and infiltration as barriers of nanomedicine for high efficacy: The current status and transcytosis strategy. *Biomaterials* (2020) 240:119902. doi: 10.1016/j.biomaterials.2020.119902

37. Hu Q, Hong Y, Qi P, Lu G, Mai X, Xu S, et al. Atlas of breast cancer infiltrated b-lymphocytes revealed by paired single-cell rna-sequencing and antigen receptor profiling. *Nat Commun* (2021) 12(1):2186. doi: 10.1038/s41467-021-22300-2

38. Helmink BA, Reddy SM, Gao J, Zhang S, Basar R, Thakur R, et al. B cells and tertiary lymphoid structures promote immunotherapy response. *Nature* (2020) 577 (7791):549–55. doi: 10.1038/s41586-019-1922-8

39. Petitprez F, de Reynies A, Keung EZ, Chen TW, Sun CM, Calderaro J, et al. B cells are associated with survival and immunotherapy response in sarcoma. *Nature* (2020) 577(7791):556–60. doi: 10.1038/s41586-019-1906-8

frontiers | Frontiers in Immunology

TYPE Original Research
PUBLISHED 14 April 2023
DOI 10.3389/fimmu.2023.1149874

Check for updates

OPEN ACCESS

EDITED BY
Rajan P. Adhikari,
Integrated BioTherapeutics, Inc.,
United States

REVIEWED BY
Rajkumar Ganesan,
Amgen, United States
Yanlu Xiong,
Fourth Military Medical University, China
Gordon Moody,
AstraZeneca, United States

*CORRESPONDENCE
Yasuyuki Fujii
ya-fujii@taisho.co.jp

SPECIALTY SECTION
This article was submitted to Autoimmune and Autoinflammatory Disorders : Autoimmune Disorders, a section of the journal Frontiers in Immunology

RECEIVED 23 January 2023
ACCEPTED 24 March 2023
PUBLISHED 14 April 2023

CITATION
Kyuuma M, Kaku A, Mishima-Tsumagari C, Ogawa B, Endo M, Tamura Y, Ishikura K, Mima M, Nakanishi Y and Fujii Y (2023) Unique structure of ozoralizumab, a trivalent anti-TNFα NANOBODY® compound, offers the potential advantage of mitigating the risk of immune complex-induced inflammation.
Front. Immunol. 14:1149874.
doi: 10.3389/fimmu.2023.1149874

COPYRIGHT
© 2023 Kyuuma, Kaku, Mishima-Tsumagari, Ogawa, Endo, Tamura, Ishikura, Mima, Nakanishi and Fujii. This is an open-access article distributed under the terms of the Creative Commons Attribution License (CC BY). The use, distribution or reproduction in other forums is permitted, provided the original author(s) and the copyright owner(s) are credited and that the original publication in this journal is cited, in accordance with accepted academic practice. No use, distribution or reproduction is permitted which does not comply with these terms.

Unique structure of ozoralizumab, a trivalent anti-TNFα NANOBODY® compound, offers the potential advantage of mitigating the risk of immune complex-induced inflammation

Masanao Kyuuma, Ayaka Kaku, Chiemi Mishima-Tsumagari, Bunichiro Ogawa, Mayumi Endo, Yunoshin Tamura, Kei-ichiro Ishikura, Masashi Mima, Yutaka Nakanishi and Yasuyuki Fujii*

Research Headquarters, Taisho Pharmaceutical Co., Ltd., Saitama, Japan

Biologics have become an important component of treatment strategies for a variety of diseases, but the immunogenicity of large immune complexes (ICs) and aggregates of biologics may increase risk of adverse events is a concern for biologics and it remains unclear whether large ICs consisting of intrinsic antigen and therapeutic antibodies are actually involved in acute local inflammation such as injection site reaction (ISR). Ozoralizumab is a trivalent, bispecific NANOBODY® compound that differs structurally from IgGs. Treatment with ozoralizumab has been shown to provide beneficial effects in the treatment of rheumatoid arthritis (RA) comparable to those obtained with other TNFα inhibitors. Very few ISRs (2%) have been reported after ozoralizumab administration, and the drug has been shown to have acceptable safety and tolerability. In this study, in order to elucidate the mechanism underlying the reduced incidence of ISRs associated with ozoralizumab administration, we investigated the stoichiometry of two TNFα inhibitors (ozoralizumab and adalimumab, an anti-TNFα IgG) ICs and the induction by these drugs of Fcγ receptor (FcγR)-mediated immune responses on neutrophils. Ozoralizumab-TNFα ICs are smaller than adalimumab-TNFα ICs and lack an Fc portion, thus mitigating FcγR-mediated immune responses on neutrophils. We also developed a model of anti-TNFα antibody-TNFα IC-induced subcutaneous inflammation and found that ozoralizumab-TNFα ICs do not induce any significant inflammation at injection sites. The results of our studies suggest that ozoralizumab is a promising candidate for the treatment of RA that entails a lower risk of the IC-mediated immune cell activation that leads to unwanted immune responses.

KEYWORDS

tumor necrosis factor, VHH, rheumatoid arthritis, injection site reaction, immunogenicity, Fcγ receptor, anti-TNFα antibody, immune complex

1 Introduction

Rheumatoid arthritis (RA) is one of a number of systemic autoimmune diseases that are accompanied by inflammation and both joint pain and swelling due to the inflammation. The roles of TNFα in the pathogenesis of RA have been reported (1, 2), and biologics that inhibit TNFα have made significant improvements in the treatment of RA (3–7). Five TNF inhibitors are now available for clinical use in RA, and the following four of them (the exception being certolizumab pegol) contain the Fc (Fragment crystallizable) portion: etanercept, a TNF receptor Fc fusion protein (3); infliximab, an anti-TNFα chimeric monoclonal antibody (4); adalimumab and golimumab, anti-TNFα human monoclonal antibodies (5, 6); and certolizumab pegol, a pegylated anti-TNFα humanized antibody Fab' fragment (7).

The Fc portion of IgG antibodies mediates various immune response by interacting with the complement system or with Fcγ receptor (FcγR), which is widely expressed on several types of immune cells (dendritic cells, mast cells, neutrophils, monocytes, and macrophages). The effector functions of IgG antibodies, such as complement-dependent cytotoxicity (CDC) and antibody-dependent cellular cytotoxicity (ADCC), are thought to be important mechanisms underlying the actions of therapeutic antibodies aimed at cytotoxicity, such as rituximab and trastuzumab (8). However, these Fc-mediated responses also entail the risk of inducing various unwanted immune responses (9). Accumulating evidence has shown that the unwanted inflammatory response is closely associated with injection site reactions (ISRs) or systemic hypersensitivity reactions (10–12). These unwanted immune responses can be an important factor in deciding to discontinue biotherapy and in selecting biological therapeutics (13–15).

Cross-linking of FcγRs by multimerized IgG as a result of immune complex (IC) formation is known to be one of the triggers of these unwanted immune responses (9, 16, 17). The extent of FcγR-mediated activation has been reported to be correlated with IC size (18). The traditional IgG antibodies, such as adalimumab and infliximab, can generate extremely large ICs under certain conditions, because an IgG antibody interacts with only one TNFα molecule of TNFα trimers in the complex as the result of the low flexibility of IgG in the distance between two antigen binding domains (19, 20). Moreover, studies that used a reporter assay have found a correlation between the size of the ICs and FcγRII and FcγRIII receptor-downstream signaling (21), suggesting that ICs composed of anti-TNFα antibodies and TNFα would be capable of inducing an unwanted immune response. However, the results were obtained in studies that used FcγR-overexpressing cells, and no studies have ever been performed using primary cells directly isolated from the hematopoietic system. Moreover, it is unclear whether the activation of FcγR-expressing cells by ICs leads to acute inflammation at the local injection site.

The next-generation anti-TNFα therapeutic ozoralizumab is a 38kDa humanized trivalent NANOBODY® compound that consists of two anti-human TNFα NANOBODY® VHHs and an anti-human serum albumin (HSA) NANOBODY® VHH, and it is structurally different from anti-TNFα IgGs such as adalimumab (22–24). Unlike previously reported IgG mAbs (19, 20), the very flexible geometry of three small NANOBODY® VHHs fused together with a 9GS linker enables both anti-human TNFα NANOBODY® VHHs to bind to two of the TNFα molecules of same TNFα trimers, and as a result ozoralizumab tends not to form large ICs with TNFα trimers. Moreover, since ozoralizumab lacks an Fc portion, ICs containing ozoralizumab might not be recognized by FcγRs expressed on immune cells. Consequently, ozoralizumab is expected to cause fewer immune responses caused by cross-linking of FcγRs with ICs. Treatment with ozoralizumab has been shown to have beneficial effects in the treatment of RA comparable to those of other TNF inhibitors and has been shown to have acceptable tolerability in Phase II/III clinical trials (25). The incidence of ISRs has been as low as 2%. The incidence of ISRs in the clinical studies of ozoralizumab has been similar to the incidence observed in clinical studies of certolizumab pegol (26), which also lacks an Fc portion, suggesting that the immune response *via* the Fc portion in antibody therapeutics is associated with the incidence of ISRs. In our previous paper, we demonstrated the immunogenicity assessment of biologics from biologics induce ADA production, indicating that the different structure of ozoralizumab compared to other TNF inhibitors is advantageous for the adaptive and systemic immune response induced by repeated administration (24). However, it remained unclear whether ozoralizumab is involved in localized acute inflammation.

In the present study, we therefore compared the effects of ICs formed with ozoralizumab or adalimumab (the latter as representative of antibodies that contain an Fc portion) on FcγR-mediated immune responses. We determined the molecular masses and hence stoichiometries of ICs by Size Exclusion Chromatography (SEC) and investigated whether ozoralizumab-TNFα ICs are capable of activating FcγR-expressing immune cells. We also developed a model of anti-TNFα antibodies and TNFα IC-induced subcutaneous inflammation to predict the potential clinical benefit of ozoralizumab in avoiding or reducing certain types of unwanted immune responses.

2 Materials and methods

2.1 Size exclusion chromatography

Ozoralizumab or adalimumab (0.65 nmol) was mixed with 0.072, 0.217, 0.65, or 1.95 nmol of TNFα trimer in 250 μL of PBS. Each mixture was incubated overnight at 4°C and then loaded onto a Superdex 200 Increase 10/300 column equilibrated with PBS. Representative results from two independent experiments are shown in Figure 1. The molecular weight estimated by the elution volume at the column has been calibrated by using a Gel Filtration Calibration Kit (Cytiva, United States), Carbonic Anhydrase (29 kDa, Sigma, United States), Cytochrome C (12.4 kDa, Sigma, United States), and Aprotinin (6.5 kDa, Nakarai, Japan). The molecular masses of the complexes obtained were estimated by SEC Principles & Methods (Cytiva, United States). After mixing 0.65 nmol of ozoralizumab with 1.3 nmol HSA (Sigma-Aldrich, United States) and 0.072, 0.217, 0.65, or 1.95 nmol of TNFα trimer

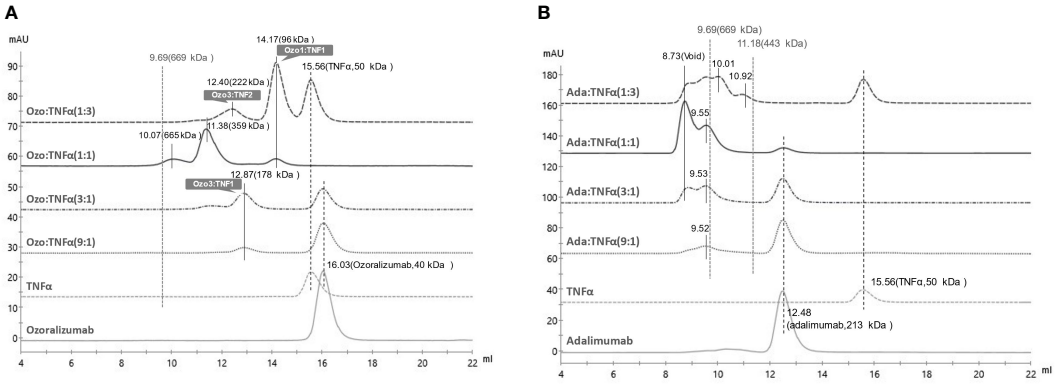

FIGURE 1
Size Exclusion Chromatography (SEC) of immunocomplexes of TNFα with ozoralizumab or adalimumab. **(A)** chromatograms of ozoralizumab-TNFα mixtures in various molar ratios. **(B)** chromatograms of adalimumab-TNFα mixtures in various molar ratios. All molecular weights were estimated by calibration with molecular weight markers.

in 250 ul of PBS, each mixture was incubated overnight at 4°C and loaded onto a Superdex 200 Increase 10/300 column equilibrated with PBS. Molecular mass was estimated as described above.

2.2 *In silico* modeling and MD simulations

Molecular modeling and visualization of the TNFα-ozoralizumab complex were performed using the Molecular Operating Environment (MOE) 2019.01 software platform (27). The initial complex structure of the two anti-TNFα NANOBODY® VHHs in ozoralizumab and hTNFα trimer was built based on the crystal structures of a TNFα and an anti-h TNFα NANOBODY® VHH complex (PDB ID: 5M2J) (23). The structure of an anti-TNFα NANOBODY® VHH ozoralizumab was modeled with a #VHH2 template by using the protein modeler tool in the "MOE/Homology Modeler" suite. The structure of an anti-HSA NANOBODY® VHH was also modeled using the "MOE/Antibody Modeler" tools. The linkers (9 amide acids: GGGGSGGGS) between the anti-TNFα and anti-HSA NANOBODIES ® were constructed by using the "MOE/Loop/Linker Modeler" tools. The structure (protonation, cap and build loop) for the crystal TNFα trimer structure was prepared with the "MOE/Structure Preparation" tools. In addition, the model structures were optimized by using the Amber10: EHT force field in generalized Born approximation, and all heavy atoms were fixed at the X-ray structure coordinates, except the two linkers. Molecular dynamics (MD) simulations of the ozoralizumab and TNFα trimer complex were then performed with GROMACS 2020.6 software (28) to confirm the validity of our predicted model. MD simulations were performed according to the procedure described below. The complex was placed in a truncated octahedron simulation box with a periodic boundary condition filled with TIP3P model water molecules (29). The water molecules were replaced with Na+ and Cl− ions to an NaCl concentration of 150 mM. The ff99SB force field parameter was assigned to the protein. To equilibrate the simulation system, a 20,000-step structural optimization and a 0.2 ns NVT MD simulation with position restraints for heavy atoms except water molecules were carried out. Then, the 0.2 ns MD without restraints under NPT conditions was continued. The temperature was maintained at 310 K and the pressure at 1 bar by using the stochastic dynamics algorithm (30) and the Berendsen algorithm (31), respectively. The long-range electrostatic interaction was processed by using the particle mesh Ewald method (32). An additional 0.2 ns MD simulation and a 100 ns production MD simulation were performed by applying the Nosé-Hoover and Parrinello-Rahman algorithm (33–35).

2.3 Isolation of primary mouse neutrophils

Mouse neutrophils were isolated from bone marrow by using a Neutrophil Isolation Kit (Cayman Chemical, United States) according to the manufacturer's instructions. Neutrophils were isolated from blood at room temperature by using sterile, endotoxin-free reagents. Cells were kept at room temperature in CL medium (a modified RPMI 1640 medium without phenol red and sodium hydrogen carbonate [Merck, Germany] containing 20 mM HEPES [Thermo Fisher Scientific, United States]) as described previously (36) until used (usually within 60 min). Cells were pre-treated for 20 min with 50 ng/ml TNFα prior to IC stimulation and then incubated for 10 minutes with/without BUF041B, FcγRII/CD32, and RIII/CD16 neutralized antibodies.

2.4 Detection of reactive oxygen species

Ozoralizumab was generated at Wyeth Research in the manner previously described (37). Adalimumab was purchased from Eisai Co., Ltd (Japan). Recombinant human TNFα alpha was purchased from R&D Systems (United States). All samples were diluted with PBS (Thermo Fisher Scientific, United States) or saline (Otsuka, Japan). A 20.3 μM solution of ozoralizumab or adalimumab was mixed with 2.3 μM, 6.6 or 6.8 μM, 20.3 μM, or 60.8 μM solution of TNFα trimer and incubated overnight at 4°C. Mixtures of the

respective antibodies and TNF were added to mouse neutrophils to a final antibody concentration of 33-34 nM. Reactive Oxygen Species (ROS) were measured by using L-012 sodium salt (8-Amino-5-chloro-2,3-dihydro-7-phenyl-pyrido[3,4-d] pyridazine sodium salt) (38). Neutrophils (5 x 105 cells/well) in CL medium containing 50 μM L-012 (FUJIFILM Wako Pure Chemical, Japan) were transferred to white microplates (Greiner Bio-One, Austria), and ROS-dependent chemiluminescence was measured with an ARVO microplate reader (PerkinElmer, United States). ROS released by the neutrophils were monitored for 1 min at 37°C.

2.5 Mice

Six-eight-week-old C57BL/6J male mice were purchased from Charles River Japan (Japan). The animals were housed under controlled temperature (23°C ± 3°C), humidity (55% ± 20%), and lighting (lights on from 0700 to 1900 hours) conditions. All animal experiments reported here were reviewed and approved by the Institutional Animal Care and Use Committee of Taisho Pharmaceutical Co., Ltd., and were in accordance with the Guidelines for Proper Conduct of Animal Experiments (Science Council of Japan, 2006).

2.6 Immune complex-induced subcutaneous inflammation

The dorsal skin of anesthetized mice was shaved, and 30 μL of PBS, ozoralizumab (6.6 μM, 0.25 mg/mL or 26.3 μM, 1 mg/mL), and adalimumab (6.8 μM, 1 mg/mL) mixed with 10 μg TNFα were injected intradermally at specific sites. Then, 0.5% Evans blue dye was immediately injected *via* the tail vein. The mice were sacrificed 4 hours after being injected, and the skin was removed at the fascia level above skeletal muscle, and reversed. Photographs were taken immediately and used to quantitate the degree of plasma exudation elicited by IC-induced subcutaneous inflammation. The blue dye intensity at each injection site was quantified with ImageJ software (National Institutes of Health, Bethesda, MD). The injection sites were then removed with a disposable sterile 6-mm punch biopsy (Kai, Japan), and after weighing them to evaluate edema, the tissues were immediately flash-frozen in liquid nitrogen and stored at −80°C.

2.7 Determination of MPO levels in skin

The flash-frozen skin tissues were blended and homogenized with RIPA Lysis and Extraction buffer (Thermo Fisher Scientific, United States) containing Halt Protease and Phosphatase Inhibitor (Thermo Fisher Scientific, United States). The homogenates were centrifuged at 10,000 g for 5 min, and the supernatant was collected. MPO levels in the tissue supernatant were measured by using a mouse ELISA kit (Abcam, United Kingdom) according to the manufacturer's instructions.

2.8 Histopathology

The injection sites collected from the dorsal skin of the mice (n = 3/group) were fixed in 10% neutral buffered formalin fixation, trimmed, and embedded in paraffin. Hematoxylin and eosin stained slides were prepared, and they were examined histopathologically with a BX53; microscope (Olympus Corporation, Japan).

2.9 Determination of ADCC activity

Infliximab and adalimumab were locally purchased from Med World Pharmacy. 7AAD staining solution was purchased from BD Biosciences (United States). NS0-TNF-D13 cells were produced by transfecting NS0 cells with a plasmid encoding the membrane bound form of TNFα. NK cells were isolated from the blood of healthy donors by negative selection with the RosetteSep™ Human NK cell enrichment cocktail obtained from Stemcell Technologies (Canada). NS0-TNF-D13 cells labeled with CSFE were used as targets to assess ADCC activity. The assays were run in RPMI, 1% heat-inactivated FBS, 2 mM L-glutamine, 10 mM HEPES, 50 U/ml penicillin, and 50 μg/ml streptomycin. A 0.25 x 10^5 number of NS0-TNF-D13 cells (targets cells) in 50 μl in a 96-well U-bottom plate was mixed with 50 μl of appropriately diluted anti-TNF agents or control antibody. After incubating the plates at 37°C for 20 min, effector cells were added at a target:effector ratio of at least 1:4, i.e., >0.12 x 10^6 cells/well in 50 μl. The plates were then incubated for 4 hours at 37°C. 7AAD was added for the last 10 min, and the cells were acquired by flow cytometry. The flow cytometry data were analyzed with FlowJo software 7.2.2 (BD Biosciences, United States), and % ADCC activity was calculated by gating on the CSFE + target cell population and calculating the percentage of cells that were 7AAD+. ADCC activity was determined at Wyeth Research, United States.

2.10 Determination of CDC activity

Infliximab, adalimumab, and etanercept were locally purchased from Med World Pharmacy. Sterile baby rabbit complement was purchased from Cedarlane Laboratories (Canada). Propidium Iodide staining solution was bought from BD Pharmingen (United States). The CHO- TNFα-NC2 cell line was produced by using CHO.DUKX cells that were transfected with a plasmid encoding a form of TNFα that is expressed both on the cell surface and in a secreted form. The cells were adapted to suspension media (CHO cell Media) containing R5CD1, 50 U/ml penicillin, 50 μg/ml streptomycin, 2 mM L-glutamine, and 20 nM Methotrexate and grown in a shaker flask at a 37°C in a shaker incubator under a 5% CO2 atmosphere. The plates were incubated in a 5% CO2 incubator for 3 hours 30 min at 37°C. To measure CDC activity, propidium iodide (6 μg/ml), a viability probe, was added to the cells, and after incubating them for 10 min at room temperature, 150 ul of PBS was added to all the wells. PI uptake was determined by using an HTS plate reader on a Becton-Dickinson

LSR II flow cytometer, and the data were analyzed with FlowJo software 7.2.2 (BD Biosciences, United States). CDC activity was determined at Wyeth Research, United States.

2.11 Statistical analysis

Tukey's post-test was used to compare the neutrophil activation chemiluminescence data. One-way ANOVA with Tukey's post-test was used to compare the data obtained in the IC-induced subcutaneous inflammation model and to analyze differences in means among the groups.

3 Results

3.1 Differences in complex formation with TNFα between IgG antibody and trivalent NANOBODY® compound

We previously demonstrated that ozoralizumab does not form large ICs in Ouchterlony double diffusion assays (24). However, since the stoichiometries of the ICs consisting of ozoralizumab and TNFα trimer are unclear, we evaluated the binding stoichiometry of ozoralizumab and adalimumab with TNFα trimer by SEC.

When ozoralizumab was pre-incubated with a threefold molar excess of TNFα trimers, SEC yielded three peaks. The major peak eluted at 14.17 ml (MW 96 kDa) was attributed to an ozoralizumab/TNFα trimer complex with a 1:1 stoichiometry, and the minor peak at 12.40 ml (MW around 222 kDa) was estimated to be an ozoralizumab/TNFα trimer complex with a 2:3 stoichiometry (three ozoralizumab molecules to two TNFα trimers) (Figure 1A). Unbound TNFα trimer was eluted at an elution volume of 15.56 ml (MW 50 kDa). When ozoralizumab and TNFα trimers were pre-incubated in equal molar ratios, two major peaks, at 11.38 ml (MW 359 kDa) and 10.07 ml (MW 665 kDa), attributed to heterogeneous ozoralizumab-TNFα ICs, and a small peak with an apparent MW of 96 kDa, attributed to an ozoralizumab/TNFα trimer complex with a 1:1 stoichiometry, were observed. When a threefold or ninefold molar excess of ozoralizumab was pre-incubated with TNFα, a peak at 12.87 ml (MW 178 kDa) attributed to an ozoralizumab/TNFα trimer complex with a 3:1 stoichiometry and a peak at 16.03 ml (MW 40 kDa) corresponding to unbound ozoralizumab were observed.

Similar experiments were performed with adalimumab. When adalimumab was pre-incubated with a threefold molar excess of TNFα trimers, broad peaks eluted ranging from 8.73 ml (void volume, MW ≥2000 kDa) to 10.92 ml (MW 443 kDa), attributed to heterogeneous sizes of adalimumab/TNFα trimer complexes, and a minor peak at 15.56 ml (MW 50 kDa) corresponding to TNFα trimer, were observed (Figure 1B). The ratio of the largest ICs was maximal when adalimumab and TNFα trimer were preincubated in equal molar ratios. The results demonstrated that ozoralizumab was unable to form large ICs eluted at void volume with TNFα at any molar ratio tested.

3.2 Structural *in silico* modeling and MD simulation of ozoralizumab and TNFα trimer complexes

As stated above, ozoralizumab is capable of forming a 1:1 complex with TNFα trimer under certain conditions. To confirm that one ozoralizumab is able to simultaneously bind to two TNFα in the TNFα trimer molecule, we predicted the 3-dimensional structure of the ozoralizumab-TNFα complex by in silico modeling and MD simulation. First, we modeled the structure of the TNFα - anti-TNFα NANOBODY® VHH domain of the ozoralizumab complex by using the crystal structures of an IC between TNFα and - anti- TNFα NANOBODY® VHH (#VHH2), whose amino acid sequence differs by 5 amino acids (PDB ID: 5M2J) (23). The 3-dimensional structure of the anti-HSA NANOBODY® domain of ozoralizumab was then modeled in the same way with MOE software. Finally, the entire structure of ozoralizumab in which the two anti-TNFα NANOBODIES® and anti-HSA NANOBODY® VHH were connected with a 9-amino acid linker (GGGGSGGGS) was constructed by using the "MOE/Loop/Linker Modeler" tools.

Since, based on the co-crystal structure of #VHH2 (23), these residues do not seem to be involved in the binding to the TNFα, it was considered appropriate to use #VHH2 as a template structure for in silico modeling of ozoralizumab TNFαNANOBODY®. We then performed MD simulations of the predicted TNFα-ozoralizumab complex structure to determine whether the 1:1 complex form was sufficiently stable. Figure 2 shows the final snapshot of the 100 ns MD simulation of the TNFα-ozoralizumab complex. The average distance between the C-terminus of one anti-TNFα NANOBODY® VHH and the N-terminus of the other anti-TNFα NANOBODY® VHH was 58.1 angstrom (standard deviation: ± 5.9 angstrom), which seemed to be a reasonable length for the anti-HSA NANOBODY® VHH located between the two anti-TNFα NANOBODIES® by the amino acid linkers. The TNFα trimer — ozoralizumab complex we had modeled was maintained during the MD simulations described in Section 2 (Materials and Methods).

3.3 The Fc portion is indispensable to the generation of oxidative bursts in mouse neutrophils in response to antibody-TNFα IC-dependent stimuli

Low-affinity FcγRs, IgG receptors that avidly bind to ICs, are key determinants of leukocyte activation (39). We evaluated oxidative bursts in mouse neutrophils in response to ozoralizumab-TNFα and adalimumab-TNFα, and the results confirmed the Fc portion - FcγRs contribution to anti-TNFα antibody-TNFα ICs-mediated stimulation. We isolated neutrophils from mouse bone marrow and incubated them with each of the TNFα inhibitor-TNFα ICs. Oxidative bursts were assessed by evaluating the production of mMPO-dependent ROS, which is considered a hallmark of neutrophil activation.

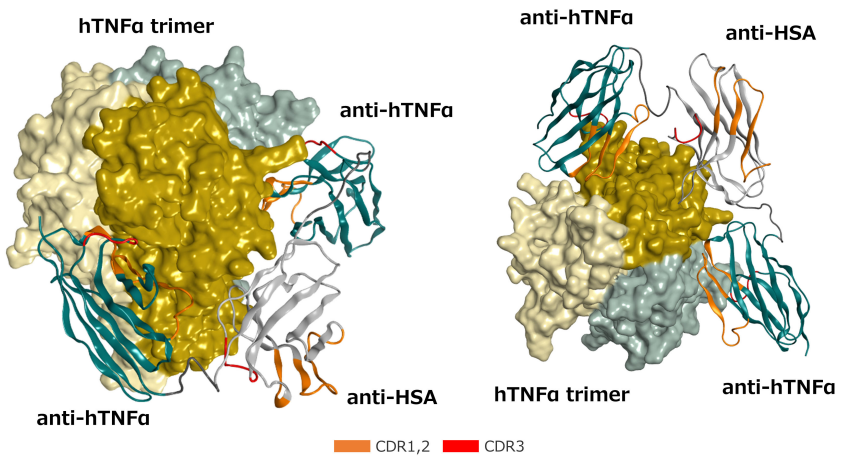

FIGURE 2
Front (Left) and bottom (Right) views of the predicted 3-dimensional structure of the ozoralizumab-TNFα trimer complex. The TNFα trimer molecule is shown with the molecular surface of each TNFα monomer unit colored dark yellow, light yellow, and light gray, respectively. The framework of the anti-TNFα NANOBODY® and the framework of the anti-HSA NANOBODY® are colored green and white, respectively. The CDRs are defined according to the Kabat numbering scheme and colored orange (CDR 1 and 2) and red (CDR3), respectively, and the two linkers are colored dark gray.

Adalimumab-TNFα ICs significantly induced ROS production by mouse neutrophils *in vitro*, but no ROS production was induced by ozoralizumab-TNFα ICs under the same conditions. In parallel studies, mouse neutrophil activation by stimulation with adalimumab-TNFα ICs was abrogated by the inclusion of blocking antibodies against both FcγRII/CD32 and RIII/CD16 (Figure 3A).

Large ICs have been reported to show stronger affinity for low-affinity FcγRs than smaller ICs do (18). Since the stoichiometry of ICs varies with the antigen-antibody molar ratio, each TNF inhibitor was mixed with TNFα in different molar ratios ([TNFα trimer]:[TNF inhibitor] = 1:3, 1:1, 3:1, and 9:1) and assessed for neutrophil activation. Marked ROS production was observed with the adalimumab-TNFα ICs at all molar ratios, and maximum activation occurred at the 1:1 molar ratio. ROS production in response to all adalimumab-TNFα IC molar ratios tested was completely suppressed by the inclusion of FcγRII/CD32 and RIII/CD16 blocking antibodies (Figure 3B). Expectedly, no ROS production was observed with the ozoralizumab-TNFα ICs under any of the conditions tested. The results suggest that the neutrophil activation induced by the TNFα inhibitor-TNFα ICs was caused by the interaction between the Fc portion of TNFα inhibitor and low-affinity FcγRs. While ROS production that results from cross-linking of Fc receptors differs depending on the stoichiometry of the ICs, the Fc-FcgR interaction is, however, critical for this response.

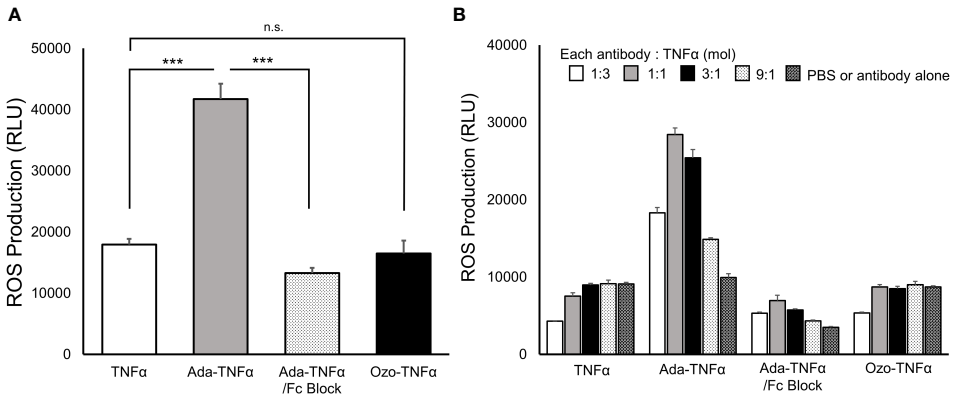

FIGURE 3
Production of ROS in mouse neutrophils activated by anti-TNFα antibody-TNFα ICs. Representative chemiluminescence values of extracellular MPO-dependent ROS as measured by the L-012 chemiluminescence assays are shown. ROS production by neutrophils (5×10^5 cells/well in CL medium) after incubation for 1 min at 37°C with uncomplexed TNFα, adalimumab-TNFα ICs (Ada-TNFα), adalimumab-TNFα ICs with MOUSE SEROBLOCK FcR (Ada-TNFα/Fc Blocker), and ozoralizumab-TNFα ICs (Ozo-TNFα) was monitored. Equimolar amounts of anti-TNFα antibodies and TNFα were mixed for IC preparation in experiment **(A)**. In experiment **(B)**, ICs were prepared by adding anti-TNFα antibodies to TNFα in four different molar ratios. PBS, ozoralizumab, and adalimumab alone were used as controls in the experiments. Data are representative of three independent experiments, and values are expressed as the mean ± SEM. n.s., not significant; n=3 ***p <0.001 vs. TNFα. (Tukey's test).

3.4 Administration of ozoralizumab-TNFα ICs did not induce a significant inflammatory response in a model of IC-induced subcutaneous inflammation

ISRs are the major adverse events reported after the administration of TNF inhibitors (10, 11). Although ISRs are a type of hypersensitivity reaction caused by an excessive immune response (11), the contribution of IC formed between TNFα trimers and TNF antibodies to the occurrence of such a reaction is unclear. We therefore investigated whether intradermally administered ozoralizumab-TNFα ICs and adalimumab-TNFα ICs would induce topical inflammation in animals. Vascular permeability and plasma neutrophil extravasation, which are hallmarks of the IC-induced immunopathologic cascade, can be visualized by the extravasation of intravenously injected Evan blue dye and quantified by tissue weight.

To maximize the size of the ICs, ozoralizumab (6.6 μM, 0.25 mg/mL: ozoralizumab-TNFα IC1) and adalimumab (6.8 μM, 1 mg/mL) were mixed with equimolar TNFα (6.5 μM), and ozoralizumab (26.3 μM, 1 mg/mL: ozoralizumab-TNFα IC2) was mixed with 6.5 μM of TNFα to evaluate the size dependency of the ICs for topical inflammation. After pre-incubation, these ICs or PBS was intradermally injected into mice. The blue dye intensity was significantly higher at sites injected with adalimumab-TNFα ICs ($P < 0.001$) than at the sites injected with PBS (Figures 4A, B), whereas the blue dye intensity at the sites injected with ozoralizumab-TNFα IC1 and 2 was almost the same as at the sites injected with PBS (Figures 4A, B). Similar results were obtained when the wet weight of skin biopsy specimens from IC injection sites were measured as an indicator of edema (Figure 4C). The skin injected with adalimumab-TNFα ICs weighed significantly more ($P < 0.001$) than the skin injected with PBS (Figure 4C). By contrast, no weight changes were observed in the skin injected with ozoralizumab-TNFα IC 1 or 2, or with TNFα alone. No changes in dye intensity or skin weight were observed at the sites injected with antibody alone (Supplementary Figure 1). These results indicated adalimumab-TNFα ICs, which can form large ICs containing the Fc portion, induced edema and vascular hyperpermeability at the injection site, but the ozoralizumab-TNFα ICs did not. It is noteworthy that the adalimumab-TNFα ICs had sufficient ability to induce a local response, whereas similarly administered ozoralizumab-TNFα ICs did not induce any significant local immune response.

3.5 Ozoralizumab-TNFα ICs dose MPO induction, but do not induce any marked neutrophil infiltration at injection sites

MPO is a peroxidase enzyme that is expressed most abundantly in neutrophil granules, and it is a critical component of the

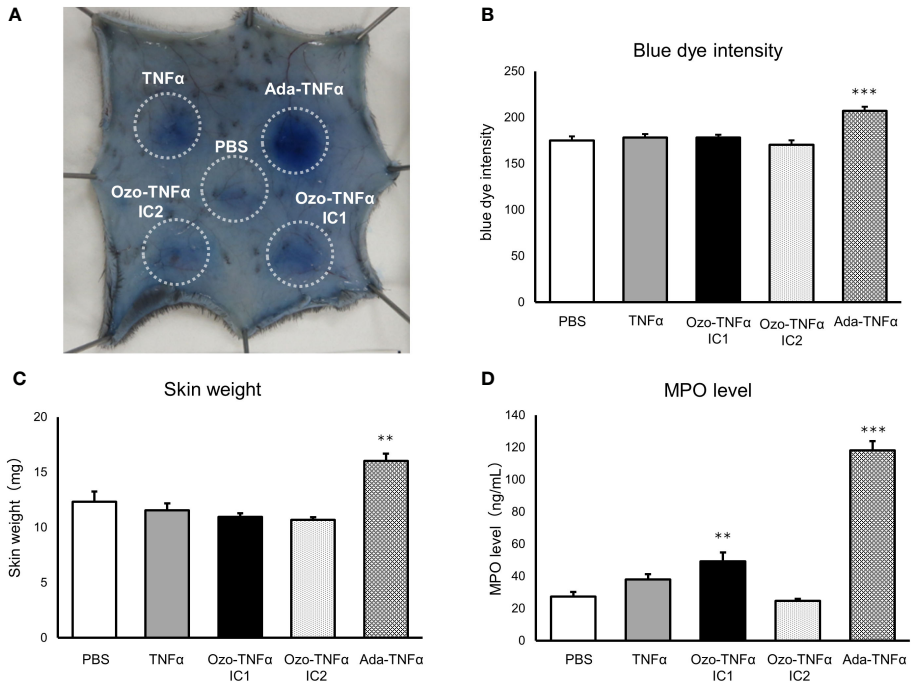

FIGURE 4
Inflammatory responses in skin tissue injected with pre-incubated ICs. C57BL/6J mice were intradermally injected with PBS, TNFα, ozoralizumab-TNFα IC1 (Ozo-TNFα IC1), ozoralizumab-TNFα IC2 (Ozo-TNFα IC2), or adalimumab-TNFα ICs (Ada-TNFα ICs). Degree of plasma exudation was evaluated by monitoring after intravenous injection of 0.5% Evans blue. **(A)** Representative macroscopic appearance of the subcutaneous inflammation. The circles surround the exuded Evans blue dye at each injection site. **(B)** Blue dye intensity quantified with ImageJ software. **(C)** Weight of 6-mm skin punch biopsy specimens. **(D)** MPO levels in tissue supernatant extracted from the 6-mm skin punch biopsy specimens. Data are expressed as mean ± SE. n = 7-8 $^{**}p < 0.01$, $^{***}p < 0.001$ vs. PBS (Tukey's test).

phagocytic microorganism-killing activities of the innate immune system (40). Measuring MPO in the skin is a well-established method of estimating its neutrophil content in cutaneous inflammation (41, 42). In this study we evaluated neutrophil accumulation by measuring the MPO content of skin punches by an ELISA. The results showed that the local MPO concentration in the skin 4 hours after injection with adalimumab-TNFα ICs was markedly higher (118.22 ± 5.66 ng/mL) than in the skin injected with PBS (27.34 ± 2.99 ng/mL) (Figure 4D). By contrast, ozoralizumab TNFα IC2-injected sites or TNFα-injected sites were not significantly different from PBS-injected sites (24.65 ± 1.32 ng/mL and 37.94 ± 3.34 ng/mL, respectively). Local MPO concentrations at the ozoralizumab TNFα IC1 injection site (49.15 ± 5.62 ng/mL) were significantly different from PBS injection site and lower than local MPO concentrations at the adalimumab injection site. Since ozoralizumab TNFα IC2 is thought to form smaller ICs than ozoralizumab TNFα IC1, the results indicate that MPO level is dependent on the size of the ICs.

To visualize the intensity and characteristics of the inflammation in response to the IC challenges, the skin sections taken from each group of mice were subjected to histopathological examination (Figure 5, Table 1). Skin sections from the adalimumab-TNFα IC-injected mice revealed an inflammatory cell infiltration predominantly composed of neutrophils, recognized by their multilobulated nuclei (Figures 5M–O), and representative pictures demonstrated that higher numbers of neutrophils had been recruited than in the mice injected with PBS (Figures 5A–C) or TNFα (Figures 5D–F). The arrows in the photomicrographs indicate focal neutrophil infiltration in the subcutaneous tissue at an adalimumab-TNFα IC-injected site (Figure 5M). By contrast, the skin sections from the mice injected with ozoralizumab-TNFα IC1 (Figures 5G–I) or ozoralizumab-TNFα IC2 (Figures 5J–L) did not show evidence of inflammatory cell infiltration, nor did the skin sections from the PBS-injected mice (Figures 5A–C). These histopathological findings confirmed the results obtained by the dye extravasation method (Figure 4), suggesting that, adalimumab-TNFα ICs are capable of triggering an IC-induced immune response accompanied by neutrophil infiltration, but that ozoralizumab-TNFα ICs are not.

4 Discussion

The first step in the immune response is recognition of a foreign substance by tissue-resident innate immune cells, such as by mast cells and macrophages sensing ICs by their FcγRs, complement receptors and pattern recognition receptors (PRR) (43, 44), which results in the production of secondary mediators such as TNFα and chemokines, and subsequently promotes neutrophil infiltration (45). Large ICs consisting of intrinsic antigen and therapeutic antibodies are more likely to be recognized by FcγRs on the surface of innate immune cells, and they can induce immune responses *in vitro*, such as the secretion of pro-inflammatory cytokines and chemokines (46). However, it is not clear whether these ICs consisting of anti-TNFα antibodies and TNFα can induce acute inflammation at local site.

The properties of the target molecules are also important to the formation of large ICs. Theoretically, large ICs can be formed only by a combination of multimeric antigen and multivalent antibodies. TNFα forms a trimer and TNFα trimers tend to be to form large ICs with bivalent antibodies. However, as demonstrated in Figure 1, ozoralizumab did not form large ICs eluted at void volume in the SEC under any of the conditions tested; in contrast, adalimumab did form them under certain conditions. The difference may be attributable to the TNFα trimer binding styles of the IgG antibody and ozoralizumab. It may be impossible for conventional IgGs to bind to two TNFα molecules in the same TNFα trimer with its two antigen-binding sites because of the large size of Fab and limited flexibility of the hinges. Actually, no elution peaks corresponding to adalimumab-TNFα trimer (1:1) complexes were observed under any of the conditions tested (Figure 1B). Thus, anti-TNFα IgGs are naturally prone to form larger ICs by cross-linking two TNFα trimers. On the other hand, as shown in Figure 2, ozoralizumab was well designed to be able to capture two TNFα molecules in the same TNFα trimer with its two anti-TNFα NANOBODY® VHHs, which have flexibility linkers, resulting in improved binding affinity and neutralizing activity (23, 24). Indeed, ozoralizumab-TNFα trimer (1:1) complexes were observed under certain conditions (Figure 1A). Ozoralizumab contains an anti-HSA NANOBODY® VHH that can bind to HSA, but it was unclear whether ozoralizumab/TNFα/HSA heterotrimers are formed. After addition of a 2-fold molar excess of HSA, the ozoralizumab/TNF IC elution peak and single ozoralizumab elution peak were no longer seen, and an ozoralizumab/TNFα/HSA heterotrimer peak corresponding to HSA binding was observed under all conditions (Supplementary Figure 2). Interestingly, the heterogeneous ozoralizumab-TNFα IC (Ozo ^{n}: TNFα trimers ^{n}) peak at 11.38 ml (MW 359 kDa) observed in the absence of HSA (Figure 1A, Ozo : TNFα (1:1)) was no longer seen, and a dominant peak with an apparent MW of 250 kDa attributed to ozoralizumab/TNFα/HSA complexes with a 1:1:1 stoichiometry was observed (Supplementary Figure 2, Ozo : TNFα [1:1]). The results demonstrated that ozoralizumab binding to HSA did not inhibit binding to TNFα, but may instead reduce the formation of high-order ICs. Thus, because of its unique structure, ozoralizumab appears to be superior to other anti-TNFα IgG antibodies which tend to form larger ICs.

A minimal threshold of interaction between ICs and low affinity FcγRs is required for FcγR-expressing cell activation. In our *in vitro* experiment, adalimumab-TNFα ICs significantly induced ROS production by mouse neutrophils, whereas no ROS production was induced by ozoralizumab-TNFα ICs under the same conditions. The difference between the induction of ROS production by the two ICs suggested a difference between the interactions of the two ICs and FcγRs on neutrophils. The ROS induction by adalimumab-TNFα ICs was completely abrogated by the addition of anti-FcγRII and anti-FcγRIII neutralizing antibodies, and the ozoralizumab-TNFα ICs, which lack an Fc portion, did not induce ROS production (Figure 3). These findings suggest the important role of the Fc portion in adalimumab in neutrophil activation *via* cross-linking of FcγRs. As shown in Figure 1B and previously reported (18, 47), adalimumab is able to form large ICs

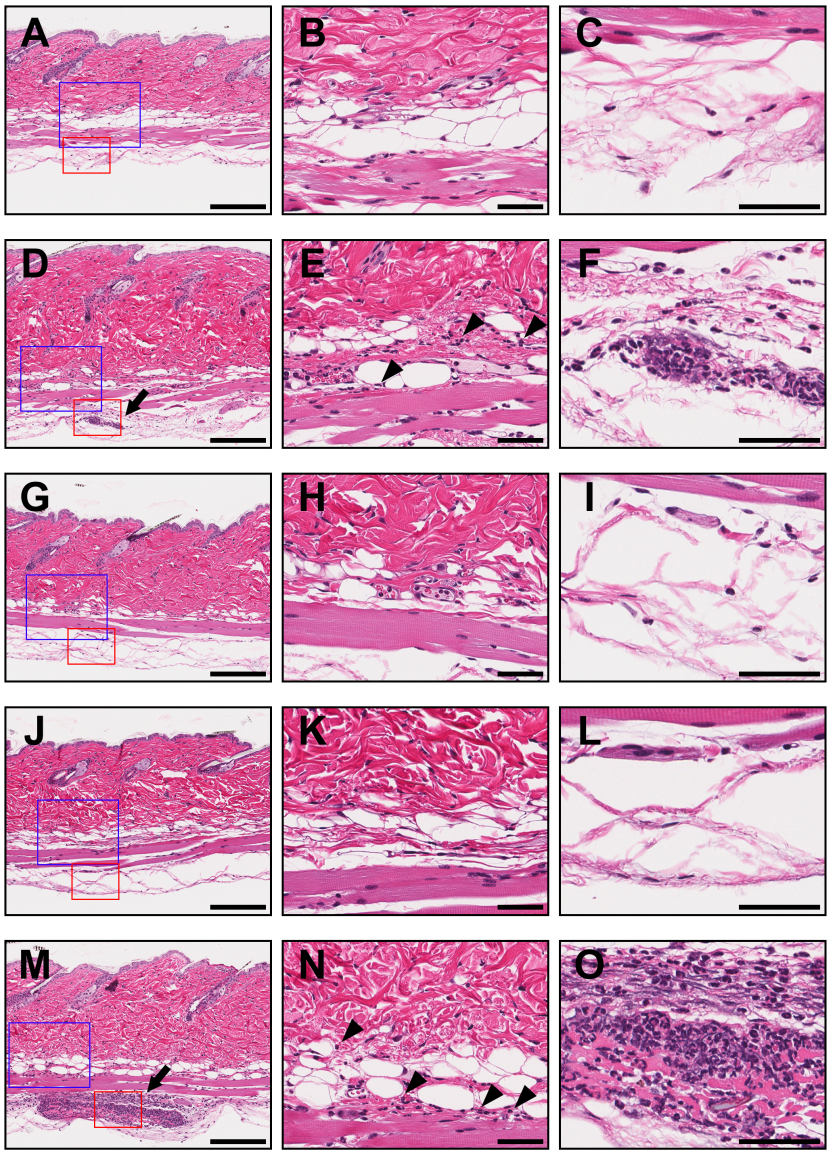

FIGURE 5
Histopathological examination of injection sites in a mouse model of IC-induced subcutaneous inflammation. The skin biopsy specimens collected from injected areas of PBS **(A–C)**, TNFα **(D–F)**, ozoralizumab-TNFα IC1 **(G–I)**, ozoralizumab-TNFα IC2 **(J–L)**, and adalimumab-TNFα ICs **(M–O)** were examined histopathologically after hematoxylin and eosin staining. The center column and right column are high magnification views of the blue boxes and red boxes, respectively, in the left column. The arrows point to focal neutrophil infiltration in the deeper layer of the subcutaneous tissue in the TNFα **(D)** and adalimumab-TNFα IC **(M)** injected areas. Neutrophils had also sporadically infiltrated the superficial layer of subcutaneous tissue (arrowheads) in the TNFα **(E)** and adalimumab-TNFα IC **(N)** injected areas. By contrast, the areas injected with ozoralizumab-TNFα IC1 **(G–I)**, ozoralizumab-TNFα IC2 **(J–L)**, and PBS **(A–C)** did not show any evidence of inflammatory cell infiltration. Scale bars: 200 μm (left), 50 μm (center and right).

TABLE 1 Histopathologic findings in a mouse model of immune complex (IC)-induced subcutaneous inflammation.

Groups	PBS			TNFα			Ozoralizumab-TNFα IC1			Ozoralizumab-TNFα IC2			Adalimumab-TNFα ICs		
Number of animals	3			3			3			3			3		
Grade	–	±	+	–	±	+	–	±	+	–	±	+	–	±	+
Skin (injection site)															
Subcutaneous neutrophil infiltration	3	0	0	2	1	0	3	0	0	3	0	0	0	1	2

-, None/Negligible, ±, Minimal/Very slight, +, Mild/Slight.
ICs, immune complexes; PBS, phosphate-buffered saline; TNF, tumor necrosis factor.

with TNFα trimers (≥2000kDa) under certain conditions. The neutrophil activation by adalimumab-TNFα ICs (Figure 3B) seemed to be correlated with the amounts of large ICs (Figure 1B). Adalimumab-TNFα ICs prepared from equimolar amounts of the antibodies and TNFα trimers have been reported to induce maximal FcγRII- and FcγRIII-mediated cell signaling, as shown in reporter cell lines (21), a finding that is in consistent with the findings in our studies using primary cells. The small ICs formed by ozoralizumab do not establishe the threshold between ICs and low affinity FcγRs, thus indicating that ozoralizumab-ICs are not part of the FcγR-mediated activation. In addition, did not induce ADCC, one of the effector responses that are regulated by FcγRs (Supplementary Figure 3). Taken together ozoralizumab could be freed from the unwanted immune response of the FcγR function.

We developed a model of anti-TNFα antibodies and TNFα IC-induced subcutaneous inflammation and demonstrated that adalimumab-TNFα ICs can induce acute subcutaneous inflammation at injection sites in animals, but that ozoralizumab-TNFα ICs cannot (Figures 4A–C). FcγRIII-deficient mice, which lack IgG-mediated mast cell degranulation, are resistant to IgG-dependent passive cutaneous anaphylaxis, and exhibit an impaired Arthus reaction, which suggests the importance of FcγRs in the IC-mediated immune response (48). The FcγR-mediated signaling deficiency led to a reduction in extravasation and neutrophil accumulation of at the inflammation site, consistent with our observations. Ozoralizumab-TNFα ICs did not induce increased vascular permeability and plasma extravasation, which were visualized with Evans blue dye (Figures 4A–C). The complement system is known to be involved in vascular permeability and plasma extravasation, and complement depletion with cobra venom factor has been shown to abrogate extravasation in FcγIII α chain–deficient mice (48, 49). Ozoralizumab did not cause CDC in an assay using transmembrane TNFα-expressing CHO- TNFα-NC2 cell line as target cells and baby rabbit complement, although adalimumab, infliximab, and etanercept did (Supplementary Figure 3). Unexpectedly, ozoralizumab-TNFα IC1 induced slight neutrophil recruitment based on the MPO levels (Figure 4D), suggesting that they were sensed by tissue-resident innate immune cells *via* another mechanism besides FcγRs. Ozoralizumab-TNFα IC2, which contains more ozoralizumab, did not induce any marked MPO induction, indicating that the sensing was not due to recognition of the foreign sequence in ozoralizumab. The sensing of biologic aggregation by PRRs, such as TLRs, is known to lead to significant increases in inflammatory cytokine secretion (50, 51). Ozoralizumab-TNFα ICs may be sensed by innate immune systems *via* PRRs. It has been suggested that the immune response activation by aggregated biologics depends on the number of particles and their surface area (52). Since IC size decreases under antibody excess conditions (Figure 1), the difference between the ozoralizumab-TNFα IC1 and ozoralizumab-TNFα IC2 immune responses suggests that the size of ICs may contribute to the Fc portion-independent immune response. Despite no neutrophil recruitment was seen in the histopathological examination (Figure 5), the increased MPO levels seen in Figure 4D. The increase in MPO levels in local injection site may have been induced by immune cells such as macrophages; it is possible that the immune response seen with ozoralizumab-TNFα IC1 administration was not sufficient to recruit neutrophils and subsequently not have led to the induce inflammatory symptoms such as extravasation and edema. These results indicated that ICs composed of anti-TNFα antibodies and TNFα ould induce acute inflammation at the local injection site, and therefore ozoralizumab, which does not interact with complement and does not cross-link FcγR is easy to operate biologics that is free from the acute inflammation caused by the FcγR and complement-related effector functions.

Our findings suggest that differences between the characteristics of ICs formed by different antibody formats can partially explain the different incidences of ISRs observed during treatment with anti-TNFα antibodies (Figures 4, 5) (10, 11, 25, 26). The administered biologics diffuse from the site of administration (subcutaneous tissue) and are absorbed through capillaries and transferred into the bloodstream. During these diffusion processes, microscopically, they are thought to undergo antigen-antibody ratios that tend to form large ICs, such as those shown in the SEC. Large ICs are recognized by tissue-resident innate immune cells and complement, leading to neutrophil recruitment. In addition, the deposition of ICs under the subcutaneous tissue and capillary endothelium can exacerbate further inflammation. These reactions are a kind of type III hypersensitivity reactions (ICs-mediated reaction) and can cause symptoms of ISRs. Indeed, ISRs were reported in a small proportion of patients treated with ozoralizumab (2%) and with certolizumab pegol (4.3%), which like ozoralizumab lacks the Fc portion and forms small ICs. Taken together, these findings suggest that biologics without Fc portion and with small ICs formation capacity has shown the potential to lead to a mitigation in local acute inflammation.

In summary, unlike adalimumab, ozoralizumab mitigates FcγR-mediated immune responses on neutrophils and does not induce any significant inflammation at injection sites. The differences were most likely attributable to the size of ICs and involvement of the Fc portion. Based on our finding, biologics without Fc portion and with low immune complex formation capacity has shown the potential to lead to a mitigation in local hypersensitivity reactions. Therefore, ozoralizumab mitigates the risk of acute inflammation, which may be reflected in the low incidence of ISRs. The unique structure of ozoralizumab provide a beneficial treatment for RA patients.

Data availability statement

The original contributions presented in the study are included in the article/Supplementary Material. Further inquiries can be directed to the corresponding author.

Ethics statement

All experimental procedures involving animal handling were approved by the Institutional Animal Care and Use Committee of Taisho Pharmaceutical Co., LTD., and were in accordance with the Guidelines for Proper Conduct of Animal Experiments (Science Council of Japan, 2006).

Author contributions

MK, and YF contributed to conception and design of the study. MK, AK and KI performed the *in vivo* experiments. MK, CT and MM performed the *in vitro* experiments. BO and YN performed the histopathology. ME and YT organized the *in silico* modeling. MK wrote the first draft of the manuscript. AK, BO, ME, MM, and YN wrote sections of the manuscript. All authors contributed to the article and approved the submitted version.

Acknowledgments

We wish to thank Tomoya Hasegawa, Kunihiko Iwamoto, and Tomofumi Kurokawa, Taisho Pharmaceutical Co., Ltd., for their help in performing the experiments. Ablynx discovered and performed the initial development of the NANOBODY® compound ozoralizumab (NANOBODY® is a registered trademark of Ablynx N.V. Ablynx N.V. is an affiliate of Sanofi).

Conflict of interest

All author are employed by Taisho Pharmaceutical Co., Ltd.

This study received funding from Taisho Pharmaceutical Co., Ltd. The funder had the following involvement with the study: the study design, collection, analysis, interpretation of data, the writing of this article or the decision to submit it for publication.

Publisher's note

All claims expressed in this article are solely those of the authors and do not necessarily represent those of their affiliated organizations, or those of the publisher, the editors and the reviewers. Any product that may be evaluated in this article, or claim that may be made by its manufacturer, is not guaranteed or endorsed by the publisher.

Supplementary material

The Supplementary Material for this article can be found online at: https://www.frontiersin.org/articles/10.3389/fimmu.2023.1149874/full#supplementary-material

SUPPLEMENTARY FIGURE 1

Inflammatory responses in the skin of mice to intradermally injected with anti TNFα antibody alone and pre-incubated ICs. Mice were intradermally injected with PBS, ozoralizumab-TNFαICs (Ozo-TNFα IC1, the same conc/ratio as in Figure 4), adalimumab-TNFαICs (Ada-TNFα ICs, the same conc/ratio as in Figure 4), ozoralizumab (Ozo) and adalimumab (Ada) and then intravenously injected with 0.5% Evans blue. **(A)** Representative macroscopic appearance of the subcutaneous inflammation. The circles surround exuded Evans blue dye at each injection site. **(B)** Blue dye intensity was quantified with ImageJ software. **(C)** Skin weight of 6-mm skin punch biopsy specimens. n = 6 *** p <0.001 vs. PBS (Tukey's test).

SUPPLEMENTARY FIGURE 2

Size Exclusion Chromatography (SEC) of immunocomplexes of ozoralizumab-TNFα-HSA. All molecular weights were estimated by calibration with molecular weight markers.

SUPPLEMENTARY FIGURE 3

(A) ADCC activity of infliximab, adalimumab, and a control IgG1 antibody (a human IgG1 antibody raised against the HIV envelop) were compared with ozoralizumab by using CFSE-labeled NS0-TNFD13 cells as targets and human NK cells as effectors. % ADCC activity values were calculated as the percentage of target cells that were $7AAD^+$. **(B)** CDC activity of etanercept, adalimumab, infliximab, and a control IgG1 antibody (a human IgG1 antibody raised against the HIV envelope) was compared with the CDC activity of ozoralizumab on the CHO-TNF NC2 line *in vitro* in the presence of baby rabbit complement. Cytotoxicity was assessed by measuring PI uptake of the dead cells. Values plotted are percentages of PI+ cells with the test and control subtracted from % PI- cells in the presence of complement alone.

References

1. Scott DL, Wolfe F, Huizinga TW. Rheumatoid arthritis. *Lancet* (2010) 376 (9746):1094–108. doi: 10.1016/S0140-6736(10)60826-4

2. McInnes IB, Schett G. Pathogenetic insights from the treatment of rheumatoid arthritis. *Lancet* (2017) 389(10086):2328–37. doi: 10.1016/S0140-6736(17)31472-1

3. Moreland LW, Baumgartner SW, Schiff MH, Tindall EA, Fleischmann RM, Weaver AL, et al. Treatment of rheumatoid arthritis with a recombinant human tumor necrosis factor receptor (P75)-fc fusion protein. *N Engl J Med* (1997) 337(3):141–7. doi: 10.1056/NEJM199707173370301

4. Elliott MJ, Maini RN, Feldmann M, Kalden JR, Antoni C, Smolen JS, et al. Randomised double-blind comparison of chimeric monoclonal antibody to tumour necrosis factor α (cA2) versus placebo in rheumatoid arthritis. *Lancet* (1994) 344 (8930):1105–10. doi: 10.1016/s0140-6736(94)90628-9

5. Weinblatt ME, Keystone EC, Furst DE, Moreland LW, Weisman MH, Birbara CA, et al. Adalimumab, a fully human anti-tumor necrosis factor alpha monoclonal antibody, for the treatment of rheumatoid arthritis in patients taking concomitant methotrexate: the ARMADA trial. *Arthritis Rheumatol* (2003) 48(1):35–45. doi: 10.1002/art.10697

6. Zhou H, Jang H, Fleischmann RM, Bouman-Thio E, Xu Z, Marini JC, et al. Pharmacokinetics and safety of golimumab, a fully human anti-TNF-Alpha monoclonal antibody, in subjects with rheumatoid arthritis. *J Clin Pharmacol* (2007) 47(3):383–96. doi: 10.1177/0091270006298188

7. Choy EHS, Hazleman B, Smith M, Moss K, Lisi L, Scott DGI, et al. Efficacy of a novel PEGylated humanized anti-TNF fragment (CDP870) in patients with rheumatoid arthritis: A phase II double-blinded, randomized, dose-escalating trial. *Rheumatol (Oxf)* (2002) 41(10):1133–7. doi: 10.1093/rheumatology/41.10.1133

8. Clynes RA, Towers TL, Presta LG, Ravetch JV. Inhibitory fc receptors modulate in vivo cytoxicity against tumor targets. *Nat Med* (2000) 6(4):443–6. doi: 10.1038/74704

9. Nimmerjahn F, Ravetch JV. Fcγ receptors as regulators of immune responses. *Nat Rev Immunol* (2008) 8(1):34–47. doi: 10.1038/nri2206

10. Matsui T, Umetsu R, Kato Y, Hane Y, Sasaoka S, Motooka Y, et al. Age-related trends in injection site reaction incidence induced by the tumor necrosis factor-α (TNF-α) inhibitors etanercept and adalimumab: the food and drug administration adverse event reporting system, 2004-2015. *Int J Med Sci* (2017) 14(2):102–9. doi: 10.7150/ijms.17025

11. Murdaca G, Spanò F, Puppo F. Selective TNF-α inhibitor-induced injection site reactions. *Expert Opin Drug Safety* (2013) 12(2):187–93. doi: 10.1517/14740338.2013.755957

12. Leach MW, Rottman JB, Hock MB, Finco D, Rojko JL, Beyer JC. Immunogenicity/Hypersensitivity of biologics. *Toxicol Pathol* (2014) 42(1):293–300. doi: 10.1177/0192623313510987

13. Böhm R, Proksch E, Schwarz T, Cascorbi I. Drug hypersensitivity: Diagnosis, genetics, and prevention. *Deutsches Ärzteblatt Int* (2018) 115:501–12. doi: 10.3238/arztebl.2018.0501

14. Sauna ZE, Lagassé D, Pedras-Vasconcelos J, Golding B, Rosenberg AS. Evaluating and mitigating the immunogenicity of therapeutic proteins. *Trends Biotechnol* (2018) 36(10):1068–84. doi: 10.1016/j.tibtech.2018.05.008

15. Barton J. Patient preferences and satisfaction in the treatment of rheumatoid arthritis with biologic therapy. *Patient Preference Adherence* (2009) 3:335. doi: 10.2147/ppa.s5835

16. Bournazos S, Gupta A, Ravetch JV. The role of IgG fc receptors in antibody-dependent enhancement. *Nat Rev Immunol* (2020) 20(10):633–43. doi: 10.1038/s41577-020-00410-0

17. Krishna M, Nadler SG. Immunogenicity to biotherapeutics the role of anti-drug immune complexes. *Front Immunol* (2016) 7:21. doi: 10.3389/fimmu.2016.00021

18. Lux A, Yu X, Scanlan CN, Nimmerjahn F. Impact of immune complex size and glycosylation on IgG binding to human FcγRs. *J Immunol* (2013) 190(8):4315–23. doi: 10.4049/jimmunol.1200501

19. Kohno T, Tam LT, Stevens SR, Louie JS. Binding characteristics of tumor necrosis factor receptor-fc fusion proteins vs anti-tumor necrosis factor MAbs. *J Invest Dermatol Symposium Proc* (2007) 12(1):5–8. doi: 10.1038/sj.jidsymp.5650034

20. Scallon B, Cai A, Solowski N, Rosenberg A, Song X, Shealy D, et al. Binding and functional comparisons of two types of tumor necrosis factor antagonists. *J Pharmacol Exp Ther* (2002) 301(2):418–26. doi: 10.1124/jpet.301.2.418

21. Krayukhina E, Noda M, Ishii K, Maruno T, Wakabayashi H, Tada M, et al. Analytical ultracentrifugation with fluorescence detection system reveals differences in complex formation between recombinant human TNF and different biological TNF antagonists in various environments. *MAbs* (2017) 9(4):664–79. doi: 10.1080/19420862.2017.1297909

22. Coppieters K, Dreier T, Silence K, De Haard. H, Lauwereys M, Casteels P, et al. Formatted antitumor necrosis factor α VHH proteins derived from camelids show superior potency and targeting to inflamed joints in a murine model of collagen-induced arthritis. *Arthritis Rheumatism* (2006) 54(6):1856–66. doi: 10.1002/art.21827

23. Beirnaert E, Desmyter A, Spinelli S, Lauwereys M, Aarden L, Dreier T, et al. Bivalent llama single-domain antibody fragments against tumor necrosis factor have picomolar potencies due to intramolecular interactions. *Front Immunol* (2017) 8:867. doi: 10.3389/fimmu.2017.00867

24. Ishiwatari-Ogata C, Kyuuma M, Ogata H, Yamakawa M, Iwata K, Ochi M, et al. Ozoralizumab, a humanized anti-TNFα NANOBODY' compound, exhibits efficacy not only at the onset of arthritis in a human TNF transgenic mouse but also during secondary failure of administration of an anti-TNFα IgG. *Front Immunol* (2022) 13:853008. doi: 10.3389/fimmu.2022.853008

25. Takeuchi T, Kawanishi M, Nakanishi M, Yamasaki H, Tanaka Y. Phase II/III results of the anti-TNF multivalent NANOBODY® compound 'ozoralizumab' in patient with rheumatoid arthritis (OHZORA trial). *Arthritis Rheumatol* (2022) 74 (11):1776–85. doi: 10.1002/art.42273

26. Goel N, Stephens S. Certolizumab pegol. *MAbs* (2010) 2(2):137–47. doi: 10.4161/mabs.2.2.11271

27. Chemical Computing Group ULC. *Molecular operating environment (MOE), 2020.0901*. Montreal, QC, Canada: Chemical Computing Group ULC (2020).

28. Abraham MJ, Murtola T, Schulz R, Páll S, Smith JC, Hess B, et al. GROMACS: High performance molecular simulations through multi-level parallelism from laptops to supercomputers. *SoftwareX* (2015) 1-2:19–25. doi: 10.1016/j.softx.2015.06.001

29. Jorgensen WL, Chandrasekhar J, Madura JD, Impey RW, Klein ML. Comparison of simple potential functions for simulating liquid water. *J Chem Physics.* (1983) 79(2):926–35. doi: 10.1063/1.445869

30. Hess B, Kutzner C, Spoel DVD, Lindahl E. GROMACS 4:' algorithms for highly efficient, load-balanced, and scalable molecular simulation. *J Chem Theory Computation* (2008) 4(3):435–47. doi: 10.1021/ct700301q

31. Berendsen HJC, Postma JPM, Gunsteren WFV, DiNola A, Haak JR. Molecular dynamics with coupling to an external bath. *J Chem Physics* (1984) 81(8):3684–90. doi: 10.1063/1.448118

32. Bayly CI, Cieplak P, Cornell W, Kollman PA. A well-behaved electrostatic potential based method using charge restraints for deriving atomic charges: the RESP model. *J Phys Chem* (1993) 97(40):10269–80. doi: 10.1021/j100142a004

33. Nosé S. A molecular dynamics method for simulations in the canonical ensemble. *Mol Physics* (1984) 52(2):255–68. doi: 10.1080/00268978400101201

34. Hoover WG. Canonical dynamics: Equilibrium phase-space distributions. *Phys Rev A* (1985) 31(3):1695–7. doi: 10.1103/PhysRevA.31.1695

35. Parrinello M, Rahman A. Polymorphic transitions in single crystals: a new molecular dynamics method. *J Appl Physics* (1981) 52(12):7182–90. doi: 10.1063/1.328693

36. Behnen M, Leschczyk C, Möller S, Batel T, Klinger M, Solbach W, et al. Immobilized immune complexes induce neutrophil extracellular trap release by human neutrophil granulocytes *Via* FcγRIIIB and mac-1. *J Immunol* (2014) 193(4):1954–65. doi: 10.4049/jimmunol.1400478

37. Coppieters K, Dreier T, Silence K, De Haard H, Lauwereys M, Casteels P, et al. Formatted anti-tumor necrosis factor alpha VHH proteins derived from camelids show superior potency and targeting to inflamed joints in a murine model of collagen-induced arthritis. *Arthritis Rheum* (2006) 54(6):1856–66. doi: 10.1002/art.21827

38. Imada I, Sato EF, Miyamoto M, Ichimori Y, Minamiyama Y, Konaka R, et al. Analysis of reactive oxygen species generated by neutrophils using a chemiluminescence probe l-012. *Analytical Biochem* (1999) 271(1):53–8. doi: 10.1006/abio.1999.4107

39. Jönsson F, Mancardi DA, Albanesi M, Bruhns P. Neutrophils in local and systemic antibody-dependent inflammatory and anaphylactic reactions. *J Leukocyte Biol* (2013) 94(4):643–56. doi: 10.1189/jlb.1212623

40. Klebanoff SJ. Myeloperoxidase: friend and foe. *J Leukocyte Biol* (2005) 77 (5):598–625. doi: 10.1189/jlb.1204697

41. Bradley PP, Priebat DA, Christensen RD, Rothstein G. Measurement of cutaneous inflammation: estimation of neutrophil content with an enzyme marker. *J Invest Dermatol* (1982) 78(3):206–9. doi: 10.1111/1523-1747.ep12506462

42. Carbo C, Yuki K, Demers M, Wagner DD, Shimaoka M. Isoflurane inhibits neutrophil recruitment in the cutaneous arthus reaction model. *J Anesthesia* (2013) 27 (2):261–8. doi: 10.1007/s00540-012-1508-1

43. Schmidt RE, Gessner JE. Fc receptors and their interaction with complement in autoimmunity. *Immunol Letters* (2005) 100(1):56–67. doi: 10.1016/j.imlet.2005.06.022

44. Pallardy MJ, Turbica I, Biola-vidamment A. Why the immune system should be concerned by nanomaterials? *Front Immunol* (2017) 8:544. doi: 10.3389/fimmu.2017.00544

45. Mayadas TN, Tsokos GC, Tsuboi N. Mechanisms of immune ComplexMediated neutrophil recruitment and tissue injury. *Circulation* (2009) 120(20):2012–24. doi: 10.1161/CIRCULATIONAHA.108.771170

46. Jefferis R. Aggregation, immune complexes and immunogenicity. *MAbs* (2011) 3 (6):503–4. doi: 10.4161/mabs.3.6.17611

47. Kim M, Lee S, Song M, Yoo TH, Lee B, Kim Y. Comparative analyses of complex formation and binding sites between human tumor necrosis factor-alpha and its three antagonists elucidate their different neutralizing mechanisms. *J Mol Biol* (2007) 374 (5):1374–88. doi: 10.1016/j.jmb.2007.10.034

48. Hazenbos WL, Gessner J, Hofhuis FM, Kuipers H, Meyer D, Heijnen IA, et al. Impaired IgG-dependent anaphylaxis and arthus reaction in FcγRIII (CD16) deficient mice. *Immunity* (1996) 5(2):181–8. doi: 10.1016/S1074-7613(00)80494-X

49. Williams TJ. Vascular permeability changes induced by complement-derived peptides. *Agents Actions* (1983) 13(5-6):451–5. doi: 10.1007/BF02176415

50. Tian J, Avalos AM, Mao S, Chen B, Senthil K, Wu H, et al. Toll-like receptor 9dependent activation by DNA-containing immune complexes is mediated by HMGB1 and RAGE. *Nat Immunol* (2007) 8(5):487–96. doi: 10.1038/ni1457

51. Joubert MK, Hokom M, Eakin C, Zhou L, Deshpande M, Baker MP, et al. Highly aggregated antibody therapeutics can enhance the in vitro innate and late-stage T-cell immune responses. *J Biol Chem* (2012) 287(30):25266–79. doi: 10.1074/jbc.M111.330902

52. Lundahl MLE, Fogli S, Colavita PE, Scanlan EM. Aggregation of protein therapeutics enhances their immunogenicity: Causes and mitigation strategies. *RSC Chem Biol* (2021) 2(4):1004–20. doi: 10.1039/d1cb00067e

frontiers | Frontiers in Immunology

TYPE Original Research
PUBLISHED 21 April 2023
DOI 10.3389/fimmu.2023.1152035

Check for updates

OPEN ACCESS

EDITED BY
Silke Paust,
The Scripps Research Institute,
United States

REVIEWED BY
Khashayarsha Khazaie,
Mayo Clinic Arizona, United States
Lenneke A. M. Cornelissen,
Radboud University Medical Centre,
Netherlands

*CORRESPONDENCE
Nicholas J. Shields
nicholas.shields@sydney.edu.au

SPECIALTY SECTION
This article was submitted to
Cancer Immunity
and Immunotherapy,
a section of the journal
Frontiers in Immunology

RECEIVED 27 January 2023
ACCEPTED 10 April 2023
PUBLISHED 21 April 2023

CITATION
Shields NJ, Peyroux EM, Ferguson AL, Steain M, Neumann S and Young SL (2023) Late-stage MC38 tumours recapitulate features of human colorectal cancer – implications for appropriate timepoint selection in preclinical studies.
Front. Immunol. 14:1152035.
doi: 10.3389/fimmu.2023.1152035

COPYRIGHT
© 2023 Shields, Peyroux, Ferguson, Steain, Neumann and Young. This is an open-access article distributed under the terms of the Creative Commons Attribution License (CC BY). The use, distribution or reproduction in other forums is permitted, provided the original author(s) and the copyright owner(s) are credited and that the original publication in this journal is cited, in accordance with accepted academic practice. No use, distribution or reproduction is permitted which does not comply with these terms.

Late-stage MC38 tumours recapitulate features of human colorectal cancer – implications for appropriate timepoint selection in preclinical studies

Nicholas J. Shields[1,2]*, Estelle M. Peyroux[2], Angela L. Ferguson[1,3,4], Megan Steain[1], Silke Neumann[2] and Sarah L. Young[1,5]

[1]School of Medical Sciences, Faculty of Medicine and Health, The University of Sydney, Sydney, NSW, Australia, [2]Department of Pathology, Otago Medical School, University of Otago, Dunedin, New Zealand, [3]Liver Injury and Cancer Program, Centenary Institute, Sydney, NSW, Australia, [4]Charles Perkins Centre, University of Sydney, Sydney, NSW, Australia, [5]Faculty of Science, University of Canterbury, Christchurch, New Zealand

Anti-tumour T cell responses play a crucial role in controlling the progression of colorectal cancer (CRC), making this disease a promising candidate for immunotherapy. However, responses to immune-targeted therapies are currently limited to subpopulations of patients and specific types of cancer. Clinical studies have therefore focussed on identifying biomarkers that predict immunotherapy responses and elucidating the immunological landscapes of different cancers. Meanwhile, our understanding of how preclinical tumour models resemble human disease has fallen behind, despite their crucial role in immune-targeted drug development. A deeper understanding of these models is therefore needed to improve the development of immunotherapies and the translation of findings made in these systems. MC38 colon adenocarcinoma is a widely used preclinical model, yet how it recapitulates human colorectal cancer remains poorly defined. This study investigated the tumour-T cell immune landscape of MC38 tumours using histology, immunohistochemistry, and flow cytometry. We demonstrate that early-stage tumours exhibit a nascent TME, lacking important immune-resistance mechanisms of clinical interest, while late-stage tumours exhibit a mature TME resembling human tumours, with desmoplasia, T cell exhaustion, and T cell exclusion. Consequently, these findings clarify appropriate timepoint selection in the MC38 model when investigating both immunotherapies and mechanisms that contribute to immunotherapy resistance. Overall, this study provides a valuable resource that will enable appropriate application of the MC38 model and expedite the development and clinical translation of new immunotherapies.

KEYWORDS

colorectal cancer, immunotherapy, syngeneic preclinical models, MC38, immune exclusion, t cell exhaustion, tumour microenvironment

1 Introduction

Murine tumour models have been crucial for the preclinical development and optimisation of many cancer therapies (1, 2). However, in the case of immunotherapies, progress has been hindered in part by the lack of suitable models that accurately predict successful clinical responses in humans (1). Mounting evidence illustrates that human tumours and the composition of their immune infiltrates are highly heterogeneous (3, 4) and that effective anti-tumour immunity can be hindered by numerous immune evasion and suppression mechanisms (5). Consequently, various clinical studies have focussed on identifying biomarkers and immune signatures that can predict responses to immunotherapy (4, 6–9). In addition, there is an increasing emphasis on elucidating the immunological landscapes of different cancers and cancer subtypes (10–12), even down to the inherent immunological status of individual cancer patients (13). In the context of colorectal cancer (CRC), clinical studies examining the immune landscape of distinct CRC subtypes have occurred at such pace that they have outstripped our understanding of preclinical tumour models and how these relate to human disease. Consequently, a deeper understanding of preclinical tumour models and how these models resemble human CRC is vital for the clinical translation of results obtained in these systems.

The MC38 cell line was originally derived in 1975 from a colon adenocarcinoma induced by subcutaneous injection of dimethylhydrazine in a female C57BL/6 mouse (14). Due to the intact immune system of syngeneic C57BL/6 hosts, this cell line (among others derived from different tumour types) has been extensively used as a transplantable tumour model for investigating anti-tumour immunity and novel immunotherapies (15–17). As in other syngeneic tumour models, MC38 tumour cells are implanted subcutaneously owing to the advantages of this approach – namely the simplicity and reproducibility of inoculation and the ease of monitoring subsequent tumour growth (1, 18). While this approach obviously fails to recapitulate the complexity of colorectal carcinogenesis *in situ*, the MC38 model has been reported as a reliable representation of advanced disease that has escaped immune selection (19). One obvious limitation of this approach is that the immune microenvironment in subcutaneous tissue is significantly different from the gastrointestinal tract (20). Consequently, orthotopic models have been developed using the MC38 cell line, which involve tumour cell implantation in the mouse colon wall (20, 21). This approach is advantageous over subcutaneous inoculation in that it mimics the growth of primary tumours within the colonic microenvironment (1). However, the complexity of surgical implantation procedures limits the feasibility of this approach, while trauma and inflammation arising from the surgical procedure can create a non-physiologic tumour microenvironment (TME) (20, 21). In addition, it is difficult to monitor tumour growth in the mouse colon. Hence, despite its caveats, subcutaneous implantation of the MC38 cell line remains a useful and practical preclinical model for the study of anti-tumour immune responses.

In contrast to the extensive molecular characterisation of human CRC (22–24), contemporary studies have only recently begun to define the features of preclinical tumour models and how they recapitulate human disease (19, 25, 26). Of note, the genomic and transcriptomic landscape of the MC38 cell line has been characterised using whole-exome sequencing, single-nucleotide polymorphism (SNP) array analysis, and RNA sequencing (19). This study found that the MC38 cell line exhibited DNA mismatch-repair (MMR) deficiency and a propensity for C > A/G > T transversions – mutational signatures that are associated with hypermutated human CRC tumours containing defects in the DNA polymerases Pol δ (*POLD1*) and Pol ϵ (*POLE*) (19, 27). Consistent with this notion, the MC38 genome was shown to harbour mutations in *POLD1* and the MMR gene, *MSH3* (19). In terms of known CRC driver mutations present in the MC38 genome, striking similarities to human CRC (23, 24) are present, with genetic alterations in components of the WNT/β-catenin, TGF-β, EGFR and downstream MAPK signalling pathways (19). Consequently, the MC38 cell line has been purported as a valid model for hypermutated and/or microsatellite instability-high (MSI-H) human CRC (19).

In accordance with its characterisation as a valid model of hypermutated/MSI-H human CRC – and consistent with human consensus molecular subtype 1 (CMS1) tumours (28, 29) – the MC38 model is responsive to immune checkpoint inhibition of the PD-1/PD-L1 axis (15, 30). Consequently, MC38 tumours are widely considered as immunogenic and this model has been used extensively for the preclinical development and optimisation of new immunotherapeutic strategies (17, 30, 31). Studies investigating therapeutically-induced immune responses in the MC38 model have shown that these tumours evade anti-tumour immunity through a variety of different mechanisms, including the recruitment of regulatory $CD4^+$ T cells (T_{REG}) (19), the expression of inhibitory ligands such as PD-L1 by tumour and myeloid cells (15), and by inducing the dysfunction of infiltrating $CD8^+$ T cells (32, 33). Importantly, these immune features closely emulate those observed in human CRC tumours and are associated with unfavourable patient outcomes in CRC and other malignancies (34–38). However, despite widespread use of the MC38 model in cancer immunotherapy research, spontaneous or 'naturally-occurring' T cell responses against this cell line (that occur in the absence of therapeutic interventions) are poorly characterised. Furthermore, the spatiotemporal dynamics of T cell infiltration in MC38 tumours during their establishment and progression is largely undefined. Given the importance of the immune landscape in human CRC tumours – both for patient prognosis and predicting therapeutic responses to immunotherapy (9, 39, 40) – a deeper understanding of the immune microenvironment in MC38 tumours is needed.

This study therefore investigated the tumour-T cell immune landscape in the MC38 model, using histology, immunohistochemistry (IHC) and flow cytometry to longitudinally profile endogenous T cell responses in outgrowing tumours. We demonstrate that the progression of MC38 tumours following subcutaneous implantation

is a dynamic process, with profound changes in the nature of T cell infiltration and the structural architecture of the MC38 TME. Our findings demonstrate the importance of appropriate timepoint selection when investigating novel immunotherapies and mechanisms of immunotherapy resistance in this model. Collectively, this study provides a resource that may improve the translation of effective immunotherapies to human patients.

2 Materials and methods

2.1 Mice and cell culture

6- to 10-week-old female C57BL/6 mice were obtained from the Hercus-Taieri Research Unit (HTRU) at the University of Otago, Dunedin, New Zealand. All mice were maintained under specific pathogen-free conditions and all experiments were conducted in accordance with protocols approved by the University of Otago Animal Ethics Committee. The MC38 colon adenocarcinoma cell line was maintained in DMEM media (Gibco, Waltham, MA, USA) supplemented with 10% heat-inactivated FCS (Moregate Biotech, Hamilton, NZ), 100 U/mL penicillin and 100 mg/mL streptomycin (Gibco) and harvested using DPBS (Gibco) containing 0.02% EDTA. Cells were routinely tested for mycoplasma contamination using a commercial mycoplasma detection kit (QuickTest, Bimake, Houston, TX, USA) in accordance with the manufacturer's instructions. Primary murine cells were cultured in RPMI 1640 medium (Gibco) supplemented with 10% FCS (Moregate Biotech), 100 U/mL penicillin, 100 U/mL streptomycin and 50 μM 2-mercaptoethanol (2-ME, all from Gibco). Bone marrow-derived dendritic cells (BMDCs) were generated by culturing bone marrow progenitors (isolated from C57BL/6 mice) with 20 ng/mL recombinant murine GM-CSF (BioLegend, San Diego, CA, USA) as previously described (41). To assess PD-L1 and MHC class I (MHC-I, H-2K^b) expression *in vitro*, MC38 tumour cells were cultured in the presence or absence of 10 ng/mL recombinant murine interferon-γ (IFN-γ, Prospec-Tany TechnoGene, Rehovot, Israel). At indicated timepoints, cells were stained with PerCP-Cy5.5 anti-H-2K^b and PE-Cy7 anti-PD-L1 antibodies (both from BioLegend, refer to Supplementary Table 1) and assessed by flow cytometry.

2.2 MC38 tumour model

MC38 tumour cells were harvested, washed extensively, and resuspended in DPBS (Gibco). C57BL/6 mice were inoculated with 1×10^5 MC38 cells (suspended in 100 μL DPBS) by subcutaneous (s.c.) injection in the right hind flank. In some experiments, mice were inoculated with 0.5×10^6 or 1.0×10^6 MC38 cells. Injections were performed using 0.5 mL insulin syringes with 0.33 mm (29G) x 12.7 mm needles (BD, Franklin Lakes, NJ, USA). Tumour size (mm^2) was monitored daily or every two days using a digital calliper and calculated as the product of the largest perpendicular diameters. Mice were euthanised once tumours reached an area of 150 mm^2.

2.3 Histology, immunohistochemistry and image acquisition

Tumours were fixed in 10% neutral buffered formalin (Sigma-Aldrich) for 24 hours at room temperature, dehydrated, and embedded in paraffin. Sequential 3 μm tissue sections were cut from tumours at the region of greatest diameter and mounted on slides for staining procedures.

Haematoxylin and eosin (H&E) and reticular fibre staining was performed according to standard procedures by the Otago Micro and Nanoscale Imaging (OMNI) Histology Unit (University of Otago). For H&E staining, Gill II haematoxylin and eosin were obtained from Leica Biosystems, Wetzlar, Germany. Potassium permanganate, oxalic acid, ferric ammonium sulphate, ammoniacal silver solution, gold chloride, sodium thiosulphate and Nuclear Fast Red solution used for reticular fibre staining were all obtained from Sigma-Aldrich. Stained sections were dehydrated through ethanol and xylene, and then coverslipped with DPX mountant (Sigma-Aldrich).

Immunohistochemistry (IHC) for CD3, CD4, CD8 and CD31 was performed by the OMNI Histology Unit (University of Otago) on a BOND RX^m automated stainer (Leica Microsystems, Bannockburn, IL, USA). Staining was performed using the BOND Polymer Refine Detection kit (Leica Biosystems) according to optimised protocols. Briefly, 3 μm tumour sections were deparaffinised and rehydrated, before blocking endogenous peroxidase activity with 3 – 4% (v/v) hydrogen peroxide (Peroxidase Block, Leica Biosystems). Heat-induced epitope retrieval was performed using either BOND Epitope Retrieval Solution 1 (ER1, citrate-based, pH 6.0) or BOND Epitope Retrieval Solution 2 (ER2, EDTA-based, pH 9.0; both from Leica Biosystems). After blocking in 2 – 10% (w/v) BSA, sections were incubated with primary antibodies for optimised durations. Primary antibodies were diluted 1:1000 in BOND Primary Antibody Diluent (Leica Biosystems) or Da Vinci Green Diluent (Biocare Medical, Pacheco, CA, USA) and are listed as follows: recombinant rabbit monoclonal anti-CD31 (clone EPR17259, ab182981, Abcam), rabbit polyclonal anti-CD3 antibody (ab5690, Abcam), recombinant rabbit monoclonal anti-CD4 (clone EPR19514, ab183685, Abcam), and rabbit monoclonal anti-CD8 (clone SP16, ab101500, Abcam). Following the manufacturer's instructions (BOND Polymer Refine Detection kit, Leica Biosystems), primary antibody binding was visualised using 3,3'-diaminobenzidine (DAB) tetrahydrochloride hydrate and counterstained with haematoxylin. The sections were then washed, dehydrated, and coverslipped using DPX mountant (Sigma-Aldrich). In all IHC staining, murine spleen tissue was used for positive anatomical controls, and tumour tissue with primary antibodies omitted was used for negative controls (no-primary controls).

Whole slide images of stained sections were generated using an Aperio ScanScope automated scanner (Leica Biosystems) using the 20× (0.50 μm/pixel resolution) and ×40 (0.25 μm/pixel resolution) objectives to produce uniplanar digital slides. Aperio ImageScope software (Leica Biosystems) was used to extract images of entire

tumour sections for subsequent analysis (TIFF format, full resolution at 20× magnification). Quantitative evaluation of IHC images was performed according to published methodology (42) using ImageJ software (NIH) and is described in Supplementary Material (Supplementary Figures 1–3).

2.4 Enzyme-linked immunosorbent assay for total TGF-β1

To generate tumour-conditioned media, MC38 cell culture supernatants were harvested after 24 and 48 hours and centrifuged to remove tumour cells. Tumour homogenate samples were prepared from MC38 tumours excised 14- and 21-days post-inoculation. Briefly, resected tumours were weighed and then homogenised in controlled volumes of RPMI media, before collecting the supernatants after centrifugation. Total TGF-β1 levels in MC38 tumour-conditioned media and resected tumour homogenates were quantified using a murine TGF-β1 ELISA kit (Invitrogen, Carlsbad, CA, USA) according to the manufacturer's instructions. RPMI media (no FCS) and complete DMEM media (containing 10% FCS) were used as background controls for tumour homogenates and tumour-conditioned media samples, respectively. Absorbance was measured at 450 and 570 nm using a Victor X4 plate reader (Perkin Elmer) and absorbance values for samples were blank and background subtracted. TGF-β1 concentrations (pg/mL) were interpolated from a standard curve generated using Prism 8.0.1 software (GraphPad). For tumour homogenate samples, the total amount of TGF-β1 per tumour (pg) was normalised to tumour mass (pg/mg).

2.5 Tissue processing and tumour-infiltrating lymphocyte isolation

Mice were euthanised after 7, 14 and 21 days (post tumour inoculation) and single-cell suspensions prepared from tumours and tumour-draining inguinal lymph nodes (LNs). Mechanical dissociation was employed for the isolation of TILs, following a validated protocol with slight alterations (43). Briefly, resected tumours were weighed and then processed into <1 mm^3 pieces using a scalpel in cold RPMI 1640 media. Tumour fragments were transferred into mechanical dissociator C tubes (Miltenyi Biotec) and homogenised on a GentleMACS dissociator (Miltenyi Biotec). Cell strainers and C tubes were rinsed to collect residual cells and tumour homogenates were passed through 70 μm cell strainers, which were rinsed repeatedly with cold media. Filtrates were collected and centrifuged, before the resulting cell pellets were resuspended in DPBS and layered onto Ficoll-Paque PLUS (GE Healthcare, Uppsala, Sweden) for density gradient centrifugation (as per the manufacturer's instructions). Cells were collected from the high-density solution interface using a transfer pipette and washed twice in DPBS containing 5% FCS at 4°C. LNs were processed on ice in cold DPBS containing 5% FCS and homogenised by forcing the tissue through 70 μm nylon cell strainers. Resulting homogenates were then passed through 40 μm nylon cell strainers to remove residual tissue. Isolated tumour and LN cells were resuspended in media or DPBS at the appropriate density for subsequent procedures.

2.6 Flow cytometry and antibodies

Single-cell suspensions were stained using the Zombie Yellow Fixable Viability kit (BioLegend) or the LIVE/DEAD Fixable Violet Dead Cell Stain kit (Invitrogen) to exclude dead cells. Non-specific antibody binding was blocked using anti-mouse CD16/CD32 Fc Block solution (BD Biosciences, San Diego, CA, USA) following the manufacturer's protocol. For cell surface staining, cells were incubated with fluorophore-conjugated antibodies in FACS buffer (PBS with 0.1% w/v BSA, 0.01% w/v sodium azide, 0.2 mM Na_2 EDTA, pH 7.4) for 15 minutes at 4°C. Intracellular staining for transcription factors and cytokines was performed using the True-Nuclear Buffer Set (BioLegend) according to the manufacturer's protocol. All antibodies used for flow cytometry are detailed in Supplementary Table 1. After antibody staining, cells were washed extensively in FACS buffer and analysed on a Gallios flow cytometer (10 colour configuration equipped with blue (488 nm), red (633 nm) and violet (405 nm) lasers) using Kaluza Acquisition and Analysis software (all from Beckman Coulter, Fullerton, CA, USA). A standard gating strategy was employed for data analysis, involving doublet exclusion based on forward scatter (FSC) and side scatter (SSC) characteristics, and the exclusion of dead cells based on viability staining. Populations of interest were subjected to further analysis after gating on fluorescence parameters for lineage-specific markers (e.g. CD3 and CD4/CD8). Fluorescence-minus-one (FMO) controls were used to establish gating thresholds for positivity (44).

2.7 *Ex vivo* T cell stimulation assays

For phorbol 12-myristate 13-acetate (PMA)/ionomycin stimulation, $CD3^+$ T cells were enriched from D14 and D21 MC38 tumour dissociates using the Pan T Cell Isolation kit (negative selection), autoMACS columns, and an autoMACS Pro automated separator according to the manufacturer's instructions (all from Miltenyi Biotec). Following enrichment, cells were rested overnight in complete medium supplemented with 5 ng/mL recombinant murine interleukin-7 (IL-7, Prospec-Tany TechnoGene) and then stimulated with 50 ng/mL PMA and 500 ng/mL ionomycin (both from Sigma-Aldrich) or left untreated (unstimulated controls). Cells were incubated for 5 hours in the presence of 5 μg/mL brefeldin A (BFA; BioLegend) and then harvested, washed, and stained for flow cytometric analysis. Intracellular staining for IFN-γ, IL-2, IL-10, TNF and granzyme B (GzmB) was performed using the True-Nuclear Buffer Set (BioLegend) according to the manufacturer's protocol.

For peptide stimulation, $CD8^+$ T cells were isolated from D14 and D21 MC38 tumours and tumour-draining lymph nodes (TdLNs) using the CD8α+ T cell isolation kit (Miltenyi Biotec) and then rested overnight in complete medium supplemented with

5 ng/mL rmIL-7 (Prospec-Tany TechnoGene). BMDCs were either left untreated (no peptide) or pulsed with 1 μg/mL of the following peptides (all from Mimotopes, Mulgrave, VIC, AU): MuLV $p15E_{604-611}$ (KSPWFTTL), $Adpgk_{R304M}$ (ASMTNMELM), $Dpagt1_{V213L}$ (SIIVFNLL), or $OVA_{257-264}$ (SIINFEKL; irrelevant peptide). BMDCs were incubated for 3 hours, washed, and then plated in triplicate wells per condition (10^5 cells/well). $CD8^+$ T cells were added to BMDCs at a 10:1 ratio and incubated for 6 hours in the presence of 5 μg/mL BFA (BioLegend). Cells were then harvested, washed, and stained for flow cytometric analysis. Antigen-specific $CD8^+$ T cell responses were detected *via* intracellular staining for TNF and IFN-γ as described above.

2.8 Statistical analysis

All statistical analyses were performed using GraphPad Prism 8.0.1 software (GraphPad Software, La Jolla, CA, USA). Specific statistical tests performed are indicated in corresponding figure legends. *p*-values of <0.05 were considered statistically significant and significance levels are annotated as: *$p \leq 0.05$; **$p \leq 0.01$; ***$p \leq 0.001$; ****$p \leq 0.0001$. All graphs depict the mean ± the standard error of the mean (SEM; error bars).

3 Results

3.1 Growth kinetics and histological characteristics of MC38 colon adenocarcinoma *in vivo*

Firstly, the optimal number of tumour cells required to reproducibly induce slow growing subcutaneous tumours was determined. In our hands, inoculation with 0.1×10^6 MC38 cells produced consistent engraftment and desirable tumour growth kinetics (compared to higher inoculums), with tumour size reaching ≥150 mm^2 after a mean of 23 days (Figure 1A).

To understand the evolution of the MC38 TME over progressive outgrowth, tumours resected at days 7, 14 and 21 (after inoculation; D7, D14 & D21) were processed for analyses (Figure 1B). Across all timepoints, H&E staining revealed MC38 tumours exhibited hallmarks of high-grade neoplasms *in vivo*, with frequent mitotic figures and pleomorphic, hyperchromatic nuclei containing prominent nucleoli (Figure 1C). Changes in stromal architecture during tumour progression were apparent, particularly at the invasive tumour margin (Figure 1D). At the earliest timepoint (D7), MC38 tumours displayed diffuse margins with tumour cells infiltrating surrounding adipose tissue (outer tumour region; Figure 1D). D14 MC38 tumour margins were more defined with an increase in extracellular matrix (ECM) deposition, while D21 MC38 tumours displayed well-defined margins exhibiting desmoplasia with pervasive deposition of fibrous ECM (Figure 1D, adjacent stroma). Stromal cells embedded within this ECM exhibited morphological characteristics of cancer-associated fibroblasts (CAF), with spindle-shaped profiles and plump nuclei (Figure 1D, arrows).

Within the inner tumour region (core), adipocytes were present throughout D7 tumours, while D14 and D21 tumours exhibited dense, hypercellular cores with spindle-shaped tumour cells forming a sarcomatoid-like pattern of haphazard, interlacing bundles (inner tumour region; Figure 1D). In established MC38 tumours (D14), focal areas of both ischemic and haemorrhagic necrosis were evident, suggestive of inadequate or defective tumour vasculature (Supplementary Figure 4A).

3.2 T cell infiltration in MC38 tumours progressively decreases during outgrowth, culminating in an immune-excluded phenotype

Given the prognostic importance of T cell infiltration in CRC (39), IHC for CD3, CD4 and CD8 was performed to define the spatiotemporal dynamics of T cell infiltration in MC38 tumours. Staining was quantified in two tumour compartments: the 'outer tumour region' defined as the area 250 μm inwards from the stromal–tumour interface (tumour margin); and the 'inner tumour region' (tumour core) defined as the area encompassed by the outer tumour region. Identical trends for all T cell markers were observed, whereby the density of infiltration by $CD3^+$, $CD4^+$ and $CD8^+$ cells progressively decreased during tumour outgrowth in terms of the total tumour area (Figures 2A, B) and within the outer and inner tumour regions (Figures 2C–E). Higher densities of $CD3^+$, $CD4^+$ and $CD8^+$ cells were also localised to the outer tumour region compared to the inner tumour core (Figures 2C–E). In late-stage D21 tumours, areas of dense T cell accumulation were evident at the tumour margin and adjacent tissue, with pronounced restriction of T cells at the stromal–tumour interface (Figure 2F).

3.3 MC38 tumours exhibit structurally abnormal vasculature and progressive reticulin fibre deposition at the tumour margin

Increasing metabolic demands of outgrowing tumours requires the generation of new blood vessels (angiogenesis), while T cells are dependent on tumour vasculature to infiltrate and execute their anti-tumour functions. To assess angiogenesis and the microvasculature in MC38 tumours, IHC for the endothelial cell marker CD31 was performed over the course of tumour outgrowth (Figure 3A). In early D7 MC38 tumours, vascularisation was pronounced (in terms of both $CD31^+$ area and vessel density) compared to intermediate and late-stage tumours (Figures 3B, C). There was a trend towards increased vascularisation in D21 versus D14 tumours, however, this was not statistically significant (Figure 3B). In relatively avascular D14 tumours, extensive areas of necrosis were present (Supplementary Figure 4A), suggesting that tumour vasculature was inadequate for nutrient and oxygen demands at this stage of outgrowth.

The inner core of D7 tumours exhibited higher vessel density compared to the outer regions of these tumours ($CD31^+$ objects/mm^2),

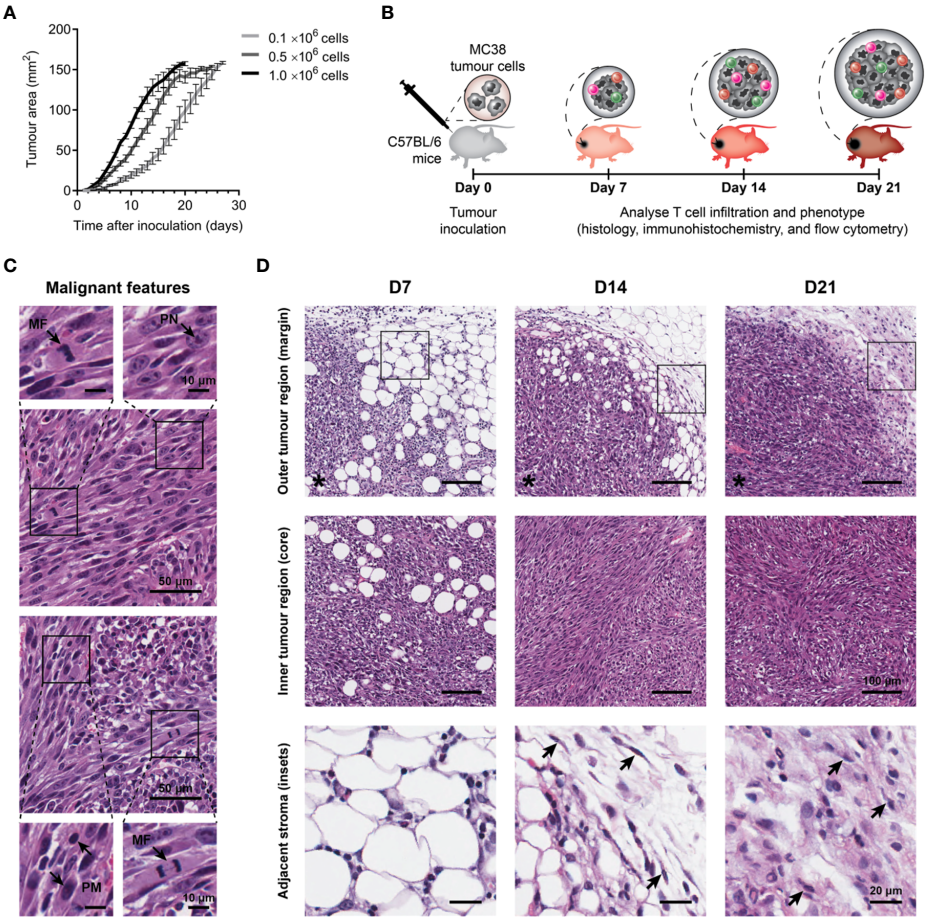

FIGURE 1
Growth kinetics and histological features of MC38 tumours. **(A)** Growth kinetics of MC38 tumours *in vivo*. Syngeneic C57BL/6 mice were inoculated with indicated numbers of MC38 cells by subcutaneous injection at the right hind flank (n = 10 per group). Growth curves depict the mean and standard error of the mean (SEM, error bars). **(B)** Study design to characterise T cell infiltration. MC38 tumours were resected 7-, 14- and 21-days post-inoculation and processed for histology, immunohistochemistry, or flow cytometry. **(C)** Histological features in haematoxylin and eosin (H&E) stained MC38 tumour sections. Arrows indicate characteristics of high-grade neoplasms, including hyperchromatic nuclei containing multiple, prominent nucleoli (PN; arrow, top left inset), mitotic figures (MF; arrows, bottom left and top right insets) and pleomorphism (PM; arrows, bottom right inset). **(D)** H&E images depicting structural changes in the outer (top row) and inner (middle row) regions of MC38 tumours during outgrowth (D7, D14 and D21) and high magnification images of adjacent stroma at the tumour margin (bottom row, ROI shown in top row). Arrows indicate stromal cells with morphological features typical of normal fibroblasts in D14 tumours (thin, wavy, spindle-shaped cells), and cancer-associated fibroblasts (CAFs) in D21 tumours (large cells with plump nuclei). Asterisks (*) denote the side of the tumour in images of the tumour margin. Scale bar dimensions are shown at the right of each row (10, 20, 50 and 100 µm).

while there were no statistical differences in the distribution of $CD31^+$ vessels in D14 and D21 tumour regions (Figure 3C). Structurally, MC38 tumour vasculature was highly disorganised, with an irregular pattern of interconnection that became increasingly pronounced in late-stage D21 tumours (Figure 3A). $CD31^+$ vessels in adjacent connective tissue surrounding MC38 tumours appeared dilated but exhibited relatively normal vessel structure characterised by intact $CD31^+$ endothelium supported by fine, perivascular connective tissue (Supplementary Figure 4B). By contrast, $CD31^+$ vessels in both the periphery and centre of D21 MC38 tumours were structurally defective, with aberrant endothelium which was either reduced in thickness or entirely absent (Supplementary Figure 4B).

In addition to abnormal tumour vasculature, excessive production of ECM components leading to tumour fibrosis (desmoplasia) can mediate the physical exclusion of T cells from tumours (45). To assess the ECM architecture in the MC38 TME, tumours were subjected to reticulin staining – a non-specific silver impregnation method that visualises argyrophillic ECM fibres (reticulin fibres). Extensive fibrosis was evident throughout the MC38 TME, with reticulin fibres increasing in both frequency and thickness during progressive outgrowth (Figure 3A). Distinct differences in the architecture and orientation of reticulin fibres were also observed between the outer and inner tumour regions. Within the tumour core, early tumours (D7) exhibited a delicate meshwork of fine reticulin fibrils, which transitioned to thick, elongated fibres in intermediate (D14) and late-stage (D21) tumours (arrows, Figure 3A). In D14 and D21 tumours, these thick intratumoural fibres were orientated along aggregates of interlacing tumour cell bundles, forming a supportive reticular network (Figure 3A, insets). At the tumour margin, D7 tumours exhibited a network of fine reticulin fibrils (similar to that in the

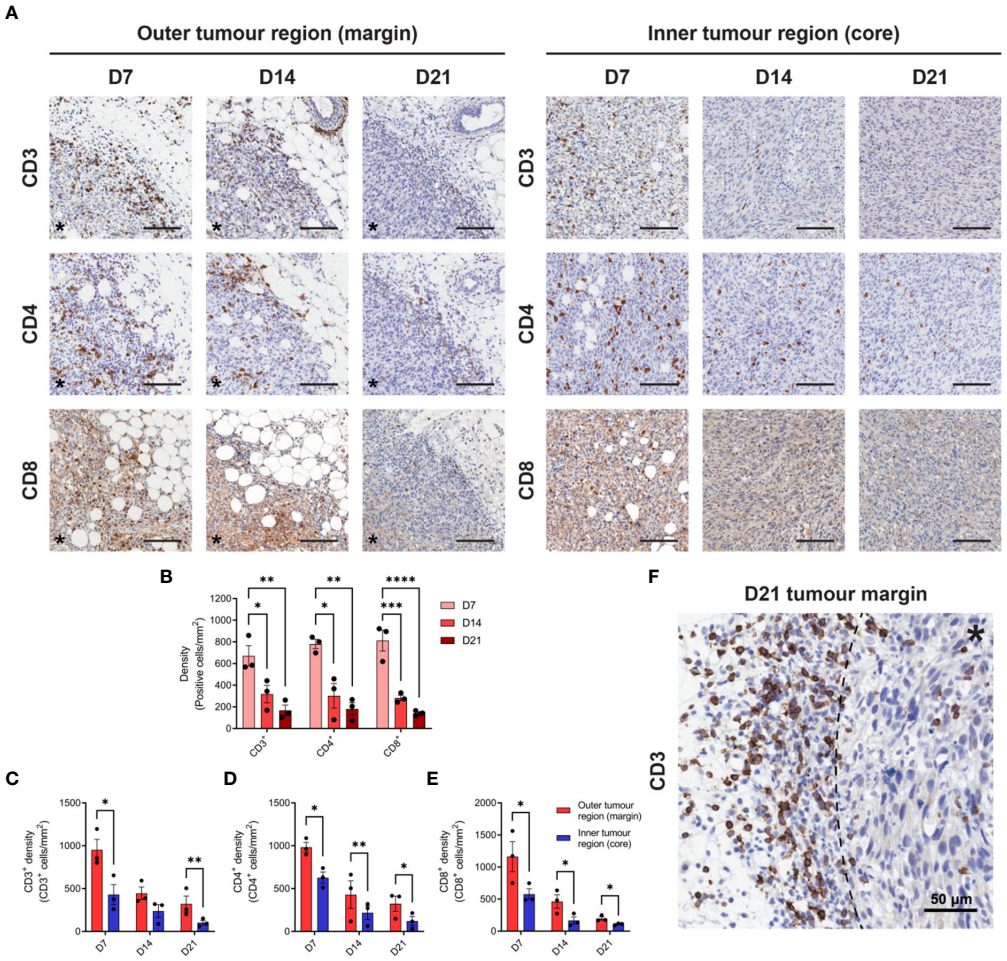

FIGURE 2
T cell infiltration in MC38 tumours during progressive outgrowth. **(A)** MC38 tumours were resected from mice 7-, 14- and 21-days post-inoculation (n = 3 biological replicates per timepoint) and processed for IHC. Images depict immunohistochemical staining for CD3, CD4, or CD8 (DAB, brown with haematoxylin counterstain) in the outer (left panel) and inner (right panel) regions of MC38 tumours (D7, D14 and D21). All scale bars depict 100 µm. **(B)** Quantification of CD3, CD4, and CD8 infiltration in MC38 tumours (total tumour area) during progressive outgrowth. **(C–E)** Quantification of CD3 **(C)**, CD4 **(D)**, and CD8 **(E)** infiltration in the outer and inner regions of MC38 tumours at indicated timepoints. $CD3^+$, $CD4^+$, and $CD8^+$ density was quantified as the absolute number of positive cells per mm^2 (positive cells/mm^2). **(F)** Representative image depicting dense accumulation of $CD3^+$ cells at the stromal–tumour interface (dashed line) in late-stage D21 tumours. Asterisks (*) denote the side of the tumour in images of the tumour margin. Graphs represent the mean and standard error of the mean (SEM, error bars). Statistical analyses were performed using one-way ANOVA with *post-hoc* Tukey test to correct for multiple comparisons **(B)** or two-tailed paired Student's t-tests **(C–E)**. *$p \leq 0.05$; **$p \leq 0.01$; ***$p \leq 0.001$; ****$p \leq 0.0001$.

inner tumour region/core), while D14 and D21 tumours displayed extensive deposition of thick reticulin fibres in the stroma along the invasive front (Figure 3A). In contrast to the core of these tumours, these thick reticulin fibres were largely aligned in parallel to the tumour margin, forming a prominent barrier that mirrored the exclusion of infiltrating T cells in D21 tumours (dashed line, Figure 3D).

3.4 TGF-β secretion and PD-L1 expression are intrinsic immune-suppressive mechanisms present in MC38 tumour cells

Tumour cells employ a variety of mechanisms to evade anti-tumour immunity, including the secretion of cytokines and expression of inhibitory cell surface molecules. To elucidate potential mechanisms utilised by MC38, we assessed TGF-β secretion and PD-L1 expression – two well-established immune-suppressive and evasive mechanisms of clinical interest. Secretion of TGF-β by MC38 tumour cells *in vitro* was quantified in tumour-conditioned media, while *ex vivo* TGF-β within the MC38 TME was determined from resected MC38 tumour supernatants. TGF-β was detected in MC38-conditioned media and increased with the duration of culture, indicating secretion of this cytokine by MC38 tumour cells (Figure 4A). TGF-β was also abundant in the MC38 TME but decreased in D21 tumours compared to D14 tumours (normalised to tumour mass, pg/mg; Figure 4B). Interestingly, there was a relationship between TGF-β levels and the size of MC38 tumours, wherein TGF-β concentrations exponentially decayed with increasing tumour burden (Figure 4C).

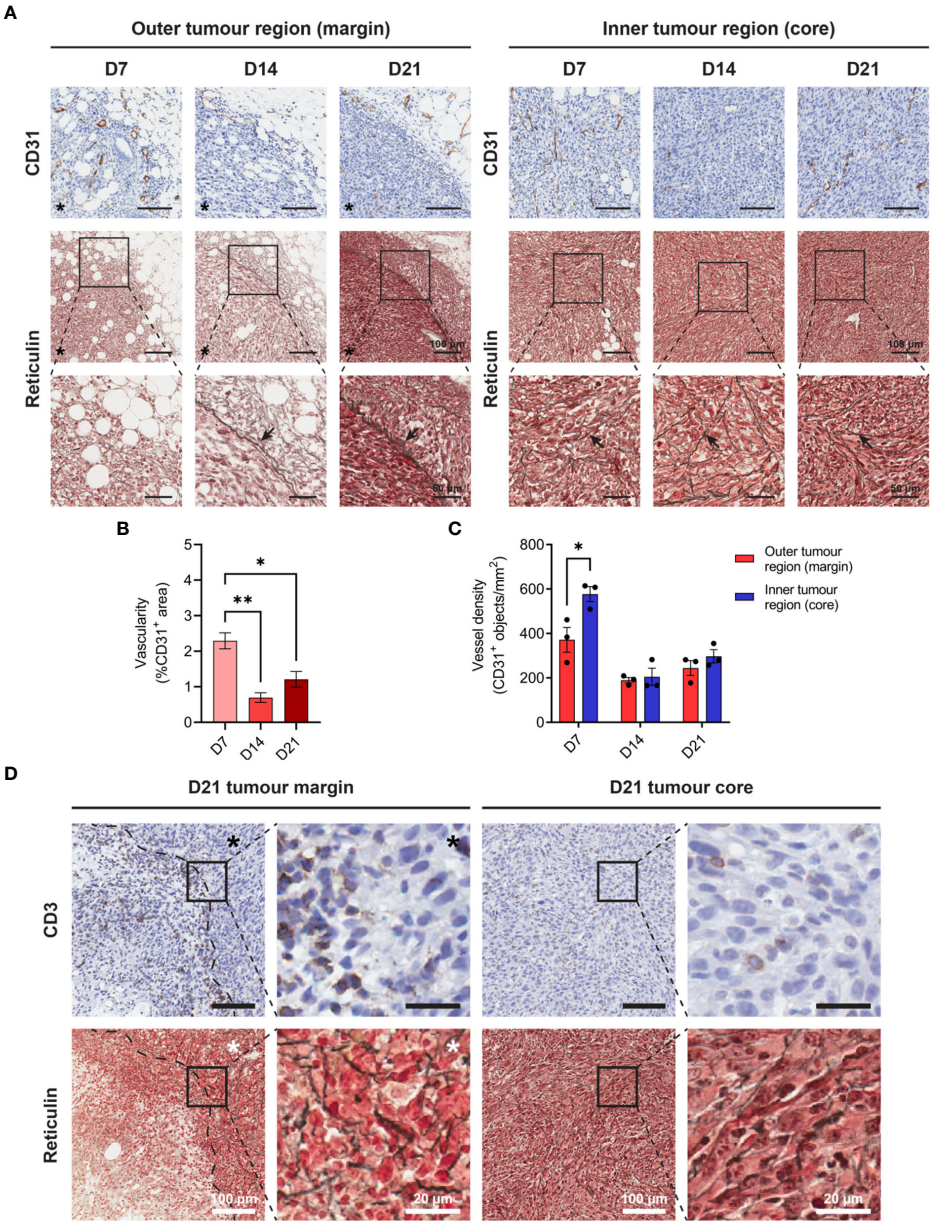

FIGURE 3
Angiogenesis, reticulin fibrosis, and immune exclusion in MC38 tumours. **(A)** MC38 tumours were resected from mice 7-, 14- and 21-days post-inoculation (n = 3 biological replicates per timepoint) and processed for CD31 IHC and reticulin staining. Images depict immunohistochemical staining for CD31 (brown with haematoxylin counterstain, top row) and reticulin silver staining of argyrophillic 'reticular fibres' (black, arrows) with Nuclear Fast Red counterstain (nuclei, red). Scale bars depict 100 µm and 50 µm in low and high magnification images, respectively. **(B)** Vascularity of MC38 tumours determined as the $CD31^+$ area proportional to the total tumour area (%$CD31^+$ area of total tumour). **(C)** $CD31^+$ vessel density in the outer and inner regions of MC38 tumours at indicated timepoints. Vessel density was quantified as the absolute number of $CD31^+$ blood vessels per mm^2 ($CD31^+$ objects/mm^2). **(D)** CD3 IHC and reticulin staining of sequential D21 tumour sections. Top row images depict immunohistochemical staining for CD3 (brown) with haematoxylin counterstain (blue) and bottom row images depict reticulin staining for collagenous 'reticular fibres' (black) with Nuclear Fast Red counterstain (red). Asterisks (*) denote the side of the tumour in images of the tumour margin. Scale bars depict 100 µm and 20 µm in low and high magnification images, respectively. Graphs represent the mean and standard error of the mean (SEM, error bars). Statistical analyses were performed using one-way ANOVA with *post-hoc* Tukey test to correct for multiple comparisons **(B)** or two-tailed paired Student's t-tests **(C)**. *$p \leq 0.05$; **$p \leq 0.01$.

PD-L1 can be constitutively expressed by tumour cells or induced by exposure to interferons – in particular IFN-γ produced by tumour-specific T cells (46, 47). Hence, while IFN-γ promotes tumour cell recognition *via* the upregulation of MHC-I (48), simultaneous upregulation of PD-L1 can suppress T cell-mediated killing in a process known as adaptive immune resistance (47). Therefore, expression of PD-L1 and MHC-I (H-$2K^b$) was assessed at both baseline and in response to IFN-γ exposure. MC38 cells constitutively expressed PD-L1 *in vitro*, which was markedly upregulated in response to IFN-γ and peaked in expression after 24 hours (Figure 4D). Similarly, H-$2K^b$ expression increased dramatically in response to IFN-γ but exhibited differing kinetics

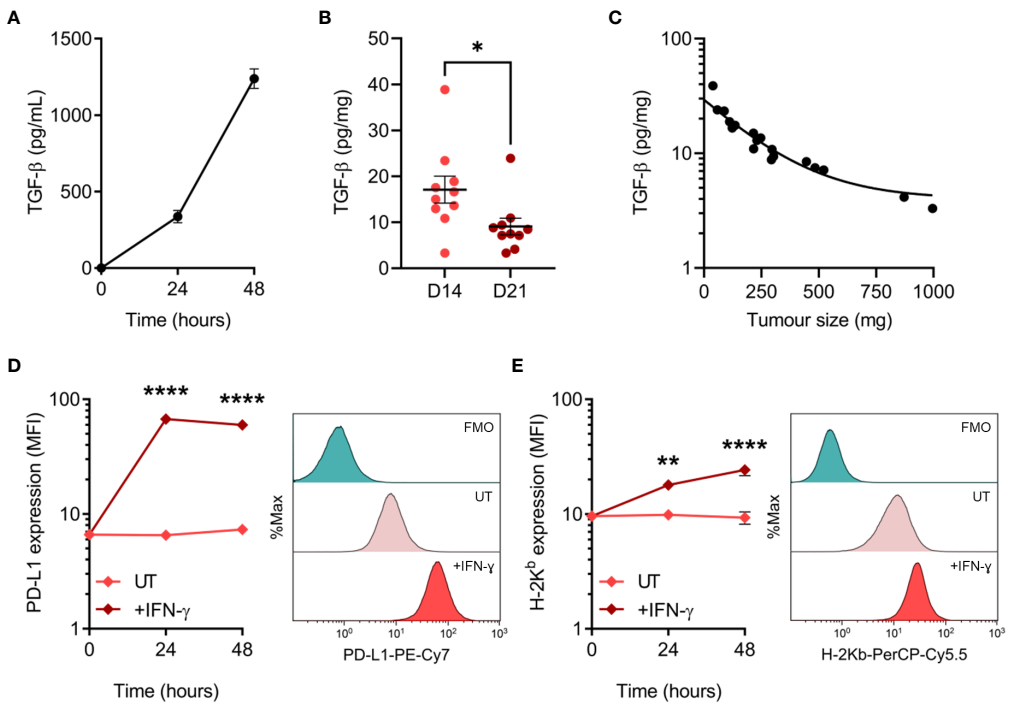

FIGURE 4
TGF-β secretion and PD-L1 expression by MC38 tumour cells. **(A)** Total TGF-β secreted by MC38 tumour cells over indicated durations *in vitro* (pg/mL). Data are representative of three independent experiments. **(B)** Total TGF-β concentrations in supernatants obtained from D14 and D21 MC38 tumours (n = 10 biological replicates per timepoint). TGF-β levels were normalised to tumour mass (pg/mg). **(C)** Scatter plot showing the relationship between TGF-β concentrations within MC38 tumours (pg/mg) and tumour size/burden (mg). **(D, E)** PD-L1 and MHC class I (H-2K^b) expression in untreated and IFN-γ-stimulated (10 ng/mL) MC38 tumour cells (median fluorescence intensity, MFI). Representative histogram overlays (right) depict expression in untreated and IFN-γ-stimulated cells after 48 hours and corresponding fluorescence-minus-one (FMO) controls. Data are representative of three independent experiments. Graphs represent the mean and standard error of the mean (SEM, error bars). Statistical analyses were performed using two-tailed unpaired Student's t-test **(B)**, or two-way ANOVA with *post-hoc* Sidak test to correct for multiple comparisons (comparing IFN-γ-treated samples to untreated controls; **(D, E)**). *p ≤ 0.05; **p ≤ 0.01; ****p ≤ 0.0001.

with expression peaking after 48 hours (Figure 4E). These results suggest that TGF-β secretion and PD-L1 upregulation are potential mechanisms utilised by MC38 tumour cells to evade anti-tumour immunity.

3.5 Dynamic changes in the composition of tumour-infiltrating T cells during MC38 tumour development

Having determined the spatiotemporal dynamics of T cell infiltration in MC38 tumours, the phenotype and functional orientation of these cells were characterised. Changes in the composition and phenotypes of tumour-infiltrating lymphocytes (TILs) were examined by performing flow cytometric analysis on tumour dissociates isolated throughout the course of MC38 tumour progression (D7, D14 & D21; Figure 1B). Relative ratios of various T cell subsets in MC38 tumours were examined as a surrogate marker for the inflammatory status of tumour infiltrates. During MC38 tumour outgrowth, tumour infiltration by CD8$^+$ T cells markedly increased relative to CD4$^+$ T cells (decreasing CD4$^+$/CD8$^+$ ratio, Figure 5A), with the proportion of CD8$^+$ effectors (T_{EFF}) increasing relative to regulatory CD4$^+$ T cells (T_{REG}; decreasing CD4$^+$FoxP3$^+$/CD8$^+$T-bet$^+$ ratio, Figure 5B). Similarly, the proportion of CD4$^+$ T helper 1 (T_H1) effectors increased relative to regulatory CD4$^+$ T_{REG} cells in intermediate (D14) and late stage (D21) tumours (decreasing CD4$^+$FoxP3$^+$/CD4$^+$T-bet$^+$ ratio, Figure 5C). These data suggest that the T cell infiltrate in MC38 tumours becomes increasing inflammatory over the course of tumour progression, with an increase in the proportion of effector cell populations and T cell subsets associated with anti-tumour immunity (49).

3.6 Activated effector memory (T_{EM}) CD4$^+$ and CD8$^+$ TILs increase during MC38 tumour progression

Next, the activation status of TILs was analysed as a surrogate marker for anti-tumour T cell responses within the endogenous T cell repertoire. Within the CD4$^+$ TIL compartment, there was a progressive increase in proportion of cells expressing the T cell activation markers CD25, CD69, and CD137 (4-1BB), consistent with increased infiltration or expansion of activated CD4$^+$ T cells within the MC38 TME (D7→D21; Figures 5D, E). Notably, CD25 and CD137 were co-expressed by CD4$^+$ TILs (data not shown). Over the course of MC38 tumour progression, there was a significant increase in CD8$^+$ TILs expressing CD69 (15→86%;

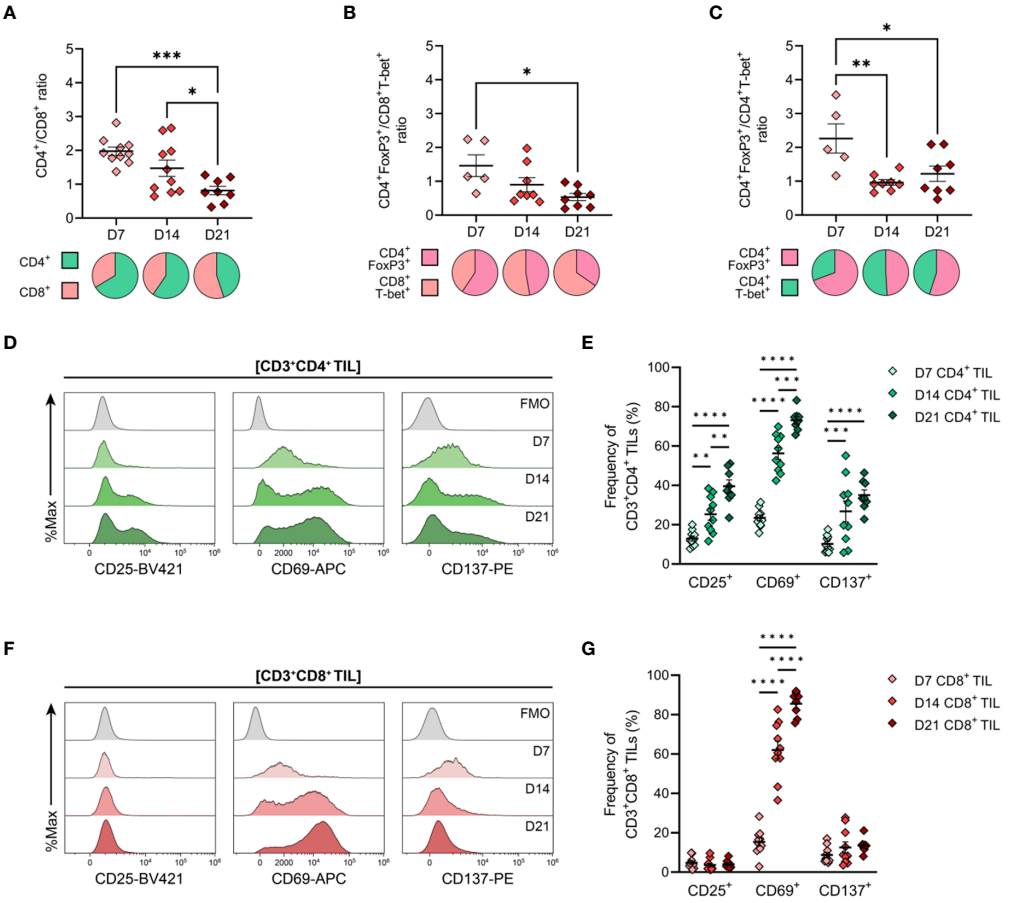

FIGURE 5
General features of T cell infiltration in MC38 tumours and expression of activation markers by $CD4^+$ and $CD8^+$ TILs. MC38 tumours were resected 7-, 14- and 21-days post-inoculation (D7, D14 and D21; n = 5-10 biological replicates per timepoint) and mechanically dissociated. Tumour-infiltrating lymphocytes (TILs) were then isolated from tumour homogenates and analysed by flow cytometry. **(A–C)** Graphs depict the ratio of $CD3^+CD4^+$ to $CD3^+CD8^+$ TILs ($CD4^+/CD8^+$ ratio, **(A)**, $FoxP3^+CD3^+CD4^+$ to $T\text{-}bet^+CD3^+CD8^+$ TILs ($CD4^+$ $T_{REG}/CD8^+$ T_{EFF} ratio, **(B)**) and $FoxP3^+CD3^+CD4^+$ to $T\text{-}bet^+CD3^+CD4^+$ TILs ($CD4^+$ $T_{REG}/CD4^+$ T_H1 ratio, **(C)**) during tumour outgrowth (D7, D14 and D21). All ratios were calculated as the quotient of the absolute number of events collected for each of the indicated populations. Pie charts depict relative proportions of indicted populations. **(D, F)** Representative histogram overlays depicting the expression of activation markers (CD25, CD69 and CD137) by total $CD3^+CD4^+$ (**(D)**, green) and $CD3^+CD8^+$ (**(F)**, red) tumour-infiltrating lymphocytes (TIL) isolated from MC38 tumours 7-, 14- and 21-days post-inoculation (D7, D14 and D21). Corresponding fluorescence-minus-one controls (FMO, grey) are also shown. **(E, G)** Frequencies of total $CD3^+CD4^+$ (**(E)**, green) and $CD3^+CD8^+$ (**(G)**, red) TIL expressing indicated activation markers during MC38 tumour outgrowth (D7, D14 and D21). All data are representative of 5-10 biological replicates per timepoint. Graphs represent the mean and standard error of the mean (SEM, error bars). Statistical analyses were performed using one-way **(A–C)** or two-way **(E, G)** ANOVA with *post-hoc* Tukey test to correct for multiple comparisons. *$p \leq 0.05$; **$p \leq 0.01$; ***$p \leq 0.001$; ****$p \leq 0.0001$.

Figures 5F, G), with these cells also co-expressing PD-1 (data not shown). The majority of $CD8^+$ TILs did not express CD25 or CD137 (<5% and <14% of total $CD8^+$ TILs, respectively), with $CD25^+$ and $CD137^+$ $CD8^+$ TIL frequencies remaining stable throughout tumour outgrowth (Figures 5F, G). Altogether, these data indicate an endogenous T cell response against MC38 tumours, which is characterised by increased recruitment and/or expansion of activated $CD4^+$ and $CD8^+$ effectors within the TME.

To further characterise TILs infiltrating MC38 tumours, the differentiation status of $CD4^+$ and $CD8^+$ TILs over the course of MC38 tumour progression was investigated. To this end, the distribution of naïve, memory and effector subsets within MC38 TILs was assessed on the basis of CD44 and CD62L expression (50, 51). In both $CD4^+$ and $CD8^+$ TIL compartments, the proportion of effector memory (T_{EM}; $CD44^{HI}CD62L^-$) cells progressively increased, while the proportion of naïve (T_N; $CD44^{LO}CD62L^+$) and central memory (T_{CM}; $CD44^{HI}CD62L^+$) subsets decreased (Figures 6A, B). T_{EM} cells were the predominant population throughout the course of tumour outgrowth (>63% and >52% of total $CD4^+$ and $CD8^+$ TILs, respectively), but early-stage tumours (D7) exhibited substantial infiltration by naïve $CD44^{LO}CD62L^+$ T_N cells (24% and 25% of total $CD4^+$ and $CD8^+$ TILs, respectively; Figures 6A, B). Infiltration by T_{CM} ($CD44^{HI}CD62L^+$) $CD4^+$ and $CD8^+$ subsets was consistently low throughout tumour outgrowth (>13% and >20% of total $CD4^+$ and $CD8^+$ TILs, respectively; Figures 6A, B).

To further define these TIL subsets, their expression of CD27, CD28, CD127 (IL-7Rα) and PD-1 was analysed in late-stage D21 MC38 tumours. Within both $CD4^+$ and $CD8^+$ TIL compartments, naïve (T_N, $CD44^{LO}CD62L^+$) and T_{CM} ($CD44^{HI}CD62L^+$) subsets

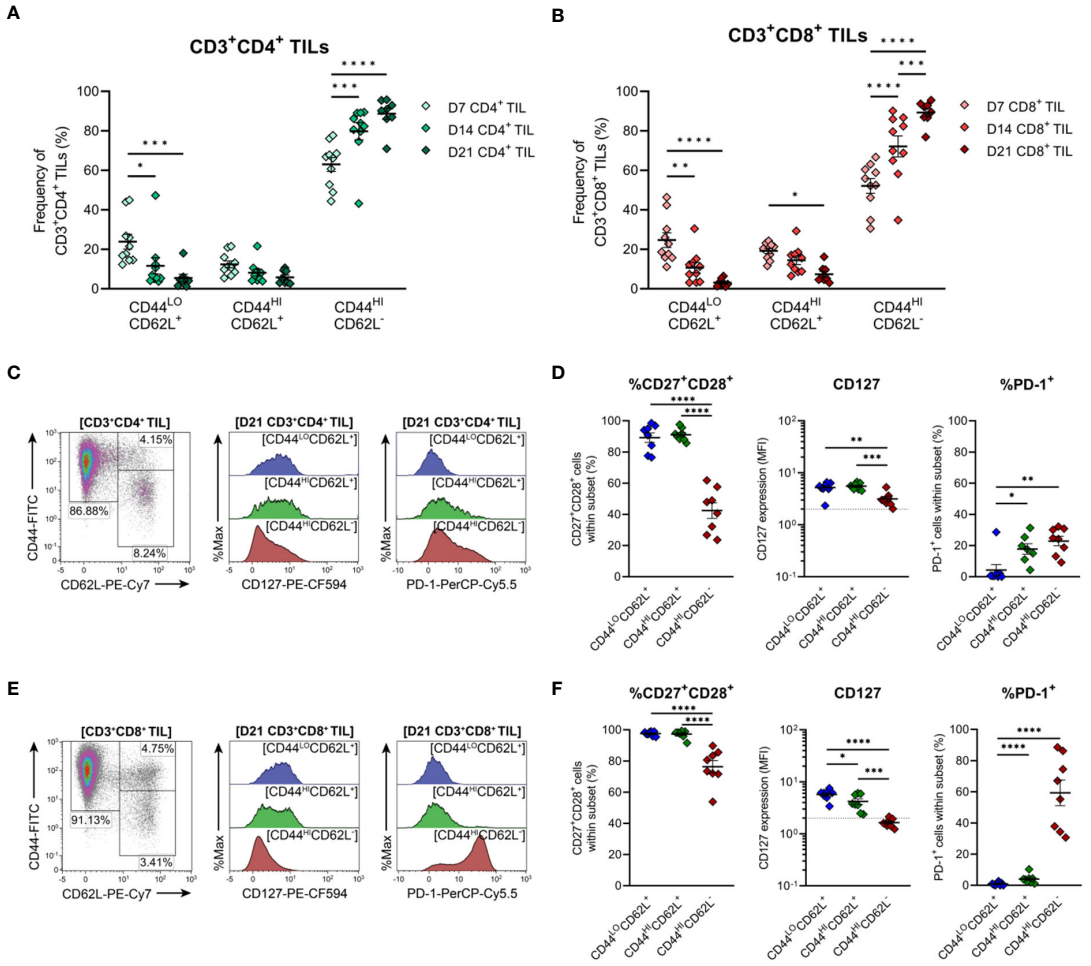

FIGURE 6
Distribution of CD4$^+$ and CD8$^+$ T cell subsets infiltrating MC38 tumours. **(A, B)** Frequencies of naïve (CD44^{LO}CD62L$^+$), central (CD44^{HI}CD62L$^+$), and effector (CD44^{HI}CD62L$^-$) memory T cells among CD3$^+$CD4$^+$ **(A)** and CD3$^+$CD8$^+$ **(B)** TILs during progressive MC38 tumour outgrowth (D7, D14 and D21). **(C, E)** Representative flow plots depicting the distribution of T cell subsets (based on CD44 and CD62L expression) and CD127 (IL-7Rα) and PD-1 expression in naïve (CD44^{LO}CD62L$^+$; blue), central memory/T_{CM} (CD44^{HI}CD62L$^+$; green) and effector memory/T_{EM} (CD44^{HI}CD62L$^-$; red) T cell subsets within CD3$^+$CD4$^+$ **(C)** and CD3$^+$CD8$^+$ **(E)** TIL isolated from D21 MC38 tumours. **(D, F)** Expression of both CD27 and CD28 (%CD27$^+$CD28$^+$), CD127 (MFI) or PD-1 (%PD-1$^+$) within CD44 and CD62L subsets of CD3$^+$CD4$^+$ **(D)** and CD3$^+$CD8$^+$ **(F)** TIL isolated from D21 MC38 tumours. In graphs depicting CD127 expression, dotted lines represent the threshold for CD127 positivity determined from fluorescence-minus-one controls. All density plot percentages indicate frequencies as the proportion of the gated population (indicated in bold titles with square brackets). All data are representative of 8-10 biological replicates per timepoint. Graphs represent the mean and standard error of the mean (SEM, error bars). Statistical analyses were performed using two-way **(A, B)** or one-way **(D, F)** ANOVA with *post-hoc* Tukey test to correct for multiple comparisons. *p ≤ 0.05; **p ≤ 0.01; ***p ≤ 0.001; ****p ≤ 0.0001.

exhibited high co-expression of costimulatory molecules (CD27 and CD28), and high CD127 expression, consistent with the less-differentiated status of these T cell subsets (Figures 6C–F). Indicative of terminal differentiation, CD4$^+$ and CD8$^+$ T_{EM} (CD44^{HI}CD62L$^-$) cells displayed low (CD4$^+$) or no (CD8$^+$) expression of CD127 and down-regulated CD27 expression (Figures 6D, F). PD-1 expression was enriched within both CD4$^+$ and CD8$^+$ T_{EM} TIL subsets (Figures 6D, F) but absent in less-differentiated CD8$^+$ T_N (CD44^{LO}CD62L$^+$) and T_{CM} (CD44^{HI}CD62L$^+$) subsets (Figure 6F). Consistent with observations in human CRC (52, 53), these data demonstrate that the progression of MC38 tumours is characterised by increased infiltration of CD4$^+$ and CD8$^+$ T_{EM} cells (as a proportion of total CD4$^+$ and CD8$^+$ T cells). Furthermore, in late-stage D21 tumours, a subset of these cells within the CD8$^+$ TIL compartment exhibit features of terminal differentiation.

3.7 Infiltration of MC38 tumours by CD4$^+$ T_H1 effector cells and suppressive regulatory T cells increases during tumour outgrowth

The functional polarisation of MC38 TILs was then assessed by examining expression of the T_H1/cytotoxic T lymphocyte (CTL) transcription factors, T-bet and Eomes, and FoxP3, the master

regulator of T_{REG} function. $CD4^+$ TILs exhibited heterogeneous expression of both T-bet and FoxP3 in established tumours (D14 & D21), while $CD4^+$ TILs in early-stage tumours (D7) were mainly $FoxP3^-T\text{-}bet^-$ (75% of total $CD4^+$ TILs; Figure 7A). These data imply that MC38 tumours are initially infiltrated by naïve $CD4^+$ T cells, given that a significant proportion of D7 $CD4^+$ TILs also exhibit a naïve $CD44^{LO}CD62L^+$ phenotype (Figure 6A).

As tumours progressed, the frequency of $CD4^+$ $FoxP3^-T\text{-}bet^-$ TILs decreased but still accounted for 55% of total $CD4^+$ TILs in D21 tumours, while T_H1 ($FoxP3^-T\text{-}bet^+$) and T_{REG} ($FoxP3^+T\text{-}bet^-$) subsets remained relatively stable (Figure 7A). Given the high proportion of $CD4^+$ TILs exhibiting an effector memory phenotype ($CD44^{HI}CD62L^-$) in intermediate and late-stage tumours (D14 & D21; Figure 6A), these data suggest that as MC38 tumours progress, they are infiltrated by $CD4^+$ effector subsets other than T_H1 and T_{REG} cells, likely T_H2 or T_H17 cells. Accompanying these changes in the composition of $CD4^+$ TILs, the proportion of $CD4^+$ $FoxP3^+T\text{-}bet^+$ cells increased during tumour outgrowth (Figure 7A).

To gain further insight into the functional status of $CD4^+$ TIL subsets present, PD-1 expression in $CD4^+$ TILs isolated from late-stage MC38 tumours (D21) was examined (Figure 7C). Consistent with an activated or exhausted effector phenotype, a significant proportion of $CD4^+$ T_H1 ($FoxP3^-T\text{-}bet^+$) and T_{REG} ($FoxP3^+T\text{-}bet^-$

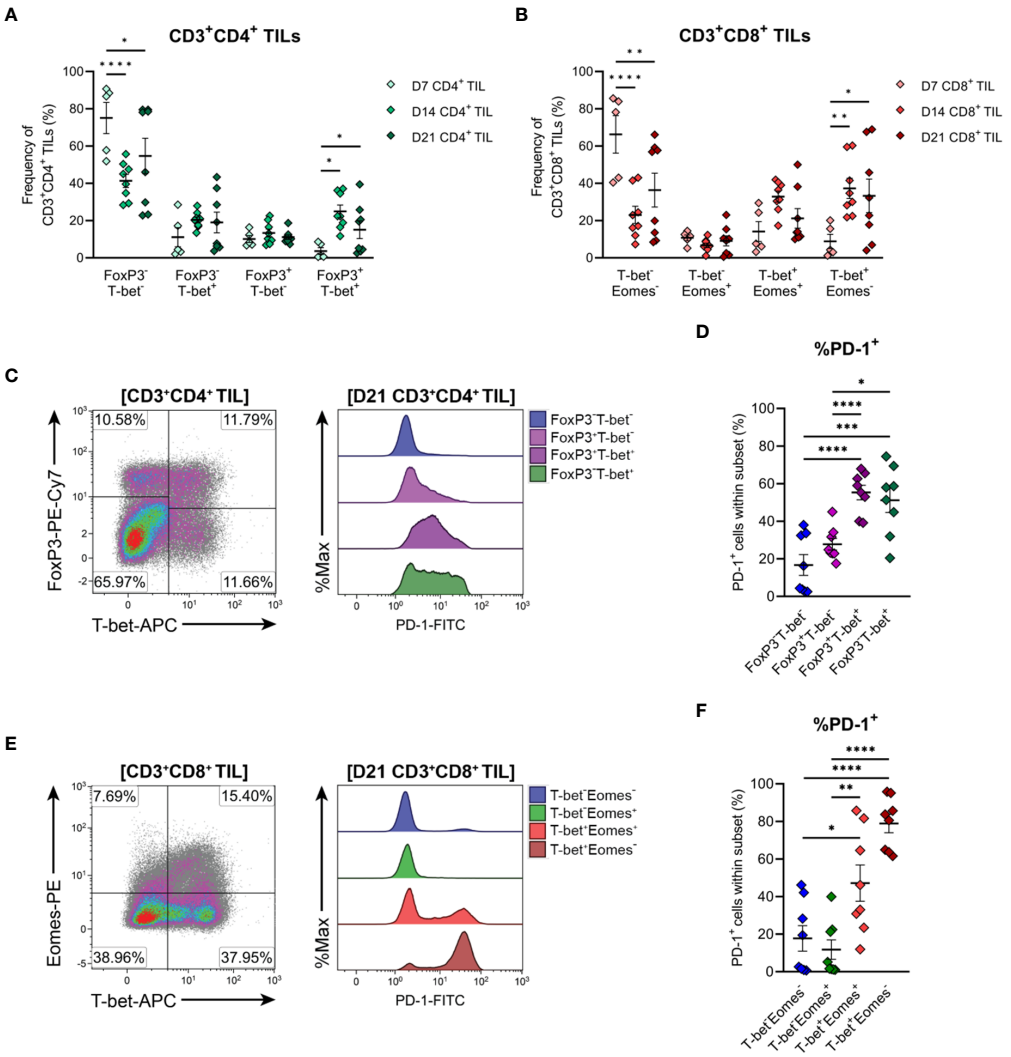

FIGURE 7
Differentiation status of $CD4^+$ and $CD8^+$ T cells infiltrating MC38 tumours. **(A)** Frequencies of T-bet and FoxP3 subsets within total $CD3^+CD4^+$ TIL. **(B)** Frequencies of T-bet and Eomes subsets within total $CD3^+CD8^+$ TIL. **(C)** Representative flow plots depicting the distribution of T-bet and FoxP3 subsets and their expression of PD-1 in $CD3^+CD4^+$ TIL isolated from D21 MC38 tumours. **(D)** Expression of PD-1 (%PD-1^+) within FoxP3 and T-bet subpopulations of D21 $CD3^+CD4^+$ TIL. **(E)** Representative flow plots depicting the distribution of T-bet and Eomes subsets and their expression of PD-1 in $CD3^+CD8^+$ TIL isolated from D21 MC38 tumours. **(F)** Expression of PD-1 (%PD-1^+) within T-bet and Eomes subpopulations of D21 $CD3^+CD8^+$ TIL. All density plot percentages indicate frequencies as the proportion of the gated population (indicated in bold titles with square brackets). All data are representative of 8-10 biological replicates per timepoint. Graphs represent the mean and standard error of the mean (SEM, error bars). Statistical analyses were performed using two-way **(A, B)** or one-way **(D, F)** ANOVA with *post-hoc* Tukey test to correct for multiple comparisons. *$p \leq 0.05$; **$p \leq 0.01$; ***$p \leq 0.001$; ****$p \leq 0.0001$.

and FoxP3$^+$T-bet$^+$) cells expressed PD-1 (51%, 25% and 55% PD-1$^+$, respectively), whereas most naïve-like cells (FoxP3$^-$T-bet$^-$) lacked PD-1 expression (84% PD-1$^-$; Figure 7D). Notably, PD-1 expression was highest in CD4$^+$ T$_H$1 (FoxP3$^-$T-bet$^+$, 51% PD-1$^+$) and FoxP3$^+$T-bet$^+$ T$_{REG}$ (55% PD-1$^+$) subsets, which may reflect exhaustion (54) and enhanced suppressive function (55, 56) in these subsets, respectively (Figure 7D). Altogether, these results indicate that during progressive outgrowth, MC38 tumours are increasingly infiltrated by both anti-tumour T$_H$1 effector and suppressive T$_{REG}$ CD4$^+$ subsets. However, the polarisation of a large proportion of CD4$^+$ TILs (40-75% FoxP3$^-$T-bet$^-$) cannot be confirmed, suggesting that MC38 tumours are also infiltrated by other T helper subsets not identified here.

3.8 Terminally differentiated CD8$^+$ effector cell infiltration of MC38 tumours increases during progressive tumour growth

T-bet and Eomes expression within CD8$^+$ TILs was also examined to further define their differentiation status. CD8$^+$ TILs exhibited distinct single-positive and double-positive T-bet and Eomes populations (Figures 7B, E). Similar to observations in CD4$^+$ TILs, a large proportion of CD8$^+$ TILs in early-stage tumours (D7) were double-negative for both transcription factors (T-bet$^-$Eomes$^-$, 66% of total CD8$^+$ TILs; Figure 7B). Again, given the CD44^{LO}CD62L$^+$ phenotype of a significant proportion of D7 CD8$^+$ TILs (Figure 6B), these data suggest that MC38 tumours are initially infiltrated by naïve CD8$^+$ T cells. During subsequent tumour outgrowth, the frequency of T-bet$^-$Eomes$^-$ CD8$^+$ TILs decreased, while the proportion of effector memory-like (57, 58) T-bet$^-$Eomes$^+$ and T-bet$^+$Eomes$^+$ CD8$^+$ TILs remained relatively constant (Figure 7B). There was also an increase in the proportion of CD8$^+$ T-bet$^+$Eomes$^-$ cells, which composed 30-32% of the total CD8$^+$ infiltrate in D14 and D21 MC38 tumours (versus 9% at D7; Figure 7B).

To further characterise CD8$^+$ TIL populations, the expression of PD-1 in late-stage tumours (D21) was assessed. T-bet$^-$Eomes$^+$ and T-bet$^-$Eomes$^-$ CD8$^+$ TILs largely lacked PD-1 expression (12% and 18% PD-1$^+$, respectively), in accordance with their memory- and naïve- like transcription factor profiles, respectively (Figures 7E, F). In contrast, a large proportion of the T-bet$^+$Eomes$^+$ CD8$^+$ subset expressed PD-1 (46%), consistent with the acquisition of an activated or exhausted effector phenotype (Figure 7F). PD-1 expression was highest in T-bet$^+$Eomes$^-$ CD8$^+$ TILs, with majority of these cells expressing PD-1 (81%; Figure 7F). Given the high expression of T-bet by these cells, this subset likely represents a population of terminally differentiated effectors with a more severe exhausted phenotype (59, 60). Hence, similar to the kinetics of CD4$^+$ TIL infiltration, MC38 tumours are increasingly infiltrated by CD8$^+$ effectors during progressive tumour outgrowth. However, in later stages of tumour outgrowth, a large proportion of these cells exhibit features of terminal differentiation, particularly the subset distinguished by a T-bet$^+$Eomes$^-$ phenotype.

3.9 CD8$^+$ TILs undergo progressive exhaustion during tumour outgrowth and display a severely exhausted phenotype in late-stage MC38 tumours

Expression of the inhibitory receptors PD-1 and TIM-3 can be used to classify T cells along a spectrum of dysfunction toward terminal differentiation and exhaustion. At opposing ends of this functional spectrum, PD-1$^+$TIM-3$^+$ cells are considered severely dysfunctional or 'terminally exhausted', whereas PD-1$^-$TIM-3$^-$ cells represent functional effectors (33, 59, 61). In between these phenotypic extremes, PD1$^+$TIM3$^-$ cells are thought to represent T cells in a transitional status, termed 'transitional exhausted' cells (62). Therefore, to clarify the exhaustion status of MC38 TILs, the distribution of PD-1/TIM-3 subsets within CD4$^+$ and CD8$^+$ TILs were examined along with the expression of additional exhaustion-associated markers in these subsets. The composition of PD-1 and TIM-3 subsets within CD4$^+$ TILs remained relatively stable throughout the course of MC38 tumour progression, with distinct PD-1$^-$TIM-3$^-$ (34-44%), PD-1$^+$TIM-3$^-$ (24-26%) and PD-1$^+$TIM-3$^+$ (29-39%) populations apparent (Figures 8A, B). In contrast to CD4$^+$ TILs, the composition of PD-1 and TIM-3 subsets within CD8$^+$ TILs changed over the course of tumour outgrowth (Figures 8C, D). In early-stage tumours (D7), CD8$^+$ TILs were predominantly PD-1$^-$TIM-3$^-$, but as tumours progressed, there was a decrease in the proportion of PD-1$^-$TIM-3$^-$ cells (37→20%) and a concomitant increase in the proportion of terminally exhausted PD-1$^+$TIM-3$^+$ cells (19→59%; Figure 8D). Meanwhile, the proportion of transitional exhausted PD-1$^+$TIM-3$^-$ cells remained relatively stable (Figure 8D). Consistent with progressive T cell exhaustion, the simultaneous expression of additional inhibitory receptors – specifically LAG-3 and CD39 – increased across PD-1 and TIM-3 subsets in both CD4$^+$ and CD8$^+$ TILs in a hierarchical manner (% CD39$^+$LAG-3$^+$; PD-1$^-$TIM-3$^-$<PD-1$^+$TIM-3$^-$<PD-1$^+$TIM-3$^+$; Figures 8E–H). Notably, the majority of PD-1$^+$TIM-3$^+$ cells co-expressed CD39 and LAG-3 (61% and 81% for CD4$^+$ and CD8$^+$ subsets, respectively; Figures 8F, H). Furthermore, CD8$^+$ TILs exhibited hierarchical downregulation of CD127 across PD-1 and TIM-3 subsets, wherein the terminally exhausted PD-1$^+$TIM-3$^+$ subset lacked CD127 expression – a hallmark of terminal differentiation (63) (Figure 8H). Altogether, these data suggest that CD8$^+$ TILs undergo progressive exhaustion during the outgrowth of MC38 tumours.

3.10 Tumour-infiltrating CD4$^+$ and CD8$^+$ T cells that express PD-1 are polyfunctional and display rapid effector functions *ex vivo*

The functional qualities of CD4$^+$ and CD8$^+$ T cells infiltrating D14 and D21 tumours were examined *ex vivo* following tumour dissociation. Effector function was assessed by intracellular cytokine staining following acute PMA and ionomycin stimulation and in unstimulated controls. Following stimulation, CD4$^+$ TILs mainly

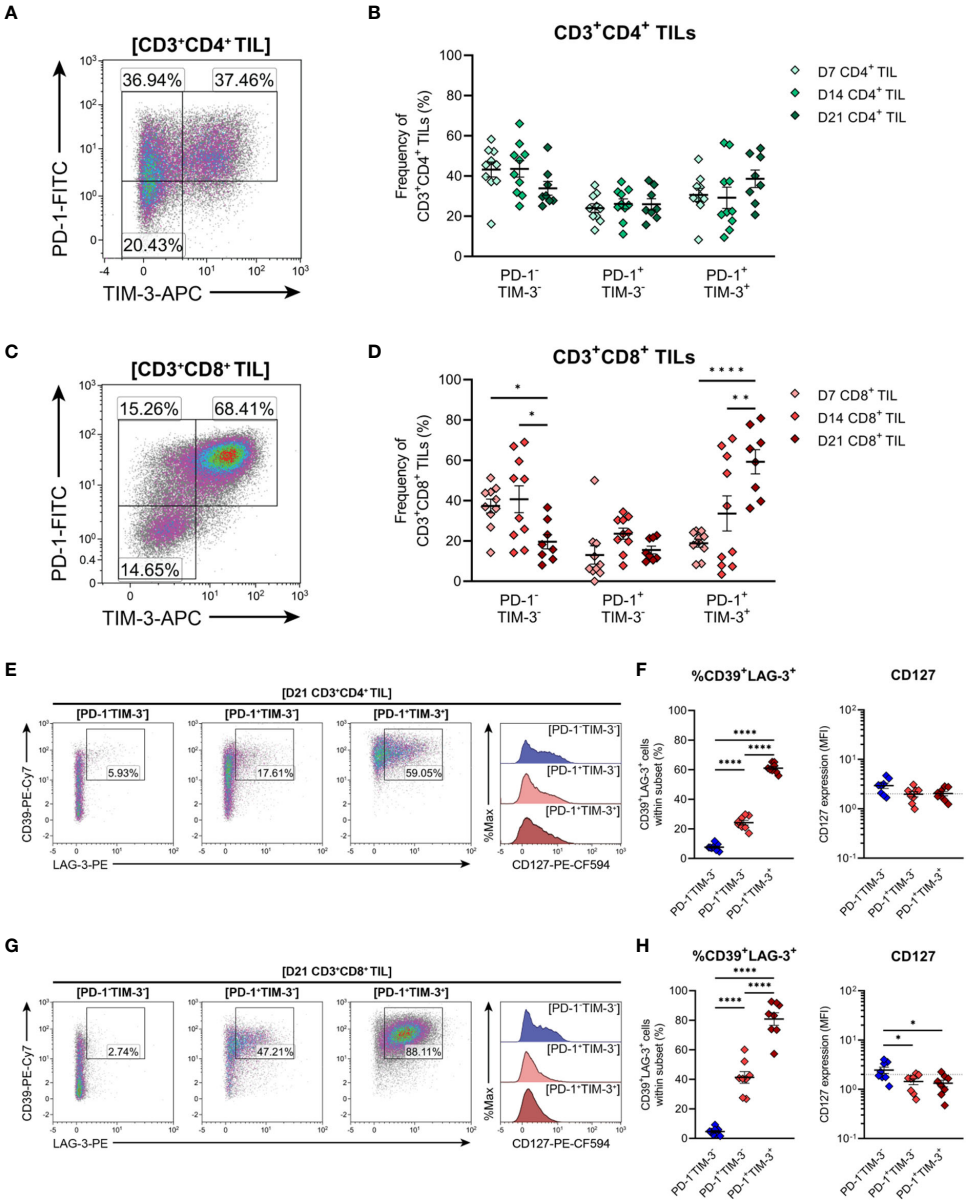

FIGURE 8
Expression of inhibitory receptors associated with exhaustion by CD4$^+$ and CD8$^+$ T cells infiltrating MC38 tumours. **(A, C)** Representative density plots depicting the distribution of PD-1 and TIM-3 subsets within total CD3$^+$CD4$^+$ **(A)** and CD3$^+$CD8$^+$ **(C)** TILs. **(B, D)** Frequencies of naïve-like (PD-1$^-$TIM-3$^-$), progenitor exhausted (PD-1$^+$TIM-3$^-$) and terminally exhausted (PD-1$^+$TIM-3$^+$) T cells among CD3$^+$CD4$^+$ **(B)** and CD3$^+$CD8$^+$ **(D)** TILs. **(E, G)** Representative flow plots depicting LAG-4, CD39 and CD127 expression in naïve-like (PD-1$^-$TIM-3$^-$; blue), progenitor exhausted (PD-1$^+$TIM-3$^-$; light red) and terminally exhausted (PD-1$^+$TIM-3$^+$; dark red) T cell subsets within CD3$^+$CD4$^+$ **(E)** and CD3$^+$CD8$^+$ **(G)** TIL isolated from D21 MC38 tumours. **(F, H)** Expression of both CD39 and LAG-3 (%CD39$^+$LAG-3$^+$) and CD127 (MFI) within PD-1 and TIM-3 subsets of CD3$^+$CD4$^+$ **(F)** and CD3$^+$CD8$^+$ **(H)** TIL isolated from D21 MC38 tumours. All density plot percentages indicate frequencies as the proportion of the gated population (indicated in bold titles with square brackets). All data are representative of 8-10 biological replicates per timepoint. Graphs represent the mean and standard error of the mean (SEM, error bars). Statistical analyses were performed using two-way **(B, D)** or one-way **(F, H)** ANOVA with *post-hoc* Tukey test to correct for multiple comparisons. *p ≤ 0.05; **p ≤ 0.01; ****p ≤ 0.0001.

produced TNF, with low frequencies of cells producing IFN-γ or both cytokines (<10%; Figure 9A). Compared to CD4$^+$ TILs, a greater proportion of CD8$^+$ TILs produced IFN-γ and were polyfunctional, producing both IFN-γ and TNF (13% versus 5%; Figure 9B). A similar proportion of CD8$^+$ TILs also expressed granzyme B (9-13% GzmB$^+$; Figure 9B). However, production of IL-2 or IL-10 in either CD4$^+$ or CD8$^+$ TILs could not be detected (data not shown) and unstimulated controls did not exhibit significant frequencies of cytokine-producing cells (~1%; Figures 9A, B, representative density plots). In response to stimulation, there were no significant differences in the frequencies of cytokine-producing CD4$^+$ or CD8$^+$ cells between D14 and D21 tumours (%IFN-γ$^+$, %TNF$^+$, %IFN-γ$^+$TNF$^+$ and %GzmB$^+$; Figures 9A, B).

In addition to the progressive upregulation of inhibitory receptors (particularly PD-1), T cell exhaustion is typically characterised by the stepwise loss of effector functions such as

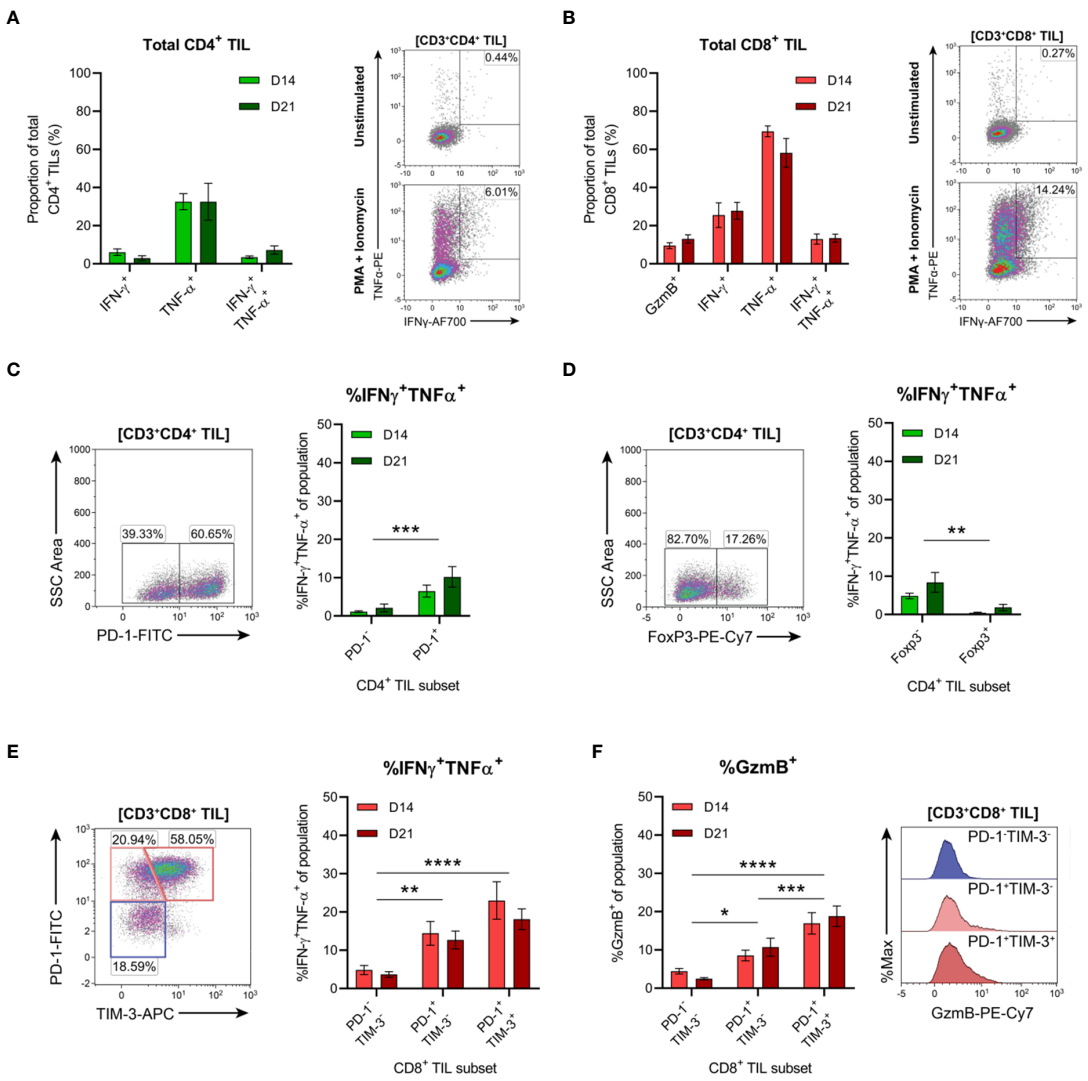

FIGURE 9
Tumour-infiltrating CD4$^+$ and CD8$^+$ T cell subsets exhibit distinct functional properties. **(A, B)** Frequency of cytokine producing cells within total CD3$^+$CD4$^+$ **(A)** and CD3$^+$CD8$^+$ **(B)** TILs. Representative density plots depict IFN-γ and TNF-α production by total CD3$^+$CD4$^+$ and CD3$^+$CD8$^+$ TILs in unstimulated controls (top) and following PMA+ionomycin stimulation (bottom). **(C, D)** Representative density plots depicting PD-1 **(C)** and FoxP3 **(D)** subset gating in CD3$^+$CD4$^+$ TILs and frequencies of cells producing both IFN-γ and TNF-α (%IFN-γ$^+$TNF-α$^+$) within PD-1 and FoxP3 subsets. **(E)** Representative density plot depicting PD-1 and TIM-3 subset gating in CD3$^+$CD8$^+$ TILs and frequencies of cells producing both IFN-γ and TNF-α (%IFN-γ$^+$TNF-α$^+$) within these subsets. **(F)** Frequency of cells producing granzyme B (%GzmB$^+$) within PD-1 and TIM-3 subsets (CD3$^+$CD8$^+$ TILs) and representative histogram overlays. All density plot percentages indicate frequencies as the proportion of the gated population (indicated in bold titles with square brackets). Graphs represent the mean and standard error of the mean (SEM, error bars). Statistical analyses were performed using two-way ANOVA with *post-hoc* Tukey test to correct for multiple comparisons, or by multiple unpaired Student's *t*-tests, using the Holm-Sidak method to correct for multiple comparisons. *p ≤ 0.05; **p ≤ 0.01; ***p ≤ 0.001; ****p ≤ 0.0001.

cytokine polyfunctionality and lytic activity (64, 65). Therefore, we investigated whether PD-1 expression was associated with the loss of effector functions within CD4$^+$ and CD8$^+$ TILs. Co-production of IFN-γ and TNF was analysed within CD4$^+$ TIL subsets based on the presence or absence of PD-1 or FoxP3 expression (Figures 9C, D). Polyfunctional CD4$^+$ TILs (IFN-γ$^+$TNF$^+$) were enriched within cells lacking FoxP3 expression (compared to FoxP3$^+$ counterparts) and within PD-1$^+$ cells (compared to PD-1$^-$ counterparts; Figures 9C, D). There was no difference in the proportion of polyfunctional PD-1$^+$ CD4$^+$ TILs between D14 and D21 tumours, suggesting that their functionality did not decline during progressive tumour growth (Figure 9C). These data support the notion that FoxP3$^+$ CD4$^+$ TILs represent subsets of T_{REG} cells, while CD4$^+$ T_H1 effectors are enriched in the PD-1$^+$ TIL fraction.

In CD8$^+$ TILs, IFN-γ and TNF co-production along with granzyme B expression was assessed within PD-1 and TIM-3 subsets (Figures 9E, F). Despite their exhausted phenotype, a greater proportion of PD-1$^+$TIM-3$^+$ CD8$^+$ TILs produced both IFN-γ and TNF and displayed increased cytolytic potential (with a higher frequency of granzyme B-positive cells) compared to the PD-1$^+$TIM-3$^-$ and PD-1$^-$TIM-3$^-$ subsets (Figures 9E, F). Within all CD8$^+$ TIL subsets, there were no differences in the frequencies of polyfunctional or granzyme B-expressing cells between D14 and D21 tumours, suggesting that these subsets also maintain their

10.3389/fimmu.2023.1152035

functional status during tumour progression (Figures 9E, F). Together, these data indicate that despite their exhausted phenotype, PD-1$^+$TIM-3$^+$ CD8$^+$ TILs retain rapid effector functions *ex vivo* and display enhanced polyfunctionality compared to other CD8$^+$ TIL subsets. Furthermore, both CD4$^+$ and CD8$^+$ T cells with anti-tumour functionality (particularly IFN-γ and TNF co-production) are enriched within the PD-1$^+$ fraction of MC38 TILs.

3.11 Endogenous CD8$^+$ T cell responses to MC38 are dominated by recognition of the p15E tumour antigen over Adpgk and Dpagt1 neoantigens

Three MHC-I-restricted neoantigens have been reported in the MC38 colon adenocarcinoma cell line (66). These neoantigens derive from non-synonymous point-mutations in the genes encoding ADP-dependent glucokinase (Adpgk), dolichyl-phosphate N-acetylglucosaminephosphotransferase 1 (Dpagt1) and RalBP1-associated Eps domain-containing 1 (Reps1) (66). To validate these neoantigens as potential targets for endogenous CD8$^+$ T cell responses, the presence of these mutations was assessed in our MC38 cell line. Two mutated neoantigens (Adpgk$_{R304M}$ and Dpagt1$_{V304L}$) were detected, while the C→G point mutation reported in *Reps1* (Reps1$_{P45A}$) was absent in our version of the MC38 cell line (Supplementary Figure 5).

Having confirmed that MC38 cells harboured mutations in *Adpgk* and *Dpagt1*, the recognition of neo-epitopes derived from these mutations by endogenous CD8$^+$ T cells was assessed (Adpgk$_{R304M}$, ASMTNMELM; Dpagt1$_{V213L}$, SIIVFNLL). In addition, CD8$^+$ T cell responses to p15E (p15E$_{604-611}$, KSPWFTTL) – an envelope protein of a murine endogenous retrovirus (MERV) and an immunodominant tumour antigen expressed by the MC38 cell line (67, 68) – was also examined. CD3$^+$CD8$^+$ T cells were isolated from D14 and D21 tumour-bearing mice and stimulated *ex vivo* with peptide-pulsed bone marrow-derived dendritic cells (BMDCs). Antigen-specific CD8$^+$ T cell responses were then evaluated by intracellular cytokine staining for IFN-γ and TNF (Figure 10A). No antigen-specific activation of CD3$^+$CD8$^+$ T cells isolated from tumour-draining lymph nodes (TdLN) could be detected (Figure 10B). However, CD8$^+$ TILs strongly responded to p15E$_{604-611}$, with p15E-reactive CD8$^+$ TILs readily detectable in D14 and D21 tumours (Figure 10C). Polyfunctional responses against the Adpgk$_{R304M}$ neo-epitope could be detected in some mice, although to a lesser magnitude than p15E, composing up to 3.3% and 3.6% of total CD3$^+$CD8$^+$ in D14 and D21 tumours, respectively (Figure 10C). Although Dpagt1$_{V213L}$-reactive CD8$^+$ TILs were detectable in some animals, this neo-epitope did not elicit strong activation of CD8$^+$ TILs from either D14 or D21 tumours (Figure 10C). These data suggest that the CD8$^+$ T cell response against MC38 tumours is dominated by recognition of the endogenous retroviral envelope protein, p15E, over the identified neoantigens, Adpgk$_{R304M}$ and Dpagt1$_{V213L}$. Importantly, CD8$^+$ T cell responses against p15E and Adpgk$_{R304M}$ occur spontaneously in MC38 tumour-bearing mice, making these tumour antigens relevant immunotherapeutic targets in this model.

3.12 p15E-reactive CD8$^+$ TILs display phenotypic features of exhaustion which exacerbate during tumour progression

After confirming the presence of functional tumour-specific CD8$^+$ T cells in MC38 tumours, their phenotypic status was examined – specifically, the expression of inhibitory receptors by p15E-reactive CD8$^+$ TILs. Bulk CD8$^+$ TILs from D14 and D21 tumours were heterogeneous in their expression of both PD-1 and TIM-3, while virtually all p15E-reactive CD8$^+$ TILs were PD-1$^+$ (>99% in both D14 and D21 tumours) with a subset of these cells co-expressing TIM-3 (Figures 10D, E). Hence, despite their functional status *ex vivo* (IFN-γ and TNF production), these tumour-specific CD8$^+$ T cells exhibited phenotypic features of exhaustion, containing populations of both transitional exhausted (PD-1$^+$TIM-3$^-$) and terminally exhausted (PD-1$^+$TIM-3$^+$) cells. Further analysis of p15E-reactive TILs revealed that the proportion of terminally exhausted PD-1$^+$TIM-3$^+$ cells increased during tumour progression, with a concomitant decrease in the proportion of transitional exhausted PD-1$^+$TIM-3$^-$ cells (D21 versus D14 tumours; Figure 10F). These data demonstrate that tumour-specific T cells within MC38 tumours acquire the expression of inhibitory receptors in a stepwise manner during tumour progression.

4 Discussion

Immune-competent murine tumour models are crucial tools for the development and optimisation of cancer immunotherapies. However, understanding how these models recapitulate the biology of human disease is vital for the translation of preclinical findings into the clinical setting. In this study, the landscape of T cell infiltration in MC38 tumours was systematically examined, with the aim of determining how this model reflects features of human CRC.

We present an overview of the tumour-T cell immune landscape in subcutaneous MC38 tumours and how the MC38 TME evolves over the course of tumour progression (Figure 11). Early MC38 tumours (D7) exhibit a nascent TME, with perfuse infiltration throughout the tumour mass by T cells that predominately display naïve and early effector phenotypes. Subsequently, T cell infiltration is increasingly restricted from the tumour core, which coincides with the accumulation of fibrotic, desmoplastic stroma and the deposition of dense reticular fibres at the invasive margin. Intermediate MC38 tumours (D14) begin to acquire features of a mature TME – with ECM remodelling and a shift in the composition and phenotype of infiltrating T cells towards effector populations – while late-stage tumours (D21) exhibit a mature TME reminiscent of human tumours, with desmoplasia, CD8$^+$ T cell exhaustion, and T cell exclusion from the tumour core. MC38 tumours also display extensive vascularisation throughout the tumour mass. However, while T

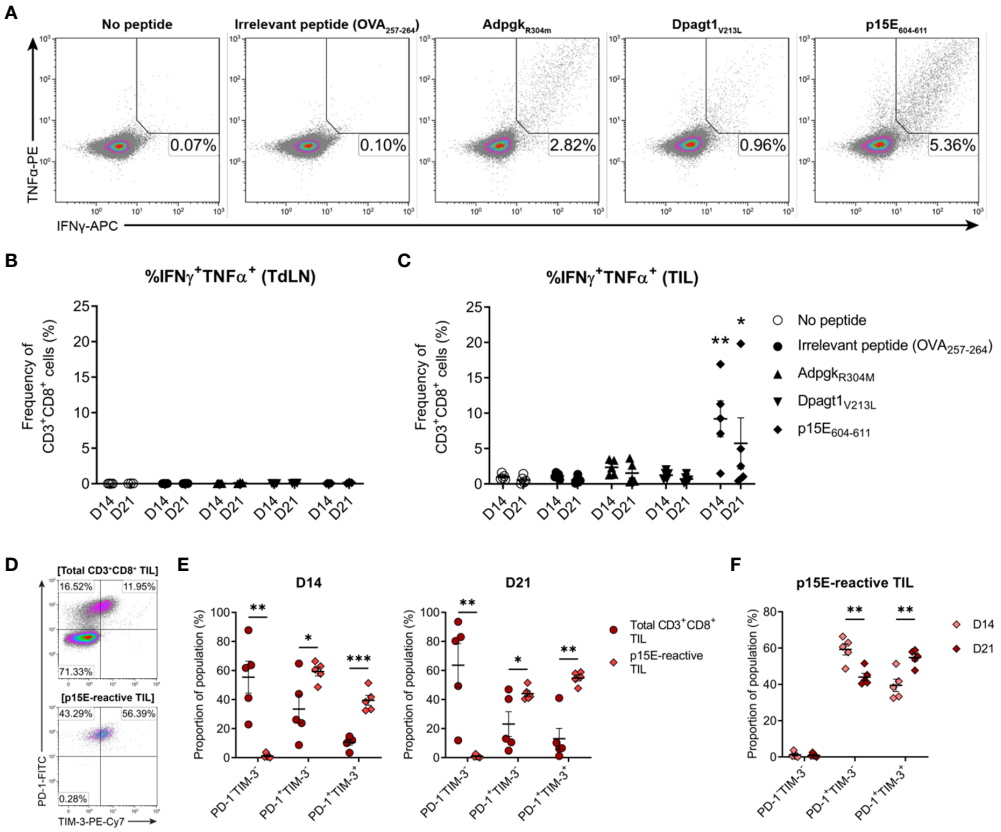

FIGURE 10
The endogenous CD8+ T cell response to MC38 is dominated by recognition of the p15E tumour antigen. **(A)** Representative density plots showing TNFα and IFNγ production by CD8+ TILs stimulated *ex vivo* with BMDCs pulsed with 1 μg/mL of H-2K^b/D^b-restricted tumour antigen peptides (p15E$_{604-611}$, KSPWFTTL; Adpgk$_{R304M}$, ASMTNMELM; and Dpagt1$_{V213L}$, SIIVFNLL), unpulsed BMDCs (no peptide) or BMDC pulsed with 1 μg/mL OVA$_{257-264}$ peptide (SIINFEKL; irrelevant peptide). Percentages indicate peptide-reactive CD8+ T cell frequencies (%IFNγ+TNFα+) as the proportion of total CD3+CD8+ cells. **(B, C)** Frequency of polyfunctional CD3+CD8+ cells – isolated from TdLNs **(B)** and TILs **(C)** – producing IFNγ and TNFα in response to indicated treatments (%IFNγ+TNFα+). **(D)** Representative density plots showing PD-1 and TIM-3 expression by total CD3+CD8+ TILs (top) and p15E-reactive CD3+CD8+ TILs (IFNγ+TNFα+, bottom) isolated from D21 MC38 tumours. Percentages indicate subset frequencies as the proportion of the gated populations. **(E)** Comparison of PD-1 and TIM-3 subset compositions in total CD3+CD8+ TILs (•) and p15E-reactive CD3+CD8+ TILs (♦) from D14 and D21 MC38 tumours. **(F)** Comparison of PD-1 and TIM-3 subset compositions in p15E-reactive CD3+CD8+ TILs from D14 and D21 MC38 tumours. All data are representative of five biological replicates per timepoint. Graphs represent the mean (line) and standard error of the mean (SEM, error bars). Statistical analyses were performed using two-way ANOVA with *post-hoc* Dunnett's test, comparing tumour antigen peptide-reactive frequencies to irrelevant peptide controls **(B, C)**, or multiple unpaired Student's t-tests using the Holm-Sidak method to correct for multiple comparisons **(E, F)**. *p ≤ 0.05; **p ≤ 0.01; ***p ≤ 0.001.

cell extravasation is permitted by vessels in adjacent connective tissue and more structurally 'normal' vessels at the periphery of tumours, T cells are unable to access the tumour interior *via* intratumoural vasculature. Hence, MC38 tumour progression is characterised by the development of an T cell-excluded phenotype, which appears to be mediated by physical barriers, particularly dense ECM and aberrant tumour vasculature.

Relevant to these changes, we observed that MC38 tumour cells secreted TGF-β *in vitro* and that high levels of this cytokine were present within the MC38 TME. Notably, TGF-β plays a central role in the recruitment of fibroblasts to tumours and their conversion to cancer-associated fibroblasts, while increased TGF-β expression correlates with the accumulation of fibrotic desmoplastic stroma (69) and is strongly associated with T cell exclusion in human tumours (17, 70, 71). Thus, high TGF-β concentrations within the MC38 TME – coinciding with the development of desmoplastic stroma and T cell exclusion at the tumour margin – may imply a role for this cytokine in the induction of this phenotype. Consistent with this notion, others have identified TGF-β as a mechanism of immune evasion employed by MC38 tumours, acting to impair anti-tumour T cell function while promoting T cell exclusion (17).

In the context of human CRC, high levels of TGF-β and ECM remodelling are defining features of CMS4 tumours (mesenchymal subtype), which exhibit the poorest prognosis across all CRC subtypes (22). Akin to our observations in MC38 tumours, CMS4 tumours frequently display an immune-excluded phenotype with prominent desmoplasia and are dependent on a TGF-β-driven stromal gene program, in which cancer-associated fibroblasts promote tumour progression (72–74). However, CMS4 tumours are predominately microsatellite stable (MSS) and exhibit high chromosomal instability (CIN), whereas the MC38 model is hypermutated and exhibits high microsatellite instability (MSI-H) which are defining characteristics of human CMS1 tumours (MSI immune subtype) (19, 22). Despite this disparity between the

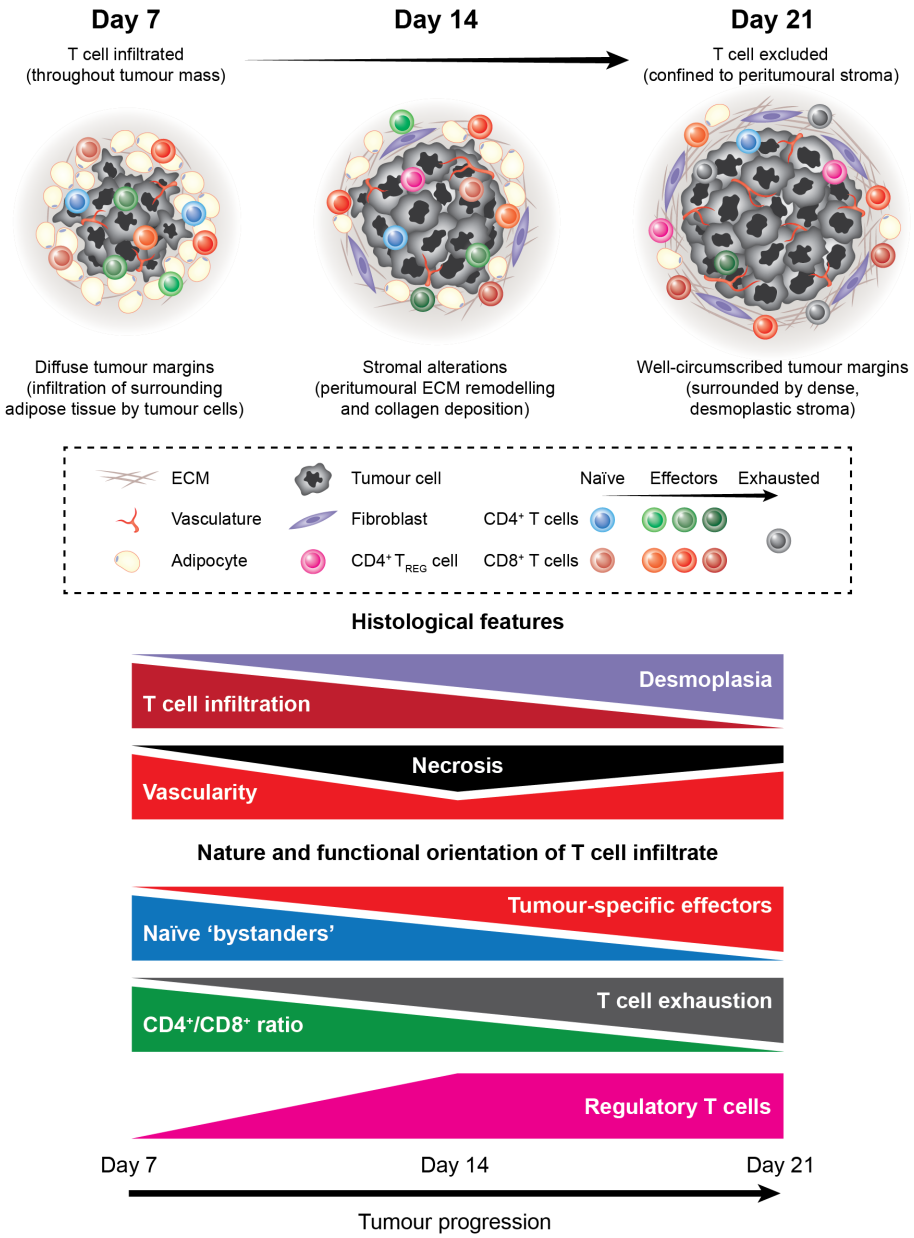

FIGURE 11
The tumour-T cell immune landscape in MC38 tumours during progressive outgrowth. Extensive characterisation of outgrowing MC38 tumours revealed dynamic histological changes and shifts in the nature and functional orientation of infiltrating T cells. Histological changes included stromal alterations, particularly peritumoural ECM deposition and remodelling that resulted in the formation of dense desmoplastic stroma at the tumour margin. This coincided with decreasing T cell infiltration into the tumour core, with late-stage MC38 tumours exhibiting a T cell-excluded phenotype. In addition, necrosis, angiogenesis, and vascular abnormalities were apparent within the MC38 tumour microenvironment. Longitudinal immunophenotyping of TILs in MC38 tumours revealed dynamic changes in the composition, phenotype, and function of these cells. Notably, the T cell infiltrate in MC38 tumours shifted from cells with a naïve-like phenotype toward a more pro-inflammatory composition during progressive outgrowth. This was characterised by an increase in $CD8^+$ effectors and a decrease in the $CD4^+/CD8^+$ ratio within MC38 tumours. In parallel, $CD8^+$ TILs progressively acquired phenotypic features of dysfunction, which cumulated in a profoundly exhausted phenotype in late-stage MC38 tumours. Our data also indicate that unfavourable immune populations such as suppressive $CD4^+$ regulatory T cells also accumulate in outgrowing MC38 tumours.

genomic features of human CMS4 tumours and MC38, our findings show that late-stage MC38 tumours recapitulate archetypal features of the TME in human CMS4 tumours. This study therefore supports the use of MC38 as a relevant model for the immune-excluded phenotype observed in CMS4 tumours and for investigating therapeutic strategies that aim to reverse T cell exclusion.

Longitudinal immunophenotyping of TILs over the course of MC38 tumour progression revealed dynamic changes in the composition, phenotype, and function of these cells (Figure 11). Notably, decreases in the ratios of $CD4^+/CD8^+$, $CD4^+FoxP3^+$/T-bet^+CD8^+ and $CD4^+$T-$bet^+/CD4^+FoxP3^+$ TILs were observed during progressive tumour outgrowth, suggesting that the T cell infiltrate in MC38 tumours shifts toward a more pro-inflammatory

composition during progressive outgrowth. However, at the same time, T cells are increasingly excluded from the vicinity of tumour cells. Immune exclusion – as well as other immunosuppressive mechanisms – may therefore explain the unabated growth of these tumours despite a strong endogenous anti-tumour T cell response.

While pronounced T cell infiltration in tumours is generally considered a manifestation of an ongoing host immune response against malignant cells, the mere presence of TILs is not necessarily indicative of an effective anti-tumour immune response. Rather, the ability of TILs to mediate tumour regression relies on both the quantity and the quality of responding T cell infiltrates (75, 76). Consequently, the phenotypes of T cells isolated from MC38 tumours were examined, revealing striking alterations over the course of tumour progression. Regarding $CD8^+$ T cells, infiltration by $CD8^+$ effectors increased during outgrowth of MC38 tumours, but these cells progressively acquired phenotypic features of exhaustion. Interestingly, PD-1 and CD69 were co-expressed within a large proportion of $CD8^+$ TILs, which may imply these cells are tissue-resident memory cells (T_{RM} cells) (77, 78), although further phenotypic analysis is required to confirm this phenotype. However, as T_{RM} formation is strictly dependent on TGF-β (79, 80), it is plausible that abundant TGF-β within the MC38 TME drives $CD8^+$ T_{RM} differentiation, while also mediating the exclusion of these cells from the tumour parenchyma (71).

In late-stage MC38 tumours, $CD8^+$ TILs displayed a profoundly exhausted phenotype characterised by simultaneous expression of multiple inhibitory receptors (PD-1, TIM-3, LAG-3 and CD39) and low expression of CD127. In addition, an increasing proportion of $CD8^+$ TILs exhibited high T-bet expression and low expression of Eomes as tumours progressed. Given the association of high T-bet expression with the acquisition of effector function (81, 82), and the requirement for Eomes expression in memory formation (57, 58), these $CD8^+$ T-bet$^+$Eomes$^-$ TILs likely represent dysfunctional, terminally differentiated effectors. We also observed that tumour-specific $CD8^+$ TILs recognising the p15E tumour antigen displayed phenotypic features of exhaustion and that the proportion of these cells displaying a terminally exhausted PD-1$^+$TIM-3$^+$ phenotype increased with tumour progression. Interestingly, in contradiction to their dysfunctional phenotype, these cells were capable of rapid IFN-γ and TNF production *ex vivo*, while $CD8^+$ TILs with anti-tumour functionality *ex vivo* (IFN-γ and TNF co-production) were predominately PD-1$^+$. While these data imply that these cells are not exhausted, it more likely reflects their highly differentiated state skewed toward potent effector function when simulated *ex vivo*. By contrast, these cells would be highly vulnerable to suppression within the TME given their expression of multiple inhibitory receptors (PD-1, TIM-3, LAG-3 and CD39), which could render them dysfunctional and unable mediate effective tumour control *in situ*. Although the factors driving the exhaustion of $CD8^+$ T cells in MC38 tumours is unclear, chronic tumour antigen stimulation (83) and/or suppressive factors within the tumour microenvironment (65) are likely involved. Indeed, PD-L1 expression by both MC38 tumour cells and tumour-infiltrating myeloid cells has been shown to suppress of anti-tumour $CD8^+$ T cell responses in this model (15, 84). Consequently, this study supports the use of the MC38 model in studies investigating immunotherapies targeting T cell exhaustion and the PD-1/PD-L1 axis and as a model for microsatellite instable-high (MSI-H) human CRCs that exhibit high PD-L1 expression and responsiveness to PD-1 blockade (28, 85).

While $CD8^+$ TILs isolated from MC38 tumours displayed well-defined phenotypes, $CD4^+$ TILs were highly heterogenous and difficult to define in this study. Indeed, $CD4^+$ T cell polarisation and function is extremely diverse, requiring more comprehensive phenotyping than that used in this study to delineate subpopulations. Notably, the majority of $CD4^+$ TILs in MC38 tumours did not express FoxP3 or T-bet (40-75%), suggesting that MC38 tumours are heavily infiltrated by effector subsets other than T_H1 and T_{REG} cells, likely T_H2 or T_H17 cells. Nevertheless, tumour progression was accompanied by increased infiltration of activated effector memory $CD4^+$ T cells and T_H1 (FoxP3$^-$T-bet$^+$) and T_{REG} (FoxP3$^+$T-bet$^-$) subsets were present in established tumours. We also observed a proportion of $CD4^+$ TILs with a FoxP3$^+$T-bet$^+$ phenotype that increased during tumour outgrowth. Interestingly, $CD4^+$ T cells exhibiting this phenotype have been identified as a subset of highly suppressive T_{REG} cells which accumulate at sites of type-1 inflammation and potently inhibit local T_H1 immune responses (86–88). $CD4^+$ TIL subpopulations also exhibited CD25$^+$CD137$^+$ and CD39$^+$TIM-3$^+$ phenotypes (data not shown), supporting the notion that $CD4^+$ T_{REG} cells accumulate in MC38 tumours given that these markers are highly and selectively expressed by this subset (89–92). In established tumours, $CD4^+$ T_H1 TILs displayed high PD-1 expression, which was also associated with polyfunctional IFN-γ and TNF production *ex vivo*. Altogether, these data suggest that recruitment of T_{REG} cells is an active immunosuppressive mechanism in the MC38 model and that $CD4^+$ T_H1 effectors may undergo a similar fate to $CD8^+$ TILs, acquiring an exhausted phenotype within the MC38 TME.

Aside from the phenotypic features of T cell infiltration in MC38 tumours, this study also characterised the frequency of $CD8^+$ TILs responsive to peptide stimulation with tumour antigens (TAs) identified in the MC38 model. In an interesting observation, detectable tumour-specific $CD8^+$ T cell responses were dominated by recognition of the p15E ERV antigen over two defined mutated neoantigens, with functional p15E-reactive clones composing up to ~20% of total $CD8^+$ TILs in late-stage tumours. Although mutated neoantigens have generated intense interest as immunotherapy targets (93), TAs derived from endogenous retroviral elements are increasingly promising alternatives (94). Unlike neoantigens – which derive from mutations and are often unique to individual patients – ERV-derived TAs arise through epigenetic dysregulation of the cancer genome and are shared across different patients and tumour types (95, 96). Consequently, this class of TAs is amenable to the development of off-the-shelf therapies for patients with shared HLA class I alleles. MC38 and the p15E tumour antigen may therefore represent a useful preclinical model for developing immunotherapies that target shared ERV TAs.

One limitation of this study is the use of peptide stimulation, which can only detect responsive or 'reactive' T cells and is therefore prone to underestimating the true frequency of antigen-specific T cells. Indeed, other studies using more reliable peptide-MHC

tetramer staining have reported higher frequencies tumour-specific T cells in the MC38 model, with Dpagt1-specific $CD8^+$ T cells composing over 20% of $CD8^+$ TILs in D13 tumours (97). A recent study also identified another neoantigen in the MC38 model derived from a mutation in the ribosomal protein L18 (Rpl18) (98). Strikingly, recognition of this neo-epitope was shown to dominate endogenous $CD8^+$ T cell responses compared to other identified neoantigens, including $Adpgk_{R304M}$ (98). Future studies utilising peptide-MHC tetramers should comprehensively examine the immunodominance of defined TAs in the MC38 model, including ERV-derived TAs, mutated neoantigens, and unaltered self-proteins that are overexpressed (such as p53 (99), survivin (100) and topoisomerase II-α (101)). Another question that remains to be addressed regards the identity of MHC class II-restricted tumour antigens recognised by $CD4^+$ T cells in the MC38 model. Indeed, there is increasing interest in targeting MHC class II-restricted antigens in immunotherapies (102–104) and mutated neoantigens that stimulate anti-tumour $CD4^+$ T cell responses have recently been identified in other syngeneic tumour models (103, 105, 106). A deeper understanding of the immunodominance of different TA classes will help to inform the development of effective immunotherapies.

In human patients with clinically-manifest or advanced disease, tumours have been shaped by years – if not decades – of tumour-immune interactions (107) and are frequently resistant to immunotherapeutic interventions (108). By contrast, tumour-immune interactions in preclinical mouse models occur over a timeframe of days to weeks and studies typically begin therapeutic inventions only days after tumour inoculation. Consequently, how accurately these models recapitulate tumour-immune interactions in humans and the selection of appropriate timepoints in these studies are issues frequently overlooked.

Our observations have important implications for optimal timepoint selection in the MC38 model. Many seminal immunotherapy studies that provide rational for subsequent clinical trials initiate treatment 5-9 days post-inoculation when MC38 tumours are newly established (17, 30, 31, 84, 109–112). However, at these timepoints, we show that MC38 tumours exhibit a nascent TME which lacks both important hallmarks of human tumours and pre-empts the manifestation of the immune-resistance mechanisms that these therapies target (such as T cell exhaustion and immune exclusion). Consequently, at early timepoints, the ability of these immunotherapies to induce tumour regression likely reflects their efficacy before immune-resistant mechanisms in the MC38 TME are established, rather than their ability to reverse these mechanisms or permit anti-tumour immunity in the context of a mature TME. Indeed, antibodies targeting CTLA-4 or TIM-3 have been shown to be effective in various mouse tumour models when administered early (day 3 post-inoculation) but are largely ineffective against established tumours (day 11 post-inoculation) (113). Premature timepoint selection in preclinical tumour models may therefore contribute to disparities between the results of these studies and subsequent clinical trials.

The application of more relevant timepoints (when tumours more accurately reflect the TME in human tumours) may improve the clinical translation of immunotherapies developed in preclinical models such as MC38. Our findings demonstrate that MC38 tumours more faithfully resemble human tumours after 14 days and advocate for the initiation of therapeutic interventions at this timepoint in studies investigating immunotherapies. However, one important caveat concerns balancing the use of more appropriate timepoints with the ethical use of laboratory animals. Although more relevant, the implementation of later timepoints in murine tumour studies may encroach on humane endpoints (based on tumour size) and impair animal welfare. This is a vital consideration, as researchers have a responsibility to perform studies to the highest quality whilst also ensuring the ethical and humane care and use of animals. Ultimately, more accurate application of preclinical models will improve clinical translation and, in accordance with the 3Rs (Replacement, Reduction and Refinement), aid in reducing animal usage.

To conclude, this study describes the dynamics of endogenous T cell responses in the MC38 model, including the spatiotemporal features, composition, phenotype, function, and nature of tumour antigen recognition. Future work should characterise the broader immune context of the MC38 TME, particularly the tumour-infiltrating myeloid compartment given the important role of these cells in tumour immunity and the MC38 model (15, 114). We also identify immune-resistance mechanisms in this model that recapitulate aspects of human CRC subtypes and highlight the importance of appropriate timepoint selection when investigating features of the TME – particularly T cell exclusion and exhaustion. Although cancer immunotherapies hold immense promise, human tumours are heterogeneous and utilise multiple resistance mechanisms that restrain anti-tumour immunity. Therefore, targeting the specific mechanisms active in any given tumour is likely a prerequisite for therapeutic response. Accordingly, personalised combination strategies that are tailored to individual patients' specific TMEs hold immense promise for the next generation of cancer immunotherapies (115). However, the development of rational combination strategies will be dependent on the appropriate application of preclinical models matched to distinct tumour-immune profiles seen in human patients. Collectively, our findings provide a valuable resource that enables appropriate application of the MC38 model in preclinical studies and will aid in the development and clinical translation of new immunotherapies.

Data availability statement

The original contributions presented in this study are included in the article and Supplementary Material. Further inquiries can be directed to the corresponding author.

Ethics statement

The animal study was reviewed and approved by University of Otago Animal Ethics Committee.

Author contributions

NS was the primary designer, performer, and interpreter of experiments, and writer of this manuscript. EP and SN assisted with experimental work, the interpretation of data, and writing the manuscript. AF and MS provided supervision, interpreted results, and reviewed and edited the manuscript. SY was the principal investigator responsible for supervision, conceived the study, provided funding and resources, and reviewed and edited the manuscript. All authors contributed to the article and approved the submitted version.

Funding

This work was supported by an internal grant from the Division of Health Sciences, University of Otago.

Acknowledgments

The authors would like to acknowledge Otago Micro and Nanoscale Imaging (OMNI) for performing histology and immunohistochemistry and University of Otago Genetic Analysis Services for providing DNA sequencing services. We also thank Amanda Fisher (Histology Unit, Department of Pathology, University of Otago) for their expertise and assistance in histology and IHC, and Nada Guirguis (Department of Pathology, University of Otago) for their expertise and assistance in histology and pathology.

Conflict of interest

The authors declare that the research was conducted in the absence of any commercial or financial relationships that could be construed as a potential conflict of interest.

Publisher's note

All claims expressed in this article are solely those of the authors and do not necessarily represent those of their affiliated organizations, or those of the publisher, the editors and the reviewers. Any product that may be evaluated in this article, or claim that may be made by its manufacturer, is not guaranteed or endorsed by the publisher.

Supplementary material

The Supplementary Material for this article can be found online at: https://www.frontiersin.org/articles/10.3389/fimmu.2023.1152035/full#supplementary-material

References

1. Dranoff G. Experimental mouse tumour models: what can be learnt about human cancer immunology? *Nat Rev Immunol* (2012) 12(1):61–6. doi: 10.1038/nri3129

2. Zitvogel L, Pitt JM, Daillère R, Smyth MJ, Kroemer G. Mouse models in oncoimmunology. *Nat Rev Cancer.* (2016) 16(12):759–73. doi: 10.1038/nrc.2016.91

3. Punt CJ, Koopman M, Vermeulen L. From tumour heterogeneity to advances in precision treatment of colorectal cancer. *Nat Rev Clin Oncol* (2017) 14(4):235–46. doi: 10.1038/nrclinonc.2016.171

4. Charoentong P, Finotello F, Angelova M, Mayer C, Efremova M, Rieder D, et al. Pan-cancer immunogenomic analyses reveal genotype-immunophenotype relationships and predictors of response to checkpoint blockade. *Cell Rep* (2017) 18 (1):248–62. doi: 10.1016/j.celrep.2016.12.019

5. Motz GT, Coukos G. Deciphering and reversing tumor immune suppression. *Immunity.* (2013) 39(1):61–73. doi: 10.1016/j.immuni.2013.07.005

6. Łuksza M, Riaz N, Makarov V, Balachandran VP, Hellmann MD, Solovyov A, et al. A neoantigen fitness model predicts tumour response to checkpoint blockade immunotherapy. *Nature.* (2017) 551(7681):517–20. doi: 10.1038/nature24473

7. Jiang P, Gu S, Pan D, Fu J, Sahu A, Hu X, et al. Signatures of T cell dysfunction and exclusion predict cancer immunotherapy response. *Nat Med* (2018) 24(10):1550–8. doi: 10.1038/s41591-018-0136-1

8. Samstein RM, Lee C-H, Shoushtari AN, Hellmann MD, Shen R, Janjigian YY, et al. Tumor mutational load predicts survival after immunotherapy across multiple cancer types. *Nat Genet* (2019) 51(2):202–6. doi: 10.1038/s41588-018-0312-8

9. Herbst RS, Soria J-C, Kowanetz M, Fine GD, Hamid O, Gordon MS, et al. Predictive correlates of response to the anti-PD-L1 antibody MPDL3280A in cancer patients. *Nature.* (2014) 515(7528):563–7. doi: 10.1038/nature14011

10. Bruni D, Angell HK, Galon J. The immune contexture and immunoscore in cancer prognosis and therapeutic efficacy. *Nat Rev Cancer.* (2020) 20(11):662–80. doi: 10.1038/s41568-020-0285-7

11. Bindea G, Mlecnik B, Tosolini M, Kirilovsky A, Waldner M, Obenauf AC, et al. Spatiotemporal dynamics of intratumoral immune cells reveal the immune landscape in human cancer. *Immunity.* (2013) 39(4):782–95. doi: 10.1016/j.immuni.2013.10.003

12. Blank CU, Haanen JB, Ribas A, Schumacher TN. The "cancer immunogram". *Science.* (2016) 352(6286):658–60. doi: 10.1126/science.aaf2834

13. Chen DS, Mellman I. Elements of cancer immunity and the cancer–immune set point. *Nature.* (2017) 541(7637):321. doi: 10.1038/nature21349

14. Corbett T, Griswold D, Roberts B, Peckham J, Schabel F. Tumor induction relationships in development of transplantable cancers of the colon in mice for chemotherapy assays, with a note on carcinogen structure. *Cancer Res* (1975) 35 (9):2434–9.

15. Lau J, Cheung J, Navarro A, Lianoglou S, Haley B, Totpal K, et al. Tumour and host cell PD-L1 is required to mediate suppression of anti-tumour immunity in mice. *Nat Commun* (2017) 8(1):1–11. doi: 10.1038/ncomms14572

16. Gordon SR, Maute RL, Dulken BW, Hutter G, George BM, McCracken MN, et al. PD-1 expression by tumour-associated macrophages inhibits phagocytosis and tumour immunity. *Nature* (2017) 545(7655):495–9. doi: 10.1038/nature22396

17. Mariathasan S, Turley SJ, Nickles D, Castiglioni A, Yuen K, Wang Y, et al. TGFβ attenuates tumour response to PD-L1 blockade by contributing to exclusion of T cells. *Nature.* (2018) 554(7693):544. doi: 10.1038/nature25501

18. Olson B, Li Y, Lin Y, Liu ET, Patnaik A. Mouse models for cancer immunotherapy research. *Cancer discovery.* (2018) 8(11):1358–65. doi: 10.1158/2159-8290.CD-18-0044

19. Efremova M, Rieder D, Klepsch V, Charoentong P, Finotello F, Hackl H, et al. Targeting immune checkpoints potentiates immunoediting and changes the dynamics of tumor evolution. *Nat Commun* (2018) 9(1):32. doi: 10.1038/s41467-017-02424-0

20. Zhao X, Li L, Starr TK, Subramanian S. Tumor location impacts immune response in mouse models of colon cancer. *Oncotarget.* (2017) 8(33):54775. doi: 10.18632/oncotarget.18423

21. Zigmond E, Halpern Z, Elinav E, Brazowski E, Jung S, Varol C. Utilization of murine colonoscopy for orthotopic implantation of colorectal cancer. *PloS One* (2011) 6(12):e28858. doi: 10.1371/journal.pone.0028858

22. Guinney J, Dienstmann R, Wang X, de Reyniès A, Schlicker A, Soneson C, et al. The consensus molecular subtypes of colorectal cancer. *Nat Med* (2015) 21(11):1350–6. doi: 10.1038/nm.3967

23. Sjöblom T, Jones S, Wood LD, Parsons DW, Lin J, Barber TD, et al. The consensus coding sequences of human breast and colorectal cancers. *science*. (2006) 314 (5797):268–74. doi: 10.1126/science.1133427

24. Cancer Genome Atlas Network. Comprehensive molecular characterization of human colon and rectal cancer. *Nature*. (2012) 487(7407):330. doi: 10.1038/nature11252

25. Castle JC, Loewer M, Boegel S, de Graaf J, Bender C, Tadmor AD, et al. Immunomic, genomic and transcriptomic characterization of CT26 colorectal carcinoma. *BMC Genomics* (2014) 15(1):1–12. doi: 10.1186/1471-2164-15-190

26. Zhong W, Myers JS, Wang F, Wang K, Lucas J, Rosfjord E, et al. Comparison of the molecular and cellular phenotypes of common mouse syngeneic models with human tumors. *BMC Genomics* (2020) 21(1):1–17. doi: 10.1186/s12864-019-6344-3

27. Alexandrov LB, Nik-Zainal S, Wedge DC, Aparicio SA, Behjati S, Biankin AV, et al. Signatures of mutational processes in human cancer. *Nature*. (2013) 500 (7463):415–21. doi: 10.1038/nature12477

28. Overman MJ, McDermott R, Leach JL, Lonardi S, Lenz H-J, Morse MA, et al. Nivolumab in patients with metastatic DNA mismatch repair-deficient or microsatellite instability-high colorectal cancer (CheckMate 142): an open-label, multicentre, phase 2 study. *Lancet Oncol* (2017) 18(9):1182–91. doi: 10.1016/S1470-2045(17)30422-9

29. Overman MJ, Lonardi S, Wong KYM, Lenz H-J, Gelsomino F, Aglietta M, et al. Durable clinical benefit with nivolumab plus ipilimumab in DNA mismatch repair-deficient/microsatellite instability-high metastatic colorectal cancer. *J Clin Oncol* (2018) 36(8):773–9. doi: 10.1200/JCO.2017.76.9901

30. Woo S-R, Turnis ME, Goldberg MV, Bankoti J, Selby M, Nirschl CJ, et al. Immune inhibitory molecules LAG-3 and PD-1 synergistically regulate T-cell function to promote tumoral immune escape. *Cancer Res* (2012) 72(4):917–27. doi: 10.1158/0008-5472.CAN-11-1620

31. Kuai R, Yuan W, Son S, Nam J, Xu Y, Fan Y, et al. Elimination of established tumors with nanodisc-based combination chemoimmunotherapy. *Sci advances*. (2018) 4(4):eaao1736. doi: 10.1126/sciadv.aao1736

32. Kurtulus S, Madi A, Escobar G, Klapholz M, Nyman J, Christian E, et al. Checkpoint blockade immunotherapy induces dynamic changes in PD-1– CD8+ tumor-infiltrating T cells. *Immunity*. (2019) 50(1):181–94.e6. doi: 10.1016/j.immuni.2018.11.014

33. Miller BC, Sen DR, Al Abosy R, Bi K, Virkud YV, LaFleur MW, et al. Subsets of exhausted CD8+ T cells differentially mediate tumor control and respond to checkpoint blockade. *Nat Immunol* (2019) 20(3):326–36. doi: 10.1038/s41590-019-0312-6

34. Curiel TJ, Coukos G, Zou L, Alvarez X, Cheng P, Mottram P, et al. Specific recruitment of regulatory T cells in ovarian carcinoma fosters immune privilege and predicts reduced survival. *Nat Med* (2004) 10(9):942–9. doi: 10.1038/nm1093

35. Saito T, Nishikawa H, Wada H, Nagano Y, Sugiyama D, Atarashi K, et al. Two FOXP3+ CD4+ T cell subpopulations distinctly control the prognosis of colorectal cancers. *Nat Med* (2016) 22(6):679. doi: 10.1038/nm.4086

36. Li Y, He M, Zhou Y, Yang C, Wei S, Bian X, et al. The prognostic and clinicopathological roles of PD-L1 expression in colorectal cancer: a systematic review and meta-analysis. *Front Pharmacol* (2019) 10:139. doi: 10.3389/fphar.2019.00139

37. Wu X, Zhang H, Xing Q, Cui J, Li J, Li Y, et al. PD-1$^+$ CD8$^+$ T cells are exhausted in tumours and functional in draining lymph nodes of colorectal cancer patients. *Br J Cancer*. (2014) 111(7):1391–9. doi: 10.1038/bjc.2014.416

38. Granier C, Dariane C, Combe P, Verkarre V, Urien S, Badoual C, et al. Tim-3 expression on tumor-infiltrating PD-1+ CD8+ T cells correlates with poor clinical outcome in renal cell carcinoma. *Cancer Res* (2017) 77(5):1075–82. doi: 10.1158/0008-5472.CAN-16-0274

39. Galon J, Costes A, Sanchez-Cabo F, Kirilovsky A, Mlecnik B, Lagorce-Pagès C, et al. Type, density, and location of immune cells within human colorectal tumors predict clinical outcome. *Science*. (2006) 313(5795):1960–4. doi: 10.1126/science.1129139

40. Pagès F, Mlecnik B, Marliot F, Bindea G, Ou F-S, Bifulco C, et al. International validation of the consensus immunoscore for the classification of colon cancer: a prognostic and accuracy study. *Lancet* (2018) 391(10135):2128–39. doi: 10.1016/S0140-6736(18)30789-X

41. Inaba K, Inaba M, Romani N, Aya H, Deguchi M, Ikehara S, et al. Generation of large numbers of dendritic cells from mouse bone marrow cultures supplemented with granulocyte/macrophage colony-stimulating factor. *J Exp Med* (1992) 176(6):1693–702. doi: 10.1084/jem.176.6.1693

42. Väyrynen JP, Vornanen JO, Sajanti S, Böhm JP, Tuomisto A, Mäkinen MJ. An improved image analysis method for cell counting lends credibility to the prognostic significance of T cells in colorectal cancer. *Virchows Archiv*. (2012) 460(5):455–65. doi: 10.1007/s00428-012-1232-0

43. Garaud S, Gu-Trantien C, Lodewyckx J-N, Boisson A, De Silva P, Buisseret L, et al. A simple and rapid protocol to non-enzymatically dissociate fresh human tissues for the analysis of infiltrating lymphocytes. *JoVE (Journal Visualized Experiments)* (2014) 94):e52392–e. doi: 10.3791/52392

44. Maecker HT, Trotter J. Flow cytometry controls, instrument setup, and the determination of positivity. *Cytometry Part A*. (2006) 69(9):1037–42. doi: 10.1002/cyto.a.20333

45. Salmon H, Franciszkiewicz K, Damotte D, Dieu-Nosjean M-C, Validire P, Trautmann A, et al. Matrix architecture defines the preferential localization and migration of T cells into the stroma of human lung tumors. *J Clin Invest* (2012) 122 (3):899–910. doi: 10.1172/JCI45817

46. Dunn GP, Koebel CM, Schreiber RD. Interferons, immunity and cancer immunoediting. *Nat Rev Immunol* (2006) 6(11):836. doi: 10.1038/nri1961

47. Garcia-Diaz A, Shin DS, Moreno BH, Saco J, Escuin-Ordinas H, Rodriguez GA, et al. Interferon receptor signaling pathways regulating PD-L1 and PD-L2 expression. *Cell Rep* (2017) 19(6):1189–201. doi: 10.1016/j.celrep.2017.04.031

48. Zhou F. Molecular mechanisms of IFN-γ to up-regulate MHC class I antigen processing and presentation. *Int Rev Immunol* (2009) 28(3-4):239–60. doi: 10.1080/08830180902978120

49. Antony PA, Piccirillo CA, Akpinarli A, Finkelstein SE, Speiss PJ, Surman DR, et al. CD8$^+$ T cell immunity against a Tumor/Self-antigen is augmented by CD4$^+$ T helper cells and hindered by naturally occurring T regulatory cells. *J Immunol* (2005) 174(5):2591–601. doi: 10.4049/jimmunol.174.5.2591

50. Sallusto F, Lenig D, Förster R, Lipp M, Lanzavecchia A. Two subsets of memory T lymphocytes with distinct homing potentials and effector functions. *Nature*. (1999) 401(6754):708–12. doi: 10.1038/44385

51. Tan JT, Ernst B, Kieper WC, LeRoy E, Sprent J, Surh CD. Interleukin (IL)-15 and IL-7 jointly regulate homeostatic proliferation of memory phenotype CD8+ cells but are not required for memory phenotype CD4+ cells. *J Exp Med* (2002) 195 (12):1523–32. doi: 10.1084/jem.20020066

52. Phillips S, Banerjea A, Feakins R, Li S, Bustin S, Dorudi S. Tumour-infiltrating lymphocytes in colorectal cancer with microsatellite instability are activated and cytotoxic. *Br J surgery*. (2004) 91(4):469–75. doi: 10.1002/bjs.4472

53. Pagès F, Berger A, Camus M, Sanchez-Cabo F, Costes A, Molidor R, et al. Effector memory T cells, early metastasis, and survival in colorectal cancer. *New Engl J Med* (2005) 353(25):2654–66. doi: 10.1056/NEJMoa051424

54. Crawford A, Angelosanto JM, Kao C, Doering TA, Odorizzi PM, Barnett BE, et al. Molecular and transcriptional basis of CD4+ T cell dysfunction during chronic infection. *Immunity*. (2014) 40(2):289–302. doi: 10.1016/j.immuni.2014.01.005

55. Park HJ, Park JS, Jeong YH, Son J, Ban YH, Lee B-H, et al. PD-1 upregulated on regulatory T cells during chronic virus infection enhances the suppression of CD8+ T cell immune response *via* the interaction with PD-L1 expressed on CD8+ T cells. *J Immunol* (2015) 194(12):5801–11. doi: 10.4049/jimmunol.1401936

56. Kim HR, Park HJ, Son J, Lee JG, Chung KY, Cho NH, et al. Tumor microenvironment dictates regulatory T cell phenotype: upregulated immune checkpoints reinforce suppressive function. *J ImmunoTherapy Cancer*. (2019) 7 (1):339. doi: 10.1186/s40425-019-0785-8

57. Banerjee A, Gordon SM, Intlekofer AM, Paley MA, Mooney EC, Lindsten T, et al. Cutting edge: the transcription factor eomesodermin enables CD8+ T cells to compete for the memory cell niche. *J Immunol* (2010) 185(9):4988–92. doi: 10.4049/jimmunol.1002042

58. Intlekofer AM, Takemoto N, Wherry EJ, Longworth SA, Northrup JT, Palanivel VR, et al. Effector and memory CD8+ T cell fate coupled by T-bet and eomesodermin. *Nat Immunol* (2005) 6(12):1236. doi: 10.1038/ni1268

59. Fourcade J, Sun Z, Benallaoua M, Guillaume P, Luescher IF, Sander C, et al. Upregulation of Tim-3 and PD-1 expression is associated with tumor antigen–specific CD8+ T cell dysfunction in melanoma patients. *J Exp Med* (2010) 207(10):2175–86. doi: 10.1084/jem.20100637

60. Schietinger A, Philip M, Krisnawan VE, Chiu EY, Delrow JJ, Basom RS, et al. Tumor-specific T cell dysfunction is a dynamic antigen-driven differentiation program initiated early during tumorigenesis. *Immunity*. (2016) 45(2):389–401. doi: 10.1016/j.immuni.2016.07.011

61. Sakuishi K, Apetoh L, Sullivan JM, Blazar BR, Kuchroo VK, Anderson AC. Targeting Tim-3 and PD-1 pathways to reverse T cell exhaustion and restore anti-tumor immunity. *J Exp Med* (2010) 207(10):2187–94. doi: 10.1084/jem.20100643

62. Ma J, Zheng B, Goswami S, Meng L, Zhang D, Cao C, et al. PD1 Hi CD8+ T cells correlate with exhausted signature and poor clinical outcome in hepatocellular carcinoma. *J ImmunoTherapy Cancer*. (2019) 7(1):1–15. doi: 10.1186/s40425-019-0814-7

63. Bachmann MF, Wolint P, Schwarz K, Jäger P, Oxenius A. Functional properties and lineage relationship of CD8+ T cell subsets identified by expression of IL-7 receptor α and CD62L. *J Immunol* (2005) 175(7):4686–96. doi: 10.4049/jimmunol.175.7.4686

64. Yi JS, Cox MA, Zajac AJ. T-Cell exhaustion: characteristics, causes and conversion. *Immunology*. (2010) 129(4):474–81. doi: 10.1111/j.1365-2567.2010.03255.x

65. Wherry EJ, Kurachi M. Molecular and cellular insights into T cell exhaustion. *Nat Rev Immunol* (2015) 15(8):486–99. doi: 10.1038/nri3862

66. Yadav M, Jhunjhunwala S, Phung QT, Lupardus P, Tanguay J, Bumbaca S, et al. Predicting immunogenic tumour mutations by combining mass spectrometry and exome sequencing. *Nature*. (2014) 515(7528):572–6. doi: 10.1038/nature14001

67. White HD, Roeder DA, Green WR. An immunodominant kb-restricted peptide from the p15E transmembrane protein of endogenous ecotropic murine leukemia virus (MuLV) AKR623 that restores susceptibility of a tumor line to anti-AKR/Gross MuLV cytotoxic T lymphocytes. *J virology*. (1994) 68(2):897–904. doi: 10.1128/jvi.68.2.897-904.1994

68. Yang JC, Perry-Lalley D. The envelope protein of an endogenous murine retrovirus is a tumor-associated T-cell antigen for multiple murine tumors. *J Immunother* (2000) 23(2):177–83. doi: 10.1097/00002371-200003000-00001

69. Kalluri R, Zeisberg M. Fibroblasts in cancer. *Nat Rev Cancer*. (2006) 6(5):392–401. doi: 10.1038/nrc1877

70. Tauriello DV, Palomo-Ponce S, Stork D, Berenguer-Llergo A, Badia-Ramentol J, Iglesias M, et al. TGFβ drives immune evasion in genetically reconstituted colon cancer metastasis. *Nature*. (2018) 554(7693):538. doi: 10.1038/nature25492

71. Gunderson AJ, Yamazaki T, McCarty K, Fox N, Phillips M, Alice A, et al. TGFβ suppresses CD8+ T cell expression of CXCR3 and tumor trafficking. *Nat Commun* (2020) 11(1):1–13. doi: 10.1038/s41467-020-15404-8

72. Calon A, Lonardo E, Berenguer-Llergo A, Espinet E, Hernando-Momblona X, Iglesias M, et al. Stromal gene expression defines poor-prognosis subtypes in colorectal cancer. *Nat Genet* (2015) 47(4):320–9. doi: 10.1038/ng.3225

73. Isella C, Terrasi A, Bellomo SE, Petti C, Galatola G, Muratore A, et al. Stromal contribution to the colorectal cancer transcriptome. *Nat Genet* (2015) 47(4):312–9. doi: 10.1038/ng.3224

74. Calon A, Espinet E, Palomo-Ponce S, Tauriello DV, Iglesias M, Céspedes MV, et al. Dependency of colorectal cancer on a TGF-β-driven program in stromal cells for metastasis initiation. *Cancer Cell* (2012) 22(5):571–84. doi: 10.1016/j.ccr.2012.08.013

75. Ladányi A, Somlai B, Gilde K, Fejös Z, Gaudi I, Tímár J. T-Cell activation marker expression on tumor-infiltrating lymphocytes as prognostic factor in cutaneous malignant melanoma. *Clin Cancer Res* (2004) 10(2):521–30. doi: 10.1158/1078-0432.CCR-1161-03

76. Moran AE, Polesso F, Weinberg AD. Immunotherapy expands and maintains the function of high-affinity tumor-infiltrating CD8 T cells in situ. *J Immunol* (2016) 197(6):2509–21. doi: 10.4049/jimmunol.1502659

77. Ganesan A-P, Clarke J, Wood O, Garrido-Martin EM, Chee SJ, Mellows T, et al. Tissue-resident memory features are linked to the magnitude of cytotoxic T cell responses in human lung cancer. *Nat Immunol* (2017) 18(8):940. doi: 10.1038/ni.3775

78. Schenkel JM, Masopust D. Tissue-resident memory T cells. *Immunity*. (2014) 41 (6):886–97. doi: 10.1016/j.immuni.2014.12.007

79. Mackay LK, Rahimpour A, Ma JZ, Collins N, Stock AT, Hafon M-L, et al. The developmental pathway for CD103+ CD8+ tissue-resident memory T cells of skin. *Nat Immunol* (2013) 14(12):1294–301. doi: 10.1038/ni.2744

80. Mackay LK, Wynne-Jones E, Freestone D, Pellicci DG, Mielke LA, Newman DM, et al. T-Box transcription factors combine with the cytokines TGF-β and IL-15 to control tissue-resident memory T cell fate. *Immunity*. (2015) 43(6):1101–11. doi: 10.1016/j.immuni.2015.11.008

81. Joshi NS, Cui W, Chandele A, Lee HK, Urso DR, Hagman J, et al. Inflammation directs memory precursor and short-lived effector CD8+ T cell fates *via* the graded expression of T-bet transcription factor. *Immunity*. (2007) 27(2):281–95. doi: 10.1016/j.immuni.2007.07.010

82. Sullivan BM, Juedes A, Szabo SJ, von Herrath M, Glimcher LH. Antigen-driven effector CD8 T cell function regulated by T-bet. *Proc Natl Acad Sci USA* (2003) 100 (26):15818–23. doi: 10.1073/pnas.2636938100

83. Bucks CM, Norton JA, Boesteanu AC, Mueller YM, Katsikis PD. Chronic antigen stimulation alone is sufficient to drive CD8+ T cell exhaustion. *J Immunol* (2009) 182(11):6697–708. doi: 10.4049/jimmunol.0800997

84. Juneja VR, McGuire KA, Manguso RT, LaFleur MW, Collins N, Haining WN, et al. PD-L1 on tumor cells is sufficient for immune evasion in immunogenic tumors and inhibits CD8 T cell cytotoxicity. *J Exp Med* (2017) 214(4):895–904. doi: 10.1084/jem.20160801

85. Llosa NJ, Cruise M, Tam A, Wicks EC, Hechenbleikner EM, Taube JM, et al. The vigorous immune microenvironment of microsatellite instable colon cancer is balanced by multiple counter-inhibitory checkpoints. *Cancer discovery*. (2015) 5(1):43–51. doi: 10.1158/2159-8290.CD-14-0863

86. Kachler K, Holzinger C, Trufa DI, Sirbu H, Finotto S. The role of Foxp3 and tbet co-expressing treg cells in lung carcinoma. *Oncoimmunology*. (2018) 7(8):e1456612. doi: 10.1080/2162402X.2018.1456612

87. Koch MA, Perdue NR, Killebrew JR, Urdahl KB, Campbell DJ. The transcription factor T-bet controls regulatory T cell homeostasis and function during type 1 inflammation. *Nat Immunol* (2009) 10(6):595. doi: 10.1038/ni.1731

88. Levine AG, Mendoza A, Hemmers S, Moltedo B, Niec RE, Schizas M, et al. Stability and function of regulatory T cells expressing the transcription factor T-bet. *Nature*. (2017) 546(7658):421–5. doi: 10.1038/nature22360

89. Freeman ZT, Nirschl TR, Hovelson DH, Johnston RJ, Engelhardt JJ, Selby MJ, et al. A conserved intratumoral regulatory T cell signature identifies 4-1BB as a pan-cancer target. *J Clin Invest* (2020) 130(3):1405–16. doi: 10.1172/JCI128672

90. Sakaguchi S. Naturally arising CD4+ regulatory T cells for immunologic self-tolerance and negative control of immune responses. *Annu Rev Immunol* (2004) 22:531–62. doi: 10.1146/annurev.immunol.21.120601.141122

91. Deaglio S, Dwyer KM, Gao W, Friedman D, Usheva A, Erat A, et al. Adenosine generation catalyzed by CD39 and CD73 expressed on regulatory T cells mediates immune suppression. *J Exp Med* (2007) 204(6):1257–65. doi: 10.1084/jem.20062512

92. Yan J, Zhang Y, Zhang J-P, Liang J, Li L, Zheng L. Tim-3 expression defines regulatory T cells in human tumors. *PloS One* (2013) 8(3):e58006. doi: 10.1371/journal.pone.0058006

93. Yarchoan M, Johnson BAIII, Lutz ER, Laheru DA, Jaffee EM. Targeting neoantigens to augment antitumour immunity. *Nat Rev Cancer*. (2017) 17(4):209–22. doi: 10.1038/nrc.2016.154

94. Smith CC, Selitsky SR, Chai S, Armistead PM, Vincent BG, Serody JS. Alternative tumour-specific antigens. *Nat Rev Cancer*. (2019) 19(8):465–78. doi: 10.1038/s41568-019-0162-4

95. Bonaventura P, Alcazer V, Mutez V, Tonon L, Martin J, Chuvin N, et al. Identification of shared tumor epitopes from endogenous retroviruses inducing high-avidity cytotoxic T cells for cancer immunotherapy. *Sci advances*. (2022) 8(4):eabj3671. doi: 10.1126/sciadv.abj3671

96. Laumont CM, Vincent K, Hesnard L, Audemard É, Bonneil É, Laverdure J-P, et al. Noncoding regions are the main source of targetable tumor-specific antigens. *Sci Trans Med* (2018) 10(470):eaau5516. doi: 10.1126/scitranslmed.aau5516

97. Cornelissen LA, Blanas A, van der Horst JC, Kruijssen L, Zaal A, O'Toole T, et al. Disruption of sialic acid metabolism drives tumor growth by augmenting CD8+ T cell apoptosis. *Int J cancer*. (2019) 144(9):2290–302. doi: 10.1002/ijc.32084

98. Hos BJ, Camps MG, Jvd B, Tondini E, Ende T, Ruano D, et al. Identification of a neo-epitope dominating endogenous CD8 T cell responses to MC-38 colorectal cancer. *OncoImmunology* (2019) 9(1):e1673125. doi: 10.1080/2162402X.2019.1673125

99. Ryan MH, Abrams SI. Characterization of CD8+ cytotoxic T lymphocyte/tumor cell interactions reflecting recognition of an endogenously expressed murine wild-type p53 determinant. *Cancer Immunology Immunother* (2001) 49(11):603–12. doi: 10.1007/s002620000156

100. Gameiro SR, Higgins JP, Dreher MR, Woods DL, Reddy G, Wood BJ, et al. Combination therapy with local radiofrequency ablation and systemic vaccine enhances antitumor immunity and mediates local and distal tumor regression. *PloS One* (2013) 8(7):e70417. doi: 10.1371/journal.pone.0070417

101. Park J-S, Kim H-S, Park M-Y, Kim C-H, Chung Y-J, Hong Y-K, et al. Topoisomerase II alpha as a universal tumor antigen: antitumor immunity in murine tumor models and h-2Kb-restricted T cell epitope. *Cancer immunology Immunother* (2010) 59(5):747–57. doi: 10.1007/s00262-009-0795-3

102. Iiizumi S, Ohtake J, Murakami N, Kouro T, Kawahara M, Isoda F, et al. Identification of novel HLA class II-restricted neoantigens derived from driver mutations. *Cancers*. (2019) 11(2):266. doi: 10.3390/cancers11020266

103. Alspach E, Lussier DM, Miceli AP, Kizhvatov I, DuPage M, Luoma AM, et al. MHC-II neoantigens shape tumour immunity and response to immunotherapy. *Nature*. (2019) 574(7780):696–701. doi: 10.1038/s41586-019-1671-8

104. Veatch JR, Jesernig BL, Kargl J, Fitzgibbon M, Lee SM, Baik C, et al. Endogenous CD4+ T cells recognize neoantigens in lung cancer patients, including recurrent oncogenic KRAS and ERBB2 (Her2) driver mutations. *Cancer Immunol Res* (2019) 7(6):910–22. doi: 10.1158/2326-6066.CIR-18-0402

105. Castle JC, Kreiter S, Diekmann J, Löwer M, Van de Roemer N, de Graaf J, et al. Exploiting the mutanome for tumor vaccination. *Cancer Res* (2012) 72(5):1081–91. doi: 10.1158/0008-5472.CAN-11-3722

106. Kreiter S, Vormehr M, Van de Roemer N, Diken M, Löwer M, Diekmann J, et al. Mutant MHC class II epitopes drive therapeutic immune responses to cancer. *Nature*. (2015) 520(7549):692–6. doi: 10.1038/nature14426

107. Dunn GP, Old LJ, Schreiber RD. The three Es of cancer immunoediting. *Annu Rev Immunol* (2004) 22:329–60. doi: 10.1146/annurev.immunol.22.012703.104803

108. Sharma P, Hu-Lieskovan S, Wargo JA, Ribas A. Primary, adaptive, and acquired resistance to cancer immunotherapy. *Cell*. (2017) 168(4):707–23. doi: 10.1016/j.cell.2017.01.017

109. Williford J-M, Ishihara J, Ishihara A, Mansurov A, Hosseinchi P, Marchell TM, et al. Recruitment of CD103+ dendritic cells via tumor-targeted chemokine delivery enhances efficacy of checkpoint inhibitor immunotherapy. *Sci advances*. (2019) 5(12): eaay1357. doi: 10.1126/sciadv.aay1357

110. Tang H, Wang Y, Chlewicki LK, Zhang Y, Guo J, Liang W, et al. Facilitating T cell infiltration in tumor microenvironment overcomes resistance to PD-L1 blockade. *Cancer Cell* (2016) 29(3):285–96. doi: 10.1016/j.ccell.2016.02.004

111. Taylor MA, Hughes AM, Walton J, Coenen-Stass AM, Magiera L, Mooney L, et al. Longitudinal immune characterization of syngeneic tumor models to enable model selection for immune oncology drug discovery. *J immunotherapy cancer*. (2019) 7(1):1–16. doi: 10.1186/s40425-019-0794-7

112. Deng L, Liang H, Burnette B, Beckett M, Darga T, Weichselbaum RR, et al. Irradiation and anti–PD-L1 treatment synergistically promote antitumor immunity in mice. *J Clin Invest* (2014) 124(2):687–95. doi: 10.1172/JCI67313

113. Ngiow SF, von Scheidt B, Akiba H, Yagita H, Teng MW, Smyth MJ. Anti-TIM3 antibody promotes T cell IFN-γ–mediated antitumor immunity and suppresses established tumors. *Cancer Res* (2011) 71(10):3540–51. doi: 10.1158/0008-5472.CAN-11-0096

114. Jain A, Song R, Wakeland EK, Pasare C. T Cell-intrinsic IL-1R signaling licenses effector cytokine production by memory CD4 T cells. *Nat Commun* (2018) 9 (1):1–13. doi: 10.1038/s41467-018-05489-7

115. Smyth MJ, Ngiow SF, Ribas A, Teng MW. Combination cancer immunotherapies tailored to the tumour microenvironment. *Nat Rev Clin Oncol* (2016) 13(3):143–58. doi: 10.1038/nrclinonc.2015.209

frontiers | Frontiers in Immunology

TYPE Review
PUBLISHED 09 May 2023
DOI 10.3389/fimmu.2023.1183895

Check for updates

OPEN ACCESS

EDITED BY
Silke Paust,
The Scripps Research Institute,
United States

REVIEWED BY
Esraah Alharris,
University of Al-Qadisiyah, Iraq
Yoshie Kametani,
Tokai University, Japan

*CORRESPONDENCE
Fei Zeng
1055361571@qq.com
Junrong Zou
ydzjr@gmu.edu.cn

RECEIVED 10 March 2023
ACCEPTED 24 April 2023
PUBLISHED 09 May 2023

CITATION
He H, Luo H, Xu H, Qian B, Zou X, Zhang G, Zeng F and Zou J (2023) Preclinical models and evaluation criteria of prostatitis.
Front. Immunol. 14:1183895.
doi: 10.3389/fimmu.2023.1183895

COPYRIGHT
© 2023 He, Luo, Xu, Qian, Zou, Zhang, Zeng and Zou. This is an open-access article distributed under the terms of the Creative Commons Attribution License (CC BY). The use, distribution or reproduction in other forums is permitted, provided the original author(s) and the copyright owner(s) are credited and that the original publication in this journal is cited, in accordance with accepted academic practice. No use, distribution or reproduction is permitted which does not comply with these terms.

Preclinical models and evaluation criteria of prostatitis

Hailan He[1,2], Hui Luo[1,2], Hui Xu[2,3,4], Biao Qian[2,3,4], Xiaofeng Zou[2,3,4], Guoxi Zhang[2,3,4], Fei Zeng[1]* and Junrong Zou[2,3,4]*

[1]The First Clinical College, Gannan Medical University, Ganzhou, Jiangxi, China, [2]Department of Urology, The First Affiliated Hospital of Gannan Medical University, Ganzhou, Jiangxi, China, [3]Institute of Urology, The First Affiliated Hospital of Gannan Medical University, Ganzhou, Jiangxi, China, [4]Department of Urology, Jiangxi Engineering Technology Research Center of Calculi Prevention, Ganzhou, Jiangxi, China

Prostatitis is a common urological condition that affects almost half of all men at some point in their life. The prostate gland has a dense nerve supply that contributes to the production of fluid to nourish sperm and the mechanism to switch between urination and ejaculation. Prostatitis can cause frequent urination, pelvic pain, and even infertility. Long-term prostatitis increases the risk of prostate cancer and benign prostate hyperplasia. Chronic non-bacterial prostatitis presents a complex pathogenesis, which has challenged medical research. Experimental studies of prostatitis require appropriate preclinical models. This review aimed to summarize and compare preclinical models of prostatitis based on their methods, success rate, evaluation, and range of application. The objective of this study is to provide a comprehensive understanding of prostatitis and advance basic research.

KEYWORDS

prostatitis, chronic non-bacterial prostatitis, animal models, evaluation criteria, infectious prostatitis

1 Introduction

Prostatitis is an inflammatory disease of the prostate glands with a variety of complicated symptoms, including generalized pain in the pelvic and lower abdomen areas and obstructive and erectile dysfunction (1). Prostatitis is classified into four categories: acute bacterial prostatitis (I)), chronic bacterial prostatitis (II), chronic prostatitis/chronic pelvic pain syndrome (CP/CPPS)(III), and asymptomatic inflammatory prostatitis (IV) (Table 1). Type III CP/CPPS is further divided into IIIA and IIIB based on the presence or absence of leukocyte infiltration in prostate specimens (3). The prevalence of prostatitis is 8–25% in the urological surgery clinic, with Type III CP/CPPS being the most common, accounting for about 90–95% of cases (2, 4). Prostatitis, especially non-bacterial ones, is etiologically and pathogenetically complex. Prostatitis is associated with infectious and non-bacterial factors, such as spontaneousness, immune disorders, hormones, diet, stress, chemicals, urine reflux, exosomes, and autonomic nerves.

There are several treatments for prostatitis, including antibiotics, painkillers, Alpha blockers, physiotherapy, prostate massage and lifestyle changes. These current treatments for prostatitis depend largely on the underlying cause and severity. Antibiotics fight bacterial infections; painkillers relieve pain and discomfort, and Alpha blockers relax the muscles around the prostate and relieve urinary symptoms. In the pelvic region, physiotherapy reduces pain and improves muscle function (5, 6). However, most treatments treat the symptoms but not the root cause, mainly because the mechanism is not clear. The causative factors of prostatitis are so diverse that it is essential to promptly choose the associated preclinical models from the various models to easily and efficiently investigate the condition. This review compared and summarized anatomy and histology of the human and rodent prostate, site of origin, function, symptoms, progression and immune system, as well as current preclinical models of prostatitis in method, successful rate, evaluation, and range of application.

2 Differences between men and rodents' prostatitis

2.1 Prostate anatomy, histology and sites of prostatitis

The human prostate is a complex gland with diverse histological structures situated below the urinary bladder and anterior to the rectum. Comprising the prostatic urinary tract, the prostate gland encompasses the central zone (CZ), peripheral zone (PZ), and transitional zone (TZ), with the seminal vesicles located on both sides of the foundation. The CZ constitutes most of the base of the prostate and surrounds the ejaculatory ducts, while the PZ envelopes most of the central area and stretches caudally, partially enveloping the distal part of the urethra (7).

The glandular epithelium is composed of acinus and ducts lined with three types of cells, including luminal cells, basal cells, and neuroendocrine cells. Luminal cells are specialized cells that secrete a variety of products into the lumen, including prostate-specific antigen (PSA). Immunohistochemistry for PSA is strongly positive in luminal cells. The interstitium of the prostate is fibromuscular with abundant smooth muscle cells mixed with fibroblasts, blood vessels, and nerves. Notably, adipose tissue is absent in the prostate. This fibromuscular interstitium is much more pronounced than the comparatively thin fibromuscular interstitium found in the mouse prostate (8).

In rodents, the prostate is also located below the bladder, enveloping the prostatic urethra, but it does not form a singular anatomical structure like in humans. Instead, the rodent prostate consists of four distinct lobular structures: the anterior lobe (also known as the coagulation gland), dorsal lobe, ventral lobe, and lateral lobe (Figure 1). The final appearance of each lobe is different due to differences in lobe-specific branching morphogenesis (9). The cytological distribution of rodent prostate tissue is of the identical type, but PSA is expressed and secreted in human, rather than mouse, intraluminal prostate cells. The most striking histological difference lies in the stromal component, which is highly developed as a pre-fibro-muscular region in humans, whereas in mice, it is sparse with very few smooth muscle cells. Moreover, the main histological features necessary for the different murine lobes vary (10).

Besides, the human PZ is a primary site of prostatitis and prostate cancer (7). The human prostate usually displays a variety of modifications in the epithelium and stroma. Atrophy of the epithelium and hyperplasia of the basal cells are extremely frequent. Chronic inflammation is also very prevalent, with varying degrees of acute inflammation seen, ranging from localized to widespread, forming abscesses (8). However, in rodents, the bulk of prostatitis occurs in the dorsal, ventral, and lateral lobes, with little inflammation occurring in the anterior ones. It has been shown that the proximal and distal regions of each prostate lobe in mice are most related to the ductal and acinar regions, respectively, and that the mouse lateral lobes are most closely related to the peripheral region in humans (11). Immune-mediated prostatitis models, hormone-disordered prostatitis models, and diet-related models appear to have dorsolateral/ventral lobe prostatitis in most models, similar to human prostatitis. This is consistent with the frequent occurrence of prostatitis in the peripheral zone, which facilitates the study of prostatitis. However, in the autonomic disorder model, prostatitis appears to occur predominantly in the anterior lobes.

TABLE 1 Categories of prostatitis.

Categories		Symptoms/analysis		Prevalence
Infectious prostatitis (I and II)		Acute or recurrent symptoms, with the same microgram		–
Chronic prostatitis/chronic pelvic pain syndrome (CP/CPPS) (III)	Inflammation (IIIA)	Leukocytes found in testing samples	No demonstrations of infection but recurrent symptoms	90%–95% (2)
	Non-inflammation (IIIB)	No leukocytes found in testing samples		
Asymptomatic inflammatory prostatitis(IV)		Leukocytes found in testing samples without related-symptoms		–

Symbol "-" means that there is no relevant literature to provide data.

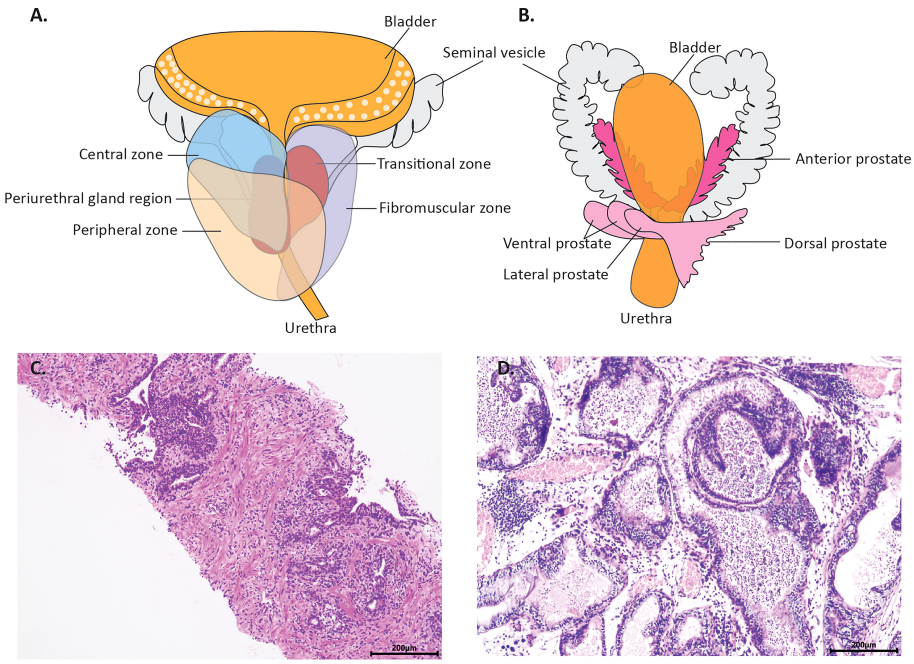

FIGURE 1
The anatomy of normal prostate and microscopic changes of prostatitis in a man and rodent. **(A)** is the schema human prostate. It consists of the central zone (CZ), the peripheral zone (PZ) and the transitional zone (TZ). **(B)** is the schema of rodents' prostate. It consists of four distinct lobular structures: the anterior lobe the dorsal lobe, the ventral lobe and the lateral lobe, distributed on the left and right flanks. **(C)** shows the typical histology of prostatitis from a biopsy specimen, with inflammatory cell infiltration between the epithelial cells and in the interstitium. **(D)** shows the typical histology of prostatitis in a gonadectomized rats, with inflammatory cells in the interstitium and lumen.

2.2 Immune response during prostatitis

The immune response to antigenic stimulation in humans and rodents is broadly similar, involving cellular and humoral immunity (12). However, there are significant differences in the development, activation, and antigen response of the innate and adaptive immune systems in humans and rodents (13). The proportion of immune cells involved in inflammatory responses also varies, with neutrophils being more abundant than lymphocytes in humans, and lymphocytes being more dominant in mice (13). Notably, the rodent immune system is more similar to that of neonatal humans, with lower innate immune activation and naiver lymphocytes (14). While rodent models of prostatitis may not consistently reflect human immune system responses, they remain valuable tools for investigating the pathogenesis and treatment of the disease. Immunodeficient mice, in particular, have proven useful in a variety of medical research areas, including preclinical trials, regenerative medicine, transplant rejection studies, and immunotherapy (15).

Overall, current models of prostatitis have limitations. The anatomy, cytology, pathogenic zone, and disease pathogenesis of human and rodent prostate tissue differ, and rodent models fail to fully mimic the age of onset of human prostatitis. These limitations stem mainly from evolutionary differences between humans and rodents. However, the rodent prostate LP is most similar to the human peripheral zone, and immune-mediated, hormone-disordered, and diet-related models of prostatitis often show DLP/VP involvement, which are also affected in human prostatitis. This highlights the potential value of rodent models for studying the disease. This review focuses on currently reported models of prostatitis, including those involving specific bacterial infections, aging, autoimmune responses, hormonal disorders, dietary metabolic problems, stress-induced, chemical injury, exosome injection, mechanical introduction, and autonomic abnormalities. However, no definitive models of prostatitis caused by psychiatric, frequent sexual intercourse, pelvic floor dysfunction, or other factors have been reported in animal models.

3 Infectious prostatitis models

Infectious prostatitis is a disease caused by bacteria that infects the prostate gland. This inflammation has acute or chronic symptoms. The common pathogenesis is pathogens infection, including UPEC strain CP9 or C85, p. aeruginosa strain ATCC 27853, E. coli, or Chlamydia psittaci.

3.1 Acute bacterial prostatitis (I)

The prostate is predisposed to acute inflammation caused by bacterial infection. In rats and mice, pathogens damage tissues, causing acute inflammation, including UPEC strains *CP9* and *C85* (16), *p.aeruginosa* strain ATCC 27853 (17), *E. coli* (18–22) or *Chlamydia psittaci* (23). Acute bacterial prostatitis provides a better understanding of pathological changes, the location of

pathogen entry, and the relationship between genetic background and bacterial invasion. Prostates can be infected by pathogens in two different ways. Mice can be injected with bacteria into their prostates (16, 18, 19, 23), or Wistar rats or Sprague-Dawley rats can be injected with pathogens through catheters into their prostates (17). During the first 18 days after infection, acute bacterial prostatitis causes lesions in the dorsolateral and ventral lobes, characterized by inflammation in the glandular lumens and interstitial tissue. After day 18, there was little evidence of inflammation (18). The intensity and concentration of pathogens determine the severity of acute prostatitis. Most bacteria damage the prostate of mice over 80%; specifically, *Chlamydia psittaci* and *E coli* infections cause 100% of mice to develop acute prostatitis (16, 22, 23).

3.2 Chronic bacterial prostatitis(II)

Prostatic damage caused by pathogens causes chronic bacterial prostatitis, typically taking 1–3 months longer. Pathology involves neutrophils and mononuclear cells infiltration in the interstitium or glandular cavity, as well as abnormal lesions of prostate tissue including occlusive changes and atrophy in acinus, epithelial hyperplasia and dysplasia. Chronic inflammation is challenging to cure, recurrent, and can be studied using mouse and rat chronic models for therapeutic research; after two months of exposure to *Escherichia coli Z17* (O2: K1: H-), 86.7% or 62% of Wistar rats developed chronic inflammation (24, 25), compared to 100% two weeks after *Chlamydia psittaci* infection (23). Two weeks after the onset of symptoms, Wistar rats displayed severe inflammation in the dorsolateral and ventral lobes, and 2–3 months later, they developed mild monocyte infiltration (23). C3H/HeOuJ mice manifested acute prostatitis with *E. coli* on the fifth day. It developed chronic inflammation 12 weeks later, characterized by reactive epithelial changes, including epithelial hyperplasia and dysplasia, as well as the level of Ki-67 increased which was known as a cellular marker for proliferation (21).

In acute and chronic inflammation, rodents are linked and differentiated from humans. In rodent bacterial prostatitis, there is a significant increase in neutrophils and macrophages in the interstitial, intraluminal or interepithelial cells of the prostate in the early acute phase, with T lymphocytes and macrophages infiltrating the tissue in the late acute stage (26). Yet, in humans, an acute inflammatory response occurs after the organism has recognized bacteria, stimulating the recruitment of neutrophils, monocytes and macrophages at the site of prostate infection (27, 28).

Upon development of chronic prostatitis, in the human prostate, the majority of infiltrating inflammatory cells are chronically activated T lymphocytes and macrophages (29, 30). Mouse models of inflammation show an infiltrative component closely resembling that of human prostate inflammation. A large number of lymphocytes infiltrate the mesenchyme, between the epithelium or in the lumen of the gland, including Th1, Th2 and Th17 cells (26, 31).

Prostatitis is usually caused by bacterial infection, and chronic bacterial prostatitis is often the result of prolonged acute infection. The lipid-like membrane barrier on the prostate surface is highly resistant to some therapeutic antibiotics, thus reducing desired medical concentrations and limiting potential therapeutic levels. Therefore, it is essential to develop models of bacterial prostatitis for research into a more effective treatment. While animal models are similar to humans regarding the clinical pattern of morbidity and histological lesion, they are predisposed to severe infection to death and remove bacteria so that chronic prostatitis is not quickly developed. Wistar or Sprague-Dawley rats are more susceptible to acute prostatitis (100%) than chronic prostatitis (50% or 62%). However, C3H/HeOuJ mice are more acceptable because they can develop chronic inflammation in the prostates and acute inflammation, and their success rate is 100%. These mice can be applied to the search for effective therapies. The advantages of cell models in noble medical analysis are that they are inexpensive, easy to access, and stable compared to mice. Cell models are also time-saving, successful, and can be used effectively for microscopic studies. However, these simple models do not represent the actual condition of complex multisystem patients. Optimization of animal and cell models should consider their limitations and maximize their benefits.

4 Non-bacterial prostatitis models

Chronic prostatitis has more complicated pathological changes than infectious prostatitis and is more obscure. Currently, there are several accepted animal models, such as spontaneousness, immune mediation, hormonal disorders, diet, lactation, stress, chemicals, urinal reflux, autonomic nervous dysfunction, and exosome (Figure 2).

4.1 Spontaneous prostatitis models

Rats and mice are predisposed to chronic non-bacterial prostatitis according to their genetic background and age in the absence of any treatment. This process takes a long time, but it is easy, and there are no medications or traumatic treatments. Inflammatory cells can be studied as part of the immune response by using this technique (32), the comparison of inflammation under different gene backgrounds (33, 34), different parts of inflammatory reaction in the prostate (33), the relationship between the occurrence and development of prostatitis and age (35, 36), oxidative stress response (37), and the role of specific genes in the occurrence and development of chronic prostatitis can also be explored. Rats of distinct types were more prone to spontaneous prostatitis than others Lewis rats are known to have an elevated susceptibility to the induction of many experimental inflammatory diseases such as inducible arthritis, glomerulonephritis, experimental myocarditis, autoimmune encephalitis, autoimmune thyroiditis and small bowel colitis (38). A total of 72% of Lewis rats developed spontaneous prostatitis by the age of 10–13 months (39, 40). In Wistar rats aged 10-13 months, 27% had spontaneous

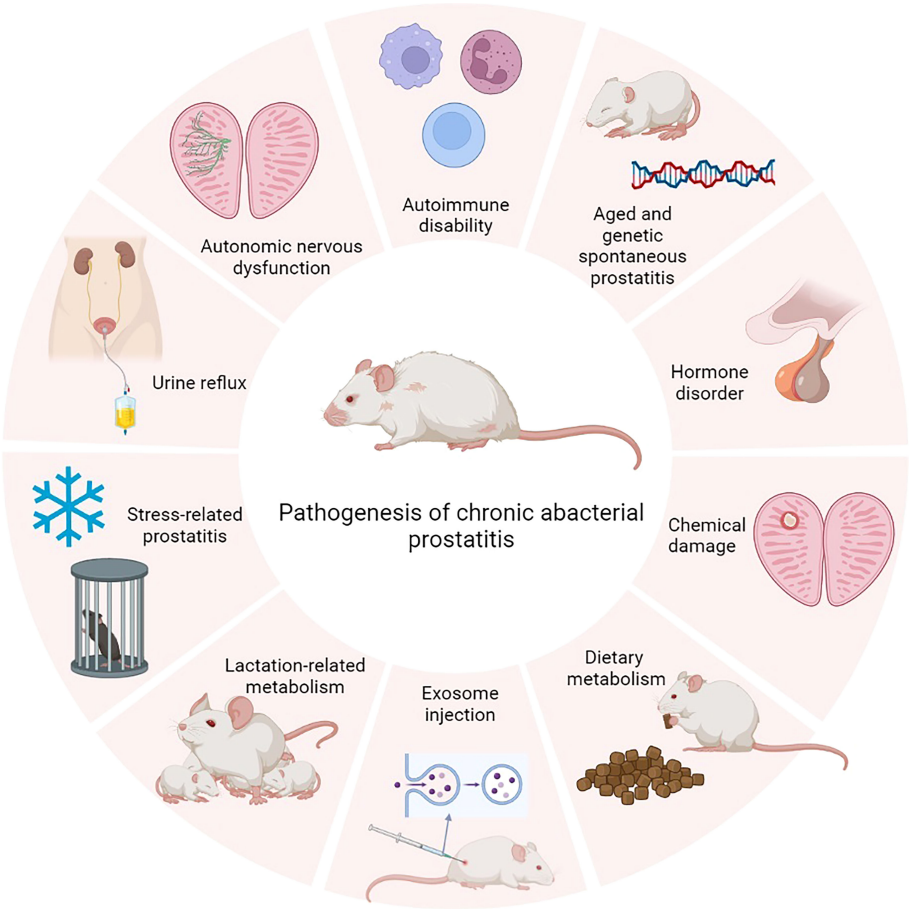

FIGURE 2
The pathogenesis of chronic prostatitis.

prostatitis (32, 39). After 13 weeks, 80% of older or younger developed spontaneous inflammation (41). In contrast to them, however, Sprague-Dawley rats are less sensitive to autoimmune related diseases. Only 16.6% of adult male Sprague-Dawley rats manifested prostatitis after a regular diet for 11 weeks (34). Noble rats of 9 months also developed prostatitis, but the success rate was uncertain (37).

Mice can be used to study prostatitis severity across genetic backgrounds. Spontaneous prostatitis occurred in Nonobese Diabetes-Resistant (NOR) and Nonobese Diabetic (NOD) mice at seven weeks of age, which became more severe and remained stable at 28 weeks (35, 36). They have a genetic susceptibility to autoimmune diabetes, and also have a tendency to other autoimmune diseases, including autoimmune thyroid disease and salpingitis (42). NZB (New Zealand Black, H-2d) mice are typically characterized by markedly receding thymus tissue, a functional defect in thymic epithelial cells compared to normal mice and an important autoimmune susceptibility factor (43). NZB strains also showed prostatitis at 14 weeks but were less sensitive and showed a lower inflammation score than NOD mice. At 18 weeks, prostatitis disappeared (36).

In summary, this spontaneous prostatitis occurred under natural conditions with fewer artificial factors and reduced artificial trauma. The models are stable and can be maintained for an extended period. This spontaneous non-bacterial prostatitis has a pathological picture similar to that of clinical patients and therefore is suitable for human chronic prostatitis research. Accordingly, it is more reliable than other models. Wistar rats can develop spontaneous prostatitis because they are more likely to succeed (80%), take less time to develop (13 weeks), and have a pathological picture closer to that of clinical patients. It is important to note that this model has numerous uncontrolled experimental factors and low targetability. The repeatability of this model is poor with prostatitis, as it takes three to thirteen months.

4.2 Immune-mediated prostatitis models

Autoimmunity is a double-edged sword. Too much strength or disorder can cause damage to the body's tissues, including the prostate. Thymectomy, autoimmunity, and specific cell transplants can cause immune-mediated prostatitis, which was studied to

determine the relationship between immune reaction and prostatitis pathogenesis.

4.2.1 Thymectomy-related prostatitis models

The nonactivated suppressor T cells played a crucial role in preventing spontaneous prostatitis. CD4+CD25+ T cells appear as energetic regulators in the peripheral immune system at three days. After thymectomy for the postnatal three days, regulatory CD4+CD25+ T cells were significantly reduced, and spontaneous prostatitis occurred (Figure 3) (44–48). There is a correlation between autoimmune disorders and prostatitis that can be explored. Besides suffering from prostatitis after a thymectomy three days after birth, mice also suffered from inflammation in other organs after 150 days due to a systemic immune system disorder. A total of 73% (C3H/HeMs x 129/J) F1 developed prostatitis in this way, characterized by lymphocyte infiltration and parasecretion in epithelial cells within the anterior and dorsal lobes. The mice also developed gastritis, epididymitis, sialadenitis, and thyroiditis (44, 45). It was found that 58.6% of B6A mice also presented with lacrimal gland adenitis in addition to prostatitis (46). A total of 73% of NZM2328 mice had prostatitis along with thyroiditis and dacryoadenitis (48). Postnatal three-day thymectomy of SNF1 mice was associated with 61.5% prostatitis, orchitis, and aortitis (47).

This model provides an opportunity to study the basic principles of suppressor T cells, activated T cells, and androgen involved in self-tolerance. NZM2328 mice are more predisposed to prostatitis (73%) than other strains to investigate the autoimmune pathogenesis and function of various subpopulation T cells in prostatitis. However, it is complex and time-consuming to perform and administer a thymectomy due to the need for tracheal intubation and respiratory support. Furthermore, they have prostatitis and respond to other organs such as the testis, aorta, thyroid, lacrimal gland, and others.

4.2.2 Experimental autoimmune prostatitis models

Experimental autoimmune prostatitis (EAP) is a disease that can be viewed as an experimental model of non-bacterial prostatitis in humans. Using specific antigens to induce autoimmunity produces specific autoantibodies to attack prostate tissue (Figure 4). Therefore, the prostate tissue is subsequently damaged, resulting in prostatitis. Specific antigens include male accessory gland (MAG) homogenate (prostate, seminal vesicles, and coagulating glands) (35, 49–59), prostate extract (36, 60–63), peptide T2 (64–66), rat prostatic steroid-binding proteins(PSBP) (35, 59, 61, 67–69), prostatic acid phosphatase(PAP) (70), ethanol plus dinitrobenzene sulfonic acid (DNBS) (71, 72), MBP-SVS2 or MBP (73) or prostate-specific proteins p25 (74). To increase the likelihood of prostatitis, adjuvants that boost the immune response are often used, such as CFA, aluminum hydroxide adjuvant, and liposomes. It is important to note that antigenic immunity can occur within a species or among species. Prostate tissue from mice or rats can be extracted to induce autoimmune disorders in the

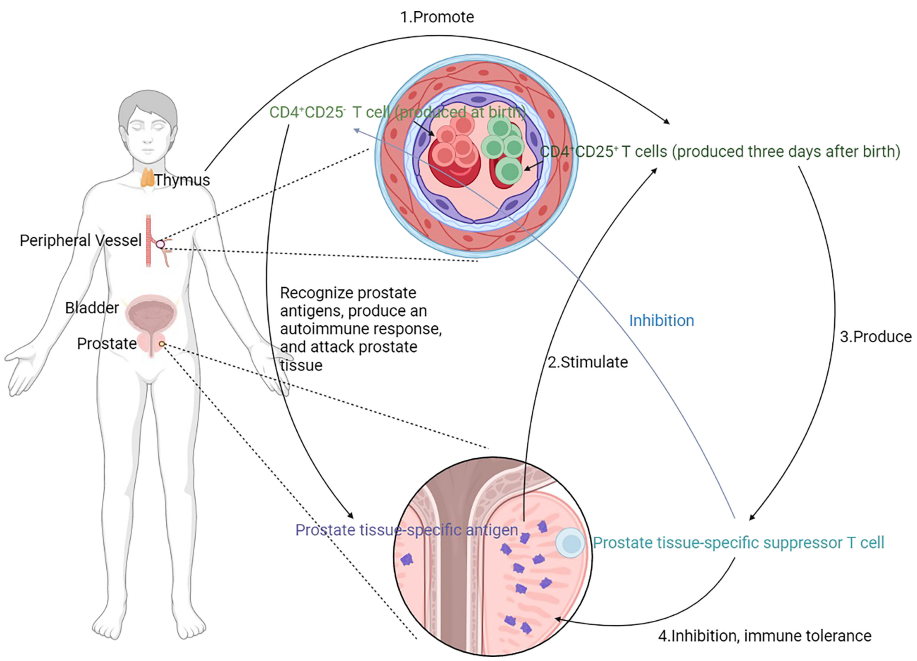

FIGURE 3
Mechanism of prostatitis induced by thymectomy. CD4+ T cells are crucial in the development of prostatitis. CD4+ CD25- T cells recognize prostate tissue-specific antigens and produce autoimmunity to attack prostate tissue. CD4+CD25+ T cells, on the other hand, inhibit this autoimmune response and only appear in the peripheral immune system 3 days after birth, stimulated by prostate tissue-specific antigens and promoted by the thymus. Prostate tissue-specific suppressor T cells are generated to suppress prostate tissue-specific antigens induced autoimmunity and produce immune tolerance. Moreover, the prostate tissue-specific suppressor T cells inhibit CD4+ CD25- T cells. Removal of the thymus at 3 days of life leads to an increase in CD4+CD25+ T cells, and a relative increase in CD4+CD25- T cells, which leads to an imbalance and the development of prostatitis.

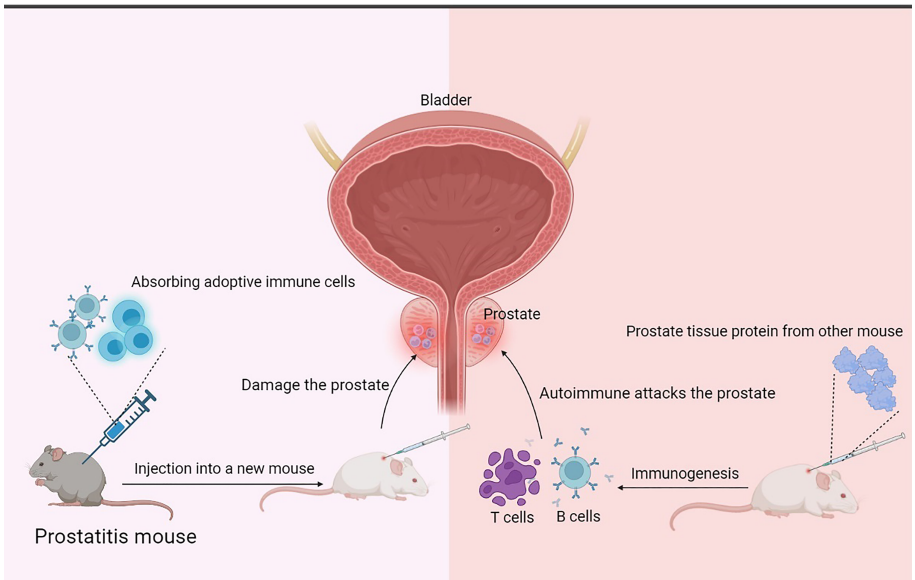

FIGURE 4
Mechanism of prostatitis induced by injection of prostatic antigen or adoptive immune cells. The principle of the EAP model is that proteins extracted from rat or mouse prostate tissue are injected subcutaneously to stimulate the mouse's autoimmune response to produce inflammatory cells such as B cells and T cells associated with the injected prostate proteins, which migrate to the prostate tissue, infiltrate, and attack the prostate tissue, causing prostate damage and prostatitis. Cell transplantation-related prostatitis models are based on the principle that relevant immune cells are extracted from a model that has already produced prostatitis and injected into new mice, and that these adaptive immune cells may be specific enough to specifically travel to prostate tissue and attack it, causing damage and prostatitis.

same species of mice or rats (49–53, 60–63, 67, 69, 75), and prostate tissue from rats can also be used to induce other species of mice (35, 36, 56, 58, 59, 68). Both methods can induce prostatitis. Autoimmune reactions are one of the pathogenesis of chronic prostatitis that has been widely accepted and adopted. Furthermore, the procedure is relatively straightforward and requires two to three injections. There is less sensitivity in rats, with 38% of Wistar rats and 33% of Lewis rats presenting prostatitis.

Mice were more susceptible to EAP models than rats, including nonobese diabetic (NOD) (35, 36, 56, 58, 59, 68, 69, 76), C57BL/6 (56, 63, 65, 66, 72, 73), C57bl/6 lpr, SJL, AJ (63), NZB, SWR (36), BALB/c (36, 63, 69) and SWXJ (H-2q, s) (74). Most of these mice have autoimmune susceptibility. NOD mice have a genetic susceptibility to autoimmune diabetes and a predisposition to other autoimmune diseases, including autoimmune thyroid disease. C57bl/6 lpr mice develop within 3-6 moths a range of abnormalities of congenital disease, which describe the 'lpr phenotype' and permit them to progress to autoimmune abnormalities and multi-organ damage (77–79). Swiss James Lambert(SJL)mouse (80–82), A/J mouse (83), SWR mouse (84) and SWXJ (H-2q, s) mouse (85) have also been used for their increased susceptibility to autoimmune disease. The New Zealand Black (NZB) strain has the most similar clinical disease and genetic complexity to human disease (86, 87). BALB/c and C57Bl/6 mice also have autoimmune susceptibility because of a specific genetic background. The two mice have distinct structural and functional parameters of the immune system. secretion of IL-2, IL-3, IL-4, IL-10 and TNF-α is significantly higher in BALB/c mice than in C57Bl/6 mice. C57Bl/6 mice possess higher splenic NK cell inhibitory activity (88). Thus, injection of specific prostate tissue antigens triggers an autoimmune response in these mice, whereby the prostate tissue is assaulted by inflammatory cells, damage occurs, and prostatitis develops. These autoimmune diseases in mice often entail inflammation of multiple organs. The issue of what specific pathophysiological features of the prostate gland lead to prostatitis is not conclusive. However, it has been suggested that IgG4-related disease (IgG4-RD) manifests as autoimmune pancreatitis (AIP), but also as prostatitis. Histopathologically, there is a dense inflammatory infiltrate in the prostate interstitium and immunohistochemical morphometry shows 10 IgG4-positive plasma cells/high-power fields (HPF). There may be specific genes in the prostate that lead to inflammatory cell infiltration in the prostate tissue in autoimmunity, resulting in prostatitis (89). It has also been shown that prostate-specific antigen (PSA)-related autoimmune reactions develop, leading to the development of prostatitis (90).

C57BL/6 mice are commonly used for this model. The prostate supernatant was extracted from rats and emulsified with an equal quantity of complete Freund adjuvant (CFA), with a final antigen concentration diluted to more than 500 μg/ml. CFA is an immune adjuvant that enhances the immune response. It was challenging to induce autoimmune prostatitis with too low concentrations of prostate tissue extract, indicating that antigen concentration was the key to successful modeling. C57BL/6 mice have been subcutaneously injected into multiple sites with 0.5ml of this extract and 1 ng/200 μl Bordetella pertussis (BP) toxin. BP induced an autoimmune response in mice. After 30 days, all of them were perceived to have lymphocytic infiltration in the prostatic stroma, periglandular and perivascular areas (63).

The autoimmune disorder is a pathogenesis of chronic abacterial prostatitis that has been widely accepted and adopted. Treatment and immune changes are currently unclear and require more comprehensive studies in EAP models. C57BL/6 mice immunized with singular homologous prostate extracts are more likely to develop prostatitis than rats, with 100% showing signs of inflammation after 30 days. Nevertheless, this model had many disadvantages, such as the experiment always lasted 30-50 days, even 1-3 months, so the exact duration was not known; intricate factors affected the temporal consumption. The success of this experiment depended on the type of antigen, strain, and age of the rats, but also on the frequency, time, and parts of the inoculation. Due to 1–3 times immunizations and long or short interval time to establish prostatitis models, the method was complicated; the success rate differed from 33% to 100%.

4.2.3 Cell transplantation-related prostatitis models

Cell transplantation-related prostatitis models are animals inoculated with isolated splenocytes from treated animals (immunization, hormonal treatment, or special gene background) (45, 73, 75, 91–93), GMTAMP-C1/C2 cells, TRAMP-C1/C2 cells (94), B7-TC1 cells (95) or T-cell receptor transgenic T-cells (91, 96–98). These splenocytes can attack the prostate tissue, leaving it damaged and inflamed (Figure 4).

The role of T and B cells in the pathogenesis of chronic prostatitis can be investigated using a cell transplantation model. It is also important to study and understand the function of immunocytes in chronic prostatitis. These observations suggest that immunological induction of prostatitis requires specific antigen organs, depletion of specific immune suppressive cells, or activation of suppressor cells. These models illustrate the basic principles of specific immunity, immune tolerance, and immune activity of chronic prostatitis. They also play an important role in researching the relationship between hormonal therapy and immunity, prostate cancer, and inflammation. To conduct research on the T cell response to specific antigens within prostatitis conveniently and proficiently, transgenic mice expressing prostate ovalbumin (POET) mice can generate a high level of membrane-bound ovalbumin/transferrin receptor fusion protein (mOVA) in prostate lobes under the action of ARR2PB promotors. Adaptive transfer with mOVA-specific T cells, will result in specific immunity (91, 96–98). This model can be applied to T cells that respond to specific organs of antigens. The POET mouse specifically contains mOVA expressed in prostate tissue but not in other organs. When the POET mouse is infused with mOVA-specific T cells, these T cells specifically bind to the mOVA expressed in the prostate and attack the corresponding area, resulting in tissue damage and prostatitis. This approach is designed to investigate the development and regulation of prostatitis, which occurs in the EAP but is also induced in other organs due to autoimmunity. However, the POET mouse allows inflammation to occur specifically in the prostate gland only by allowing specifically labelled T cells to attack prostate tissue directly. Furthermore, this model allows a clear and unambiguous view of the specific prostate lobe where inflammation occurs, ventral and dorsolateral lobes more sensitive to inflammation than anterior ones.

In addition, this POET mouse model can be applied to detect the effect of inflammation on the development and progression of prostate cancer. Because the duration of prostatitis in this model is longer compared to the EAP model, where inflammation lasts about 15 days, whereas the POET model lasts 70-80 days, it is beneficial to study the relationship between long-term stimulation of inflammation and the development of prostate cancer.

The Transgenic adenocarcinoma of the mouse prostate (TRAMP) model can also be studied for the association of inflammation with the development of prostate cancer. The GMTRAMP-C vaccine is derived from TRAMP epithelial cells and is tumorigenic. The GMTRAMP-C vaccine was administered to enhance the response of TRAMP to antigenic challenge, and TRAMP mice with strong antigenic challenge were then treated with anti CTLA-4, a protein on T cells that prevents T cells from killing other cells, including cancer cells, and anti-CTLA-4 Treatment causes T cells in TRAMP mice to be active and attack prostate tissue, causing damage and thus prostatitis. In addition to TRAMP mice, wild-type mice and non-transgenic C57BL/6 male mice sensitized with GMTRAMP-C1/C2 vaccine and treated with anti-CTLA-4 showed inflammatory infiltration of prostate tissue and even tissue damage including destruction of alveolar structures. Normal mice injected with GMTRAMP-C1/C2, a prostate tumor cell, promote immunogenetics, including T cells. T cells assault the prostate tissue, leading to structural destruction and prostatitis (94).

Adaptive transfer with spleen cells from female mice or castrated male mice at birth, C3.129 nu/nu mice are susceptible to prostatitis (45). The presence of specific antigens on the prostate tissue allows CD4+ CD25- T cells in the humoral fluid to recognize and induce autoimmunity on the one hand and promotes the production of prostate tissue-specific suppressor T cells to tolerate the immune response on the other (Figure 3). Female or castrated male mice at birth fail to produce prostate tissue-specific suppressor T cells to tolerate the immune response and instead have large numbers of CD4+ CD25- T cells, which are relayed to C3.129 nu/nu mice. C3.129 nu/nu mice have no thymus and are consequently immunodeficient, meaning that they are unable to mount an immune response to foreign substances. After relaying, CD4+ CD25- T cells recognize specific antigens on the prostate tissue of C3.129 nu/nu mice and induce autoimmunity to occur, which attacks the prostate tissue and damage occurs, resulting in prostatitis. It indicated that prostate tissue-specific suppressor T cells and nonactivated suppressor T cells play an important role in immune tolerance against prostate antigens.

4.2.4 Knockout prostatitis models

IFN-γ -deficient NOD mice were perceived to significantly reduce the number of cell infiltration (35, 36). Interferon-γ (IFNγ) is an important mediator of the cellular immune response and is an inflammatory cytokine secreted by T lymphocytes and natural killer cells (NK cells), involved in the immune response *in vivo* (99). Mice lacking IFN-γ expression had significantly less inflammatory cell infiltration in prostate tissue relative to controls in autoimmunity,

indicating that IFN-γ -producing cells played a vital role in the development of infiltration in the prostate.

Autoimmune regulator (Aire) is essential for establishing central immune tolerance and preventing autoimmunity, and abnormalities or knockouts of *Aire* contribute to multi-organ autoimmune abnormalities in the body (100). It has been shown that *Aire-KO* mice inflamed multiple organs, in addition to inflammation in eyes, salivary glands, ovaries, stomach, and inflammatory cell infiltration in prostate tissue (101, 102). Autoimmune abnormalities resulting from *Aire* deficiency also contribute to inflammatory cells reaching, infiltrating, attacking and damaging prostate tissue, the exact mechanisms of which are unclear.

Taken these, thymectomy, autoimmunity, and specific cell transplants can cause the body to produce prostate tissue-related immune cells that attack and damage the prostate tissue, causing prostatitis. *IFN-γ*-deficient NOD mice and *Aire-KO* mice can be used as reproducible genetic models for studying the pathogenesis, prevention, control, and treatment of autoimmune prostatitis.

4.3 Gonadectomy and hormone-related prostatitis models

The relative level gives negative feedback to the hypothalamus dopamine and then promotes the pituitary gland to release prolactin, which activates specific receptors in the prostate glands to respond to androgen, thereby regulating the growth and development of the epithelium. However, by castration or hormone treatment, the hormone disorder induces a humoral and cell-mediated autoimmune reaction, the expression of inflammatory cytokines, or the destruction of the prostatic blood-lymph barrier to cause prostatitis and atrophy of prostate tissue. Hormone disorders are more likely to occur with age in humans. Therefore, hormone disorder treatment is generally accepted to establish models of abacterial prostatitis, including Hypo-gonadal (hpg) mice (103), (C3H/HeMs x 129/J)Fl mice (44, 46), Han-NMRI mice (104), Noble rats (105–107), Sprague-Dawley rats (108, 109), Lewis rats (39, 40) and Wistar rats (32, 39, 106, 110–115). Treatment methods include gonadectomy and 17β-estradiol injection, and one or both can achieve the model effect. Wistar rats were universally applied for this kind of model. This model was established within 14-36 days for some Wistar rats; for others, it took up to 18 weeks (106). Temporal consumption of this method depends on age, castration, and hormone treatment. Aged rats were more predisposed to prostatitis than young ones (32, 39, 111–113). Castration could shorten time based on hormone treatment (32, 111–115). In this model, inflammation appeared in ventral and dorsolateral lobes, while Aumüller G et al. discovered that all lobes had lesions after treatment with 17β-estradiol, testosterone, and castration in old rats (32). Furthermore, the lateral lobes manifested inflammation earlier than the dorsal lobes, and the ventral ones were the latest, characterized by neutrophil infiltration into the glandular lumen and plasma cells and lymphocytes infiltration into the interstitial area (110, 111). Wistar rats were treated daily with a total volume of 0.1ml 0.25 mg/kg 17β-estradiol for 30 days, and 100% of them demonstrated inflammation within lateral lobes, characterized with serious, multifocal, significant inflammation in a lobule, but in lateral prostates, there were no signs of inflammation (39). Different lobes of the prostate may have different sensitivities to hormonal disturbances.

Genetically modified Mice are available to research the development of prostatitis from specific genetic backgrounds. *AROM+* mice are laboratory mice that have been genetically modified to overexpress aromatase in the brain. Aromatase is an enzyme that converts testosterone to estrogen, and its overexpression in the brain leads to increased local estrogen levels, which can be used to study the connection between hormone disruption and prostatitis. Eighty-eight percent of *AROM+* mice were predisposed to prostatitis at 52 weeks. With androgen deficiency and rise in estrogen, multiple acute and chronic infiltration of inflammatory cells and increased chemokine and estrogen receptor alpha in prostatic epithelial cells resulted in prostatic intraepithelial neoplasia (116). Mice with different genetic backgrounds had different characteristics of prostatitis and affected the occurrence and development of prostatitis.

This model is reproducible, simple, inexpensive, and resembles the onset and persistence of chronic non-bacterial prostatitis in humans. The etiology of this disease may be similar to that of humans, which usually develops after birth when androgen levels are disturbed. Many models are evolving mice and rats, but the latter are more susceptible. Wistar rats are helpful models, as they are only treated with 17-estradiol, have a high probability of success, are reasonably straightforward to operate, and need less time to develop lesions. Both hormonal injections and castration are used in the model established by numerous researchers. However, castrated operation requires advanced aseptic techniques, and it is complex to perform and very difficult to perform on neonatal rats in some research. *AROM+* mice can be used as reproducible genetic disease models for studying the pathogenesis, prevention, control, and treatment of hormone-related prostatitis.

Furthermore, model phenotypes are often significantly correlated with estrogen dosage, time of exposure, and presence of androgens, which means that modeling results are unstable. Various ratios of estradiol may play an important role in inflammation. Additionally, high doses of medicine injection may result in toxicity, hepatic injury, and endocrine disruption.

4.4 Diet and lactation-related prostatitis models

Models of diet-related prostatitis involve rats or mice that exhibit prostatitis through simple feeding rather than injection or surgery, evolving diet soy-free (34), soy-extracted genistein with daidzein-rich Isoflavone (117), high fat (118–121) and lipid (122). Several studies have been conducted on the relationship between metabolism and prostatitis. Sprague-Dawley rats demonstrated prostatitis with a soy-free diet after 11 weeks (34). Following oral administration of genistein and daidzein-rich isoflavone extracted from soy, almost 83% of these rats developed dorsolateral

prostatitis. During histopathological examinations, many neutrophils and lymphocytes were found to invade the stroma and glandular lumen, but body weight, prostate weight, and serous androgen levels did not change (117). High-fat diet(HFD) for 1–3 months, and even at seven months, established prostatitis models successfully, including Sprague-Dawley rat (119), NF-κB-Luciferase transgenic mice (121), aged FVB mice (118), and C57BL/6 mice (120). With HFD for 4 weeks, C57BL/6 mice presented different degrees of lymphocyte aggregates in the dorsolateral lobes and a significant increase in IL-1β, IL-6, IL-17, and TNFα (120). Lipid diet also caused prostatitis and was associated with mice with different genetic backgrounds. C57/BL6 mice had smaller prostates, a wider lumen, and shorter epithelium with linseed oil in the ventral lobes while increasing epithelial volume with soybean oil and inflammatory infiltration with pork fat for 32 weeks. Pork fat, conversely, caused Mongolian gerbils to develop larger epithelial lesions and larger inflammatory foci, whereas linseed and soybean oil caused a reverse effect (122). With or without treatment, the majority of newborns displayed prostatitis at the age of 90 or 120 days after lactation for 25 or 56 days from dams fed at the time of gestation(GD) or neonatal period for several days with different substances, including methoxychlor, pimozide (123, 124), atrazine, bromocriptine (125), tamoxifen, 17β-estradiol (123), estradiol benzoate (108), high fat diet (119) or vinclozolin (126–128). The role of lactating mothers with abnormal metabolic levels in the occurrence and development of neonatal prostatitis can be explored. Wistar rats were predisposed to inflammation and fibrotic alteration in the ventral and lateral lobes after perinatal exposure to methoxychlor, pimozide, trazine, 17-estradiol, or bromocriptine (123–125). Sprague-Dawley rats presented prostatitis with lactation from the administration of estradiol benzoate administration (108), a high-fat diet (119), and vinclozolin (126–128). Vinclozolin is a widely used dicarboxamide fungicide whose primary action is due to its competitive androgen receptor antagonism and antiandrogenic activity. Females were administered orally daily on GD14–GD19 with 100 mg/kg vinclozolin. On postnatal day 56, all newborns developed prostatitis, with significant and focal areas of infiltration of inflammatory cells into the ducts and blood vessels, especially leukocytes and macrophages, degenerate epithelial cells, decayed duct structures, and reduced epithelial cells androgen receptors and decreased secretory epithelium (128).

In summary, oral treatment is more straightforward and inexpensive than parenteral administration. Compared to inoculation, the genistein diet is safer because it is challenging to ensure a suitable injection dosage. A high dose of genistein inoculation may cause drug toxicity, hepatic injury, and endocrine disorder. Thus, Sprague-Dawley rats effectively prevent prostatitis by taking oral isoflavones rich in genistein and daidzein extracted from soy. Metabolic disease is a constant concern, and a high-fat diet can help prevent prostatitis. C57BL/6 mice are perceived to have visible prostatitis with HFD for four weeks because they can quickly develop into severe obesity, fat accumulation, and impaired glucose tolerance to appear prostatitis. To investigate the effects of maternal hormone on newborns, vinclozolin is widely used for the induction of prostatitis. Lactation of dams taking this medicine reverted prostatitis in 100% of Sprague-Dawley rats.

Furthermore, vinclozolin does not cause maternal toxicity, or normal pregnancy. The disadvantages of these prostatitis models are that they require a longer experimental period and are influenced by variations in the ratio of diet, the type of lipids and the form of the diet. It is also essential to ensure the reproducibility and similarity of the nutrient composition for a long time. These models are affected by many other factors, including strains, age, and time. The treatment of lactation and natural mating can be complicated by the intrauterine environment, breastfeeding, parent handling, and behavioral differences.

4.5 Multifarious prostatitis models

Stress, chemicals, exosome injections, mechanical operation of urine reflux, and autonomic nervous blockers induce chronic prostatitis models.

4.5.1 Stress-related prostatitis models

The mechanism of stress induced prostatitis may be a change in the internal environment or an undiscovered mechanism needed to be further explored. When Sprague-Dawley rats were treated with stress conditions, such as starvation, 4°C temperature, and narrow cages, they developed prostatitis after ten days. Histopathological analysis in rats found an embedded acinus in the prostate, which contained active prostate epithelial stroma with less secretion. More inflammatory cells were in the acinus and stroma and a greater density of acinus and stroma. However, the foci and many inflammatory cells in the prostate prevented accurate classification (129, 130).

4.5.2 Chemical-related prostatitis models

Chronic prostatitis was produced by direct chemical injection, including λ-carrageenan (131–133), capsaicin (134–136), and doxycycline (40). This method was assigned to help study the neurobiological mechanisms of male pelvic pain, although it caused damage, destruction, or degeneration of the prostates. A high dosage of chemical treatment could cause stress reactions and even death in rats. Hence, controlling time, dose, and injection parts was critical. Chen CS et al. elucidated that 100% of Sprague-Dawley rats were perceived to have prostatitis in the ventral lobes after one day and maintained the two weeks with 3% λ-carrageenan in accordance with thermal hyperalgesia, mechanical allodynia, inflammatory cell count, COX2 expression and Evans blue (131–133). In this study, a high level of inflammatory cell infiltration was detected, such as monocytes, lymphocytes, fibrous connective tissue hyperplasia, interstitial congestion, and edema, in addition to other chronic inflammatory conditions. Furthermore, inoculation with doxycycline caused 100% of Lewis rats to develop granulocytes in the lumen and inflammation in the stroma (40).

4.5.3 Exosome-related prostatitis models

Exosomes are membrane-bound extracellular vesicles produced in the intranuclear region in most eukaryotic cells. They comprise a wide range of biomolecules, including proteins, lipids and nucleic acids such as RNA and DNA. Exosomes are involved in intercellular

communication and play a role in a variety of physiological and pathological processes. They are secreted by a wide range of cells, including immune cells. Exosomes secreted by immune cells can stimulate an immune response (137). There are not currently many studies on exosome and prostatitis. Baixiong Zhao et al. established a noble prostatitis model with exosome injections (138). They extracted exosomes from prostatic fluid samples of CP/CPPS patients and then injected them into the ventral lobes of Sprague-Dawley rats. After one-week, numerous inflammatory cells infiltrated interstitial tissue because these exosomes were selectively loaded with miRNA-155 and heavily phagocytosed by prostate stromal cells to activate the immune response and induce inflammation. This model may be a novel method for studying the pathogenesis of chronic prostatitis.

4.5.4 Urine reflux-related prostatitis models

Rats were artificially assigned to prostatitis through urine reflux to study another pathogenesis of chronic prostatitis. They were perfused with urine through the urethral orifice, the interstitial area was significantly enlarged, and polymorphic cells were diffusely distributed in the prostate after seven days. The acini did not contain inflammatory cells like the bacterial prostatitis model. Moreover, no effect was observed in the bladder due to histological changes. Inflammation-related proteins (IL-1A, IL-1B, IL-6, and TNFa) and oxidative stress markers (MDA and HIF-1A) increased in this model (139).

4.5.5 Autonomic nervous dysfunction-related prostatitis models

The autonomic nervous system and the immune system are closely linked, and they communicate with each other through various pathways. For example, the sympathetic nervous system can regulate the activity of immune cells (such as T cells and natural killer cells) through the release of neurotransmitters such as norepinephrine and epinephrine (140). Likewise, immune cells generate cytokines and other signaling molecules to influence the activity of the Autonomic nervous system, and abnormal regulation of the Autonomic nervous system is relevant to a variety of immune-related disorders such as autoimmune diseases, chronic inflammation and allergies (141). Notably, the autonomic nervous system is involved in the occurrence and development of prostatitis. C57BL/6 mice received 5 mg/kg body weight of 1-adrenergic or 2-adrenergic receptor agonists intraperitoneally for five days and developed chronic prostatitis, characterized by increased pro-inflammatory cytokines TNF, IL-6, and chemokines CCL2, CCL3. After blocking the sympathetic and parasympathetic nerves, the mice developed persistent chronic prostatitis. This is a phenomenon, the detailed mechanisms of which are not yet known. It suggests, nevertheless, that there is a correlation between abnormal autonomic nerves and the development of prostatitis. Furthermore, adrenoceptor Beta 2 (Adrb2) and the accumulation of CD11b + F4/80 + macrophages were highly expressed in the prostate without sympathetic nerves. Chronic prostatitis can be studied by examining autonomic nervous and immune responses (142).

In summary, stress and urine treatment can be the pathogenesis of prostatitis, and it took less time than other models, just 7-9 days, which is advantageous for establishing this type of model. The autonomic nervous dysfunctional model related to exosomes may be novel methods for studying the pathogenesis of chronic prostatitis. The advantages of chemical treatment are simplicity, cost-effectiveness, and reproducibility, and it has strengths in research on gene-environment interactions and chemoprevention. This model tends to self-medicate and does not follow a chronic course but can cause severe lesions if administered in a high dosage of chemicals. Attention must be paid to the batch of chemicals, the breed, and source of the animal, the chemical supplier, dosage, frequency, and duration. Cellular models present advantages such as stability, high success rates, and savings of time and money. We can study microscopic examination in cells, but they are very different from the condition and consist of multiple treatment systems. It is possible to pre-estimate novel treatments in cellular models with efficient and time-saving outcomes before animal experiments.

5 Evaluation criteria

Pathological changes, biochemical analysis, behavioral testing, cutaneous allodynia evaluation, body weights or prostate, and urodynamic measurements can be used to diagnose the success of the prostatitis model.

5.1 Pathological changes

Pathology, including macro- and microscopic analysis, is critical for detecting prostatitis in animals. Macroscopic analysis is intuitive, simple, and convenient for grossly morphologically estimate the situation of inflammation within the prostates. After dissection, gross morphological analysis of infected prostates is observed for obvious signs of inflammation, including edema, congestion, and hyperemia (16, 71, 72).

Microscopic changes are more detailed and accurate than macroscopic changes, including acute and chronic prostatitis. In acute prostatitis, the dense infiltrate of acute inflammatory cells (neutrophils) in the periglandular stroma, interstitial edema, focal hemorrhage, and abundant shedding of epithelial cells into the lumen of the prostatic gland of acute prostatic tissue are revealed by the microscope (21). In chronic prostatitis, changes in the lesion were scored based on three histological conditions: edema, hemorrhage, and infiltration of leukocytes. This method depends on the subjectivity of observers by comparing the severity of appearance and diving into four grades (16, 143, 144).

5.2 Biochemical analysis

Prostatitis is characterized by an aberrant immune response and a cascade of inflammatory cytokines. These cytokines, such as interleukin-1, interleukin-6, interleukin-8 and tumor necrosis factor-alpha (TNF-alpha), play a critical role in the modulation and

amplification of the immune response, as well as the propagation of inflammation. In the context of prostatitis, the overproduction of these cytokines by immune cells is closely associated with the development of the inflammatory response. Therefore, the measurement of cytokine expression, particularly IL-1, IL-6, IL-8 and TNF-α, provides a reliable indicator of the success of the prostatitis model (19, 61, 64, 68, 76, 145).

Prostate inflammation also involves various molecules and signaling pathways. Among these are the C-C motif chemokine ligand (CCL) family, a group of chemokines that play crucial roles in immune responses and inflammation. The CCL family encompasses a range of chemokines, including CCL2, CCL3, CCL4, and CCL5, all of which contribute to the development of inflammatory responses. In chronic bacterial prostatitis, there is a significant increase in the expression of CCL2 and CCL3 in prostate tissue. This upregulation of CCL2 and CCL3 is known to promote the recruitment of immune cells to the site of inflammation, thereby exacerbating the inflammatory response. Moreover, recent studies have identified CCL2 and CCL3 as significant biomarkers for inflammatory IIIA and non-inflammatory IIIB chronic pelvic pain symptoms, underscoring their potential clinical significance in the diagnosis and management of prostatitis (146).

In general, tests for IL-1, IL-6, IL-8 and TNF-α expression levels can be an indicator to verify the success of prostatitis. CCL2 and CCL3 expression levels have been found to be altered in prostatitis, although they are not necessarily markers.

5.3 Multifarious analysis

Behavioral testing, evaluation of cutaneous allodynia, body or prostate, and urodynamic measurements can be used to diagnose the success of the prostatitis model. Behavioral testing is often used in the evolution of pain assessment (57, 69, 74) and cutaneous allodynia assessment of chronic pelvic pain (76, 112). Both can be used to test for the pain of chronic prostatitis. Weights of the body or prostate can be used to determine the changes in prostate tissue before and after treatment (74, 106, 108, 113, 117). Prostatitis causes changes in urodynamic measurements, elucidating that prostatitis models reduced the frequency of urination and the prolonged urination time, and the residual urine volume of hormone-treated rats tended to increase (106, 107, 112).

6 Conclusion and prospects

Prostatitis is a common condition observed in the urology department, with a high prevalence. Despite the complexity and uncertainty of the pathogenesis and etiology, effective treatment is imperative, so it is crucial to choose the appropriate models quickly and conveniently. Based on the models of prostatitis mechanically described above, different settlements have different manufacturing

TABLE 2 Summary of present prostatitis models.

Categories		Model	Treatment	Duration	Lesion sides	Advantages	Disadvantages	Success rate	Recommend	References
Infectious prostatitis models	Acute bacterial prostatitis	RWPE-1 cell	AIEC strains, lipoteichoic acid, Trichomonas vaginalis	2, 3, 24 hours	/	Inexpensive, easily accessible, stable, high success, microscopic studies, earlier, saving time and money.	Considerable difference from actual conditions of patients.	/	/	(147–150)
		Rat: Wistar, Sprague-Dawley	, *E. coli*, Chlamydia psittaci	0-18 days	Dorsolateral, ventral lobes	High incidence, morbidity and histological lesion similar with human,	Predisposal to severe infection to death, self-healing at short time	83.3%-100% (16, 22, 23)	Sprague-Dawley rats C3H/HeOuJ mice (16, 21–23)	(16–23)
		Mouse: C3H/HeJ	E. coli	5 days				100% (20)		
	Chronic bacterial prostatitis	Rat: Wistar, Sprague-Dawley	Escherichia coli, Chlamydia psittaci	1-3 months			Less sensitive than acute prostatitis, bacterial infection predisposal to recovery and difficult to chronic inflammation.	50% (22), 62% (24), 86.7% (25).	C3H/HeOuJ mice (21)	(21–25)
		C3H/HeOuJ mouse	E. coil	12 weeks				100%		
Spontaneous prostatitis model		Rat: Lewis, Wistar, Sprague-Dawley	/	3-13 months	Dorsolateral, ventral lobes	Fewer artificial factors, less artificial trauma, stable, long period of time, similar to the clinical patients,	Full with uncontrolled experimental factors and low targetability, spending a long period in prostatitis, ranging from 3-13 months, poor repeatability.	Lewis:30% -72% (39, 40); Wistar:27% -80% (32, 39, 41); Sprague-Dawley:16.6% diet for 11 weeks (34).	Wistar rats (41)	(32–37, 39–41, 43)

(Continued)

TABLE 2 Continued

Categories		Model	Treatment	Duration	Lesion sides	Advantages	Disadvantages	Success rate	Recommend	References
		Mouse: NOD, NZB	/	7-28 or 40 weeks	Ventral, dorsal or whole lobes	age-related, specific genetic		/	NOD, NZB (35, 36, 43)	
Immune-mediated prostatitis models	Thymectomy-related	Mouse: (C3H/HeMs x 129/J) F1, B6A, SNF1, NZM2328	Thymectomy of postnatal 3 days	40-150 days	Anterior, dorsal, ventral (infrequency) lobes	Self-tolerance, such as suppressor T cells and activated T cells from thymus.	Difficult to thymectomy, multiple inflammation	(C3H/HeMs x 129/J)F1: 27%-73% of prostatitis (44, 45); B6A:58.6% of prostatitis (46); SNF1: 61.5% of prostatitis (47) NZM2328: 73% of prostatitis (48).	NZM2328 mice (48)	(44–48)
	EAP -related prostatitis models	Rats: Wistar, Lewis, Sprague-Dawley, Copenhagen	Antigen,1-3 times of immunizations.	12 hours, 30-50 days, 1-3 months	Dorsal, ventral and lateral lobes	High clinical similarity, dose-dependent manner, genetic background, different sensitivity	Depend on operating enviroment, volume and purity of antigen, the frequency, time and parts of inoculation	Wistar: 38% (49) Lewis:33% of prostatitis (75) Sprague-Dawley:100% (64, 71) Copenhagen:80% (70)	C57BL/6 mice (63)	(35, 36, 49–53, 56, 58, 59, 61–66, 68–76)
		Mouse: NOD, C57BL/6, SJL, AJ, BALB/c, NZB, SWR		2, 10-42 or 63 days	All	NOD:100% (56, 59); C57BL/6: 37.5%-100% (56, 63, 65, 66, 73) SWXJ (H-2q, s):100% (74).				
	Cells injection-related prostatitis models	Rat: Lewis, Wistar	Splenocytes	7,10,30 days	Dorsal and ventral	The pathogenesis and function of immunocytes of chronic prostatitis can be examined	Limit and difficult to take a comprehensive acknowledge of development of prostatitis.	62.5% (75); 90% (93),100% (92)	POET (91, 96–98), C3.129mice (45), POET-3mice (91), TRAMP mice (94).	(45, 73, 75, 91–93, 95, 96)
		Mouse: C57BL/6, POET1/3,		About 60-90 days	ventral anterior dorsolateral	*C3.129 nu/nu*:more than 90% (45) *RAG-KO B6*:100% (73) C57BL/6: 100% (95) POET1/3:100% (96)				
	Knockout prostatitis models	Mouse: IFN-γ -deficient NOD, Aire-KO	Knockout	/	Ventral, dorsolateral lobes	The ability to look specifically at the mechanisms by which prostatitis develops, down to specific molecules or genes.	Basic life activities are severely affected and feeding is difficult.	Aire-KO:71% prostatitis (73).	IFN-γ -deficient NOD (35), Aire-KO:71% prostatitis (73).	(35, 73)
Gonadectomy and hormone-related prostatitis models		Rat: Lewis, Wistar, Noble, Sprague-Dawley	Orchiectomized, 17β-estradiol	2-6 weeks, 10-18 weeks	Ventral and dorsolateral lobes	Reproducible, simple, inexpensive, a resemblance to the onset and persistence of chronic nonbacterial prostatitis in humans, the etiology of this disease be similar to humans.	Complex to to perform on neonatal rats, drug toxicity, hepatic injury and endocrine disorder.	Lewis:100% (39, 40) Wistar:100%of prostatitis (32, 39, 111–114)	Wistar rats (39)	(32, 39, 40, 44, 46, 103–114, 116)
		Mouse: *hpg*, Han-NMRI, AROM+	17β-estradiol, castration	42 or 90 days	Anterior, dorsolateral and ventral lobes			(C3H/HeMs x 129/J) F1: 54% (44) Han-NMRI: 100% (104). AROM+: 21%-88% prostatitis; 33% PIN lesion; 60% scrotal hernias (116)		

(Continued)

TABLE 2 Continued

Categories		Model	Treatment	Duration	Lesion sides	Advantages	Disadvantages	Success rate	Recommend	References
Diet/ lactation-related prostatitis models	Diet-related	Sprague-Dawley rat	soy-free, genistein, high fat	9-11,26-29 weeks	Dorsolateral lobes	Simple and inexpensive, to explore the effect of maternal hormonal on newborns, C57BL/6 mice can easily develop into severe obesity, fat accumulation and impaired glucose tolerance to appear prostatitis	Longer experimental period, influence by various elements, variation in the ratio of high fat diet, intrauterine environment, breastfeeding, parental handling, and behavioral differences	80% (34);83% (117)	Sprague-Dawley rats (117, 128), C57BL/6 mice (120).	(34, 108, 117–128)
		Mouse:C57/BL6		4-9, 12, 32 weeks	Ventral dorsolateral lobe			/		
	Lactation-related	Rat: Wistar, Sprague-Dawley	17β-estradiol fat diet vinclozolin	12-15 weeks	Ventral dorsolateral lobes			Methoxychlor:60% (123); Tamoxifen: 27.89% (123); 17β-estradiol: 90% (123); Estradiol:20% (124); Vinclozolin:100% (126–128)		
Multifarious prostatitis models	Stress-related	Sprague-Dawley rat	Starvation/4 °C temperature/ narrow cages	10 days	/	Simplicity, cost-effectiveness, reproducibility, strengths in research on gene-environment interactions and chemoprevention;	Chemical-related models are self-medication, not to follow a chronic course, severe lesion if a high dosage of chemicals, influence by the batch of chemicals, the breed, sex and source of the animal, the chemical supplier, dosage, frequency and duration. The cellular models are very different from the actual condition consist of multiple systems regulation of human.	/	Sprague-Dawley rats (129–133, 138, 139)	(40, 55, 129–133, 138, 139, 151–154)
	Chemical-related	Rat: Sprague-Dawley, Lewis	3%λ-carrageenan/ capsaicin/ doxycycline	1 day	Ventral lobe			Sprague-Dawley:100% (132) Lewis:100% (40)		
	Exosome-related	Sprague-Dawley rat	Exosome from prostatic fluid	7 days	Ventral lobe	Novel research direction about exosome		/		
	Urine reflux-related	Sprague-Dawley rat	urine	7 days	/	Novel research direction about urine reflux		/		
	Autonomic nervous dysfunction-related	C57BL/6 mice	β2-adrenergic receptor agonists	5 days	Anterior lobe	Study of relationship between autonomic nerve and prostatitis		/	C57BL/6 mice (142)	

methods, durations, inflammatory lobes, success rates, disadvantages, and evaluation criteria (Table 2). The search for more suitable models to explain the etiology, pathogenesis, and clinical manifestations of prostatitis should continue in the future.

Author contributions

JZ and HH designed the manuscript and outline for the review. HH, HL, and HX searched related publications. HH and FZ drafted the manuscript. JZ, XZ, and GZ reviewed the manuscript and polished the grammar. All authors contributed to the manuscript revision and approved the submitted version.

Funding

This work was supported by the National Natural Science Foundation of China (No. 81860456), the Natural Science Foundation of Jiangxi Province (20202BABL206031 and 20224BAB216024), and the Magidden Young Scientist Fund (MJR20201201).

Acknowledgments

All figures are created with Adobe Illustrator and BioRender.

Conflict of interest

The authors declare that the research was conducted in the absence of any commercial or financial relationships that could be construed as a potential conflict of interest.

Publisher's note

All claims expressed in this article are solely those of the authors and do not necessarily represent those of their affiliated organizations, or those of the publisher, the editors and the reviewers. Any product that may be evaluated in this article, or claim that may be made by its manufacturer, is not guaranteed or endorsed by the publisher.

References

1. Breser ML, Salazar FC, Rivero VE, Motrich RD. Immunological mechanisms underlying chronic pelvic pain and prostate inflammation in chronic pelvic pain syndrome. *Front Immunol* (2017) 8:898. doi: 10.3389/fimmu.2017.00898

2. Habermacher GM, Chason JT, Schaeffer AJ. Prostatitis/chronic pelvic pain syndrome. *Annu Rev Med* (2006) 57:195–206. doi: 10.1146/annurev.med.57.011205.135654

3. Krieger JN, Nyberg LJr., Nickel JC. NIH Consensus definition and classification of prostatitis. *Jama* (1999) 282(3):236–7. doi: 10.1001/jama.282.3.236

4. Krieger JN, Lee SW, Jeon J, Cheah PY, Liong ML, Riley DE. Epidemiology of prostatitis. *Int J antimicrobial Agents* (2008) 31 Suppl 1(Suppl 1):S85–90. doi: 10.1016/j.ijantimicag.2007.08.028

5. Franco JV, Turk T, Jung JH, Xiao YT, Iakhno S, Tirapegui FI, et al. Pharmacological interventions for treating chronic prostatitis/chronic pelvic pain syndrome. *Cochrane Database systematic Rev* (2019) 10(10):Cd012552. doi: 10.1002/14651858.CD012552.pub2

6. Franco JV, Turk T, Jung JH, Xiao YT, Iakhno S, Garrote V, et al. Non-pharmacological interventions for treating chronic prostatitis/chronic pelvic pain syndrome. *Cochrane Database systematic Rev* (2018) 5(5):Cd012551. doi: 10.1002/14651858.CD012551.pub2

7. McNeal JE. Anatomy of the prostate and morphogenesis of BPH. *Prog Clin Biol Res* (1984) 145:27–53.

8. Amin MB, Tickoo SK. Diagnostic Pathology: Genitourinary E-Book. *Elsevier Health Sciences* (2022).

9. Sugimura Y, Cunha GR, Donjacour AA, Bigsby RM, Brody JR. Whole-mount autoradiography study of DNA synthetic activity during postnatal development and androgen-induced regeneration in the mouse prostate. *Biol Reprod* (1986) 34(5):985–95. doi: 10.1095/biolreprod34.5.985

10. Oliveira DS, Dzinic S, Bonfil AI, Saliganan AD, Sheng S, Bonfil RD. The mouse prostate: a basic anatomical and histological guideline. *Bosnian J basic Med Sci* (2016) 16(1):8–13. doi: 10.17305/bjbms.2016.917

11. Crowley L, Cambuli F, Aparicio L, Shibata M, Robinson BD, Xuan S, et al. et al: a single-cell atlas of the mouse and human prostate reveals heterogeneity and conservation of epithelial progenitors. *eLife* (2020) 9. doi: 10.7554/eLife.59465

12. Wang X, Wang H, Jiang K, Zhang Y, Zhan C, Ying M, et al. et al: liposomes with cyclic RGD peptide motif triggers acute immune response in mice. *J Controlled release* (2019) 293:201–14. doi: 10.1016/j.jconrel.2018.12.003

13. Mestas J, Hughes CC. Of mice and not men: differences between mouse and human immunology. *J Immunol (Baltimore Md 1950)* (2004) 172(5):2731–8. doi: 10.4049/jimmunol.172.5.2731

14. Tao L, Reese TA. Making mouse models that reflect human immune responses. *Trends Immunol* (2017) 38(3):181–93. doi: 10.1016/j.it.2016.12.007

15. Serr I, Kral M, Scherm MG, Daniel C. Advances in human immune system mouse models for personalized treg-based immunotherapies. *Front Immunol* (2021) 12:643544. doi: 10.3389/fimmu.2021.643544

16. Rippere-Lampe KE, Lang M, Ceri H, Olson M, Lockman HA, O'Brien AD. Cytotoxic necrotizing factor type 1-positive escherichia coli causes increased inflammation and tissue damage to the prostate in a rat prostatitis model. *Infect Immun* (2001) 69(10):6515–9. doi: 10.1128/IAI.69.10.6515-6519.2001

17. Rifaioglu MM, Nacar A, Yuksel R, Yonden Z, Karcioglu M, Zorba OU, et al. Antioxidative and anti-inflammatory effect of thymoquinone in an acute pseudomonas prostatitis rat model. *Urol Int* (2013) 91(4):474–81. doi: 10.1159/000351261

18. Kaplan L, Lee C, Schaeffer AJ. Effect of castration on experimental bacterial prostatitis in rats. *Prostate* (1983) 4(6):625–30. doi: 10.1002/pros.2990040608

19. Inci M, Davarci M, Inci M, Motor S, Yalcinkaya FR, Nacar E, et al. Anti-inflammatory and antioxidant activity of thymoquinone in a rat model of acute bacterial prostatitis. *Hum Exp Toxicol* (2013) 32(4):354–61. doi: 10.1177/0960327112455068

20. Elkahwaji JE, Ott CJ, Janda LM, Hopkins WJ. Mouse model for acute bacterial prostatitis in genetically distinct inbred strains. *Urology* (2005) 66(4):883–7. doi: 10.1016/j.urology.2005.04.013

21. Elkahwaji JE, Zhong W, Hopkins WJ, Bushman W. Chronic bacterial infection and inflammation incite reactive hyperplasia in a mouse model of chronic prostatitis. *Prostate* (2007) 67(1):14–21. doi: 10.1002/pros.20445

22. Nickel JC, Olson ME, Costerton JW. Rat model of experimental bacterial prostatitis. *Infection* (1991) 19 Suppl 3:S126–130. doi: 10.1007/BF01643681

23. Jantos CA, Augustin J, Durchfeld-Meyer B, Baumgärtner W, Schiefer HG. Experimental genital tract infection with chlamydia psittaci (GPIC agent) in male rats. *Infection* (1998) 26(2):126–30. doi: 10.1007/BF02767776

24. Seo SI, Lee SJ, Kim JC, Choi YJ, Sw SW, Hwang TK, et al. Effects of androgen deprivation on chronic bacterial prostatitis in a rat model. *Int J Urol* (2003) 10(9):485–91. doi: 10.1046/j.1442-2042.2003.00666.x

25. Cho YH, Lee SJ, Lee JY, Kim SW, Lee CB, Lee WY, et al. Antibacterial effect of intraprostatic zinc injection in a rat model of chronic bacterial prostatitis. *Int J Antimicrob Agents* (2002) 19(6):576–82. doi: 10.1016/S0924-8579(02)00115-2

26. Boehm BJ, Colopy SA, Jerde TJ, Loftus CJ, Bushman W. Acute bacterial inflammation of the mouse prostate. *Prostate* (2012) 72(3):307–17. doi: 10.1002/pros.21433

27. Paulis G, Conti E, Voliani S, Bertozzi MA, Sarteschi ML, Menchini Fabris F. Evaluation of the cytokines in genital secretions of patients with chronic prostatitis. *Archivio italiano di urologia andrologia* (2003) 75(4):179–86.

28. Nadler RB, Koch AE, Calhoun EA, Campbell PL, Pruden DL, Bennett CL, et al. IL-1beta and TNF-alpha in prostatic secretions are indicators in the evaluation of men with chronic prostatitis. *J Urol* (2000) 164(1):214–8.

29. Steiner GE, Stix U, Handisurya A, Willheim M, Haitel A, Reithmayr F, et al. et al: cytokine expression pattern in benign prostatic hyperplasia infiltrating T cells and impact of lymphocytic infiltration on cytokine mRNA profile in prostatic tissue. *Lab investigation J Tech Methods Pathol* (2003) 83(8):1131–46. doi: 10.1097/01.LAB.0000081388.40145.65

30. Theyer G, Kramer G, Assmann I, Sherwood E, Preinfalk W, Marberger M, et al. Phenotypic characterization of infiltrating leukocytes in benign prostatic hyperplasia. *Lab investigation J Tech Methods Pathol* (1992) 66(1):96–107.

31. Rautajoki KJ, Kylaniemi MK, Raghav SK, Rao K, Lahesmaa R. An insight into molecular mechanisms of human T helper cell differentiation. *Ann Med* (2008) 40(5):322–35. doi: 10.1080/07853890802068582

32. Vykhovanets EV, Resnick MI, Marengo SR. Intraprostatic lymphocyte profiles in aged wistar rats with estradiol induced prostate inflammation. *J Urol* (2006) 175(4):1534–40. doi: 10.1016/S0022-5347(05)00652-X

33. Aumüller G, Enderle-Schmitt U, Seitz J, Müntzing J, Chandler JA. Ultrastructure and immunohistochemistry of the lateral prostate in aged rats. *Prostate* (1987) 10(3):245–56. doi: 10.1002/pros.2990100307

34. Sharma OP, Adlercreutz H, Strandberg JD, Zirkin BR, Coffey DS, Ewing LL. Soy of dietary source plays a preventive role against the pathogenesis of prostatitis in rats. *J Steroid Biochem Mol Biol* (1992) 43(6):557–64. doi: 10.1016/0960-0760(92)90244-D

35. Penna G, Amuchastegui S, Cossetti C, Aquilano F, Mariani R, Giarratana N, et al. Spontaneous and prostatic steroid binding protein peptide-induced autoimmune prostatitis in the nonobese diabetic mouse. *J Immunol* (2007) 179(3):1559–67. doi: 10.4049/jimmunol.179.3.1559

36. Jackson CM, Flies DB, Mosse CA, Parwani A, Hipkiss EL, Drake CG. Strain-specific induction of experimental autoimmune prostatitis (EAP) in mice. *Prostate* (2013) 73(6):651–6. doi: 10.1002/pros.22606

37. Ghatak S, Ho SM. Age-related changes in the activities of antioxidant enzymes and lipid peroxidation status in ventral and dorsolateral prostate lobes of noble rats. *Biochem Biophys Res Commun* (1996) 222(2):362–7. doi: 10.1006/bbrc.1996.0749

38. Zhou X, Weiser P, Pan J, Qian Y, Lu H, Zhang L. Chondroitin sulfate and abnormal contact system in rheumatoid arthritis. *Progress in molecular biology and translational science* (2010) 93:423–42.

39. Naslund MJ, Strandberg JD, Coffey DS. The role of androgens and estrogens in the pathogenesis of experimental nonbacterial prostatitis. *J Urol* (1988) 140(5):1049–53. doi: 10.1016/S0022-5347(17)41924-0

40. Lundgren R, Holmquist B, Hesselvik M, Müntzing J. Treatment of prostatitis in the rat. *Prostate* (1984) 5(3):277–84. doi: 10.1002/pros.2990050305

41. Keith IM, Jin J, Neal DJr., Teunissen BD, Moon TD. Cell relationship in a wistar rat model of spontaneous prostatitis. *J Urol* (2001) 166(1):323–8. doi: 10.1016/S0022-5347(05)66153-8

42. Chen D, Thayer TC, Wen L, Wong FS. Mouse models of autoimmune diabetes: the nonobese diabetic (NOD) mouse. *Methods Mol Biol (Clifton NJ)* (2020) 2128:87–92. doi: 10.1007/978-1-0716-0385-7_6

43. Wallace DJ, Hahn BH eds. *Dubois' lupus erythematosus and related syndromes. Ninth Edition*. London: Elsevier (2019).

44. Taguchi O, Kojima A, Nishizuka Y. Experimental autoimmune prostatitis after neonatal thymectomy in the mouse. *Clin Exp Immunol* (1985) 60(1):123–9. doi: 10.1084/jem.165.1.146

45. Taguchi O, Nishizuka Y. Self tolerance and localized autoimmunity. mouse models of autoimmune disease that suggest tissue-specific suppressor T cells are involved in self tolerance. *J Exp Med* (1987) 165(1):146–56. doi: 10.1084/jem.165.1.146

46. Taguchi O, Kontani K, Ikeda H, Kezuka T, Takeuchi M, Takahashi T, et al. Tissue-specific suppressor T cells involved in self-tolerance are activated extrathymically by self-antigens. *Immunology* (1994) 82(3):365–9.

47. Bagavant H, Thompson C, Ohno K, Setiady Y, Tung KS. Differential effect of neonatal thymectomy on systemic and organ-specific autoimmune disease. *Int Immunol* (2002) 14(12):1397–406. doi: 10.1093/intimm/dxf105

48. Bagavant H, Tung KS. Failure of CD25+ T cells from lupus-prone mice to suppress lupus glomerulonephritis and sialoadenitis. *J Immunol* (2005) 175(2):944–50. doi: 10.4049/jimmunol.175.2.944

49. Depiante-Depaoli M, Pacheco-Rupil B, Britos S, Casas A. Experimental autoimmune damage to rat male accessory glands. i. transfer of autoimmune response by spleen cells. *Am J Reprod Immunol* (1984) 5(1):9–14. doi: 10.1111/j.1600-0897.1984.tb00280

50. Maccioni M, Rivero V, Riera CM. Autoantibodies against rat prostate antigens. association of specific IGG2b and IGG2c with the DTH response. *J Autoimmun* (1996) 9(4):485–91. doi: 10.1006/jaut.1996.0065

51. Galmarini M, Ferro ME, Riera CM. Delayed hypersensitivity and lesions following isoimmunization with modified rat male accessory glands: kinetics of induction. *J Reprod Immunol* (1988) 13(2):147–57. doi: 10.1016/0165-0378(88)90058-7

52. Pistoresi-Palencia MC, Romero-Piffiguer M, Ferro ME. Effect of aging on the autoimmune response to rat male accessory glands: deficit of I-e-positive peritoneal cells capable of inducing suppression. *Eur J Immunol* (1991) 21(7):1685–9. doi: 10.1002/eji.1830210715

53. Orsilles MA, Depiante-Depaoli M. Oxidative stress-related parameters in prostate of rats with experimental autoimmune prostatitis. *Prostate* (1998) 34(4):270–4. doi: 10.1002/(SICI)1097-0045(19980301)34:4<270::AID-PROS4>3.0.CO;2-L

54. Correa SG, Riera CM. Adjuvant effect of liposomes in the autoimmune response to rat male accessory glands. *Immunol Lett* (1991) 28(1):39–46. doi: 10.1016/0165-2478(91)90125-T

55. Jin BR, Ju JY, Nugroho A, Lee M, An HJ. Carica papaya leaf extract inhibits prostatitis-associated prostatic hyperplasia *via* the TRAF6/TAK1/MEK/NF-κB pathway. *BioMed Pharmacother* (2021) 135:111197. doi: 10.1016/j.biopha.2020.111197

56. Rivero VE, Cailleau C, Depiante-Depaoli M, Riera CM, Carnaud C. Non-obese diabetic (NOD) mice are genetically susceptible to experimental autoimmune prostatitis (EAP). *J Autoimmun* (1998) 11(6):603–10. doi: 10.1006/jaut.1998.0248

57. Rudick CN, Schaeffer AJ, Thumbikat P. Experimental autoimmune prostatitis induces chronic pelvic pain. *Am J Physiol Regul Integr Comp Physiol* (2008) 294(4):R1268–1275. doi: 10.1152/ajpregu.00836.2007

58. Penna G, Amuchastegui S, Cossetti C, Aquilano F, Mariani R, Sanvito F, et al. Treatment of experimental autoimmune prostatitis in nonobese diabetic mice by the vitamin d receptor agonist elocalcitol. *J Immunol* (2006) 177(12):8504–11. doi: 10.4049/jimmunol.177.12.8504

59. Rivero V, Carnaud C, Riera CM. Prostatein or steroid binding protein (PSBP) induces experimental autoimmune prostatitis (EAP) in NOD mice. *Clin Immunol* (2002) 105(2):176–84. doi: 10.1006/clim.2002.5281

60. Kurita M, Yamaguchi H, Okamoto K, Kotera T, Oka M. Chronic pelvic pain and prostate inflammation in rat experimental autoimmune prostatitis: effect of a single treatment with phosphodiesterase 5 inhibitors on chronic pelvic pain. *Prostate* (2018) 78(15):1157–65. doi: 10.1002/pros.23690

61. Motrich RD, Maccioni M, Ponce AA, Gatti GA, Oberti JP, Rivero VE. Pathogenic consequences in semen quality of an autoimmune response against the prostate gland: from animal models to human disease. *J Immunol* (2006) 177(2):957–67. doi: 10.4049/jimmunol.177.2.957

62. Qi X, Han L, Liu X, Zhi J, Zhao B, Chen D, et al. Prostate extract with aluminum hydroxide injection as a novel animal model for chronic prostatitis/chronic pelvic pain syndrome. *Urology* (2012) 80(6):1389.e1389–1315. doi: 10.1016/j.urology.2012.07.030

63. Keetch DW, Humphrey P, Ratliff TL. Development of a mouse model for nonbacterial prostatitis. *J Urol* (1994) 152(1):247–50. doi: 10.1016/S0022-5347(17)32871-9

64. Ihsan AU, Khan FU, Nawaz W, Khan MZ, Yang M, Zhou X. Establishment of a rat model of chronic Prostatitis/Chronic pelvic pain syndrome (CP/CPPS) induced by immunization with a novel peptide T2. *BioMed Pharmacother* (2017) 91:687–92. doi: 10.1016/j.biopha.2017.05.004

65. Khan FU, Ihsan AU, Nawaz W, Khan MZ, Yang M, Wang G, et al. A novel mouse model of chronic prostatitis/chronic pelvic pain syndrome induced by immunization of special peptide fragment with aluminum hydroxide adjuvant. *Immunol Lett* (2017) 187:61–7. doi: 10.1016/j.imlet.2017.05.008

66. Zhang L, Ihsan AU, Cao Y, Cheng Y, Zhou X. Establishment of experimental autoimmune prostatitis model by T(2) peptide in aluminium hydroxide adjuvant. *Andrologia* (2018) 50(3). doi: 10.1111/and.12922

67. Maccioni M, Rivero VE, Riera CM. Prostatein (or rat prostatic steroid binding protein) is a major autoantigen in experimental autoimmune prostatitis. *Clin Exp Immunol* (1998) 112(2):159–65. doi: 10.1046/j.1365-2249.1998.00588.x

68. Motrich RD, van Etten E, Baeke F, Riera CM, Mathieu C, Rivero VE. Crucial role of interferon-gamma in experimental autoimmune prostatitis. *J Urol* (2010) 183(3):1213–20. doi: 10.1016/j.juro.2009.11.008

69. Breser ML, Motrich RD, Sanchez LR, Rivero VE. Chronic pelvic pain development and prostate inflammation in strains of mice with different susceptibility to experimental autoimmune prostatitis. *Prostate* (2017) 77(1):94–104. doi: 10.1002/pros.23252

70. Fong L, Ruegg CL, Brockstedt D, Engleman EG, Laus R. Induction of tissue-specific autoimmune prostatitis with prostatic acid phosphatase immunization: implications for immunotherapy of prostate cancer. *J Immunol* (1997) 159(7):3113–7. doi: 10.4049/jimmunol.159.7.3113

71. Lang MD, Nickel JC, Olson ME, Howard SR, Ceri H. Rat model of experimentally induced abacterial prostatitis. *Prostate* (2000) 45(3):201–6. doi: 10.1002/1097-0045(20001101)45:3<201::AID-PROS1>3.0.CO;2-Q

72. Stanton MM, Nelson LK, Benediktsson H, Hollenberg MD, Buret AG, Ceri H. Proteinase-activated receptor-1 and immunomodulatory effects of a PAR1-activating peptide in a mouse model of prostatitis. *Mediators Inflammation* (2013) 2013:748395. doi: 10.1155/2013/748395

73. Hou Y, DeVoss J, Dao V, Kwek S, Simko JP, McNeel DG, et al. An aberrant prostate antigen-specific immune response causes prostatitis in mice and is associated with chronic prostatitis in humans. *J Clin Invest* (2009) 119(7):2031–41. doi: 10.1172/JCI38332

74. Altuntas CZ, Daneshgari F, Veizi E, Izgi K, Bicer F, Ozer A, et al. et al: a novel murine model of chronic prostatitis/chronic pelvic pain syndrome (CP/CPPS) induced by immunization with a spermine binding protein (p25) peptide. *Am J Physiol Regul Integr Comp Physiol* (2013) 304(6):R415–422. doi: 10.1152/ajpregu.00147.2012

75. Liu KJ, Chatta GS, Twardzik DR, Vedvick TS, True LD, Spies AG, et al. Identification of rat prostatic steroid-binding protein as a target antigen of experimental autoimmune prostatitis: implications for prostate cancer therapy. *J Immunol* (1997) 159(1):472–80. doi: 10.4049/jimmunol.159.1.472

76. Zhang LG, Chen J, Meng JL, Zhang Y, Liu Y, Zhan CS, et al. Effect of alcohol on chronic pelvic pain and prostatic inflammation in a mouse model of experimental autoimmune prostatitis. *Prostate* (2019) 79(12):1439–49. doi: 10.1002/pros.23866

77. Eisenberg RA, Craven SY, Warren RW, Cohen PL. Stochastic control of anti-Sm autoantibodies in MRL/Mp-lpr/lpr mice. *J Clin Invest* (1987) 80(3):691–7. doi: 10.1172/JCI113123

78. Corneth OBJ, Schaper F, Luk F, Asmawidjaja PS, Mus AMC, Horst G, et al. Lack of IL-17 receptor a signaling aggravates lymphoproliferation in C57BL/6 lpr mice. *Sci Rep* (2019) 9(1):4032. doi: 10.1038/s41598-019-39483-w

79. Takeda K, Dennert G. The development of autoimmunity in C57BL/6 lpr mice correlates with the disappearance of natural killer type 1-positive cells: evidence for their suppressive action on bone marrow stem cell proliferation, b cell immunoglobulin secretion, and autoimmune symptoms. *J Exp Med* (1993) 177(1):155–64. doi: 10.1084/jem.177.1.155

80. Tzou SC, Lupi I, Landek M, Gutenberg A, Tzou YM, Kimura H, et al. Autoimmune hypophysitis of SJL mice: clinical insights from a new animal model. *Endocrinology* (2008) 149(7):3461–9. doi: 10.1210/en.2007-1692

81. Rosenberg NL, Ringel SP, Kotzin BL. Experimental autoimmune myositis in SJL/J mice. *Clin Exp Immunol* (1987) 68(1):117–29.

82. Case LK, Wall EH, Dragon JA, Saligrama N, Krementsov DN, Moussawi M, et al. The y chromosome as a regulatory element shaping immune cell transcriptomes and susceptibility to autoimmune disease. *Genome Res* (2013) 23(9):1474–85. doi: 10.1101/gr.156703.113

83. Sellers RS, Clifford CB, Treuting PM, Brayton C. Immunological variation between inbred laboratory mouse Strains:Points to consider in phenotyping genetically immunomodified mice. *Vet Pathol* (2012) 49(1):32–43. doi: 10.1177/0300985811429314

84. Raval P. Systemic (non-organ specific) autoimmune disorders☆. In: *Reference module in biomedical sciences*. Elsevier (2014), 1-6. doi: 10.1016/B978-008055232-3.60773-1

85. Lin Y-H, Liu G, Kavran M, Altuntas CZ, Gasbarro G, Tuohy VK, et al. Lower urinary tract phenotype of experimental autoimmune cystitis in mouse: a potential animal model for interstitial cystitis. *BJU international* (2008) 102(11):1724–30. doi: 10.1111/j.1464-410X.2008.07891.x

86. Dubois EL, Horowitz RE, Demopoulos HB, Teplitz R. NZB/NZW mice as a model of systemic lupus erythematosus. *Jama* (1966) 195(4):285–9. doi: 10.1001/jama.1966.03100040091025

87. Chused TM, McCoy KL, Lal RB, Malek TR, Brown EM, Edison LJ, et al. Autoimmune disease in new Zealand mice. In: Smolen JS, Zielinski CC, editors. *Systemic lupus erythematosus: clinical and experimental aspects*. Berlin, Heidelberg: Springer Berlin Heidelberg (1987). p. 50–9. doi: 10.1046/j.1365-2249.1998.00588.x

88. Trunova GV, Makarova OV, Diatroptov ME, Bogdanova IM, Mikchailova LP, Abdulaeva SO. Morphofunctional characteristic of the immune system in BALB/c and C57BL/6 mice. *Bull Exp Biol Med* (2011) 151(1):99–102. doi: 10.1007/s10517-011-1268-1

89. Bourlon MT, Sánchez-Ávila M, Chablé-Montero F, Arceo-Olaiz R. IgG4-related autoimmune prostatitis: is it an unusual or underdiagnosed manifestation of IgG4-related disease? *Case Rep Urol* (2013) 2013:295472. doi: 10.1155/2013/295472

90. Rivero VE, Motrich RD, Maccioni M, Riera CM. Autoimmune etiology in chronic prostatitis syndrome: an advance in the understanding of this pathology. *Crit Rev Immunol* (2007) 27(1):33–46. doi: 10.1615/CritRevImmunol.v27.i1.30

91. Haverkamp JM, Charbonneau B, Crist SA, Meyerholz DK, Cohen MB, Snyder PW, et al. An inducible model of abacterial prostatitis induces antigen specific inflammatory and proliferative changes in the murine prostate. *Prostate* (2011) 71(11):1139–50. doi: 10.1002/pros.21327

92. Seethalakshmi L, Bala RS, Malhotra RK, Austin-Ritchie T, Miller-Graziano C, Menon M, et al. 17 beta-estradiol induced prostatitis in the rat is an autoimmune disease. *J Urol* (1996) 156(5):1838–42. doi: 10.1016/S0022-5347(01)65548-4

93. Pacheco-Rupil B, Depiante-Depaoli M, Casadio B. Experimental autoimmune damage to rat male accessory glands. II. T cell requirement in adoptive transfer of specific tissue damage. *Am J Reprod Immunol* (1984) 5(1):15–9. doi: 10.1111/j.1600-0897.1984.tb00281.x

94. Hurwitz AA, Foster BA, Kwon ED, Truong T, Choi EM, Greenberg NM, et al. Combination immunotherapy of primary prostate cancer in a transgenic mouse model using CTLA-4 blockade. *Cancer Res* (2000) 60(9):2444–8.

95. Gilardoni MB, Rabinovich GA, Oviedo M, Depiante-Depaoli M. Prostate cancer induction in autoimmune rats and modulation of T cell apoptosis. *J Exp Clin Cancer Res* (1999) 18(4):493–504.

96. Lees JR, Charbonneau B, Hayball JD, Diener K, Brown M, Matusik R, et al. T-Cell recognition of a prostate specific antigen is not sufficient to induce prostate tissue destruction. *Prostate* (2006) 66(6):578–90. doi: 10.1002/pros.20307

97. Zhang J, Thomas TZ, Kasper S, Matusik RJ. A small composite probasin promoter confers high levels of prostate-specific gene expression through regulation by androgens and glucocorticoids *in vitro* and *in vivo*. *Endocrinology* (2000) 141 (12):4698–710. doi: 10.1210/endo.141.12.7837

98. Andriani F, Nan B, Yu J, Li X, Weigel NL, McPhaul MJ, et al. Use of the probasin promoter ARR2PB to express bax in androgen receptor-positive prostate cancer cells. *J Natl Cancer Inst* (2001) 93(17):1314–24. doi: 10.1093/jnci/93.17.1314

99. Kemna J, Gout E, Daniau L, Lao J, Weißert K, Ammann S, et al. IFNγ binding to extracellular matrix prevents fatal systemic toxicity. *Nat Immunol* (2023) 24(3):414–22. doi: 10.1038/s41590-023-01420-5

100. Oftedal BE, Hellesen A, Erichsen MM, Bratland E, Vardi A, Perheentupa J, et al. Dominant mutations in the autoimmune regulator AIRE are associated with common organ-specific autoimmune diseases. *Immunity* (2015) 42(6):1185–96. doi: 10.1016/j.immuni.2015.04.021

101. Anderson MS, Venanzi ES, Klein L, Chen Z, Berzins SP, Turley SJ, et al. Projection of an immunological self shadow within the thymus by the aire protein. *Science* (2002) 298(5597):1395–401. doi: 10.1126/science.1075958

102. Jiang W, Anderson MS, Bronson R, Mathis D, Benoist C. Modifier loci condition autoimmunity provoked by aire deficiency. *J Exp Med* (2005) 202(6):805–15. doi: 10.1084/jem.20050693

103. Bianco JJ, Handelsman DJ, Pedersen JS, Risbridger GP. Direct response of the murine prostate gland and seminal vesicles to estradiol. *Endocrinology* (2002) 143 (12):4922–33. doi: 10.1210/en.2002-220493

104. Strauss L, Mäkelä S, Joshi S, Huhtaniemi I, Santti R. Genistein exerts estrogen-like effects in male mouse reproductive tract. *Mol Cell Endocrinol* (1998) 144(1-2):83–93. doi: 10.1016/S0303-7207(98)00152-X

105. Tam NN, Ghatak S, Ho SM. Sex hormone-induced alterations in the activities of antioxidant enzymes and lipid peroxidation status in the prostate of noble rats. *Prostate* (2003) 55(1):1–8. doi: 10.1002/pros.10169

106. Konkol Y, Vuorikoski H, Streng T, Tuomela J, Bernoulli J. Characterization a model of prostatic diseases and obstructive voiding induced by sex hormone imbalance in the wistar and noble rats. *Transl Androl Urol* (2019) 8(Suppl 1):S45–s57. doi: 10.21037/tau.2019.02.03

107. Bernoulli J, Yatkin E, Talvitie EM, Santti R, Streng T. Urodynamic changes in a noble rat model for nonbacterial prostatic inflammation. *Prostate* (2007) 67(8):888–99. doi: 10.1002/pros.20567

108. Prins GS. Neonatal estrogen exposure induces lobe-specific alterations in adult rat prostate androgen receptor expression. *Endocrinology* (1992) 130(6):3703–14. doi: 10.1210/endo.130.6.1597166

109. Camargo ACL, Constantino FB, Santos SAA, Colombelli KT, Dal-Pai-Silva M, Felisbino SL, et al. Influence of postnatal prolactin modulation on the development and maturation of ventral prostate in young rats. *Reprod Fertil Dev* (2018) 30(7):969–79. doi: 10.1071/RD17343

110. Harris MT, Feldberg RS, Lau KM, Lazarus NH, Cochrane DE. Expression of proinflammatory genes during estrogen-induced inflammation of the rat prostate. *Prostate* (2000) 44(1):19–25. doi: 10.1002/1097-0045(20000615)44:1<19::AID-PROS3>3.0.CO;2-S

111. Robinette CL. Sex-hormone-induced inflammation and fibromuscular proliferation in the rat lateral prostate. *Prostate* (1988) 12(3):271–86. doi: 10.1002/pros.2990120310

112. Yamaguchi H, Kurita M, Okamoto K, Kotera T, Oka M. Voiding behavior and chronic pelvic pain in two types of rat nonbacterial prostatitis models: attenuation of chronic pelvic pain by repeated administration of tadalafil. *Prostate* (2019) 79(5):446–53. doi: 10.1002/pros.23750

113. Kamijo T, Sato S, Kitamura T. Effect of cernitin pollen-extract on experimental nonbacterial prostatitis in rats. *Prostate* (2001) 49(2):122–31. doi: 10.1002/pros.1126

114. Wilson MJ, Woodson M, Wiehr C, Reddy A, Sinha AA. Matrix metalloproteinases in the pathogenesis of estradiol-induced nonbacterial prostatitis in the lateral prostate lobe of the wistar rat. *Exp Mol Pathol* (2004) 77(1):7–17. doi: 10.1016/j.yexmp.2004.02.004

115. Tangbanluekal L, Robinette CL. Prolactin mediates estradiol-induced inflammation in the lateral prostate of wistar rats. *Endocrinology* (1993) 132 (6):2407–16. doi: 10.1210/endo.132.6.8504745

116. Ellem SJ, Wang H, Poutanen M, Risbridger GP. Increased endogenous estrogen synthesis leads to the sequential induction of prostatic inflammation (prostatitis) and prostatic pre-malignancy. *Am J Pathol* (2009) 175(3):1187–99. doi: 10.2353/ajpath.2009.081107

117. Kwon SM, Kim SI, Chun DC, Cho NH, Chung BC, Park BW, et al. Development of rat prostatitis model by oral administration of isoflavone and its characteristics. *Yonsei Med J* (2001) 42(4):395–404. doi: 10.3349/ymj.2001.42.4.395

118. Lamas CA, Kido LA, Hermes TA, Nogueira-Lima E, Minatel E, Collares-Buzato CB, et al. Brazilian Berry extract (Myrciaria jaboticaba): a promising therapy to minimize prostatic inflammation and oxidative stress. *Prostate* (2020) 80(11):859–71. doi: 10.1002/pros.24017

119. Tikoo K, Vikram A, Shrivastava S, Jena G, Shah H, Chhabra R. Parental high-fat diet promotes inflammatory and senescence-related changes in prostate. *Oxid Med Cell Longev* (2017) 2017:4962950. doi: 10.1155/2017/4962950

120. Shankar E, Vykhovanets EV, Vykhovanets OV, Maclennan GT, Singh R, Bhaskaran N, et al. High-fat diet activates pro-inflammatory response in the prostate through association of stat-3 and NF-κB. *Prostate* (2012) 72(3):233–43. doi: 10.1002/pros.21425

121. Vykhovanets EV, Shankar E, Vykhovanets OV, Shukla S, Gupta S. High-fat diet increases NF-κB signaling in the prostate of reporter mice. *Prostate* (2011) 71 (2):147–56. doi: 10.1002/pros.21230

122. Ferrucci D, Silva SP, Rocha A, Nascimento L, Vieira AS, Taboga SR, et al. Dietary fatty acid quality affects systemic parameters and promotes prostatitis and pre-neoplastic lesions. *Sci Rep* (2019) 9(1):19233. doi: 10.1038/s41598-019-55882-5

123. Stoker TE, Robinette CL, Cooper RL. Perinatal exposure to estrogenic compounds and the subsequent effects on the prostate of the adult rat: evaluation of inflammation in the ventral and lateral lobes. *Reprod Toxicol* (1999) 13(6):463–72. doi: 10.1016/S0890-6238(99)00049-0

124. Stoker TE, Robinette CL, Britt BH, Laws SC, Cooper RL. Prepubertal exposure to compounds that increase prolactin secretion in the male rat: effects on the adult prostate. *Biol Reprod* (1999) 61(6):1636–43. doi: 10.1095/biolreprod61.6.1636

125. Stoker TE, Robinette CL, Cooper RL. Maternal exposure to atrazine during lactation suppresses suckling-induced prolactin release and results in prostatitis in the adult offspring. *Toxicol Sci* (1999) 52(1):68–79. doi: 10.1093/toxsci/52.1.68

126. Wolf CJ, LeBlanc GA, Ostby JS, Gray LEJr. Characterization of the period of sensitivity of fetal male sexual development to vinclozolin. *Toxicol Sci* (2000) 55 (1):152–61. doi: 10.1093/toxsci/55.1.152

127. Cowin PA, Gold E, Aleksova J, O'Bryan MK, Foster PM, Scott HS, et al. Vinclozolin exposure *in utero* induces postpubertal prostatitis and reduces sperm production *via* a reversible hormone-regulated mechanism. *Endocrinology* (2010) 151 (2):783–92. doi: 10.1210/en.2009-0982

128. Cowin PA, Foster P, Pedersen J, Hedwards S, McPherson SJ, Risbridger GP. Early-onset endocrine disruptor-induced prostatitis in the rat. *Environ Health Perspect* (2008) 116(7):923–9. doi: 10.1289/ehp.11239

129. Gatenbeck L, Aronsson A, Dahlgren S, Johansson B, Strömberg L. Stress stimuli-induced histopathological changes in the prostate: an experimental study in the rat. *Prostate* (1987) 11(1):69–76. doi: 10.1002/pros.2990110109

130. Aronsson A, Dahlgren S, Gatenbeck L, Strömberg L. Predictive sites of inflammatory manifestation in the prostatic gland: an experimental study on nonbacterial prostatitis in the rat. *Prostate* (1988) 13(1):17–24. doi: 10.1002/pros.2990130103

131. Zeng F, Chen H, Yang J, Wang L, Cui Y, Guan X, et al. Development and validation of an animal model of prostate inflammation-induced chronic pelvic pain: evaluating from inflammation of the prostate to pain behavioral modifications. *PloS One* (2014) 9(5):e96824. doi: 10.1371/journal.pone.0096824

132. Chen CS, Chang PJ, Lin WY, Huang YC, Ho DR. Evidences of the inflammasome pathway in chronic prostatitis and chronic pelvic pain syndrome in an animal model. *Prostate* (2013) 73(4):391–7. doi: 10.1002/pros.22580

133. Radhakrishnan R, Nallu RS. Development and characterisation of a novel animal model of prostate inflammation-induced chronic pelvic pain. *Inflammopharmacology* (2009) 17(1):23–8. doi: 10.1007/s10787-008-8051-6

134. Wang HJ, Tyagi P, Chen YM, Chancellor MB, Chuang YC. Low energy shock wave therapy inhibits inflammatory molecules and suppresses prostatic pain and hypersensitivity in a capsaicin induced prostatitis model in rats. *Int J Mol Sci* (2019) 20(19). doi: 10.3390/ijms20194777

135. Yuan Y, Dong FX, Liu X, Xiao HB, Zhou ZG. Liquid chromatograph-mass spectrometry-based non-targeted metabolomics discovery of potential endogenous biomarkers associated with prostatitis rats to reveal the effects of magnoflorine. *Front Pharmacol* (2021) 12:741378. doi: 10.3389/fphar.2021.741378

136. Chuang YC, Yoshimura N, Huang CC, Wu M, Chiang PH, Chancellor MB. Intraprostatic botulinum toxin a injection inhibits cyclooxygenase-2 expression and suppresses prostatic pain on capsaicin induced prostatitis model in rat. *J Urol* (2008) 180(2):742–8. doi: 10.1016/j.juro.2007.07.120

137. Dieudé M, Bell C, Turgeon J, Beillevaire D, Pomerleau L, Yang B, et al. The 20S proteasome core, active within apoptotic exosome-like vesicles, induces autoantibody production and accelerates rejection. *Sci Trans Med* (2015) 7(318):318ra200. doi: 10.1126/scitranslmed.aac9816

138. Zhao B, Zheng J, Qiao Y, Wang Y, Luo Y, Zhang D, et al. Prostatic fluid exosome-mediated microRNA-155 promotes the pathogenesis of type IIIA chronic prostatitis. *Transl Androl Urol* (2021) 10(5):1976–87. doi: 10.21037/tau-21-139

139. Funahashi Y, Majima T, Matsukawa Y, Yamamoto T, Yoshida M, Gotoh M. Intraprostatic reflux of urine induces inflammation in a rat. *Prostate* (2017) 77(2):164–72. doi: 10.1002/pros.23257

140. Carnevale L, Pallante F, Perrotta M, Iodice D, Perrotta S, Fardella S, et al. Celiac vagus nerve stimulation recapitulates angiotensin II-induced splenic noradrenergic activation, driving egress of CD8 effector cells. *Cell Rep* (2020) 33(11):108494. doi: 10.1016/j.celrep.2020.108494

141. Kox M, van Eijk LT, Zwaag J, van den Wildenberg J, Sweep FC, van der Hoeven JG, et al. Voluntary activation of the sympathetic nervous system and attenuation of the innate immune response in humans. *Proc Natl Acad Sci United States America* (2014) 111(20):7379–84. doi: 10.1073/pnas.1322174111

142. Hu H, Cui Y, Yang J, Cao Y. Loss of the sympathetic signal produces sterile inflammation of the prostate. *Front Mol Neurosci* (2022) 15:855376. doi: 10.3389/fnmol.2022.855376

143. Wang X, Zhong S, Xu T, Xia L, Zhang X, Zhu Z, et al. Histopathological classification criteria of rat model of chronic prostatitis/chronic pelvic pain syndrome. *Int Urol Nephrol* (2015) 47(2):307–16. doi: 10.1007/s11255-014-0868-x

144. Nickel JC, True LD, Krieger JN, Berger RE, Boag AH, Young ID. Consensus development of a histopathological classification system for chronic prostatic inflammation. *BJU Int* (2001) 87(9):797–805. doi: 10.1046/j.1464-410x.2001.02193.x

145. Penna G, Mondaini N, Amuchastegui S, Degli Innocenti S, Carini M, Giubilei G, et al. Seminal plasma cytokines and chemokines in prostate inflammation: interleukin 8 as a predictive biomarker in chronic prostatitis/chronic pelvic pain syndrome and benign prostatic hyperplasia. *Eur Urol* (2007) 51(2):524–33. doi: 10.1016/j.eururo.2006.07.016

146. Desireddi NV, Campbell PL, Stern JA, Sobkoviak R, Chuai S, Shahrara S, et al. Monocyte chemoattractant protein-1 and macrophage inflammatory protein-1alpha as possible biomarkers for the chronic pelvic pain syndrome. *J Urol* (2008) 179(5):1857–61. doi: 10.1016/j.juro.2008.01.028

147. Conte MP, Aleandri M, Marazzato M, Conte AL, Ambrosi C, Nicoletti M, et al. The Adherent/Invasive escherichia coli strain LF82 invades and persists in human prostate cell line RWPE-1, activating a strong inflammatory response. *Infect Immun* (2016) 84(11):3105–13. doi: 10.1128/IAI.00438-16

148. Kim JH, Kim KH, Kim HJ, Lee J, Myung SC. Expression of beta-defensin 131 promotes an innate immune response in human prostate epithelial cells. *PloS One* (2015) 10(12):e0144776. doi: 10.1371/journal.pone.0144776

149. Han IH, Song HO, Ryu JS. IL-6 produced by prostate epithelial cells stimulated with trichomonas vaginalis promotes proliferation of prostate cancer cells by inducing M2 polarization of THP-1-derived macrophages. *PloS Negl Trop Dis* (2020) 14(3): e0008126. doi: 10.1371/journal.pntd.0008126

150. Kushwaha B, Devi A, Maikhuri JP, Rajender S, Gupta G. Inflammation driven tumor-like signaling in prostatic epithelial cells by sexually transmitted trichomonas vaginalis. *Int J Urol* (2021) 28(2):225–40. doi: 10.1111/iju.14431

151. Jeon SH, Zhu GQ, Kwon EB, Lee KW, Cho HJ, Ha US, et al. Extracorporeal shock wave therapy decreases COX-2 by inhibiting TLR4-NFκB pathway in a prostatitis rat model. *Prostate* (2019) 79(13):1498–504. doi: 10.1002/pros.23880

152. Zhu GQ, Jeon SH, Lee KW, Tian WJ, Cho HJ, Ha US, et al. Electric stimulation hyperthermia relieves inflammation *via* the suppressor of cytokine signaling 3-toll like receptor 4 pathway in a prostatitis rat model. *World J Mens Health* (2020) 38(3):359–69. doi: 10.5534/wjmh.190078

153. Feng B, Dong Z, Wang Y, Yan G, Yang E, Cheng H, et al. Li-ESWT treatment reduces inflammation, oxidative stress, and pain *via* the PI3K/AKT/FOXO1 pathway in autoimmune prostatitis rat models. *Andrology* (2021) 9(5):1593–602. doi: 10.1111/andr.13027

154. Meng H, Shen Y, Shen J, Zhou F, Shen S, Das UN. Effect of n-3 and n-6 unsaturated fatty acids on prostate cancer (PC-3) and prostate epithelial (RWPE-1) cells. *vitro Lipids Health Dis* (2013) 12:160. doi: 10.1186/1476-511X-12-160

frontiers | Frontiers in Immunology

TYPE Original Research
PUBLISHED 10 July 2023
DOI 10.3389/fimmu.2023.1173728

Check for updates

OPEN ACCESS

EDITED BY
Silke Paust,
The Scripps Research Institute,
United States

REVIEWED BY
Weihong Zeng,
International Peace Maternity and Child Health Hospital, China
Ankit Jain,
Texas A&M University, United States

*CORRESPONDENCE
Yoshie Kametani
y-kametn@is.icc.u-tokai.ac.jp;
ky49214@tsc.u-tokai.ac.jp

RECEIVED 25 February 2023
ACCEPTED 26 June 2023
PUBLISHED 10 July 2023

CITATION
Kametani Y, Ito R, Ohshima S, Manabe Y, Ohno Y, Shimizu T, Yamada S, Katano N, Kirigaya D, Ito K, Matsumoto T, Tsuda B, Kashiwagi H, Goto Y, Yasuda A, Maeki M, Tokeshi M, Seki T, Fukase K, Mikami M, Ando K, Ishimoto H and Shiina T (2023) Construction of the systemic anticancer immune environment in tumour-bearing humanized mouse by using liposome-encapsulated anti-programmed death ligand 1 antibody-conjugated progesterone. *Front. Immunol.* 14:1173728. doi: 10.3389/fimmu.2023.1173728

COPYRIGHT
© 2023 Kametani, Ito, Ohshima, Manabe, Ohno, Shimizu, Yamada, Katano, Kirigaya, Ito, Matsumoto, Tsuda, Kashiwagi, Goto, Yasuda, Maeki, Tokeshi, Seki, Fukase, Mikami, Ando, Ishimoto and Shiina. This is an open-access article distributed under the terms of the Creative Commons Attribution License (CC BY). The use, distribution or reproduction in other forums is permitted, provided the original author(s) and the copyright owner(s) are credited and that the original publication in this journal is cited, in accordance with accepted academic practice. No use, distribution or reproduction is permitted which does not comply with these terms.

Construction of the systemic anticancer immune environment in tumour-bearing humanized mouse by using liposome-encapsulated anti-programmed death ligand 1 antibody-conjugated progesterone

Yoshie Kametani[1,2]*, Ryoji Ito[3], Shino Ohshima[1], Yoshiyuki Manabe[4,5], Yusuke Ohno[1,3], Tomoka Shimizu[1], Soga Yamada[1], Nagi Katano[1], Daiki Kirigaya[1], Keita Ito[4], Takuya Matsumoto[4], Banri Tsuda[6], Hirofumi Kashiwagi[7], Yumiko Goto[7], Atsushi Yasuda[8], Masatoshi Maeki[9], Manabu Tokeshi[9], Toshiro Seki[8], Koichi Fukase[4,5], Mikio Mikami[7], Kiyoshi Ando[10,11], Hitoshi Ishimoto[7] and Takashi Shiina[1,2]

[1]Department of Molecular Life Science, Division of Basic Medical Science, Tokai University School of Medicine, Isehara, Japan, [2]Institute of Advanced Biosciences, Tokai University, Hiratsuka, Kanagawa, Japan, [3]Human Disease Model Laboratory, Department of Applied Research for Laboratory Animals, Central Institute for Experimental Animals, Kawasaki, Japan, [4]Department of Chemistry, Graduate School of Science, Osaka University, Osaka, Japan, [5]Forefront Research Center, Osaka University, Osaka, Japan, [6]Department of Palliative Medicine, Tokai University School of Medicine, Isehara, Japan, [7]Department of Obstetrics and Gynecology, Tokai University School of Medicine, Isehara, Japan, [8]Department of Internal Medicine, Division of Nephrology, Endocrinology, and Metabolism, Tokai University School of Medicine, Isehara, Japan, [9]Faculty of Engineering, Hokkaido University, Sapporo, Japan, [10]Department of Hematology and Oncology, Tokai University School of Medicine, Isehara, Japan, [11]Department of Hematology and Oncology, Research Institute for Radiation Biology and Medicine, Hiroshima University, Hiroshima, Japan

Immune checkpoint inhibitors highlight the importance of anticancer immunity. However, their clinical utility and safety are limited by the low response rates and adverse effects. We focused on progesterone (P4), a hormone produced by the placenta during pregnancy, because it has multiple biological activities related to anticancer and immune regulation effects. P4 has a reversible immune regulatory function distinct from that of the stress hormone cortisol, which may drive irreversible immune suppression that promotes T cell exhaustion and apoptosis in patients with cancer. Because the anticancer effect of P4 is induced at higher than physiological concentrations, we aimed to develop a new anticancer drug by encapsulating P4 in liposomes. In this study, we prepared liposome-encapsulated anti-programmed death ligand 1 (PD-L1) antibody-conjugated P4 (Lipo-anti-PD-L1-P4) and evaluated the effects on the growth of MDA-MB-231 cells, a PD-L1-expressing triple-negative breast cancer cell line, *in vitro* and in NOG-hIL-4-Tg mice transplanted with human peripheral blood mononuclear cells (humanized

mice). Lipo-anti-PD-L1-P4 at physiological concentrations reduced T cell exhaustion and proliferation of MDA-MB-231 *in vitro*. Humanized mice bearing MDA-MB-231 cells expressing PD-L1 showed suppressed tumor growth and peripheral tissue inflammation. The proportion of B cells and CD4+ T cells decreased, whereas the proportion of CD8+ T cells increased in Lipo-anti-PD-L1-P4-administrated mice spleens and tumor-infiltrated lymphocytes. Our results suggested that Lipo-anti-PD-L1-P4 establishes a systemic anticancer immune environment with minimal toxicity. Thus, the use of P4 as an anticancer drug may represent a new strategy for cancer treatment.

KEYWORDS

breast cancer, immune environment, liposome, progesterone, programmed death ligand 1, humanized mouse

1 Introduction

Immune checkpoint blockade is a powerful tool in cancer treatment. However, the overall treatment response rate is low and patients experience acute and chronic immune-related adverse events, suggesting that systemic anticancer immune responses are impaired by the establishment of a local tumor microenvironment (1, 2). Cancers of different origins have developed similar strategies for evading the immune system. For example, cancer cells frequently escape immune surveillance by downregulating the major histocompatibility complex expression and/or expressing programmed death ligand 1 (PD-L1) (3, 4). Cancer cells share these characteristics and gene expression patterns with placental trophoblasts (5). However, trophoblast invasion of the endometrium and decidua during pregnancy is highly regulated; the invasion stops in the myometrium to prevent dispersion into the maternal circulation (6, 7). After 10 months of gestation, trophoblasts are excreted or undergo apoptosis. The immune system of pregnant women is active in order to protect against infectious diseases; this was evident by the statistically insignificant difference between the death rate of pregnant women with coronavirus disease 2019 and that of non-pregnant women (8, 9). Moreover, pregnancy does not promote cancer progression (10).

We tried to construct an anticancer immune environment by using molecules involved in the immune system during pregnancy. We focused on progesterone (P4), which is produced in the placenta during pregnancy (11), because it is a multiple-target transcription factor and has various biological activities, such as regulation of the maternal–fetal tolerance (12) and anticancer effects (13, 14). P4 inhibits epithelial-to-mesenchymal transition (15), and its derivative induces the transition from endoplasmic reticulum stress to apoptosis (16). P4 also affects mitochondrial processes involved in apoptosis induction (17). Resting T cells survive and retain competency in the presence of P4 but die when activated by a high concentration of it (18). We also found that P4 treated cells expanded CD8 T cells extensively in humanized mice (18). Therefore, if a high amount of P4 is administered, both cancer cells and activated T cells that induce immune-related adverse events (irAEs) will die and naive T cells and resting memory T cells will survive; thus, cancer growth and irAEs might be reduced and naïve T cells might activate after the treatment. Especially, cytotoxic T cells might proliferate to induce high anticancer effects.

Glucocorticoids induce T cell exhaustion irrespective of activation state (18). Glucocorticoids suppress T cell effector functions by secreting IL-10 following the irreversible induction of T cell exhaustion (19). The use of glucocorticoids in patients with cancer which show irAEs may promote cancer progression owing to the immunosuppressive function of glucocorticoids (20). Thus, P4 may be a suitable alternative to glucocorticoids. However, the concentration of P4 required to induce antitumor effects and immune regulation is higher than its normal physiological levels.

Therefore, effective delivery is essential to achieve the dual benefits of P4. Large quantities of exosomes are secreted into placental villi (21), the contents of which reflect those of the parent cells (22). As syncytiotrophoblasts produce large amounts of P4, exosomes may contain high concentrations of hydrophobic P4 in their plasma and/or endoplasmic reticulum membranes. To mimic intrauterine exosomes, we encapsulated P4 in liposomes, which have been extensively investigated and whose toxicity and safety have been evaluated. To specifically target cancerous cells, P4 has been conjugated to the anti-PD-L1 monoclonal antibody atezolizumab (23). To study the effects of Lipo-anti-PD-L1-P4, it is insufficient to use conventional experimental animals, because the immune system is specific to each species (24). Therefore, we developed a humanized mouse model using NOD/SCID/γcnull (NOG) mice (25); it can be used to evaluate patient immunity—especially humoral immunity (26). We developed a second-generation immunodeficient mouse model (NOG-hIL-4-Tg) that expressed human IL-4 (27). These mice did not develop graft-versus-host disease after the transplantation of human peripheral blood mononuclear cells (PBMC). Mature human B cells can be engrafted into NOG-hIL-4-Tg mice, suggesting that the human immune environment can be recreated. We found that the immunity of healthy donors and patients with breast cancer could be compared by transplanting PBMCs into NOG-hIL-4-Tg mice (28). In this study, we evaluated the effects of Lipo-anti-PD-L1-P4

by analyzing the kinetic profile and localization of lymphocytes *in vitro* and *in vivo* using a humanized mouse model.

2 Materials and methods

2.1 Ethical approval

This study was conducted in accordance with the guidelines of the Declaration of Helsinki and Japanese federal regulations required for the privacy protection of human participants. The study protocol was approved by Tokai University (12R-002/20R211/21R277) and the Central Institute for Experimental Animals (08-01) Human Research Committees. Written informed consent was obtained from all participants. All animal procedures were conducted in accordance with the Guidelines for the Care and Use of Laboratory Animals and were approved by the Animal Care Committees of Tokai University School of Medicine (185016/191073/202049/213047/224039) and the Central Institute for Experimental Animals (20045). The study was conducted in compliance with the ARRIVE guidelines. As we created the healthy donor's immune environment in multiple mice, the experimental design did not need blinding.

2.2 Cell lines

The human triple-negative breast adenocarcinoma (MDA-MB-231) cell line was purchased from the European Collection of Authenticated Cell Cultures, cultured in L15 medium supplemented with 15% fetal calf serum (FCS) (Sigma-Aldrich, St. Louis, MO, USA), and maintained at 37°C without CO_2 equilibration. The myeloma (Karpas 707H) cell line was kindly gifted by Dr. Karpus from Cambridge University. Human placental choriocarcinoma (JEG-3 and BeWo) and embryonic kidney (HEK-293) cells were purchased from the American Type Collection Center (ATCC) (CLS Cat# 300192/p777_HEK293, RRID: CVCL_0045) and stored at the Tokai University School of Medicine. JEG-3 cells were cultured in low-glucose DMEM supplemented with 10% FCS and maintained at 37°C under 5% CO_2. BeWo cells were cultured in Ham's F12 medium supplemented with 10% FCS and maintained at 37°C under 5% CO_2. HEK-293 cells were cultured in high-glucose DMEM supplemented with 10% FCS and maintained at 37°C in 5% CO_2. Karpas 707H cells were cultured in RPMI-1640 medium (Nissui Co. Ltd., Tokyo, Japan) supplemented with 10% FCS and maintained at 37°C under 5% CO_2.

2.3 Human PBMCs

Peripheral blood samples (approximately 30 mL) from 42 healthy donors without a history of malignancy (23 males and 19 female individuals; age, 21–64 years) were collected in Vacutainer ACD tubes containing heparin (Becton Dickinson, Franklin Lakes, NJ, USA). The samples were immediately placed in 10 mL of Ficoll-Paque PLUS (Cytiva, London, UK). PBMCs were isolated under density gradient centrifugation (500 ×*g* for 30 min at 20°C) and washed with phosphate-buffered saline (PBS) (300 ×*g* for 5 min at 4°C).

2.4 *In vitro* culture of PBMCs

The PBMCs (1×10^6/mL) were stimulated with 1 μg/mL of toxic shock syndrome toxin 1 (TSST-1;Toxin Technology Inc., Sarasota, FL, USA) in RPMI-1640 medium supplemented with 10% fetal FCS and antibiotics (streptomycin, 0.1 mg/mL; penicillin, 100 U/mL [Meiji Seika, Tokyo, Japan]) in the presence or absence of different concentrations of P4 (Sigma-Aldrich), cortisol (Sigma-Aldrich), atezolizumab (Chugai Pharmaceutical Co. Ltd., Tokyo, Japan), or liposome-encapsulated atezolizumab-conjugated steroids, and cultured for 72 h at 37°C under 5% CO_2. The cells were harvested and washed with PBS, and 5×10^5 cells/tube were used for flow cytometry.

2.5 Flow cytometry

Fluorochrome-conjugated anti-human monoclonal antibodies were used to identify human immune cells. Cells were incubated with appropriate dilutions of fluorescently labeled mouse anti-human monoclonal antibodies (Table S1) for 15 min at 4°C, washed with PBS containing 1% (w/v) bovine serum albumin (Sigma-Aldrich), and analyzed using FACS Fortessa or Verse flow cytometer (BD Biosciences, Franklin Lakes, NJ, USA). For each analysis, a live gate with white blood cells or lymphocytes was used based on human CD45 expression. The data were analyzed using FlowJo, PRID:SCR_008520 (BD Biosciences).

The culture supernatants were collected. Debris was removed by centrifugation (300 ×*g* 5 *min* at 4°C). Cytokine quantification was performed using LEGENDplex v8.0 (BioLegend, San Diego, CA, USA). Briefly, 25 μL of the supernatant was mixed with 25 μL of capture beads and incubated for 2 h at 25 °C. The beads were washed, mixed with detection antibodies, and incubated for 1 h at 25 °C. Streptavidin–phycoerythrin was added, and the mixture was incubated for 30 min at 25 °C. The beads were washed and analyzed using a FACSVerse flow cytometer (BD Biosciences). Data (pg/mL) were analyzed using LEGENDplex v8.0.

2.6 NOG-hIL-4-Tg mice

P4- or cortisol-treated human PBMCs were transplanted into NOG-hIL-4-Tg (NOD.Cg-Prkdc^{scid}Il2rg^{tm1Sug}/Tg(CMV-IL4)/Jic) mice, which were maintained under specific pathogen-free conditions at the animal facilities of the Tokai University School of Medicine and the Central Institute for Experimental Animals. To determine the effector function of P4- or cortisol-treated human PBMCs, T and B cells were evaluated because human PBMCs can engraft in NOG-hIL-4-Tg mice without causing graft-versus-host disease (27). Offspring expressing human IL-4 were identified as

previously described (27). DNA was extracted from the ear tissue collected at the time of genotyping. Human IL-4 protein level was measured using the Human IL-4 ELISA Set BD OptEIA Kit (BD Biosciences).

2.7 Lipo-anti-PD-L1-P4

First, the following solutions were prepared: lipid solution (1,2-dioleoyl-*sn*-glycero-3-phosphocholine [35.8 mg (45.5 μmol)] [COATSOME MC-8181; NOF Corp., Tokyo, Japan] and *N*-[(3-maleimide-1-oxopropyl)aminopropyl polyethyleneglycol-carbamyl] distearoylphosphatidyl-ethanolamine [11.7 mg (4.0 μmol)] [SUNBRIGHT DSPE-020MA; NOF Corp.]) and P4 (9.56 mg [30.4 μmol]) (160-24511; FUJIFILM Wako Pure Chemical Industries Ltd., Osaka, Japan) in ethanol (5.0 mL). The lipid solution and 25 mM acetate buffer (pH 4.0) were injected into a microfluidic device (iLiNP) at flow rates of 50 and 150 μL/min, respectively, using microsyringes and microsyringe pumps (70-2208; Harvard Apparatus, Holliston, MA, USA) (29). The mixed solution from the outlet was collected in a microtube (18 ml) and dialyzed against PBS for 12 h at 4°C using Spectra/Por 4 Dialysis Membrane Standard RC Tubing (12–14 kDa cutoff) (08-667B; Spectrum Laboratories Inc., San Francisco, CA, USA). The solution containing P4 liposomes (15 mL) was concentrated to 4.5 mL using the Amicon Ultra-15 Centrifugal Filter Device (100 kDa cutoff) (UFC910024; Merck Millipore, Burlington, MA, USA) at 1,000 ×*g* for 70 min at 4°C. The size and ζ-potential of P4 liposomes were measured using a ZetaSizer Ultra (Malvern Instruments, Worcestershire, UK). The concentration of P4 incorporated into liposomes was quantified using high-performance liquid chromatography (column: COSMOSIL 5C18-AR-300 2.0 × 150 mm [37991-61; Nacalai Tesque, Kyoto, Japan]; eluent: linear gradient 2%→98% acetonitrile aqueous solution containing 0.1% trifluoroacetic acid for 48 min, followed by isocratic elution of 98% acetonitrile aqueous solution containing 0.1% trifluoroacetic acid for 7 min; flow rate: 0.2 mL/min; detection: 220 nm UV) (Shimadzu Prominence UFLC; Shimadzu Corp., Kyoto, Japan). This quantification revealed that out of the 8.6 mg of P4 introduced to the iLiNP device, 0.71 mg of it was encapsulated in liposomes (8%), and all experiments were performed based on this quantification. Given that all its constituent lipids (DOPC and DSPE-PEG-MAL) are incorporated into the liposome, the P4 content in the liposomes was calculated to be 1.5% (w/w).

P4 leakage test: P4-loaded liposomes (100 μL) were placed in a dialysis membrane (14 kDa cutoff, 046-30911; FUJIFILM Wako Pure Chemical Industries Ltd., Osaka, Japan) and dialyzed with more than 1,000-flod PBS at 37°C. The decrease in P4 concentration in the dialysis tube was monitored over time. These experiments revealed that P4 was gradually released over a period of approximately 12 h (Figure S1A).

Half-antibody-conjugated P4 liposomes were prepared as follows: 2-mercaptoethanol (8.8 mL [120 μmol]; final concentration: 50 mM) (135-07522; FUJIFILM Wako Pure Chemical Industries Ltd.) and ethylenediaminetetraacetic acid (3.5 mg [12 μmol]; final concentration: 5 mM) (15105-35; Nacalai Tesque) were added to atezolizumab in PBS (2.4 mL [2.0 mg/mL]). After incubation at 37 °C for 1.5 h, the solution was centrifuged using the Amicon Ultra-15 Centrifugal Filter Device (10 kDa cutoff) (UFC901024; Merck Millipore) at 2,580 ×*g* for 30 min at 4°C. PBS (14 mL) was added to the high molecular weight fraction and centrifuged again. This procedure was repeated thrice. Protein concentration was adjusted to 1 mg/mL and measured using a Nanodrop Lite spectrophotometer (ND-LITE-PR; Thermo Fisher Scientific, Waltham, MA, USA). Half-antibody (1 mg/mL) and P4 liposome (78.5 μg/mL) solutions were mixed in a 1:1 (v/v) ratio and shaken for 2 h at 25°C to obtain half-antibody-conjugated P4 liposomes (Lipo-anti-PD-L1-P4).

2.8 Transplantation and treatment of NOG-hIL-4-Tg mice

Human PBMCs (5×10^6 cells) were injected intravenously into 8-week-old NOG-hIL-4-Tg mice. Atezolizumab (250 μg/head), Lipo-anti-PD-L1-P4 (250 μg atezolizumab was contained in the administered liposome/head), and empty liposomes (250 μg atezolizumab was contained in the administered liposome/head) were administered intraperitoneally every five days for a total of six times. As a negative control, an equal volume of PBS was injected into NOG-hIL-4-Tg mice transplanted with human PBMCs (hu-PBL hIL-4 NOG mice). The mice were sacrificed 28 **d** after the PBMC transplantation.

For the tumor-bearing humanized mouse model, 5×10^6 MDA-MB-231 cells were transplanted subcutaneously into the flanks of 7- to 9-week-old NOG-hIL-4-Tg mice. After two weeks, 5×10^6 PBMCs were transplanted intravenously. Atezolizumab, Lipo-anti-PD-L1-P4, empty liposomes, and PBS were administered every five days intraperitoneally. Solid tumor diameters were measured every alternate day using a micrometer caliper. The tumor volume was calculated as {day X long diameter (mm) × short diameter (mm) × short diameter (mm) - day-0 long diameter (mm) × short diameter (mm) × short diameter (mm)}/2.

2.9 Immunohistochemistry

NOG-hIL-4-Tg mouse spleen, lung, liver, and tumor tissues were fixed in Mildform (FUJIFILM Wako Pure Chemical Industries, Ltd.) and embedded in paraffin. The paraffin blocks were micro-sectioned and deparaffinized. Post-fixed tissue sections were stained with hematoxylin and eosin.

For immunohistochemistry, the tissues were fixed in formalin, washed, and mounted onto glass slides. Endogenous peroxidase activity was blocked with 1% goat serum for 10 min at 25°C. The sections were blocked with goat serum for 30 min, washed, and incubated with primary monoclonal antibodies (Table S1). Subsequent incubation with peroxidase-labeled anti-mouse Ig antibody (Histofine Simple Stain MAX-PO; Nichirei Biosciences INC, Tokyo, Japan) was performed according to the manufacturer's protocol.

2.10 Quantification of cytokine secretion

NOG-mouse spleen cells, previously stored at -80°C, were stained with anti-human CD4 and CD8 antibodies, and CD4 and CD8 T cells were sorted using the FACSAria Cell sorter (BD Biosciences). For the CD3+ cells, the Pan T Cell Isolation Kit (Miltenyi Biotec B.V. & CO. KG, Germany) was used for T cell sorting. Briefly, the cells were washed and incubated with the Pan T cell biotin-antibody cocktail at 4°C for 5 min. Afterwards the mixture was washed with wash buffer and 20 µL of Pan T cell micro bead cocktail was added and then incubated at 4°C for 10 min. The T cells were sorted using the Automacs system (program: depletion; Miltenyi Biotec). The purified cells ($1x10^5$/well) were stimulated with Dynabeads™ Human T-Activator CD3/CD28 (Thermo Fisher Scientific) at 37°C, 5% CO_2 for 72 h. Supernatants of the cultured cells were submitted for cytokine quantitation using the bead-based multiplex LEGENDplex (BioLegend) according to the manufacturer's instructions. Briefly, the supernatant was mixed with capture beads and incubated for 2 h at 25°C. The beads were then washed and incubated with detection antibodies for 1 h at 25°C. Subsequently, streptavidin-phycoerythrin was added, and the mixture was incubated for 30 min at 25°C. Finally, the beads were washed and analyzed using FCM as mentioned above. Then the IL-5, IL-13, IL-2, IL-6, IL-9, IL-10, IFN- γ, TNF- α, IL-17A, IL-17F, IL-4, and IL-22 cytokines were quantified. The analysis was performed using the BD FACSVerse™ Flow Cytometer (BD Biosciences). The data were analyzed in pg/mL using LEGENDPlex™ V8.0 (BioLegend).

2.11 Statistical Analysis

Data are presented as mean ± standard deviation. After the normality testing, significant differences between groups were determined using a one-way analysis of variance or two-sided Student's *t*-test for *in vitro* analyses. Regarding the mice data, we conducted a Mann-Whitney U test and evaluated the statistical significance. All statistical analyses were performed in Microsoft Excel, RRID:SCR_016137 (Microsoft Corp., Redmond, WA, USA).

3 Results

3.1 P4 suppresses T Cell activation and tumor growth

We previously reported that a high concentration (200 µM) of P4 transiently suppresses T-cell activation (18). This was confirmed by the results presented in Figure 1A using the gating strategy shown in Figure S2. We activated PBMCs with toxic shock syndrome toxin 1 (TSST-1; a superantigen molecule that can activate non-specific T cells via antigen-presenting cells (APCs)) in the presence (2–200 µM) and absence (0 µM) of P4. T cells expressed the early activation marker CD25 and late activation marker PD-1 after 3 d in the absence of P4. However, the expression of both activation markers was suppressed in the presence of 20–200 µM P4 on both CD4 and CD8 T cells. We also examined whether P4 exerted anticancer effects on cancer cells as previously reported (13, 14). The growth of JEG-3, BeWo, MDA-MB-231, and HEK-293 cells was severely suppressed in the presence of 200 µM P4, whereas no suppression was observed in the presence of cortisol, an immunosuppressive steroid drug. The presence of 20 µM P4 did not significantly suppress the growth of Karpas 707H cells compared with cortisol. However, this suppression was comparable to that of cortisol in the presence of 200 µM P4 (Figure 1B).

These results suggest that a high concentration (200 µM) of P4 suppresses T cell activation and tumor growth, especially in adenocarcinomas.

3.2 P4 and atezolizumab decrease the expression of immune checkpoint molecules

T cell activation was suppressed when human T cells were stimulated with a high concentration (200 µM) of P4. However, T and B cells may express immune checkpoint molecules, such as programmed death 1 (PD-1) receptor and PD-L1, promoting T cell exhaustion. Because immune checkpoint antibodies suppress T cell exhaustion by blocking the interaction between PD-1 and PD-L1, we hypothesized that the co-administration of P4 and atezolizumab (an anti-PD-L1 monoclonal antibody) may preserve the quiescent state of T cells by preventing T cell exhaustion. Therefore, we activated PBMCs with TSST-1 in the presence (20 and 200 µM) and absence (0 µM) of P4. P4 decreased PD-1 and PD-L1 expression in T cells (Figures 2A–D). In the presence of atezolizumab and in the absence of P4, PD-L1 and PD-1 single-positive (SP) cells proportion tended to decrease and increase, respectively, compared to that of the control. Double-positive (DP) cells showed intermediate patterns. Co-administration of P4 and atezolizumab further suppressed PD-1 and PD-L1 expressing T cell proportion, although effective suppression required the administration of P4 at a high concentration (200 µM) of P4. The mean fluorescence intensity (MFI) of PD-1 and PD-L1 expressing cells showed a similar tendency. These results suggest that the co-administration of P4 and atezolizumab is effective in preserving the quiescent state of T cells.

3.3 Liposome encapsulation enhances the inhibitory effect of P4

In pregnant women, P4 is mainly synthesized by placental syncytiotrophoblasts. Placental intervillous blood contains approximately 10-fold more P4 than the peripheral blood, with a maximum concentration of approximately 20 µM. Even if P4 is proven to have an immune regulatory effect, the effective dose is too high for clinical administration because it is 10-fold higher than its normal physiological concentration. As syncytiotrophoblasts secrete large amounts of exosomes, we attempted to encapsulate

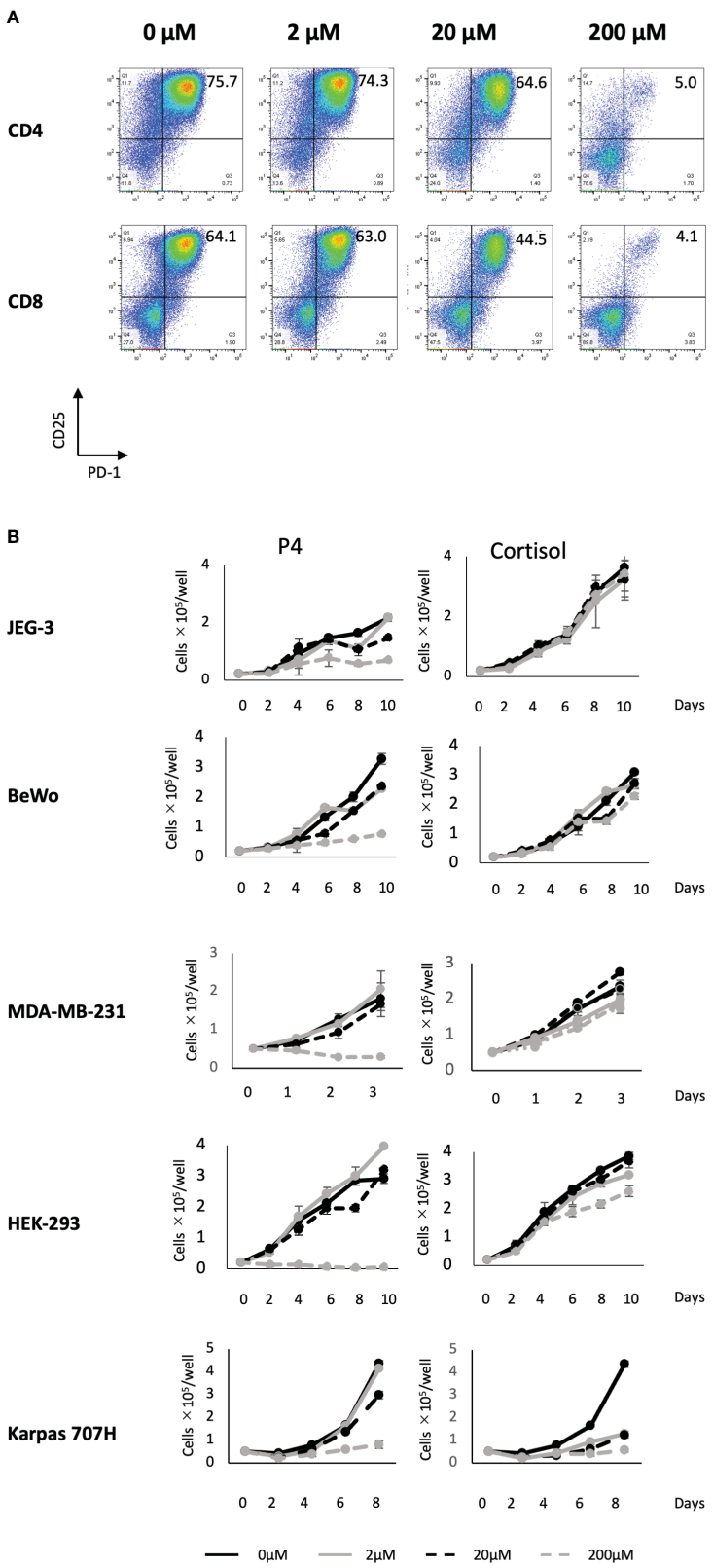

FIGURE 1
Effect of P4 on human T cells and cancer cell lines. **(A)** Peripheral blood mononuclear cells (PBMCs) were stimulated with toxic shock syndrome toxin 1 in the presence of 0, 2, 20, and 200 μM of P4. T cell activation was analyzed using flow cytometry. Upper panels: CD4+ T cells; lower panels: CD8+ T cells. The levels of activated CD25+/PD-1+ T cells are shown. **(B)** JEG-3, BeWo, MDA-MB-231, HEK-293, and Karpas 707H cells cultured with P4 (left panels) or cortisol (right panels). Solid black lines: 0 μM; broken black lines: 2 μM; solid gray lines: 20 μM; broken gray lines: 200 μM. Data are presented as the mean ± standard deviation of three independent experiments. P4, progesterone.

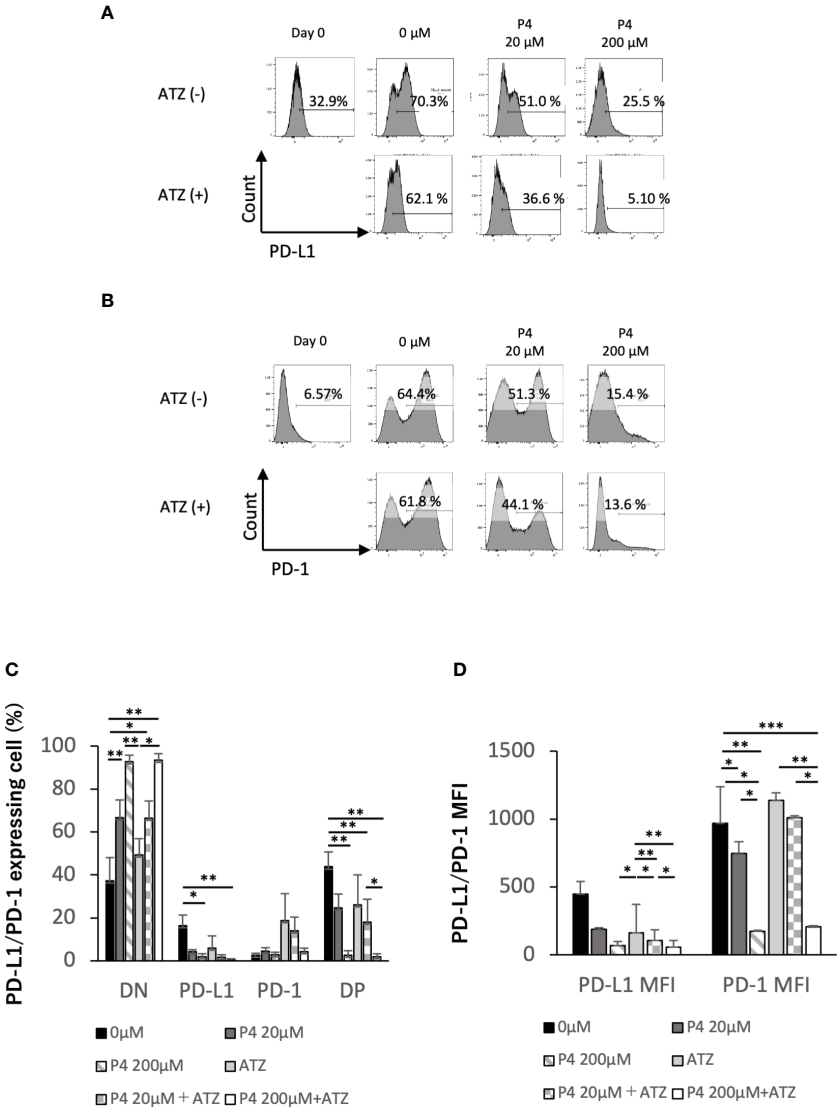

FIGURE 2
Effect of atezolizumab on the expression of immune checkpoint molecules. **(A)** PD-L1 and **(B)** PD-1 expression on T cells. P4 (0–200 μM) was added to human PBMCs and stimulated with TSST-1 for 72 h. PD-L1 expression in CD3-gated cells are shown as histograms. The culture with/without atezolizumab is shown as [ATZ(+)] or [ATZ (−)]. "Day 0" means the PBMCs before culture and "0μM" means the TSST-1 treatment without P4. Percentages shown in each panel of T cells are the PD-L1(A)- and PD-1(B)-positive cell ratios. Numbers shown in each panel of ATZ, atezolizumab; P4, progesterone; PD-1, programmed death 1; PD-L1, programmed death ligand 1. **(C)** PD-L1/PD-1 expressing cells (%). **(D)** MFI of PD-L1 or PD-1 in the CD3+ cells. Data are presented as mean ± standard deviation (S.D.) $^{**}P < 0.01$ (one-way analysis of variance or Student's *t*-test) [$n = 5$].

P4 in liposomes (Figure 3A) for targeted delivery to cells. As shown in Figure 3B, the liposome diameter was <100 nm. The liposome size remained stable for more than one month if maintained at 4°C (Figure S1B).

Human PBMCs were cultured in the presence of Lipo-anti-PD-L1-P4. Lipo-anti-PD-L1-P4 containing 20 μM P4 significantly suppressed T cell activation, especially in PD-1+/PD-L1+ T cells (Figure 4A). The MFI was reduced (Figure 4A) and the levels of activated CD25+/PD-1+ T cells in the presence of Lipo-anti-PD-L1-P4 were similar to those of CD8+ T cells in the presence of P4 10-fold higher than the normal levels (Figure 4B), suggesting that the construct enhanced the inhibitory effect of P4 on T cells. This construct enabled P4 to regulate the immune system at physiological concentrations.

When JEG-3 and MDA-MB-231 cells, both of which express PD-L1, were cultured *in vitro*, Lipo-anti-PD-L1-P4 containing 20 μM P4 suppressed cell proliferation to the same extent as 200 μM P4. In Karpas 707H cells that did not express PD-L1, Lipo-anti-PD-L1-P4 suppressed cell proliferation to a lesser extent (Figure 4C). These results suggest that Lipo-anti-PD-L1-P4 effectively suppresses T cell activation and the growth of PD-L1-expressing cancer cells at physiological concentrations of P4.

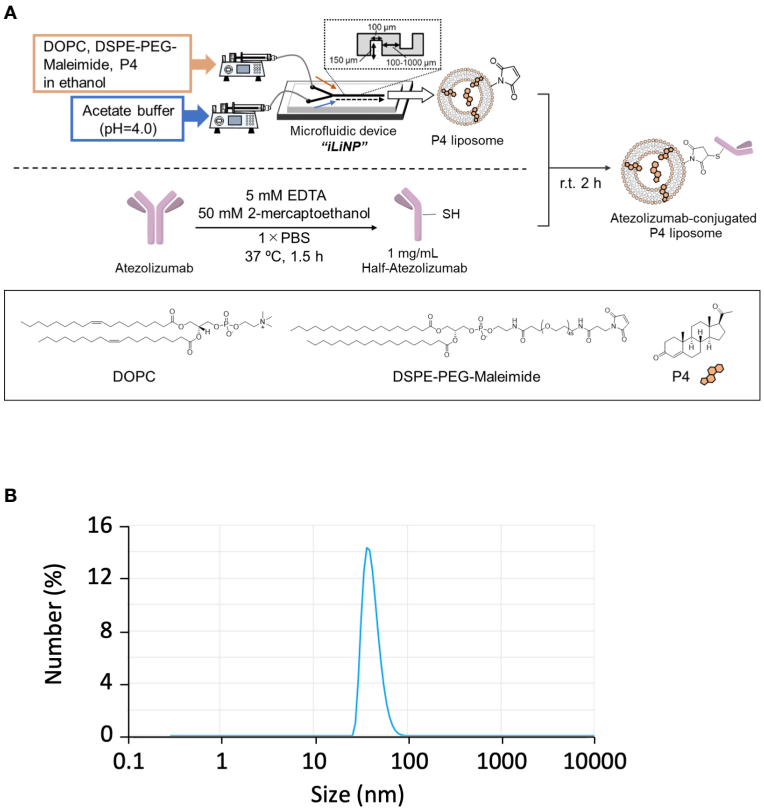

FIGURE 3
Preparation of Lipo-anti-PD-L1-P4. **(A)** Protocol for the preparation of Lipo-anti-PD-L1-P4. **(B)** Representative result of liposome size distribution. Average size: 44 nm; polydispersity index: 0.22; ζ-potential: −20.1 kV; P4 concentration: 78.5 μg/mL. **(C)** P4 leakage test. DOPC, 1,2-dioleoyl-*sn*-glycero-3-phosphocholine; DSPE-PEG-Maleimide, *N*-[(3-maleimide-1-oxopropyl)aminopropyl polyethyleneglycol-carbamyl] distearoylphosphatidylethanolamine; EDTA, ethylenediaminetetraacetic acid; Lipo-anti-PD-L1-P4, liposome-encapsulated anti-programmed death ligand 1 antibody-conjugated P4; P4, progesterone; PBS, phosphate-buffered saline; r.t., room temperature.

3.4 Establishment of a tumor-bearing humanized mouse model

To evaluate the role of immune checkpoint antibodies in immunity, we established a tumor-bearing humanized mouse model using NOG-hIL-4-Tg mice transplanted with human PBMCs (Figure 5A). MDA-MB-231 cells were subcutaneously transplanted into the NOG-hIL-4-Tg mice. After two weeks of observation, the mice were transplanted with PBMCs from healthy donors. Atezolizumab was administered to a subset of tumor-bearing humanized mice. The tumors engrafted and expanded (Figure 5B). T cell infiltration was not commonly observed in control mice (Figure 5C). Along with tumor growth, the percentage of B cells also increased (Figures 6A, B, Table 1). Most B cells developed into plasmablast-like cells (Figure S3). Tumor volume did not differ significantly between the atezolizumab-treated and control groups. However, atezolizumab-treated mice showed suppressed tumor growth and increased T cell populations, especially CD8+ T cells. Tumor-infiltrating T cells were observed in the atezolizumab-treated group (Figure 5C). We checked the CD45RA and CD62L memory markers and found that almost all cells were central and effector memory cells, and no significant differences were observed between the two treatment groups (Figure S4). These results suggest that our novel tumor-bearing humanized mouse model partially mimics breast cancer immunity, supported by our previous report on the percentage of B cells being high in patients with breast cancer (30).

3.5 Lipo-anti-PD-L1-P4 suppresses the growth of PD-L1-expressing tumor cells

Next, we used our novel tumor-bearing humanized mouse model to examine the effects of Lipo-anti-PD-L1-P4 on the tumor size and immunity. We also injected empty liposomes into tumor-bearing humanized mice to determine whether tumor growth was suppressed because liposomes themselves may have an adjuvant effect. Tumor size did not differ significantly among the control (PBS), atezolizumab-treated, Lipo-anti-PD-L1-P4-treated, and empty liposome-treated groups in the first week. Thereafter, tumor growth was suppressed in the Lipo-anti-PD-L1-P4-treated group compared with that in the other groups. After four weeks, the tumor size in the Lipo-anti-PD-L1-P4-treated group was significantly smaller than that in the other three groups. The empty liposome group showed similar kinetics as the atezolizumab-treated group, suggesting that the anticancer effect

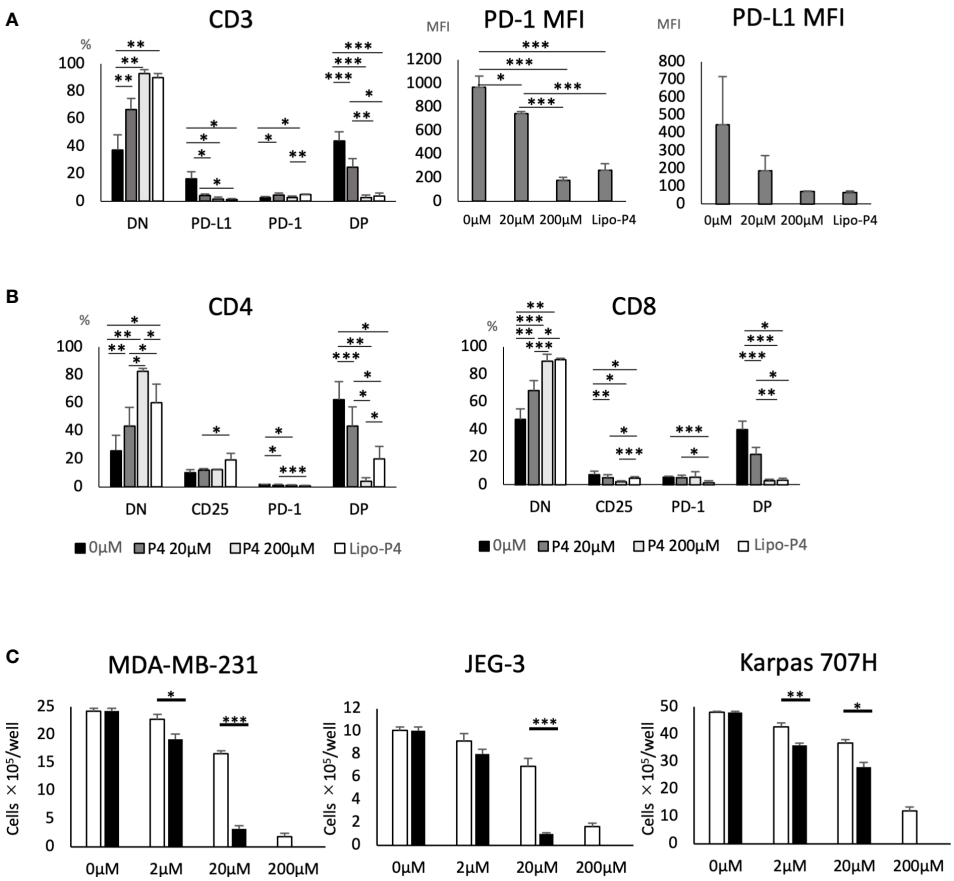

FIGURE 4
Effect of Lipo-anti-PD-L1-P4 on cell proliferation. PD-1 and PD-L1 expression on T cells **(A, B)** and **(C)** cancer cells. **(A)** Left panel: Percentage of PD-1 and PD-L1 expressing cells in CD3+ T cells. Right panels: PD-1 and PD-L1 mean fluorescence intensities of CD3+ T cells. **(B)** Left panel: percentage of PD-1 and PD-L1 expressing cells in CD4+ T cells; right panel: percentage of PD-1 and PD-L1 expressing cells in CD8+ T cells. **(C)** MDA-MB-231, JEG-3, and Karpas 707H cells were cultured in the presence or absence of P4 (open bars) or Lipo-anti-PD-L1-P4 (solid bars). Vertical lines represent the cell number after 3 d of culture. *$P < 0.05$; **$P < 0.01$; ***$P < 0.001$ (one-way analysis of variance or two-sided Student's *t*-test). Data are presented as the mean ± standard deviation of four independent experiments. DN, double-negative; DP, double-positive; Lipo-anti-PD-L1-P4 (Lipo-P4), liposome-encapsulated anti-programmed death ligand 1 antibody-conjugated P4; MFI, mean fluorescence intensity; PD-1, programmed death 1; PD-L1, programmed death ligand 1.

of empty liposomes was induced mainly by atezolizumab. In the atezolizumab and empty liposome groups, tumor growth was initially suppressed; however, after four weeks, the tumor size was the same as that in the control group (Figure 5B).

We also examined the T/B and CD4+/CD8+ T cell ratios in human CD45+ cells localized in the spleen. Almost all human lymphocytes engrafted in NOG-hIL-4-Tg mice differentiated into T cells after Lipo-anti-PD-L1-P4 treatment (Figures 6A, B, Table 1). Moreover, the percentage of CD19+ B cells significantly decreased, and that of CD8+ T cells significantly increased in the Lipo-anti-PD-L1-P4-treated group. Most of the T cells identified in these groups were central and effector memory T cells and no significant difference was observed in the expression of memory markers compared to the PBS or atezolizumab-treated groups (Figure S4). The proportions of B and CD8+/CD4+ T cells in the empty liposome group diverged, and on average, did not differ significantly from those in the atezolizumab-treated and control groups (Figures 6A, B, Table 1). Immunohistochemistry showed that among the three (PBS, ATZ and Lipo-anti-PD-L1-P4) groups, the infiltration of T cells into the tumor was the strongest in the Lipo-anti-PD-L1-P4-treated mice (Figure 5C). The infiltrated cells contained CD4 T cells and CD8 T cells and expressed a significant amount of IFN-γ (Figure S5). We purified and stimulated these CD3+ T cells and examined whether they were functional and secreted enough cytokines (Figure 5D). T cells from all three treatment groups secreted a significant amount of IFN- γ and low level of TNF- α. PBS-treated T cells and atezolizumab-treated T cells also secreted IL-5 and IL-13, which are Th2 cytokines. When the CD4 and CD8 T cells were purified and independently analyzed, these cytokines were detected in CD4 T cells, and CD8 T cells secreted only IFN-γ, TNF- α and IL-2, suggesting that the CD8 T cells showed typical cytokine profiles and CD4 T cells secreted only Th1 and Th2 cytokines (Figure S6). Furthermore, the amount of IFN-γ secreted by Lipo-P4-aPDL1-treated mouse T cells tended to be low compared to those secreted by the cells of PBS or atezolizumab-treated mice (Figures 5D, S6). While a significant amount of IFN-γ and TNF-α was secreted by CD4 T cells of the Lipo-anti-PD-L1-P4-treated #22 mouse, no detectable cytokine production was observed for the CD8 T cells of the same mouse.

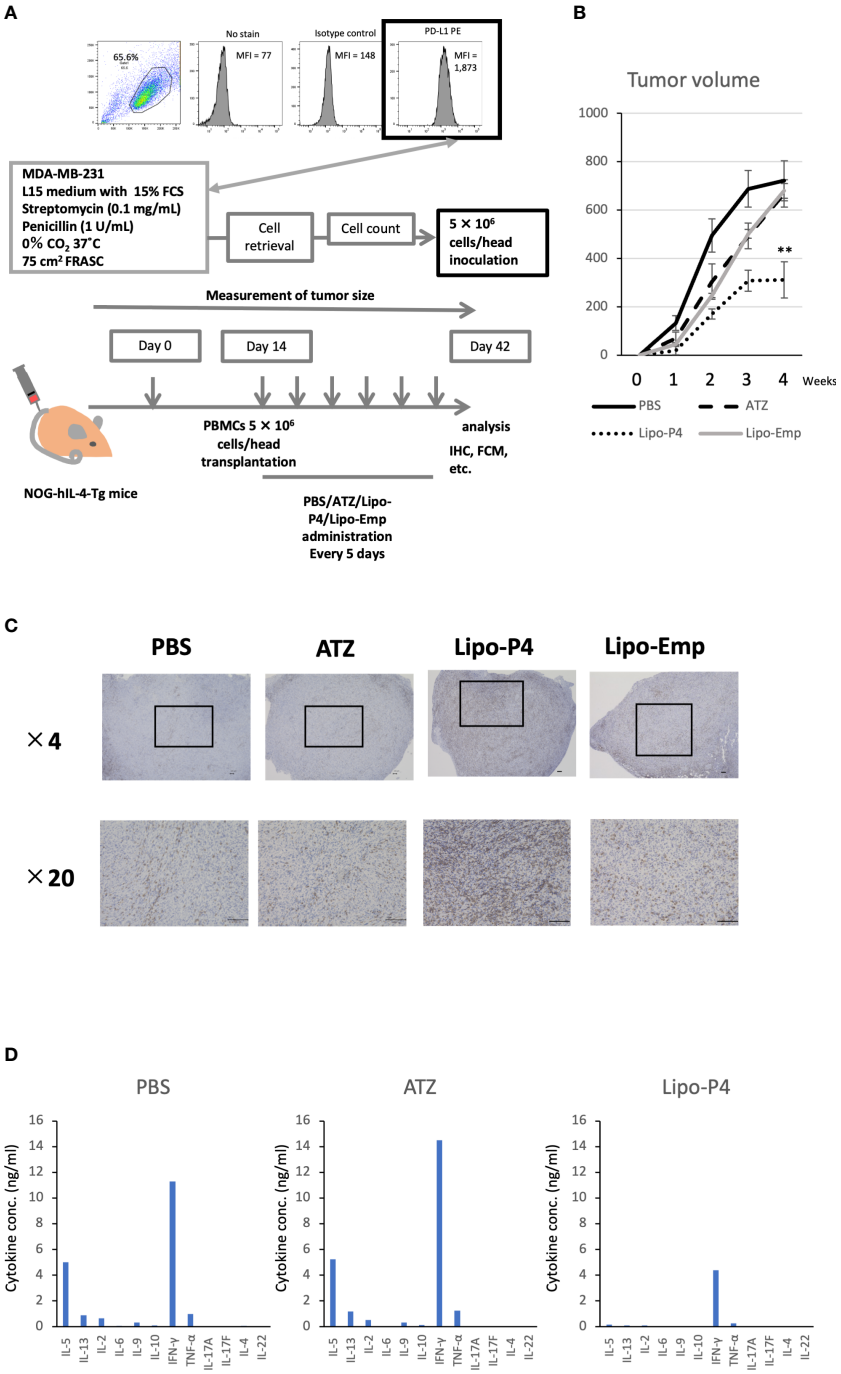

FIGURE 5
Effect of Lipo-anti-PD-L1-P4 on tumor growth in tumor-bearing humanized NOG-hIL-4-Tgmice. **(A)** Protocol for establishing the NOG-hIL-4-Tg mouse model. PD-L1 expression in MDA-MB-231 cells was analyzed using flow cytometry. **(B)** Kinetics of tumor growth in NOG-hIL-4-Tg mice. Tumor growth was measured from PBMC transplantation (Day 0). The mean volume ± standard error was calculated for each week. After four weeks, the mice were sacrificed. $^{**}P < 0.01$ (one-way analysis of variance or Student's *t*-test) (PBS [n = 11], ATZ [n = 9], Lipo-P4 [n = 7], Lipo-Emp [n = 3]). **(C)** Representative immunohistochemistry of CD3 expression in tumor tissues. Indicated bars in the tissue sections represent 100 μm. **(D)** Representative cytokine production patterns of CD3 T cells purified from NOG-hIL-4-Tg mouse spleens and stimulated with CD3/CD28. ATZ, atezolizumab; FCM, flow cytometry; FCS, fetal calf serum; IHC, immunohistochemistry; Lipo-anti-PD-L1-P4 (Lipo-P4), liposome-encapsulated anti-programmed death ligand 1 antibody-conjugated P4; Lipo-Emp, empty liposomes; MFI, mean fluorescence intensity; PBMC, peripheral blood mononuclear cell; PD-L1, programmed death ligand 1.

When the same reduced dose as that used clinically was administered, the anticancer effect was still observed but at a significantly lower level compared with that observed at the higher dose administration (Figure S7). One of the three low-dose Lipo-anti-PD-L1-P4-treated mice had more B cells and another mouse had more CD4+ T cells than CD8+ T cells (Table 1). These results suggested that atezolizumab, but not liposomes, slightly affected tumor growth. Lipo-anti-PD-L1-P4 showed a greater

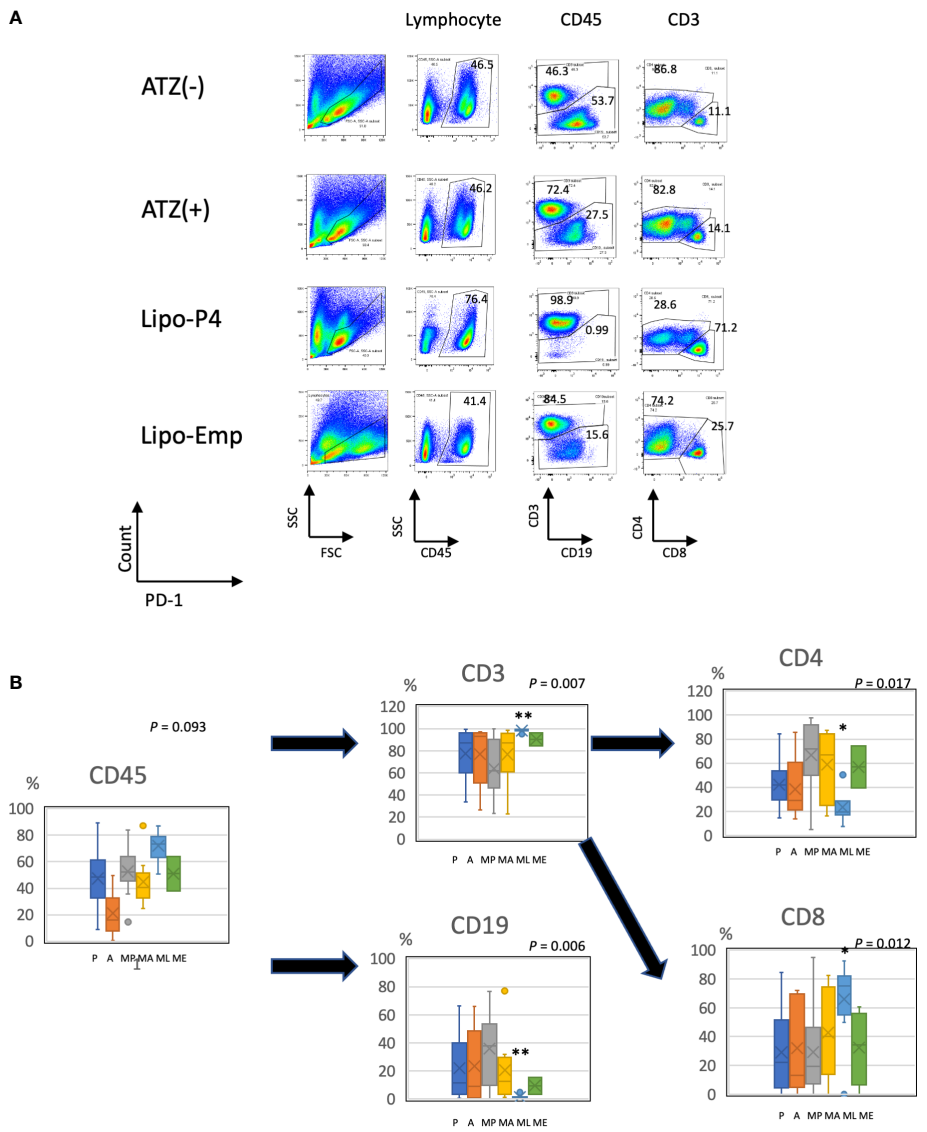

FIGURE 6
Profile of human lymphocytes in the spleen of tumor-bearing humanized mise. **(A)** Typical patterns of human lymphocytes in the NOG-hIL-4-Tg mouse spleen. Cells were gated as shown in Supplementary Figure S1. The gated fractions are shown above each panel. Vertical and horizontal lines represent the markers analyzed using flow cytometry. **(B)** Box-and-whisker plots of lymphocyte subsets. *$P < 0.05$; **$P < 0.01$ (one-way analysis of variance or Student's *t*-test) (PBS [n = 11], ATZ [n = 9], Lipo-P4 [n = 7], Lipo-Emp [n = 3]). ATZ [A], atezolizumab; Lipo-Emp, empty liposome; Lipo-anti-PD-L1-P4 (Lipo-P4), liposome-encapsulated anti-programmed death ligand 1 antibody-conjugated P4; MA, MDA-MB-231 cells transplanted with atezolizumab; ME, MDA-MB-231 cells transplanted with Lipo-Emp; ML, MDA-MB-231 cells transplanted with Lipo-anti-PD-L1-P4; MP, MDA-MB-231 cells transplanted with PBS; PBS [P], phosphate-buffered saline.

dose-dependent anticancer effect than atezolizumab in a novel tumor-bearing humanized mouse model.

3.6 Lipo-anti-PD-L1-P4 modulates immune cell migration in non-tumor tissues in tumor-bearing humanized mice

Lipo-anti-PD-L1-P4 is an effective anticancer agent because it suppresses tumor growth and may enhance T-cell infiltration in peripheral tissues, causing severe immune-related adverse events. Therefore, we analyzed T cell infiltration in the lungs and livers of Lipo-anti-PD-L1-P4-treated mice. T cell infiltration was more pronounced in the lungs and livers of Lipo-anti-PD-L1-P4-treated mice than in the control mice. However, tissue destruction was not severe (Figure S8). CD8+ T cells localized in the spleen did not express high levels of CD25 and PD-1, suggesting that cytotoxic T cell activation was moderate in the non-tumor tissues of Lipo-anti-PD-L1-P4-treated mice (Figure S9), while the memory phenotype of T cells was not significantly different among PBS, ATZ, and Lipo-anti-PDL1-P4 treatments (Figure S4).

The engraftment of human hematopoietic stem cells in immunodeficient mice is usually evaluated using CD45+ bone marrow cells. Evaluating the engraftment of human PBMCs in immunodeficient mice is difficult because CD45+ bone marrow cells cause severe graft-versus-host disease. Therefore, the T cell

TABLE 1 Proportion of human lymphocyte subsets in the tumor-bearing humanized mouse.

				/CD45		/CD3		/CD4/CD3				/CD8/CD3			
Mouse	Treatment	Spleen cell #	CD45 %	CD3 %	CD19 %	CD4 %	CD8 %	DN %	CD25 %	PD-1 %	DP %	DN %	CD25 %	PD-1 %	DP %
1	PBS	7.1E+07	54.5	29.5	70.5	92.9	7.1	17.8	7.3	33.9	41.1	57.2	31.8	5.46	5.6
2	PBS	9.8E+07	63.9	62	37.9	50.0	49.9	15.8	13.8	48.3	22.1	32	49.7	3.59	14.8
3	PBS	1.7E+07	4.98	41.4	58.6	86.5	12.4	59.7	11.6	20.5	8.19	92.5	2.5	2.5	2.5
4	PBS	4.2E+07	51.2	23.4	76.6	92.0	8.0	51	3.54	34.3	11.2	77.3	4.94	10.6	7.08
5	PBS	2.7E+07	72.7	89.5	10.7	16.4	73.1	77.6	11.9	7.63	2.84	91	5.31	2.43	1.3
6	PBS	7.8E+07	45.6	46.3	53.7	86.8	11.1	38.6	7.45	40.2	13.7	86.5	5.99	6.56	0.93
7	PBS	1.7E+08	83.9	99.7	0.22	4.93	94.9	62.6	10.9	18.3	8.16	70.4	4.31	19.5	5.76
8	PBS	8.2E+07	52.1	94	4.9	62.7	36.6	27	3.67	47.7	21.7	67.4	5.38	21.6	5.59
9	PBS	7.4E+07	35.7	53.5	45.5	97.8	1.71	16.8	6.12	51	26	49	3.41	35.5	12
10	PBS	7.8E+06	14.6	52.1	47.9	91	9	82.4	6.34	7.87	1.42	89.9	3.83	4.84	1.43
11	PBS	1.0E+08	52.2	90.2	9.78	72.1	27.8	68.1	6.27	18.9	6.7	82.9	11	4.2	1.92
AVERAGE	**PBS**	**7.0E+07**	**48.3**	**62.0**	**37.8**	**68.5**	**30.1**	**47.0**	**8.1**	**29.9**	**14.8**	**72.4**	**11.7**	**10.6**	**5.4**
12	ATZ	2.4E+08	87.2	92.5	5.54	26.3	73.6	18.2	16.8	42.2	22.8	56.1	34	2.95	6.91
13	ATZ	2.6E+07	24.7	87.2	12.8	87.2	66.5	27.5	12.1	47.2	13.2	27.5	12.1	47.2	13.2
14	ATZ	6.6E+07	35.9	22.9	77.1	86.2	13.7	45.2	6.04	34	14.8	70.2	8.69	16.8	4.3
15	ATZ	3.4E+07	38.5	98.6	1.4	16.2	82.4	51.5	21.4	14.2	12.9	79.7	8.21	7.68	4.36
16	ATZ	3.4E+07	40.4	98.6	1.37	23.3	76.6	59.4	24.9	8.18	7.53	69.8	10.8	12.2	7.19
17	ATZ	8.4E+07	45.8	72.4	27.5	82.8	14.1	46	9.69	31.6	12.7	60.3	19.5	13.7	6.59
18	ATZ	1.5E+07	5.3	95.6	2.89	49.5	48.7	39.7	6.03	34.5	19.7	74.6	3.08	20.4	1.91
19	ATZ	2.3E+07	29.8	68.5	32	80.4	19.5	58.5	15.9	16.8	8.74	77.5	8.61	11.1	2.85
20	ATZ	7.5E+07	57	92	7.98	66.8	33.1	73.4	7.04	15.6	3.95	75	10.5	11.3	3.17
AVERAGE	**ATZ**	**6.6E+07**	**40.5**	**80.9**	**18.7**	**57.6**	**47.6**	**46.6**	**13.3**	**27.1**	**12.9**	**65.6**	**12.8**	**15.9**	**5.6**
21	Lipo-P4	5.0E+04	42.1	96.7	2.9	40.6	59.1	80.9	13.9	2.63	2.59	80.9	13.9	2.63	2.59
22	Lipo-P4	2.4E+07	78.2	99.2	0.74	7.48	92.5	60.7	26.6	6.53	5.99	93.8	3.87	1.59	0.78
23	Lipo-P4	2.4E+07	79	98.9	0.99	28.6	71.2	51	4.69	37.2	7.14	86	2.67	10.5	0.81
24	Lipo-P4	1.2E+08	73.4	98.1	1.7	19.7	75.1	56	1.84	34.5	7.66	87.7	2.15	8.98	1.21

(Continued)

10.3389/fimmu.2023.1173728

TABLE 1 Continued

				/CD45		/CD3		/CD4/CD3				/CD8/CD3			
Mouse	Treatment	Spleen cell #	CD45 %	CD3 %	CD19 %	CD4 %	CD8 %	DN %	CD25 %	PD-1 %	DP %	DN %	CD25 %	PD-1 %	DP %
25	Lipo-P4	5.2E+07	63.1	99.5	0.17	16.9	82.1	18.3	3.07	51.5	27.1	66.2	1.51	30	2.33
26	Lipo-P4	1.4E+08	87.1	99.1	0.7	17.7	81.7	52.3	5.43	30.7	11.6	78.1	5.25	13.3	3.33
27	Lipo-P4	1.7E+07	41.6	79.3	21.2	73.8	26.1	77.7	10.2	8.31	3.74	87.4	7.91	3.73	0.91
28	Lipo-P4	1.5E+08	50.7	95.1	4.85	50.2	49.8	74.2	6.88	12.9	6	78.1	10.9	7.45	3.55
AVERAGE	**Lipo-P4**	**7.6E+07**	**67.6**	**95.6**	**4.3**	**30.6**	**68.4**	**55.7**	**8.4**	**25.9**	**9.9**	**82.5**	**4.9**	**10.8**	**1.8**
29	Lipo-Emp	1.7E+07	7.21	86.5	13	87.5	12.4	55.2	25.2	12.3	7.27	77.5	15.4	5.19	1.86
30	Lipo-Emp	8.8E+07	38.1	84.5	15.6	74.2	25.7	64.1	7.74	21.2	6.99	74.6	12.6	10.1	2.74
31	Lipo-Emp	1.4E+08	64	96.4	3.52	39.3	60.6	71.5	7.17	16.5	4.85	79.2	8.53	9.32	2.96
AVERAGE	**Lipo-Emp**	**8.1E+07**	**36.4**	**89.1**	**10.7**	**67.0**	**32.9**	**63.6**	**13.4**	**16.7**	**6.4**	**77.1**	**12.2**	**8.2**	**2.5**
32	ATZ (Low)	1.6E+07	0.18	91.2	3.04	85.6	6.48	52.4	20.4	5.11	22.1	75.7	10.8	8.11	5.41
33	ATZ (Low)	7.8E+07	53.1	76.2	22.1	96.2	2.33	41.6	2.92	43.8	11.6	74.9	11.5	9.23	4.41
34	ATZ (Low)	7.0E+07	66	99.5	0.2	20.8	78.8	17.6	1.49	47.7	33.2	73.4	1.36	21.9	3.29
35	ATZ (Low)	5.6E+07	67.7	98.7	1.07	58.5	41	36.7	15.1	30	18.2	75.3	4.96	16.2	3.52
AVERAGE	**ATZ (Low)**	**5.5E+07**	**46.7**	**91.4**	**6.6**	**65.3**	**32.2**	**37.1**	**10.0**	**31.7**	**21.3**	**74.8**	**7.2**	**13.9**	**4.2**
36	Lipo-P4 (Low)	9.6E+07	44.9	93	1.91	82.6	17.3	50.9	7.82	24.7	16.6	47.1	22	16.1	14.8
37	Lipo-P4 (Low)	7.4E+07	62.6	63.3	33.9	88.1	10.1	25	3.09	55.8	16.1	37.5	12	36.6	13.9
38	Lipo-P4 (Low)	4.3E+07	81.3	96.4	2.82	23.7	75.6	17.3	2.83	57.6	22.3	48.4	1.92	45.8	3.86
AVERAGE	**Lipo-P4 (Low)**	**7.1E+07**	**62.9**	**84.2**	**12.9**	**64.8**	**34.3**	**31.1**	**4.6**	**46.0**	**18.3**	**44.3**	**12.0**	**32.8**	**10.9**

The bold values mean that they are average of the groups shown in the upper site.

10.3389/fimmu.2023.1173728

population in the bone marrow can help predict the adverse effects of anticancer drugs. We compared human lymphocytes in the spleen and bone marrow and calculated the correlation coefficient. In non-tumor-bearing NOG-hIL-4-Tg mice, spleen cells were positively correlated with bone marrow cells (Figure S10).

Next, we compared the profiles of spleen and bone marrow lymphocytes of tumor-bearing humanized NOG-hIL-4-Tg mice. There was no correlation between the proportions of lymphocyte subsets in the spleen and bone marrow of the control (PBS) mice. Conversely, atezolizumab treatment induced a positive correlation between the proportion of lymphocyte subsets in the spleen and the bone marrow of conventional NOG-hIL-4-Tg mice. The effect of Lipo-anti-PD-L1-P4 was negatively correlated with CD45+, T, and B cell proportions in the spleen and bone marrow, whereas the CD4+/CD8+ ratio was highly correlated with the proportions of the two cell types (Figure 7). These results suggested that the inflammation caused in non-tumor tissues by Lipo-anti-PD-L1-P4 was moderate and not severe in our tumor-bearing humanized mouse model. Spleen and bone marrow cells are complementary and not related to engraftment, in contrast to that in conventional NOG-hIL-4-Tg mice administered with atezolizumab. Lipo-anti-PD-L1-P4 treatment increases the efficiency of human lymphocyte engraftment into peripheral lymphoid tissues. Meanwhile, severe inflammation in the peripheral non-tumor tissues was avoided.

4 Discussion

In this study, we showed that Lipo-anti-PD-L1-P4 suppressed tumor growth without causing severe inflammation in the peripheral tissues of tumor-bearing humanized NOG-hIL-4-Tg mice. The effect was 10 times higher than that of free P4 in terms of tumor cell growth, and CD8+ T cell proliferation was considered.

We recently reported that the high-dose of P4 treatment induced transient suppression of T cell activation and enhancement of T cell localization in the spleen (18), whereas previous studies demonstrated the anticancer effects of P4 (13, 14). As MDA-MB-231 cells express the membrane P4 receptor PGRMC1 (31), and P4 suppresses cell proliferation by inhibiting PGRMC1, the anticancer effect was predicted. However, to the best of our knowledge no *in vivo* studies have reported tumor growth suppression or non-tumor tissue protection by P4.

Our results suggest that P4-based immunoregulatory agents are immuno-protective and possess antitumor effects, demonstrating

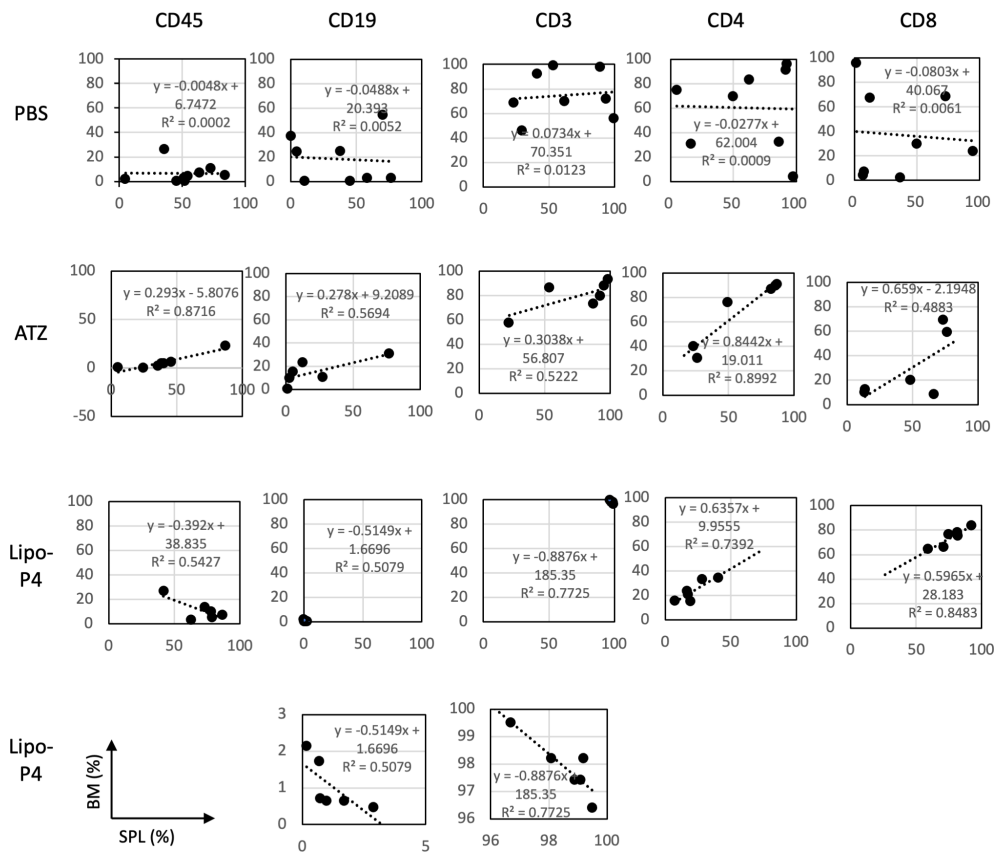

FIGURE 7
Profiles of spleen and bone marrow lymphocytes of tumor-bearing humanized NOG-hIL-4-Tg mice. The proportions (%) of human CD45+ cells/lymphocyte gated-cells, CD19+/CD45+ cells, CD3+/CD45+ cells, CD4+/CD3+ cells, and CD8+/CD3+ cells in the spleen (horizontal lines) and bone marrow (vertical lines) of NOG-hIL-4-Tg mice are plotted. Approximate straight lines and correlation coefficients are shown (PBS [n = 8], ATZ [n = 6], Lipo-P4 [n = 6]). ATZ, atezolizumab; Lipo-P4, liposome-encapsulated anti-programmed death ligand 1 antibody-conjugated P4; PBS, phosphate-buffered saline. Lower two panels of Lipo-P4 present the same graphs shown in the upper panels, but the vertical axis was expanded. Correlation lines and correlation coefficients (R^2) are shown in the panels.

the potential of immunoregulatory drugs for cancer treatment. Therefore, these agents may be safer than cortisol, which diminishes the immune response. However, the concentration required to effectively suppress the immune system and tumor growth was approximately 200 μM, which is 10-fold higher than its physiological concentration. This observation highlights the difficulty in using P4 as an alternative immune regulator to cortisol. Therefore, we aimed to deliver P4 to cells more efficiently.

Previously, it was believed that steroid hormones were secreted via simple diffusion (32). However, vesicle-mediated steroid hormone secretion has recently been reported in *Drosophila* (33). Syncytiotrophoblasts secrete large amounts of P4 (11) and exosomes into the placental villi (21). We hypothesized that exosomes would support the delivery of steroids. By encapsulating P4 in liposomes, the suppression of T cell activation and cancer cell proliferation was induced in the presence of physiological concentrations of P4 *in vitro*. In the tumor-bearing humanized mouse model, while tumor growth was suppressed and the proportion of CD8+ T cells increased, T cell infiltration into peripheral tissues did not significantly increase, and no symptoms of graft-versus-host disease were observed. Empty liposomes did not suppress tumor growth in the same manner as Lipo-anti-PD-L1-P4 did. Moreover, the empty liposomes did not enhance CD8+ T cell expansion in the spleen. These results suggested that the anticancer effect was induced by P4. A similar phenomenon may occur at the maternal–fetal interface to suppress anti-fetal immunity. Therefore, the effect of Lipo-anti-PD-L1-P4 may mimic the regulation of extravillous trophoblast migration and/or survival, and allo-specific immune activation.

During pregnancy, women develop an immune tolerance, which allows them to accept a semi-allogeneic fetus (34). In the mother, placental trophoblasts, which share the same characteristics as cancer cells, are confined to the uterus (6, 7). P4 has multiple functions involved in the trophoblast confinement (11). P4 has been reported to induce IL-4 secretion and Th2 shift, which do not enhance cytotoxicity, but enhance B-cell responses (12, 35). We previously reported that the proportion of CD8+ T cells was significantly increased in P4-pretreated PBMC-transplanted NOG-hIL-4-Tg mice (18). Kawata et al. (36) reported that short-term exposure of T cells to high concentrations of P4 induced the transient expression of T-bet. Therefore, a high concentration of P4 may induce transient T-bet expression in placental T cells to acquire the Th1 phenotype. During pregnancy, serum glucocorticoid levels increase because of stress (37). While glucocorticoids irreversibly diminish the immune system, increased levels of P4 may suppress glucocorticoid function to protect the mother's immune system from T cell exhaustion. P4 suppresses glucocorticoid function, which may suppress the development of B-cell-derived plasmablasts, resulting in the absence of B cells in the humanized mouse model.

Humanized mouse models are a powerful tool for evaluating immune-related drugs because the immune system is highly divergent between species. Many platforms have been constructed to analyze the human immune microenvironment (38, 39). However, to date, no such system has been used to evaluate mature B cell responses (26). Various platforms have been constructed to evaluate the effects of antibody-based anticancer drugs on human immunity in immunodeficient mice (40). However, these models are based on T cells and the innate immune response. The humanized mouse model used in this study was established using NOG-hu-IL-4-Tg mice transplanted with human PBMCs (27). Human B cells engraft, and a large proportion differentiate into plasmablast-like cells. Interestingly, only the transplantation of cancer cell lines tended to increase B cell subsets in our humanized mouse model. Xu et al. (41) reported similar B-cell subsets in their wild-type mouse model. The cancer microenvironment may induce glucocorticoid production because glucocorticoids are stress hormones. Glucocorticoids have been reported to enhance BLIMP-1 expression (42), which may promote premature B-cell differentiation into autoreactive plasmablasts. Recently, B-reg, an IL-10-secreting B-cell subset, was reported to have a phenotype similar to that of plasmablasts (43). Thus, it is plausible that B cells contribute to the cancer microenvironment. B cells have been previously reported to promote tumor growth by producing IL-10 (44). An increase in plasmablasts may create an environment that promotes cancer immune evasion, whereas the presence of B cells in the tumor microenvironment is reported to be associated with anticancer immunity if memory B cells are dominant (45). Garaud et al. (46) reported that plasmablast-like B cells may become immunosuppressive and promote tumor growth. In humanized mice, B cells may promote tumor growth in a similar manner. We previously reported that patient-derived plasmablasts secrete antibodies but produce specific antibodies at low levels (28). The cytokines secreted by B cells may be immunosuppressive. Non-specific or autoreactive antibodies may interact with Fc receptors to block optical surveillance of opsonized cancer cells by natural killer cells and macrophages. This mouse model may be sufficient to elucidate the functions of B cells in the cancer microenvironment.

Lipo-anti-PD-L1-P4 induces T cell infiltration in cancer tissues and decreases plasma cell levels. However, the underlying mechanism is unclear, although one study showed a reduction in the number of plasmablasts in P4 cultures (47). Here, in PBMCs from healthy donors, almost all the B cells were naïve memory/transitional B cells and not plasmablasts. As non-activated naïve and memory B cells may survive in a high P4 environment, similar to the T cell fate in P4, most B cells might survive in healthy donors. If the environment is replaced by a P4-induced anticancer immune environment, plasmablasts may disappear and cytotoxic T cells may become dominant.

Lipo-anti-PD-L1-P4 did not significantly enhance peripheral tissue inflammation. This was another striking feature of P4. Previously, we reported that a high concentration of P4 suppresses T-cell activation (18). Similarly, Papapavlou et al. (48) reported that P4 inhibits T cell activation at high concentrations, which may be an immune regulatory function specific to P4. We found an increase in CD8 T cell number and a decrease in IFN-γ secretion per cell, which might increase the threshold of inflammation caused by low-affinity autoreactive T cells that have migrated in the peripheral tissues. However, we need to examine the possibility that the Lipo-anti-PD-L1-P4-treated T cells extensively attacked the cancer cells and were highly exhausted after one month

of action, and the underlying molecular mechanisms need to be clarified in future studies.

While the 6 h treatment with a high-dose of P4 was enough for the remodeling of the lymphocyte profile and characteristics in humanized mice (18), the P4 leakage from the liposome was rather quick under biological conditions. Therefore, although the anticancer drug may be functional in this liposomal formulation, further studies are required for its optimization and implementation. First, the stable encapsulation of the P4 in the formula is essential. As we observed a dose-dependent effect of P4, it is crucial to encapsulate quantitative amount of P4 in liposomes. The composition of liposomes should also be determined by extensive examination of the entrapment efficiency, toxicity, and stability. The scalability of the key outcome is also important for the implementation. As for the entrapment efficacy and loading percentage, electromicroscopic analyses are needed. It is also necessary to determine how Lipo-anti-PD-L1-P4 can be used in the treatment. A large portion of liposomes tend to accumulate in the liver and lung, in which capillaries are abundant. Therefore, it might be difficult to target the liposomes to the tumor. For this purpose, the ratio of antibodies and the diameter of the liposomes should be optimized. Moreover, the route of administration should be optimized. Along with these optimization studies, pharmacokinetic and biodistribution studies should be performed.

Second, as the killing efficiency of Lipo-anti-PD-L1-P4 against Karpas 707H was lower than that against MDA-MB-231 and JEG-3 cells, its cancer treatment efficacy may be limited. Further experiments should be conducted using other cell types. Especially, since progesterone is a sex steroid so its relationship with reproductive organ-related cancers such as ovarian and prostate cancer should be examined. Moreover, as we used cancer cell lines, further analyses of heterogeneous cancer tissues should be performed. Cancer screening is required to determine the limitations of mice transplanted with patient-derived xenografts.

Third, our mice did not develop lymph nodes that contained human lymphocytes. Therefore, lymph node metastasis could not be analyzed. Fourth, B cells differentiated into plasmablasts in the mouse model. Fifth, the mice used human PBMCs for the immune humanization. Therefore, the cells have a limitation of survival period. This makes it difficult to evaluate the survival rate of tumor-bearing mice after several months, because the number of human immune cells decrease after three months and the effect of lymphocytes could not be evaluated correctly. There is a need to establish a new humanized mouse model to maintain lymphocytes in a naïve/memory state and evaluate the contribution of these cells to the anticancer effect. Other issues may be addressed using our model. However, if the relationship between *in vitro* and *in vivo* (patients and humanized mice, respectively) analyses is confirmed, the mouse system will become a useful tool for evaluating the response of patients to ICIs.

Nevertheless, our results strongly suggested Lipo-anti-PD-L1-P4 as an anticancer drug candidate. Lipo-anti-PD-L1-P4 suppressed the hyperactivation of acquired immunity and exerted a strong anticancer effect. It also induced a shift in the cancer immune microenvironment towards a state of inducing tumor T cell infiltration, tumor necrosis, and natural killer/T cell proliferation, and inhibiting plasmablast-like cell differentiation. To date, no other molecule has simultaneously achieved these effects. Lipo-anti-PD-L1-P4 enhances T-cell infiltration into the tumor tissue, resulting in the suppression of tumor growth. Thus, Lipo-anti-PD-L1-P4 is a promising anticancer drug. Our tumor-bearing humanized mouse model is a promising tool for the development of immune-related anticancer drugs.

Data availability statement

The original contributions presented in the study are included in the article/Supplementary Material. Further inquiries can be directed to the corresponding author.

Ethics statement

The studies involving human participants were reviewed and approved by Tokai University Human Research Committees. The patients/participants provided their written informed consent to participate in this study. The animal study was reviewed and approved by Animal Care Committees of Tokai University School of Medicine and Central Institute for Experimental Animals.

Author contributions

YK, RI, and YM contributed to the conception and design of the study. RI, TosS, YM, MMa, MT, and YK contributed to the development of the methodology. HK, SO, YO, TomS, SY, NK, YG, DK, KI, TM, and AY contributed to the acquisition and analysis of data. YK, RI, YM, MMi, KA, HI, and TosS contributed to the writing, review, and/or revision of the manuscript. HK, TaS, YG, RI, and BT provided administrative, technical, or material support. KF, MMi, KA, HI, TaS, and YK supervised the study. All authors contributed to the article and approved the submitted version.

Funding

This work was supported by MEXT KAKENHI (22220007), an AMED Translational Research Grant (A259TS, A321TS; to YK), the Tokai University School of Medicine Project Research (to YK), and a Tokai University Grant-in-Aid (to YK).

Acknowledgments

We thank the members of the Teaching and Research Support Center at Tokai University School of Medicine for their technical skills. We also thank Yumiko Nakagawa for her excellent animal-care skills. We would like to thank Editage (www.editage.com) for the English language editing.

Conflict of interest

The authors declare that the research was conducted in the absence of any commercial or financial relationships that could be construed as a potential conflict of interest.

Publisher's note

All claims expressed in this article are solely those of the authors and do not necessarily represent those of their affiliated organizations, or those of the publisher, the editors and the reviewers. Any product that may be evaluated in this article, or claim that may be made by its manufacturer, is not guaranteed or endorsed by the publisher.

Supplementary material

The Supplementary Material for this article can be found online at: https://www.frontiersin.org/articles/10.3389/fimmu.2023.1173728/full#supplementary-material

References

1. He X, Xu C. Immune checkpoint signaling and cancer immunotherapy. *Cell Res* (2020) 30(8):660–9. doi: 10.1038/s41422-020-0343-4

2. Johnson DB, Nebhan CA, Moslehi JJ, Balko JM. Immune-checkpoint inhibitors: long-term implications of toxicity. *Nat Rev Clin Oncol* (2022) 19(4):254–67. doi: 10.1038/s41571-022-00600-w

3. McGranahan N, Rosenthal R, Hiley CT, Rowan AJ, Watkins TBK, Wilson GA, et al. Allele-specific hla loss and immune escape in lung cancer evolution. *Cell* (2017) 171(6):1259–71 e11. doi: 10.1016/j.cell.2017.10.001

4. Iwai Y, Ishida M, Tanaka Y, Okazaki T, Honjo T, Minato N. Involvement of pd-L1 on tumor cells in the escape from host immune system and tumor immunotherapy by pd-L1 blockade. *Proc Natl Acad Sci U.S.A.* (2002) 99(19):12293–7. doi: 10.1073/pnas.192461099

5. Pang H, Lei D, Guo Y, Yu Y, Liu T, Liu Y, et al. Three categories of similarities between the placenta and cancer that can aid cancer treatment: cells, the microenvironment, and metabolites. *Front Oncol* (2022) 12:977618. doi: 10.3389/fonc.2022.977618

6. Gauster M, Moser G, Wernitznig S, Kupper N, Huppertz B. Early human trophoblast development: from morphology to function. *Cell Mol Life Sci* (2022) 79 (6):345. doi: 10.1007/s00018-022-04377-0

7. Kojima J, Ono M, Kuji N, Nishi H. Human chorionic villous differentiation and placental development. *Int J Mol Sci* (2022) 23(14):8003. doi: 10.3390/ijms23148003

8. Di Toro F, Gjoka M, Di Lorenzo G, De Santo D, De Seta F, Maso G, et al. Impact of Covid-19 on maternal and neonatal outcomes: a systematic review and meta-analysis. *Clin Microbiol Infect* (2021) 27(1):36–46. doi: 10.1016/j.cmi.2020.10.007

9. Wastnedge E, Reynolds R, Boeckel S, Stock S, Denison F, Maybin J, et al. Pregnancy and Covid-19. *Physiol Rev* (2021) 101(1):303–18. doi: 10.1152/physrev.00024.2020

10. Daniilidis A, Giannoulis C, Sardeli C, Dinas K, Nasioutziki M, Tantanasis T, et al. Pregnancy-associated breast cancer–a review analysis. *Eur J Gynaecol Oncol* (2010) 31(5):485–90.

11. Chatuphonprasert W, Jarukamjorn K, Ellinger I. Physiology and pathophysiology of steroid biosynthesis, transport and metabolism in the human placenta. *Front Pharmacol* (2018) 9:1027. doi: 10.3389/fphar.2018.01027

12. Lissauer D, Eldershaw S, Inman C, Coomarasamy A, Moss P, Kilby M. Progesterone promotes maternal–fetal tolerance by reducing human maternal T-cell polyfunctionality and inducing a specific cytokine profile. *Eur J Immunol* (2015) 45:2858–72. doi: 10.1002/eji.201445404

13. Mahbub AA, Aslam A, Elzubier ME, El-Boshy M, Abdelghany AH, Ahmad J, et al. Enhanced anti-cancer effects of oestrogen and progesterone Co-therapy against colorectal cancer in males. *Front Endocrinol (Lausanne)* (2022) 13:941834. doi: 10.3389/fendo.2022.941834

14. Fedotcheva T, Fedotcheva N, Shimanovsky N. Progestins as anticancer drugs and chemosensitizers, new targets and applications. *Pharmaceutics* (2021) 13:1616. doi: 10.3390/pharmaceutics13101616

15. van der Horst PH, Wang Y, Vandenput I, Kuhne LC, Ewing PC, van Ijcken WF, et al. Progesterone inhibits epithelial-to-Mesenchymal transition in endometrial cancer. *PloS One* (2012) 7(1):e30840. doi: 10.1371/journal.pone.0030840

16. Cao W, Gao W, Zheng P, Sun X, Wang L. Medroxyprogesterone acetate causes the alterations of endoplasmic reticulum related mrnas and lncrnas in endometrial cancer cells. *BMC Med Genomics* (2019) 12(1):163. doi: 10.1186/s12920-019-0601-9

17. Fedotcheva NI, Teplova VV, Fedotcheva TA, Rzheznikov VM, Shimanovskii NL. Effect of progesterone and its synthetic analogues on the activity of mitochondrial permeability transition pore in isolated rat liver mitochondria. *Biochem Pharmacol* (2009) 78(8):1060–8. doi: 10.1016/j.bcp.2009.05.028

18. Kashiwagi H, Seki T, Oshima S, Ohno Y, Shimizu T, Yamada S, et al. High-progesterone environment preserves T cell competency by evading glucocorticoid effects on immune regulation. *Front Immunol* (2022) 13:1000728. doi: 10.3389/fimmu.2022.1000728

19. Taves MD, Ashwell JD. Glucocorticoids in T cell development, differentiation and function. *Nat Rev Immunol* (2021) 21(4):233–43. doi: 10.1038/s41577-020-00464-0

20. Obradovic MMS, Hamelin B, Manevski N, Couto JP, Sethi A, Coissieux MM, et al. Glucocorticoids promote breast cancer metastasis. *Nature* (2019) 567(7749):540–4. doi: 10.1038/s41586-019-1019-4

21. Bai K, Li X, Zhong J, Ng E, Yeung W, Lee C, et al. Placenta-derived exosomes as a modulator in maternal immune tolerance during pregnancy. *Front Immunol* (2021) 12:671093. doi: 10.3389/fimmu.2021.671093

22. Mincheva-Nilsson L. Immunosuppressive protein signatures carried by syncytiotrophoblast-derived exosomes and their role in human pregnancy. *Front Immunol* (2021) 12:717884. doi: 10.3389/fimmu.2021.717884

23. Sun L, Zhang L, Yu J, Zhang Y, Pang X, Ma C, et al. Clinical efficacy and safety of anti-Pd-1/Pd-L1 inhibitors for the treatment of advanced or metastatic cancer: a systematic review and meta-analysis. *Sci Rep* (2020) 10(1):2083. doi: 10.1038/s41598-020-58674-4

24. Mestas J, Hughes C. Of mice and not men: differences between mouse and human immunology. *J Immunol* (2004) 172(5):2731–8. doi: 10.4049/jimmunol.172.5.2731

25. Ito M, Hiramatsu H, Kobayashi K, Suzue K, Kawahata M, Hioki K, et al. Nod/Scid/Gamma(C)(Null) mouse: an excellent recipient mouse model for engraftment of human cells. *Blood* (2002) 100(9):3175–82. doi: 10.1182/blood-2001-12-0207

26. Kametani Y, Ohno Y, Ohshima S, Tsuda B, Yasuda A, Seki T, et al. Humanized mice as an effective evaluation system for peptide vaccines and immune checkpoint inhibitors. *Int J Mol Sci* (2019) 20(24):6337. doi: 10.3390/ijms20246337

27. Kametani Y, Katano I, Miyamoto A, Kikuchi Y, Ito R, Muguruma Y, et al. Nog-Hil-4-Tg, a new humanized mouse model for producing tumor antigen-specific igg antibody by peptide vaccination. *PloS One* (2017) 12(6):e0179239. doi: 10.1371/journal.pone.0179239

28. Ohno Y, Ohshima S, Miyamoto A, Kametani F, Ito R, Tsuda B, et al. Her2-Antigen-Specific humoral immune response in breast cancer lymphocytes transplanted in hu-pbl hil-4 nog mice. *Sci Rep* (2021) 11(1):12798. doi: 10.1038/s41598-021-92311-y

29. Kimura N, Maeki M, Sato Y, Note Y, Ishida A, Tani H, et al. Development of the ilinp device: fine tuning the lipid nanoparticle size within 10 nm for drug delivery. *ACS Omega* (2018) 3(5):5044–51. doi: 10.1021/acsomega.8b00341

30. Tsuda B, Miyamoto A, Yokoyama K, Ogiya R, Oshitanai R, Terao M, et al. B-cell populations are expanded in breast cancer patients compared with healthy controls. *Breast Cancer* (2018) 25(3):284–91. doi: 10.1007/s12282-017-0824-6

31. Fragni M, Fiorentini C, Rossini E, Fisogni S, Vezzoli S, Bonini SA, et al. *In vitro* antitumor activity of progesterone in human adrenocortical carcinoma. *Endocrine* (2019) 63(3):592–601. doi: 10.1007/s12020-018-1795-x

32. White BA, Porterfield SP. *Introduction to the endocrine system*. Philadelphia: Mosby/Elsevier (2012).

33. Yamanaka N, Marques G, O'Connor MB. Vesicle-mediated steroid hormone secretion in drosophila melanogaster. *Cell* (2015) 163(4):907–19. doi: 10.1016/j.cell.2015.10.022

34. Durgam SS, Alegre ML, Chong AS. Toward an understanding of allogeneic conflict in pregnancy and transplantation. *J Exp Med* (2022) 219(5):e20211493. doi: 10.1084/jem.20211493

35. Tan IJ, Peeva E, Zandman-Goddard G. Hormonal modulation of the immune system - a spotlight on the role of progestogens. *Autoimmun Rev* (2015) 14(6):536–42. doi: 10.1016/j.autrev.2015.02.004

36. Kawana K, Kawana Y, Schust D. Female steroid hormones use signal transducers and activators of transcription protein-mediated pathways to modulate the expression of T-bet in epithelial cells: a mechanism for local immune regulation in the human reproductive tract. *Mol endocriology* (2005) 19(8):2047–59. doi: 10.1210/me.2004-0489

37. Solano M, Arck P. Steroids, pregnancy and fetal development. *Front Immunol* (2020) 10:3017. doi: 10.3389/fimmu.2019.03017

38. Ito R, Takahashi T, Katano I, Ito M. Current advances in humanized mouse models. *Cell Mol Immunol* (2012) 9(3):208–14. doi: 10.1038/cmi.2012.2

39. Walsh NC, Kenney LL, Jangalwe S, Aryee KE, Greiner DL, Brehm MA, et al. Humanized mouse models of clinical disease. *Annu Rev Pathol* (2017) 12:187–215. doi: 10.1146/annurev-pathol-052016-100332

40. Ye W, Chen Q. Potential applications and perspectives of humanized mouse models. *Annu Rev Anim Biosci* (2022) 10:395–417. doi: 10.1146/annurev-animal-020420-033029

41. Xu Y, Wei Z, Feng M, Zhu D, Mei S, Wu Z, et al. Tumor-infiltrated activated B cells suppress liver metastasis of colorectal cancers. *Cell Rep* (2022) 40(9):111295. doi: 10.1016/j.celrep.2022.111295

42. Franco L, Gadkari M, Howe K, Sun J, Kardava L, Kumar P, et al. Immune regulation by glucocorticoids can be linked to cell type–dependent transcriptional responses. *J Exp Ned* (2019) 216:384–406. doi: 10.1084/jem.20180595

43. Fillatreau S. Regulatory functions of B cells and regulatory plasma cells. *BioMed J* (2019) 42(4):233–42. doi: 10.1016/j.bj.2019.05.008

44. Monteiro C, Kasahara T, Sacramento P, Dias A, Leite S, Silva V, et al. Human pregnancy levels of estrogen and progesterone contribute to humoral immunity by activating Tfh/B cell axis. *Eur J Immunol* (2021) 51:167–79. doi: 10.1002/eji.202048658

45. Garaud S, Buisseret L, Solinas C, Gu-Trantien C, de Wind A, Van den Eynden G, et al. Tumor infiltrating b-cells signal functional humoral immune responses in breast cancer. *JCI Insight* (2019) 5:e129641. doi: 10.1172/jci.insight.129641

46. Garaud S, Dieu-Nosjean M-C, Willard-Gallo K. T Follicular helper and b cell crosstalk in tertiary lymphoid structures and cancer immunotherapy. *Nat Commun* (2022) 13:2259. doi: 10.1038/s41467-022-29753-z

47. Shen P, Fillatreau S. Antibody-independent functions of B cells: a focus on cytokines. *Nat Rev Immunol* (2015) 15(7):441–51. doi: 10.1038/nri3857

48. Papapavlou G, Hellberg S, Raffetseder J, Brynhildsen J, Gustafsson M, Jenmalm MC, et al. Differential effects of estradiol and progesterone on human T cell activation in vitro. *Eur J Immunol* (2021) 51(10):2430–40. doi: 10.1002/eji.202049144

frontiers | Frontiers in Immunology

TYPE Original Research
PUBLISHED 21 July 2023
DOI 10.3389/fimmu.2023.1187388

Check for updates

OPEN ACCESS

EDITED BY
Silke Paust,
The Scripps Research Institute,
United States

REVIEWED BY
Theodore Nowicki,
University of California, Los Angeles,
United States
Melissa G. Lechner,
University of California, Los Angeles,
United States
Jeffrey A. Knauf,
Cleveland Clinic, United States

*CORRESPONDENCE
Sun Wook Cho
swchomd@snu.ac.kr
Kyu Eun Lee
kyueunlee@snu.ac.kr

†These authors have contributed equally to this work and share first authorship

RECEIVED 16 March 2023
ACCEPTED 23 June 2023
PUBLISHED 21 July 2023

CITATION
Xu Z, Shin HS, Kim YH, Ha SY, Won J-K, Kim S-j, Park YJ, Parangi S, Cho SW and Lee KE (2023) Modeling the tumor microenvironment of anaplastic thyroid cancer: an orthotopic tumor model in C57BL/6 mice. *Front. Immunol.* 14:1187388. doi: 10.3389/fimmu.2023.1187388

COPYRIGHT
© 2023 Xu, Shin, Kim, Ha, Won, Kim, Park, Parangi, Cho and Lee. This is an open-access article distributed under the terms of the Creative Commons Attribution License (CC BY). The use, distribution or reproduction in other forums is permitted, provided the original author(s) and the copyright owner(s) are credited and that the original publication in this journal is cited, in accordance with accepted academic practice. No use, distribution or reproduction is permitted which does not comply with these terms.

Modeling the tumor microenvironment of anaplastic thyroid cancer: an orthotopic tumor model in C57BL/6 mice

Zhen Xu[1,2†], Hyo Shik Shin[3†], Yoo Hyung Kim[4†], Seong Yun Ha[1], Jae-Kyung Won[5,6], Su-jin Kim[1,7,8], Young Joo Park[3,4,9], Sareh Parangi[10], Sun Wook Cho[3,4*] and Kyu Eun Lee[1,7,8*]

[1]Cancer Research Institute, Seoul National University College of Medicine, Seoul, Republic of Korea, [2]Department of Surgery, YanBian University Hospital, Yanji, Jilin, China, [3]Department of Internal Medicine, Seoul National University College of Medicine, Seoul, Republic of Korea, [4]Department of Internal Medicine, Seoul National University Hospital, Seoul, Republic of Korea, [5]Department of Pathology, Seoul National University Hospital, Seoul, Republic of Korea, [6]Department of Pathology, College of Medicine, Seoul National University, Seoul, Republic of Korea, [7]Department of Surgery, Seoul National University College of Medicine, Seoul, Republic of Korea, [8]Division of Surgery, Thyroid Center, Seoul National University Cancer Hospital, Seoul, Republic of Korea, [9]Department of Molecular Medicine and Biopharmaceutical Sciences Graduate School of Convergence Science and Technology, Seoul National University, Seoul, Republic of Korea, [10]Department of Surgery, Massachusetts General Hospital, Harvard Medical School, Boston, MA, United States

Introduction: Securing a well-established mouse model is important in identifying and validating new therapeutic targets for immuno-oncology. The C57BL/6 mouse is one of the most fully characterised immune system of any animal and provides powerful platform for immuno-oncology discovery. An orthotopic tumor model has been established using TBP3743 (murine anaplastic thyroid cancer [ATC]) cells in B6129SF1 hybrid mice, this model has limited data on tumor immunology than C57BL/6 inbred mice. This study aimed to establish a novel orthotopic ATC model in C57BL/6 mice and characterize the tumor microenvironment focusing immunity in the model.

Methods: Adapted TBP3743 cells were generated via *in vivo* serial passaging in C57BL/6 mice. Subsequently, the following orthotopic tumor models were established via intrathyroidal injection: B6129SF1 mice injected with original TBP3743 cells (original/129), B6129SF1 mice injected with adapted cells (adapted/129), and C57BL/6 mice injected with adapted cells (adapted/B6).

Results: The adapted TBP3743 cells de-differentiated but exhibited cell morphology, viability, and migration/invasion potential comparable with those of original cells *in vitro*. The adapted/129 contained a higher Ki-67$^+$ cell fraction than the original/129. RNA sequencing data of orthotopic tumors revealed enhanced oncogenic properties in the adapted/129 compared with those in the original/129. In contrast, the orthotopic tumors grown in the adapted/B6 were smaller, with a lower Ki-67$^+$ cell fraction than those in the adapted/129. However, the oncogenic properties of the tumors within the adapted/B6 and adapted/129 were similar. Immune-related pathways were enriched in the adapted/B6 compared with those in the adapted/129. Flow cytometric analysis of the orthotopic tumors revealed higher cytotoxic CD8$^+$ T cell and monocytic-

myeloid-derived suppressor cell fractions in the adapted/B6 compared with the adapted/129. The estimated $CD8^+$ and $CD4^+$ cell fractions in the adapted/B6 were similar to those in human ATCs but negligible in the original/B6.

Conclusion: A novel orthotopic tumor model of ATC was established in C57BL/6 mice. Compared with the original B6129SF1 murine model, the novel model exhibited more aggressive tumor cell behaviours and strong immune responses. We expect that this novel model contributes to the understanding tumor microenvironment and provides the platform for drug development.

KEYWORDS

anaplastic thyroid cancer, syngeneic, tumor microenvironment, immunotherapy, BRAF V600E

Introduction

Anaplastic thyroid carcinoma (ATC) is a highly aggressive malignant tumor accounting for 1–2% of all thyroid cancers (1–5). Upon initial presentation, most patients exhibit extensive local invasion or distant metastatic lesions (stage IVA-IVC) (2). Thus, the associated prognosis is poor, with a median overall survival of 5–12 months (2, 4, 6).

Tremendous research efforts have sought to characterize the genetic and molecular pathogenesis of ATC (4, 7–9), leading to the development of novel targeted therapies. For instance, the $BRAF^{V600E}$ mutation is frequently found in ATCs (20–50% of the cases) (7, 8, 10). The combination therapy of BRAF and MEK inhibitors has demonstrated therapeutic efficacy in $BRAF^{V600E}$-mutated ATCs (11), leading to its approval in 2018 by the United States Food and Drug Administration. However, progression-free and median overall survival remain relatively low (6.7 and 14.5 months, respectively) even after the combination therapy (12).

One of requirements for the development of anti-cancer drugs is the establishment of a mouse model that replicates the histology and microenvironment of human tumors (13). The cultivated cell-line derived xenograft model (CDXM) is currently the most widely used model for drug screening and development (14). Although the CDXM exhibits rapid tumor development and excellent experimental reproducibility, it is unsuitable for investigating tumor microenvironments as it is established in immune-compromised mice. Meanwhile, the genetically engineered model (GEM) has been successfully applied to replicate and analyse tumor microenvironments. However, tumor formation requires a longer period in the GEM than in the xenograft model, and the rate of tumor formation varies among mice (15–17). Thus, by combining the advantages of the CDXM and GEM, a model for transplanting murine tumor cells from the GEM back into mice has been developed. The TBP3743 murine ATC cell line generated from mice with a thyroid-specific *Braf*^{V600E} mutation and *Trp53* deletion (18, 19) exhibits rapid and consistent tumor growth following orthotopic injection in B6129SF1 hybrid mice (19). Although this model has been tried to explore the tumor microenvironment and assess the anti-tumor efficacy of immune checkpoint inhibitors (20), B6129SF1 hybrid mice have little cumulative data regarding tumor biology and drug development compared to inbred C57BL/6 mice (21).

In this study, we performed *in vivo* adaptation of TBP3743 cells within inbred C57BL/6 mice and established an orthotopic model of ATC. We characterized the differentiation status, oncogenic molecular features, and immune signatures of the tumors from the original and the adapted TBP3743 cells. The findings of this study describe a suitable preclinical mouse model for investigating the ATC tumor microenvironment and developing anti-cancer drugs for immunotherapy.

Methods

Maintenance of tumor cells *in vitro*

The original TBP3743 cell line (19), generated from B6129SF1 mice with thyroid-specific *Braf*^{V600E} and thyroid-specific *Trp53* deletion, was kindly gifted from Dr. Sareh Parangi (Department of Surgery, Massachusetts General Hospital, Harvard Medical School, Boston, MA, USA). These cells were maintained in RPMI-1640 media supplemented with 10% fetal bovine serum (FBS; WELGENE, Seoul, Korea), 2 mM GlutaMAX™ (Gibco, New York, NY, USA), and 100 U/mL penicillin-streptomycin (Gibco).

Generation of adapted TBP3743 cells in C57BL/6 mice

Six-week-old female C57BL/6 and B6129SF1 mice were purchased from Orient Bio, Inc. (Seongnam, Korea) and the Jackson Laboratory (Bar Harbor, ME, USA), respectively. A mixture of 1×10^7 original TBP3743 cells and Matrigel (BD Biosciences, Franklin Lakes, NJ) was injected subcutaneously into C57BL/6 mice ($n = 5$) for generating adapted TBP3743 cells. Two-

dimensional tumor size was measured twice per week, and the tumor volume was calculated using Eq. (1):

$$Volume = {}^{1}/_{2} \times a \times b^{2} \quad (1)$$

where a is the longest diameter, and b is the perpendicular diameter (22). First, the mice were euthanized and the largest tumor was selected, surgically removed, minced, and incubated with phosphate-buffered saline (PBS) containing 2 mg/mL collagenase type 1 on a shaker at 37°C for 3 h. The cells were then maintained in RPMI-1640 media supplemented with 10% FBS. Expanded tumor cells were re-implanted in new C57BL/6 mice (n = 5) in the same manner as described above.

Establishment of the murine orthotopic tumor model of ATC

The orthotopic tumor model was established by intrathyroidal injection of tumor cells. For intrathyroidal injection, 1×10^5 tumor cells in 10 μL of PBS were injected into the left thyroid gland of mice using a Hamilton syringe with a 30G needle.

Six-week-old female C57BL/6 or B6129SF1 mice underwent intrathyroidal injection of the original or adapted TBP3743 cells. The original cells were injected into the B6129SF1 mice (original/129 group). Adapted cells after 3rd and 6th adaptation passage were injected into the B6129SF1 mice (adapted/129 group) or C57BL/6 (adapted/B6 group and SC6/B6 group, respectively). To evaluate the effect of tumor-host immune interactions in tumor growth, we injected the original and adapted cells into athymic mice (Orient Bio, Inc., Seongnam, Korea). Tumor size and volume were measured 9 days after tumor cell injection.

Evaluation of the *in vivo* anti-tumor response to BRAF inhibitor in mice injected with adapted TBP3743 cells

To evaluate the anti-tumor response to a BRAF inhibitor, we labelled adapted TBP3743 cells with luciferase protein before generating the orthotopic thyroid cancer model. Beginning three days after tumor cell injection, mice were intraperitoneally injected daily with 10 mg/kg of PLX-4032 (Selleckchem, Houston, TX, USA; n = 8) or saline (untreated group; n = 8). To obtain *in vivo* bioluminescence imaging, mice were intraperitoneally injected with 100 μL (3 mg/mL PBS) of D-Luciferin (Perkin Elmer, Wellesley, MA). Bioluminescence imaging (IVIS spectrum, Perkin Elmer) was performed two weeks after tumor cell injection.

Evaluation of the *in vivo* anti-tumor response to anti-PD-L1 antibody in mice injected with adapted TBP3743 cells

To evaluate the anti-tumor response to anti-PD-L1 antibody, we intraperitoneally injected daily with 0.2 mg/kg of anti-PD-L1 antibody (kindly gifted from Pf. Dae Hee Kim, Kangwon National University, Gangwon-do, Republic of Korea) or Ig G controls from 5 days after tumor cell injection. Tumor size and volume were measured 10 days after tumor cell injection.

Immunohistochemical staining

The harvested tumors were fixed in 4% paraformaldehyde and embedded in paraffin. Immunohistochemistry (IHC) staining was performed with the following primary antibodies: anti-CD3 (1:100, ab5690, Abcam, Cambridge, UK), anti-CD4 (1:100, ab183685, Abcam), anti-CD8 (1:100, ab209775, Abcam), F4/80 (1:50, 14-4801-81, Invitrogen, San Diego, CA, USA), anti-CD163 (1:200, ab182422, Abcam), and anti-Ki67 (1:200, MA5-14520, Invitrogen).

Cell viability assay

To compare the viability of original and adapted TBP3743 cells, 8×10^3 cells/mL were seeded into a 96-well tissue culture plate with 100 μL of media. Subsequently, 10 μL of the CCK-8 solution (Dojindo, Kumamoto, Japan) was added to each well after 12, 36, and 60 h. The cells were incubated for an additional 2 h, and the absorbance was measured at 450 nm with a microplate reader (SpectraMax 190; Molecular Devices, San Jose, CA, USA).

To assess the drug response to the BRAF inhibitor, the original and adapted TBP3743 cells (1×10^3/well) were seeded in 384-well plates and treated with PLX-4032 (0.05, 0.15, 0.46, 1.37, 4.12, 12.35, 37.03, 111.11, 333.33, or 1000 μM). Cell viability was evaluated using a CellTiter-Glo Luminescent Cell Viability Assay (Promega) after 72 h of PLX-4032 treatment.

Real-time PCR assay

Total RNA was extracted using TRIzol reagent (Invitrogen) from *in vitro* maintained tumor cells or *in vivo* orthotopic tumors, and cDNA was synthesized using the M-MLV Reverse Transcriptase kit (Invitrogen). The real-time PCR was performed with the StepOne Plus real-time PCR system (Applied Biosystems) and TB green Premix (Takara Bio Inc., Otsu, Japan). The assay was performed according to the manufacturer's protocol. Results were presented as the average of three independent experiments. Detailed primer sequences are listed in supplementary data (Supplementary Table 1).

Cell migration assay

Cell migration was assessed using the Transwell system (Corning, NY, USA). Briefly, polycarbonate membranes with 8 μm pores were coated with 0.2% gelatin solution for 1 h and dried overnight. Cells were added to the upper chamber and placed into a 24-well plate. The lower chamber was filled with 650 μL of serum-free media. After 12 h, non-migrating cells were swabbed with a

cotton-tipped applicator. Migrating cells to lower chamber were fixed in methanol for 30 min, and stained with 1% crystal violet for 30 min. The results were quantified with ImageJ.

3D invasion assay

A 3D invasion assay was performed with the original and adapted TBP3743 cells using a Cultrex 3D Spheroid Cell Invasion Assay (Trevigen, Inc., Gaithersburg, MD, USA). Briefly, 2×10^3 cells were dispensed in 50 µL of Spheroid Formation Extracellular Matrix (ECM) per well and incubated at 37 °C for 72 h. After three days, 50 µL of the Invasion Matrix was added to each well and incubated at 37°C for seven days. Cell invasion was observed microscopically using the 4× objective, and spheroid images were analysed by ImageJ.

Flow cytometry

Tumors were minced and incubated with Hanks' Balanced Salt solution (HBSS) containing 2 mg/mL collagenase type 1 on a shaker at 37 °C for 3 h. Cells were washed and suspended in PBS supplemented with 2% FBS, followed by staining with fluorochrome-conjugated antibodies: anti-CD45 (1:250, 103138, BioLegend, San Diego, CA, USA), anti-CD3 (1:60, 35-0031-82, Invitrogen), anti-CD4 (1:60, 100422, BioLegend), anti-CD8 (1:60, 100714, BioLegend), anti-CD25 (1:10, MA5-17818, Invitrogen), anti-FoxP3 (1:10, 17-5773-82, Invitrogen), anti-CD11b (1:50, 101206, BioLegend), anti-Ly6C (1:50, 128026, BioLegend), anti-Ly6G (1:100, 560599, BD Biosciences, Franklin Lakes, NJ, USA), anti-F4/80 (1:50, 12-4801-82, Invitrogen), anti-CD80 (1:50, 562504, BD Biosciences), anti-CD206 (1:50, 46-2061-82, Invitrogen), anti-MHC Class 1 (1:50, ab95572, Abcam), and anti- NK1.1 (1:50, 61-5941-82, Invitrogen). Multicolour flow cytometry was performed using The MACSQuant® Analyzer 16 (Miltenyi Biotec B.V. & Co. KG, Bergisch Gladbach, Germany) and analysed with FlowJo software (BD Biosciences, OR, USA).

Bulk RNA sequencing and data analysis

RNA was isolated from three tumor tissues in the original/129, adapted/129, and adapted/B6 groups. Total RNA was used to construct cDNA libraries with the TrueSeq RNA library kit (Illumina, San Diego, CA, USA) according to the manufacturer's instructions. Next, sequencing was performed using an Illumina HiSeq2000 (Illumina) platform with ~100 nt paired-end reads. The quality of raw sequence data was assessed using FastQC (FastQC 0.11.3). Sequenced reads were aligned to the mm10 mouse genome assembly (GRCm38) reference genome with HISAT2 aligner (HISAT2 2.2.1). Raw read counts were used to analyse the differentially expressed genes (DEGs) among the groups by applying the Cuffdiff workflow (Cuffdiff 2.2.1). DEGs were defined as genes with a false discovery rate (FDR)< 0.05 and an absolute log2 fold change >1.

Curated gene sets were derived from the Kyoto Encyclopedia of Genes and Genomes (KEGG) pathway database and the Broad Institute Molecular Signatures Database. Over-representation analysis with the DEGs was performed using the DAVID functional annotation tool, and enriched gene sets were those with an FDR< 0.05. Single sample gene set enrichment analysis (ssGSEA) was performed with R package gene set variation analysis.

In the network analysis, nodes represented enriched gene sets that were significantly over-represented by DEGs, while edges represented gene expression profiles that were significantly correlated (similarity > 0.5) across samples/gene sets. Interpretation and plotting of the network were performed with R package igraph.

Immune cell proportions were analysed by CIBERSORT using the LM22 gene signature. Gene expression data of tumors from original/129, adapted/129, or adapted/B6, and human ATCs from the previously published data (8) were normalized as fragments per kilobase of transcript per million (FPKM) by Cuffnorm and uploaded to the CIBERSORT web portal (https://cibersort.stanford.edu/). Twenty-two human hematopoietic cell proportions per sample were provided.

Statistical analysis

Statistical analyses were performed using GraphPad PRISM version 8.0.0 (GraphPad Software, San Diego, CA, USA). Data were presented as mean ± standard deviation. The independent *t*-test, paired *t*-test, or Mann–Whitney U-test (n< 10) was used to compare continuous variables. Statistical significance was defined as two-sided *P*-values< 0.05. Statistical analyses and plotting for bulk RNA sequencing were performed using R Statistical Software (version 4.0.3).

Results

Establishment of the adapted TBP3743 cell line via *in vivo* passaging to the C57BL/6 mice

To generate the adapted TBP3743 cells in C57BL/6 mice, six rounds of *in vivo* serial passaging were performed (Figure 1A). Cells harvested from round-1, -3, and -6 tumors were designated as SC1, SC3, and SC6 cells, respectively, and injected into another C57BL/6 mouse for the subsequent round. Tumors after rounds 3 were stably established three weeks after the injection (Supplementary Table 2). SC3 and SC6 exhibited comparable tumor growth *in vivo* (Figure 1B). The gross morphology of the original cells was similar to those of SC1, SC3, and SC6 cells (Figure 1C). The $Braf^{V600E}$ mutation was identified in all SC1–4 cells (Supplementary Figure 1). We compared the expression of genes associated with thyroid differentiation. The mRNA expressions of *Tshr*, *Pax8*, *Nis*, and *Ttf1* were significantly downregulated in SC3 and SC6 cells compared with the original TBP3743 cells, but comparable between SC3 and SC6 (Figure 1D). Consistently, protein expression of PAX8 was completely lost in SC3 and SC6,

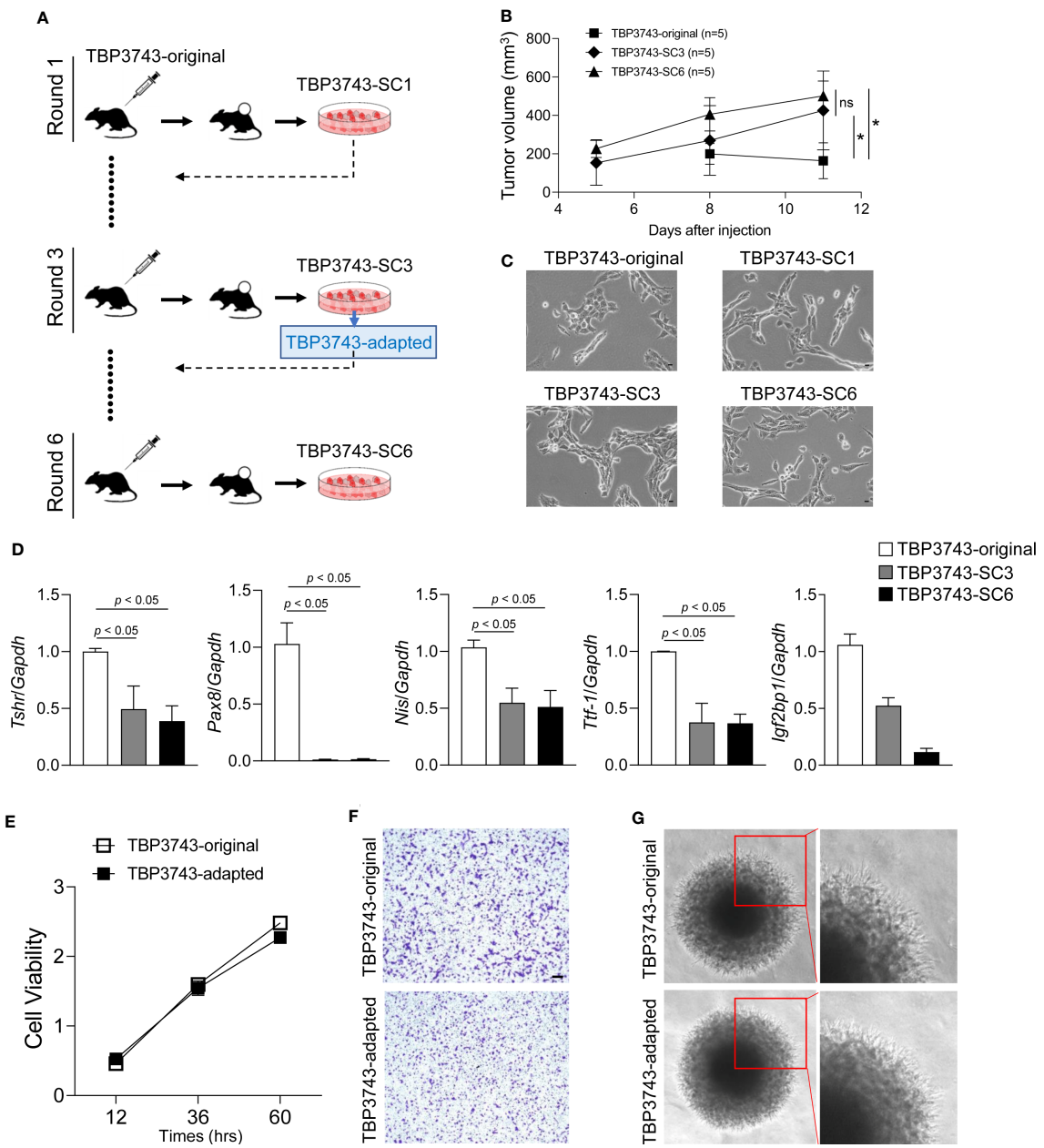

FIGURE 1
In vivo passaging of TBP3743 cells. TBP3743 cells were subcutaneously injected into C57BL/6 mice and tumor growth were observed for 21 days in 1st and 2nd round, and 10-15 days in 3rd, 4th 5th, and 6th round of *in vivo* passaging. At each round, the two largest tumors were harvested, primary single cell culture were performed, and established cells were used for the next round of *in vivo* passaging. **(A)** Scheme for TBP3743 adaptation into C57BL/6 mice. **(B)** Tumor growth curves of the original, 3rd and 6th round from day 5 to 11. **(C)** The morphology of TBP3743 original or subclones (scale bars: 200 μm). **(D)** Thyroid differentiation genes were analyzed by real-time RT-PCR. To characterize TBP3743-original or -adapted cells, **(E)** Cell proliferation were measured by the CCK-8 assay at the indicated time, **(F)** Cell migration assay were performed using Transwell system (scale bars: 50 μm), **(G)** Cell invasion ability were measured by spheroid culture system. SC, subclone.

and that of TTF1 was lower, but still preserved in SC3 and SC6 compared with the original TBP3743 cells. TSHR protein expression was negligible in the original cell, SC3, and SC6 (Supplementary Figure 2). In addition, the expression of *Igf2bp1*, which has recently been identified as a marker for ATC (23), was observed to be significantly downregulated gradually from the original state to SC3 and further to SC6 (Figure 1D). In summary, the SC3 and SC6 cells were de-differentiated clones compared with the original cells. *In vivo* tumorigenic capacities between SC3 and SC6 in C57BL/6 mice were similar. *In vitro* cell morphology and the expressions of thyroid differentiation genes were all comparable between SC3 and SC6. Both SC3 and SC6 maintained the molecular characteristics of ATC. Thus, we designated SC3 as the adapted TBP3743 cells for further use.

Next, *in vitro* characteristics were investigated between the original and adapted TBP3743 cells. Cell viability was similar between two cell types (Figure 1E). The migration (Figure 1F, Supplementary Figure 3) and invasion (Figure 1G) capacity of these two cells were also comparable. Consistent with a previous report (19), loss of E-cadherin was observed in both cells. The abundances of N-cadherin and vimentin were similar (Supplementary Figure 4A). Regarding oncogenic signalling, the phosphorylation of AKT was significantly increased in the adapted TBP3743 cells compared to the original cells (Supplementary Figure 4B). Additionally, ERK phosphorylation was higher in the adapted TBP3743 cells compared to the original cells, but the difference did not reach statistical significance (Supplementary Figure 4B). Collectively, cell viability, migration, and invasion capacity were similar between the original and adapted cells, while the PI3K-AKT pathway showed a modest increase in the adapted TBP3743 cells compared with the original cells.

Establishment of an orthotopic tumor model using adapted TBP3743 cells

Orthotopic tumor growth was investigated two weeks after tumor cell injection. The mean volume and weight of tumors collected from the adapted/129 group was greater than that of the original/129 group (volume: 343.8 ± 179.2 mm^3 vs. 599.1 ± 278.9 mm^3, $P< 0.05$; weight: 0.33 ± 0.19 g vs. 0.55 ± 0.22 g, $P< 0.05$, respectively; Figure 2A). The Ki-67^+ cell fraction was markedly higher in the adapted/129 group than the original/129 group (Figures 2B, C). Histological features were similar among the groups, presenting with spindle sarcoma-like tumor cells with pleomorphic nuclei and high mitotic count, which are consistent with ATC features (Figure 2B). Hence, the adapted TBP3743 cells exhibited more proliferative characteristics than the original cells in the B6129SF1 mice. However, the tumor volume, weight, and Ki-67^+ cell fraction from the adapted/B6 group were considerably

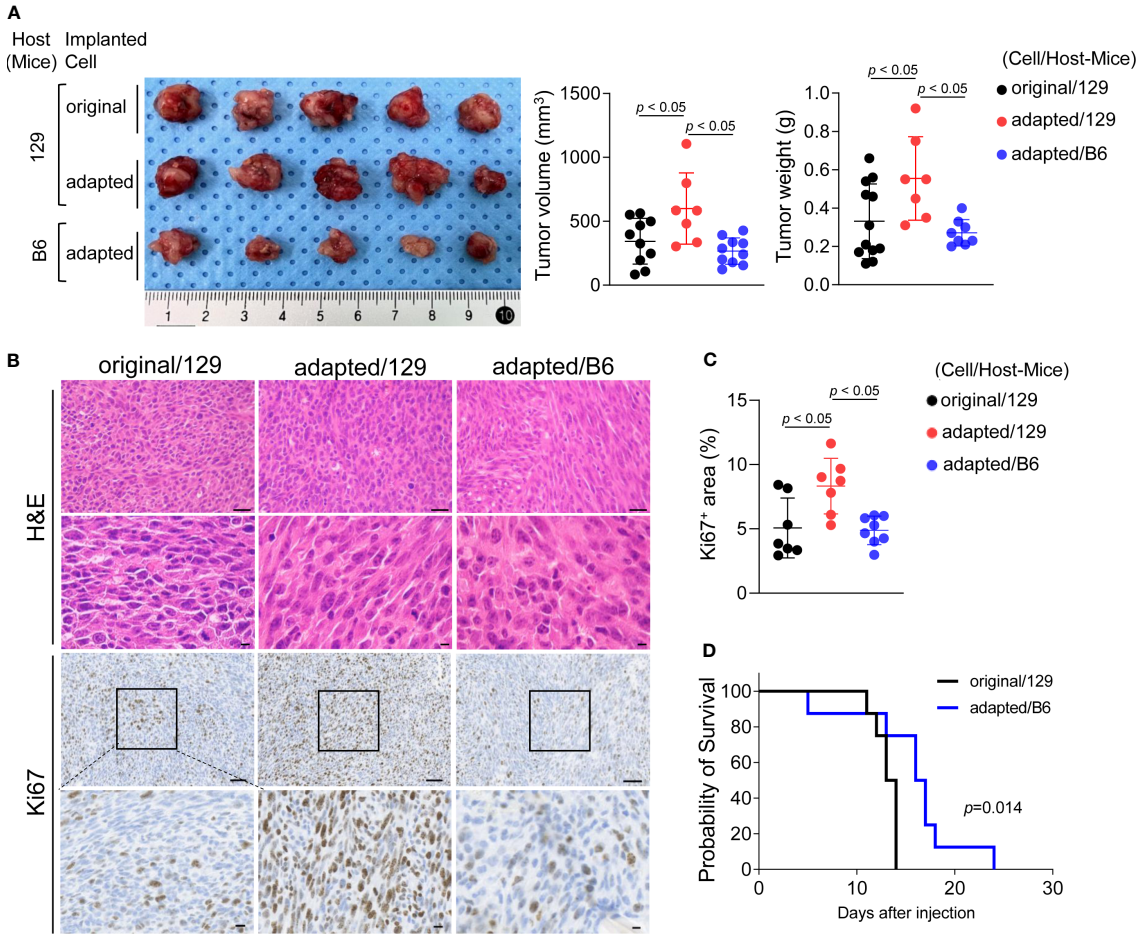

FIGURE 2
Establishment of orthotopic tumor model using TBP3743-B6 cells. B6129SF1 mice were implanted with 10^5 cells of each cell line (TBP3743-original and -adapted cells) and C57BL/6 mice were implanted with 10^5 cells of TBP3743-adapted. After 14 days post-implantation, tumors were harvested. **(A)** Representative image of tumors and, quantification of tumor volume and weight. **(B)** Representative image of H&E staining and Ki67 immunohistochemistry staining on each tumors (H&E upper panel scale bars: 50 μm; lower panel scale bars: 10 μm; Ki67 panel scale bar: 50 μm; lower panel scale bars: 10 μm). **(C)** Quantification of Ki67$^+$ area in tumors. **(D)** FACS analysis of MHC class 1 on TBP3743-original, -adapted, and SC6 tumors. 129, B6129SF1; B6, C57BL/6. All data are expressed as mean ± SD.

lower than those from the adapted/129 group. Additionally, the median survival was significantly shorter in the original/129 group compared to those of the adapted/B6 group (median [range], 13.5 [11-14] vs 16.5 [5-24] days, P=0.014, Figure 2D)

Molecular characteristics of adapted TBP3743 cell-derived orthotopic tumors

To investigate the molecular characteristics of each orthotopic tumor, total RNA sequencing analysis was performed on the tumor tissues. Compared to the original/129 group, the adapted/129 and adapted/B6 groups exhibited many DEGs. Meanwhile, a relatively small number of DEGs were detected between the adapted/129 and adapted/B6 groups (Figure 3A).

Gene sets involved in oncogenic signalling, including *Raf*, *Vegf-a*, and *Akt*, were highly enriched in the adapted/129 and adapted/B6 groups compared with those in the original/129 group (Figures 3B, C), in a similar vein, the activities of gene sets in tumor suppressor signalings, such as *Pten* and *P53*, were attenuated (Figures 3B, D). Furthermore, gene sets associated with epithelial and mesenchymal stem cell proliferation and cell migration were significantly enriched in the adapted/129 and adapted/B6 groups compared with those in the original/129 group (Figures 3E, F). Hence, the oncogenic properties in the adapted cells were more enhanced than the original cells, resulting in more aggressive tumor features.

Molecular characteristics of the immune microenvironment in adapted TBP3743 cell-derived orthotopic tumors

We next analysed RNA sequencing data to compare the tumor microenvironments among those groups. Notably, immune-related pathways were over-represented in the up-regulated DEGs of the adapted/129 and adapted/B6 groups compared with the original/

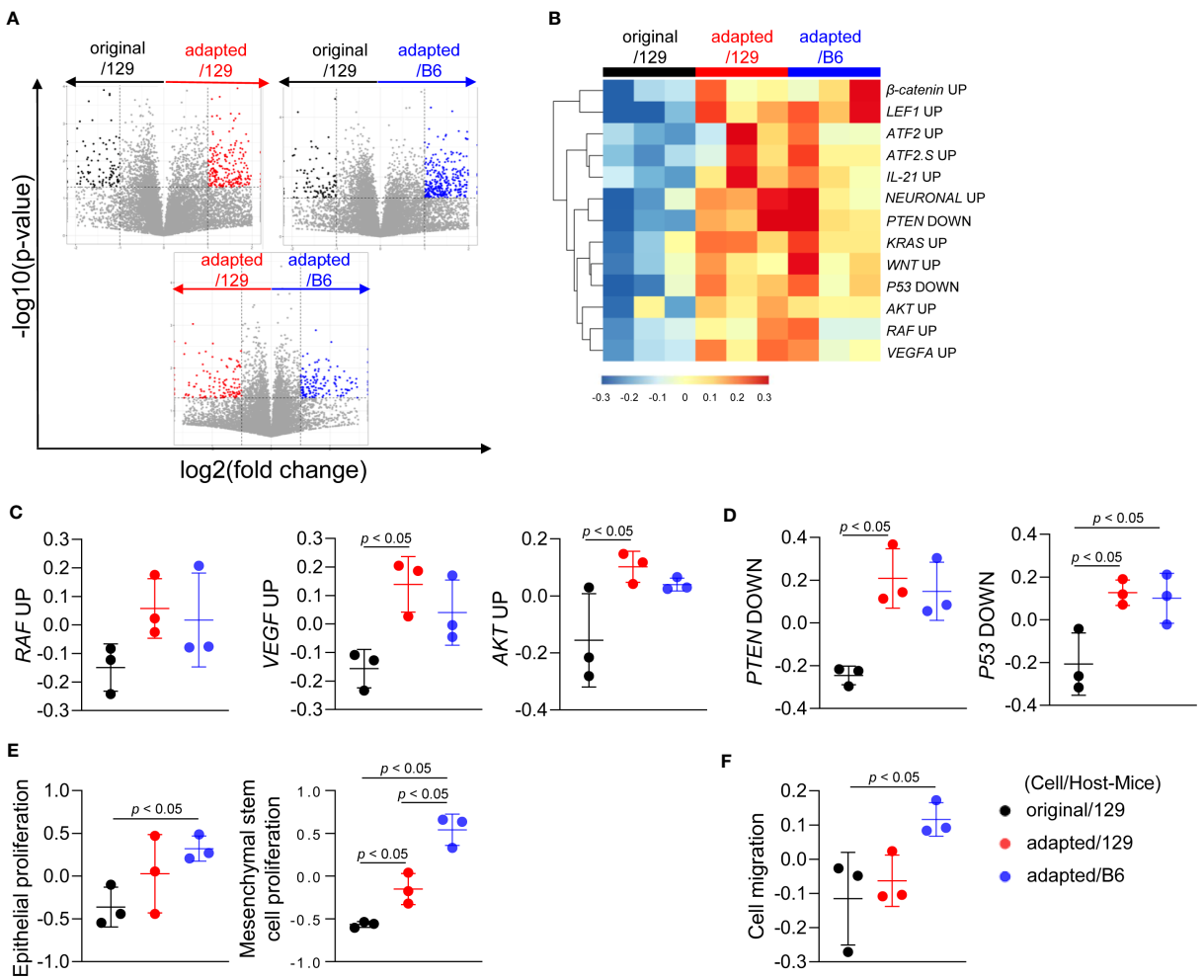

FIGURE 3
Molecular characteristics of orthotopic tumors from the adapted TBP3743 cells. B6129SF1 mice were implanted with 10^5 cells of each cell line (TBP3743-original and -adapted cells) and C57BL/6 mice were implanted with 10^5 cells of TBP3743-adapted. After 14 days post-implantation, tumors were harvested. Total RNA was harvested from whole tumor lysates and sequenced. **(A)** Volcano plots showing changes of gene expression. **(B)** Heatmap of changes in oncogenic signalling pathways and **(C, D)** each of oncogenic pathways. **(E)** Proliferation of epithelial and mesenchymal stem cells and **(F)** cell migration analysis. 129, B6129SF1; B6, C57BL/6. All data are expressed as mean ± SD.

129 group (Figure 4A). Network analysis of the over-represented gene sets further revealed that immune-related pathways were closely organized according to their mutual overlap (Figure 4B). Specifically, heatmap analysis demonstrated that the gene sets related to adaptive (T and B cells) and innate (NK T cells and cytokine production) immune responses were upregulated in the adapted/129 or adapted/B6 group compared with the original/129 group (Figure 4C). That is, immune response to tumor cells and immune inhibitory signalling pathways were enriched in the adapted/B6 group compared to the original/129 group (Figure 4D). Among the immune checkpoint related genes, both immune stimulatory (*Il2rb* and *Cd28*) and inhibitory (*Ctla4* and *Pdl1*) genes were significantly up-regulated in the adapted/129 or adapted/B6 groups compared with the original/129 group (Figure 4E). *In vitro* RT-PCR analysis revealed that inhibitory immune checkpoint genes were up-regulated in the adapted cells compared to the original TBP3743 cells (Supplementary Table 3), which were consistent with *in vivo* analysis, while stimulatory immune checkpoint genes were down-regulated in the adapted cells compared with the original TBP3743 cells (Supplementary Table 3). Collectively, the immune responses were activated in the adapted/129 and adapted/B6 groups compared with the original/129 group. In the comparison between the adapted/129 and adapted/B6 groups, while it could not be statistically assessed, the fold enrichments were higher in the adapted/B6 group (Figure 4A). More over-represented gene sets from the adapted/B6 participated in the network compared with the adapted/129 group (Figure 4B). Moreover, the expression of *Pdl1* was considerably higher in the adapted/B6 group than adapted/129 group. These results suggest that the anti-tumor immune responses might be more enhanced in the adapted/B6 group compared with the adapted/129 group.

To validate the distinctive immune characteristics observed in the adapted TBP3743 cell-derived orthotopic tumors, particularly with regard to tumor-T cell immune interactions, additional *in vivo* experiments were conducted under two immune-modifying conditions. Firstly, athymic nude mice, lacking T cell populations including $CD4^+$ and $CD8^+$ T cells, were utilized to investigate the impact of tumor-T cell interaction on tumor growth. Surprisingly, we observed comparable tumor volumes and weights between the original and adapted cell groups over the 9-day period following tumor cell injection (Supplementary Figure 5). These findings indicate the pivotal role of T cells in the tumorigenesis of the adapted model.

To further investigate the interplay between tumor cells and T cells in the adapted model microenvironment, we proceeded with a comparison of the anti-tumor efficacy of an anti-PD-L1 antibody between the original/129 group and the adapted/B6 group. Consistent with a previous study (20), treatment with the anti-PD-L1 antibody alone did not demonstrate a significant treatment response in the original model (Figure 4F). However, in the adapted model, both tumor volume and weight were significantly reduced by 60% and 55%, respectively (Figure 4G). This finding aligns with the gene expression data presented in Figure 4E, which reveals an upregulation of immune checkpoint modifying genes in the adapted model.

Immune cell profiling of the orthotopic tumor microenvironment

Flow cytometric analysis was additionally performed to characterize immune microenvironment among groups. The $CD45^+$ immune cell fraction was significantly greater in the adapted/B6 group compared with the original/129 group (39.1 ± 7.1% vs 17.4 ± 5.9%, $P< 0.05$; Figure 5A). The fractions of $CD45^+CD8^+$ cytotoxic T cells and $CD45^+CD4^+$ helper T cells were higher in the adapted/B6 group compared with the original/129 group, while $CD45^+CD3^+$ T cell fraction did not differ among groups (Figure 5B). The immune activating M1-macrophage ($CD45^+CD11b^+F4/80^+CD80^+CD206^-$) fraction was greater in the adapted/B6 group compared with the original/129 group (3.5 ± 2.1% vs 0.3 ± 0.3%, $P< 0.05$; Figure 5C), while those of total macrophage ($CD45^+CD11b^+F4/80^+$) and the immune suppressive M2 macrophages ($CD45^+CD11b^+F4/80^+CD80^-CD206^+$) did not differ (Figure 5C). The immune suppressive monocytic myeloid-derived suppressor cell (M-MDSC) ($CD45^+CD11b^+Ly6C^+Ly6G^-$) fraction was bigger in the adapted/B6 group than the adapted/129 group (10.6 ± 4.7% vs 4.1 ± 0.9%, $P< 0.05$; Figure 5D). Flow cytometric subset analysis for T cell and macrophage in the original/129, the adapted/B6, and the SC6/B6 also supported this notion. Those immune cell changes observed between the original and adapted model did not differ between the adapted/B6 and SC6/B6 (Supplementary Figure 6). Collectively, both activating and suppressive immune responses were up-regulated in the adapted/B6 group compared with the original/129 group. However, these differences were not observed between the original/129 and adapted/129 groups.

In addition to the increased immune infiltrate, especially characterized by increased T cell, immune escape cause by losing major histocompatibility (MHC) class I molecule can be another possible immune response in the process of the adapted cell tumorigenesis (24). Thus, we further analysed the expression of MHC class I molecules. *In vitro* mRNA expression of MHC class I gene was not lost, rather significantly upregulated in both SC3 and SC6 cells compared with the original cell (Supplementary Figure 7A). Additionally, flow cytometric analysis showed that under interferon-γ stimulation, the functional expression of MHC class I in SC3 cells was comparable to that of original cells, while SC6 cells showed a decrease in interferon-γ-mediated upregulation of MHC class I expression (Supplementary Figure 7B). These results suggest that immune escape through functional loss of MHC class I molecules may contribute to tumorigenesis in adapted cells, particularly in the later phase (represented by SC6 cells) rather than the early phase (represented by SC3 cells).

A bulk mRNA sequencing-based deconvolution analysis was performed to compare the immune profiles of murine tumor models to those of human ATC harbouring BRAF mutation. Supplementary Table 4 showed baseline characteristics of them (n=8). In the comparisons of fractions in $CD4^+$ T cell, $CD8^+$ T cell, and macrophages, human ATC showed higher $CD4^+$ T cell fractions than the murine tumors (Figure 5E). Given that heavy infiltration of M2-like macrophage is the characteristics of human

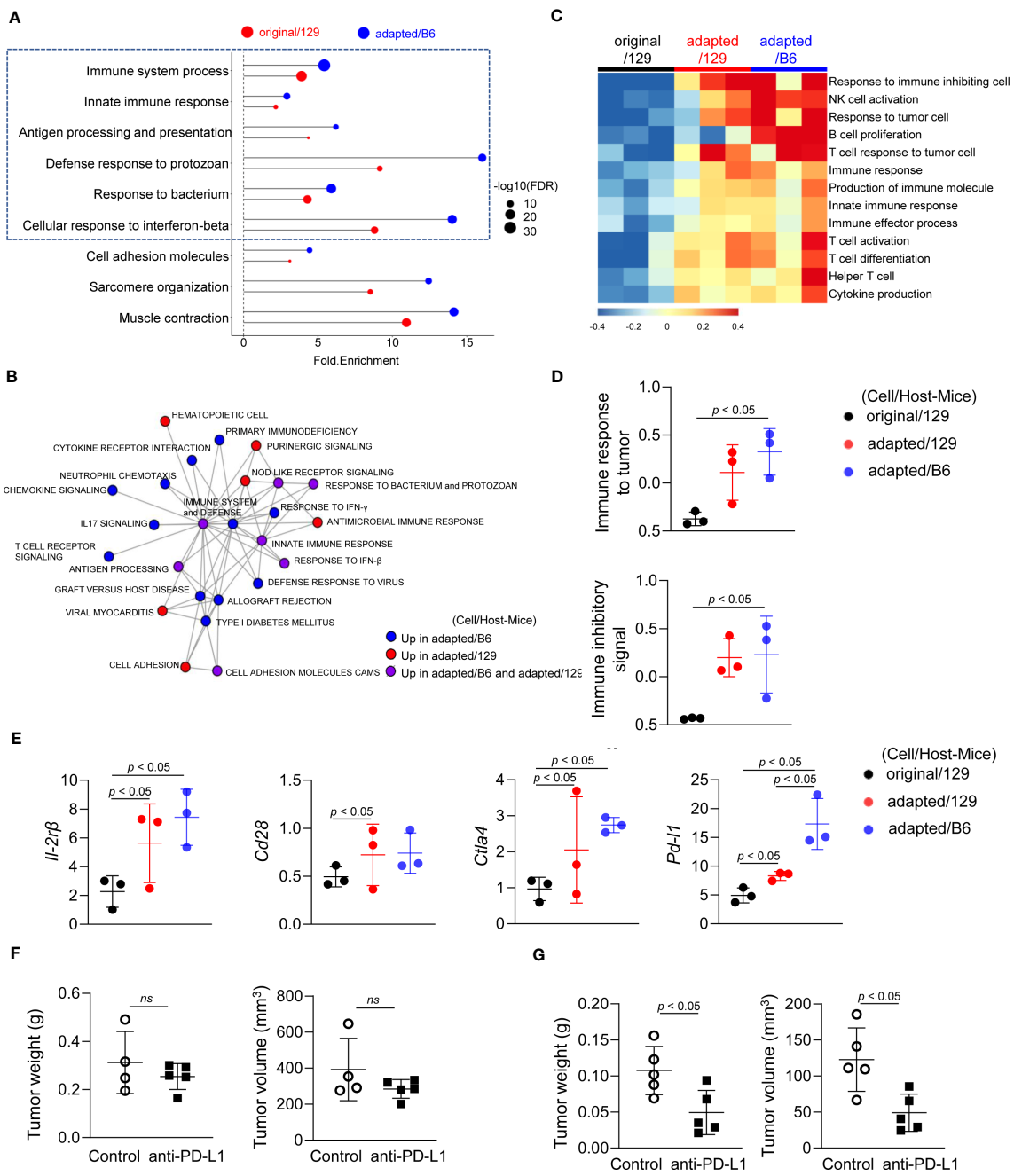

FIGURE 4
Molecular characteristics of the immune microenvironment in adapted TBP3743 cell-derived orthotopic tumors. B6129SF1 mice were implanted with 10^5 cells of each cell line (TBP3743-original and -adapted cells) and C57BL/6 mice were implanted with 10^5 cells of TBP3743-adapted. After 14 days post-implantation, tumors were harvested. Total RNA was harvested from whole tumor lysates and sequenced. **(A)** Classification of gene set enrichment analysis and **(B)** the networking of enriched pathways of immune category. **(C)** Heatmap of changes in immune response signalling pathways and **(D)** change of immune response to tumor and change of immune inhibitory signal. **(E)** Alteration of immune stimulatory related marker and immune inhibitory related marker. **(F)** B6129SF1 mice were implanted with 10^5 cells of TBP3743-original cells. After 10 days post-implantation, tumors were harvested. Anti-PD-L1 (0.2 mg/kg) was intraperitoneally injected from 5 days after tumor cell injection. Quantification of tumor volume and weight. **(G)** C57BL/6 mice were implanted with 10^5 cells of TBP3743-adapted cells. After 10 days post-implantation, tumors were harvested. Anti-PD-L1 (0.2 mg/kg) was intraperitoneally injected from 5 days after tumor cell injection. Quantification of tumor volume and weight. 129, B6129SF1; B6, C57BL/6. All data are expressed as mean ± SD.

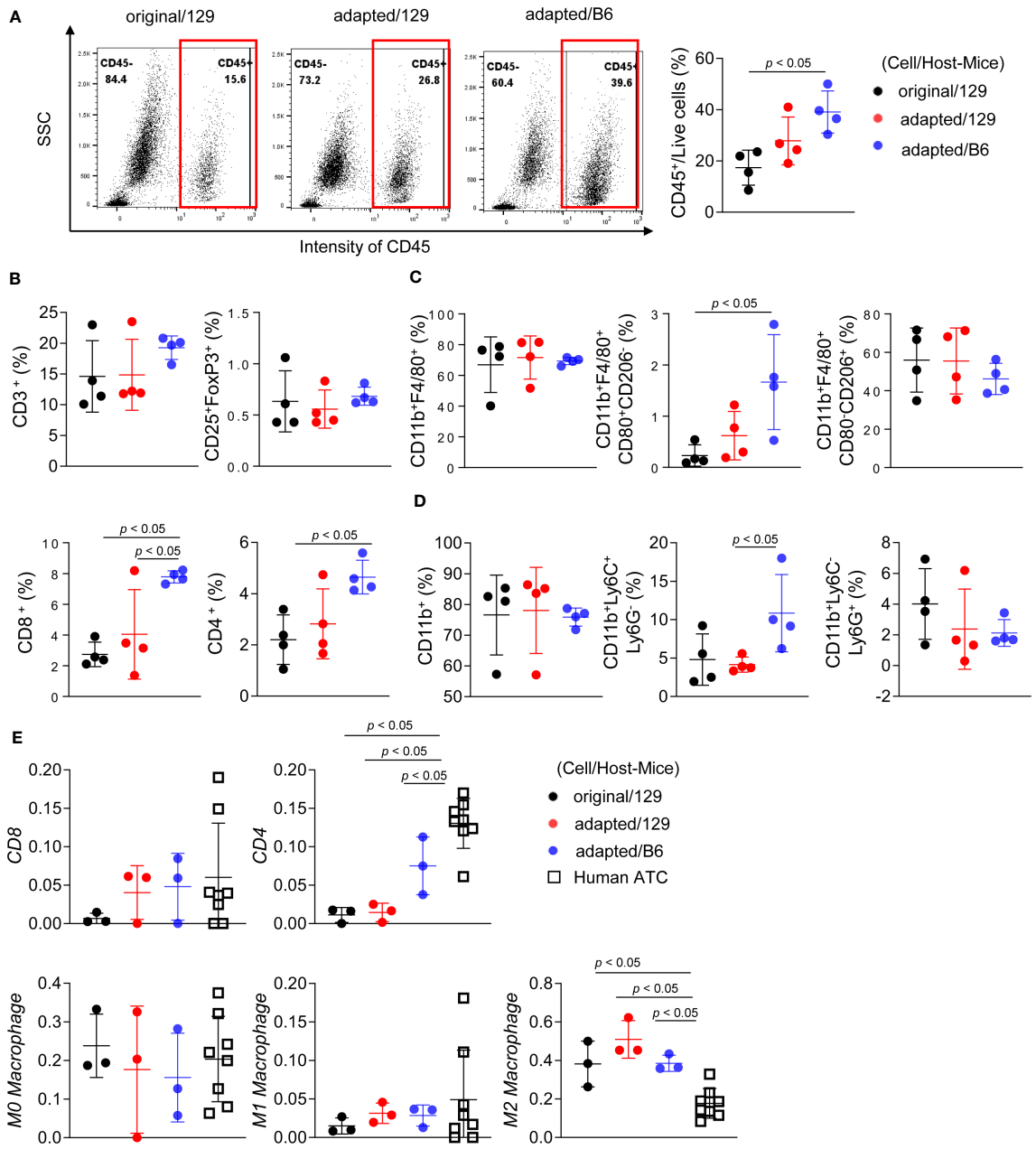

FIGURE 5
Immune cell profiling of the orthotopic tumor microenvironment. B6129SF1 mice were implanted with 10^5 cells of each cell line (TBP3743-original and -adapted cells) and C57BL/6 mice were implanted with 10^5 cells of TBP3743-adapted. After 14 days post-implantation, tumors were harvested. **(A-D)** Immune cell fractions were analysed by flow cytometry analysis using whole tumor lysates. **(A)** Representative plots and quantified graphs of $CD45^+$ cells in each tumors. Subpopulation of **(B)** T-lymphocytes ($CD3^+$ pan T; $CD8^+$ cytotoxic T; $CD4^+$ helper T; and $CD25^+FoxP3^+$ regulatory T), **(C)** macrophages ($CD11b^+F4/80^+$ pan macrophage; $CD11b^+F4/80^+CD80^+CD206^-$ M1-macrophage; and $CD11b^+F4/80^+CD80^-CD206^+$ M2-macrophage), and **(D)** myeloid cells (CD11b+ pan myeloid; $CD11b^+Ly6C^+Ly6G^-$ M-MDSC; and $CD11b^+Ly6C^-Ly6G^+$ PMC-MDSC). **(E)** RNA sequencing data of 8 human ATC samples were collected from (8) and deconvolution analysis were performed for comparing immune cell fractions between mice tumors from each group and human ATCs. M-MDSC, mononuclear myeloid-derived suppressor cells; PMN-MDSC, polymorphonuclear myeloid-derived suppressor cells; 129, B6129SF1; B6, C57BL/6. All data are expressed as mean ± SD.

ATC (3), M2-like macrophage fraction of human ATC was 16.5% (12.6%-21.1%). Those of the murine tumors were 38.4% (32.3%-44.2%) in the original/129 group, 45.4% (45.3-53.8%) in the adapted/129 group, and 36.3% (36.1%-39.9%) in the adapted/B6 group, which were all higher than that of human ATC.

Effects of a BRAF inhibitor on adapted TBP3743 cell-derived orthotopic tumors

Finally, drug responses to PLX-4032, a selective $BRAF^{V600E}$ kinase inhibitor, were explored *in vitro* and *in vivo*. *In vitro*, the

inhibitory effects of PLX-4032 on cell viability were similar between the original ($IC_{50,}$ 4.7 μM) and adapted ($IC_{50,}$ 3.5 μM) cells (Figure 6A). However, PLX-4032 treatment in the adapted/B6 group significantly reduced tumor burden by 84%, as determined by bioluminescence imaging, and tumor weight by 43% compared with the untreated group (Figures 6B, C).

Considering that a previous study reported immune modulatory effects of BRAF kinase inhibitor (20), the T cell and macrophage densities within the tumor microenvironment were assessed by IHC. Consistent with the previous study (20), the $CD3^+$, $CD4^+$, and $CD8^+$ T cell proportions were increased in the PLX-4032-treated group compared to the untreated group (Figure 6D). Moreover, the $F4/80^+$ macrophage proportion exhibited no difference, while that of $CD163^+$ M2-macrophages was decreased (Figure 6D). Collectively, the adapted TBP3743 cells responded to PLX-4032 appropriately, and the adapted/B6 model proved applicable for evaluation of the anti-tumor efficacy and immune modulatory effects of drugs.

Discussion

In the present study, we adapted the B6129SF1 mouse-derived ATC cell line, TBP3743, harbouring $Braf^{V600E}$ mutation and *Trp53* deletion (19), into C57BL/6 inbred mice and established a novel orthotopic tumor model of ATC. Although the adapted TBP3743 cells were de-dedifferentiated, they exhibited similar gross morphology, cell viability, and migration/invasion potential as the original TBP3743 cells *in vitro*. Moreover, our novel orthotopic tumor model in C57BL/6 mice showed similar histological features to human ATC with high oncogenic properties and activated anti-tumor immune responses. Indeed, the anti-tumor effects and

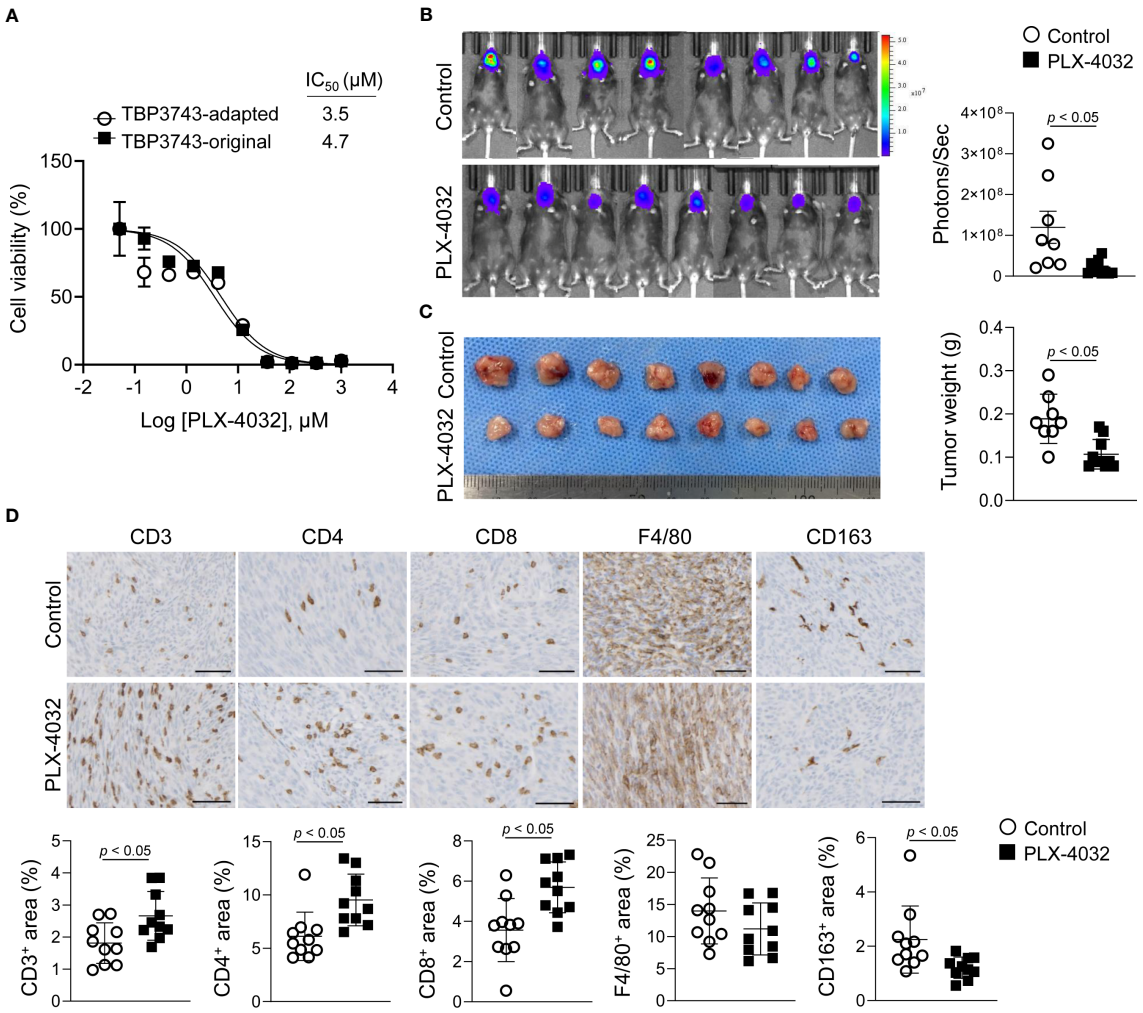

FIGURE 6
Effects of $BRAF^{V600E}$ inhibitor on TBP3743 cells. **(A)** Effect of PLX-4032 on TBP3743-original and -adapted cells were measured by cell viability assay. **(B-D)** TBP3743-adapted cells (1×10^5/10μL PBS) were injected into the murine thyroid via orthotopic injection, and mice were daily treated with 10 mg/kg of PLX-4032. At 2 weeks after injection, tumors were harvested. **(B)** bioluminescence imaging and **(C)** representative image of tumors, and quantification of tumor weight. **(D)** Representative images of IHC for T cell (CD3), helper T cell (CD4), cytotoxic T cell (CD8), macrophage (F4/80), and M2-macrophage (CD163) in each group tumors. scale bars: 50 μm. All data are expressed as mean ± SD.

immune modulatory effects of a BRAF inhibitor were observed in the model.

The adapted cells represented de-differentiated clones. During *in vivo* serial passaging, PAX8 expression was completely lost, while the expressions of TTF-1 and TSH-R were low but preserved. In contrast to the typical pattern observed in human ATC, where PAX8 is generally preserved (25, 26) and TTF-1 and TSH-R are lost earlier in the de-differentiation process (27), the TBP3743 cell line used in our study exhibited a different order of gene deletion. The adapted cells showed a reduction in mRNA expression of *TTF-1* and *TSH-R* compared to the original cells, but preservation of protein expressions of TTF-1, while the protein levels of TSH-R were negligible. Additionally, the recently described ATC marker gene, IGF2BP1 (23), was preserved in both the original and adapted cells. These findings indicate that the adapted ATC cells were still undergoing the de-differentiation process observed in human thyroid cancer.

The histologic features of the original/129, adapted/129, and adapted/B6 cells were consistent with human sarcomatoid ATC, characterized by spindle sarcoma-like tumor cells with pleomorphic nuclei and a high mitotic count. The complete loss of PAX8 in the adapted cells can be explained by previous reports indicating low positivity of PAX8 in human sarcomatoid ATC (less than 50%) (25, 26). Therefore, the adapted cells and the adapted/B6 model, paired with the original cells and original/129 model, provide a valuable tool for investigating the pathophysiology of the de-differentiation process in ATC.

The present study focused on analysing the molecular characteristics of ATC tumors using RNA sequencing data. *In vitro* analysis revealed that the gross cancer cell behaviours, including cell proliferation rates, with or without BRAF inhibitors, or migration/3D invasion potentials, were similar between the original and adapted cells. However, the rate of *in vivo* tumor growth and the Ki-67 index was significantly higher in B6129SF1 mice injected with the adapted TBP3743 cells compared to those injected with original TBP3743 cells. Molecular analyses supported these phenotypic differences demonstrating that gene sets associated with driver mutation pathways, such as RAF upregulation and PTEN and P53 down-regulation, as well as other oncogenic pathways, were enhanced in the tumors derived from adapted TBP3743 cells compared to original cells in B6129SF1 mice. These findings highlight the marked differences in cancer cell behaviour within *in vivo* and *in vitro* systems; thus, *in vitro* results must be interpreted carefully.

The evaluation of MHC molecule expression provides further insight into the adaptation mechanism studied here. In general, the selected clones exhibited loss of MHC genes, which has the potential to lead to immune evasion (28). Interestingly, the original cells and SC3 clone, representing an early adapted cell, retained their antigen-presentation functions by expressing MHC class I molecules. However, the SC6 clone exhibited significant loss of functional MHC class I under interferon-γ stimulation, highlighting the critical role of immune evasion in the later stages of the adapted model, while not observed in the early adaptation model. Therefore, careful selection and optimization of subclone passages are necessary for further study.

Interestingly, the tumor growth rate differed between murine hosts (i.e., B6129SF1 391 versus C57BL/6), even following the implantation of the same adapted TBP3743 cells. The adapted TBP3743 cells enhanced immune responses to tumors in all mice; however, the effect was stronger in C57BL/6 than in B6129SF1 mice. Not only were the immune stimulatory responses, including cytotoxic T cell or M1 macrophage proportions, enhanced in C57BL/6 mice compared to B6129SF1 mice, but also the immune suppressive responses, such as the M-MDSC proportion and *Pdl1* expression. This homeostasis of immune responses might account for the overall reduced tumor growth in C57BL/6 mice compared with B6129SF1 mice. Indeed, these findings highlight the importance of the interactions between the tumor microenvironment and cancer cells. This was further demonstrated *in vitro* by the downregulated expression of immune checkpoint genes in the adapted TBP3743 cells *in vitro*, which became upregulated following *in vivo* generation of tumors within C57BL/6 mice. Hence, cancer cells exhibit dynamic molecular responses to the host immune responses.

ATC stands out among various solid cancers as a highly immunogenic tumor characterized by dense infiltration of tumor-associated macrophages (TAMs) (3). Additionally, recent single-cell transcriptomics data have demonstrated that the tumor immune microenvironment undergoes significant reprogramming during ATC progression. This reprogramming is initiated by the substantial infiltration of immune cells, including macrophages and T cells, during the anaplastic transformation (28). Hence, understanding cancer-immune cell interactions is crucial in ATC research (29, 30). Our deconvolution analysis of total RNA sequencing data confirms the abundant presence of $CD4^+$ and $CD8^+$ T cells in human ATC samples, consistent with previous studies (31). Notably, the adapted/B6 model closely recapitulates the degree of tumor-infiltrating T cells observed in human ATC samples compared to other murine tumor groups. With the development of various T cell-targeting anti-tumor drugs over the past decade (32–34), some of which have demonstrated success in clinical settings (35–37), our model provides an improved platform for the ongoing advancement of immune-modulating therapeutics for ATC. Specifically, it enables more sensitive verification of the anti-tumor and immune-modulatory effects of candidate drugs in a model that closely mirrors the immune response observed in human ATC. Furthermore, the adapted model's median survival which is approximately 14 days offers an extended timeframe to assess drug response. Indeed, the adapted model demonstrated a notable response to anti-PD-L1 therapeutics, whereas the original model exhibited limited efficacy, consistent with previous findings (20).

Overall, the pros and cons of the adapted model is summarized as follows. The adapted model is the representative model of human ATC: The adapted cells are de-differentiated, possess molecular characteristics of human ATC. *In vivo* tumor with the adapted cells in C57BL/6 results in heavy infiltration of immune cells, which possibly resembles distinct tumor-host immune interaction of human ATC. The tumor growth rate and median survival is appropriate to investigate responses of anti-tumor drugs. Despite our interpretation that the adapted model represents the characteristics of de-differentiated clones and enhanced immune

response similar to "hot tumors" in human ATCs, it is possible that the observed enhanced immunity is partially due to simple allogenic rejection. Additionally, while we claimed that the prolonged survival in the adapted model is more suitable for drug development, it may raise concerns that this prolongation conflicts with the features of human ATC. However, it should be noted that the median survival of our model (16.5 days) is significantly shorter than the orthotopic mouse model using the 8505c human ATC cell-line, which showed steady tumor growth over 35 days without any deaths (38).

In conclusion, a novel orthotopic tumor model of ATC has been established by successful cell adaptation via *in vivo* passage in inbred C57BL/6 mice. This new syngenic ATC mouse model will advance the current understanding of the tumor microenvironment, particularly from an immunological context, and will prove effective as a preclinical platform for ATC drug discovery.

Data availability statement

The data presented in the study are deposited in the GEO repository, accession number GSE234282. The other data used in this study are available from the authors upon request.

Ethics statement

The animal study was reviewed and approved by The Institutional Animal Care and Use Committee approved the protocols for the animal study (No. SNU-190214-1-3), and all animals were maintained in accordance with the Guidelines for the Care and Use of Laboratory Animals of the Institute of Laboratory Animal Resources, Seoul National University.

Author contributions

ZX and HS performed all *in vivo* experiments and generated the data. HS and SH performed *in vitro* experiments and generated the data. YK analysed mRNA sequencing data and generated the figures. JKW performed histologic analysis and provided important insights. ZX, HS, YK, and SC wrote and edited the manuscript. S-jK, YP, and SP reviewed and edited the manuscript. SC and KL conceptualized the study and supervised the project. KL was responsible for funding acquisition for this study. All authors contributed to the article and approved the submitted version.

Funding

This research was supported by Korea Drug Development Fund funded by Ministry of Science and ICT, Ministry of Trade, Industry, and Energy, and Ministry of Health and Welfare, Republic of Korea (RS-2022-00166371), the National R&D Program for Cancer Control, Ministry of Health and Welfare, Republic of Korea (No. HA17C0040 to S.W.C.), Korean Foundation for Cancer Research (KFCR-2020-001), and the SNUH Research Fund (grant No. 0420193080 and 0420203120).

Acknowledgments

We thank Dr. Min-Kyoung Song (Department of Internal Medicine, Seoul National University Hospital) for her excellent review and comments. We greatly appreciate Pf. Dae Hee Kim (Kangwon National University) for kindly providing the anti-PD-L1 antibody and Jae Ah Kim, BA (Seoul National University Hospital) for technical supports.

Conflict of interest

SC is a co-founder of Cellus, Inc.

The remaining authors declare that the research was conducted in the absence of any commercial or financial relationships that could be construed as a potential conflict of interest.

Publisher's note

All claims expressed in this article are solely those of the authors and do not necessarily represent those of their affiliated organizations, or those of the publisher, the editors and the reviewers. Any product that may be evaluated in this article, or claim that may be made by its manufacturer, is not guaranteed or endorsed by the publisher.

Supplementary material

The Supplementary Material for this article can be found online at: https://www.frontiersin.org/articles/10.3389/fimmu.2023.1187388/full#supplementary-material

References

1. Simoes-Pereira J, Capitao R, Limbert E, Leite V. Anaplastic thyroid cancer: clinical picture of the last two decades at a single oncology referral centre and novel therapeutic options. *Cancers (Basel)* (2019) 11(8):1188. doi: 10.3390/cancers11081188

2. Maniakas A, Dadu R, Busaidy NL, Wang JR, Ferrarotto R, Lu C, et al. Evaluation of overall survival in patients with anaplastic thyroid carcinoma, 2000-2019. *JAMA Oncol* (2020) 6(9):1397–404. doi: 10.1001/jamaoncol.2020.3362

3. Jung KY, Cho SW, Kim YA, Kim D, Oh BC, Park DJ, et al. Cancers with higher density of tumor-associated macrophages were associated with poor survival rates. *J Pathol Transl Med* (2015) 49(4):318–24. doi: 10.4132/jptm.2015.06.01

4. Kim DI, Kim E, Kim YA, Cho SW, Lim JA, Park YJ. Macrophage densities correlated with cxc chemokine receptor 4 expression and related with poor survival in anaplastic thyroid cancer. *Endocrinol Metab (Seoul)* (2016) 31(3):469–75. doi: 10.3803/EnM.2016.31.3.469

5. Iyer PC, Dadu R, Gule-Monroe M, Busaidy NL, Ferrarotto R, Habra MA, et al. Salvage pembrolizumab added to kinase inhibitor therapy for the treatment of anaplastic thyroid carcinoma. *J Immunother Cancer* (2018) 6(1):68. doi: 10.1186/s40425-018-0378-y

6. Rao SN, Zafereo M, Dadu R, Busaidy NL, Hess K, Cote GJ, et al. Patterns of treatment failure in anaplastic thyroid carcinoma. *Thyroid* (2017) 27(5):672–81. doi: 10.1089/thy.2016.0395

7. Landa I, Ibrahimpasic T, Boucai L, Sinha R, Knauf JA, Shah RH, et al. Genomic and transcriptomic hallmarks of poorly differentiated and anaplastic thyroid cancers. *J Clin Invest* (2016) 126(3):1052–66. doi: 10.1172/JCI85271

8. Yoo SK, Song YS, Lee EK, Hwang J, Kim HH, Jung G, et al. Integrative analysis of genomic and transcriptomic characteristics associated with progression of aggressive thyroid cancer. *Nat Commun* (2019) 10(1):2764. doi: 10.1038/s41467-019-10680-5

9. Yoo SK, Song YS, Park YJ, Seo JS. Recent improvements in genomic and transcriptomic understanding of anaplastic and poorly differentiated thyroid cancers. *Endocrinol Metab (Seoul)* (2020) 35(1):44–54. doi: 10.3803/EnM.2020.35.1.44

10. Kunstman JW, Juhlin CC, Goh G, Brown TC, Stenman A, Healy JM, et al. Characterization of the mutational landscape of anaplastic thyroid cancer via whole-exome sequencing. *Hum Mol Genet* (2015) 24(8):2318–29. doi: 10.1093/hmg/ddu749

11. Subbiah V, Kreitman RJ, Wainberg ZA, Cho JY, Schellens JHM, Soria JC, et al. Dabrafenib and trametinib treatment in patients with locally advanced or metastatic braf V600-mutant anaplastic thyroid cancer. *J Clin Oncol* (2018) 36(1):7–13. doi: 10.1200/JCO.2017.73.6785

12. Subbiah V, Kreitman RJ, Wainberg ZA, Cho JY, Schellens JHM, Soria JC, et al. Dabrafenib plus trametinib in patients with braf V600e-mutant anaplastic thyroid cancer: updated analysis from the phase ii roar basket study. *Ann Oncol* (2022) 33 (4):406–15. doi: 10.1016/j.annonc.2021.12.014

13. Jeon MJ, Haugen BR. Preclinical models of follicular cell-derived thyroid cancer: an overview from cancer cell lines to mouse models. *Endocrinol Metab (Seoul)* (2022) 37(6):830–8. doi: 10.3803/EnM.2022.1636

14. Jin Y, Liu M, Sa R, Fu H, Cheng L, Chen L. Mouse models of thyroid cancer: bridging pathogenesis and novel therapeutics. *Cancer Lett* (2020) 469:35–53. doi: 10.1016/j.canlet.2019.09.017

15. Charles RP, Iezza G, Amendola E, Dankort D, McMahon M. Mutationally activated Braf(V600e) elicits papillary thyroid cancer in the adult mouse. *Cancer Res* (2011) 71(11):3863–71. doi: 10.1158/0008-5472.CAN-10-4463

16. Richmond A, Su Y. Mouse xenograft models vs gem models for human cancer therapeutics. *Dis Model Mech* (2008) 1(2-3):78–82. doi: 10.1242/dmm.000976

17. Becher OJ, Holland EC. Genetically engineered models have advantages over xenografts for preclinical studies. *Cancer Res* (2006) 66(7):3355–8, discussion 8-9. doi: 10.1158/0008-5472.CAN-05-3827

18. McFadden DG, Vernon A, Santiago PM, Martinez-McFaline R, Bhutkar A, Crowley DM, et al. P53 constrains progression to anaplastic thyroid carcinoma in a braf-mutant mouse model of papillary thyroid cancer. *Proc Natl Acad Sci USA* (2014) 111(16):E1600–9. doi: 10.1073/pnas.1404357111

19. Vanden Borre P, McFadden DG, Gunda V, Sadow PM, Varmeh S, Bernasconi M, et al. The next generation of orthotopic thyroid cancer models: immunocompetent orthotopic mouse models of braf V600e-positive papillary and anaplastic thyroid carcinoma. *Thyroid* (2014) 24(4):705–14. doi: 10.1089/thy.2013.0483

20. Gunda V, Gigliotti B, Ndishabandi D, Ashry T, McCarthy M, Zhou Z, et al. Combinations of braf inhibitor and anti-Pd-1/Pd-L1 antibody improve survival and tumor immunity in an immunocompetent model of orthotopic murine anaplastic thyroid cancer. *Br J Cancer* (2018) 119(10):1223–32. doi: 10.1038/s41416-018-0296-2

21. Song HK, Hwang DY. Use of C57bl/6n mice on the variety of immunological researches. *Lab Anim Res* (2017) 33(2):119–23. doi: 10.5625/lar.2017.33.2.119

22. Tomayko MM, Reynolds CP. Determination of subcutaneous tumor size in athymic (Nude) mice. *Cancer Chemother Pharmacol* (1989) 24(3):148–54. doi: 10.1007/BF00300234

23. Haase J, Misiak D, Bauer M, Pazaitis N, Braun J, Potschke R, et al. Igf2bp1 is the first positive marker for anaplastic thyroid carcinoma diagnosis. *Modern Pathol* (2021) 34(1):32–41. doi: 10.1038/s41379-020-0630-0

24. Garrido F, Aptsiauri N. Cancer immune escape: mhc expression in primary tumors versus metastases. *Immunology* (2019) 158(4):255–66. doi: 10.1111/imm.13114

25. Bishop JA, Sharma R, Westra WH. Pax8 immunostaining of anaplastic thyroid carcinoma: a reliable means of discerning thyroid origin for undifferentiated tumors of the head and neck. *Hum Pathol* (2011) 42(12):1873–7. doi: 10.1016/j.humpath.2011.02.004

26. Lai WA, Hang JF, Liu CY, Bai YH, Liu ZY, Gu HY, et al. Pax8 expression in anaplastic thyroid carcinoma is less than those reported in early studies: a multi-institutional study of 182 cases using the monoclonal antibody mrq-50. *Virchows Arch* (2020) 476(3):431–7. doi: 10.1007/s00428-019-02708-4

27. Miettinen M, Franssila KO. Variable expression of keratins and nearly uniform lack of thyroid transcription factor 1 in thyroid anaplastic carcinoma. *Hum Pathol* (2000) 31(9):1139–45. doi: 10.1053/hupa.2000.16667

28. Lu L, Wang JR, Henderson YC, Bai S, Yang J, Hu M, et al. Anaplastic transformation in thyroid cancer revealed by single-cell transcriptomics. *J Clin Invest* (2023) 133(11):e169653. doi: 10.1172/JCI169653

29. Ferrari SM, Fallahi P, Galdiero MR, Ruffilli I, Elia G, Ragusa F, et al. Immune and inflammatory cells in thyroid cancer microenvironment. *Int J Mol Sci* (2019) 20 (18):4413. doi: 10.3390/ijms20184413

30. Chakraborty S, Carnazza M, Jarboe T, DeSouza N, Li XM, Moscatello A, et al. Disruption of cell-cell communication in anaplastic thyroid cancer as an immunotherapeutic opportunity. *Adv Exp Med Biol* (2021) 1350:33–66. doi: 10.1007/978-3-030-83282-7_2

31. Luo H, Xia X, Kim GD, Liu Y, Xue Z, Zhang L, et al. Characterizing dedifferentiation of thyroid cancer by integrated analysis. *Sci Adv* (2021) 7(31): eabf3657. doi: 10.1126/sciadv.abf3657

32. Zanello A, Bortolotti M, Maiello S, Bolognesi A, Polito L. Anti-Pd-L1 immunoconjugates for cancer therapy: are available antibodies good carriers for toxic payload delivering? *Front Pharmacol* (2022) 13:972046. doi: 10.3389/fphar.2022.972046

33. Choi Y, Shi Y, Haymaker CL, Naing A, Ciliberto G, Hajjar J. T-Cell agonists in cancer immunotherapy. *J Immunother Cancer* (2020) 8(2):e000966. doi: 10.1136/jitc-2020-000966

34. Waldman AD, Fritz JM, Lenardo MJ. A guide to cancer immunotherapy: from T cell basic science to clinical practice. *Nat Rev Immunol* (2020) 20(11):651–68. doi: 10.1038/s41577-020-0306-5

35. Michielin O, Lalani AK, Robert C, Sharma P, Peters S. Defining unique clinical hallmarks for immune checkpoint inhibitor-based therapies. *J Immunother Cancer* (2022) 10(1):e003024. doi: 10.1136/jitc-2021-003024

36. Kyi C, Postow MA. Immune checkpoint inhibitor combinations in solid tumors: opportunities and challenges. *Immunotherapy* (2016) 8(7):821–37. doi: 10.2217/imt-2016-0002

37. Schadendorf D, Hodi FS, Robert C, Weber JS, Margolin K, Hamid O, et al. Pooled analysis of long-term survival data from phase ii and phase iii trials of ipilimumab in unresectable or metastatic melanoma. *J Clin Oncol* (2015) 33 (17):1889–94. doi: 10.1200/JCO.2014.56.2736

38. Nucera C, Nehs MA, Mekel M, Zhang X, Hodin R, Lawler J, et al. A novel orthotopic mouse model of human anaplastic thyroid carcinoma. *Thyroid* (2009) 19 (10):1077–84. doi: 10.1089/thy.2009.0055

frontiers | Frontiers in Immunology

TYPE Review
PUBLISHED 07 September 2023
DOI 10.3389/fimmu.2023.1236965

Check for updates

OPEN ACCESS

EDITED BY
Daniel R. Principe,
University of Illinois Chicago, United States

REVIEWED BY
Simon Young,
University of Texas Health Science Center at Houston, United States
Joanne Lysaght,
Trinity College Dublin, Ireland

*CORRESPONDENCE
An Coosemans
An.Coosemans@kuleuven.be

RECEIVED 08 June 2023
ACCEPTED 23 August 2023
PUBLISHED 07 September 2023

CITATION
Berckmans Y, Ceusters J, Vankerckhoven A, Wouters R, Riva M and Coosemans A (2023) Preclinical studies performed in appropriate models could help identify optimal timing of combined chemotherapy and immunotherapy. *Front. Immunol.* 14:1236965. doi: 10.3389/fimmu.2023.1236965

COPYRIGHT
© 2023 Berckmans, Ceusters, Vankerckhoven, Wouters, Riva and Coosemans. This is an open-access article distributed under the terms of the Creative Commons Attribution License (CC BY). The use, distribution or reproduction in other forums is permitted, provided the original author(s) and the copyright owner(s) are credited and that the original publication in this journal is cited, in accordance with accepted academic practice. No use, distribution or reproduction is permitted which does not comply with these terms.

Preclinical studies performed in appropriate models could help identify optimal timing of combined chemotherapy and immunotherapy

Yani Berckmans[1], Jolien Ceusters[1], Ann Vankerckhoven[1], Roxanne Wouters[1,2], Matteo Riva[1,3] and An Coosemans[1]*

[1]Department of Oncology, Laboratory of Tumor Immunology and Immunotherapy, Leuven Cancer Institute, KU Leuven, Leuven, Belgium, [2]Oncoinvent AS, Oslo, Norway, [3]Department of Neurosurgery, Centre Hospitalier Universitaire (CHU) UCLouvain Namur, University Hospital of Godinne, Yvoir, Belgium

Immune checkpoint inhibitors (ICI) have been revolutionary in the field of cancer therapy. However, their success is limited to specific indications and cancer types. Recently, the combination treatment of ICI and chemotherapy has gained more attention to overcome this limitation. Unfortunately, many clinical trials testing these combinations have provided limited success. This can partly be attributed to an inadequate choice of preclinical models and the lack of scientific rationale to select the most effective immune-oncological combination. In this review, we have analyzed the existing preclinical evidence on this topic, which is only limitedly available. Furthermore, this preclinical data indicates that besides the selection of a specific drug and dose, also the sequence or order of the combination treatment influences the study outcome. Therefore, we conclude that the success of clinical combination trials could be enhanced by improving the preclinical set up, in order to identify the optimal treatment combination and schedule to enhance the anti-tumor immunity.

KEYWORDS

immune checkpoint inhibitors, chemotherapy, preclinical models, combination treatment, cancer therapy

1 Rise in combination therapies with immune checkpoint inhibitors after limited effectivity in monotherapy

In recent years, attention towards cancer immunotherapy has grown (1, 2). The goal is to shift the balance from tumor promoting immunosuppression towards anti-tumor immune activation, to support and promote the immune-mediated attack of cancer cells. Immune checkpoint inhibitors (ICI) are an example of such immunotherapeutic modality aiming to

release the tumor induced immune brakes (3). Many of these brakes, or checkpoint molecules, have been identified, such as programmed death ligand 1 (PD-1) or its ligand PD L1, cytotoxic T-lymphocyte associated protein 4 (CTLA-4), T-cell immunoglobin and mucin domain 3 (TIM 3), lymphocyte activation gene 3 (LAG-3) and others (4). Seven such ICIs are currently approved for use in patients across all cancer types. The first approved was the anti-CTLA-4 ipilimumab followed by three anti-PD-1 ICI, nivolumab, cemiplimab and pembrolizumab, and three anti-PD-L1 inhibitors, durvalumab, avelumab and atezolizumab (4, 5). However, as the efficacy of these ICI was mostly observed in a restricted subset of patients, their use is limited to specific indications in cancers such as melanoma, breast cancer, colorectal, classical Hodgkin's lymphoma and non-small cell lung cancer (NSCLC) (4, 6). In an estimated 60-70% of patients, they remain ineffective (3, 6). To overcome this clinical challenge, attention for combination therapies has grown. In 2018, the clinical research program of the Cancer Research Institute (Anna-Maria Kellen Clinical Accelerator, NY, USA) published an overview of immune-oncological trials, describing the rise in combination trials using PD-1/L1 targeting agents with other immunotherapies, radiotherapy and chemotherapies over the past five years. From the 1105 reported combination studies, the most prevalent combinations included anti-PD-1/L1 with either anti-CTLA-4 (n=251) or chemotherapy (n=170) (7). An update in 2021 showed the continued increase in the number of trials testing a combination of anti-PD-1/L1 and chemotherapy with 145 new trials started in the first three quarters of 2020 alone (8).

2 Rationale for combination of chemotherapy with immune checkpoint inhibitors

To develop combination treatments, not only oncological but also immunological changes should be considered. Galluzzi et al. described different immune effects induced by different types of chemotherapy (9). In the past, some chemotherapeutics have been described as immunosuppressive agents, which explained their use for the treatment of severe autoimmune diseases (10). Examples of such chemotherapeutics are cyclophosphamide and methotrexate, which can both impair the proliferation and function of effector T-cells (10, 11). Moreover, doxorubicin has been shown to increase the expansion of myeloid derived suppressor cells, resulting in increased immunosuppression (11). The immense chemotherapeutically induced release of tumor-associated antigens has also been suggested to suppress the anti-tumor immune response. However, evidence supporting this mechanism is currently not available (10). In contrast, cytotoxic chemotherapies have also been reported to promote immunogenicity. For example, one of the immune effects reported for doxorubicin was the enhanced proliferation of tumor targeting CD8+ T-cells, while other conventional chemotherapies like gemcitabine and paclitaxel, were shown to decrease immunosuppressive myeloid derived suppressor cells and regulatory T-cells cells, respectively (9). Similar immunological effects have been discussed in a review by Brown et al., such as the increase of antigen presentation through the upregulation of MHC class 1 on tumor cells by a number of the DNA-damaging therapeutics including gemcitabine, cyclophosphamide and oxaliplatin (12). Our group has shown that carboplatin-paclitaxel resulted in a superior immune-composition compared to several other chemotherapeutics in an ovarian cancer mouse model (13), which was in line with observations in patients (14). Another argument in favor of combining chemotherapy and ICI therapy has been the upregulation of co-inhibitory ligands, such as PD-L1, promoted by numerous chemotherapeutics including paclitaxel, 5-fluorouracil and cisplatin (15). Furthermore, certain chemotherapeutics such as doxorubicin, oxaliplatin and cyclophosphamide could also induce immunogenic cell death (ICD) (12, 16). All together, these immune-related effect of chemotherapy promote the rationale for a combination with ICI treatment to further stimulate the anti-tumor adaptive immune response and T-cell expansion (6, 15). However, all described immune effects can be drug, dose and time dependent, highlighting the importance of optimal knowledge and preclinical evidence (16).

3 Combinations of immune checkpoint inhibitors and chemotherapy still fail in the majority of clinical trials

Combinatorial approaches resulted in selected clinical successes (17). In the AtezoTRIBE trial (NCT03721653), previously untreated metastatic colorectal cancer patients showed improved median PFS (HR 0,69; 80% CI [0,56–0,85]) with the addition of the ICI atezolizumab to the treatment schedule consisting of chemotherapy (FOLFOXIRI, a combination of folinic acid, fluorouracil, oxaliplatin and irinotecan) and anti-VEGF (bevacizumab), with all treatments being administered simultaneously using a 48h intravenous infusion with cyclic repeat every 14 days (18). The KEYNOTE-021 trial (NCT02039674) showed improved objective response rate (ORR) (p=0,0016) in NSCLC patients receiving carboplatin/pemetrexed combined with pembrolizumab compared to chemotherapy alone (19). These findings were confirmed in the KEYNOTE-189 trial (NCT02578680) in which overall survival (OS) (HR 0,49; 95% CI [0,38-0,64]) and progression free survival (PFS) (HR 0,52; 95% CI [0,43-0,64]) were significantly increased in the combination therapy-receiving patients (20). Both KEYNOTE-021 and KEYNOTE-189 trials administered pembrolizumab simultaneously with platin-based chemotherapy and pemetrexed for four cycles, repeated every three weeks, as well as maintenance therapy for up to 24 months in combination with pemetrexed (19, 20). Additionally, in patients with metastatic triple negative breast cancer (TNBC) testing positive for PD-L1 expression, the combination of atezolizumab with the chemotherapeutic nab-paclitaxel showed promising results on PFS (HR 0,62; 95% CI [0,49-0,78]) and OS (HR 0,67; 95% CI [0,53-0,86]) (IMpassion130; NCT02425891) when administered simultaneously through intravenous injection on day 1 and 15 of a 28-day cycle which was repeated until disease progression was observed (21). Similar valuable outcomes were observed in the KEYNOTE-522 trial (NCT03036488), where addition of

pembrolizumab to neoadjuvant carboplatin paclitaxel chemotherapy yielded a greater response compared to chemotherapy alone in early TNBC patients (HR 0,63; 95% CI [0,43-0,93]) (22).

However, the majority of trials testing an immune-oncological combination produced disappointing results (17). For example, in gastroesophageal cancer patients, the combination of pembrolizumab with chemotherapy (cisplatin and fluorouracil/capecitabine) resulted in a nearly equal OS compared to chemotherapy alone (HR 0,85; 95% CI [0,70-1,03]) in the phase 3 KEYNOTE-062 trial (NCT02494583) (23). Similarly, in the KEYNOTE-361 trial (NCT02853305), no improved PFS (HR 0,78; 95% CI [0,65-0,95]) or OS (HR 0,86; 95% CI [0,72-1,02]) was reported after combination treatment with pembrolizumab and chemotherapy (comprising of gemcitabine and cisplatin/carboplatin) compared to chemotherapy alone, for the treatment of advanced urothelial carcinoma. In this trial, the ICI and chemotherapy were administered simultaneously through intravenous injection on day 1 of a three- weekly cycle with a maximum of six chemotherapy cycles and 35 cycles of pembrolizumab (24). For ovarian cancer, three large phase 3 trials have been published, all reporting negative results. The phase 3 JAVELIN Ovarian 200 trial (NCT02580058) reported no improved response between groups receiving either avelumab (every two weeks, intravenously) combined with pegylated liposomal doxorubicin (PLD) (every four weeks, intravenously) or PLD monotherapy (PFS: HR 0,78; CI [0,59-1,24]; OS: HR 0,89: CI [0,74-1;24]) (25, 26). Likewise, in the JAVELIN Ovarian 100 trial (NCT02718417), the primary objectives of increasing the PFS were not met. In this study, two combination regimens were compared to the control group receiving carboplatin paclitaxel chemotherapy alone; chemotherapy followed by avelumab (HR 1,43; 95% CI [1,05-1,95]) and chemotherapy plus avelumab followed by avelumab (HR 1,14; 95% CI [0,83-1,56]). Remarkably, both combination regimens seemed to perform worse than chemotherapy alone (27, 28). Interim analysis of the IMagyn050 trial (NCT03038100) in newly diagnosed ovarian cancer patients underscored this, as no difference in PFS was seen after addition of atezolizumab to chemotherapy (carboplatin paclitaxel) followed by anti-VEGF (bevacizumab) (HR 0,92; 95% CI [0,97-1,07]). All treatments were administered intravenously on day 1 of a three- weekly cycle. Additionally, both adjuvant and neoadjuvant schedules were included in this trial. However, no discrepancies have been reported between the two groups (29).

4 Limited relevant preclinical research could relate to failing clinical trials

The large number of failed clinical trials testing the combination of ICI with chemotherapy is alarming. The question arises if this could have been anticipated using relevant preclinical research. We performed a PubMed literature search using the minimal search term (chemotherapy [Title/Abstract] AND checkpoint[Title/Abstract] NOT (Review[Publication Type]). This search resulted in 2863 articles on November 12th 2021 of which only 92 research articles were dedicated to preclinical testing of ICI and chemotherapy combinations (See Supplementary Material 1). Figure 1 gives an overview of all different cancer types used in these research articles. Remarkably, almost half (47.8%) of these articles study either colorectal cancer or breast cancer, in which ICI are already accepted for use under specific conditions. More specifically, the U.S. Food and Drug Administration (FDA) approved both pembrolizumab as first line treatment, as well as the combination of ipilimumab and nivolumab in second line treatment of metastatic colorectal cancer in specific conditions. For breast cancer, both atezolizumab and pembrolizumab have been approved for metastatic TNBC patients (4). Although preclinical results are scarce for the majority of other cancer types, clinical trials testing this immune-oncological combination are conducted in a wide range of disease profiles.

Figures 1B, C display the different chemotherapeutics and ICI tested in these preclinical studies, respectively. A wide variety of chemotherapeutics have been tested, which can be explained by the different cancer types that were studied and their standard of care in the clinic. In contrast, only two types of ICI prevail: anti-PD-1/L1 and anti-CTLA-4 checkpoint inhibitors. Other ICI modalities are scarcely represented in these preclinical studies. Generally, the choice of preclinical model should be looked at critically before each experiment. Besides the pathogenesis of the disease which should be properly reproduced, it is equally crucial to assure that the biological target of the tested therapy is conserved in the chosen model (30). Therefore, when testing ICI therapy, it is most reasonable to choose an immune competent preclinical model in which the engagement of the ICI with its target on immune cells can be ensured. In the majority of the 92 articles, preclinical research was performed in syngeneic mouse models with C57BL/6 or Balb/c background (Figure 1D). Both C57BL/6 and Balb/c are inbred immune competent mice strains. Some inter-strain immunological differences are present, consisting in a prevailing humoral immune response in Balb/c mice, while in C57Bl/6 murine cellular immunity dominates (31). Additionally in other studies, C57Bl/6 mice appeared to have a Th1 dominant immune response in contrast to Balb/c mice where Th2 dominated the immune response (32). Besides these discrepancies, syngeneic models are overall characterized by a fully functioning immune system, which is their main advantage besides their uncomplicated establishment and fair cost. In contrast, five studies could be identified using immunodeficient mouse strains. The use of immunodeficient mouse strains to create models such as patient derived xenografts (PDX) has been proven successful as a preclinical platform (33) and has shown to accurately reflect the gene expression profile and histology of the primary human tumor (34). However, PDX models do not recapitulate the full physiological biology of the human tissue due to the lack of an intact immune system making them less suitable for testing immunotherapeutic strategies (35). Additionally, the response to chemotherapy can also depend on the presence of a fully functioning immune system. In a study by Kroemer and Galluzzi et al., chemotherapy response was shown to be suboptimal in immunodeficient mice compared to syngeneic tumor-bearing mice. This discrepancy could be related to the lack of immunogenic cell death and activation of the subsequent anti-tumor immune response (36). Humanization of these mice created a strategy to overcome the immune limitations seen in immunodeficient xenograft models (37). Different methods for

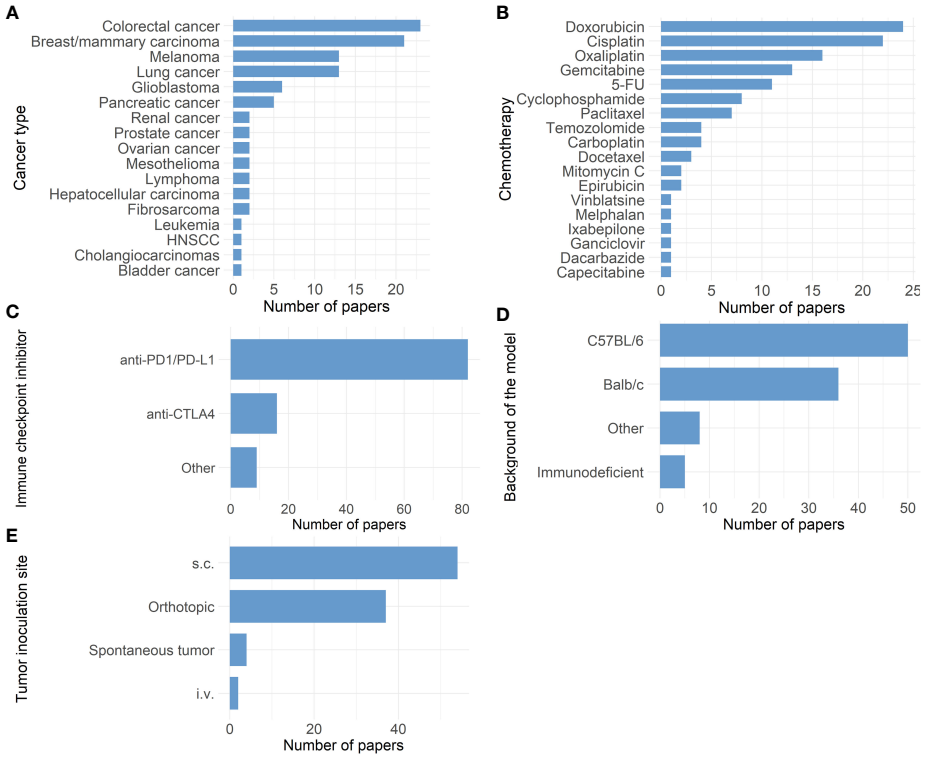

FIGURE 1
Overview of 92 research papers in which a combination of immune checkpoint inhibitors and chemotherapy was tested preclinically. **(A)** Bar chart showing the different cancer types studied. **(B)** Bar chart showing the distribution of different chemotherapies tested. (5-FU: 5-fluorouracil) **(C)** Bar chart showing the distribution of different immune-checkpoint inhibitors tested. (Other: anti-B7-H3, anti-CD47, anti-CD96, anti-4-1BB, anti-40 and anti-HLA-G) **(D)** Bar chart showing the background of different mouse models used. (Other: C3H, CBA/CaJ, DBA/2J, FVB, KRAS LSL- G12D+; p53-/-: LSL, 129S1/SvImJ, B10.D2, μMt) .**(E)** Bar chart showing the distribution of inoculation sites in the mouse models used. (s.c.: subcutaneous, i.v.: intravenous).

creating humanized mouse models exist such as transplantation of human peripheral blood mononuclear cells or human hematopoietic stem cells into immunodeficient mice after which they can be inoculated using human tumor cells or patient derived tissue (37). This offers an interesting approach to test immunotherapies in models bearing human tumors in combination with a humanized immune system. Multiple caveats however still need to be overcome, such as the development of graft versus host disease and the high cost.

While currently the syngeneic immune competent mouse models are explored most in immune-oncology research, it can be argued that in order to mimic heterogeneous and progressive cancers *in vivo*, genetically engineered mouse models offer added physiological relevance (37). Genetically engineered mouse models carry altered oncogenes and/or tumor suppressor genes and can therefore develop tumor spontaneously (38). Advantages include the orthotopic origin of the tumor with physiological intra-tumoral heterogeneity and an intact immune system, while the extensive variability in tumor development, low mutational burden and the time-consuming process are the largest disadvantages (35, 37). An example of such an established spontaneous cancer model are KPC mice (KrasLSL-G12D+;Trp53LSL-R172H/+;p48Cre in C57Bl/6 mice) which stochastically develop intra-epithelial neoplasms in the pancreas (39). These types of mouse models were only present in four out of the 92 research articles, including models for breast cancer, head and neck squamous cell carcinoma and lung cancer (See Supplementary Material 1; Martinez-Usatorre et al., Sci Transl Med, 2021; Sirait-Fischer et al., Front Oncol, 2020; Spielbauer et al., Otolaryngology–Head and Neck Surgery, 2018; Workenhe et al., Commun Biol, 2020).

Lastly, though none of the 92 articles found in our literature search deferred from using mice, in preclinical immune-oncological research, other species are increasingly being considered for use due to their similar immunological, anatomical or pathological features to humans. Syrian hamsters are viewed as ideal preclinical animal model for cancer immunotherapy studies due to the complex tumor microenvironment, tumor histology and cancer progression resembling the human scenario (40). Another advantage of this species are the cheek pouches which are considered an immune desert due to the lack of lymphatic drainage pathways offering the potential of long-term transplantation of foreign material, such as patient derived tumor tissue without immune rejection (40). Secondly, ferrets can be suitable models as they have a particularly high cancer prevalence, which could give insights into the biological development of cancer, and have shown useful in immunology studies (41, 42). Higher animal models such as canines and swine are also available. Canines can spontaneously develop tumors, showing large homology to human cancers both genetically and in relation to the surrounding tumor immune microenvironment (43). They are fully immune competent and

possess more comparable immune constituents to the human immune system compared to murine models (43, 44). Swine models can be applied in oncological research and are mostly used to test new devices and surgical procedures (45). Immunological applications can also be explored as swine are genetically and immunologically relevant to humans and have shown to respond similarly to anti-cancer drugs (46). Different models exist such as genetically modified swine capable of developing tumors and wild-type immune competent swine bearing xenograft tumors (45). Lower models such as zebrafish or Xenopus could also provide opportunities to study certain therapeutic effects on cancer cells depending on the research question (44). Homologous to humans, zebrafish possess two branches in their immune system, the innate and the adaptive component. However, one difference is the delay in adaptive immunity development causing the zebrafish to rely solely on the innate immunity in the first stages of their lives. This provides the opportunity for specific studies into the innate immune system using recently hatched (72 hours post fertilization) zebrafish which harbor a fundamentally similar macrophage lineage to humans. At this stage, inoculation of human cancer cells has an increased engraftment chance due to the absence of adaptive immune cells (47). In later stages of zebrafish development, immune-oncological research may be limited due to their biological and anatomical differences, such as the lack of lymph nodes, and less complex immune system compared to humans (44).

Besides animal models, alternative methods for preclinical research are being explored, which is increasingly promoted by governmental and ethical services, but has proven difficult when the immune system is involved. One hopeful approach is the use of *ex vivo*, three dimensional cultures derived from human tumor tissue called explants (48, 49). This methodology has already been successful for multiple cancer types. Moreover, the explant culturing method for NSLC by Karekla et al. showed reproducible drug responses to cisplatin (49). Furthermore, these types of cultures have the potential to provide a platform for evaluating immunological responses to ICI therapy, as reported by Voabil and colleagues (50).

Another point of attention when working with animal models for the purpose of translational research is the fact that the tumor inoculation site can impact the tumor immune environment and subsequently the immunotherapy response (51). Most of these 92 studies use subcutaneous (s.c.) mouse models (Figure 1E). Subcutaneously mimicking a tumor that from origin grows in another organ is less ideal as the invasive potential of the tumor is limited due to the presence of s.c. connective tissue, therefore creating a different tumor microenvironment (most likely also influencing the function/role of tissue resident immune cells) (52). This can impact the translatability of these models for immunotherapeutic research. For example, in preclinical melanoma models the tumor location was shown to influence the recruitment of tissue-specific tumor-associated macrophages (51, 52). Orthotopically inoculated tumors in immune-competent mice can surmount some of these limitations. Overall, it seems that the chosen model and inoculation site can impact the outcome in these preclinical studies.

5 The therapeutic combinatorial schedule influences treatment response

Our group has previously described the shift in survival in a syngeneic orthotopic mouse model for ovarian cancer when changing the sequence of the chemotherapy and immunotherapy combination (53). To identify the optimal immune-oncological combination regimen, we looked into the different administration schedules of the 92 preclinical studies (Figure 2). In the majority (76,1%; 70/92), administration of ICI and chemotherapy was simultaneous, mostly even started the same day (47/92). Only 16,3% (15/92) of preclinical studies were designed with a sequential administration of treatment, nearly all of them starting with chemotherapy prior to ICI treatment (14/15). Only a small percentage of studies (7,6%; 7/92) investigated multiple different administration schedules. These seven articles will be further discussed below. Additionally, two preclinical studies not identified through our search strategy, but similarly looking into the impact of combination treatment scheduling, have been added manually to the discussion below. An overview of all nine studies can be found in Table 1.

Lesterhuis et al. studied the combination of anti-CTLA-4 and gemcitabine chemotherapy in a s.c. mesothelioma mouse model. A significant survival benefit was reported in mice receiving simultaneous administration of both treatments compared to the regimen where gemcitabine was administered either before or after anti-CTLA-4,

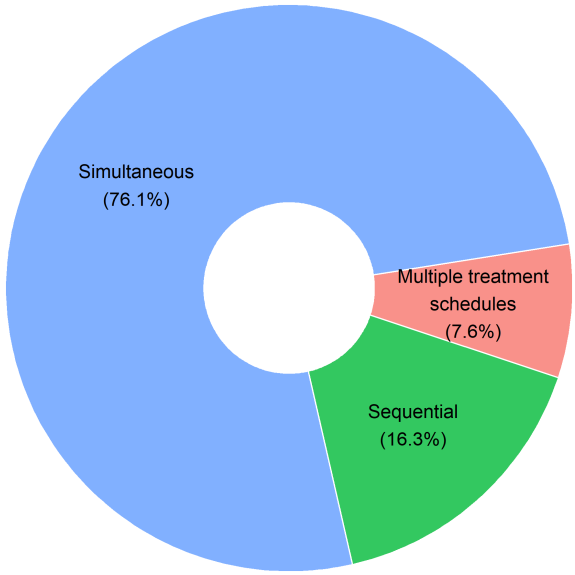

FIGURE 2
Pie chart on administration schedules in 92 preclinical research articles. Studies with simultaneous treatment administration include all studies with same start date of both therapies (47/92), studies where immune-checkpoint inhibitor treatment started first (6/92) or chemotherapeutic treatment started first (17/92) before simultaneous administration of the combination treatment was continued. Sequential treatment administration includes studies where no overlap between both treatments occurred. Treatments were given consecutively with either first chemotherapy (14/92) or first immune-checkpoint inhibitor therapy (1/92). In 7 out of the 92 studies (7.6%), multiple treatment administration schedules were tested in one preclinical experiment.

TABLE 1 Overview of different combinations of chemotherapy and ICI used in nine research articles comparing multiple therapeutic regimens.

Author – Year	Cancer type	ICI	Chemo-therapy	Regimen of administration tested	Superior regimen	Limitations
Lesterhuis WJ. et al. – 2013 (54)	Meso-thelioma	anti-CTLA4	Gemcitabine	• Simultaneous • Sequential – first chemo • Sequential – first ICI	Simultaneous	s.c. mouse model
Martin-Ruiz A. et al. – 2020 (55)	Lung carcinoma	anti-PD-1	Cisplatin	• Simultaneous • Sequential – first chemo • Sequential – first ICI	Simultaneous	Immuno-deficient mouse model (NSG)
Zhao X. et al. – 2020 (56)	Colorectal carcinoma	anti-PD-1	5-fluorouracil	• Simultaneous • Sequential – first chemo	Sequential – first chemo	s.c. mouse model
Fu D. et al. – 2020 (57)	Colorectal carcinoma	anti-PD-1/L1	Cisplatin or Oxaliplatin	• Simultaneous • Sequential – first chemo, 3 days later ICI • Sequential first – chemo, 6 days later ICI	Sequential – first chemo, 3 days later ICI	s.c. mouse model
Golchin S. et al. – 2019 (58)	Colorectal carcinoma	anti-PD-L1	Oxaliplatin	• Simultaneous • Sequential – first chemo • Sequential – first ICI	Sequential – first ICI	s.c. mouse model
Alimohammadi R. et al. – 2020 (59)	Melanoma	anti-CTLA-4	Doxel	• Simultaneous • Sequential – first chemo • Sequential – first ICI	Sequential – first ICI	/
Yan Y. et al. – 2018 (60)	Melanoma	anti-PD-1/L1	Carboplatin + Paclitaxel	• Simultaneous • First ICI followed by simultaneous ICI + chemo	First ICI followed by simultaneous ICI + chemo	/
Coosemans et al. – 2019 (53)	Ovarian cancer	anti-PD-1	Carboplatin + Paclitaxel	• Simultaneous – first ICI followed by ICI + chemo • Simultaneous – first chemo followed by chemo + ICI	Simultaneous – first ICI followed by ICI + chemo	/
Riva et al. – 2020 (61)	High-Grade Glioma	anti-PD-1	Temozolomide	• Simultaneous • Sequential – first chemo • Sequential – first ICI	No difference	/

(ICI, immune checkpoint inhibitor; s.c., subcutaneous; NSG, NOD scid gamma).

although no (immunological) explanation was provided or discussed (54). One other study similarly observed reduced tumor growth when anti-PD-1 was given simultaneously with cisplatin compared to both sequential regimens. Of note, the authors used an immunodeficient mouse model (patient derived xenograft, NOS-SCID gamma mouse) for lung cancer, restricting the reliability of the immune response (55).

Sequential administration of 5-fluorouracil chemotherapy followed by anti-PD-1 appeared to be the best treatment schedule compared to simultaneous administration of both treatments in colorectal cancer. According to this study by Zhao et al., sequential administration of both treatments resulted in increased frequencies of total tumor infiltrated T-cells, as well as the increased expression of PD-L1 on tumor cells. From this, it was suggested that the survival benefit of this combination regimen could be related to the optimal scheduling of the individual immunological effects (56). In accordance to this, another study in colorectal cancer by Fu et al. reported an increased survival when the ICI anti-PD-1/L1 was administered with a specific delay of three days after platin-based chemotherapy compared to simultaneous administration. However, increasing the delay to six days abrogated this beneficial outcome. Subsequent flow cytometric analysis of tumor infiltrating lymphocytes showed an increase of PD-1 positive T cells three days after chemotherapy, followed by a decrease on day seven. This immunological evidence could relate to the narrow window for optimal treatment scheduling (57). In contrast, in a similar s.c. colorectal mouse model, sequential treatment with first anti-PD-L1 followed by oxaliplatin was identified as the most promising treatment regimen compared to both simultaneous treatment or chemotherapy followed by ICI administration (non-significant). This result could be explained by the more pronounced influx of CD8+ T-cells observed in this specific treatment regimen compared to other regimen in this study (58). The discrepancy between the results of the two latter studies could be attributed to the use of different mouse models, MC38 cells in C57BL/6 mice and CT26 cells in Balb/c mice, respectively. As described above, the choice of the preclinical model can influence the immune response and subsequent study outcome.

The sequential schedule in which the ICI was administered prior to chemotherapy, was demonstrated to be superior in two studies performed in orthotopic melanoma mouse models. Both studies showed a rise in CD8+ T-cells with this treatment schedule (59, 60). In the first study, the combination of anti-CTLA-4 followed by Doxil (a liposomal doxorubicin) was superior to both simultaneous and sequential administration in the reverse order (59). Likewise, significant increase in survival was noted in the second melanoma study testing the combination regimen where anti-PD-L1 was administered before carboplatin-paclitaxel compared to simultaneous start of both therapies (60).

It is important to note that in all these research articles, mainly tumor infiltrating effector CD8+ T-cells were evaluated. Analysis of other therapeutically induced immune effects such as influence on the innate immune system or the stimulation of ICD was underrepresented.

As previously mentioned, our group also tested different immune-oncological combination regimens in a syngeneic orthotopic ID8-fLuc ovarian cancer mouse model using a survival analysis. The most beneficial schedule was identified as anti-PD-1 followed by simultaneous carboplatin/paclitaxel chemotherapy. Of note, this combination did not show significant improved survival compared to mice receiving chemotherapy alone. However, inferior results were observed when chemotherapy was started prior to the addition of the ICI therapy (53). Additionally, our group studied different schedules combining (for the first time at the preclinical level) anti-PD-1 with chemotherapy-radiotherapy in an orthotopic high-grade glioma mouse model. However, we did not observe any significant difference, nor in survival, nor in immune composition, between either simultaneous or sequential administration (61).

It is clear from these nine articles (Table 1), although they have some limitations, that the order/sequence of treatments can influence the tumor growth and survival preclinically. On the other hand, clinically tested treatment schedules and doses will always differ from those given to preclinical models due to the large variability in treatment options depending on tumor type and stage of cancer patients, compared to animals. This is an unavoidable limitation due to the inherent biological difference between humans and animals. Nevertheless, the influence on the immune system can be identified and extrapolated. For example, positive preclinical results with CTLA-4 inhibitors in mice and non-human primates resulted in the development of the human monoclonal antibody ipilimumab and the following clinical trial successes (62). Additionally, failing clinical trials using combined anti-PD1 and chemotherapy for the treatment of ovarian cancer such as JAVELIN ovarian 100 could be replicated in preclinical studies in an orthotopic syngeneic ovarian cancer mouse model, showing the potential translatability of rationally designed preclinical research (28, 53). P reclinical research is therefore indispensable to ameliorate the outcome of clinical combination trials, in order to determine the optimal sequence for each immune-oncological combination therapy based on their individual immunological effects (recruitment of immune cells, induction of ICD, etc.) and to provide relevant scientific evidence for designing further clinical trials to increase their success rate.

6 Conclusion

To conclude, even though a large number of clinical trials testing ICI and chemotherapy combinations have been conducted, a majority of these trials produced disappointing results. A lack of rationally designed preclinical research could partially explain why these trials fail to induce synergy between therapies. Here, preclinical research articles testing this immune-oncological combination treatments were reviewed. Together, the articles discussed in this review show the importance of choosing a relevant model for preclinical research in order to increase the translatability and gather evidence for optimizing the clinical trial design, of preclinical research using the correct preclinical models and of preclinical research evaluating different treatment schedules when combining therapies. Most importantly, combination strategies have to take into consideration the different immunological effects and mechanisms of both the specific chemotherapeutic and ICIs. Increasing the investment into detailed preclinical research focused on identifying the optimal therapeutic regimen, could drastically improve the chance for success in subsequent clinical trials.

Author contributions

Study concept by AC. Study design by YB. Data analysis and interpretation by YB and JC. Manuscript preparation by YB. Manuscript review by AC, JC, AV, RW, MR. Final manuscript editing by AC. All authors contributed to the article and approved the submitted version.

Funding

This research was funded by Kom Op Tegen Kanker (Stand up to Cancer), the Flemish cancer society (2019/11955/1 to AC).

Acknowledgments

We thank Prof. Jitka Fucikova (Sotio, Department of immunology, Charles University, Second Faculty of medicine and University Hospital Motol, Prague, Czech Republic) for providing her insight and comments on this review. We also want to express our gratitude to the recently deceased Prof. Dr. Jeffrey W. Pollard (Queen's Medical Research Institute, The University of Edinburgh, UK) for providing us with his valuable advice during the preparation of this manuscript.

Conflict of interest

Author RW was employed by the company Oncoinvent AS.

The remaining authors declare that the research was conducted in the absence of any commercial or financial relationships that could be construed as a potential conflict of interest.

Publisher's note

All claims expressed in this article are solely those of the authors and do not necessarily represent those of their affiliated organizations, or those of the publisher, the editors and the reviewers. Any product that may be evaluated in this article, or claim that may be made by its manufacturer, is not guaranteed or endorsed by the publisher.

Supplementary material

The Supplementary Material for this article can be found online at: https://www.frontiersin.org/articles/10.3389/fimmu.2023.1236965/full#supplementary-material

References

1. Chen DS, Mellman I. Oncology meets immunology: the cancer-immunity cycle. *Immun* (2013) 39(1):1–10. doi: 10.1016/j.immuni.2013.07.012

2. Schreiber RD, Old LJ, Smyth MJ. Cancer immunoediting: integrating immunity's roles in cancer suppression and promotion. *Sci (1979)* (2011) 331(6024):1565–70. doi: 10.1126/science.1203486

3. Barbari C, Fontaine T, Parajuli P, Lamichhane N, Jakubski S, Lamichhane P, et al. Immunotherapies and combination strategies for immuno-oncology. *Int J Mol Sci MDPI AG* (2020) 21:1–28. doi: 10.3390/ijms21145009

4. Vaddepally RK, Kharel P, Pandey R, Garje R, Chandra AB. Review of indications of FDA-approved immune checkpoint inhibitors per NCCN guidelines with the level of evidence. *Cancers* (2020) 12:738. doi: 10.3390/cancers12030738

5. Twomey JD, Zhang B. Cancer immunotherapy update: FDA-approved checkpoint inhibitors and companion diagnostics. *AAPS J Springer Sci Business Media Deutschland GmbH* (2021) 23:39. doi: 10.1208/s12248-021-00574-0

6. Yan Y, Kumar AB, Finnes H, Markovic SN, Park S, Dronca RS, et al. Combining immune checkpoint inhibitors with conventional cancer therapy. *Front Immunol NLM (Medline)* (2018) 9:1739. doi: 10.3389/fimmu.2018.01739

7. Tang J, Shalabi A, Hubbard-Lucey VM. Comprehensive analysis of the clinical immuno-oncology landscape. *Ann Oncol* (2018) 29(1):84–91. doi: 10.1093/annonc/mdx755

8. Upadhaya S, Neftelino ST, Hodge JP, Oliva C, Campbell JR, Yu JX. Combinations take centre stage in PD1/PDL1 inhibitor clinical trials. *Nat Rev Drug Discovery* (2021) 20(3):168–9. doi: 10.1038/d41573-020-00204-y

9. Galluzzi L, Senovilla L, Zitvogel L, Kroemer G. The secret ally: Immunostimulation by anticancer drugs. *Nat Rev Drug Discov* (2012) 11:215–33. doi: 10.1038/nrd3626

10. Zitvogel L, Apetoh L, Ghiringhelli F, Kroemer G. Immunological aspects of cancer chemotherapy. *Nat Rev Immunol* (2008) 8(1):59–73. doi: 10.1038/nri2216

11. Galluzzi L, Buqué A, Kepp O, Zitvogel L, Kroemer G. Immunological effects of conventional chemotherapy and targeted anticancer agents. *Cancer Cell* (2015) 28 (6):690–714. doi: 10.1016/j.ccell.2015.10.012

12. Brown JS, Sundar R, Lopez J. Combining DNA damaging therapeutics with immunotherapy: More haste, less speed. *Br J Cance. Nat Publishing Group* (2018) 118:312–24. doi: 10.1038/bjc.2017.376

13. Vankerckhoven A, Baert T, Riva M, de Bruyn C, Thirion G, Vandenbrande K, et al. Type of chemotherapy has substantial effects on the immune system in ovarian cancer. *Transl Oncol* (2021) 14(6):101076. doi: 10.1016/j.tranon.2021.101076

14. de Bruyn C, Ceusters J, Landolfo C, Baert T, Thirion G, Claes S, et al. Neo-adjuvant chemotherapy reduces, and surgery increases immunosuppression in first-line treatment for ovarian cancer. *Cancers (Basel)* (2021) 13:5899. doi: 10.3390/cancers13235899

15. Galluzzi L, Humeau J, Buqué A, Zitvogel L, Kroemer G. Immunostimulation with chemotherapy in the era of immune checkpoint inhibitors. *Nat Rev Clin Oncol Nat Res* (2020) 17:725–41. doi: 10.1038/s41571-020-0413-z

16. Emens LA, Middleton G. The interplay of immunotherapy and chemotherapy: Harnessing potential synergies. *Cancer Immunol Res* (2015) 3(5):436–43. doi: 10.1158/2326-6066.CIR-15-0064

17. Salas-Benito D, Pérez-Gracia JL, Ponz-Sarvisé M, Rodriguez-Ruiz ME, Martínez-Forero I, Castañón E, et al. Paradigms on immunotherapy combinations with chemotherapy. *Cancer Discovery* (2021) 11(6):1353–67. doi: 10.1158/2159-8290.CD-20-1312

18. Antoniotti C, Rossini D, Pietrantonio F, Catteau A, Salvatore L, Lonardi S, et al. Upfront FOLFOXIRI plus bevacizumab with or without atezolizumab in the treatment of patients with metastatic colorectal cancer (AtezoTRIBE): a multicentre, open-label, randomised, controlled, phase 2 trial. *Lancet Oncol* (2022) 23(7):876–87. doi: 10.1016/S1470-2045(22)00274-1

19. Langer CJ, Gadgeel SM, Borghaei H, Papadimitrakopoulou VA, Patnaik A, Powell SF, et al. Carboplatin and pemetrexed with or without pembrolizumab for advanced, non-squamous non-small-cell lung cancer: a randomised, phase 2 cohort of the open-label KEYNOTE-021 study. *Lancet Oncol* (2016) 17(11):1497–508. doi: 10.1016/S1470-2045(16)30498-3

20. Gandhi L, Rodríguez-Abreu D, Gadgeel S, Esteban E, Felip E, de Angelis F, et al. Pembrolizumab plus chemotherapy in metastatic non–small-cell lung cancer. *New Engl J Med* (2018) 378(22):2078–92. doi: 10.1056/NEJMoa1801005

21. Emens LA, Adams S, Barrios CH, Diéras V, Iwata H, Loi S, et al. First-line atezolizumab plus nab-paclitaxel for unresectable, locally advanced, or metastatic triple-negative breast cancer: IMpassion130 final overall survival analysis. *Ann Oncol* (2021) 32(8):983–93. doi: 10.1016/j.annonc.2021.05.355

22. Schmid P, Cortes J, Pusztai L, McArthur H, Kümmel S, Bergh J, et al. Pembrolizumab for early triple-negative breast cancer. *New Engl J Med* (2020) 382 (9):810–21. doi: 10.1056/NEJMoa1910549

23. Shitara K, van Cutsem E, Bang YJ, Fuchs C, Wyrwicz L, Lee KW, et al. Efficacy and safety of pembrolizumab or pembrolizumab plus chemotherapy vs chemotherapy alone for patients with first-line, advanced gastric cancer. *JAMA Oncol* (2020) 6 (10):1571–80. doi: 10.1001/jamaoncol.2020.3370

24. Powles T, Csőszi T, Özgüroğlu M, Matsubara N, Géczi L, Cheng SYS, et al. Pembrolizumab alone or combined with chemotherapy versus chemotherapy as first-line therapy for advanced urothelial carcinoma (KEYNOTE-361): a randomised, open-label, phase 3 trial. *Lancet Oncol* (2021) 22(7):931–45. doi: 10.1016/S1470-2045(21)00152-2

25. Pujade-Lauraine E, Fujiwara K, Ledermann JA, Oza AM, Kristeleit R, Ray-Coquard IL, et al. Avelumab alone or in combination with chemotherapy versus chemotherapy alone in platinum-resistant or platinum-refractory ovarian cancer (JAVELIN Ovarian 200): an open-label, three-arm, randomised, phase 3 study. *Lancet Oncol* (2021) 22(7):1034–46. doi: 10.1016/S1470-2045(21)00216-3

26. Yonemori K, Matsumoto T, Nagao S, Katsumata N, Oda K, Watari H, et al. Avelumab in platinum-resistant/refractory ovarian cancer (PRROC): phase 3 results from JAVELIN Ovarian 200. *Ann Oncol* (2019) 30(October):vi89. doi: 10.1093/annonc/mdz339.028

27. Monk BJ, Colombo N, Oza AM, Fujiwara K, Birrer MJ, Randall L, et al. Chemotherapy with or without avelumab followed by avelumab maintenance versus chemotherapy alone in patients with previously untreated epithelial ovarian cancer (JAVELIN Ovarian 100): an open-label, randomised, phase 3 trial. *Lancet Oncol* (2021) 22(9):1275–89. doi: 10.1016/S1470-2045(21)00342-9

28. Ledermann JA, Colombo N, Oza AM, Fujiwara K, Birrer MJ, Randall LM, et al. Avelumab in combination with and/or following chemotherapy vs chemotherapy alone in patients with previously untreated epithelial ovarian cancer: Results from the phase 3 javelin ovarian 100 trial. *Gynecol Oncol* (2020) 159:13–4. doi: 10.1016/j.ygyno.2020.06.025

29. Moore KN, Bookman M, Sehouli J, Miller A, Anderson C, Scambia G, et al. Atezolizumab, bevacizumab, and chemotherapy for newly diagnosed stage III or IV ovarian cancer: Placebo-controlled randomized phase III trial (IMagyn050/GOG 3015/ENGOT-OV39). *J Clin Oncol* (2021) 39(17):1842–55. doi: 10.1200/JCO.21.00306

30. Storey J, Gobbetti T, Olzinski A, Berridge BR. A structured approach to optimizing animal model selection for human translation: the animal model quality assessment. *ILAR J* (2021) 62(1–2):66–76. doi: 10.1093/ilar/ilac004

31. Trunova GV, Makarova OV, Diatroptov ME, Bogdanova IM, Mikchailova LP, Abdulaeva SO. Morphofunctional characteristic of the immune system in BALB/c and C57Bl/6 mice. *Bull Exp Biol Med* (2011) 151(1):99–102. doi: 10.1007/s10517-011-1268-1

32. Bleul T, Zhuang X, Hildebrand A, Lange C, Böhringer D, Schlunck G, et al. Different innate immune responses in BALB/c and C57BL/6 strains following corneal transplantation. *J Innate Immun* (2021) 13(1):49–59. doi: 10.1159/000509716

33. Izumchenko E, Paz K, Ciznadija D, Sloma I, Katz A, Vasquez-Dunddel D, et al. Patient-derived xenografts effectively capture responses to oncology therapy in a heterogeneous cohort of patients with solid tumors. *Ann Oncol* (2017) 28(10):2595–605. doi: 10.1093/annonc/mdx416

34. Stribbling SM, Ryan AJ. The cell-line-derived subcutaneous tumor model in preclinical cancer research. *Nat Protoc* (2022) 17(9):2108–28. doi: 10.1038/s41596-022-00709-3

35. Sajjad H, Imtiaz S, Noor T, Siddiqui YH, Sajjad A, Zia M. Cancer models in preclinical research: A chronicle review of advancement in effective cancer research. *Anim Model Exp Med* (2021) 4(2):87–103. doi: 10.1002/ame2.12165

36. Kroemer G, Galluzzi L, Kepp O, Zitvogel L. Immunogenic cell death in cancer therapy. *Annu Rev Immunol* (2013) 31(1):51–72. doi: 10.1146/annurev-immunol-032712-100008

37. Sanmamed MF, Chester C, Melero I, Kohrt H. Defining the optimal murine models to investigate immune checkpoint blockers and their combination with other immunotherapies. *Ann Oncol* (2016) 27(7):1190–8. doi: 10.1093/annonc/mdw041

38. Onaciu A, Munteanu R, Munteanu VC, Gulei D, Raduly L, Feder RI, et al. Spontaneous and induced animal models for cancer research. *Diagnostics* (2020) 10 (9):660. doi: 10.3390/diagnostics10090660

39. Stromnes IM, Hulbert A, Rollins MR, Basom RS, Delrow J, Bonson P, et al. Insufficiency of compound immune checkpoint blockade to overcome engineered T cell exhaustion in pancreatic cancer. *J Immunother Cance.* (2022) 10(2):e003525. doi: 10.1136/jitc-2021-003525

40. Jia Y, Wang Y, Dunmall LSC, Lemoine NR, Wang P, Wang Y. Syrian hamster as an ideal animal model for evaluation of cancer immunotherapy. *Front Immunol* (2023) 14. doi: 10.3389/fimmu.2023.1126969

41. Hundakova A, Leva L, TOman M, Knotek Z. A ferret model of immunosuppression induced with dexamethasone. *Vet Immunol Immunopathol* (2022) 243:110362. doi: 10.1016/j.vetimm.2021.110362

42. Compton Z, Harris V, Mellon W, Rupp S, Mallo D, Kapsetaki SE, et al. Cancer prevalence across vertebrates. *BioRxiv* (2023), 527811. doi: 10.1101/2023.02.15.527881

43. Mestrinho LA, Santos RR. Translational oncotargets for immunotherapy: From pet dogs to humans. *Adv Drug Delivery Rev* (2021) 172:296–313. doi: 10.1016/j.addr.2021.02.020

44. Rossa C, D'Silva NJ. Non-murine models to investigate tumor-immune interactions in head and neck cancer. *Oncogene* (2019) 38(25):4902–14. doi: 10.1038/s41388-019-0776-8

45. Boettcher AN, Schachtschneider KM, Schook LB, Tuggle CK. Swine models for translational oncological research: an evolving landscape and regulatory considerations. *Mamm Genome* (2022) 33(1):230–40. doi: 10.1007/s00335-021-09907-y

46. Gaba RC, Elkhadragy L, Boas FE, Chaki S, Chen HH, El-Kebir M, et al. Development and comprehensive characterization of porcine hepatocellular carcinoma for translational liver cancer investigation. *Oncotarget* (2020) 11 (28):2686–701. doi: 10.18632/oncotarget.27647

47. Miao KZ, Kim GY, Meara GK, Qin X, Feng H. Tipping the scales with zebrafish to understand adaptive tumor immunity. *Front Cell Dev Biol* (2021) 20:9. doi: 10.3389/fcell.2021.660969

48. Majumder B, Baraneedharan U, Thiyagarajan S, Radhakrishnan P, Narasimhan H, Dhandapani M, et al. Predicting clinical response to anticancer drugs using an ex vivo platform that captures tumour heterogeneity. *Nat Commun* (2015) 6(1):6169. doi: 10.1038/ncomms7169

49. Karekla E, Liao WJ, Sharp B, Pugh J, Reid H, Le Quesne J, et al. Ex vivo explant cultures of non–small cell lung carcinoma enable evaluation of primary tumor responses to anticancer therapy. *Cancer Res* (2017) 77(8):2029–39. doi: 10.1158/0008-5472.CAN-16-1121

50. Voabil P, de Bruijn M, Roelofsen LM, Hendriks SH, Brokamp S, van den Braber M, et al. An ex vivo tumor fragment platform to dissect response to PD-1 blockade in cancer. *Nat Med* (2021) 27(7):1250–61. doi: 10.1038/s41591-021-01398-3

51. Lehmann B, Biburger M, Brückner C, Ipsen-Escobedo A, Gordan S, Lehmann C, et al. Tumor location determines tissue-specific recruitment of tumor-associated macrophages and antibody-dependent immunotherapy response. *Sci Immunol* (2017) 2(7):eaah6413. doi: 10.1126/sciimmunol.aah6413

52. Zhao X, Li L, Starr TK, Subramanian S. Tumor location impacts immune response in mouse models of colon cancer. *Oncotarget* (2017) 52:54775–87. doi: 10.18632/oncotarget.18423

53. Coosemans A, Vankerckhoven A, Baert T, Boon L, Ruts H, Riva M, et al. Combining conventional therapy with immunotherapy: A risky business? *Eur J Cancer* (2019) 113:41–4. doi: 10.1016/j.ejca.2019.02.014

54. Lesterhuis WJ, Salmons J, Nowak AK, Rozali EN, Khong A, Dick IM, et al. Synergistic effect of CTLA-4 blockade and cancer chemotherapy in the induction of anti-tumor immunity. *PloS One* (2013) 8(4):e61895. doi: 10.1371/journal.pone.0061895

55. Martín-Ruiz A, Fiuza-Luces C, Martínez-Martínez E, Arias CF, Gutiérrez L, Ramírez M, et al. Effects of anti-PD-1 immunotherapy on tumor regression: insights from a patient-derived xenograft model. *Sci Rep* (2020) 10(1):7078. doi: 10.1038/s41598-020-63796-w

56. Zhao X, Kassaye B, Wangmo D, Lou E, Subramanian S. Chemotherapy but not the tumor draining lymph nodes determine the immunotherapy response in secondary tumors. *iScience* (2020) 23(5):101056. doi: 10.1016/j.isci.2020.101056

57. Fu D, Wu J, Lai J, Liu Y, Zhou L, Chen L, et al. T cell recruitment triggered by optimal dose platinum compounds contributes to the therapeutic efficacy of sequential PD-1 blockade in a mouse model of colon cancer. *Am J Cancer Res* (2020) 10(2):473–90.

58. Golchin S, Alimohammadi R, Rostami Nejad M, Jalali SA. Synergistic antitumor effect of anti-PD-L1 combined with oxaliplatin on a mouse tumor model. *J Cell Physiol* (2019) 234(11):19866–74. doi: 10.1002/jcp.28585

59. Alimohammadi R, Alibeigi R, Nikpoor AR, Chalbatani GM, Jwebster T, Jaafari MR, et al. Encapsulated checkpoint blocker before chemotherapy: The optimal sequence of anti-ctla-4 and doxil combination therapy. *Int J Nanomed* (2020) 15:5279–88. doi: 10.2147/IJN.S260760

60. Yan Y, Cao S, Liu X, Harrington SM, Bindeman WE, Adjei AA, et al. CX3CR1 identifies PD-1 therapy-responsive CD8+ T cells that withstand chemotherapy during cancer chemoimmunotherapy. *JCI Insight* (2018) 3(8):e97828. doi: 10.1172/jci.insight.97828

61. Riva M, Wouters R, Sterpin E, Giovannoni R, Boon L, Himmelreich U, et al. Radiotherapy, temozolomide, and antiprogrammed cell death protein 1 treatments modulate the immune microenvironment in experimental high-grade glioma. *Neurosurgery* (2021) 88(2):E205–15. doi: 10.1093/neuros/nyaa421

62. Rausch MP, Hastings KT. Immune checkpoint inhibitors in the treatment of melanoma: from basic science to clinical application. In: *Cutaneous Melanoma: Etiology and Therapy*. Brisbane (AU): Codon Publications (2017).

frontiers | Frontiers in Immunology

TYPE Original Research
PUBLISHED 15 September 2023
DOI 10.3389/fimmu.2023.1260627

Check for updates

OPEN ACCESS

EDITED BY
Rajan P. Adhikari,
Integrated BioTherapeutics, Inc.,
United States

REVIEWED BY
Scott Kobayashi,
National Institutes of Health (NIH),
United States
Xiaobing Han,
University of Manitoba, Canada

*CORRESPONDENCE
Binh An Diep
binh.diep@ucsf.edu

†These authors have contributed equally to this work

RECEIVED 21 July 2023
ACCEPTED 22 August 2023
PUBLISHED 15 September 2023

CITATION
Nguyen NTQ, Doan TNM, Sato K, Tkaczyk C, Sellman BR and Diep BA (2023) Monoclonal antibodies neutralizing alpha-hemolysin, bicomponent leukocidins, and clumping factor A protected against *Staphylococcus aureus*-induced acute circulatory failure in a mechanically ventilated rabbit model of hyperdynamic septic shock.
Front. Immunol. 14:1260627.
doi: 10.3389/fimmu.2023.1260627

COPYRIGHT
© 2023 Nguyen, Doan, Sato, Tkaczyk, Sellman and Diep. This is an open-access article distributed under the terms of the Creative Commons Attribution License (CC BY). The use, distribution or reproduction in other forums is permitted, provided the original author(s) and the copyright owner(s) are credited and that the original publication in this journal is cited, in accordance with accepted academic practice. No use, distribution or reproduction is permitted which does not comply with these terms.

Monoclonal antibodies neutralizing alpha-hemolysin, bicomponent leukocidins, and clumping factor A protected against *Staphylococcus aureus*-induced acute circulatory failure in a mechanically ventilated rabbit model of hyperdynamic septic shock

Nhu T. Q. Nguyen[1†], Thien N. M. Doan[1†], Kei Sato[1], Christine Tkaczyk[2], Bret R. Sellman[2] and Binh An Diep[1*]

[1]Division of HIV, Infectious Diseases, and Global Medicine, Department of Medicine, University of California, San Francisco, San Francisco, CA, United States, [2]Early Vaccines and Immune Therapies, AstraZeneca, Gaithersburg, MD, United States

Background: Patients with septic shock caused by *Staphylococcus aureus* have mortality rates exceeding 50%, despite appropriate antibiotic therapy. Our objectives were to establish a rabbit model of *S. aureus* septic shock and to determine whether a novel immunotherapy can prevent or halt its natural disease progression.

Methods: Anesthetized rabbits were ventilated with lung-protective low-tidal volume, instrumented for advanced hemodynamic monitoring, and characterized for longitudinal changes in acute myocardial dysfunction by echocardiography and sepsis-associated biomarkers after *S. aureus* intravenous challenge. To demonstrate the potential utility of this hyperdynamic septic shock model for preclinical drug development, rabbits were randomized for prophylaxis with anti-Hla/Luk/ClfA monoclonal antibody combination that neutralizes alpha-hemolysin (Hla), the bicomponent pore-forming leukocidins (Luk) including Panton-Valentine leukocidin, leukocidin ED, and gamma-hemolysin, and clumping factor A (ClfA), or an irrelevant isotype-matched control IgG (c-IgG), and then challenged with *S. aureus*.

Results: Rabbits challenged with *S. aureus*, but not those with saline, developed a hyperdynamic state of septic shock characterized by elevated cardiac output (CO), increased stroke volume (SV) and reduced systemic vascular resistance (SVR), which was followed by a lethal hypodynamic state characterized by rapid decline in mean arterial pressure (MAP), increased central venous pressure, reduced CO, reduced SV, elevated SVR, and reduced left-ventricular ejection

fraction, thereby reproducing the hallmark clinical features of human staphylococcal septic shock. In this model, rabbits pretreated with anti-Hla/Luk/ClfA mAb combination had 69% reduction in mortality when compared to those pretreated with c-IgG (P<0.001). USA300-induced acute circulatory failure—defined as >70% decreased in MAP from pre-infection baseline—occurred in only 20% (2/10) of rabbits pretreated with anti-Hla/Luk/ClfA mAb combination compared to 100% (9/9) of those pretreated with c-IgG. Prophylaxis with anti-Hla/Luk/ClfA mAb combination halted progression to lethal hypodynamic shock, as evidenced by significant protection against the development of hyperlactatemia, hypocapnia, hyperkalemia, leukopenia, neutropenia, monocytopenia, lymphopenia, as well as biomarkers associated with acute myocardial injury.

Conclusion: These results demonstrate the potential utility of a mechanically ventilated rabbit model that reproduced hallmark clinical features of hyperdynamic septic shock and the translational potential of immunotherapy targeting *S. aureus* virulence factors for the prevention of staphylococcal septic shock.

KEYWORDS

***Staphylococcus aureus*, mechanical ventilated rabbit model, hyperdynamic septic shock, neutralizing monoclonal antibodies, alpha-toxin, Panton-Valentine leukocidin, leukocidin, clumping factor A**

Introduction

Centers for Disease Control estimated 119,247 cases of *S. aureus* bacteremia (SAB) occurred in 2017 in United States, with 19,832 (16.6%) associated deaths (1). CDC reported an even higher mortality rate of 55.6% for patients with septic shock (2). Numerous bacterial virulence factors are implicated in animal models as contributing to the pathogenesis of *S. aureus* sepsis, such as surface proteins that facilitate tissue adherence and immune evasion, immunomodulatory proteins and coagulases that alter the inflammatory-coagulation interface, exotoxins that damage immune cells, endothelial cells, as well as different cells of the heart, lungs, liver and kidneys (3–7). Various clinical trials targeting some of these *S. aureus* virulence factors, such as its capsular polysaccharides, iron surface determinant B, manganese transport protein C, or clumping factor A (ClfA), have failed to demonstrate efficacy (8–11).

Results from clinical trials targeting pore-forming toxins by passive immunization with single monoclonal antibodies (mAb) are mixed. Although a cross-reactive mAb, ASN100, that neutralizes alpha-hemolysin (Hla) as well as two-component pore-forming toxins (Luk)—including Panton-Valentine leukocidin F component (LukF), leukocidin D, and gamma-hemolysin B component (HlgB)—protected against lethal challenge with a highly virulent community-associated methicillin-resistant *S. aureus* strain USA300 in mouse and rabbit pneumonia models (12), its phase 2 trial was terminated for futility after a planned interim analysis (13, 14). An anti-Hla mAb, MEDI4893/suvratoxumab, that protected against lethal challenge with USA300 in ferret and mouse pneumonia models but only partial protection in the rabbit pneumonia model showed a modest 31.9% (90% CI, -7.5% to 56.8%) relative risk reduction of pneumonia in a phase 2 clinical trial (15). It now seems imprudent to target only pore-forming toxins when staphylococcal pathogenesis is widely thought to be due to many virulence determinants (3–7).

The present study was undertaken to evaluate prophylactic efficacy of an anti-Hla/Luk/ClfA mAb combination in a newly developed mechanically ventilated rabbit model of USA300-induced septic shock. The anti-Hla/Luk/ClfA mAb combination was shown recently to confer protection in mouse models of surgical site infection (16), a diabetic mouse wound infection model (17), and a rabbit model of prosthetic joint infection (18). Mouse sepsis models are often used for preclinical testing but not used to evaluate efficacy of the anti-Hla/Luk/ClfA mAb combination because mouse polymorphonuclear leukocytes (PMNs) are known to be largely resistant to Panton-Valentine leukocidin and gamma-hemolysin and susceptible only to leukocidin ED (12). In contrast, rabbit and human PMNs were highly sensitive to all these cytotoxins (12, 19, 20), thereby making the rabbit a more suitable species for preclinical efficacy testing of the anti-Hla/Luk/ClfA mAb combination. Also, mouse sepsis models were not useful in predicting clinical efficacy of *S. aureus* conjugate capsular polysaccharides (21) and iron surface determinant B (IsdB) (22–24) vaccines that ultimately failed in phase 3 clinical trials (8, 25). The translational value of mouse sepsis models may be limited by the predominance of a hypodynamic

circulation, which is typically not observed in septic shock patients (26–29). Because septic shock patients who were resuscitated adequately with fluids consistently demonstrated a hyperdynamic circulation with a high cardiac output (CO) and low systemic vascular resistance (SVR) (26–29), the recently published Minimum Quality Threshold in Preclinical Sepsis Studies *guideline* recommended that preclinical sepsis models should administer fluid resuscitation in order to separate sepsis-related events from pathological events resulting solely from progressive circulatory deterioration due to protracted hypovolemia (30). Fluid resuscitation was implemented successfully in non-human primate, canine and mouse Gram-negative sepsis models, which was critical for the development of both hyperdynamic state and myocardial depression seen in human sepsis (31–34). Unfortunately, fluid resuscitation was not implemented in commonly used mouse *S. aureus* sepsis models (21–24), likely because assessment of fluid responsiveness and its impact on sepsis-induced changes in cardiovascular performance require advanced hemodynamic monitoring and/or echocardiography, methods which are not available in most research laboratories.

To develop rabbit models that better predict the human clinical response and support drug regulatory approval, we used funding from the Food and Drug Administration to establish an experimental ICU to perform pathophysiology and preclinical efficacy studies to closely mimic clinical practice (35, 36). We describe here a new preclinical model of hyperdynamic septic shock induced by *S. aureus* in which rabbits are mechanically ventilated, instrumented for advanced hemodynamic monitoring (MAP, central venous pressure, cardiac output, stroke volume, systemic vascular resistance), evaluated for acute myocardial dysfunction by echocardiography, and assessed for changes in sepsis-associated blood biomarkers using real-time point-of-care instruments. In a natural history study, rabbits challenged intravenously with USA300 developed hallmark clinical features of a hyperdynamic state of septic shock that was followed by a short-lived and lethal hypodynamic state in which animals developed global left-ventricular dysfunction and acute circulatory failure. In a prophylactic efficacy study, rabbits pretreated with the anti-Hla/Luk/ClfA mAb combination, but not those pretreated with irrelevant isotype-matched control mAb (c-IgG), were protected against the lethal course of USA300-induced septic shock.

Methods

S. aureus preparation

A minimal-passaged SF8300 clinical strain representative of the epidemic clone USA300-0114 was used to induce lethal septic shock in the mechanically ventilated rabbit model. SF8300 was grown in 10 mL of tryptic soy broth (TSB) media (Sigma-Aldrich) overnight, then diluted 1:50 into 50 mL of TSB media in a 250 mL Erlenmeyer flask. Bacteria were grown at 37°C with shaking at 120 RPM and harvested at an $OD_{600\ nm}$ of 0.4. Cells were washed and resuspended in sterile phosphate-buffered saline (PBS) to a concentration of 1×10^{10} colony-forming units (CFU)/mL, aliquoted into individual cryovials, and immediately stored at -80°C (19). Frozen stocks were titered in triplicate on three separate occasions before use in any experiment. Based on this value, the inoculum containing 9.4 x 10^8 CFUs (in 2.2 mL saline solution) was prepared and again tittered in triplicate to document the numbers of bacterial CFUs used for intravenous challenge of rabbits.

Monoclonal antibodies

Anti-Hla mAb (37), anti-Luk mAb that cross-neutralizes LukF-PV (PVL), LukD (leukocidin ED), HlgB (γ-hemolysin) (16), and anti-ClfA mAb (38) were generated as described previously. An irrelevant isotype-matched control IgG (c-IgG) directed against the gp120 protein of HIV was used as control (37).

Mechanically ventilated rabbit model of USA300-induced septic shock

The rabbit model was reviewed and approved by the University of California San Francisco Institutional Animal Care and Use Committee. Experiments were conducted in a facility certified by the Association for Assessment and Accreditation of Laboratory Animal Care International. New Zealand White rabbits (Western Oregon Rabbit Co.), 3.4 - 4.0 kg, 16 - 20 weeks of age, both male or female rabbits, were sedated by administration of buprenorphine (0.01-0.05 mg/kg) subcutaneously, and then, after 30 minutes, injected intramuscularly with a solution containing 36 mg/kg ketamine and 5.2 mg/kg xylazine. Ophthalmic ointment was placed on each eye. Once the desired depth of anesthesia was achieved as assessed by lack of pedal reflex, a 3.0 mm cuffed endotracheal tube was introduced orally into the trachea. The endotracheal tube was connected to a neonatal ventilatory circuit (Fisher & Paykel), connected to a heated humidifier (Fisher & Paykel) and then a ventilator (ADS2000, Engler) with the following settings: peak inspiratory pressure (PIP) of 12-15 cm H_2O, positive end-expiration pressure (PEEP) of 5 cmH_2O, respiratory rate of 30 breaths/min, flow rate of 4 L/min, fraction of inspired oxygen (FiO_2) of 0.35, and 2.0-2.5% isoflurane to maintain general anesthesia. The ventilator settings remain constant for the duration of the study, except when FiO_2 is increased to 1.0 when performing suctioning for removal of mucus that built up at the distal end of the endotracheal tube. The respiratory rate may be adjusted to maintain PaO_2 between 140 and 200 mmHg and $PaCO_2$ between 35 and 45 mmHg. The left or right marginal ear vein was catheterized with a 22G x 1" IV catheter for continuous infusion of Normosol-R with 5% dextrose (4 mL/kg/h) using an infusion pump (Hospira) for fluid maintenance.

The right carotid artery was catheterized with either 4 French pediatric PiCCO catheter (Getinge) for the natural history study or 18G arterial catheter (Argon Medical Devices) for the efficacy study and positioned approximate 2-3 cm from the common aortic arch, whereas the right internal jugular vein was catheterized with a 4 French dual-lumen pediatric central venous catheter (Medline) and positioned 1-2 cm from the right atrium using a common cutdown

approach as detailed here. The surgical site was shaved, scrubbed, and prepped aseptically. The surgical site was draped out with sterile towels. The rabbit was placed in a supine position and depth of anesthesia was assessed by pinching between the toes. If rabbit was responsive, isoflurane was increased to effect. A 2-3 cm incision was made to access the right carotid artery/internal jugular vein using aseptic technique. Blunt and sharp dissection was used to identify and isolate the carotid artery from the Vagus nerve as well as the internal jugular vein. A distal 3-0 silk ligature was placed around the carotid artery/jugular vein to prevent back bleeding. A loose proximal ligature was placed around the carotid artery/jugular vein. A small (approximately 1 mm) cut was made at an angle across the vessel and the catheter was passed through the cut proximally and advanced about 5 cm so that the catheter tip was positioned approximately 2-3 cm from the common aortic arch or 1-2 cm from the right atrium. The proximal ligature was tied to secure the catheter in place. The vessels were repositioned and the wound was closed in at least 2 layers. The catheters were connected to pressure transducers with integrated flush device (Getinge) and the patient monitor (MP90, Philips Healthcare) for continuous blood pressure monitoring. To maintain patency, the catheters were continuously flushed with 3 ml/h normal saline containing 1U/ml heparin, and manually flushed every 1 h with three quick flushes of normal saline containing 1U/ml heparin.

Once the catheters were in place, the transpulmonary thermodilution method was used to measure cardiac output every 2 h by injecting a bolus of 2-mL cold normal saline through the central venous catheter. A thermistor located at the tip of the PiCCO catheter recorded the very brief drop in the blood temperature for calculation of a thermodilution curve and cardiac output (CO) on the patient monitor (MP90, Philips Healthcare). For each timepoint, CO was measured two times about 3-4 min apart, and then averaged. If the two CO measurements differed >10% from one another, a third CO measurement was performed, and the three measurements averaged. At 6 h after surgery, rabbits were challenged intravenously via the IV catheter placed in the marginal ear vein with a 2.2 ml saline solution containing 9.4 x 10^8 CFUs of USA300.

Echocardiography

Two-dimensional echocardiography was used to assess global left ventricular hypokinesia in the natural history study rabbits. Images were obtained with a cardiac ultrasound machine (iE33, Philips Healthcare) equipped with S12-4 sector array pediatric transducer. We measured the left ventricular and auricular dimensions as well as left ventricular ejection fraction (LVEF) using the parasternal long axis view of the heart via Teicholz method.

Serial blood sampling and analysis

Arterial blood samples were collected at pre-infection baseline (within 1 h of intravenous challenge with USA300), and then every 2 h for the first 24 h post infection (hpi) and every 4 h until the end of the study. Blood gas analysis was determined using RapidPoint 500 (Siemens), including partial pressure of oxygen (PaO_2) and of carbon dioxide ($PaCO_2$), bicarbonate [HCO_3^-]), base excess, sodium (Na^+), potassium (K^+), chloride (Cl^-), calcium (Ca^{++}), glucose, and lactate. The Element HT5 Veterinary Hematology Analyzer© (Heska, Loveland, CO) was used to determine complete blood count with five-part differential. VetScan VS2© (Abaxis, Union City, CA) was used for analysis of alanine aminotransferase (ALT), aspartate aminotransferase (AST), creatinine and blood urea nitrogen.

Microbiology and tissue sample processing

Heart, lung, liver, kidney, and spleen were weighed and processed for bacterial count. For each organ, 3 to 4 pieces (0.05-0.10 grams each) were removed from different parts of the organ, totaling 0.1-0.2 grams, and then homogenized for 30-90 seconds using a Tissue-Tearor (BioSpec, Bartlesville, OK). Each homogenate (100 μL) was then serially diluted in 900 μL of normal saline and 100 μL of each dilution plated onto 5% blood sheep agar and incubated for 16-24 h at 37°C for CFU count.

Statistical analysis

Our hypothesis is that survival of rabbits pretreated with c-IgG is shorter than survival of those pretreated with anti-Hla/Luk/ClfA mAb combination in a rabbit model of USA300-induced septic shock. We calculated that a sample size of 9 animals per experimental group would provide a power of 80% to detect a hazard ratio of 0.25, with a two-sided type I error 0.05 by means of a log-rank test (Schoenfeld method) using STATA version 17.0 (StataCorp). The sample size was increased to 10 animals per experimental group to account for potential exclusion of animals in this model for technical problems related to intubation, surgery for placement of catheter in the carotid artery, or occlusion of endobronchial tube from mucus buildup during mechanical ventilation (35). Survival curves were generated using the Kaplan-Meier method, and significance was assessed by means of the log rank (Mantel-Cox) test. Nonparametric statistics, median [25th percentile – 75th percentile], were computed for all variables. Bacterial count and lung weight/body weight (LW/BW) ratio were compared using a nonparametric two-sided Mann-Whitney U test. Two-sided Fisher's exact test was used to determine whether rabbits pretreated with c-IgG or anti-Hla/Luk/ClfA mAb combination differ in the proportions of categories for the various blood tests (e.g., hypocapnia). Nonparametric one-way analysis of variance (ANOVA) with Kruskal-Wallis test followed by Dunn's multiple comparison test were used to evaluate effect of pretreatment with c-IgG or anti-Hla/Luk/ClfA mAb combination on blood tests conducted at pre-infection baseline or terminal endpoint.

Results

Natural history study revealing a hyperdynamic state of USA300-induced septic shock in mechanically ventilated rabbits

We performed a natural history study to characterize the pathogenesis of USA300-induced septic shock in anesthetized rabbits that were intubated for mechanical ventilation with a lung-protective low-tidal volume (Figure 1A), as previously described (35). Anesthetized rabbits were instrumented with the PiCCO catheter and central venous catheter for advanced hemodynamic monitoring, including intermittent measurement of cardiac output by transpulmonary thermodilution method (Figures 1A, B). Rabbits were infused with a total of 60-65 mL/kg of a balanced crystalloid solution over the course of 6 h preceding *S. aureus* challenge for (*i*) fluid maintenance at 4 mL/kg/h, (*ii*) continuous flushing the arterial and central venous catheters at 3 mL/

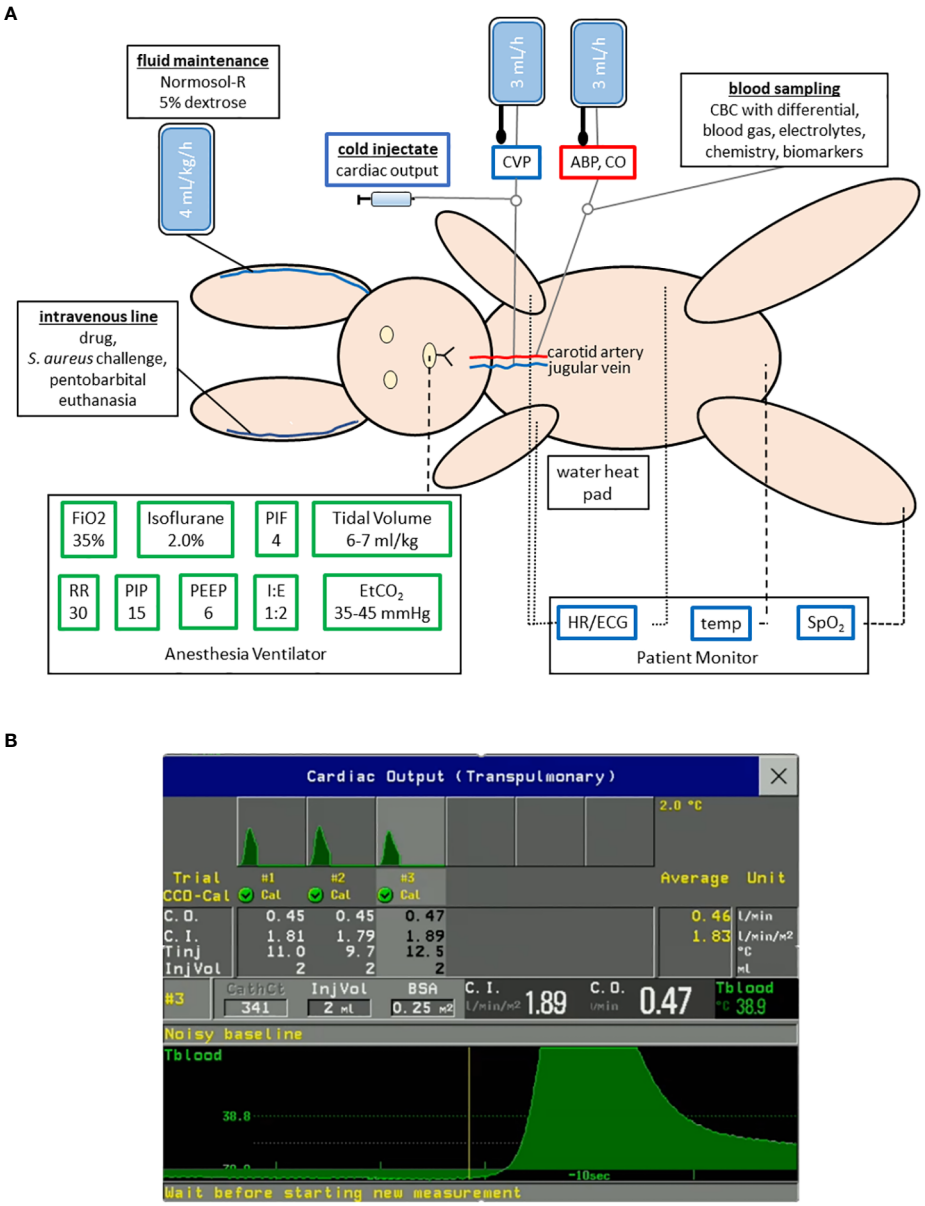

FIGURE 1
Experimental setup for a mechanically ventilated rabbit model of hyperdynamic septic shock with advanced hemodynamic monitoring. **(A)** Rabbits were anesthetized with isoflurane and mechanically ventilated with lung-protective low-tidal volume parameters as shown. A thermodilution catheter placed in the right carotid artery and central venous catheter (CVC) in the right internal jugular vein for continuous measurement of arterial blood pressure (ABP), central venous pressure (CVP), and heart rate (HR), as well as intermittent measurement of cardiac output. **(B)** Changes in blood temperature (Tblood) were measured by transpulmonary thermodilution of cold saline of known volume (InjVol) and temperature (Tinj) that was injected through the CVC and passed through the right heart, the lungs, and the left heart and then detected by the PiCCO catheter placed in the carotid artery. This procedure was repeated 2-3 times within 10 minutes to ensure that an accurate average of the cardiac output (C.O.), which is inversely related to the area under the thermodilution curve, was computed on the cardiac monitor (Philips Intellivue MP90 with PiCCO module).

h each (Figure 1A), and (*iii*) fluid resuscitation at 30 mL/kg to counteract the hypotension associated with overstimulation of Vagus nerve during carotid artery catheterization (35), thereby providing adequate volume repletion that may be crucial for the development of a hyperdynamic state of septic shock after *S. aureus* challenge.

Mortality rate was 100% (6/6) for USA300-challenged rabbits, with acute circulatory failure and death occurring between 15 and 27 h post infection (Figures 2A–F), whereas the two saline-challenged rabbits survived to the end of the study period at 36 h post challenge (Figures 2G, H). The hyperdynamic state of USA300-

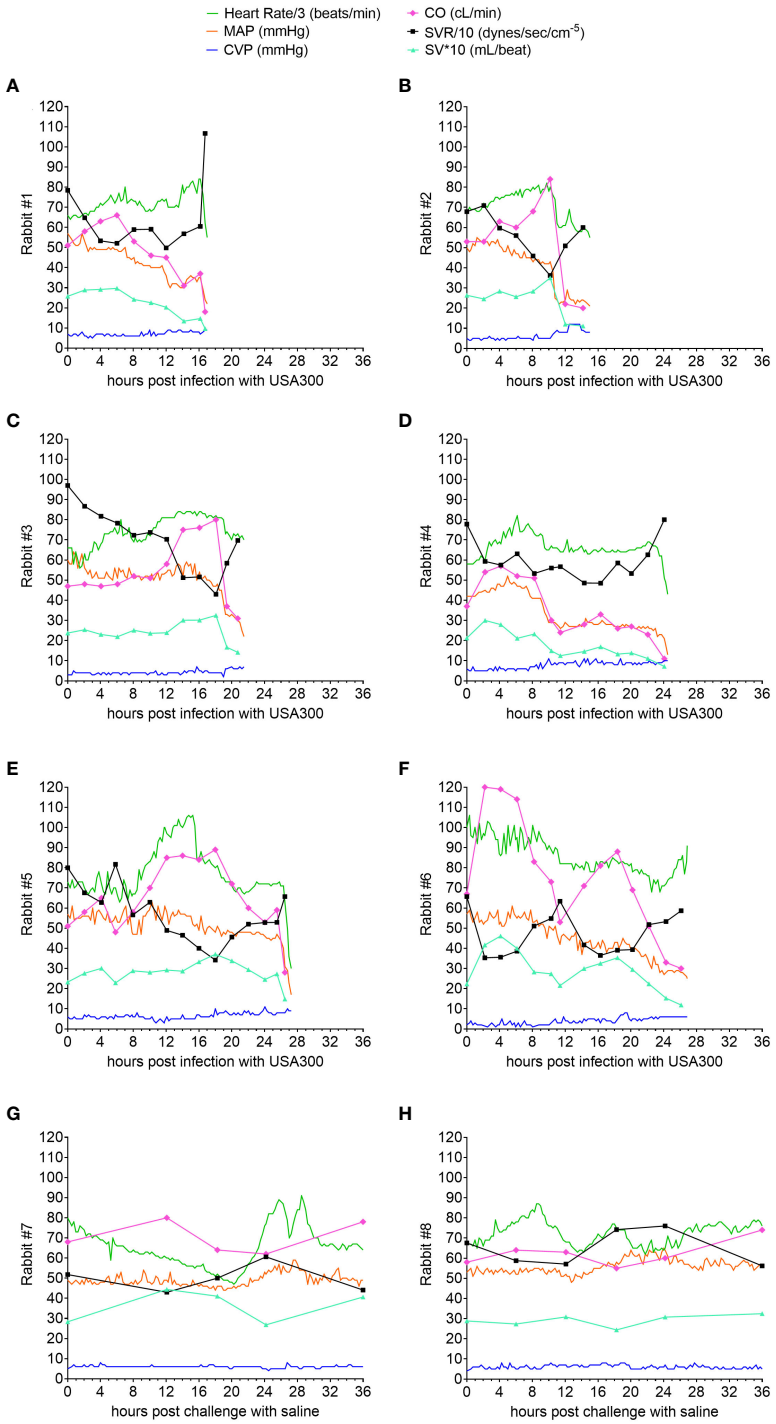

FIGURE 2
Natural history study showing hyperdynamic and hypodynamic states of USA300-induced septic shock in mechanically ventilated rabbits. Advanced hemodynamic monitoring was performed for rabbits challenged with USA300 **(A–F)** or saline **(G, H)**. Heart rate (HR), mean arterial pressure (MAP) and central venous pressure (CVP) were recorded every 15 minutes, whereas cardiac output (CO) was determined intermittently at the time points indicated in each graph. Systemic vascular resistance (SVR) and stroke volume (SV) were computed based on HR, MAP, CVP and CO. Numerical values for HR were divided by 3 and SVR by 10, and SV multiplied by 10 so that they can be displayed with the other parameters using the same scale on the y-axis.

induced septic shock, which was characterized by elevated cardiac output, increased stroke volume, and decreased systemic vascular resistance, occurred early at 2-6 h post infection in five of the rabbits (Figures 2A, B, D–F) or later at 8-18 h post infection in one rabbit (Figure 2C), thereby reproducing the clinical hyperdynamic state with increased heart rate, elevated cardiac output, increased stroke volume, and decreased systemic vascular resistance in adequately volume-resuscitated patients with septic shock (26–29). Then the ensuing hypodynamic state, which was characterized by decreased heart rate, decreased MAP, increased central venous pressure, decreased cardiac output, decreased stroke volume, and elevated systemic vascular resistance, occurred in the 4-6 h period before the rabbits succumbed to USA300-induced septic shock (Figures 2A–F), mimicking the terminal phase in non-survivor patients with hypodynamic shock and death (39). MAP, central venous pressure, cardiac output, stroke volume and systemic vascular resistance remained within normal limits for the two saline-challenged rabbits, consistent with our previous findings that our lung-protective low-tidal volume mechanical ventilation protocol and instrumentation did not negatively impact rabbits without infectious challenge (35).

Acute myocardial dysfunction in rabbits during hypodynamic shock

Transthoracic echocardiography was used in the rabbit natural history study to characterize further potential septic shock-induced acute myocardial dysfunction, including global left ventricular hypokinesia, which occurred in 60% of mechanically ventilated patients with septic shock (40). Representative M-mode echocardiographic tracings for Rabbit #1 (see Figure 2A for corresponding changes in hemodynamic parameters) obtained at pre-infection baseline (Figure 3A), at the early hypodynamic state when MAP decreased 20% from pre-infection baseline value (Figure 3B), and at the late hypodynamic state when MAP decreased >30% from pre-infection baseline value (Figure 3C) illustrated the development of progressive global left ventricular hypokinesia. For all six rabbits with USA300-induced septic shock, left

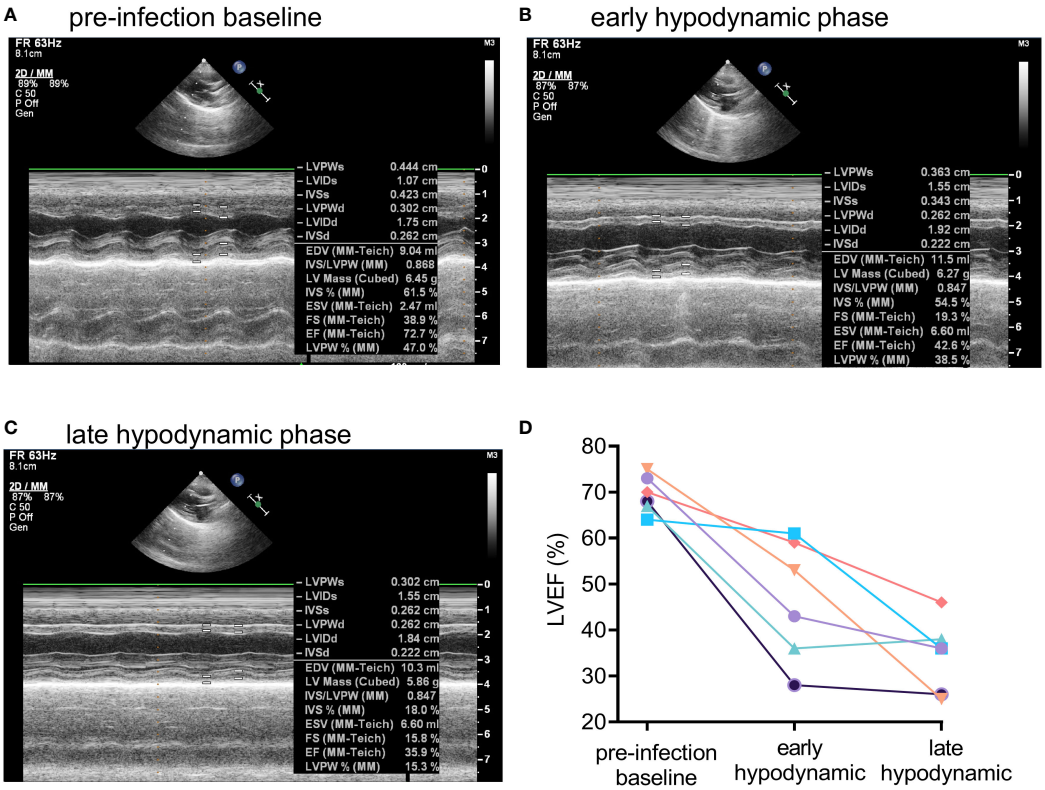

FIGURE 3
Development of global left ventricular dysfunction in early and late hypodynamic states of USA300-induced septic shock. Representative M-mode echocardiographic tracing showing systolic and diastolic left ventricular dimensions in a USA300 WT-infected for Rabbit #1 at **(A)** pre-infection baseline, **(B)** early hypodynamic state when MAP decreased by about 20% from pre-infection baseline, and **(C)** late hypodynamic state in the when MAP was decreased >30% from pre-infection baseline. **(D)** Left ventricular ejection fraction (LVEF) for six rabbits challenged with USA300 declined significantly from pre-infection baseline to the early and then late hypodynamic states (linear test for trend, $P < 0.001$). For two control rabbits challenged with saline, LVEF values were unchanged over time: 67%, 69%, 64% for Rabbit #7, and 64%, 62%, and 62% for Rabbit #8 at pre-infection baseline, 5 h post saline challenge, and 36 h post saline challenge, respectively.

ventricular ejection fraction (LVEF) was 70% (range from 64% to 75%) at pre-infection baseline, and decreased progressively to 47% (28% to 61%) during the early hypodynamic state, and then to 35% (25% - ;46%) during late hypodynamic state (test for linear trend $P<0.001$; Figure 3D).

Prophylactic efficacy of anti-Hla/Luk/ClfA mAb in a rabbit model of USA300-induced septic shock

Rabbits were randomized for intravenous injection with either 30 mg/kg each of the anti-Hla/Luk/ClfA mAb combination or irrelevant isotype-matched c-IgG. After 16-20 h, rabbits were challenged intravenously with the community-associated MRSA USA300, which is known to produce the virulence determinants targeted by our mAb combination: α-hemolysin is neutralized by anti-Hla mAb; F components of the bicomponent toxin LukF-PV (PVL), LukD (leukocidin ED), HlgB (γ-hemolysin) are cross-neutralized by anti-Luk mAb (41); and clumping factor A is neutralized by anti-ClfA mAb. Overall survival rates were 11% (1/9) for rabbits pretreated with c-IgG compared to 80% (8/10) for those pretreated with anti-Hla/Luk/ClfA mAb combination ($P<0.001$ by log-rank test; Figure 4A).

S. aureus quantified in heart and kidney samples showed significant $\log_{10}$CFU reduction ($P<0.001$ and $P=0.043$ by nonparametric Mann-Whitney test), whereas those in lung, spleen, kidney, and liver samples showed non-significant reduction in rabbits pretreated with anti-Hla/Luk/ClfA mAb combination compared to those pretreated with c-IgG (Figure 4B).

Anti-Hla/Luk/ClfA mAb combination protected against acute circulatory failure

Although cardiac output and central venous pressure were measured in the natural history study, these advanced hemodynamic parameters were not measured for the efficacy study of the anti-Hla/Luk/ClfA mAb combination because they are labor intensive, and the more expensive thermodilution and central venous catheters that we used are more prone to thrombotic occlusion due to their narrower tip design, thereby requiring removal and exchange with new catheters in 20-30% of rabbits. Nonetheless, for the efficacy study, we catheterized the right carotid artery for continuous blood pressure monitoring with a similarly sized arterial catheter in which the narrow tip was cut off with a sharp surgical blade, creating a 90° blunt tip which helped reduce the frequency of thrombotic catheter occlusion to <5% of rabbits. Mean arterial pressure (MAP) was recorded every 15 min, providing a high-resolution view of the individual rabbit's hemodynamics (Figures 5A, B). MAP declined sharply in all (9/9) c-IgG-pretreated rabbits in the 2-4 h preceding death (Figure 5A), corresponding to the hypodynamic state of septic shock described above (Figures 2, 3), whereas MAP remained within normal limits for 80% (8/10) of anti-Hla/Luk/ClfA mAb combination-pretreated rabbits that survived to the end of the study at 36 h post infection and declined sharply in only the remaining 20% (2/10) of rabbits that died (Figure 5B). The one survivor pretreated with c-IgG developed severe hypotension at 25 h post infection when MAP decreased to 14 mmHg, but then increased rapidly and remained from 25 to 32 mmHg until the animal was euthanized at 36 h post infection, the end of the study period (Figure 5A). USA300-induced acute circulatory failure, defined as >70% decreased in MAP from pre-infection baseline, occurred in 20% (2/10) of rabbits pretreated with anti-Hla/Luk/ClfA mAb combination compared to 100% (9/9) rabbits pretreated with c-IgG compared to (two-sided Fisher's exact test, $P < 0.001$; see also Figure 5C).

Hypoxemic respiratory failure not a consistent feature of this rabbit model of USA300-induced septic shock

Despite USA300 infecting the lungs of all rabbits (Figure 4B), the lung weight to body weight (LW/BW) ratio in g/kg, a quantitative measure of acute lung injury, was 4.2 [3.8 – 4.9] for

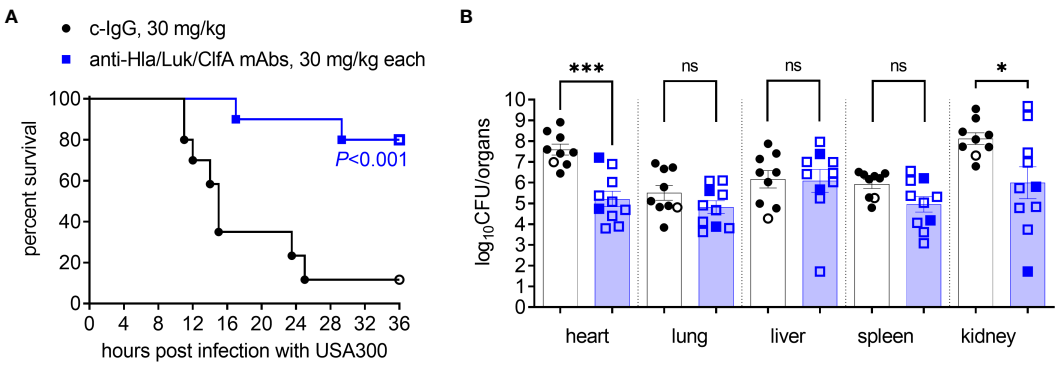

FIGURE 4
Anti-Hla/Luk/ClfA mAb combination improved survival in rabbit model of USA300-induced hyperdynamic septic shock. **(A)** Kaplan-Meier survival curves for rabbits pretreated with indicated mAbs and then challenged intravenously with 9.4 x 10^8 CFUs of USA300. Two-sided Mantel-Cox log-rank test was used to compare survival rates with $P<0.05$ considered statistically significant. **(B)** Bacterial counts of vital organs for rabbits determined at the terminal endpoint when rabbits succumbed to infection (filled symbol) or at the end of the monitoring period 36 h post infection (open symbol). Nonparametric Mann-Whitney U test was used to evaluate differences in bacterial counts in vital organs for animals pretreated with c-IgG vs. anti-Hla/Luk/ClfA antibody. *P*-values ≥0.05 are marked as ns for not significant, * if <0.05, and *** if <0.001.

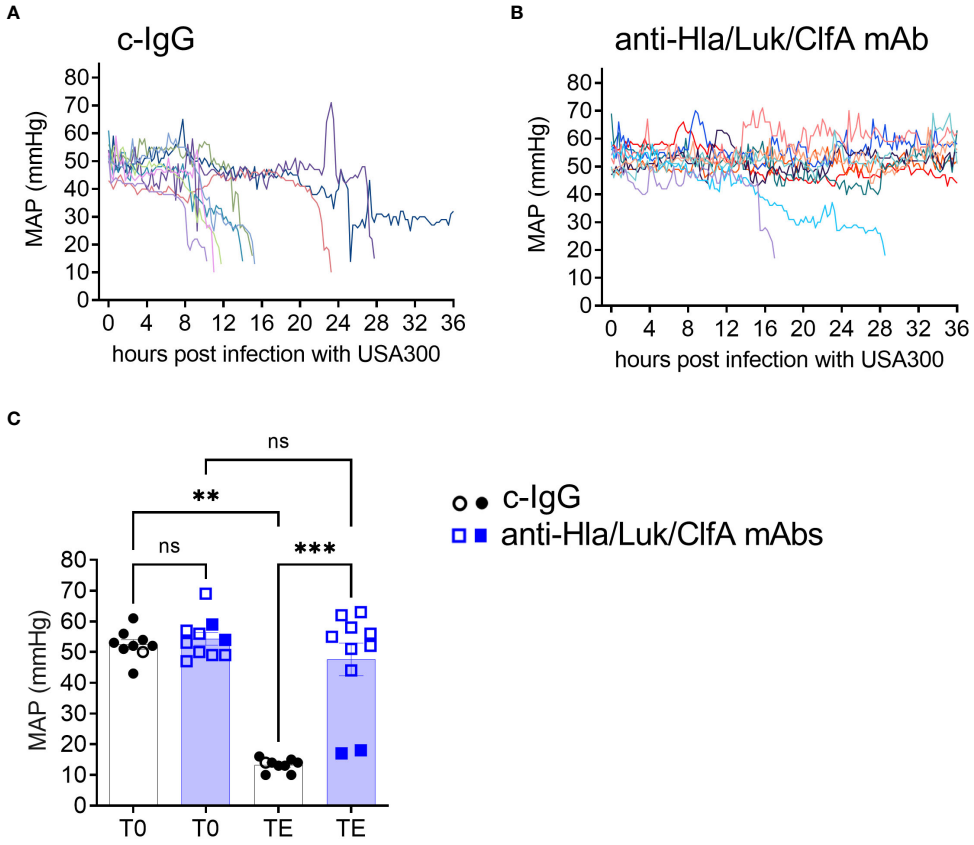

FIGURE 5
Anti-Hla/Luk/ClfA mAb combination, but not c-IgG, protected against acute circulatory failure. Mean arterial pressure (MAP) were recorded every 15 minutes in rabbits pretreated with **(A)** c-IgG or **(B)** anti-Hla/Luk/ClfA mAb combination. **(C)** MAP at pre-infection baseline (T0) or terminal endpoint (TE) for the two experimental groups were compared by nonparametric one-way analysis of variance (ANOVA) with Kruskal-Wallis test followed by Dunn's multiple comparison tests. Data points from rabbits that succumbed to infection are represented by filled symbols, and those euthanized at the end of the monitoring period 36 h post infection by open symbols. *P*-values ≥0.05 are marked as ns for not significant, ** if <0.01, and *** if <0.001.

rabbits pretreated with anti-Hla/Luk/ClfA mAb combination and 3.9 [3.7 - 4.5] for those pretreated with c-IgG (Mann Whitney test, *P*=0.50; Figure 6A), which are similar to the LW/BW ratio of 3.9 for uninfected control rabbits that were managed using the same aforementioned lung-protective ventilatory strategies (35). Accordingly, hypoxemic respiratory failure was not a consistent feature of the rabbit model because the ratio of partial pressure arterial oxygen and fraction of inspired oxygen (PaO_2/FiO_2) decreased to 100 mmHg - 300 mmHg, thresholds for mild to moderate in ARDS severity according to the Berlin definition (42), in only 20% (2/10) and 11% (1/9) of rabbits pretreated with anti-Hla/Luk/ClfA mAb combination or c-IgG, respectively (two-sided Fisher's exact test, *P* = 1.00; Figure 6B).

Temporal changes in peripheral white blood cell populations and survival in rabbits pretreated with anti-Hla/Luk/ClfA mAb combination

To determine whether temporal changes in circulating white blood cell populations are associated with survival of rabbits pretreated with anti-Hla/Luk/ClfA mAb combination or c-IgG, serial blood samples were collected from each rabbit at pre-infection baseline, 2, 4, 6, 8, 10, 12, 14, 16, 18, 20, 22, 24, 28, 32, 36 h post infection or within 1 h of the time when rabbit succumbed to infection for complete blood count with differential. Peripheral white blood cells, including neutrophils and monocytes, declined very rapidly within the first 6 h post infection for all rabbits, but then increased among the 80% (8/10) and 11% (1/9) of rabbits pretreated with anti-Hla/Luk/ClfA mAb combination or c-IgG, respectively, that survived to the end of the study at 36 h post infection (two-sided Fisher's exact test, *P* = 0.006; Figures 7A–F). Among the 8 non-survivors pretreated with c-IgG, those with the steepest decline in white blood cells, neutrophils and monocytes also developed earliest acute circulatory failure and death (Figures 7A, C, E). Lymphocyte counts also declined, but less rapidly compared to the decline of neutrophils and monocytes, in all rabbits from both experimental groups (Figures 7G, H). Compared to rabbits pretreated with c-IgG, those pretreated with anti-Hla/Luk/ClfA mAb combination had significantly greater numbers of white blood cells (4.9 [3.7 - 6.4] vs. 1.4 [0.7 - 2.9] * 10^3/μL, *P*<0.001), neutrophils (2.5 [1.7 - 3.4] vs. 0.7 [0.2 - 1.5] * 10^3/μL, *P*<0.001), monocytes (0.49 [0.29 - 0.56] vs. 0.05 [0.01 - 0.14] *

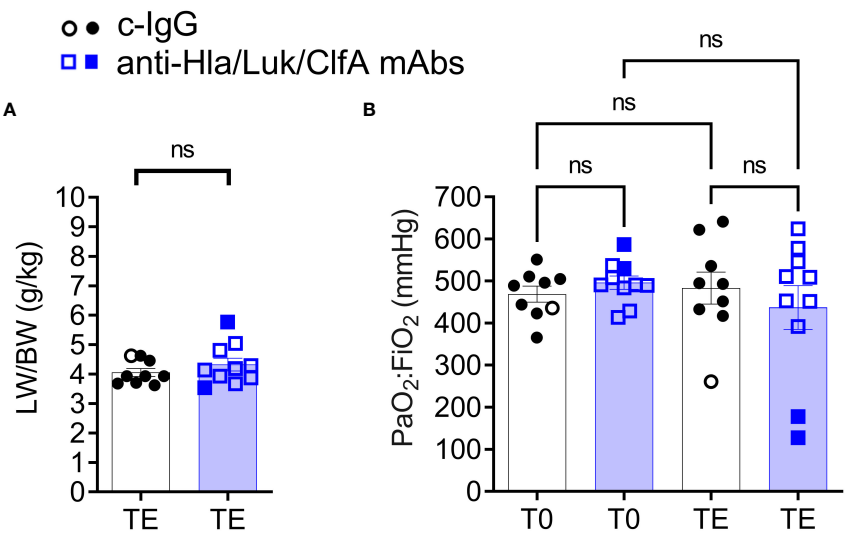

FIGURE 6
Intravenous challenge with USA300 did not cause hypoxemic respiratory failure. **(A)** Lung weight to body weight (LW/BW) ratio determined at pre-infection baseline (T0) or the terminal endpoint (TE) when rabbits succumbed to infection (filled symbol) or at the end of the monitoring period 36 h post infection (open symbol). Nonparametric Mann-Whitney U test was used to evaluate differences in LW/BW pretreated with c-IgG compared to anti-Hla/Luk/ClfA antibody. **(B)** PaO_2:FiO_2 determined at pre-infection baseline (T0) or TE and compared by nonparametric one-way analysis of variance (ANOVA) with Kruskal-Wallis test followed by Dunn's multiple comparison tests. *P*-values ≥0.05 are marked as ns for not significant.

10^3/μL, *P*=0.002), and lymphocytes (1.2 [0.9 - 1.4] vs. 0.4 [0.3 - 0.8] * 10^3/μL, *P*=0.002) at the terminal endpoint (Figures 7A–H).

Differences in biomarkers in rabbits pretreated with anti-Hla/Luk/ClfA mAb combination or c-IgG

Lactate at the terminal endpoint was 1.3 [0.8 - 6.4] mmol/L for rabbits pretreated with anti-Hla/Luk/ClfA mAb combination compared to 13.9 [9.0 - 15.7] mmol/L for those pretreated with c-IgG (multiplicity-adjusted *P*<0.01; Figure 8D). Lactate increased in all (10/10) non-survivors but remained similar to pre-infection baseline for 9/9 survivors from both experimental groups (Figure 8D), consistent with hyperlactatemia being one of the strongest prognostic biomarker of survival in patients with septic shock (43, 44).

Despite no differences at pre-infection baseline, $PaCO_2$ at the terminal endpoint was 35 [29 - 44] mmHg for rabbits pretreated with anti-Hla/Luk/ClfA mAb combination compared to 19 [11 - 27] mmHg for those pretreated with c-IgG (multiplicity-adjusted *P*<0.05; Figure 8A). Severe hypocapnia, defined as $PaCO_2$ < 25 mmHg, occurred in 10% (1/10) of rabbits pretreated with anti-Hla/Luk/ClfA mAb combination compared to 78% (7/9) of those pretreated with c-IgG (two-sided Fisher's exact test, *P* = 0.005). This is consistent with findings in patients with septic shock in which severe hypocapnia was associated with death (45, 46).

pH showed broad changes, ranging from marked acidosis to alkalosis, in rabbits from both experimental groups, and did not correlate with survival or death (Figure 8B). In contrast, bicarbonate decreased to the lowest level in all (10/10) non-survivors compared 0/9 survivors, although differences between the two experimental groups at the terminal endpoint were not statistically significant (Figure 8C).

Glucose also displayed a broad range at the terminal endpoint for rabbits in both experimental groups, with hypoglycemia (<100 mg/dL) occurring in 37% (7/19) and hyperglycemia (>200 mg/dL) in 16% (3/19) of rabbits (Figure 8E). Potassium levels at the terminal endpoint was 3.0 [2.7 - 4.8] mmol/L for rabbits pretreated with anti-Hla/Luk/ClfA mAb combination compared to 7.4 [4.5 - 8.3] mmol/L for those pretreated with c-IgG (multiplicity-adjusted *P*<0.01; Figure 8F). Extreme hyperkalemia (>6.5 mEq/L) occurred in 70% (7/10) of rabbits from both experimental groups that succumbed to USA300-induced septic shock and none (0/9) of the survivors (Figure 8F).

Changes in biomarkers associated with multiple organ dysfunction

Acute myocardial injury biomarkers, including cardiac troponin I, CK-MB, and myoglobin, increased significantly from pre-infection baseline to the terminal endpoint for rabbits pretreated with c-IgG (Figures 9A–C). In contrast, cardiac troponin I, but not CK-MB or myoglobin, increased significantly from pre-infection baseline to the terminal endpoint for rabbits pretreated with anti-Hla/Luk/ClfA mAb combination (Figures 9A–C). When comparing rabbits pretreated with c-IgG or anti-Hla/Luk/ClfA mAb combination at the terminal endpoint, significant differences were noted with cardiac troponin I (multiplicity-adjusted *P*<0.01), but not CK-MB or myoglobin (Figures 9A–C). The aspartate aminotransferase to alanine aminotransferase (AST/

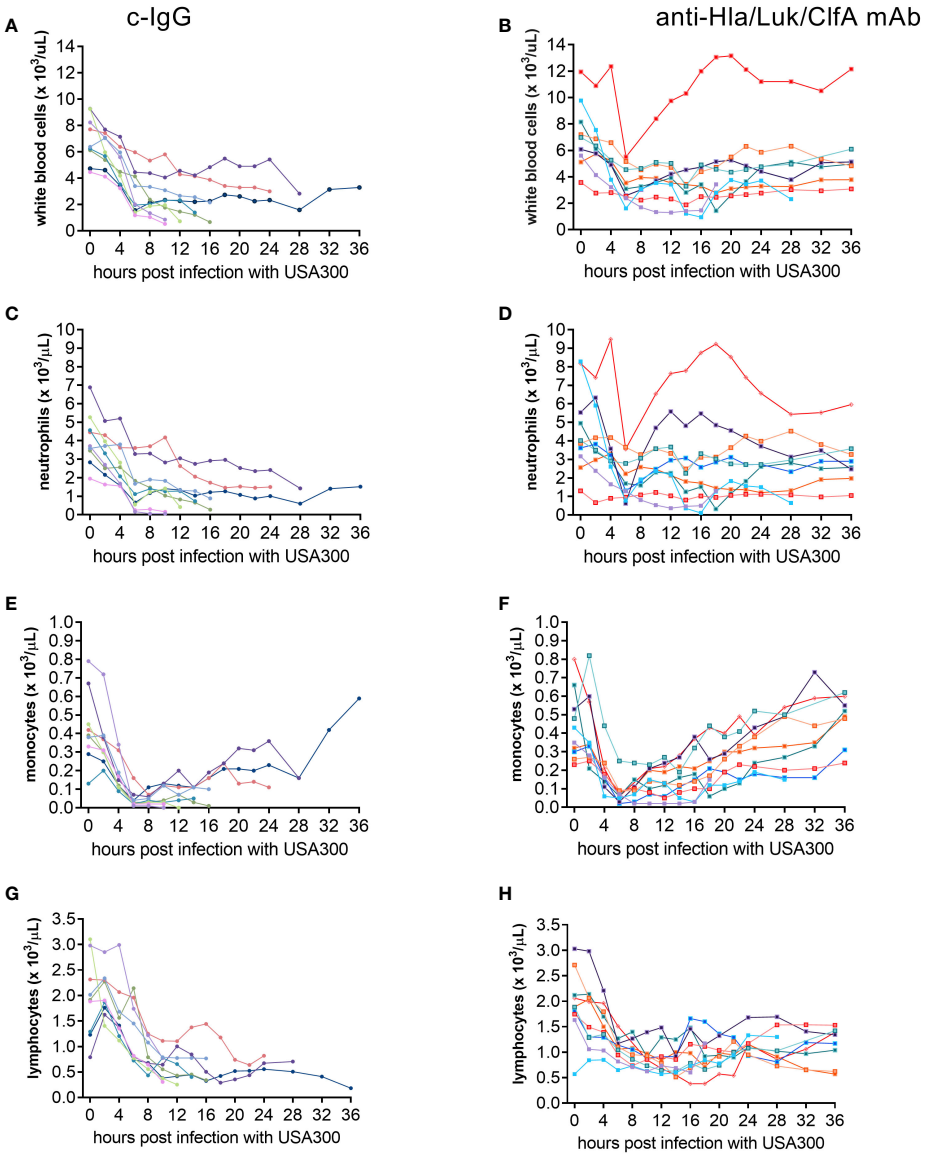

FIGURE 7
Temporal changes in circulating cell populations. Serial blood samples were collected from carotid artery and analyzed on a veterinary hematology analyzer for complete blood count with differential for rabbits pretreated with c-IgG **(A, C, E, G)** or anti-Hla/Luk/ClfA mAb combination **(B, D, F, H)**.

ALT) ratio increased to greater than 5 in 44% (4/9) rabbits pretreated with c-IgG compared to 0% (0/10) for those pretreated with anti-Hla/Luk/ClfA mAb combination (Figure 9D). In the four c-IgG-pretreated rabbits with AST/ALT >5, ALT was only mildly elevated (suggestive of minimal liver necrosis) whereas AST was markedly elevated (suggestive of myocardial necrosis) (47), which is consistent also with their markedly elevated levels of cardiac troponin I, CK-MB, and myoglobin (Figures 9A–C). Creatinine and blood urea nitrogen levels were mildly elevated in only 22% (2/9) and 10% (1/10) of rabbits pretreated with c-IgG and anti-Hla/Luk/ClfA mAb combination (two-sided Fisher's exact test, $P = 0.58$; Figures 9E–F), suggesting minimal impact of USA300-induced septic shock on kidney function.

Discussion

Our new mechanically ventilated rabbit model (Figure 1) reproduced an extended hyperdynamic state of septic shock that was characterized by elevated cardiac output, increased stroke volume, and reduced systemic vascular resistance, which was then followed by a short-lived and lethal hypodynamic state characterized by rapid decline in mean arterial pressure, increased in central venous pressure, reduced cardiac output, reduced stroke volume, elevated systemic vascular resistance (Figure 2), and reduced left-ventricular ejection fraction (Figure 3). The hyperdynamic and hypodynamic states of septic shock observed in this rabbit model closely mimicked the hallmark clinical features

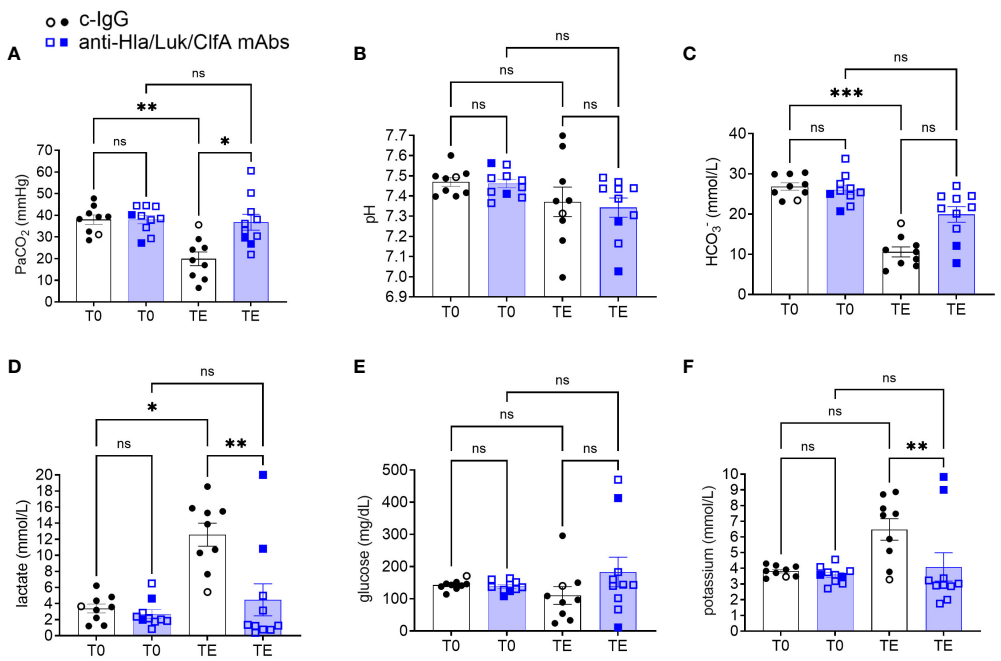

FIGURE 8
Arterial blood gas analysis in rabbits pretreated with anti-Hla/Luk/ClfA mAb combination or c-IgG. **(A)** Partial pressure of arterial carbon dioxide ($PaCO_2$), **(B)** pH, **(C)** HCO_3^-, **(D)** lactate, **(E)** glucose, and **(F)** potassium determined at pre-infection baseline (T0) or the terminal endpoint (TE) within 1 h of when rabbits succumbed to infection or at 36 h post-infection at the end of the study period for rabbits pretreated with anti-Hla/Luk/ClfA mAb combination or c-IgG. Multiplicity adjusted *P*-values were calculated by nonparametric one-way analysis of variance (ANOVA) with Kruskal-Wallis test followed by Dunn's multiple comparison test for the four comparisons indicated in each panel. *P*-values >0.05 are marked with ns for not significant, * for <0.05, ** for <0.01, and *** for <0.001.

of human septic shock (30, 48), which may prove to be critical for using this preclinical animal model as a tool to help predict clinical efficacy of novel anti-staphylococcal drug candidates.

Because the development of a hyperdynamic state in patients with septic shock and in preclinical animal models is dependent on adequate fluid resuscitation (30–34), volume repletion in our rabbit model was implemented by infusion of 60-65 mL/kg of a balanced crystalloid solution over the course of 6 h preceding *S. aureus* challenge (Figure 1A). Our non-aggressive fluid repletion approach allowed for the development of a hyperdynamic state of septic shock as evidenced by the increased stroke volume observed in all (6/6) rabbits as early as 2 h after *S. aureus* challenge (Figures 2A–F), suggesting that adequate volume repletion was administered (49, 50). It should be noted that our goal is to model in rabbits the transition from pre-sepsis to the development of *S. aureus*-induced hyperdynamic septic shock, and, as such, volume repletion in our rabbit model was implemented before infectious challenge to enable the maintenance and increase in stroke volume that occurred shortly after intravenous injection of *S. aureus*. This experimental setup allowed us to then evaluate whether prophylactic administration of anti-Hla/Luk/ClfA mAb combination prevents the development of *S. aureus* hyperdynamic and hypodynamic septic shock in the setting of pre-administration of volume repletion.

We showed here in this new rabbit model of hyperdynamic septic shock that prophylaxis with the anti-Hla/Luk/ClfA mAb combination resulted in a 69% greater survival rate compared to prophylaxis with c-IgG (Figure 4A), and that improved survival was associated with its protection against *S. aureus*-induced acute circulatory failure (Figure 5). The most severe manifestation of acute circulatory failure, aside from sudden death, is septic shock, which can be difficult to characterize in the critically ill patients because of modifying factors such as antibiotic therapy and supportive care (48). In our mechanically ventilated rabbit model, the hallmark clinical features of septic shock are readily recognized in rabbits pretreated with c-IgG. USA300-induced severe hypotension (Figure 5A) was associated with extreme hyperlactatemia (Figure 8D), a biomarker of global tissue hypoxia/hypoperfusion (51) that occurred despite adequate arterial oxygenation (Figure 6B) from our lung-protective low-tidal volume mechanical ventilation strategy. The latter stages of USA300-induced septic shock in the rabbit model were further characterized by hypocapnia (Figure 8A), hyperkalemia (Figure 8F), leukopenia (Figure 7A), neutropenia (Figure 7C), monocytopenia (Figure 7E) and lymphopenia (Figure 7G), which are common components of human septic shock (52, 53). Prophylaxis with anti-Hla/Luk/ClfA mAb combination, however, halted the progression of acute circulatory failure in 80% (8/10) of rabbits (Figure 5B), thereby preventing marked changes to these biomarkers and their grave prognosis. Importantly, the improved survival associated with anti-Hla/Luk/ClfA mAb combination may be due in part to its capacity to reduce growth and survival of USA300 in the heart (Figure 4B) and protect against acute myocardial injury (Figures 9A–C).

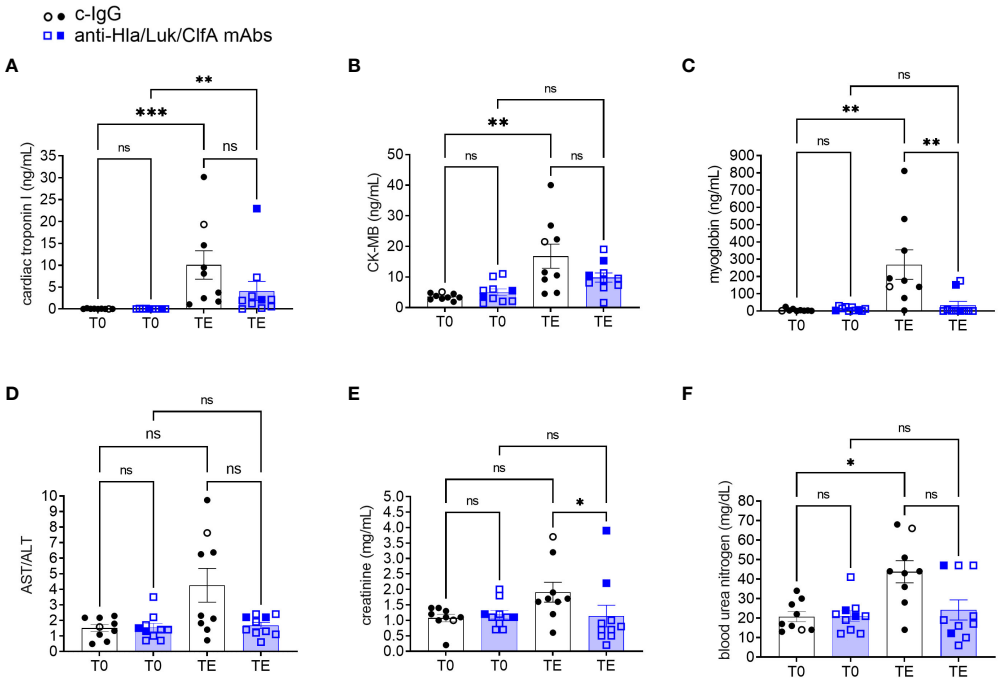

FIGURE 9
Biomarkers of multiple organ dysfunction in rabbits pretreated with anti-Hla/Luk/ClfA mAb combination or c-IgG. **(A)** Cardiac troponin I, **(B)** creatine kinase-MB (CK-MB), **(C)** myoglobin, **(D)** aspartate aminotransferase/alanine aminotransferase (AST/ALT), **(E)** creatinine, and **(F)** blood urea nitrogen determined at pre-infection baseline (T0) or the terminal endpoint (TE) within 1 h of when rabbits succumbed to infection or at 36 h post-infection at the end of the study period for rabbits pretreated with anti-Hla/F/ClfA mAb combination or c-IgG. Multiplicity adjusted *P*-values were calculated by nonparametric one-way analysis of variance (ANOVA) with Kruskal-Wallis test followed by Dunn's multiple comparison test for the four comparisons indicated in each panel. *P*-values >0.05 are marked with ns for not significant, * for <0.05, ** for <0.01, and *** for <0.001.

Our study has limitations. First, our sample size calculation was powered to detect as statistically significant a 60% difference in survival (the primary study outcome), requiring a small sample size of only nine animals per experimental group. As such, our study was not powered for statistical analysis of secondary study outcomes comparing changes in blood biomarkers that also requires accounting for multiple comparisons. Second, we did not determine the individual contributions of each mAb for protection against USA300-induced septic shock in the present study. However, it should be noted that these three mAbs when administered alone or in various combinations had demonstrated efficacy in the other preclinical models, including mouse, ferret and rabbit models of pneumonia (54–56), mouse and rabbit models of dermonecrosis (57, 58), mouse models of surgical site infection (16), a diabetic mouse wound infection model (17), and a rabbit model of prosthetic joint infection (18). Third, only the community-associated MRSA USA300 strain was used in the rabbit model of septic shock for efficacy testing because it expresses all the virulence factors targeted the anti-Hla/Luk/ClfA mAb combination. Future studies would characterize the efficacy of this mAb combination against other clinically relevant MRSA strains, including some hospital-associated MRSA strains that do not express PVL. Fourth, while we demonstrated efficacy of anti-Hla/Luk/ClfA mAb combination for pre-exposure prophylaxis, we did not address its efficacy in post-exposure exposure treatment as an adjunctive therapy to the standard of care, which includes antibiotic, fluid resuscitation and vasopressor that are vital to the management of patients with *S. aureus* septic shock. For future post-exposure treatment studies in the rabbit model, aggressive fluid resuscitation may be triggered at a later time points after *S. aureus* challenge using precise thresholds for acute hemodynamic deterioration (e.g., when MAP decreased >20% from pre-infection baseline), which aligns better with the recommendation in the Surviving Sepsis Campaign guidelines that initial fluid resuscitation begins immediately on diagnosis of sepsis and organ dysfunction (48).

In summary, prophylactic administration of the anti-Hla/Luk/ClfA mAb combination protected against acute circulatory failure and death in a rabbit model of USA300-induced hyperdynamic septic shock. Prognostic biomarkers associated with improved survival in this rabbit model may be useful for designing clinical trials to evaluate efficacy of the anti-Hla/Luk/ClfA mAb combination against *S. aureus* severe sepsis and septic shock.

Data availability statement

The raw data supporting the conclusions of this article will be made available by the authors, without undue reservation.

Ethics statement

The animal study was approved by University of California San Francisco Institutional Animal Care and Use Committee. The study was conducted in accordance with the local legislation and institutional requirements.

Author contributions

NN: Data curation, Formal Analysis, Investigation, Methodology, Writing – review & editing. TD: Data curation, Formal Analysis, Methodology, Investigation, Writing – review & editing. KS: Investigation, Writing – review & editing. CT: Investigation, Writing – review & editing, Methodology, Resources. BS: Resources, Writing – review & editing, Conceptualization, Project administration, Supervision. BD: Conceptualization, Project administration, Resources, Supervision, Writing – review & editing, Data curation, Formal Analysis, Funding acquisition, Investigation, Methodology, Visualization, Writing – original draft.

Funding

The authors declare financial support was received for the research, authorship, and/or publication of this article. Development of the mechanically ventilated rabbit model of septic shock was funded in part by the US Food and Drug Administration contract number HHSF223201710112C to BD. The FDA was not involved in the study design, collection, analysis, interpretation of data, the writing of this article or the decision to submit it for publication. The preclinical efficacy of the monoclonal antibody combination was funded by AstraZeneca.

Conflict of interest

Authors CT and BS are employed by AstraZeneca. The preclinical efficacy testing of anti-Hla/Luk/ClfA mAb combination study was funded by AstraZeneca to BD.

The remaining authors declare that the research was conducted in the absence of any commercial or financial relationships that could be construed as a potential conflict of interest.

This study received funding from AstraZeneca for preclinical efficacy testing of the monoclonal antibody combination in the mechanically ventilated rabbit model of *S. aureus* septic shock. The funder had the following involvement with the study: BS was involved in the study design, and CT prepared and characterized the monoclonal antibody combination.

Publisher's note

All claims expressed in this article are solely those of the authors and do not necessarily represent those of their affiliated organizations, or those of the publisher, the editors and the reviewers. Any product that may be evaluated in this article, or claim that may be made by its manufacturer, is not guaranteed or endorsed by the publisher.

References

1. Kourtis AP, Hatfield K, Baggs J, Mu Y, See I, Epson E, et al. Vital signs: Epidemiology and recent trends in methicillin-resistant and in methicillin-susceptible *staphylococcus aureus* bloodstream infections - United States. *MMWR Morb Mortal Wkly Rep* (2019) 68:214–9. doi: 10.15585/mmwr.mm6809e1

2. Klevens RM, Morrison MA, Nadle J, Petit S, Gershman K, Ray S, et al. Invasive methicillin-resistant *Staphylococcus aureus* infections in the United States. *JAMA* (2007) 298:1763–71. doi: 10.1001/jama.298.15.1763

3. van Hal SJ, Jensen SO, Vaska VL, Espedido BA, Paterson DL, Gosbell IB. Predictors of mortality in *Staphylococcus aureus* Bacteremia. *Clin Microbiol Rev* (2012) 25:362–86. doi: 10.1128/CMR.05022-11

4. Sampedro GR, Bubeck Wardenburg J. *Staphylococcus aureus* in the intensive care unit: Are these golden grapes ripe for a new approach? *J Infect Dis* (2017) 215:S64–70. doi: 10.1093/infdis/jiw581

5. Thomer L, Schneewind O, Missiakas D. Pathogenesis of *Staphylococcus aureus* bloodstream infections. *Annu Rev Pathol* (2016) 11:343–64. doi: 10.1146/annurev-pathol-012615-044351

6. Foster TJ, Geoghegan JA, Ganesh VK, Hook M. Adhesion, invasion and evasion: the many functions of the surface proteins of. *Staphylococcus aureus. Nat Rev Microbiol* (2013) 12:49–62. doi: 10.1038/nrmicro3161

7. Spaan AN, van Strijp JAG, Torres VJ. Leukocidins: staphylococcal bi-component pore-forming toxins find their receptors. *Nat Rev Microbiol* (2017) 15:435–47. doi: 10.1038/nrmicro.2017.27

8. Fowler VG, Allen KB, Moreira ED, Moustafa M, Isgro F, Boucher HW, et al. Effect of an investigational vaccine for preventing *Staphylococcus aureus* infections after cardiothoracic surgery: a randomized trial. *JAMA* (2013) 309:1368–78. doi: 10.1001/jama.2013.3010

9. Fowler VG Jr., Proctor RA. Where does a. *Staphylococcus aureus Vaccine stand? Clin Microbiol Infect* (2014) 20 Suppl 5:66–75. doi: 10.1111/1469-0691.12570

10. Fattom A, Matalon A, Buerkert J, Taylor K, Damaso S, Boutriau D. Efficacy profile of a bivalent *Staphylococcus aureus* glycoconjugated vaccine in adults on hemodialysis: Phase III randomized study. *Hum Vaccin Immunother* (2015) 11:632–41. doi: 10.4161/hv.34414

11. Miller LS, Fowler VG, Shukla SK, Rose WE, Proctor RA. Development of a vaccine against *Staphylococcus aureus* invasive infections: Evidence based on human immunity, genetics and bacterial evasion mechanisms. *FEMS Microbiol Rev* (2020) 44:123–53. doi: 10.1093/femsre/fuz030

12. Diep BA, Le VT, Visram ZC, Rouha H, Stulik L, Dip EC, et al. Improved Protection in a Rabbit Model of Community-Associated Methicillin-Resistant *Staphylococcus aureus* Necrotizing Pneumonia upon Neutralization of Leukocidins in Addition to Alpha-Hemolysin. *Antimicrob Agents Chemother* (2016) 60:6333–40. doi: 10.1128/AAC.01213-16

13. Release AN. *Arsanis provides update following completion of planned interim analysis of phase 2 clinical trial of ASN100* (2018). Available at: http://investors.arsanis.com/news-releases/news-release-details/arsanis-provides-update-following-completion-planned-interim (Accessed 11/15/2019).

14. Miller LS, Fowler VG, Shukla SK, Rose WE, Proctor RA. Development of a vaccine against *Staphylococcus aureus* invasive infections: Evidence-based on human immunity, genetics, and bacterial evasion mechanisms. *FEMS Microbiol Rev* (2020) 44 (1):123–53. doi: 10.1093/femsre/fuz030

15. Francois B, Jafri HS, Chastre J, Sanchez-Garcia M, Eggimann P, Dequin PF, et al. Efficacy and safety of suvratoxumab for prevention of *Staphylococcus aureus* ventilator-associated pneumonia (SAATELLITE): a multicentre, randomised, double-blind,

placebo-controlled, parallel-group, phase 2 pilot trial. *Lancet Infect Dis* (2021) 21:1313–23. doi: 10.1016/S1473-3099(20)30995-6

16. Ortines RV, Wang Y, Liu H, Dikeman DA, Pinsker BL, Miller RJ, et al. Efficacy of a Multimechanistic Monoclonal Antibody Combination against *Staphylococcus aureus* Surgical Site Infections in Mice. *Antimicrob Agents Chemother* (2019) 63(8):e00346–19. doi: 10.1128/AAC.00346-19

17. Tkaczyk C, Jones-Nelson O, Shi YY, Tabor DE, Cheng L, Zhang T, et al. Neutralizing *Staphylococcus aureus* Virulence with AZD6389, a Three mAb Combination, Accelerates Closure of a Diabetic Polymicrobial Wound. *mSphere* (2022) 7:e0013022. doi: 10.1128/msphere.00130-22

18. Mao Y, Valour F, Nguyen NTQ, Doan TMN, Koelkebeck H, Richardson C, et al. Multi-mechanistic monoclonal antibody combination targeting key *Staphylococcus aureus* virulence determinants in a rabbit model of prosthetic joint infection. *Antimicrob Agents Chemother* (2021) 65(7):e0183220. doi: 10.1128/AAC.01832-20

19. Diep BA, Chan L, Tattevin P, Kajikawa O, Martin TR, Basuino L, et al. Polymorphonuclear leukocytes mediate *Staphylococcus aureus* Panton-Valentine leukocidin-induced lung inflammation and injury. *Proc Natl Acad Sci USA* (2010) 107:5587–92. doi: 10.1073/pnas.0912403107

20. Loffler B, Hussain M, Grundmeier M, Bruck M, Holzinger D, Varga G, et al. *Staphylococcus aureus* panton-valentine leukocidin is a very potent cytotoxic factor for human neutrophils. *PLoS Pathog* (2010) 6:e1000715. doi: 10.1371/journal.ppat.1000715

21. Fattom AI, Sarwar J, Ortiz A, Naso RA. *Staphylococcus aureus* capsular polysaccharide (CP) vaccine and CP-specific antibodies protect mice against bacterial challenge. *Infect Immun* (1996) 64:1659–65. doi: 10.1128/iai.64.5.1659-1665.1996

22. Kuklin NA, Clark DJ, Secore S, Cook J, Cope LD, McNeely T, et al. A novel *Staphylococcus aureus* vaccine: iron surface determinant B induces rapid antibody responses in rhesus macaques and specific increased survival in a murine S. *aureus sepsis Model Infect Immun* (2006) 74:2215–23. doi: 10.1128/IAI.74.4.2215-2223.2006

23. Kim HK, DeDent A, Cheng AG, McAdow M, Bagnoli F, Missiakas DM, et al. IsdA and IsdB antibodies protect mice against *Staphylococcus aureus* abscess formation and lethal challenge. *Vaccine* (2010) 28:6382–92. doi: 10.1016/j.vaccine.2010.02.097

24. Joshi A, Pancari G, Cope L, Bowman EP, Cua D, Proctor RA, et al. Immunization with *Staphylococcus aureus* iron regulated surface determinant B (IsdB) confers protection via Th17/IL17 pathway in a murine sepsis model. *Hum Vaccin Immunother* (2012) 8:336–46. doi: 10.4161/hv.18946

25. Shinefield H, Black S, Fattom A, Horwith G, Rasgon S, Ordonez J, et al. Use of a *Staphylococcus aureus* conjugate vaccine in patients receiving hemodialysis. *N Engl J Med* (2002) 346:491–6. doi: 10.1056/NEJMoa011297

26. Wilson RF, Thal AP, Kindling PH, Grifka T, Ackerman E. Hemodynamic measurements in septic shock. *Arch Surg* (1965) 91:121–9. doi: 10.1001/archsurg.1965.01320130123014

27. Abraham E, Bland RD, Cobo JC, Shoemaker WC. Sequential cardiorespiratory patterns associated with outcome in septic shock. *Chest* (1984) 85:75–80. doi: 10.1378/chest.85.1.75

28. Hunter JD, Doddi M. Sepsis and the heart. *Br J Anaesth* (2010) 104:3–11. doi: 10.1093/bja/aep339

29. Merx MW, Weber C. Sepsis and the heart. *Circulation* (2007) 116:793–802. doi: 10.1161/CIRCULATIONAHA.106.678359

30. Hellman J, Bahrami S, Boros M, Chaudry IH, Fritsch G, Gozdzik W, et al. Huber-lang M. Part III: Minimum quality threshold in preclinical sepsis studies (MQTiPSS) for fluid resuscitation and antimicrobial therapy endpoints. *Shock* (2019) 51:33–43. doi: 10.1097/SHK.0000000000001209

31. Hollenberg SM, Dumasius A, Easington C, Colilla SA, Neumann A, Parrillo JE. Characterization of a hyperdynamic murine model of resuscitated sepsis using echocardiography. *Am J Respir Crit Care Med* (2001) 164:891–5. doi: 10.1164/ajrccm.164.5.2010073

32. Zanotti-Cavazzoni SL, Guglielmi M, Parrillo JE, Walker T, Dellinger RP, Hollenberg SM. Fluid resuscitation influences cardiovascular performance and mortality in a murine model of sepsis. *Intensive Care Med* (2009) 35:748–54. doi: 10.1007/s00134-008-1360-9

33. Natanson C, Fink MP, Ballantyne HK, MacVittie TJ, Conklin JJ, Parrillo JE. Gram-negative bacteremia produces both severe systolic and diastolic cardiac dysfunction in a canine model that simulates human septic shock. *J Clin Invest* (1986) 78:259–70. doi: 10.1172/JCI112559

34. Carroll GC, Snyder JV. Hyperdynamic severe intravascular sepsis depends on fluid administration in cynomolgus monkey. *Am J Physiol* (1982) 243:R131–141. doi: 10.1152/ajpregu.1982.243.1.R131

35. Nguyen NTQ, Gras E, Tran ND, Nguyen NNY, Lam HTH, Weiss WJ, et al. *Pseudomonas aeruginosa* ventilator-associated pneumonia rabbit model for preclinical drug development. *Antimicrob Agents Chemother* (2021) 65:e0272420. doi: 10.1128/AAC.02724-20

36. Byrne JM, Waack U, Weinstein EA, Joshi A, Shurland SM, Iarikov D, et al. FDA public workshop summary: Advancing animal models for antibacterial drug development. *Antimicrob Agents Chemother* (2020) 65(1):e01983-20. doi: 10.1128/AAC.01983-20

37. Hua L, Hilliard JJ, Shi Y, Tkaczyk C, Cheng LI, Yu X, et al. Assessment of an anti-alpha-toxin monoclonal antibody for prevention and treatment of *Staphylococcus aureus*-induced pneumonia. *Antimicrobial Agents chemother* (2014) 58:1108–17. doi: 10.1128/AAC.02190-13

38. Tkaczyk C, KasturIrangan S, Minola A, Jones-Nelson O, Gunter V, Shi YY, et al. Multimechanistic monoclonal antibodies (MAbs) targeting *Staphylococcus aureus* alpha-toxin and clumping factor A: Activity and efficacy comparisons of a MAb combination and an engineered bispecific antibody approach. *Antimicrob Agents Chemother* (2017) 61(8):e00629-17. doi: 10.1128/AAC.00629-17

39. Clowes GH Jr., Vucinic M, Weidner MG. Circulatory and metabolic alterations associated with survival or death in peritonitis: clinical analysis of 25 cases. *Ann Surg* (1966) 163:866–85. doi: 10.1097/00000658-196606000-00008

40. Vieillard-Baron A, Caille V, Charron C, Belliard G, Page B, Jardin F. Actual incidence of global left ventricular hypokinesia in adult septic shock. *Crit Care Med* (2008) 36:1701–6. doi: 10.1097/CCM.0b013e318174db05

41. Diep BA, Palazzolo-Ballance AM, Tattevin P, Basuino L, Braughton KR, Whitney AR, et al. Contribution of Panton-Valentine leukocidin in community-associated methicillin-resistant *Staphylococcus aureus* pathogenesis. *PLoS One* (2008) 3:e3198. doi: 10.1371/journal.pone.0003198

42. Force ADT, Ranieri VM, Rubenfeld GD, Thompson BT, Ferguson ND, Caldwell E, et al. Acute respiratory distress syndrome: the Berlin Definition. *JAMA* (2012) 307:2526–33. doi: 10.1001/jama.2012.5669

43. Nguyen HB, Rivers EP, Knoblich BP, Jacobsen G, Muzzin A, Ressler JA, et al. Early lactate clearance is associated with improved outcome in severe sepsis and septic shock. *Crit Care Med* (2004) 32:1637–42. doi: 10.1097/01.CCM.0000132904.35713.A7

44. Blair E. Acid-base balance in bacteremic shock. *Arch Intern Med* (1971) 127:731–9. doi: 10.1001/archinte.1971.00310160209017

45. Blair E. Hypocapnia and gram-negative bacteremic shock. *Am J Surg* (1970) 119:433–9. doi: 10.1016/0002-9610(70)90146-7

46. Mazzara JT, Ayres SM, Grace WJ. Extreme hypocapnia in the critically ill patient. *Am J Med* (1974) 56:450–6. doi: 10.1016/0002-9343(74)90475-6

47. Botros M, Sikaris KA. The de ritis ratio: the test of time. *Clin Biochem Rev* (2013) 34:117–30.

48. Evans L, Rhodes A, Alhazzani W, Antonelli M, Coopersmith CM, French C, et al. Surviving sepsis campaign: international guidelines for management of sepsis and septic shock 2021. *Intensive Care Med* (2021) 47:1181–247. doi: 10.1007/s00134-021-06506-y

49. Marik PE, Cavallazzi R, Vasu T, HIrani A. Dynamic changes in arterial waveform derived variables and fluid responsiveness in mechanically ventilated patients: a systematic review of the literature. *Crit Care Med* (2009) 37:2642–7. doi: 10.1097/CCM.0b013e3181a590da

50. Michard F, Teboul JL. Predicting fluid responsiveness in ICU patients: a critical analysis of the evidence. *Chest* (2002) 121:2000–8. doi: 10.1378/chest.121.6.2000

51. Garcia-Alvarez M, Marik P, Bellomo R. Sepsis-associated hyperlactatemia. *Crit Care* (2014) 18:503. doi: 10.1186/s13054-014-0503-3

52. Farkas JD. The complete blood count to diagnose septic shock. *J Thorac Dis* (2020) 12:S16–21. doi: 10.21037/jtd.2019.12.63

53. Angus DC, van der Poll T. Severe sepsis and septic shock. *N Engl J Med* (2013) 369:840–51. doi: 10.1056/NEJMra1208623

54. Cohen TS, Hilliard JJ, Jones-Nelson O, Keller AE, O'Day T, Tkaczyk C, et al. *Staphylococcus aureus* alpha toxin potentiates opportunistic bacterial lung infections. *Sci Transl Med* (2016) 8:329ra331. doi: 10.1126/scitranslmed.aad9922

55. Diep BA, Hilliard JJ, Le VT, Tkaczyk C, Le HN, Tran VG, et al. Targeting alpha toxin to mitigate its lethal toxicity in ferret and rabbit models of *Staphylococcus aureus* necrotizing pneumonia. *Antimicrob Agents Chemother* (2017) 61(4):e02456-16. doi: 10.1128/AAC.02456-16

56. Vu TTT, Nguyen NTQ, Tran VG, Gras E, Mao Y, Jung DH, et al. Protective efficacy of monoclonal antibodies neutralizing alpha-hemolysin and bicomponent leukocidins in a rabbit model of *Staphylococcus aureus* necrotizing pneumonia. *Antimicrob Agents Chemother* (2020) 64(3):e02220-19. doi: 10.1128/AAC.02220-19

57. Tkaczyk C, Hua L, Varkey R, Shi Y, Dettinger L, Woods R, et al. Identification of anti-alpha toxin monoclonal antibodies that reduce the severity of *Staphylococcus aureus* dermonecrosis and exhibit a correlation between affinity and potency. *Clin Vaccine Immunol* (2012) 19:377–85. doi: 10.1128/CVI.05589-11

58. Le VT, Tkaczyk C, Chau S, Rao RL, Dip EC, Pereira-Franchi EP, et al. Critical role of alpha-toxin and protective effects of its neutralization by a human antibody in acute bacterial skin and skin structure infections. *Antimicrob Agents Chemother* (2016) 60:5640–8. doi: 10.1128/AAC.00710-16

frontiers | Frontiers in Immunology

TYPE Original Research
PUBLISHED 18 October 2023
DOI 10.3389/fimmu.2023.1258291

Check for updates

OPEN ACCESS

EDITED BY
Rajan P. Adhikari,
Integrated BioTherapeutics, Inc.,
United States

REVIEWED BY
Jake ODonnell,
The University of Queensland, Australia
Alyssa Joy Cozzo,
University of North Carolina at Chapel Hill,
United States
Delia Jane Nelson,
Curtin University, Australia

*CORRESPONDENCE
Suzanne I. Sitnikova
suzanne.sitnikova@astrazeneca.com

RECEIVED 13 July 2023
ACCEPTED 27 September 2023
PUBLISHED 18 October 2023

CITATION
Sitnikova SI, Walker JA, Prickett LB, Morrow M, Valge-Archer VE, Robinson MJ, Wilkinson RW and Dovedi SJ (2023) Age-induced changes in anti-tumor immunity alter the tumor immune infiltrate and impact response to immuno-oncology treatments. *Front. Immunol.* 14:1258291. doi: 10.3389/fimmu.2023.1258291

COPYRIGHT
© 2023 Sitnikova, Walker, Prickett, Morrow, Valge-Archer, Robinson, Wilkinson and Dovedi. This is an open-access article distributed under the terms of the Creative Commons Attribution License (CC BY). The use, distribution or reproduction in other forums is permitted, provided the original author(s) and the copyright owner(s) are credited and that the original publication in this journal is cited, in accordance with accepted academic practice. No use, distribution or reproduction is permitted which does not comply with these terms.

Age-induced changes in anti-tumor immunity alter the tumor immune infiltrate and impact response to immuno-oncology treatments

Suzanne I. Sitnikova[1]*, Jennifer A. Walker[1], Laura B. Prickett[2], Michelle Morrow[1], Viia E. Valge-Archer[1], Matthew J. Robinson[1], Robert W. Wilkinson[1] and Simon J. Dovedi[1]

[1]Early Oncology Discovery, R&D, AstraZeneca, Cambridge, United Kingdom, [2]Early Oncology Bioscience, Research & Development (R&D), AstraZeneca, Waltham, MA, United States

Introduction: Immuno-oncology (IO) research relies heavily on murine syngeneic tumor models. However, whilst the average age for a cancer diagnosis is 60 years or older, for practical purposes the majority of preclinical studies are conducted in young mice, despite the fact that ageing has been shown to have a significant impact on the immune response.

Methods: Using aged (60-72 weeks old) mice bearing CT26 tumors, we investigated the impact of ageing on tumor growth as well as the immune composition of the tumor and peripheral lymphoid organs.

Results: We found many differences in the immune cell composition of both the tumor and tumor-draining lymph node between aged and young mice, such as a reduction in the naïve T cell population and a decreased intratumoral CD8/Treg ratio in aged animals. We hypothesized that these differences may contribute to impaired anti-cancer immune responses in aged mice and therefore assessed the anti-tumor efficacy of different IO therapies in aged mice, including both co-stimulation (using an anti-OX40 antibody) and immune checkpoint blockade (using anti-PD-L1 and anti-CTLA-4 antibodies). Whilst aged mice retained the capacity to generate anti-tumor immune responses, these were significantly attenuated when compared to the responses observed in young mice.

Discussion: These differences highlight the importance of age-related immunological changes in assessing and refining the translational insights gained from preclinical mouse models.

KEYWORDS

age, immunotherapy, CT26, OX40, PD-L1, CTLA-4

Introduction

Over half of cancers arise in individuals over the age of 60 (1) and yet the majority of preclinical studies are undertaken in comparatively young mice, typically 6-8 weeks old. These murine models are invaluable for evaluating the fundamental biology of a particular target or for delineating the mechanism of action of candidate drugs. However, these preclinical models frequently overpredict efficacy and have so far proven to be of limited predictive value to the clinical setting (2). This may be partly due to their failure to recapitulate many of the age-induced changes that impact the immune system and therefore potentially the tumor microenvironment (TME) and the efficacy of cancer immunotherapy in patients (2).

Indeed, ageing is accompanied by a progressive deterioration of the immune system, frequently termed immunosenescence, which is the result of changes intrinsic to the hematopoietic system coupled with age-associated perturbations to peripheral tissues and secondary lymphoid organs (3, 4). A principal contributor to this process is thymic involution, which drives a decline in thymic output and a greater reliance upon cytokine and (self-) antigen-driven homeostatic proliferation to maintain the peripheral T cell pool (5). Over the lifetime of an individual, this reliance upon tonic stimulation can profoundly alter the T cell repertoire, favoring the development of memory T cell populations over the naïve T cell pool (6). The numerical decline in cells of the aged immune system is compounded by age-related inflammatory processes that occur within peripheral tissues, often collectively termed 'inflamm-aging' (7). These changes promote immune cell dysfunction and increased activity of suppressive immune cell subsets, such as regulatory T cells (Treg) and myeloid-derived suppressor cells (MDSCs) (8). Thus, in ageing patients these various contributors to immunosenescence and altered tissue microenvironments have a significant potential to impact anti-tumor immunity and the efficacy of cancer immunotherapy. Nevertheless, this is not modelled in preclinical studies carried out in 6-8 week old mice which, according to correlations between mouse age and human age, represent roughly the equivalent of a teenage human (9). We therefore conducted studies to evaluate the impact of age on the anti-tumor immune response and the outcome of IO therapies to assess whether recapitulating this patient characteristic in preclinical mouse models could increase their predictive value.

Materials and methods

Animals

Female BALB/c mice were supplied by Charles River UK at 6 to 8 weeks of age (young) or 60 to 72 weeks of age (aged). These mice were aged at Charles River UK specifically for the purpose of these studies and housing conditions were kept the same as for young mice. Mice were housed under specific pathogen-free conditions in Tecniplast Green Line Sealsafe Individually Ventilated Cages (IVC) changed weekly and holding a maximum of 6 animals with irradiated aspen chip bedding, Nestlets nesting material, a tunnel and wooden chew blocks. Mice were housed on a 12/12 light/dark cycle, at 20-24°C and 45-65% humidity with *ad libitum* UV-treated water and RM1 rodent diet (SAFE). Mice underwent a minimum of 5 days of acclimatization after arrival in the animal facility before study initiation.

Tumor model and monitoring

The murine colon carcinoma cell line CT26 was obtained from ATCC and maintained in RPMI 1640 media supplemented with 10% FBS. It did not undergo any *in vivo* passaging and was maintained under limited passage from original stocks (typically under 5). It was reauthenticated using STR-based DNA profiling and multiplex polymerase chain reaction and tested for murine viruses and mycoplasma (IDEXX Bioresearch). For implantation, mice were shaved on the right flank and subcutaneously injected with 5 x 10^5 CT26 cells in 100 µL PBS. Tumor volume was measured 3 times per week using electronic callipers and calculated using the formula ($width^2 \times length$)/2. Mice were euthanized when they reached humane welfare limits pertaining to tumor volume (average diameter of 15mm) or tumor condition (ulceration of the skin above the tumor). Tumor growth rate was calculated as previously described (10) by fitting the tumor growth curve of each animal to the exponential model log10(tumor volume) = a + b * time + error, where a and b are parameters that correspond to the log initial volume and growth rate, respectively.

Experimental design

Mice were randomized to minimize differences in body weight and treated with either anti-mouse PD-L1 antibody mIgG1 D265A (AstraZeneca) intraperitoneally (IP) at 10 mg/kg twice weekly starting 4 days after tumor cell implantation for a total of 6 doses and/or anti-mouse CTLA-4 antibody (clone 9D9) mIgG1 (AstraZeneca) IP at 10 mg/kg twice weekly starting 7 days after tumor cell implantation for a total of 6 doses or anti-mouse OX40 antibody (clone OX86) mIgG2a (AstraZeneca) IP at 1 mg/kg 4 and 7 days after tumor cell implantation. Group sizes were determined using power analyses based on the variability of the tumor model in pilot studies.

Flow cytometric analysis

Tumors were disaggregated using the gentleMACS™ Mouse Tumor Dissociation kit (Miltenyi Biotec). Tumor-draining lymph nodes (or matching inguinal lymph nodes in non-tumor bearing mice) were dissociated through a 70 µm nylon cell strainer. Cells were stained with a fixable viability dye (Thermo Fisher) and blocked with antibodies against murine CD16/CD32 (eBioscience) before staining with fluorescence-conjugated antibodies (Supplementary Table S1) in flow cytometry staining buffer with Brilliant Stain Buffer (BD Biosciences). Intracellular staining was performed using the FoxP3/Transcription Factor Staining Buffer Set

(eBioscience) and cells were fixed in 3.7% formaldehyde. Counting beads (123Count eBeads; eBioscience) were added to the samples before acquisition on a BD LSRFortessa flow cytometer (BD Biosciences). Panel-specific FMO controls and single color controls were prepared for each experiment. Analysis was carried out using FlowJo (BD Biosciences). As an adjunct to conventional gating, for tumor samples the data was quality controlled using the flowAI plugin in FlowJo followed by T-distributed stochastic neighbor embedding (optSNE) dimensionality reduction and FlowSOM clustering analysis.

Statistical methods

For time-to-endpoint analysis, groups were compared using a log-rank test in GraphPad Prism. Fold changes in tumor growth rates were compared using unpaired Mann-Whitney testing in GraphPad Prism. Cell populations and growth rates were compared using either two-way ANOVA with Sidak's multiple comparisons testing or unpaired Mann-Whitney testing in GraphPad Prism.

Results

Peripheral immune changes in response to tumor growth are observed in aged mice

In this study, we sought to investigate the impact of age on the CT26 mouse syngeneic flank tumor model, which is a commonly-used preclinical model for assessment of novel anti-tumor therapies. To determine whether the characteristics of this model would be affected by age, we implanted CT26 tumor cells simultaneously in both aged (60-72 weeks of age) and young (6-8 weeks of age) female BALB/c mice. Correlations between mouse and human age suggest that this would correspond to 50-70 year-old and 15 year-old patients, respectively (9), and we confirmed that several hallmarks of ageing were observed in these mice at 60-72 weeks of age, such as thymic involution and increased adiposity (Supplementary Figure 1) (11, 12).

Given the known impact of age on the immune system, we first sought to determine whether aged animals were able to respond to the presence of a tumor by evaluating the changes triggered in the inguinal lymph node (the lymph node closest to the site of flank tumor implantation) after the addition of a tumor. We observed similar changes triggered in response to the tumor in both aged and young mice, namely a decrease in the frequency of $CD4^+$ T cells and an increase in the frequency of B cells (Figure 1A), with the latter being a phenomenon previously described after the implantation of tumor cells (13).

Despite this similar response to the presence of a tumor, we found that the immune composition of the tumor-draining lymph node was still markedly different between young and aged mice, with a reduced frequency of both $CD4^+$ and $CD8^+$ T cells and an increased frequency of B cells in the aged cohort (Figure 1B). Similar differences were also seen in the lymph nodes of non-tumor bearing mice (Figure 1C) and in the spleens of aged mice, irrespective of tumor presence (Supplementary Figures 2A, B), suggesting that these differences are mainly driven by baseline differences in the immune status between young and aged mice, rather than a difference in the response elicited by the tumor. We also further analyzed the phenotype of $CD4^+$ T cells and found that, consistent with known changes in immune homeostasis with ageing (3), the proportion of naïve T cells was significantly decreased in the inguinal lymph nodes (Figure 1D) and spleens (Supplementary Figures 2C, D) of aged mice. This decrease was also observed in tumor-draining lymph nodes, as well as increases in the central memory subset in the aged mice (Figure 1E). Taken together these findings suggest that the immune system of aged mice is able to respond to the presence of a tumor but that this response does not restore their immune phenotype to that seen in young mice, suggesting a potential for differential responses to immunotherapy in aged animals.

The tumor immune infiltrate is significantly altered in aged mice

Having observed a similar immune response elicited by the tumor despite baseline differences in the immune compartment of the aged mice compared to young mice, we next assessed whether age would impact the tumor immune cell infiltrate. We found that aged mice implanted with CT26 tumors reached welfare endpoints (a function of both tumor volume and tumor condition) faster than the young mice, with a median time-to-endpoint of 20 days for the aged mice versus 23 days for the young mice (Figure 2A, $p=0.0004$). However, analysis of the tumor growth rates of individual animals across 4 independent experiments revealed no consistent difference in the kinetics of tumor growth between aged and young mice (Figure 2B, Supplementary Figure 3). The CT26 tumor model is prone to develop ulceration of the skin above the tumor, which can lead to sacrifice of the animal for welfare reasons. We found that the proportion of animals being sacrificed due to skin ulceration at tumor volumes under $500mm^3$ was higher in aged mice compared to young mice (25% versus 15%, respectively; data not shown), suggesting that the difference detected in the time-to-endpoint analysis is driven by differences in tumor condition rather than tumor volume.

Having determined that CT26 tumors grew similarly in aged and young mice, we next assessed the impact of age on the immune cell composition of the tumors. Flow cytometric analysis of tumor-infiltrating immune cells revealed a significant decrease in the size of the $CD45^+$ immune cell infiltrate (expressed as the absolute cell count per mm^3 of tumor) in aged mice (Figure 2C, $p=0.0034$). Unsupervised clustering analysis then enabled the detection and quantification of several lymphoid (Figure 2D) and myeloid (Figure 2E) cell subsets within the TME (Supplementary Figure 4). Significant differences were observed with tumors in the aged mice containing fewer NK cells, $PD1^+$ $CD8^+$ T cells and monocytic cells (all $p<0.05$) as well as increased macrophages ($p<0.0001$) and a trend to increased Treg ($p=0.0557$) (Figure 2F). Altogether these changes in the tumor-infiltrating immune cell

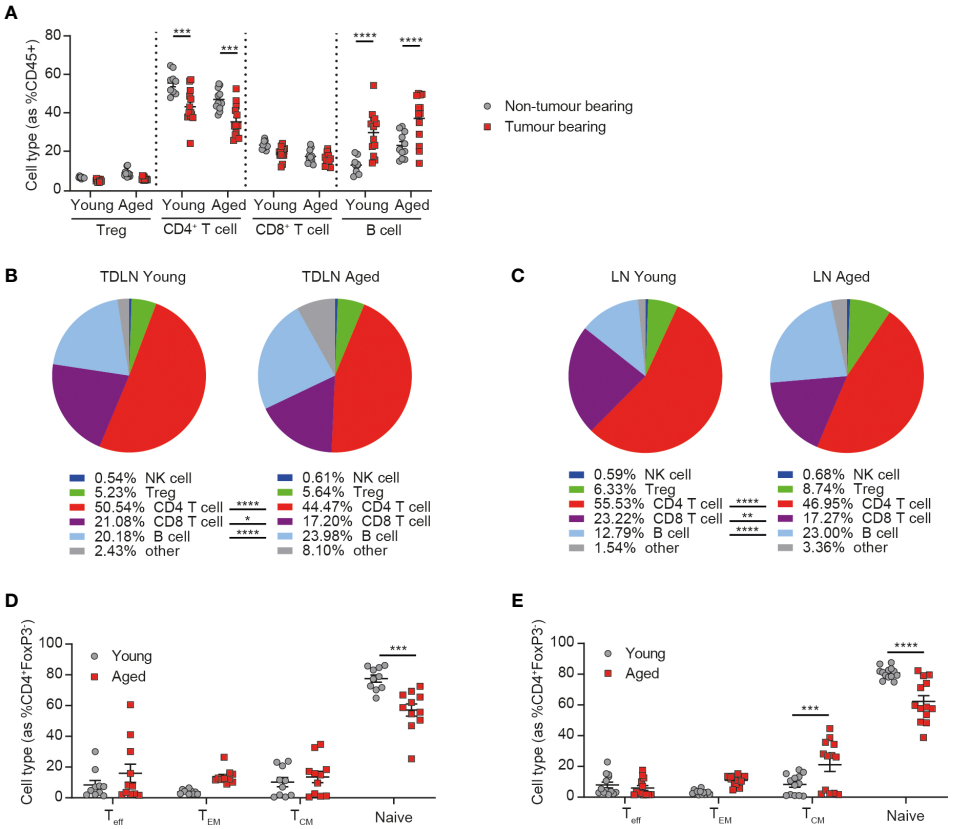

FIGURE 1
Peripheral immune changes in response to tumor growth are observed in aged mice. Inguinal lymph nodes from female BALB/c mice either at 6-8 weeks old (young) or at 60-72 weeks old (aged) were sampled in the absence or presence of CT26 tumor cells subcutaneously implanted on the flank 15-17 days prior. **(A)** Immune cell subsets within inguinal lymph nodes of tumor-bearing mice compared to non-tumor bearing mice in both young and aged mice. 5-8 mice per group. **(B)** Comparison of the immune cell subsets within inguinal tumor-draining lymph nodes (TDLN) of young (left) and aged (right) mice bearing CT26 flank tumors. 18-19 mice per group. **(C)** Comparison of the immune cell subsets within inguinal lymph nodes of young (left) and aged (right) mice in the absence of a tumor. 9-11 mice per group. **(D, E)** Frequency of $CD44^-CD62L^-$ effector (T_{eff}), $CD44^+CD62L^-$ effector memory (T_{EM}), $CD44^+CD62L^+$ central memory (T_{CM}) and $CD44^-CD62L^+$ naïve cell subsets within the $CD4^+$ T cell compartment in the inguinal lymph node **(D)** or TDLN **(E)** of both young and aged mice. The results include data from 2-3 experiments. $*P < 0.05$, $**P < 0.01$, $***P < 0.001$ and $****P < 0.0001$.

composition would suggest the potential for dampened anti-tumor immune responses in the aged mice. Indeed, we observe a reduction in key cytotoxic cell types ($CD8^+$ T cells and NK cells) that have been linked to improved prognosis in several cancer types and an increase in key immunosuppressive cells types (Treg and macrophages) that have been linked overall to poorer prognosis (14). These differences in the composition of the tumor immune infiltrate also resulted in a significant decrease in the ratio of $CD8^+$ T cells to Treg in the tumors of aged mice (Figure 2G, p=0.0007), a variable known to correlate with responsiveness to immuno-oncology therapies (15).

The anti-tumor efficacy of anti-OX40 antibody treatment is attenuated in aged mice

Having identified age-related differences in both the tumor-draining lymph node and tumor-infiltrating immune cells, we sought to investigate whether these changes would impact the response of aged mice to immunotherapy. We treated both aged and young animals with an anti-OX40 antibody and found that whilst time-to-endpoint was prolonged in both cohorts, the complete response rate was more than halved from 73% to 24% in aged mice (Figure 3A). This impact of age on the effect of treatment was confirmed by assessment of the tumor growth rate (Figure 3B, p<0.0001), with more profound anti-OX40-induced reductions in tumor growth rate observed in the young cohort, despite no age-related differences in expression of OX40 (Supplementary Figure 5A). Published work has previously associated the anti-tumor activity of OX40 agonism with depletion of Tregs within the TME (16) so we assessed whether the reduced efficacy of the anti-OX40 antibody in aged mice correlated with impaired Treg depletion within the tumor. We found that this was not the case and similar levels of Treg depletion were seen in the aged mice compared to the young mice (Figure 3C). We did not observe any impact of treatment on $CD8^+$ T cell proportions (Supplementary Figure 5B) but we observed significant differences in the response to OX40 agonism within the $CD4^+$ T cell compartment in aged mice. Whereas in young mice, treatment with the anti-OX40 antibody led to a reduction in the

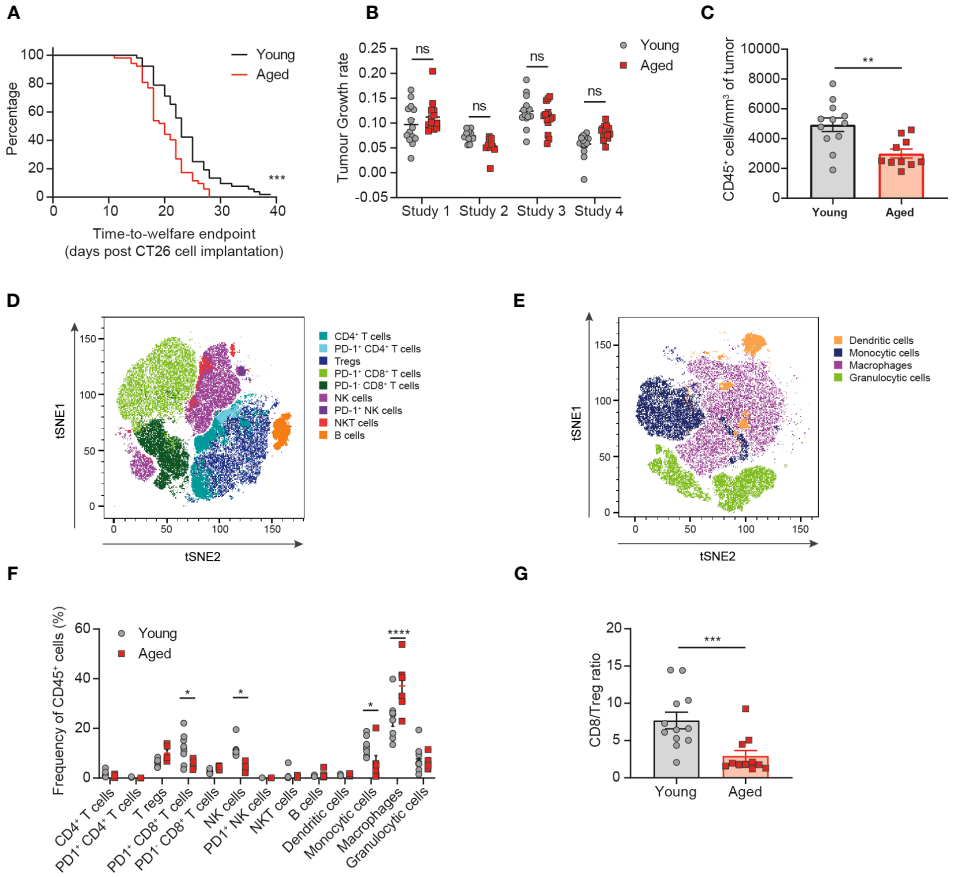

FIGURE 2
The tumor immune infiltrate is significantly altered in aged mice. CT26 tumor cells were subcutaneously implanted on the flank of female BALB/c mice either at 6-8 weeks old (young) or at 60-72 weeks old (aged). **(A)** Kaplan-Meier curves of pooled data from 4 independent experiments showing time-to-welfare endpoint of young and aged mice. 52 mice per group. **(B)** Rate of tumor growth for each animal across 4 experiments. 10-14 mice per group. **(C-G)** Flow cytometric analysis of the tumor immune infiltrate 15-17 days after tumor implantation. **(C)** Absolute cell count per mm^3 of tumor of $CD45^+$ immune cells in aged and young mice. 10-12 mice per group. **(D, E)** tSNE plot showing clusters of lymphoid **(D)** and myeloid **(E)** cell types identified by unsupervised clustering analysis. **(F)** Comparison of the proportion of immune cell clusters within the tumor of young and aged mice. 5-8 mice per group. **(G)** Comparison of the ratio of $CD8^+$ T cells to Tregs in the tumor of young and aged mice. 11-12 mice per group. The results in panels **(A, B)** include data from 4 experiments, the results in panels **(C, G)** include data from 2 experiments, the results in panels **(D-F)** include data from 1 representative of 2 experiments. ns, non-significant, $*P < 0.05$, $**P < 0.01$, $***P < 0.001$ and $****P < 0.0001$.

frequency of effector $CD4^+$ T cells and an increase in effector memory $CD4^+$ T cells, these changes were not seen in the aged mice after treatment (Figure 3D). Given the reduced induction of effector memory $CD4^+$ T cells in the aged mice, we next investigated whether a memory response could also be generated after treatment. Both aged and young mice that had achieved complete tumor clearance after treatment with anti-OX40 antibody were rechallenged with CT26 tumor cells on the opposite flank 53 days later. We observed that growth of the second tumors was prevented in both aged and young mice, suggesting that memory responses had been successfully generated in the aged mice (Figure 3E).

CTLA-4 blockade is less effective in aged mice

Given the impact of age on the anti-tumor efficacy of the immune agonist OX40 treatment, we next sought to determine how age might affect the response to immune checkpoint blockade. We investigated CTLA-4 blockade and saw a significant impact of age on treatment response. Whereas young mice displayed a prolonged time to endpoint (p=0.0023) and a 18% complete response rate after treatment with anti-CTLA-4 antibody, this was not the case in the aged mice and we saw a reduced complete response rate of only 3% (Figure 4A). This dampening in the effect of CTLA-4 blockade in aged mice was also seen in the tumor growth rate analysis, where the fold change in growth rate compared to the untreated group was significantly less pronounced in the aged mice (Figure 4B, p=0.0104).

In clinical practice, it has been observed that addition of PD-1 or PD-L1 blockade to CTLA-4 inhibition can increase the response rate and durability of responses in patients (17–19). Therefore we assessed whether addition of an anti-PD-L1 antibody could overcome the reduced responsiveness of aged mice to CTLA-4 blockade. When we first assessed PD-L1 blockade monotherapy, we saw only modest anti-tumor activity and did not see a clear impact of age on response to this treatment (Supplementary Figure 6). However, after treatment with the combination of anti-PD-L1 and

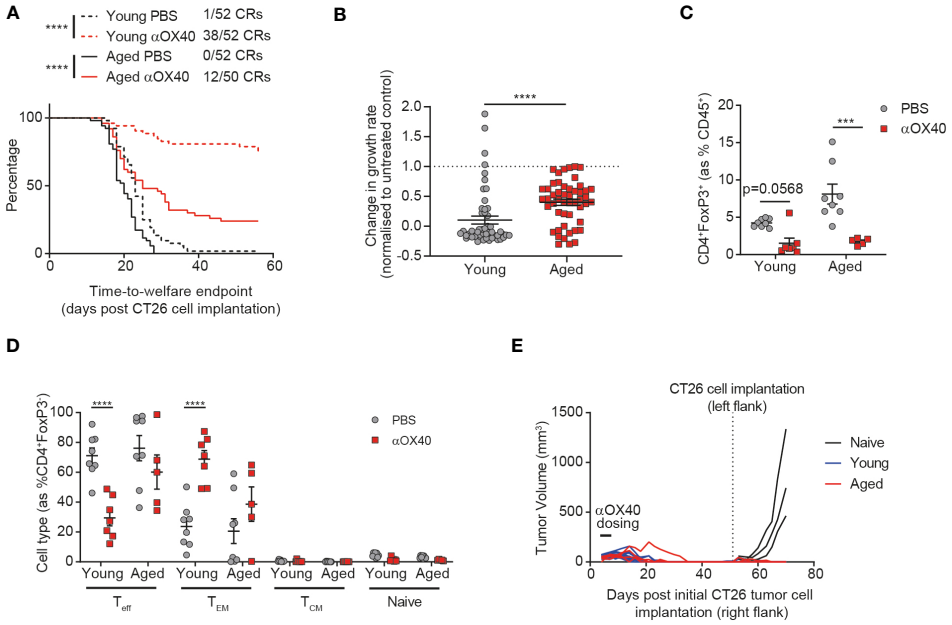

FIGURE 3
Age attenuates the anti-tumor efficacy of anti-OX40 antibody treatment. CT26 tumor cells were subcutaneously implanted on the flank of female BALB/c mice either at 6-8 weeks old (young) or at 60-72 weeks old (aged). The mice were treated with anti-OX40 antibody IP at 1 mg/kg 4 and 7 days after tumor cell implantation. **(A)** Kaplan-Meier curves showing time-to-welfare endpoint. 50-52 mice per group. **(B)** Fold change in the rate of tumor growth for each animal for both young and aged mice after anti-OX40 antibody treatment compared to untreated age-matched mice. 50-52 mice per group. **(C)** 15 days after implantation, tumors were analyzed by flow cytometry. Comparison of the proportion of Tregs in the tumor of young and aged mice after anti-OX40 antibody treatment compared to untreated mice. 5-8 mice per group. **(D)** Frequency of $CD44^{-}CD62L^{-}$ effector (T_{eff}), $CD44^{+}CD62L^{-}$ effector memory (T_{EM}), $CD44^{+}CD62L^{+}$ central memory (T_{CM}) and $CD44^{-}CD62L^{+}$ naïve cell subsets within the $CD4^{+}$ T cell compartment in the tumor of both young and aged mice after anti-OX40 antibody treatment compared to untreated mice. 5-8 mice per group. **(E)** 53 days after initial tumor implantation, 11 young mice and 4 aged mice that achieved complete tumor clearance after treatment with anti-OX40 antibody were re-implanted with CT26 tumor cells on the opposite flank and monitored for tumor growth. 3 control young mice (untreated and not previously tumor-bearing) were implanted as controls (naïve). The results in panels A and B include data from 4 experiments, the results in panels **(C, D)** include data from 1 representative of 2 experiments. ***$P < 0.001$ and ****$P < 0.0001$.

anti-CTLA-4 antibodies we saw striking age-related differences in activity of this immune checkpoint blockade regimen. Indeed, in young mice this combination led to strong anti-tumor efficacy with a 55% complete response rate (Figure 4C). In contrast, the complete response rate was only 11% in aged mice after treatment with the combination of anti-PD-L1 and anti-CTLA-4 antibodies (Figure 4C) and there was a significant decrease in the effect of the treatment on tumor growth rates (Figure 4D p=0.0002).

Discussion

In this study we evaluated the impact of age, a characteristic rarely taken into account in preclinical studies, on the anti-tumor immune response in the commonly-used syngeneic CT26 flank tumor model. There is a well-recognized need to further improve preclinical mouse tumor models to better recapitulate the characteristics of cancer patient populations (2, 20, 21) and one key aspect of this population is their advanced age (1). We sought to evaluate whether accounting for this characteristic in preclinical studies would impact the outcome of the assessment of immuno-oncology treatments and potentially reduce the discrepancy between the responses achieved in preclinical studies compared to the clinical setting. To achieve this, we used mice aged between 15 and 18 months, which we found already recapitulated the thymic involution observed in older humans. Our analysis of both the tumor-infiltrating immune cells as well as secondary lymphoid organ composition in these mice also confirmed that they recapitulated the known hallmarks of immune ageing such as a reduction in the naïve T cell compartment (22).

We assessed the impact of age on the growth kinetics of the CT26 tumor model. From the literature, these age-related changes appear to be very variable, with some groups reporting faster tumor growth in aged mice (23), whilst others report slower tumor growth (24, 25). This variability may be partly due to strain and model-specific differences in the impact of ageing. In order for our experiments to be correctly powered to detect small perturbations in tumor growth kinetics that may be associated with age, we carried out a meta-analysis of 4 independent studies. From this large dataset we concluded that there was no overall impact of age on CT26 tumor growth rate, despite the variability intrinsic to individual experiments that revealed varying trends towards enhanced or decreased growth rates. Presented data from previous studies are usually the result of a limited data set where variation may contribute towards the conclusions drawn and may account for some of the discrepancies regarding the impact of age across published studies (23–27). These conclusions could also be compounded by the use of survival analyses to compare tumor growth as this time-to-endpoint readout also takes into account other welfare aspects such as tumor condition. Indeed, we found that the impact of

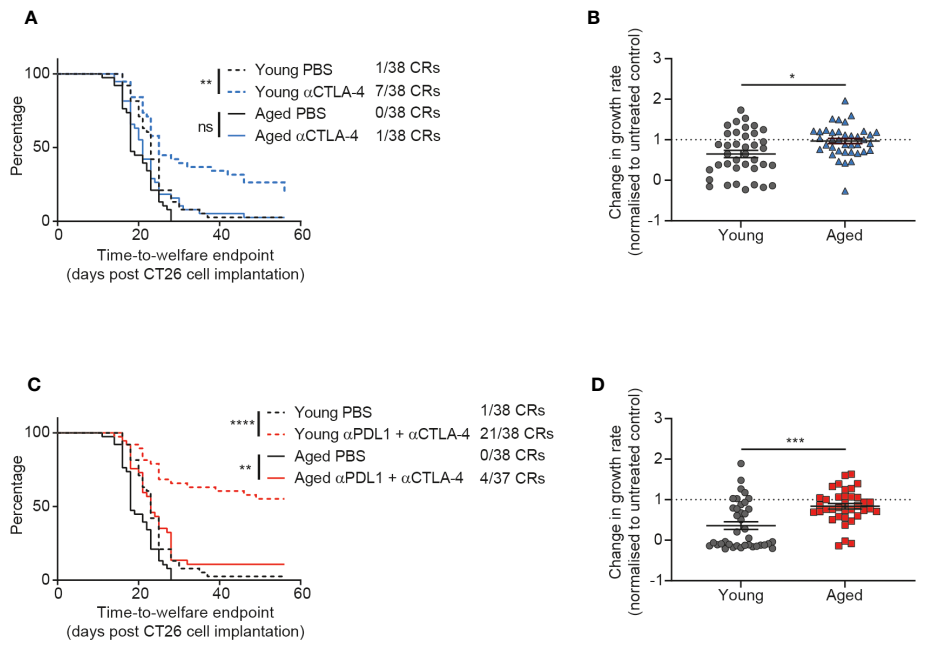

FIGURE 4
CTLA-4 blockade is less effective in aged mice. CT26 tumor cells were subcutaneously implanted on the flank of female BALB/c mice either at 6-8 weeks old (young) or at 60-72 weeks old (aged). **(A, B)** The mice were treated with anti-CTLA-4 antibody IP at 10 mg/kg twice weekly starting 7 days after tumor cell implantation for a total of 6 doses. **(A)** Kaplan-Meier curves showing time-to-welfare endpoint. 38 mice per group. **(B)** Fold change in rate of tumor growth for each animal in both young and aged mice after anti-CTLA-4 antibody treatment compared to age-matched untreated mice. 38 mice per group. **(C, D)** The mice were treated IP at 10 mg/kg twice weekly for a total of 6 doses with a combination of anti-PD-L1 antibody (starting 4 days after tumor cell implantation) and anti-CTLA-4 antibody (starting 7 days after tumor cell implantation). **(C)** Kaplan-Meier curves showing time-to-welfare endpoint. 37-38 mice per group. **(D)** Fold change in rate of tumor growth for each animal in both young and aged mice after anti-PD-L1 and anti-CTLA-4 antibodies compared to age-matched untreated mice. 37-38 mice per group. The results in panels **(A, B)** include data from 3 experiments and the results in panels **(C, D)** include data from 4 experiments. ns, non-significant, $*P < 0.05$, $**P < 0.01$, $***P < 0.001$ and $****P < 0.0001$.

age in these analyses may differ compared to measurement of tumor growth. This discrepancy was detected in our meta-analysis, where aged mice did come off study faster than young mice despite no difference in tumor growth rates. However we found that this could be at least in part driven by increased welfare issues in aged mice, especially higher rates and severity of skin ulceration above the tumors. Although the cause of this increase in skin ulceration has not been elucidated, we hypothesize that it could be linked to an overall decline in the wound healing response in aged mice (28), as these animals were also more prone to develop wounds due to implantation of microchips for animal identification (data not shown).

We also carried out immune profiling on the tumors of these aged mice and detected changes in both the frequency and the absolute numbers of several tumor-infiltrating immune cell subsets. We hypothesize that these could at least partially be due to baseline changes in immune composition driven by processes such as inflammaging [for example the observed increase in the proportion of macrophages, which are known to accumulate as a result of inflammaging and exert pro-tumorigenic effects (29, 30)] rather than entirely due to differences in the immune system's recognition of the tumor. Nevertheless, these changes did not result in a significant difference in tumor growth rate in the aged mice suggesting that even if there is reduced immune control of the tumors in aged mice, this may be counterbalanced by reduced support for tumor growth, for example due to impaired angiogenesis (31). One limitation of this flow cytometric analysis of the tumor microenvironment is the lack of information about the spatial distribution of these immune cells within the tumor that can be generated with other techniques such as immunohistochemistry. This analysis would be of interest, especially as other reports have described changes in the tumor localization of T cells in the 4T1 tumor model in aged mice (32). For this study though, the high throughput and more quantitative approach of flow cytometry was preferred, enabling us to not only enumerate immune cells within the tumor, but also to more extensively phenotype them.

In this study, we found that age did alter responses to immuno-oncology therapies. Indeed, the effects of anti-OX40 antibody treatment were much reduced in aged compared to young mice. This is consistent with a previous report describing reduced efficacy of OX40 agonism in the CT26 tumor model although that study was carried out in younger (12 month old) mice and surprisingly saw less activity of OX40 agonism in 12 month old mice than we observe in 15-18 month old mice (33). We further extended this work to include an assessment of the impact of age on response to immune checkpoint blockade and here results were even more striking, with aged mice showing a greatly reduced anti-tumor effect of treatment with the combination of anti-PD-L1 and anti-CTLA-4 antibodies. Reduced efficacy of the monotherapies has been reported in the 4T1 model (32) and of the combination in the B16 model (34), although conversely others report increased efficacy of PD-1 blockade in aged mice (35). Although published reports would not suggest that this might be due to reduced expression of PD-1 or CTLA-4, as these are

often observed to increase with ageing (36, 37), this was not the case in our experimental setting (Supplementary Figure 7) where we observed decreased levels of PD-1 and CTLA-4 on $CD8^+$ T cells within the tumor. Overall, a decrease in responsiveness to immuno-oncology treatments with age is perhaps not unexpected though (38), given that ageing has been associated with immune dysregulation including both immunosenescence (39) as well as a chronic inflammatory state known as inflamm-aging (7). Specifically, ageing has been shown to lead to a decline in the naïve T cell pool (6) as well as defects in T cell priming (40). Priming is a crucial step in boosting anti-tumor immune responses with treatments such as anti-CTLA-4 antibodies (41) and is a known contributor to the increased sensitivity of the CT26 tumor model to immunotherapy, as it is a self-priming model (42). These age-related changes would be hypothesized to affect the outcomes of CTLA-4 blockade preferentially over PD-1/PD-L1 blockade based on their mechanisms of action (41) and this is reflected both in our dataset, where we did not detect an impact of age on the efficacy of PD-L1 blockade, as well as in clinical analyses of the impact of age on treatment outcomes of patients receiving PD-1/PD-L1 blocking antibodies, which do not report a decline in responsiveness to treatment associated with age (38). These types of clinical meta-analyses though mainly compare middle-aged patients against older patients (typically with a cutoff of 65 years of age), unlike our analysis where we compare very young mice (thought to represent roughly teenage patients) against aged mice (thought to represent middle aged patients). We suggest that the reduced sensitivity to immune checkpoint blockade of the CT26 model grown in aged mice, with only a subset of animals displaying responses to anti-PD-L1 and anti-CTLA-4 antibodies rather than a majority of complete responses, is a closer approximation to the response rates observed in clinical practice and could indicate improved translatability (17). This work further supports the need, already described by several other groups (2, 20, 21), to better model the effects of immuno-oncology drug candidates in the setting of the aged immune system as we find that age can significantly impact response to therapeutic treatments in one of the most responsive mouse models commonly used in immuno-oncology drug discovery (33). Future work could further build on this to assess additional characteristics of cancer patients and increase the generalizability of our findings, for example by repeating the study in male mice where sex differences in the immune system could alter the impact of ageing on anti-tumor immune responses.

In conclusion, we show that aged mice represent valuable models for the preclinical assessment of immuno-oncology therapies and that they could prove more accurate than young mice in predicting the efficacy of novel treatments due to the clear impact of age on both natural immunity to cancer and the ability to effectively respond to specific immuno-oncology treatments.

Data availability statement

The original contributions presented in the study are included in the article/Supplementary Material. Further inquiries can be directed to the corresponding author.

Ethics statement

The animal study was approved by Babraham Institute Animal Welfare and Ethical Review Body, Cambridge, UK. The study was conducted in accordance with the local legislation and institutional requirements.

Author contributions

SS: Conceptualization, Formal Analysis, Writing – original draft. JW: Writing – original draft. LP: Formal Analysis, Writing – review & editing. MM: Writing – review & editing, Supervision. VV: Writing – review & editing, Conceptualization. MR: Writing – review & editing, Supervision. RW: Writing – review & editing. SD: Writing – review & editing, Supervision.

Funding

The author(s) declare financial support was received for the research, authorship, and/or publication of this article. This work was funded by AstraZeneca.

Acknowledgments

We would like to thank the Animal Sciences and Technology group, the Core Tissue Culture facility and the Cambridge Early Oncology Discovery *in vivo* group at AstraZeneca for technical support as well as Raphaela Mendes Fernandes De Souza Lobo.

Conflict of interest

This study was funded by AstraZeneca. The funder had the following involvement with the study: study design, data collection and analysis, decision to publish, and preparation of the manuscript. All authors were employees of and shareholders in AstraZeneca at the time of the study.

Publisher's note

All claims expressed in this article are solely those of the authors and do not necessarily represent those of their affiliated organizations, or those of the publisher, the editors and the reviewers. Any product that may be evaluated in this article, or claim that may be made by its manufacturer, is not guaranteed or endorsed by the publisher.

Supplementary material

The Supplementary Material for this article can be found online at: https://www.frontiersin.org/articles/10.3389/fimmu.2023.1258291/full#supplementary-material

References

1. Siegel RL, Miller KD, Jemal A. Cancer statistics. *2020* (2020) 70(1):7–30. doi: 10.3322/caac.21590

2. Klevorn LE, Teague RM. Adapting cancer immunotherapy models for the real world. *Trends Immunol* (2016) 37(6):354–63. doi: 10.1016/j.it.2016.03.010

3. Becklund BR, Purton JF, Ramsey C, Favre S, Vogt TK, Martin CE, et al. The aged lymphoid tissue environment fails to support naive T cell homeostasis. *Sci Rep* (2016) 6:30842. doi: 10.1038/srep30842

4. Thompson HL, Smithey MJ, Uhrlaub JL, Jeftic I, Jergovic M, White SE, et al. Lymph nodes as barriers to T-cell rejuvenation in aging mice and nonhuman primates. *Aging Cell* (2019) 18(1):e12865. doi: 10.1111/acel.12865

5. Goronzy JJ, Weyand CM. Mechanisms underlying T cell ageing. *Nat Rev Immunol* (2019) 19(9):573–83. doi: 10.1038/s41577-019-0180-1

6. Goronzy JJ, Weyand CM. Successful and maladaptive T cell aging. *Immunity* (2017) 46(3):364–78. doi: 10.1016/j.immuni.2017.03.010

7. Franceschi C, Bonafè M, Valensin S, Olivieri F, De Luca M, Ottaviani E, et al. Inflamm-aging. An evolutionary perspective on immunosenescence. *Ann New York Acad Sci* (2000) 908:244–54. doi: 10.1111/j.1749-6632.2000.tb06651.x

8. Fane M, Weeraratna AT. How the ageing microenvironment influences tumour progression. *Nat Rev Cancer* (2020) 20(2):89–106. doi: 10.1038/s41568-019-0222-9

9. Wang S, Lai X, Deng Y, Song Y. Correlation between mouse age and human age in anti-tumor research: Significance and method establishment. *Life Sci* (2020) 242:117242. doi: 10.1016/j.lfs.2019.117242

10. Hather G, Liu R, Bandi S, MettEtal J, Manfredi M, Shyu WC, et al. Growth rate analysis and efficient experimental design for tumor xenograft studies. *Cancer Inform* (2014) 13(Suppl 4):65–72. doi: 10.4137/CIN.S13974

11. Flores KG, Li J, Sempowski GD, Haynes BF, Hale LP. Analysis of the human thymic perivascular space during aging. *J Clin Invest* (1999) 104(8):1031–9. doi: 10.1172/JCI7558

12. Yang H, Youm YH, Vandanmagsar B, Rood J, Kumar KG, Butler AA, et al. Obesity accelerates thymic aging. *Blood* (2009) 114(18):3803–12. doi: 10.1182/blood-2009-03-213595

13. Harrell MI, Iritani BM, Ruddell A. Tumor-induced sentinel lymph node lymphangiogenesis and increased lymph flow precede melanoma metastasis. *Am J Pathol* (2007) 170(2):774–86. doi: 10.2353/ajpath.2007.060761

14. Bruni DA-O, Angell HA-O, Galon JA-O. The immune contexture and Immunoscore in cancer prognosis and therapeutic efficacy. *Nat Rev Cancer* (2020) 20(11):662–80. doi: 10.1038/s41568-020-0285-7

15. Goda N, Sasada S, Shigematsu H, Masumoto N, Arihiro K, Nishikawa H, et al. The ratio of CD8 + lymphocytes to tumor-infiltrating suppressive FOXP3 + effector regulatory T cells is associated with treatment response in invasive breast cancer. *Discov Oncol* (2022) 13(1):27. doi: 10.1007/s12672-022-00482-5

16. Bulliard Y, Jolicoeur R, Zhang J, Dranoff G, Wilson NS, Brogdon JL. OX40 engagement depletes intratumoral Tregs via activating FcγRs, leading to antitumor efficacy. *Immunol Cell Biol* (2014) 92(6):475–80. doi: 10.1038/icb.2014.26

17. Rotte A. Combination of CTLA-4 and PD-1 blockers for treatment of cancer. *J Exp Clin Cancer Res* (2019) 38(1):255. doi: 10.1186/s13046-019-1259-z

18. Motzer RJ, Tannir NM, McDermott DF, Aren Frontera O, Melichar B, Choueiri TK, et al. Nivolumab plus Ipilimumab versus Sunitinib in Advanced Renal-Cell Carcinoma. *N Engl J Med* (2018) 378(14):1277–90. doi: 10.1056/NEJMoa1712126

19. Larkin J, Chiarion-Sileni V, Gonzalez R, Grob JJ, Rutkowski P, Lao CD, et al. Five-year survival with combined nivolumab and ipilimumab in advanced melanoma. *N Engl J Med* (2019) 381(16):1535–46. doi: 10.1056/NEJMoa1910836

20. Hurez V, Padron AS, Svatek RS, Curiel TJ. Considerations for successful cancer immunotherapy in aged hosts. *Clin Exp Immunol* (2017) 187(1):53–63. doi: 10.1111/cei.12875

21. Bouchlaka MN, Murphy WJ. Impact of aging in cancer immunotherapy: The importance of using accurate preclinical models. *Oncoimmunology* (2013) 2(12): e27186–e. doi: 10.4161/onci.27186

22. Nikolich-Zugich J. Aging of the T cell compartment in mice and humans: from no naive expectations to foggy memories. *J Immunol* (2014) 193(6):2622–9. doi: 10.4049/jimmunol.1401174

23. Ishikawa S, Matsui Y, Wachi S, Yamaguchi H, Harashima N, Harada M. Age-associated impairment of antitumor immunity in carcinoma-bearing mice and restoration by oral administration of Lentinula edodes mycelia extract. *Cancer Immunol Immunother* (2016) 65(8):961–72. doi: 10.1007/s00262-016-1857-y

24. Pettan-Brewer C, Morton J, Coil R, Hopkins H, Fatemie S, Ladiges W. B16 melanoma tumor growth is delayed in mice in an age-dependent manner. *Pathobiol Aging Age Relat Dis* (2012) 2. doi: 10.3402/pba.v2i0.19182

25. Oh J, Magnuson A, Benoist C, Pittet MJ, Weissleder R. Age-related tumor growth in mice is related to integrin alpha 4 in CD8+ T cells. *JCI Insight* (2018) 3(21). doi: 10.1172/jci.insight.122961

26. Chen YM, Wang PS, Liu JM, Hsieh YL, Tsai CM, Perng RP, et al. Effect of age on pulmonary metastases and immunotherapy in young and middle-aged mice. *J Chin Med Assoc* (2007) 70(3):94–102. doi: 10.1016/S1726-4901(09)70338-7

27. Beheshti A, Benzekry S, McDonald JT, Ma L, Peluso M, Hahnfeldt P, et al. Host age is a systemic regulator of gene expression impacting cancer progression. *Cancer Res* (2015) 75(6):1134–43. doi: 10.1158/0008-5472.CAN-14-1053

28. Swift ME, Kleinman HK, DiPietro LA. Impaired wound repair and delayed angiogenesis in aged mice. *Lab Invest* (1999) 79(12):1479–87.

29. Duong L, Pixley FJ, Nelson DJ, Jackaman C. Aging leads to increased monocytes and macrophages with altered CSF-1 receptor expression and earlier tumor-associated macrophage expansion in murine mesothelioma. *Front Aging* (2022) 3:848925. doi: 10.3389/fragi.2022.848925

30. Jackaman C, Tomay F, Duong L, Abdol Razak NB, Pixley FJ, Metharom P, et al. Aging and cancer: The role of macrophages and neutrophils. *Ageing Res Rev* (2017) 36:105–16. doi: 10.1016/j.arr.2017.03.008

31. Lahteenvuo J, Rosenzweig A. Effects of aging on angiogenesis. *Circ Res* (2012) 110(9):1252–64. doi: 10.1161/CIRCRESAHA.111.246116

32. Sceneay J, Goreczny GJ, Wilson K, Morrow S, DeCristo MJ, Ubellacker JM, et al. Interferon signaling is diminished with age and is associated with immune checkpoint blockade efficacy in triple-negative breast cancer. *Cancer Discovery* (2019) 9(9):1208–27. doi: 10.1158/2159-8290.CD-18-1454

33. Ruby CE, Weinberg AD. OX40-enhanced tumor rejection and effector T cell differentiation decreases with age. *J Immunol* (2009) 82(3):1481–9. doi: 10.4049/jimmunol.182.3.1481

34. Padron A, Hurez V, Gupta HB, Clark CA, Pandeswara SL, Yuan B, et al. Age effects of distinct immune checkpoint blockade treatments in a mouse melanoma model. *Exp Gerontol* (2018) 105:146–54. doi: 10.1016/j.exger.2017.12.025

35. Kugel CH 3rd, Douglass SM, Webster MR, Kaur A, Liu Q, Yin X, et al. Age correlates with response to Aanti-PD1, reflecting age-related differences in intratumoral effector and regulatory T-cell populations. *Clin Cancer Res* (2018) 24 (21):5347–56. doi: 10.1158/1078-0432.CCR-18-1116

36. Garcia MG, Deng Y, Murray C, Reyes RM, Padron A, Bai H, et al. Immune checkpoint expression and relationships to anti-PD-L1 immune checkpoint blockade cancer immunotherapy efficacy in aged versus young mice. *Aging Cancer* (2022) 3 (1):68–83. doi: 10.1002/aac2.12045

37. Liu JN, Kong XS, Huang T, Wang R, Li W, Chen QF. Clinical implications of aberrant PD-1 and CTLA4 expression for cancer immunity and prognosis: A pan-cancer study. *Front Immunol* (2020) 11:2048. doi: 10.3389/fimmu.2020.02048

38. Elias R, Giobbie-Hurder A, McCleary NJ, Ott P, Hodi FS, Rahma O. Efficacy of PD-1 & PD-L1 inhibitors in older adults: a meta-analysis. *J Immunother Cancer* (2018) 6(1):26. doi: 10.1186/s40425-018-0336-8

39. Pawelec G. Age and immunity: what is "immunosenescence"? *Exp Gerontol* (2018) 105:4–9. doi: 10.1016/j.exger.2017.10.024

40. Bansal-Pakala P, Croft M. Defective T cell priming associated with aging can be rescued by signaling through 4-1BB (CD137). *J Immunol* (2002) 169(9):5005. doi: 10.4049/jimmunol.169.9.5005

41. Wei SC, Duffy CR, Allison JP. Fundamental mechanisms of immune checkpoint blockade therapy. *Cancer Discovery* (2018) 8(9):1069–86. doi: 10.1158/2159-8290.CD-18-0367

42. Huang AY, Gulden PH, Woods AS, Thomas MC, Tong CD, Wang W, et al. The immunodominant major histocompatibility complex class I-restricted antigen of a murine colon tumor derives from an endogenous retroviral gene product. *Proc Natl Acad Sci U S A* (1996) 93(18):9730–5. doi: 10.1073/pnas.93.18.9730

frontiers | Frontiers in Immunology

TYPE Review
PUBLISHED 28 November 2023
DOI 10.3389/fimmu.2023.1264882

Check for updates

OPEN ACCESS

EDITED BY
An Coosemans,
KU Leuven, Belgium

REVIEWED BY
Dina Schneider,
Lentigen Technology, United States
Jahan S. Khalili,
SystImmune Inc, United States

*CORRESPONDENCE
Gordon Moody
gordon.moody@astrazeneca.com

RECEIVED 21 July 2023
ACCEPTED 27 October 2023
PUBLISHED 28 November 2023

CITATION
Giardino Torchia ML and Moody G (2023) DIALing-up the preclinical characterization of gene-modified adoptive cellular immunotherapies. *Front. Immunol.* 14:1264882. doi: 10.3389/fimmu.2023.1264882

COPYRIGHT
© 2023 Giardino Torchia and Moody. This is an open-access article distributed under the terms of the Creative Commons Attribution License (CC BY). The use, distribution or reproduction in other forums is permitted, provided the original author(s) and the copyright owner(s) are credited and that the original publication in this journal is cited, in accordance with accepted academic practice. No use, distribution or reproduction is permitted which does not comply with these terms.

DIALing-up the preclinical characterization of gene-modified adoptive cellular immunotherapies

Maria Letizia Giardino Torchia[1] and Gordon Moody[2*]

[1]Cell Therapy Unit, Oncology Research, AstraZeneca, Cambridge, United Kingdom,
[2]Cell Therapy Unit, Oncology Research, AstraZeneca, Gaithersburg, MD, United States

The preclinical characterization of gene modified adoptive cellular immunotherapy candidates for clinical development often requires the use of mouse models. Gene-modified lymphocytes (GML) incorporating chimeric antigen receptors (CAR) and T-cell receptors (TCR) into immune effector cells require *in vivo* characterization of biological activity, mechanism of action, and preclinical safety. Typically, this characterization involves the assessment of dose-dependent, on-target, on-tumor activity in severely immunocompromised mice. While suitable for the purpose of evaluating T cell-expressed transgene function in a living host, this approach falls short in translating cellular therapy efficacy, safety, and persistence from preclinical models to humans. To comprehensively characterize cell therapy products in mice, we have developed a framework called "DIAL". This framework aims to enable an end-to-end understanding of genetically engineered cellular immunotherapies *in vivo*, from infusion to tumor clearance and long-term immunosurveillance. The acronym DIAL stands for Distribution, Infiltration, Accumulation, and Longevity, compartmentalizing the systemic attributes of gene-modified cellular therapy and providing a platform for optimization with the ultimate goal of improving therapeutic efficacy. This review will discuss both existent and emerging examples of DIAL characterization in mouse models, as well as opportunities for future development and optimization.

KEYWORDS

CAR-T cells, immunotherapy, adoptive cell therapy, tumor microenvironment, animal models

1 Introduction

Mouse models are routinely used in the preclinical characterization of gene-modified adoptive cellular immunotherapy candidates for clinical development. Adoptive transfer studies in mice, initially in the context of allograft transfer, underpin our understanding of T cell function, trafficking, and therapeutic potential (1–3). The first human studies of gene-modified T cells occurred in the 1980s (4), where a neomycin resistance cassette was retrovirally transduced into tumor-infiltrating lymphocytes (TIL) from patients with

melanoma before infusion into patients. These pioneering studies demonstrated the ability of autologous lymphocytes transferred into patients, along with interleukin-2 (IL-2) treatment, to persist for months. The persistence of the transgene was determined through a PCR-based detection assay, which enabled detection of the adoptively transferred cells. Prior to this landmark human clinical study, a similar approach employing TIL therapy was successfully implemented in mice, resulting in complete regression of syngeneic murine tumors (5). Thus, the mouse study served as a valuable early model for investigating the distribution and function of adoptively transferred tumor-infiltrating lymphocytes.

The development of gene-modified chimeric T-cell receptors that enhance T cell function toward tumor cells in an MHC-independent manner was first described by Eshhar and colleagues in 1989 (6). These chimeric receptors, termed immunoglobulin T-cell receptor (TCR) chimeras, combined an extracellular antibody-like antigen binding molecule with a TCR and an intracellular CD3 zeta (CD3ζ) signaling domain. While effective *in vitro*, these initial designs lacked the co-stimulatory framework that enabled enhanced T-cell function and persistence *in vivo*.

In 2002, the "second generation" chimeric antigen receptor (CAR) was introduced, addressing the limitations of the previous design (7). This evolved design enabled transduced T cells to produce high levels of endogenous IL-2, supporting the maintenance of cytotoxic function and persistence. Over the years, multiple second-generation CAR-T were developed, incorporating co-stimulatory domains such as CD28 or 4-1BB (8). These designs differed from the first-generation constructs by their ability to drive T cell expansion in the presence of continual antigen exposure (9). The functional improvement was further demonstrated by the requirement of co-stimulation for tumor regression in mouse models of ALL (10, 11).

A few years later, the second-generation CAR-T design was reduced to practice with the first evidence of CAR-T-mediated tumor responses in human clinical trials in advanced follicular lymphoma (12). Subsequent clinical trials led to the development of second generation CAR-T therapy targeting CD19, resulting in the approval of tisagenlecleucel and axicabtagene ciloleucel for the treatment of refractory lymphoma and pediatric leukemia. Thus, the preclinical validation of second-generation CAR-T in mice informed the subsequent clinical development and approval of gene-modified lymphocyte (GML) therapy.

In parallel with second-generation CAR-T, transgenic T-cell receptor (TCR-T) therapy gained momentum as another genetically modified approach for redirecting potent T-cell responses in solid tumors. Building upon the initial success of TIL therapy, Rosenberg et al. engineered autologous gene-modified TCR-T against the melanosome antigen MART-1 (13). These modified TCR-T cells demonstrated persistence and induced tumor regressions in a limited number of patients. The development of the PMEL-1 mouse model, targeting another prevalent melanosome antigen in mice, provided strong preclinical evidence. In this model, transgenic PMEL-1 (gp100) directed T cells were transferred into mice bearing melanotic, poorly immunogenic B16 tumors (14). In both preclinical and clinical settings, tumor regression and persistence of the TCR-T were observed, accompanied by autoimmune responses such as vitiligo, which were observed in both mice and humans (15, 16).

The future development of therapies against HLA-restricted cancer-testis (CT) antigens including NY-ESO-1, PRAME, MAGE-A3 and MAGE-A4, among others, showcased additional opportunities for the efficacy of TCR-T against solid tumors. However, the development of a fully analogous mouse model posed challenges due to the lack of homology, expression and/or cross-reactivity of TCRs with mouse peptide-MHC (pMHC). In most cases, representative antigens with known high-affinity CD8 TCRs such as PMEL-1, tyrosinase-related protein 1 (TRP1) or ovalbumin (OVA/OT-I) were used as proxies for human TCR-T.

The process of preclinical validation for GML is constantly evolving, and new guidance is emerging (17). However, the primary objective of preclinical testing remains consistent: to confirm the biological activity, mechanism of action, and preclinical safety of the therapy before its use in patients.

While animal models, particularly severely immunocompromised mice, are commonly employed for CAR-T validation, the current approach often focuses on assessing fundamental attributes such as dose-dependence, on-target on-tumor activity, and the absence of uncontrolled proliferation and toxicity. While these attributes validate the functionality of the transgene and the manufacturing process, they overlook several critical aspects that should be considered when designing GML as therapeutics for oncology.

These aspects include modeling on-target, off-tumor toxicity and exhaustion, understanding the impact of lymphodepleting chemotherapy (LDC) on toxicity or cell expansion, evaluating tumor heterogeneity and antigen escape, evaluating the tumor microenvironment (TME) with its soluble factors and immune suppressor cells, overcoming barriers to infiltration, exploring the consequences (both positive and negative) of long-term expansion and persistence, and evaluating toxicities such as cytokine-release syndrome (CRS) and immune effector-cell-associated neurotoxicity syndrome (ICANS).

To characterize the cell therapy product and its design attributes more comprehensively, we have developed a framework called "DIAL". This framework provides a holistic understanding of genetically engineered cellular immunotherapies *in vivo*, encompassing their journey from infusion to tumor regression and continued immunosurveillance. The acronym DIAL represents Distribution, Infiltration, Accumulation, and Longevity, which serve to compartmentalize the systemic attributes of gene modified cellular therapy (Figure 1). Additionally, DIAL serves as a platform for optimizing these attributes, with the ultimate goal of enhancing overall therapeutic efficacy. This review will discuss both existing and emerging examples of DIAL optimization, their characterization in mouse models, and potential avenues for future development. Given the rapidly evolving nature of this field, it is not feasible to cover each topic exhaustively with examples of each emerging technology. Instead, each section will focus on key examples, emphasizing areas for improvement and future advances.

2 Distribution

Optimal drug distribution refers to the efficient and rapid delivery of drug material to the desired site of action from the site

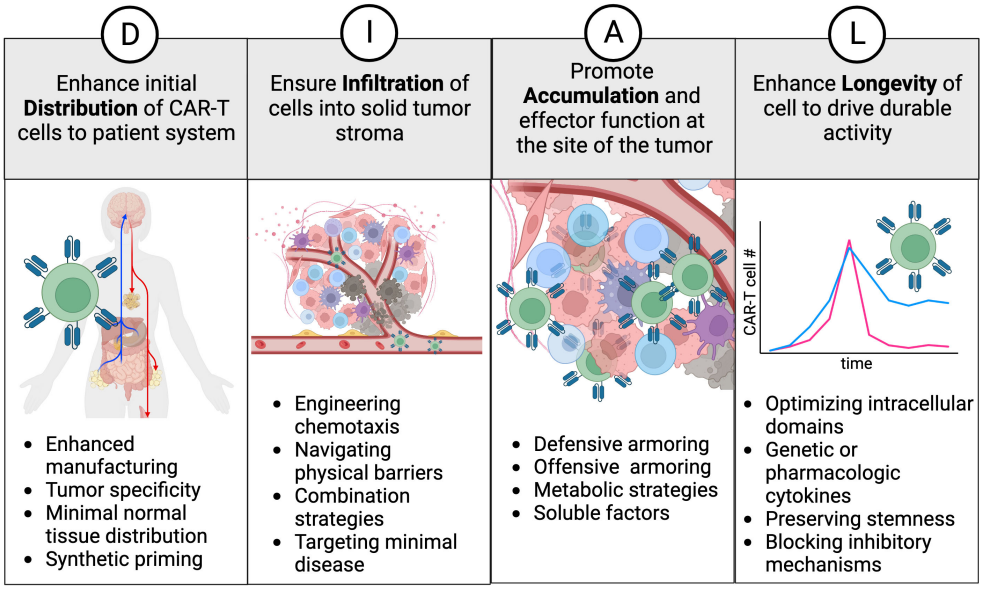

FIGURE 1
The DIAL framework. Distribution, infiltration, accumulation, and longevity are classified as key attributes and areas to focus on for enhancing cell therapy products. Examples of interventions are provided for each attribute and discussed in the text.

of administration. The distribution of adoptively transferred lymphocytes for cellular therapy is analogous to pharmacologic distribution of biologics and small molecules, with certain key distinctions.

As donor-derived "living drugs", infused GML exhibit a distribution pattern similar to endogenous lymphocytes (18–20). Following intravenous infusion, T-lymphocytes follow the vascular circulation, extravasate into tissues, diffuse into target sites, and recirculate through uptake in lymphatic tissue via high endothelial venules, ultimately returning to the vasculature through either the thoracic duct or vascular circuits (21). While the initial use of CAR-T focused on treating of B cell malignancies in the periphery it is important to note that GML also can distribute in compacted tissues and encounter their cognate antigens. This interaction allows them to receive survival and proliferation signals, promoting their expansion.

The expansion phase of GML products induced by antigen encounter sets adoptive cell therapy (ACT) apart from other therapeutic approaches. During this phase, the levels of the therapeutic cells (measured by the presence of CAR or TCR-positive cell by flow cytometry or gene copy number by PCR) increase relative to the infusion levels. The peak and duration of this elevation depends on the antigenic burden and the microenvironmental context of antigen encounter, both of which influence the extent of proliferation and expansion. Over time, the infused cells undergo apoptosis in various tissues. The initial phase of decay occurs rapidly after the initial expansion, while the second phase of decay proceeds gradually over weeks to months. This gradual decline may be attributed to factors such as loss of stimulation, activation-induced cell death, and exhaustion (22).

The composition of cell therapy infusion products plays a pivotal role in determining their distribution. When accounting for effector, memory and naïve subsets, both rodents and human exhibit a similar distribution pattern for ACT (21, 23–25). Factors such as cell size and the presence of receptors that govern lymphatic tropism (such as L-selectin and CCR7) can influence the survival and recirculation of cells post-infusion. Further, the relative composition of these subsets can impact the proliferative and metabolic potential of the transferred lymphocytes.

In the case of commonly used laboratory mice (Mus musculus), variations in CAR-T and TCR-T distribution may be attributed to factors like strain differences, extent of immune competence, and discrepancies in housing and sourcing facilities. Nonetheless, working with laboratory mice generally offers the advantage of predictability and consistency in experimental outcomes.

2.1 Distribution – cellular manufacturing

The ex vivo manipulation and expansion of GML, often referred to as cellular manufacturing, represents the initial stage where subsequent distribution patterns can be influenced. The manufacturing process involves complex interplay of factors that dictate the cellular kinetics (CK) of the grafted cells, including post-infusion cell survival, tissue infiltration, antigen-induced expansion, recirculation through the lymphatics into the bloodstream, terminal differentiation, and elimination.

Early T cell manufacturing processes focused on scaling up large numbers of cells for infusion into patients who would subsequently receive supportive doses of IL-2 (26, 27). In comparison, CAR-T therapy had key distinctions, requiring fewer cells for infusion and demonstrating the ability to persist without patient-administered IL-2. However, many of the principles established with TIL therapy, such as T cell activation though their TCR using anti-CD3 antibodies or antigen-presenting cells, and expansion in the

presence of moderately high (>100 IU/mL) levels of IL-2 for 1-2 weeks, were initially maintained in GML protocols.

However, it was observed that sustained expansion in IL-2 could lead to cell exhaustion and limited persistence *in vivo* (28). Consequently, various protocol modifications were adopted in cellular manufacturing to preserve the fitness and persistence of the transferred cells post-infusion (29, 30).

In the years following the development of the initial CD19 CAR-T therapy, numerous modifications to manufacturing protocols were explored. These included the use of CD3/CD28 beads and alternative cytokines such as IL-7, IL-15, and IL-21, which promoted a stem cell memory phenotype (31–33). Additional enhancements involved incorporating small molecules into expansion media to further boost memory characteristics, promote persistence, and increase anti-tumor activity (34–39). The results demonstrated that process modifications preserving a memory cell phenotype enabled enhanced persistence, as determined by factors such as proliferative potential, resistance to stress (e.g., serial antigen stimulation or low cell dosing), and improved distribution to lymphatics and secondary lymphoid organs, facilitating recirculation (40).

Administration of high doses of CAR-T cells after prolonged manufacturing times and in conjunction with supportive IL-2 can lead to severe toxicities and lack of long-term durability, even when the target antigen is not present in normal tissues (41). Because of these potential issues, many of the recent advancements in autologous cellular manufacturing focus on preserving GML stemness as a means of improving potency and reducing toxicity, with a heightened focus on the T memory stem-cell (T_{SCM}). This subset of memory T cells with self-renewal capacity was first identified in mice (34) and subsequently in human (28) and non-human primate (42). T_{SCM} have similar cell surface markers and metabolic potential compared to naïve T cells, and have an enhanced proliferative potential compared to other memory and effector subsets. For CAR-T, it is important to consider that recently activated naïve T cells are often not distinguished from native T_{SCM} cells and thus may differ in functional capacity and fate. There are a variety of ways to enhance the CAR- T_{SCM} fraction: mechanical enrichment of naïve/memory subsets (29, 43), addition of factors or cytokines to induce stemness (31, 37, 44), and shortening the manipulation of peripheral cells and reducing manufacturing time (45, 46). Although much of the modeling for CAR-T_{SCM} is performed using human cells in immunocompromised mice, the underlying principles can be applied to immunocompetent strains as well.

Murine T cell manufacturing processes are not optimal for translation to human CAR-T cell manufacturing. Mouse T cells exhibit many dissimilarities compared to their human counterparts. Additionally, available protocols for murine T cell transduction and expansion, as well as lymphodepletion, create disparities in comparison to humans.

To begin with, murine T cells do not expand ex vivo to the same extent as human T cells. They require different media and conditions for activation and do not consistently expand for greater than approximately 10-14 days. Furthermore, the source of cells differs between murine and human protocols. Murine protocols primarily utilize splenic T cells, whereas human protocols rely on peripheral blood T cells (47, 48).

Lastly, lymphodepletion in mouse typically involves low-dose (<5 Gy) whole-body irradiation, whereas lymphodepleting chemotherapy (LDC) is almost exclusively used in humans. These differing protocols can lead to variations in the dynamics of lymphopenic immune cell recovery and cytokine production, which are crucial for supporting the expansion of transferred cells and promoting memory phenotypes.

Despite these differences, genetically engineered fully murine model systems can still be utilized to highlight many of the advantages of generating stem-like T cells for ACT (49–55). In the future, the development and engineering of GML could benefit from a combination of both immunocompetent syngeneic murine and immunocompromised human xenograft model systems. This approach would provide a more comprehensive understanding of the various factors required to achieve optimal cell distribution.

2.2 Distribution – choice of antigen

The choice of antigen and context of antigen encounter will influence the initial distribution of the gene-modified cells. After intravenous infusion, cell therapy products follows a pattern of distribution that involves vascular circulation, extravasation, diffusion into tissue, and recirculation primarily through lymphatics and vascular circuits. GML can distribute in tissues and encounter their cognate antigens in the tumor, triggering survival and proliferation signals that allow for expansion and continued distribution (Figure 2A). Different types of lymphocytes may have varying tendencies to distribute to tissues and lymphatics.

In cases where antigen is readily accessible in blood-based tumors, the process of expansion and distribution is facilitated. However, when the antigen is confined to poorly vascularized or compacted tissues, both the accessibility and the context of antigen encounter are compromised. Non-genetically modified lymphocytes, particularly T cells, have the capability to produce cytokines and transcription factors that promote proliferation and antigen-induced expansion. GML, with their expressed receptors, further enhance antigen-induced expansion to exaggerated levels, which can be augmented by preceding lymphodepletion. It is important to note that the differences between mouse and human lymphodepletion, as discussed earlier, can also lead to discrepancies in interpreting preclinical models when evaluating antigen-specific expansion in humans.

Antigens that exhibit a tumor-specific expression profile facilitate confined and intended cell expansion. On the other hand, more promiscuous antigens increase the risk of "off-tumor" toxicities and promote effector differentiation, which can lead to eventual dysfunction. When target-directed activity induces both direct cytotoxicity and paracrine effects through cytokine production, widespread antigen expression outside the tumor can exacerbate systemic inflammation. This, in turn, hampers the cells' ability to infiltrate the tumor efficiently. This phenomenon is commonly referred to as on-target, off-tumor toxicity. However,

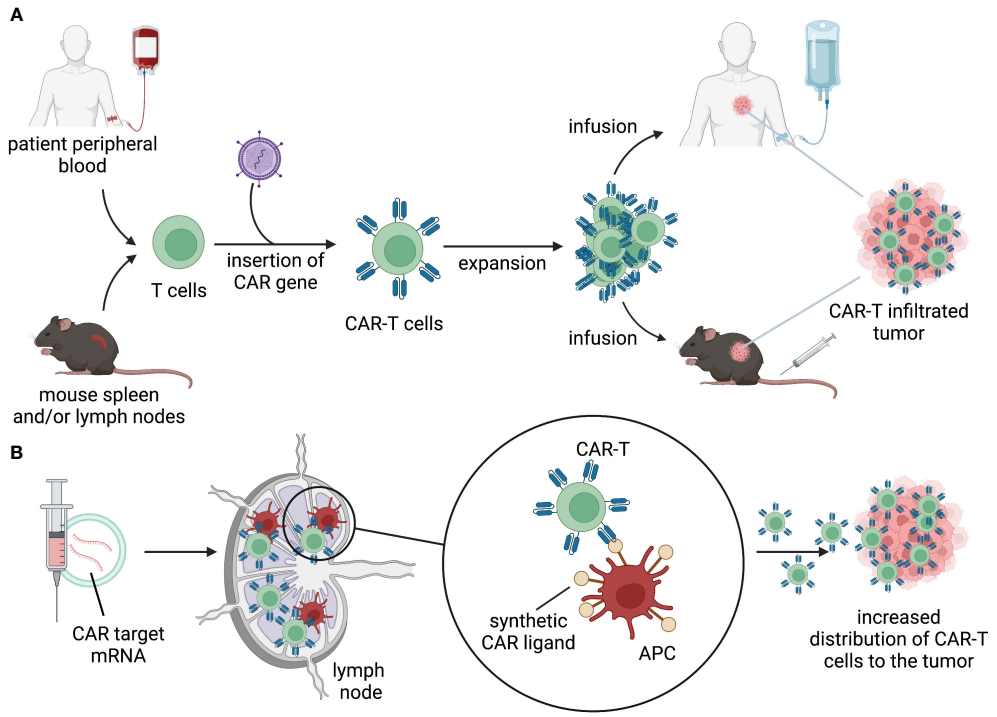

FIGURE 2
Distribution. **(A)** T cells isolated from patient's peripheral blood or mouse lymphoid organs are engineered to express a CAR. CAR-T cells are expanded ex vivo and infused back into the patient or in tumor-bearing mice. Upon infusion, CAR-T cells distribute through the body, migrate to the tumor, and kill target-expressing tumor cells. **(B)** delivery of mRNA-encoding CAR ligands using lipid nanoparticles (LNPs) to lymph nodes results in expression of the target by APC. Target-expressing APC prime and activate CAR-T cells, allowing for expansion and migration to the tumor.

promiscuous antigen expression can also impede cell expansion and distribution by diverting cells into non-tumor tissues, effectively excluding a portion of the transferred GML from their intended target.

The ideal antigen for tumor targeting would be uniquely expressed in the tumor and absent in normal tissues. However, for CAR-T therapy, such antigens are rare, with only a few examples like EGFRvIII and aberrantly glycosylated protein glycoforms such as Muc1 falling into this category (56, 57). Most CAR targets show a preference for tumor expression but are also detected in normal tissues. The most successful CAR targets have been observed in B cell malignancies, where normal expression occurs in cells that are apparently dispensable. Another wave of CAR targets is emerging, with lower levels of normal tissue expression but not complete absence. These targets aim to strike a balance between effective tumor targeting and minimizing off-target toxicities. It is challenging to achieve complete avoidance of target engagement in normal tissues, so efforts are focused on selecting targets with reduced normal tissue expression to mitigate potential toxicity while still enabling successful tumor targeting.

This expanded repertoire of CAR targets opens up new possibilities for successful immunotherapy beyond B cell malignancies, where targets expressed in dispensable tissues have shown promising outcomes. Preclinical mouse models provide certain examples where on-target, off-tumor toxicity can be monitored. However, it's important to note that these models often involve immunocompromised mice using mouse cross-reactive single-chain variable fragments (scF*vs*) or transgenic approaches to introduce the human antigen.

For instance, one study showed that a low-affinity Her2 CAR-T specifically targeted Her2-expressing tumors while avoiding accumulation in the mouse liver, where Her2 was artificially expressed using adenovirus (58). In another example, an affinity-tuned, mouse cross-reactive GPC3 CAR-T was able to avoid lethal toxicity against GPC3 expressed in the mouse lung and induce regression of human hepatocellular carcinoma tumors (59). However, caution must be exercised when interpreting off-tumor toxicities in mice, as some results may not align with human studies. For instance, a high-affinity GD2 CAR-T demonstrated lethal CNS toxicity in a mouse model of neuroblastoma (60), whereas human clinical trials using a similar GD2-targeted CAR-T via intravenous and intracerebroventricular therapy showed good tolerability without signs of off-tumor CNS toxicities (61).

In contrast to CAR therapy, GML TCR therapy offers access to certain tumor-specific targets, particularly due to its ability to recognize intracellular proteins presented as peptides in the context of the major histocompatibility complex (pMHC). These targets primarily fall into the categories of cancer-testis antigens, tumor-viral antigens, and mutant neoantigens. The presence of these unique tumor-specific targets presents opportunities for precise and personalized immunotherapy approaches.

GML TCR therapy allows for the targeting of antigens that are specifically expressed by tumor cells, offering potential advantages in terms of enhanced tumor specificity and reduced toxicity

compared to CAR therapy. This approach broadens the range of tumor-specific antigens that can be targeted, expanding the possibilities for developing effective treatments against various types of cancer. However, achieving broad targeting will necessitate the rapid development of personalized TCR-T therapies (62), which cannot be practically modeled in mice.

For the majority of the aforementioned targets, fully mouse surrogate CAR/TCR systems, transgenic mice, or cross-reactive mouse antibodies are not typically used in preclinical studies. While on-tumor activity can be measured, there remains a significant gap in the investigation of off-tumor inflammation and toxicity. Consequently, examples of off-tumor engagement by GML are predominantly observed in human clinical trials, and the overall implications for cell survival, distribution, and toxicity in these scenarios remain poorly understood.

Furthermore, it's worth noting that many GML TCR therapy approaches are often combined with interleukin-2 (IL-2) to enhance cellular expansion and persistence. However, the use of IL-2 in these therapies brings its own considerations and potential dose-limiting toxicities. These toxicities may include vascular leak syndrome, hypotension, and renal dysfunction. Modeling IL-2 toxicity in mice is challenging, primarily because mice can tolerate high levels of IL-2 without experiencing the dose-limiting toxicities observed in humans.

A recent advancement in GML engineering is the application of combinatorial antigen targeting technology. This approach aims to more precisely target tumor tissues while avoiding off-tumor inflammation and promoting optimal GML distribution. However, it is important to note that most logic-gated CAR-T systems have only been demonstrated at the preclinical level in mouse models.

Logic gating approaches typically involve two distinct binding events and can fall into different categories:

1. OR gating: Both antigen-binding fragments can simultaneously engage with the target and trigger signaling. This can occur through tandem engagement, where both antigen-binding molecules are joined and signal through a shared intracellular domain (ICD), or through the expression of separate CARs in a bicistronic format.
2. AND gating: Both antigen-binding fragments are required to engage the target in order to initiate signaling.
3. ON gating: The CAR is not expressed or fully functional until the addition of a second pharmacologic agent, which can be a small molecule, protein, or antibody-like drug. "Universal CARs" also fall in this category.
4. NOT gating: The second antigen-binding fragment can disable or "turn off" the signaling initiated by the first antigen binder, typically expressed in normal tissues.
5. IF … THEN gating: The first antigen binder drives signaling through a secondary transcription factor, leading to the expression of the second protein, which can be a fully competent CAR molecule.

While "OR" gated CAR-T, used in multiple dual and tandem formats, is being evaluated in clinical trials for hematologic malignancies, most logic-gating approaches have only been described and validated in preclinical studies in mice (63–66). Since most logic-gating strategies require two separate events to initiate signaling, they may have limitations such as leakiness or a loss of precise temporal control. For a more detailed discussion on the benefits and challenges associated with various logic-gating approaches to mitigate on-tumor, off-target toxicity, a recent review provides in-depth coverage (67).

An innovative approach aims to address some of the challenges faced by other technologies by combining distinct antigen binding domains with mutually dependent signaling domains downstream of the TCR complex. Researchers proposed coupling the intracellular domains (ICDs) of SLP76 and LAT to single-chain variable fragment (scFv) domains that recognize different antigens. By engineering mutations that prevent simultaneous binding of the Grb2 family member GADS, this approach creates a tightly regulated logic gate that has the potential to enable tumor-specific expansion of dual CAR-T cells (68).

The SLP76/LAT logic gate was validated using a commonly used xenograft model of acute lymphoblastic leukemia (NALM6) in NSG mice, where the tumor cells expressed ROR1 and CD19 antigens as dual targets. Encouragingly, this approach demonstrated an improved balance between efficacy and off-tumor toxicity compared to traditional "split CAR" and "Syn-NOTCH" logic-gating strategies. The development of technologies that provide more precise control over dual antigen targeting in the future may not only help in managing off-tumor toxicity but also enhance the distribution properties of CAR targeting molecules.

This advancement opens up possibilities for the exploration of dual-antigen-defined tumor types. It offers the potential for improved efficacy by combining the favorable attributes of TCR GML (tumor specificity) and CAR GML (targeting broader indications).

2.3 Distribution – cell priming strategies

To enhance GML expansion, strategies have been explored to mimic peripheral priming mechanisms in secondary lymphoid organs (SLO) by targeting oxygen, nutrient, and co-stimulatory ligand-accessible regions of the body. Initially, the concept of enhancing adoptive T cell therapy involved using viral-specific T cells as a platform for tumor-directed CAR or TCR transgenes. These priming responses can be engaged passively, through endogenous viral antigen presentation, or actively, via vaccination against the viral antigen (69, 70). In recent approaches, *in vitro* priming of CAR-T cells with oncolytic viruses through their native TCR has been combined with *in vivo* boosting, leading to impressive responses in preclinical models of melanoma and glioma (71).

Despite the early enthusiasm and adoption of viral-specific T cells as a CAR platform, and the development of innovative approaches to prime peripheral expansion of CAR-T, only a limited number of human clinical trials have been initiated using these approaches. It's important to note that most viral-specific T cells are being explored as an allogeneic platform due to their reduced potential for alloreactivity (NCT04288726, NCT03740256,

NCT01475058, NCT01430390). In addition to viral-specific T cells, other lymphocyte lineages such as NK cells, iNKT cells, γδ T cells, and MR1 T cells that can recognize non-MHC antigens in tumors may also be considered as GML platforms (72–75). While these alternative ACT platforms have the ability to naturally expand in the presence of their cognate ligands, similar to viral-specific T cell priming, and show potent responses in mouse models, it remains to be seen if they exhibit similar expansion and distribution potential to αβ CAR-T cells in human patients.

Recent synthetic approaches to enhance CAR-T expansion include "CAR vaccine" strategies, which involve the delivery of mRNA-encoded CAR ligands using lipid nanoparticles (LNPs) to lymph nodes (Figure 2B). This allows CAR-T cells to undergo *in vivo* expansion and stimulation in lymphatic regions. The CARVac strategy demonstrated that LNP-mediated delivery of the CLDN6 antigen to antigen-presenting cells (APCs) in the lymphoid compartments of mice could promote robust expansion of CLDN6 CAR-T cells and improved anti-tumor efficacy (76). Another approach involved *in vivo* expression of "amphiphile ligands" that could be delivered by LNPs and inserted into the membrane of APCs to present cognate ligands, facilitating GML proliferation (77, 78). Interestingly, neither of these approaches resulted in substantial elimination of the CAR-antigen expressing APCs. Clinical testing of CARVac is underway to enhance CAR-T expansion against CLDN6-positive solid tumors (NCT04503278). Although data generated in mouse models demonstrated a significant increase in expansion and improved anti-tumor efficacy, data from human trials are still in the early stages and inconclusive regarding the priming benefits of the "CAR vaccine" approach. Nonetheless, these and future strategies to safely enhance peripheral CAR-T expansion can be effectively modeled in mice and have the potential to drive GML activity using lower infused doses or lymphodepletion-free regimens.

3 Infiltration

Following successful systemic distribution, transferred immune cells may encounter various physical and chemical barriers as they navigate towards tumor-associated antigens and exert their cytotoxic function. In the case of hematologic malignancies, GML may not require extensive infiltration to encounter antigens. However, this is not the case for the majority of carcinomas. Fortunately, immune cells, such as T cells, possess receptors that facilitate extravasation from the vasculature into inflamed tissues and further penetration into the extracellular matrix (ECM) based on chemokine receptor expression, cytokines, and chemical gradients (79). While most CXC and CC chemokine receptors are already expressed on peripheral T cells at various activation stages (80), there are instances where enforced overexpression of these receptors enhances GML's ability to access tumors by leveraging native chemical gradients.

3.1 Infiltration – engineering chemotaxis

One important aspect of successful infiltration is the ability of T lymphocytes to undergo extravasation and chemotaxis towards sites of inflammation. Naturally circulating T cells acquire this capacity as a result of effector differentiation following antigen recognition and priming in secondary lymphoid organs (SLO). As described earlier, there are various methods to enhance GML priming using synthetic and natural mechanisms. Additionally, receptor overexpression in GML has been shown to augment their infiltration capacity. Some approaches focus on tumor-specific cues to modify chemotactic receptor expression, while others aim to increase lymphoid-homing capacity, recirculation, and survival in a more general manner, thereby enhancing anti-tumor function (81). Proof-of-mechanism for tumor-specific strategies primarily comes from engineered preclinical mouse models and xenograft model systems, where overexpression of the chemokine receptor can influence the infiltration and accumulation of CAR-T cells compared to their unmodified counterparts.Chemokine receptor overexpression in GML has been utilized to address potential trafficking deficiencies in solid tumors (Figure 3A). The strategic rationale behind these approaches is often similar:

1. Tumors are found to express sufficient levels of chemokine ligands, creating chemotactic gradients.
2. Peripheral T cells or endogenous tumor-infiltrating lymphocytes (TIL) show low levels or downregulation of the cognate or paired chemokine receptor(s).
3. Re-expression of the lost or downregulated receptor is shown to synthetically augment and/or restore infiltration in preclinical mouse models.

Examples of receptors engineered into GML include CCR2, CCR4, CXCR2, CXCR3, CXCR4, and CX3CR1 (82–88). Recent examples showed overexpression of CXCR2 enhanced infiltration of CAR-T hepatocellular carcinoma xenografts where the tumors were shown to express high levels of CXCR2 ligands including CCL2, CXCL1, CXCL2, and CXCL5 (89); CXCR1 overexpression enhanced T and NK CAR cells to migrate into ovarian or pancreatic tumors (90, 91) and CCR2 transduction into MSLN CAR-T cells enhanced migration into CCL2 positive malignant pleural mesotheliomas (86, 92). Although some of these examples exploit chemotactic gradients that may be generally expressed in inflamed tissues rather than specifically in tumors, a recent study used a tumor-specific strategy by forcing overexpression of the chemokine receptor CXCR6 on mesothelin-targeted CAR-T cells. This approach led to enhanced regression of pancreatic tumor xenografts. CXCR6, which is normally lowly expressed on peripheral blood T cells, is naturally attracted to its counterpart ligand CXCL16. In this case, CXCL16 was found to be highly expressed by malignant pancreatic epithelial cells, making it an attractive tumor-specific strategy (93).

Other strategies have been explored to improve infiltration and survival of transferred ACT without directly targeting the tumor. Some of these strategies involve factors such as IL-7/CCL19 or L-selectin overexpression to increase tumor penetration of ACT (81, 94). Notably, L-selectin overexpression in mice allowed for equivalent tumor infiltration and improved anti-tumor function of CAR-T cells by decreasing the activation threshold of the transferred cells, contrary to the presumed improvement in

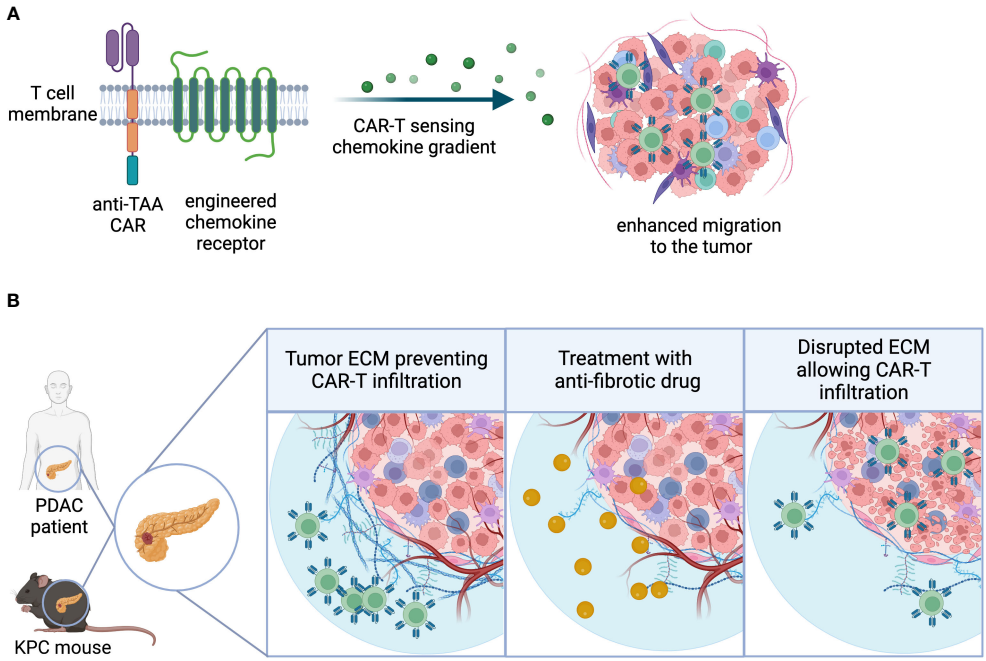

FIGURE 3
Infiltration. **(A)** Chemokine receptors can be engineered into CAR-T cells, enhancing the sensitivity to chemokine gradients and ultimately migration and infiltration to the tumor site. **(B)** Extracellular matrix-(ECM) rich tumor types physically restrict lymphocytic infiltration, creating an immune-excluded TME. Use of combination agents that directly or indirectly target tumor fibrosis may facilitate GML infiltration into the TME.

lymphoid organ homing. While these strategies have shown therapeutic merit in preclinical models, few have been validated in human clinical trials. It remains to be seen whether these strategies can enhance the success of GML-based solid tumor therapy.

A recent report suggested that ex vivo expansion of CAR-T cells in the presence of TGF-β could significantly enhance tumor infiltration and efficacy in xenograft tumor models (95). This approach aimed to epigenetically rewire peripheral blood T cells toward a resident memory T cell phenotype (T_{RM}), which would enhance accumulation and promote stemness of the transferred CAR-T cells targeting MSLN. In CAR-T_{RM} treated, regressing xenograft tumors, there was a marked increase in CAR-T cell infiltration, and depletion of CD103+ cells diminished the benefits of the so-called CAR-T_{RM} cells. Interestingly, overexpression of the T_{RM} transcription factor RUNX3, which had been used previously to enhance TRM expansion in murine tumor models, did not phenocopy the CAR-T_{RM} cells (96). This expansion strategy represented the first attempt to enhance CAR-T infiltration in murine models using ex vivo process engineering. Intriguingly, a similar protocol was used in human clinical trials to enhance neoantigen-directed TCR-T cells targeting mutant KRAS G12D pMHC (97). In this clinical trial, a TGF-β-based ex vivo expansion protocol was employed to enhance TCR-T cell infiltration in pancreatic ductal adenocarcinoma, leading to a dramatic reduction of lung lesions and a durable clinical response in one patient.

Another strategy to improve GML infiltration involves introducing chemotactic factors or cytokines into tumor-targeted therapeutics, such as engineered oncolytic viruses (OVs). Studies using mouse models demonstrated that intra-tumoral injection of adenovirus engineered to produce IL-15 and RANTES could promote GD2 CAR-T cell infiltration into solid tumors in immunocompromised mice (98), and this approach is also being explored in human clinical trials (NCT03740256). Subsequent efforts showed that intra-tumoral injection of OVs, such as vaccinia, could promote T cell infiltration by producing high systemic levels of CXCL11 (99). Other combinations propose introducing cytokine or immune checkpoint blockade (ICB) payloads into OVs, which, together with the oncolytic activity of the virus, can enhance CAR-T cell infiltration and survival in preclinical models of solid tumors (100–102). Unexpectedly, OV-mediated introduction of intra-tumoral Type 1 interferon (IFNβ) was shown to drive CAR-T cell apoptosis, which was prevented by deleting IFNAR1 in the engineered cells (103). Given that many OVs naturally induce the production of Type I interferon, a deeper understanding of the potential benefits, pitfalls, timing, and sequencing of combination OV and CAR-T therapy is warranted (104). The combination of OV and CAR-T therapy for solid tumors is a subject of ongoing research and a separate review (105).

3.2 Infiltration – navigating physical barriers

In addition to challenges posed by suboptimal chemotactic gradients, solid tumors often create physical barriers that promote immune exclusion. Immune exclusion can be caused by immune or non-immune stroma in the TME, which may impede immune cell

infiltration. The next section of this review will delve into the discussion of soluble and metabolic factors that contribute to immune exclusion. This section will primarily focus on tumors characterized by fibrogenic stromal cells, also known as cancer-associated fibroblasts (CAFs), which produce collagen-containing matrices that physically restrict lymphocytic infiltration. However, it is important to note that certain human tumors, such as pancreatic ductal adenocarcinoma, possess extensive stroma that cannot be accurately modeled in preclinical species. Despite this limitation, preclinical strategies have been developed to counteract non-immune stromal cells using CAR-T cells, either by directly eliminating CAFs or indirectly targeting stromal-derived barriers. In addition, use of combination agents that directly or indirectly target tumor fibrosis may represent an alternative strategy to improve GML infiltration into extracellular matrix-(ECM) rich tumor types (Figure 3B).

Developing strategies to target the extracellular matrix (ECM) presents multiple challenges. One of the key challenges is the development and validation of preclinical models that accurately replicate CAF-containing fibrogenic stroma observed in pancreatic, colon, hepatocellular, gastric, esophageal, head and neck, cervical, and breast cancers. While mouse models can partially capture certain aspects of fibrotic tumors, such as modeling the increased interstitial fluid pressure induced by fibrosis (106), they are likely to fall short in simulating the complexity of combining fibrosis-targeting agents with GML. Additionally, CAFs, like other components of the immune stroma, are heterogeneous and play diverse roles in cancer, some of which may not be adequately modeled in mice. Furthermore, fibrogenic stroma in humans often develops in the pre-metastatic niche, resulting from the recruitment of factors from the bone marrow and facilitating vascular access before tumor establishment. Most of the strategies mentioned above have been described using cell line-derived xenograft (CDX) or genetically engineered mouse models (GEMM), which rarely fully replicate the extent of stiff, fibrotic ECM seen in cancer patients.

Strategies encoded in GML to target fibrosis include directly eliminating fibrogenic cells in the tumor. One of the prominent targets on CAFs is the fibroblast-associated protein (FAP) (107–109). Murine reactive FAP CAR-T cells have shown effectiveness in multiple preclinical models, but potential toxicity concerns arise due to the depletion of FAP-expressing bone marrow stromal cells (110, 111). There have been limited opportunities to test this concept in human clinical trials, but FAP CAR-T cells appear to be tolerated at subtherapeutic doses (NCT01722149). Another genetic strategy to enhance access to ECM-rich tumors involves engineering CAR-T cells to secrete ECM-degrading enzymes, such as hyaluronidase or heparinase (112, 113). In both preclinical examples, the encoded and secreted enzymes did not interfere with CAR-T cell function and effectively degraded the matrix in mouse xenograft tumor models. Although these efforts have shown benefits in various murine models, there is limited proof-of-concept evidence from human clinical trials regarding ECM degradation and/or fibroblast targeting.

Myeloid cells can also impede GML infiltration into tumors. Targeting tumor-associated macrophages (TAMs) and myeloid-derived suppressor cells (MDSCs) broadly for depletion can be challenging due to potential toxicities. However, recent studies suggest that certain receptors may serve as tumor-specific targets, allowing for safer targeting of these suppressive cell types. For TAMs, targeting the folate receptor β (FRβ) with a CAR in syngeneic mouse models was shown to be safe and promoted increased infiltration of MSLN CAR-T cells in multiple tumor models (114). MDSC targeting was facilitated by a DR5 agonist costimulatory CAR expressed on the cell surface of Mucin 1 (MUC1) CAR-T cells (115). This approach demonstrated improved anti-tumor activity in an MDSC-admixed tumor model, presumably through increased infiltration, although direct evidence was not provided. Interestingly, the concept of targeting MDSCs with DR5 agonist antibodies has been previously tested in mice and humans, showing promising results and offering a novel approach to enhance GML infiltration (116, 117).

3.3 Infiltration – combination strategies

An indirect approach to disrupt factors that suppress lymphocytic infiltration involves tumor debulking through surgery, chemotherapy, or radiation. However, these therapies can have a dual effect as radiation and chemotherapy-resistant tumors often develop fibrosis as a consequence of treatment (118). This fibrotic response can vary depending on the therapeutic regimen but is a common outcome due to oxidative stress in the TME. To address therapy-induced fibrosis, targeted therapies have been explored to inhibit cancer-associated fibroblasts (CAFs), the extracellular matrix (ECM), or overall tumor architecture.

In terms of targeting the ECM, small molecule inhibitors of lysyl oxidase (LOX) and LOX-blocking antibodies have shown impressive activity in a GEMM of breast cancer. However, these approaches have not yet demonstrated success in human clinical trials (119, 120). Other small molecule inhibitors such as fasudil (ROCK inhibitor) and defacitinib (FAK inhibitor) have been used to attenuate focal adhesion signaling in tumor cells, influencing ECM remodeling by reducing matrix metalloproteinase (MMP) deposition and the desmoplastic response, respectively (121). Both fasudil and defacitinib have shown improved survival in mouse models of pancreatic cancer (LSL-KrasG12D/+; LSL-Trp53R172H/+;Pdx-1-Cre), and early-stage clinical trials combining defacitinib with immune checkpoint inhibitors (ICI) have demonstrated stable disease with increased T cell infiltration in post-treatment biopsies. Although there are currently no planned clinical studies with fasudil, its potential remains to be explored. Recombinant hyaluronidase or pegylated recombinant hyaluronidase 20 (PEGPH20) have been tested in combination with chemotherapy for pancreatic ductal adenocarcinoma (PDAC) based on strong combination activity observed in KPC mouse models (106). PEGPH20 was able to reduce interstitial fluid pressure (IFP) in these models and improve the response to chemotherapy (gemcitabine + nab-paclitaxel). However, a randomized controlled Phase III trial of this combination did not demonstrate a significant benefit. The reasons why the KPC mouse model was not predictive of an improved combination response remain unclear. Another preclinical strategy involves targeting discoidin

domain receptor 1 (DDR1) with neutralizing antibodies to disrupt collagen-containing stromal fibers (122). Targeting DDR1 to reduce collagen disposition enhanced the effects of chemotherapy and GML in orthotopic tumor models and mouse models of pancreatic cancer (KPC mice). To date, GML combinations with targeted inhibitors of ECM deposition have shown strong effects in multiple mouse models but have not translated successfully in clinical trials. This highlights the need to develop more predictive preclinical models of desmoplasia and matrix deposition to improve the infiltration of GML into tumors.

Administration of GML directly following chemotherapy may improve infiltration by exerting anti-fibrotic effects and shifting suppressive myeloid cells to a pro-inflammatory phenotype. Murad et al. demonstrated improved infiltration following chemotherapy in murine preclinical studies using cyclophosphamide prior to PSCA CAR-T administration in metastatic prostate and pancreatic cancer models (123). Interestingly, cyclophosphamide has been used to treat pulmonary fibrosis due to its lymphodepleting mechanism of action, which can suppress fibrotic inflammation (124). Alternative preconditioning therapies, such as fludarabine/cyclophosphamide (Flu/Cy) plus nab-paclitaxel (FNC), have been used in human clinical trials of CLDN18.2 CAR-T (125). These regimens, incorporating taxanes in addition to standard Flu/Cy, may improve GML efficacy by reducing tumor burden, conditioning the TME, and enhancing infiltration. However, there is a lack of preclinical mouse studies supporting the use of FNC preconditioning. The differences in metabolism of conventional chemotherapies between mice and humans make it challenging to model these combinations accurately, but exploring indication-specific regimens to improve responses should be considered.

Another potential approach to enhance GML infiltration involves intra-tumoral injection of surgically resected or debulked tumors to facilitate T cell-mediated clearance of minimal disease. Mouse models utilizing gel-embedded CAR-T have been described, demonstrating clearance of partially resected MSLN+ xenograft tumors (126). The fibrin gel-embedded MSLN CAR-T enabled clearance of tumor cells at the margin of surgical resection, minimizing on-target, off-tumor toxicity and complications associated with wound healing. The fibrin glue appeared to support CAR-T survival and infiltration into the tumor margin, clearing minimal residual tumor cells and preventing additional treatment-induced inflammation and fibrosis. A study to explore this approach in locally advanced breast cancer is planned.

4 Accumulation

In comparison to hematological malignancies, solid tumors present numerous challenges within the TME that hinder the activation and functionality of T cells, thereby limiting the efficacy of cell therapies (Figure 4A). Various factors within the TME can impede the successful accumulation and subsequent expansion of T cells, including metabolic properties (such as hypoxia, nutrient limitation, and ionic imbalance), the presence of suppressive cell types (such as TAMs, MDSCs, and Tregs), and the presence of suppressive cytokines or soluble factors (such as TGF-β and IL-10) (114, 127). Genetic engineering strategies for CAR-T cells aimed at counteracting the suppressive TME are commonly referred to as "armoring" approaches (128).

While there are diverse strategies to enhance the performance of CAR-T cells, a primary objective is to improve their accumulation within the TME. This can be achieved by enhancing their survival or promoting increased cell division rates. In this review, we classify accumulation strategies as either "defensive" or "offensive." Defensive strategies aim to protect GML from factors that suppress their proliferation or survival, while offensive strategies involve the elimination of suppressive cells or factors to facilitate GML accumulation (Figure 4B). To provide preclinical validation, we will also assess the feasibility of modeling these strategies in mice.

4.1 Accumulation - defensive strategies

4.1.1 Metabolism

T-cell metabolism plays a crucial role in determining both cell survival and the effectiveness of antitumor immune responses. However, understanding the intricate metabolic crosstalk between CAR-T cells and TME poses challenges for *in vitro* modeling. Therefore, the utilization of *in vivo* models becomes highly significant in dissecting the complex metabolic pathways involved in this interaction. Syngeneic models have emerged as valuable tools for investigating T-cell metabolism due to their flexibility in engineering specific immune subsets and accurately representing immune components within the TME.

Chang et al. utilized a sarcoma model expressing or lacking the spectrin-β2 antigen, which determines tumor rejection, to investigate T-cell fitness in different TMEs. Expanding upon these findings, the researchers further investigated T-cell metabolism using OT-I mice. Their groundbreaking work revealed a fundamental concept: the competition for glucose between CAR-T cells and the TME leads to reduced cytokine production and facilitates tumor growth (129). Additional insights into aerobic glycolysis-induced T-cell differentiation came from studies employing $CD4^{Cre}Ldha^{fl/fl}$ mice lacking LDHA in T cells. These studies demonstrated that aerobic glycolysis promotes effector T-cell differentiation, highlighting LDHA as a critical therapeutic target (130). Subsequently, transgenic PMEL-1 mice were used to explore the modulation of LDHA in cell therapy. This study demonstrated that the metabolic characteristics of antigen-specific T cells, along with their persistence, accumulation, and antitumor immunity, could be effectively modulated through the administration of exogenous cytokines (131).

The adjustment of T cells to hypoxic and nutrient-deprived tumors triggers a metabolic switch to glycolytic metabolism, primarily mediated by the transcription factor HIF-1α (132, 133). The critical role of HIF-1α in inducing T cell effector status has been demonstrated using HIF-1 or HIF-$2\alpha^{fl/fl}$ $dlck^{CRE}$ mice (134). However, under chronic hypoxia, this metabolic switch might lead to terminal differentiation, anergy, and exhaustion. This is particularly relevant for transferred lymphocytes, which lack access to native priming mechanisms that can maintain memory cell

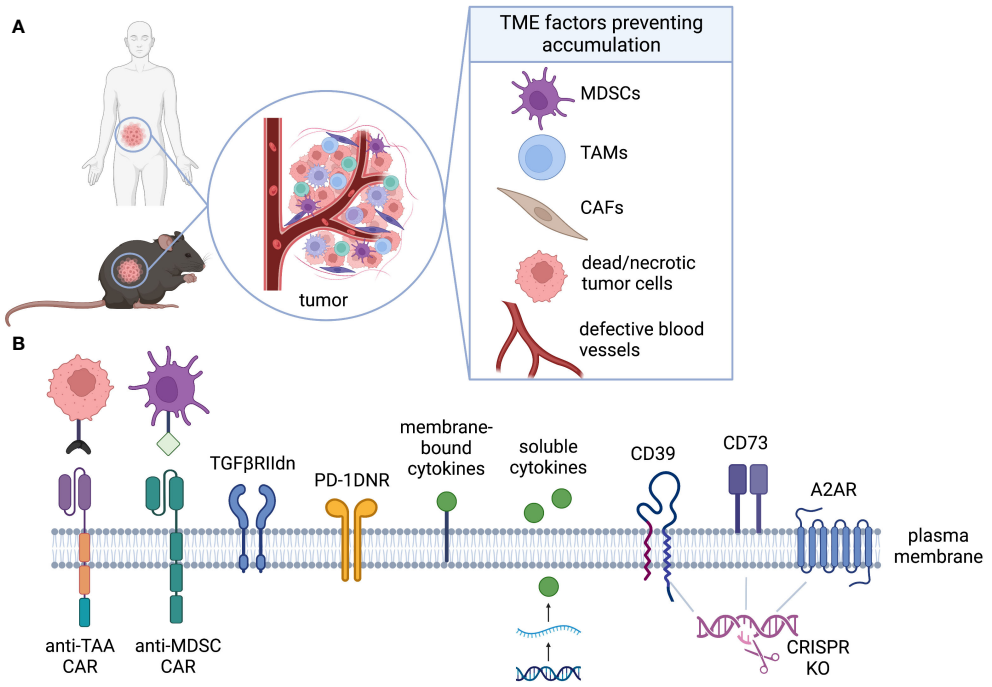

FIGURE 4
Accumulation. **(A)** The TME is rich of immunosuppressive factors that can inhibit CAR-T activation, proliferation, and accumulation even in presence of target antigen. **(B)** CAR-T can be engineered to alleviate distinct challenges of the TME. Armoring strategies can shield CAR-T cell, decreasing their sensitivity to inhibiting factors (TGFβ, PD-L1, adenosine), or can endow them with the ability to target immunosuppressive cells (anti-MDSCs).

persistence for extended periods. Therefore, rewiring the hypoxia response could potentially tailor T-cell differentiation, sustain persistence, and enhance antitumor responses in CAR-T cells.

Syngeneic mice have also played a critical role in exploring the importance of amino acids (such as arginine, tryptophan, and glutamine) in the biology of tumor-infiltrating lymphocytes (TILs). The scarcity of these amino acids in the TME can drive dysfunction of CAR-T cells and TILs. The essential role of arginine in T-cell activation, proliferation, and cytokine production has been demonstrated in TCR transgenic mouse models of CD4+ T cells specific for the influenza HA110–119 peptide (135). Sustained Arg1 activity require transport of arginine into the cell through cationic amino acid transporters. CAT2B is thought to be the most efficient in the transport of arginine into cells. Indeed, M-MDSCs or PMN-MDSCs derived from Cat2$^{-/-}$ mice adoptively transferred in tumor-bearing mice displayed a significantly reduced ability to inhibit T cell proliferation in *in vitro* assays (136). This was confirmed *in vivo* in a thymoma tumor model, where the anti-tumor activity of adoptively transferred antigen-specific CD8+ T cells was significantly enhanced in Cat2$^{-/-}$ *vs.* wild-type mice as a result of decreased ability of Cat2$^{-/-}$ MDSCs to suppress T cell function and proliferation (136, 137).

4.1.2 Soluble factors

In addition to its role in forcing metabolic reprogramming, hypoxia induces the accumulation of extracellular adenosine. The ectonucleotidases CD39 and CD73 lead to the sequential dephosphorylation of extracellular ATP and their expression on tumour cells, immune cells, fibroblasts, endothelial cells, and stromal cells is upregulated by hypoxia and TGFβ in the TME (138). Activated T effector cells can sense extracellular adenosine through the adenosine A2A receptor (A2AR), which triggers accumulation of intracellular cyclic adenosine monophosphate (cAMP) and limits TCR-mediated activation and expansion of effector T cells (139).

Numerous preclinical studies have demonstrated the potential advantages of inhibiting the adenosine pathway to augment the *in vivo* function of CAR-T cells (140–142). However, it is worth noting that the regulation of the adenosine pathway differs significantly between mice versus human. In mice, Tregs express CD39 and exhibit high levels of CD73 on their cell surface. This allows them to degrade ATP and generate adenosine, which has a dual impact: inhibiting effector T cells while enhancing the suppressive capabilities of Tregs (143, 144). Conversely, in the human T cell compartment, CD73 expression is primarily observed on the surface of naïve CD8 T cells and is only present in a small fraction of mature CD4 and CD8 memory T cells (145). Importantly, CD73 expression on Tregs is nearly absent, making the co-expression of CD73 with CD39 on Tregs a rare occurrence (146).

Transforming growth factor-β (TGFβ) is produced by multiple cells in the TME, and its expression is further enhanced by hypoxia (147). Due to its potent immunosuppressive effect and widespread presence in solid tumors, TGFβ has emerged as a popular target for cell therapy. Two commonly used strategies to modulate TGFβ activity involve the expression of dominant negative TGFβRII or targeted knockout (KO) of TGFβRII (148–155). The complex nature of TGFβ poses challenges for systemic therapies, as they

often result in a wide range of side effects. In contrast, intrinsic T cell approaches offer a more targeted solution that avoids these issues. However, it's important to note that testing the impact of TGFβ inhibition in cell therapy often relies on xenograft mouse models. While these models provide valuable insights, they do not fully replicate certain aspects such as lymphopenic proliferation following LDC or the interaction with endogenous adaptive immune cells, which are known to be influenced by TGFβ (156, 157). Therefore, the use of syngeneic or humanized murine models may be crucial to fully elucidate the effects of TGFβ-based armoring strategies on cell therapies.

4.1.3 Inhibitory molecules

Engineering inhibitory molecules to bypass negative signaling is a promising approach to enhance CAR-T cell accumulation. Inhibition of the programmed death-1 (PD-1) checkpoint pathway through the expression of a dominant negative PD-1 receptor (PD-1 DNR) has shown efficacy in enhancing the antitumor function of mesothelin-targeted CAR-T cells in xenograft models of pleural mesothelioma with high PD-1 expression (158). PD-1 DNR expression demonstrated superior efficacy compared to systemic PD-1 blockade, which required multiple doses to achieve effectiveness. Additionally, fusion receptors combining the PD-1 ectodomain and CD28 endodomain, known as switch receptors, have also been shown to enhance the antitumor function of CAR-T cells in xenograft models (158–160).

In addition to PD-1, CAR-T cells have been equipped with a dominant negative receptor for tumor necrosis factor receptor superfamily member 6 (TNFRSF6), also known as FAS. In syngeneic tumor models, expression of FAS DNR in CAR- or TCR-engineered T cells protected the cells from FAS ligand (FASL)-induced apoptosis, leading to improved *in vivo* persistence and tumor eradication (161). Lymphocyte activation gene-3 (LAG-3) knockout CAR-T cells have also been tested in xenograft models (162). However, when exploring inhibitory molecules like CTLA-4, which requires interaction with its ligands CD80 and CD86 expressed on myeloid cells, the use of syngeneic or humanized models becomes crucial (163).

4.2 Accumulation - offensive strategies

4.2.1 Cytokines

Improving the effectiveness of CAR T-cell therapy hinges on strategies that can shape the immune regulatory milieu within tumor tissue. In this context, offensive armoring strategies play a significant role. One approach is to engineer CAR-T cells with a transgenic cytokine that can overcome the insufficient production of pro-inflammatory factors in the TME. The transgenic cytokine can provide autocrine stimulation to sustain the survival and amplification of CAR-T cells, as well as paracrine modulation of the endogenous immune cell environment, thereby reducing systemic toxicity and remodeling the TME.

IL-12 has been studied as a cytokine for armoring CAR T cells, and its antitumor efficacy has been demonstrated in xenograft and immunocompetent syngeneic mouse models of ovarian cancer or hepatocellular carcinoma (164, 165). To further enhance the therapeutic potential of IL-12-secreting CAR T cells, Zhang et al. developed an NFAT-inducible membrane-bound IL-12, combining tumor-specific and inducible T-cell-mediated delivery with membrane-restricted localization (166). However, establishing a direct correlation between preclinical data and clinical toxicity remains challenging, as toxicity associated with IL-12 utilization is a primary concern. Variability in immune responses and toxicities, which occur in a dose-dependent manner, must be carefully considered in ongoing and future clinical trials (167).

IL-18 is another proinflammatory cytokine being explored in preclinical models and early clinical trials for cell therapy. Similar to IL-12, the efficacy of CAR T cells engineered to secrete IL-18 has been studied in xenograft and syngeneic mouse models (168, 169). Murine T cells expressing 19m28mz-P2A-mIL18 CAR were infused in C57BL/6 hCD19+/- mCD19+/- mouse model (169). This immune-competent, conditioning-dependent, tumor model uses systemic hCD19 modified EL4 (EL4[hCD19]) thymoma tumors infused into C57BL6 mice with a knockout murine CD19 (mCD19−/−), knock-in human CD19 (hCD19+/−) phenotype (C57BL6 [mCD19−/− hCD19+/−]) (170). These mice have restricted expression of one functional copy of the hCD19 gene in normal B cells, resulting in a retained immune-competent phenotype (170, 171). This model showed that IL-18 secreting CAR-T cells are efficacious in the absence of lymphodepleting chemotherapy. IL-18 secreting CD19 CAR-T demonstrated encouraging efficacy in an early clinical trials or the treatment of patients with relapsed/refractory B-cell non-Hodgkin lymphomas (NHL) or chronic lymphocytic leukemia (CLL) (NCT04684563) (172).

IL-15 is a pleiotropic cytokine that plays a role in innate and adaptive immune cell homeostasis and peripheral immune function. CD19 CAR T cells, IL-13Rα2 CAR T cells, and GD2 CAR T cells engineered to secrete IL-15 have shown increased expansion and *in vivo* anti-tumor activity in xenograft mouse models of Burkitt lymphoma, glioma, and metastatic neuroblastoma, respectively (173–175). However, there are concerns about prolonged exposure to IL-15, as IL-15 transgenic mice developed leukemia with a T-cell or NK-cell phenotype (176). The use of IL-15 to enhance the performance of CAR T cells will be further discussed in the section on longevity.

4.2.2 Direct targeting of immunosuppressive populations

Enhancing the accumulation of GML in the TME can be achieved by directly targeting and eliminating immunosuppressive cell populations, as discussed earlier for CAFs and MDSCs. Tumor-associated macrophages (TAMs) are another important target in cancer treatment due to their abundance in tumors and association with poor prognosis (177). One example of targeting TAMs is the use of CAR-T cells directed against CD123, which is expressed on both Hodgkin lymphoma (HL) cells and TAMs within the TME. These CAR-T cells recognize and eliminate both HL cells and TAMs, overcoming immunosuppression and exhibiting sustained clearance in xenograft models of progressive Hodgkin lymphoma. In mouse

models, rechallenging with the same tumor cell line resulted in controlled tumor growth, suggesting a protective memory response (178). However, caution should be exercised when interpreting long-term survival and persistence of T cells in immunocompromised mice, considering the role of homeostatic cytokines, potential compensatory mechanisms, and the broader context of human immunology.

Another approach involves equipping CAR-T cells with an additional CAR targeting FRβ, which is specifically expressed on immunosuppressive TAMs (114). Specific targeting and elimination of TAMs was addressed in the previous section as a means of improving infiltration into solid tumors, however, this strategy can have benefits in repolarizing the suppressive TME. In syngeneic murine tumour models of C57BL/6 mice bearing ID8 RFP-fLuc tumors (which lack mFRβ expression), transfer of CAR-T cells following cyclophosphamide preconditioning selectively eliminated FRβ+ TAMs, recruited pro-inflammatory monocytes and tumor-specific CD8+ T cells, and reduced tumor growth. This targeting approach shows promise in modulating TAMs and enhancing the antitumor immune response.

Regulatory T cells (Tregs) can also be targeted by cellular immunotherapies. However, systemic blockade of Tregs has led to life-threatening autoimmune side effects in patients due to depletion of CD25+ effector T cells. While there is early *in vitro* proof-of-concept showing that NK-92 cells expressing an anti-CD25 CAR can target Tregs, *in vivo* data are lacking, and concerns about on-target, off-tumor toxicity remain (179). *In vivo* studies in syngeneic models have shown that an immunotoxin targeting CD25 can selectively kill intratumoral Tregs while boosting endogenous immunity (180). Although incorporating such an approach into GML-based therapy is tempting, further studies are required to better understand the risk of on-target, off-tumor toxicities.

5 Longevity

One of the unique characteristics of GML which sets it apart from traditional therapeutics, is its ability to persist in the host for months or even years. This prolonged persistence enables GML to potentially drive long-term disease remission and provide ongoing immunosurveillance against residual tumor cells (Figure 5A). The potential for long-term persistence is becoming increasingly evident over time, as seen in patients with leukemia who have experienced 10 or more years of clinical remission with ongoing evidence of CD19 CAR-T cell function (181). While studies have demonstrated long-term engraftment of memory CD8 cells in mice through serial transfer (182), there is currently no known research on the persistent functional exposure of GML in mice.

Long-term engraftment of human T cells in NOD-scid IL2Rγnull (NSG) mice is complicated by xenograft-versus-host (xGvHD) immune-reactivity. This immune reactivity arises from both the MHC mismatch between human and mouse and the compromised immune system of the NSG mice, which is unable to reject the human T cell graft. Consequently, long-term engraftment studies in NSG mice may be confounded by toxicity that is specific to the model and may not accurately represent autologous GML therapy in humans. While NSG mice with Class I and Class II MHC knock-out can attenuate this toxicity (183, 184), they remain severely immunocompromised and may still generate xGvHD responses through the interaction of non-classical MHC molecules (e.g., CD1) or stress molecules (MICA/B) (185). Therefore, conducting short-term studies (~30 days) or using mouse models that can predict the consequences of long-term engraftment and endogenous immune conditioning and repertoire spreading may be more feasible and informative. Immunocompetent or syngeneic models, on the other hand, are not often used to study persistence due to challenges with T cell engineering, expansion, and the lack of models with slow tumor growth and endogenous antigen expression. Nonetheless, there are examples suggesting that transduced and expanded murine GML can be effective and persistent, and further development of these models is warranted (186).

Modifications aimed at enhancing GML longevity encompass various approaches, including alterations to intracellular domains, introduction of cytokines through genetic or pharmacological means, and deletion of intracellular inhibitory proteins that limit lymphocyte function, cytotoxicity, and persistence. These strategies not only promote the longevity of GML but can also be utilized to recruit endogenous lymphocytes, thereby extending the durability of the therapeutic response (Figure 5B).

5.1 Longevity – co-stimulatory domains

Early clinical trials with CD19 CAR T cells demonstrated that incorporating the 4-1BB co-stimulatory domain in the intracellular domain (ICD) of second-generation CARs, referred to as BBζ, resulted in enhanced persistence compared to CARs containing the CD28 co-stimulatory domain (CD28ζ). The enhanced persistence of BBζ CAR-T cells was attributed to 4-1BB's ability to activate TRAF/NF-κB signaling, promoting fatty acid oxidation and mitochondrial biogenesis, which contrasted with the predominantly glycolytic signaling downstream of CD28 (187). Clinical data showed that CD28ζ CAR-T persistence rarely exceeded 42 days (188, 189), while BBζ CAR-T persistence often exceeded 1 year in patients achieving complete responses (190).

Subsequent investigations consistently revealed distinct metabolic responses between CD28ζ and BBζ CAR-T cells, with CD28ζ CAR-T cells exhibiting a "fast burn" metabolic response driven by PI3K-induced aerobic glycolysis, and BBζ CAR-T cells displaying a "slow burn" oxidative metabolism primarily fueled by fatty acid breakdown, aligning with 4-1BB's role in T memory development and longevity (191). These findings indicated that the design of the CAR ICD can directly influence its persistence. Researchers have since developed various versions of second-generation CARs containing additional costimulatory domains such as ICOS and OX40 (192, 193), as well as third-generation CARs, aiming to enhance the balance between anti-tumor cytotoxicity and persistence (194, 195). While these versions have demonstrated strong activity in mouse xenograft tumor models using NSG mice, clinical evidence of persistence superior to second-generation BBζ CAR-T cells in humans is yet to be established (196).

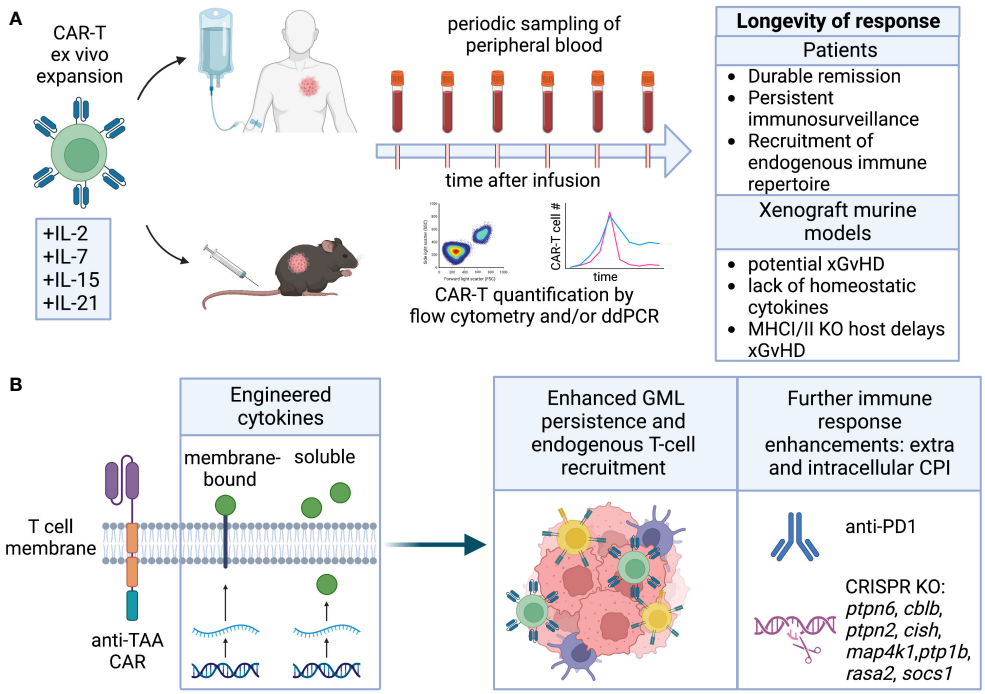

FIGURE 5
Longevity. **(A)** Cytokines employed for CAR-T ex vivo expansion can affect their differentiation and ability to self-renew and persist in the host upon infusion. Longevity is measured by quantification of CAR-T in peripheral blood, and results in durable remission. Persistence of human CAR-T in immunocompromised mice is complicated by potential GvHD and lack of homeostatic cytokines. **(B)** Engineering of cytokines enhancing CAR-T cell stemness and fitness directly or indirectly improves endogenous T cell recruitment. CRISPR KO of intracellular checkpoint inhibitors or combination with CPI blocking antibodies can further improve CAR-T persistence.

Although preclinical mouse models cannot fully replicate the persistence of engrafted T cells observed in humans, studies comparing BBζ and CD28ζ CAR-T cell performance in standard xenograft models have shown similar tumor-clearing effects between the two at high doses. However, at lower doses, BBζ CAR-T cells demonstrated functional superiority, indicating better memory conversion and resistance to the stress of low cell dosing (197). While mouse models can indirectly predict the longevity and persistence of GML based on the design of the CAR's intracellular domain (ICD), it is essential to acknowledge the limitations of these models in fully replicating the long-term engraftment and endogenous immune-conditioning observed in humans.

5.2 Longevity – role of cytokines

In clinical trials for TIL and TCR-T therapy, IL-2 is commonly used to support the function and persistence of the adoptively transferred cells. However, in the case of CAR-T therapy, IL-2 is rarely used to enhance CAR-T persistence. This may be attributed, in part, to the CAR-T cells' ability to produce paracrine IL-2 through the engagement of co-stimulatory CAR intracellular domains (ICD). Additionally, IL-2 is avoided in GML therapy due to the toxicities associated with higher doses needed to maintain the anti-tumor function of transferred T cells (198).

Recent advancements have led to the development of orthogonal versions of IL-2 that can be genetically engineered into CAR-T cells, promoting expansion and longevity with limited systemic toxicities (199, 200). By engineering CD19 CAR-T cells to express mutated IL-2Rβ receptors, which can only be activated by cell-encoded, mutated orthogonal IL-2 (ortho-IL-2), selectivity can be achieved without encountering the negative effects of IL-2 binding on wild-type T or NK cells. Two separate groups have described this mutant IL-2 "orthokine" pair and demonstrated its effectiveness in combination with suboptimal doses of CAR-T cells, leading to CAR-T expansion, tumor reduction, and persistence without the need for repeated CAR-T infusions. Interestingly, in preclinical xenograft models using NSG mice, higher doses of ortho-IL-2 were found to induce weight loss, although this toxicity was determined to be unrelated to xGvHD based on studies with TCR knockout mice. The authors speculated that the observed toxicity, which occurred at doses much higher than those required for tumor regression, was target-dependent, as weight loss and toxicity were observed in mice bearing NALM6 tumors but not in tumor-deficient mice (201). A human clinical trial testing the IL-2 orthokine and CAR-T pairing (STK-009) is currently enrolling patients with relapsed or refractory CD19 positive hematologic malignancies to evaluate the combination of autologous CD19 CAR-T cells with orthogonal IL-2 (201). This trial aims to assess the safety and efficacy of this approach in a clinical setting.

The differentiation status of T cells directly influences their longevity and antitumor activity. T cells with a stem-like phenotype, characterized by enhanced self-renewal and proliferation capacity, are associated with better clinical responses (202–207). Manipulating the differentiation status of T cells is a commonly explored strategy to improve the quality and efficacy of GML. Common-gamma chain cytokines such as IL-7 and IL-15 are frequently used in cell therapy to either promote a less differentiated product during the expansion stage or engineered into GML as an armoring strategy for *in vivo* enhancement (207).

IL-15 plays a crucial role in the homeostasis and development of CD8+ T cells by inhibiting activation-induced cell death (AICD) and upregulating antiapoptotic mediators like Mcl1 and Bcl-2 (208). IL-15-secreting CAR-T cells exhibited a less differentiated phenotype compared to unarmored CAR-T cells in a syngeneic model of subcutaneous B16 melanoma. They also showed reduced expression of PD1, prolonged persistence, and superior cellular activity (48). In another study, IL-15-armored CAR-T cells completely prevented tumor relapse in a xenograft model but were associated with severe liver toxicity and a GvHD score (209). Clinical studies have also reported IL-15 administration-related toxicity in cancer patients (210).

To mitigate IL-15 toxicity, researchers generated CD19 CAR-T cells that overexpressed both IL-15 and IL-15 receptor alpha. This strategy successfully blocked toxicity while maintaining the persistence and anti-tumor activity of CAR-T cells induced by IL-15 (209). However, the observed toxicity in mice is a subject of debate, as another study found that CD19 CAR-T cells expressing membrane-bound chimeric IL-15 delayed leukemia development, exhibited sustained resistance after tumor clearance, and generated long-lived TSCM cells without any associated toxicity (211).

Interleukin-7 (IL-7) plays a crucial role in enhancing the homeostasis and survival of memory and naïve T cells by upregulating Bcl-2 and repressing proapoptotic markers (212). Several studies have demonstrated that *in vitro* expansion of CAR-T cells with IL-7 leads to a higher frequency of cells exhibiting a memory stem cell phenotype (33). These cells retained a less differentiated phenotype and exhibited increased resistance to dysfunction upon repetitive encounters with antigens.

Early reports showed that constitutive expression of IL-7 enhanced the *in vivo* efficacy of CD19 CAR-T cells in a xenograft model of leukemia. However, it did not improve long-term persistence compared to CAR-T cells expressing IL-2 or IL-15 (213). IL-7-expressing CLDN18.2 CAR-T cells demonstrated increased proliferation, decreased apoptosis, and lower expression of exhaustion markers compared to unarmored CAR-T cells (214). However, IL-7 signaling specifically suppresses IL7Rα transcription as a homeostatic regulatory mechanism, promoting the survival of the maximum possible number of T cells given the available IL-7 (215).

To overcome the potential loss of IL-7 responsiveness, IL-7Rα was engineered into EBV-CTLs, resulting in an efficient response to IL-7 and *in vivo* activity in a xenograft model (216). Similarly, the introduction of a constitutively active IL-7 receptor (C7R) improved the *in vivo* antitumor activity of GD2-CAR-T cells in a xenograft model of metastatic neuroblastoma and EphA2-CAR-T cells in a orthotopic xenograft model of glioblastoma (217). It is important to note that GD2-CAR-T cells expressing C7R are currently being tested against relapsed or refractory neuroblastoma and other GD2-positive cancers (NCT03635632). Although autonomous or antigen-independent proliferation was not reported in this study, activating mutations of IL7R are present in 10% of pre-T-cell acute leukemias, raising concerns about unwanted proliferation associated with this approach.

Interleukin-21 (IL-21) is a crucial cytokine involved in regulating the function of CD8+ T cells and has emerged as a potential target for cancer immunotherapy. IL-21 enhances CD8+ T cell activity by promoting their proliferation, differentiation, and increasing the expression of cytotoxic molecules like perforin and granzyme B (218). Additionally, IL-21 indirectly enhances anti-tumor activity by promoting antibody production by B cells, aiding in targeting and killing tumor cells (219).

Recent studies have demonstrated the effectiveness of IL-21 in improving the anti-tumor effect of CAR-T cells. GPC3 CAR-T cells expressing IL-15 and IL-21 exhibited significantly greater anti-tumor efficacy in mice compared to CAR-T cells without IL-21 expression (220). These IL-21 expressing CAR-T cells are currently being evaluated in clinical trials for the treatment of hepatocellular carcinoma (HCC) (NCT02932956 and NCT02905188). Another study utilized NFAT-inducible secreted IL-21, which demonstrated increased anti-tumor efficacy in NSG mice and resistance to immune suppression induced by chronic lymphocytic leukemia cells (221). Engineered switch receptors have also been explored to provide IL-21 signaling. Wang et al. tested a receptor composed of the IL-4 ectodomain and the IL-21 endodomain and compared it to a receptor with the IL-7 endodomain (222). The IL-4/IL-21 inverted receptor conferred enhanced *in vivo* efficacy to GPC3 CAR-T cells against a xenograft model expressing varying levels of GPC3, compared to unarmored CAR-T cells or those with the IL-4/IL-7 inverted receptor. The study also observed a higher number of CD3+ T cells in the peripheral blood of mice receiving cells expressing the IL-4/IL-21 inverted receptor, indicating improved *in vivo* persistence (222). However, as previously mentioned, conclusions about *in vivo* persistence in xenograft models should be interpreted with caution.

Another interesting approach is the incorporation of a motif for STAT3 recruitment at the C-terminus of CD3ζ, enabling IL-21 signaling upon CAR engagement (223). CD19 CAR-T cells expressing this chimeric receptor demonstrated enhanced proliferation and cytokine polyfunctionality compared to control CAR-T cells in xenograft models of NALM6 human leukemia cells and subcutaneous CD19+ tumors, suggesting a key role for STAT3 in suppressing terminal differentiation of T cells (223–225).

5.3 Longevity – blocking inhibitory mechanisms

GML therapy can benefit from strategies that overcome co-inhibitory mechanisms, which naturally restrict long-term

proliferation of T cells. One approach is to induce intra-tumoral production of checkpoint inhibitor (CPI) antibodies, antibody-like fragments, or soluble PD1. Several studies have reported the use of CAR-T cells engineered to secrete constitutive or inducible CPI in mouse models (226–228). While these preclinical studies in xenograft mouse models have shown improved CAR-T function, such as enhanced expansion, cytolytic activity, or effector function, similar enhancements have not yet been observed in human clinical trials (229, 230). It is worth noting that the human trials utilized CPI in combination with CD19 CAR-T for CPI-insensitive indications, leaving open the possibility of using CPI-secreting CAR-T for CPI-sensitive tumors. However, since multiple versions of CPI antibodies are available as co-therapy, it remains unclear whether there are advantages or disadvantages to driving their expression from the GML itself. Further research is needed to elucidate the potential benefits and drawbacks of this approach.

Additional T cell checkpoints can hinder the expansion of GML, although their impact on longevity remains uncertain. Knocking down CTLA-4 expression using shRNA did not enhance the function or persistence of CD19 CAR-T cells based on 28ζ, but co-expression of CD80 alongside a first-generation CAR containing CD3ζ significantly increased expansion when CTLA-4 was knocked down (231). Currently, there are no known human clinical trials combining the CTLA-4 antibodies ipilumumab or tremelimumab with CAR-T or TCR-T. Trials testing CAR-T cells that produce CTLA-4 and PD1 antibodies against MUC1, EGFR, and MSLN are enrolling, but no preclinical or clinical data have been reported (NCT03179007, NCT03182816, NCT03182803). Blockade of LAG3 using CRISPR/Cas-mediated knockout did not show benefit in *in vitro* preclinical models but was not tested in mice (162). On the other hand, blockade of PD1 and Tim3, either alone or in combination, improved the activity of CD123-directed CAR-T cells in xenograft models of AML (232). Other T cell checkpoints include soluble molecules such as TGFβ and adenosine, which, as discussed in the previous section, can regulate both GML accumulation and longevity. Moreover, intracellular T cell checkpoints have been validated through gene deletion or expression of dominant-negative receptors (DNR), revealing additional mechanisms that can limit GML expansion. Several molecules, including SHP-1, CBLB, PTPN2, CISH, HPK1, PTP1B, RASA2, and SOCS1, have been identified as intrinsic checkpoints that can constrain T cell effector function, accumulation, and expansion (233–240). While targeting these intrinsic checkpoints individually is an active area of research, combinations of checkpoint deletions have also emerged (241). For instance, double knockout (DKO) of both regnase-1 and roquin-1 greatly increased T cell effector function, accumulation, and expansion in xenograft models compared to single knockout alone. However, the DKO also resulted in uncontrolled lymphoproliferation and toxicity in some mice. This finding emphasizes the need to understand the interaction of intracellular checkpoints in GML and develop mechanisms to prevent their uncontrolled expansion in patients, as unregulated persistence can have undesirable consequences.

6 Discussion

"All models are wrong, but some are useful" – George E.P. Box.

GML have transformed the therapeutic landscape for multiple B cell malignancies and are making steady progress into additional tumor types and even autoimmune diseases. As with any evolving therapeutic class, GML are undergoing continual modifications to improve their activity and safety profiles in order to broaden their applicability. As the diseases that can be targeted with GML are theoretically unlimited, the solution set for therapeutic design will inevitably diverge from those used for the treatment of B cell malignancies. In order for these designs to be validated and implemented, preclinical models are required.

Until robust three-dimensional or organotypic models that can recapitulate human tumor and normal tissue biology are readily available, GML development will continue to be dependent on the mouse as the default preclinical model to understand safety and efficacy profiles before human clinical trials. Mouse models for GML are simultaneously useful and distracting. They can be very useful to understand on-target activity and efficacy, acute GML expansion and pharmacodynamics, and proximal effector functions such as cytokine release. However, they are distracting in that they miss key aspects of GML challenges such as off-tumor toxicities, representative secondary cytokine secretion from myeloid, epithelial, or stromal cells, and control of metastatic and heterogenous disease similar to human tumors. Additional artifacts include xenograft-versus-host reactivity of human T cells engrafted in NSG mice, lack of validation of fully murinized GML designs and protocols, differences in lymphodepletion regimens, and studies in pathogen-free facilities that do not account for the influence of natural indigenous gut microbiota.

Due to the varied and unpredictable behavior of GML between mice and humans, a framework called "DIAL" has been developed to compartmentalize and study individual GML behaviors. The framework allows for understanding of aspects of the cell journey that can studied and optimized in isolation. For example, distribution studies which require vaccine-like cell priming can be studied using immunocompetent syngeneic mouse models while human GML manufacturing optimization may be best studied in NSG mice. Infiltration can be explored using genetically engineered mouse models that mimic tumor fibrosis (242), and early passage patient-derived xenograft (PDX) models in NOG or NSG mice might retain sufficient stroma to prevent immune-infiltration and exclude unmodified GML (243). PDX models can likewise be used to study accumulation, where native human tumor architecture, soluble factors, and hypoxia can affect GML survival. Likewise, syngeneic models can be deployed to complement the PDX model to capture immunosuppressive facets of TME that prevent accumulation. Strategies to enhance GML longevity can be limited due to technical factors such as development of xGvHD (NSG mice) and the challenges of optimizing murine GML manufacturing or treating rapidly growing tumors in most syngeneic models. Still, certain cytokines and intracellular designs have the potential to improve GML activity in NSG mice at

suboptimal doses, which can serve as surrogates for extended longevity. Longevity of GML response can also be demonstrated using tumor rechallenge studies in immunocompetent mice, demonstrating that GML-induced long-term immunity can be acquired via the expansion of endogenous anti-tumor T cells (244). These studies provide rationale for modification of GML with membrane bound cytokines or checkpoint inhibitors to bring about long-lasting remissions against heterogeneous tumors.

Following the success of CAR and TCR-T therapies in multiple tumor types, next-generation approaches will incorporate increasing complexity through genetic editing and engineering to augment GML functions. As each of these functions require validation through mechanistic and safety data, extensive preclinical testing in animals will be highly warranted if not required. While mice remain the most popular animal model for preclinical GML testing, canine and non-human primate (NHP) studies have also been conducted. Studies in non-murine species facilitate the study of unique GML attributes against tumors; canines present with spontaneous and heterogeneous tumors and are pathogen-exposed, as are several NHP species that provide the most genetically similar model to human, and present the most relevant model to recapitulate the consequences of LDC as well as allowing longitudinal sampling (245). Until non-murine models are more consistently used and understood, however, a mixture of murine models to deconstruct multiple GML functions will still be preferred. Future development of complex GML may benefit from co-evolution of efficient and specific murine and human gene-editing tools and vectors to more accurately predict these functions preclinically in order to decrease drug development cycle times, and improve efficacy and safety of the next wave of cell-based therapeutics.

Author contributions

GM: Conceptualization, Supervision, Writing – original draft, Writing – review & editing. MT: Writing – original draft, Writing – review & editing.

Funding

The author(s) declare that no financial support was received for the research, authorship, and/or publication of this article.

Acknowledgments

Figures were Created with BioRender.com. We thank Deborah Shuman for assistance with graphical conceptualization and design.

Conflict of interest

All authors are employees of AstraZeneca, PLC and have financial interest in the company.

Publisher's note

All claims expressed in this article are solely those of the authors and do not necessarily represent those of their affiliated organizations, or those of the publisher, the editors and the reviewers. Any product that may be evaluated in this article, or claim that may be made by its manufacturer, is not guaranteed or endorsed by the publisher.

References

1. Miller JF. Immunological function of the thymus. *Lancet* (1961) 2(7205):748–9. doi: 10.1016/S0140-6736(61)90693-6

2. Cerottini JC, Nordin AA, Brunner KT. *In vitro* cytotoxic activity of thymus cells sensitized to alloantigens. *Nature* (1970) 227(5253):72–3. doi: 10.1038/227072a0

3. Miller JF, Sprent J. Cell-to-cell interaction in the immune response. VI. Contribution of thymus-derived cells and antibody-forming cell precursors to immunological memory. *J Exp Med* (1971) 134(1):66–82. doi: 10.1084/jem.134.1.66

4. Rosenberg SA, Aebersold P, Cornetta K, Kasid A, Morgan RA, Moen R, et al. Gene transfer into humans–immunotherapy of patients with advanced melanoma, using tumor-infiltrating lymphocytes modified by retroviral gene transduction. *N Engl J Med* (1990) 323(9):570–8. doi: 10.1056/NEJM199008303230904

5. Rosenberg SA, Spiess P, Lafreniere R. A new approach to the adoptive immunotherapy of cancer with tumor-infiltrating lymphocytes. *Science* (1986) 233 (4770):1318–21. doi: 10.1126/science.3489291

6. Gross G, Waks T, Eshhar Z. Expression of immunoglobulin-T-cell receptor chimeric molecules as functional receptors with antibody-type specificity. *Proc Natl Acad Sci U S A* (1989) 86(24):10024–8. doi: 10.1073/pnas.86.24.10024

7. Maher J, Brentjens RJ, Gunset G, Riviere I, Sadelain M. Human T-lymphocyte cytotoxicity and proliferation directed by a single chimeric TCRzeta /CD28 receptor. *Nat Biotechnol* (2002) 20(1):70–5. doi: 10.1038/nbt0102-70

8. Imai C, Mihara K, Andreansky M, Nicholson IC, Pui CH, Geiger TL, et al. Chimeric receptors with 4-1BB signaling capacity provoke potent cytotoxicity against acute lymphoblastic leukemia. *Leukemia* (2004) 18(4):676–84. doi: 10.1038/sj.leu.2403302

9. Gong MC, Latouche JB, Krause A, Heston WD, Bander NH, Sadelain M. Cancer patient T cells genetically targeted to prostate-specific membrane antigen specifically lyse prostate cancer cells and release cytokines in response to prostate-specific membrane antigen. *Neoplasia* (1999) 1(2):123–7. doi: 10.1038/sj.neo.7900018

10. Brentjens RJ, Latouche JB, Santos E, Marti F, Gong MC, Lyddane C, et al. Eradication of systemic B-cell tumors by genetically targeted human T lymphocytes co-stimulated by CD80 and interleukin-15. *Nat Med* (2003) 9(3):279–86. doi: 10.1038/nm827

11. van der Stegen SJ, Hamieh M, Sadelain M. The pharmacology of second-generation chimeric antigen receptors. *Nat Rev Drug Discovery* (2015) 14(7):499–509. doi: 10.1038/nrd4597

12. Kochenderfer JN, Wilson WH, Janik JE, Dudley ME, Stetler-Stevenson M, Feldman SA, et al. Eradication of B-lineage cells and regression of lymphoma in a patient treated with autologous T cells genetically engineered to recognize CD19. *Blood* (2010) 116(20):4099–102. doi: 10.1182/blood-2010-04-281931

13. Johnson LA, Heemskerk B, Powell DJ Jr., Cohen CJ, Morgan RA, Dudley ME, et al. Gene transfer of tumor-reactive TCR confers both high avidity and tumor reactivity to nonreactive peripheral blood mononuclear cells and tumor-infiltrating lymphocytes. *J Immunol* (2006) 177(9):6548–59. doi: 10.4049/jimmunol.177.9.6548

14. Overwijk WW, Theoret MR, Finkelstein SE, Surman DR, de Jong LA, Vyth-Dreese FA, et al. Tumor regression and autoimmunity after reversal of a functionally tolerant state of self-reactive CD8+ T cells. *J Exp Med* (2003) 198(4):569–80. doi: 10.1084/jem.20030590

15. Harris JE, Harris TH, Weninger W, Wherry EJ, Hunter CA, Turka LA. A mouse model of vitiligo with focused epidermal depigmentation requires IFN-gamma for autoreactive CD8(+) T-cell accumulation in the skin. *J Invest Dermatol* (2012) 132 (7):1869–76. doi: 10.1038/jid.2011.463

16. Dudley ME, Wunderlich JR, Robbins PF, Yang JC, Hwu P, Schwartzentruber DJ, et al. Cancer regression and autoimmunity in patients after clonal repopulation with antitumor lymphocytes. *Science* (2002) 298(5594):850–4. doi: 10.1126/science.1076514

17. Research CfBEa and Administration FaD. Considerations for the development of chimeric antigen receptor (CAR) T cell products. (2022). Available at: https://www.

fda.gov/regulatory-information/search-fda-guidance-documents/considerations-development-chimeric-antigen-receptor-car-t-cell-products.

18. Zhu H, Melder RJ, Baxter LT, Jain RK. Physiologically based kinetic model of effector cell biodistribution in mammals: implications for adoptive immunotherapy. *Cancer Res* (1996) 56(16):3771–81.

19. Mackay CR, Marston WL, Dudler L. Naive and memory T cells show distinct pathways of lymphocyte recirculation. *J Exp Med* (1990) 171(3):801–17. doi: 10.1084/jem.171.3.801

20. Koya RC, Mok S, Comin-Anduix B, Chodon T, Radu CG, Nishimura MI, et al. Kinetic phases of distribution and tumor targeting by T cell receptor engineered lymphocytes inducing robust antitumor responses. *Proc Natl Acad Sci U S A* (2010) 107 (32):14286–91. doi: 10.1073/pnas.1008300107

21. Smith ME, Ford WL. The recirculating lymphocyte pool of the rat: a systematic description of the migratory behaviour of recirculating lymphocytes. *Immunology* (1983) 49(1):83–94.

22. Liu C, Ayyar VS, Zheng X, Chen W, Zheng S, Mody H, et al. Model-based cellular kinetic analysis of chimeric antigen receptor-T cells in humans. *Clin Pharmacol Ther* (2021) 109(3):716–27. doi: 10.1002/cpt.2040

23. Parente-Pereira AC, Burnet J, Ellison D, Foster J, Davies DM, van der Stegen S, et al. Trafficking of CAR-engineered human T cells following regional or systemic adoptive transfer in SCID beige mice. *J Clin Immunol* (2011) 31(4):710–8. doi: 10.1007/s10875-011-9532-8

24. Sallusto F, Lenig D, Forster R, Lipp M, Lanzavecchia A. Two subsets of memory T lymphocytes with distinct homing potentials and effector functions. *Nature* (1999) 401(6754):708–12. doi: 10.1038/44385

25. Khot A, Matsueda S, Thomas VA, Koya RC, Shah DK. Measurement and quantitative characterization of whole-body pharmacokinetics of exogenously administered T cells in mice. *J Pharmacol Exp Ther* (2019) 368(3):503–13. doi: 10.1124/jpet.118.252858

26. Rosenberg SA, Packard BS, Aebersold PM, Solomon D, Topalian SL, Toy ST, et al. Use of tumor-infiltrating lymphocytes and interleukin-2 in the immunotherapy of patients with metastatic melanoma. *A preliminary Rep N Engl J Med* (1988) 319 (25):1676–80. doi: 10.1056/NEJM198812223192527

27. Rosenberg SA, Yannelli JR, Yang JC, Topalian SL, Schwartzentruber DJ, Weber JS, et al. Treatment of patients with metastatic melanoma with autologous tumor-infiltrating lymphocytes and interleukin 2. *J Natl Cancer Inst* (1994) 86(15):1159–66. doi: 10.1093/jnci/86.15.1159

28. Gattinoni L, Lugli E, Ji Y, Pos Z, Paulos CM, Quigley MF, et al. A human memory T cell subset with stem cell-like properties. *Nat Med* (2011) 17(10):1290–7. doi: 10.1038/nm.2446

29. Sabatino M, Hu J, Sommariva M, Gautam S, Fellowes V, Hocker JD, et al. Generation of clinical-grade CD19-specific CAR-modified CD8+ memory stem cells for the treatment of human B-cell Malignancies. *Blood* (2016) 128(4):519–28. doi: 10.1182/blood-2015-11-683847

30. Turtle CJ, Hanafi LA, Berger C, Gooley TA, Cherian S, Hudecek M, et al. CD19 CAR-T cells of defined CD4+:CD8+ composition in adult B cell ALL patients. *J Clin Invest* (2016) 126(6):2123–38. doi: 10.1172/JCI85309

31. Cieri N, Camisa B, Cocchiarella F, Forcato M, Oliveira G, Provasi E, et al. IL-7 and IL-15 instruct the generation of human memory stem T cells from naive precursors. *Blood* (2013) 121(4):573–84. doi: 10.1182/blood-2012-05-431718

32. Barrett DM, Singh N, Liu X, Jiang S, June CH, Grupp SA, et al. Relation of clinical culture method to T-cell memory status and efficacy in xenograft models of adoptive immunotherapy. *Cytotherapy* (2014) 16(5):619–30. doi: 10.1016/j.jcyt.2013.10.013

33. Xu Y, Zhang M, Ramos CA, Durett A, Liu E, Dakhova O, et al. Closely related T-memory stem cells correlate with in *vivo* expansion of CAR.CD19-T cells and are preserved by IL-7 and IL-15. *Blood* (2014) 123(24):3750–9. doi: 10.1182/blood-2014-01-552174

34. Gattinoni L, Zhong XS, Palmer DC, Ji Y, Hinrichs CS, Yu Z, et al. Wnt signaling arrests effector T cell differentiation and generates CD8+ memory stem cells. *Nat Med* (2009) 15(7):808–13. doi: 10.1038/nm.1982

35. Zheng W, O'Hear CE, Alli R, Basham JH, Abdelsamed HA, Palmer LE, et al. PI3K orchestration of the in *vivo* persistence of chimeric antigen receptor-modified T cells. *Leukemia* (2018) 32(5):1157–67. doi: 10.1038/s41375-017-0008-6

36. Klebanoff CA, Crompton JG, Leonardi AJ, Yamamoto TN, Chandran SS, Eil RL, et al. Inhibition of AKT signaling uncouples T cell differentiation from expansion for receptor-engineered adoptive immunotherapy. *JCI Insight* (2017) 2(23):e95103. doi: 10.1172/jci.insight.95103

37. Pilipow K, Scamardella E, Puccio S, Gautam S, De Paoli F, Mazza EM, et al. Antioxidant metabolism regulates CD8+ T memory stem cell formation and antitumor immunity. *JCI Insight* (2018) 3(18):e122299. doi: 10.1172/jci.insight.122299

38. Foskolou IP, Barbieri L, Vernet A, Bargiela D, Cunha PP, Velica P, et al. The S enantiomer of 2-hydroxyglutarate increases central memory CD8 populations and improves CAR-T therapy outcome. *Blood Adv* (2020) 4(18):4483–93. doi: 10.1182/bloodadvances.2020002309

39. Xia L, Liu JY, Zheng ZZ, Chen YJ, Ding JC, Hu YH, et al. BRD4 inhibition boosts the therapeutic effects of epidermal growth factor receptor-targeted chimeric antigen receptor T cells in glioblastoma. *Mol Ther* (2021) 29(10):3011–26. doi: 10.1016/j.ymthe.2021.05.019

40. Zhao Z, Condomines M, van der Stegen SJC, Perna F, Kloss CC, Gunset G, et al. Structural design of engineered costimulation determines tumor rejection kinetics and persistence of CAR T cells. *Cancer Cell* (2015) 28(4):415–28. doi: 10.1016/j.ccell.2015.09.004

41. Goff SL, Morgan RA, Yang JC, Sherry RM, Robbins PF, Restifo NP, et al. Pilot trial of adoptive transfer of chimeric antigen receptor-transduced T cells targeting EGFRvIII in patients with glioblastoma. *J Immunother* (2019) 42(4):126–35. doi: 10.1097/CJI.0000000000000260

42. Lugli E, Dominguez MH, Gattinoni L, Chattopadhyay PK, Bolton DL, Song K, et al. Superior T memory stem cell persistence supports long-lived T cell memory. *J Clin Invest* (2013) 123(2):594–9. doi: 10.1172/JCI66327

43. Cao H, Kim DH, Howard A, Moz H, Wasnik S, Baylink DJ, et al. Ex vivo isolation, expansion and bioengineering of CCR7+CD95-/or CD62L+CD45RA+ tumor infiltrating lymphocytes from acute myeloid leukemia patients' bone marrow. *Neoplasia* (2021) 23(12):1252–60. doi: 10.1016/j.neo.2021.11.003

44. Kishton RJ, Vodnala SK, Vizcardo R, Restifo NP. Next generation immunotherapy: enhancing stemness of polyclonal T cells to improve anti-tumor activity. *Curr Opin Immunol* (2022) 74:39–45. doi: 10.1016/j.coi.2021.10.001

45. Ghassemi S, Durgin JS, Nunez-Cruz S, Patel J, Leferovich J, Pinzone M, et al. Rapid manufacturing of non-activated potent CAR T cells. *Nat BioMed Eng* (2022) 6 (2):118–28. doi: 10.1038/s41551-021-00842-6

46. Dickinson MJ, Barba P, Jager U, Shah NN, Blaise D, Briones J, et al. A novel autologous CAR-T therapy, YTB323, with preserved T-cell stemness shows enhanced CAR T-cell efficacy in preclinical and early clinical development. *Cancer Discovery* (2023) 13(9):1982–97. doi: 10.1158/2159-8290.24091927.v1

47. Lee J, Sadelain M, Brentjens R. Retroviral transduction of murine primary T lymphocytes. *Methods Mol Biol* (2009) 506:83–96. doi: 10.1007/978-1-59745-409-4_7

48. Lanitis E, Rota G, Kosti P, Ronet C, Spill A, Seijo B, et al. Optimized gene engineering of murine CAR-T cells reveals the beneficial effects of IL-15 coexpression. *J Exp Med* (2021) 218(2):e20192203. doi: 10.1084/jem.20192203

49. Gautam S, Fioravanti J, Zhu W, Le Gall JB, Brohawn P, Lacey NE, et al. The transcription factor c-Myb regulates CD8(+) T cell stemness and antitumor immunity. *Nat Immunol* (2019) 20(3):337–49. doi: 10.1038/s41590-018-0311-z

50. Hanada KI, Yu Z, Chappell GR, Park AS, Restifo NP. An effective mouse model for adoptive cancer immunotherapy targeting neoantigens. *JCI Insight* (2019) 4(10): e124405. doi: 10.1172/jci.insight.124405

51. Vodnala SK, Eil R, Kishton RJ, Sukumar M, Yamamoto TN, Ha NH, et al. T cell stemness and dysfunction in tumors are triggered by a common mechanism. *Science* (2019) 363(6434):eaau0135. doi: 10.1126/science.aau0135

52. Klebanoff CA, Scott CD, Leonardi AJ, Yamamoto TN, Cruz AC, Ouyang C, et al. Memory T cell-driven differentiation of naive cells impairs adoptive immunotherapy. *J Clin Invest* (2016) 126(1):318–34. doi: 10.1172/JCI81217

53. Sukumar M, Liu J, Mehta GU, Patel SJ, Roychoudhuri R, Crompton JG, et al. Mitochondrial membrane potential identifies cells with enhanced stemness for cellular therapy. *Cell Metab* (2016) 23(1):63–76. doi: 10.1016/j.cmet.2015.11.002

54. Corria-Osorio J, Carmona SJ, Stefanidis E, Andreatta M, Ortiz-Miranda Y, Muller T, et al. Orthogonal cytokine engineering enables novel synthetic effector states escaping canonical exhaustion in tumor-rejecting CD8(+) T cells. *Nat Immunol* (2023) 24(5):869–83. doi: 10.1038/s41590-023-01477-2

55. Hu X, Majchrzak K, Liu X, Wyatt MM, Spooner CJ, Moisan J, et al. *In vitro* priming of adoptively transferred T cells with a RORgamma agonist confers durable memory and stemness in vivo. *Cancer Res* (2018) 78(14):3888–98. doi: 10.1158/0008-5472.CAN-17-3973

56. Kuan CT, Wikstrand CJ, Archer G, Beers R, Pastan I, Zalutsky MR, et al. Increased binding affinity enhances targeting of glioma xenografts by EGFRvIII-specific scFv. *Int J Cancer* (2000) 88(6):962–9. doi: 10.1002/1097-0215(20001215)88:6<962::AID-IJC20>3.0.CO;2-U

57. Van Elssen CH, Frings PW, Bot FJ, Van de Vijver KK, Huls MB, Meek B, et al. Expression of aberrantly glycosylated Mucin-1 in ovarian cancer. *Histopathology* (2010) 57(4):597–606. doi: 10.1111/j.1365-2559.2010.03667.x

58. Castellarin M, Sands C, Da T, Scholler J, Graham K, Buza E, et al. A rational mouse model to detect on-target, off-tumor CAR T cell toxicity. *JCI Insight* (2020) 5 (14):e136012. doi: 10.1172/jci.insight.136012

59. Giardino Torchia ML, Gilbreth R, Merlino A, Sult E, Monks N, Chesebrough J, et al. Rational design of chimeric antigen receptor T cells against glypican 3 decouples toxicity from therapeutic efficacy. *Cytotherapy* (2022) 24(7):720–32. doi: 10.1016/j.jcyt.2022.03.008

60. Richman SA, Nunez-Cruz S, Moghimi B, Li LZ, Gershenson ZT, Mourelatos Z, et al. High-affinity GD2-specific CAR T cells induce fatal encephalitis in a preclinical neuroblastoma model. *Cancer Immunol Res* (2018) 6(1):36–46. doi: 10.1158/2326-6066.CIR-17-0211

61. Majzner RG, Ramakrishna S, Yeom KW, Patel S, Chinnasamy H, Schultz LM, et al. GD2-CAR T cell therapy for H3K27M-mutated diffuse midline gliomas. *Nature* (2022) 603(7903):934–41. doi: 10.1038/s41586-022-04489-4

62. Levy PL, Gros A. Fast track to personalized TCR T cell therapies. *Cancer Cell* (2022) 40(5):447–9. doi: 10.1016/j.ccell.2022.04.013

63. Wilkie S, van Schalkwyk MC, Hobbs S, Davies DM, van der Stegen SJ, Pereira AC, et al. Dual targeting of ErbB2 and MUC1 in breast cancer using chimeric antigen

receptors engineered to provide complementary signaling. *J Clin Immunol* (2012) 32 (5):1059–70. doi: 10.1007/s10875-012-9689-9

64. Kloss CC, Condomines M, Cartellieri M, Bachmann M, Sadelain M. Combinatorial antigen recognition with balanced signaling promotes selective tumor eradication by engineered T cells. *Nat Biotechnol* (2013) 31(1):71–5. doi: 10.1038/nbt.2459

65. Fedorov VD, Themeli M, Sadelain M. PD-1- and CTLA-4-based inhibitory chimeric antigen receptors (iCARs) divert off-target immunotherapy responses. *Sci Transl Med* (2013) 5(215):215ra172. doi: 10.1126/scitranslmed.3006597

66. Srivastava S, Salter AI, Liggitt D, Yechan-Gunja S, Sarvothama M, Cooper K, et al. Logic-gated ROR1 chimeric antigen receptor expression rescues T cell-mediated toxicity to normal tissues and enables selective tumor targeting. *Cancer Cell* (2019) 35 (3):489–503.e8. doi: 10.1016/j.ccell.2019.02.003

67. Flugel CL, Majzner RG, Krenciute G, Dotti G, Riddell SR, Wagner DL, et al. Overcoming on-target, off-tumour toxicity of CAR T cell therapy for solid tumours. *Nat Rev Clin Oncol* (2023) 20(1):49–62. doi: 10.1038/s41571-022-00704-3

68. Tousley AM, Rotiroti MC, Labanieh L, Rysavy LW, Kim WJ, Lareau C, et al. Co-opting signalling molecules enables logic-gated control of CAR T cells. *Nature* (2023) 615(7952):507–16. doi: 10.1038/s41586-023-05778-2

69. Caruana I, Weber G, Ballard BC, Wood MS, Savoldo B, Dotti G. K562-derived whole-cell vaccine enhances antitumor responses of CAR-redirected virus-specific cytotoxic T lymphocytes in vivo. *Clin Cancer Res* (2015) 21(13):2952–62. doi: 10.1158/1078-0432.CCR-14-2998

70. Tanaka M, Tashiro H, Omer B, Lapteva N, Ando J, Ngo M, et al. Vaccination targeting native receptors to enhance the function and proliferation of chimeric antigen receptor (CAR)-modified T cells. *Clin Cancer Res* (2017) 23(14):3499–509. doi: 10.1158/1078-0432.CCR-16-2138

71. Evgin L, Kottke T, Tonne J, Thompson J, Huff AL, van Vloten J, et al. Oncolytic virus-mediated expansion of dual-specific CAR T cells improves efficacy against solid tumors in mice. *Sci Transl Med* (2022) 14(640):eabn2231. doi: 10.1126/scitranslmed.abn2231

72. Liu E, Marin D, Banerjee P, Macapinlac HA, Thompson P, Basar R, et al. Use of CAR-transduced natural killer cells in CD19-positive lymphoid tumors. *N Engl J Med* (2020) 382(6):545–53. doi: 10.1056/NEJMoa1910607

73. Makkouk A, Yang XC, Barca T, Lucas A, Turkoz M, Wong JTS, et al. Off-the-shelf Vdelta1 gamma delta T cells engineered with glypican-3 (GPC-3)-specific chimeric antigen receptor (CAR) and soluble IL-15 display robust antitumor efficacy against hepatocellular carcinoma. *J Immunother Cancer* (2021) 9(12):e003441. doi: 10.1136/jitc-2021-003441

74. Simonetta F, Lohmeyer JK, Hirai T, Maas-Bauer K, Alvarez M, Wenokur AS, et al. Allogeneic CAR invariant natural killer T cells exert potent antitumor effects through host CD8 T-cell cross-priming. *Clin Cancer Res* (2021) 27(21):6054–64. doi: 10.1158/1078-0432.CCR-21-1329

75. Crowther MD, Dolton G, Legut M, Caillaud ME, Lloyd A, Attaf M, et al. Genome-wide CRISPR-Cas9 screening reveals ubiquitous T cell cancer targeting *via* the monomorphic MHC class I-related protein MR1. *Nat Immunol* (2020) 21(2):178–85. doi: 10.1038/s41590-019-0578-8

76. Reinhard K, Rengstl B, Oehm P, Michel K, Billmeier A, Hayduk N, et al. An RNA vaccine drives expansion and efficacy of claudin-CAR-T cells against solid tumors. *Science* (2020) 367(6476):446–53. doi: 10.1126/science.aay5967

77. Ma L, Dichwalkar T, Chang JYH, Cossette B, Garafola D, Zhang AQ, et al. Enhanced CAR-T cell activity against solid tumors by vaccine boosting through the chimeric receptor. *Science* (2019) 365(6449):162–8. doi: 10.1126/science.aav8692

78. Ma L, Hostetler A, Morgan DM, Maiorino L, Sulkaj I, Whittaker CA, et al. Vaccine-boosted CAR T crosstalk with host immunity to reject tumors with antigen heterogeneity. *Cell* (2023). doi: 10.1136/jitc-2023-SITC2023.0286

79. Vaday GG, Franitza S, Schor H, Hecht I, Brill A, Cahalon L, et al. Combinatorial signals by inflammatory cytokines and chemokines mediate leukocyte interactions with extracellular matrix. *J Leukoc Biol* (2001) 69(6):885–92. doi: 10.1189/jlb.69.6.885

80. Ward SG, Westwick J. Chemokines: understanding their role in T-lymphocyte biology. *Biochem J* (1998) 333(Pt 3):457–70. doi: 10.1042/bj3330457

81. Adachi K, Kano Y, Nagai T, Okuyama N, Sakoda Y, Tamada K. IL-7 and CCL19 expression in CAR-T cells improves immune cell infiltration and CAR-T cell survival in the tumor. *Nat Biotechnol* (2018) 36(4):346–51. doi: 10.1038/nbt.4086

82. Rapp M, Grassmann S, Chaloupka M, Layritz P, Kruger S, Ormanns S, et al. C-C chemokine receptor type-4 transduction of T cells enhances interaction with dendritic cells, tumor infiltration and therapeutic efficacy of adoptive T cell transfer. *Oncoimmunology* (2016) 5(3):e1105428. doi: 10.1080/2162402X.2015.1105428

83. Garetto S, Sardi C, Martini E, Roselli G, Morone D, Angioni R, et al. Tailored chemokine receptor modification improves homing of adoptive therapy T cells in a spontaneous tumor model. *Oncotarget* (2016) 7(28):43010–26. doi: 10.18632/oncotarget.9280

84. Siddiqui I, Erreni M, van Brakel M, Debets R, Allavena P. Enhanced recruitment of genetically modified CX3CR1-positive human T cells into Fractalkine/CX3CL1 expressing tumors: importance of the chemokine gradient. *J Immunother Cancer* (2016) 4:21. doi: 10.1186/s40425-016-0125-1

85. Muller N, Michen S, Tietze S, Topfer K, Schulte A, Lamszus K, et al. Engineering NK cells modified with an EGFRvIII-specific chimeric antigen receptor to overexpress CXCR4 improves immunotherapy of CXCL12/SDF-1alpha-secreting glioblastoma. *J Immunother* (2015) 38(5):197–210. doi: 10.1097/CJI.0000000000000082

86. Moon EK, Carpenito C, Sun J, Wang LC, Kapoor V, Predina J, et al. Expression of a functional CCR2 receptor enhances tumor localization and tumor eradication by retargeted human T cells expressing a mesothelin-specific chimeric antibody receptor. *Clin Cancer Res* (2011) 17(14):4719–30. doi: 10.1158/1078-0432.CCR-11-0351

87. Peng W, Ye Y, Rabinovich BA, Liu C, Lou Y, Zhang M, et al. Transduction of tumor-specific T cells with CXCR2 chemokine receptor improves migration to tumor and antitumor immune responses. *Clin Cancer Res* (2010) 16(22):5458–68. doi: 10.1158/1078-0432.CCR-10-0712

88. Li K, Zhu Z, Luo J, Fang J, Zhou H, Hu M, et al. Impact of chemokine receptor CXCR3 on tumor-infiltrating lymphocyte recruitment associated with favorable prognosis in advanced gastric cancer. *Int J Clin Exp Pathol* (2015) 8(11):14725–32.

89. Liu G, Rui W, Zheng H, Huang D, Yu F, Zhang Y, et al. CXCR2-modified CAR-T cells have enhanced trafficking ability that improves treatment of hepatocellular carcinoma. *Eur J Immunol* (2020) 50(5):712–24. doi: 10.1002/eji.201948457

90. Jin L, Tao H, Karachi A, Long Y, Hou AY, Na M, et al. CXCR1- or CXCR2-modified CAR T cells co-opt IL-8 for maximal antitumor efficacy in solid tumors. *Nat Commun* (2019) 10(1):4016. doi: 10.1038/s41467-019-11869-4

91. Ng YY, Tay JCK, Wang S. CXCR1 expression to improve anti-cancer efficacy of intravenously injected CAR-NK cells in mice with peritoneal xenografts. *Mol Ther Oncolytics* (2020) 16:75–85. doi: 10.1016/j.omto.2019.12.006

92. Wang Y, Wang J, Yang X, Yang J, Lu P, Zhao L, et al. Chemokine receptor CCR2b enhanced anti-tumor function of chimeric antigen receptor T cells targeting mesothelin in a non-small-cell lung carcinoma model. *Front Immunol* (2021) 12:628906. doi: 10.3389/fimmu.2021.628906

93. Lesch S, Blumenberg V, Stoiber S, Gottschlich A, Ogonek J, Cadilha BL, et al. T cells armed with C-X-C chemokine receptor type 6 enhance adoptive cell therapy for pancreatic tumours. *Nat BioMed Eng* (2021) 5(11):1246–60. doi: 10.1038/s41551-021-00737-6

94. Watson HA, Durairaj RRP, Ohme J, Alatsatianos M, Almutairi H, Mohammed RN, et al. L-selectin enhanced T cells improve the efficacy of cancer immunotherapy. *Front Immunol* (2019) 10:1321. doi: 10.3389/fimmu.2019.01321

95. Jung IY, Noguera-Ortega E, Bartoszek R, Collins SM, Williams E, Davis M, et al. Tissue-resident memory CAR T cells with stem-like characteristics display enhanced efficacy against solid and liquid tumors. *Cell Rep Med* (2023) 4(6):101053. doi: 10.1016/j.xcrm.2023.101053

96. Milner JJ, Toma C, Yu B, Zhang K, Omilusik K, Phan AT, et al. Runx3 programs CD8(+) T cell residency in non-lymphoid tissues and tumours. *Nature* (2017) 552 (7684):253–7. doi: 10.1038/nature24993

97. Leidner R, Sanjuan Silva N, Huang H, Sprott D, Zheng C, Shih YP, et al. Neoantigen T-cell receptor gene therapy in pancreatic cancer. *N Engl J Med* (2022) 386 (22):2112–9. doi: 10.1056/NEJMoa2119662

98. Nishio N, Diaconu I, Liu H, Cerullo V, Caruana I, Hoyos V, et al. Armed oncolytic virus enhances immune functions of chimeric antigen receptor-modified T cells in solid tumors. *Cancer Res* (2014) 74(18):5195–205. doi: 10.1158/0008-5472.CAN-14-0697

99. Moon EK, Wang LS, Bekdache K, Lynn RC, Lo A, Thorne SH, et al. Intratumoral delivery of CXCL11 *via* a vaccinia virus, but not by modified T cells, enhances the efficacy of adoptive T cell therapy and vaccines. *Oncoimmunology* (2018) 7(3): e1395997. doi: 10.1080/2162402X.2017.1395997

100. Rosewell Shaw A, Porter CE, Watanabe N, Tanoue K, Sikora A, Gottschalk S, et al. Adenovirotherapy delivering cytokine and checkpoint inhibitor augments CAR T cells against metastatic head and neck cancer. *Mol Ther* (2017) 25(11):2440–51. doi: 10.1016/j.ymthe.2017.09.010

101. Tanoue K, Rosewell Shaw A, Watanabe N, Porter C, Rana B, Gottschalk S, et al. Armed oncolytic adenovirus-expressing PD-L1 mini-body enhances antitumor effects of chimeric antigen receptor T cells in solid tumors. *Cancer Res* (2017) 77(8):2040–51. doi: 10.1158/0008-5472.CAN-16-1577

102. Watanabe K, Luo Y, Da T, Guedan S, Ruella M, Scholler J, et al. Pancreatic cancer therapy with combined mesothelin-redirected chimeric antigen receptor T cells and cytokine-armed oncolytic adenoviruses. *JCI Insight* (2018) 3(7):e99573. doi: 10.1172/jci.insight.99573

103. Evgin L, Huff AL, Wongthida P, Thompson J, Kottke T, Tonne J, et al. Oncolytic virus-derived type I interferon restricts CAR T cell therapy. *Nat Commun* (2020) 11(1):3187. doi: 10.1038/s41467-020-17011-z

104. Evgin L, Vile RG. Parking CAR T cells in tumours: oncolytic viruses as valets or vandals? *Cancers (Basel)* (2021) 13(5):1106. doi: 10.3390/cancers13051106

105. Ajina A, Maher J. Synergistic combination of oncolytic virotherapy with CAR T-cell therapy. *Prog Mol Biol Transl Sci* (2019) 164:217–92. doi: 10.1016/bs.pmbts.2019.06.015

106. Provenzano PP, Cuevas C, Chang AE, Goel VK, Von Hoff DD, Hingorani SR. Enzymatic targeting of the stroma ablates physical barriers to treatment of pancreatic ductal adenocarcinoma. *Cancer Cell* (2012) 21(3):418–29. doi: 10.1016/j.ccr.2012.01.007

107. Kakarla S, Chow KK, Mata M, Shaffer DR, Song XT, Wu MF, et al. Antitumor effects of chimeric receptor engineered human T cells directed to tumor stroma. *Mol Ther* (2013) 21(8):1611–20. doi: 10.1038/mt.2013.110

108. Schuberth PC, Hagedorn C, Jensen SM, Gulati P, van den Broek M, Mischo A, et al. Treatment of Malignant pleural mesothelioma by fibroblast activation protein-specific re-directed T cells. *J Transl Med* (2013) 11:187. doi: 10.1186/1479-5876-11-187

109. Lo A, Wang LS, Scholler J, Monslow J, Avery D, Newick K, et al. Tumor-promoting desmoplasia is disrupted by depleting FAP-expressing stromal cells. *Cancer Res* (2015) 75(14):2800–10. doi: 10.1158/0008-5472.CAN-14-3041

110. Roberts EW, Deonarine A, Jones JO, Denton AE, Feig C, Lyons SK, et al. Depletion of stromal cells expressing fibroblast activation protein-alpha from skeletal muscle and bone marrow results in cachexia and anemia. *J Exp Med* (2013) 210 (6):1137–51. doi: 10.1084/jem.20122344

111. Tran E, Chinnasamy D, Yu Z, Morgan RA, Lee CC, Restifo NP, et al. Immune targeting of fibroblast activation protein triggers recognition of multipotent bone marrow stromal cells and cachexia. *J Exp Med* (2013) 210(6):1125–35. doi: 10.1084/jem.20130110

112. Zhao R, Cui Y, Zheng Y, Li S, Lv J, Wu Q, et al. Human hyaluronidase PH20 potentiates the antitumor activities of mesothelin-specific CAR-T cells against gastric cancer. *Front Immunol* (2021) 12:660488. doi: 10.3389/fimmu.2021.660488

113. Caruana I, Savoldo B, Hoyos V, Weber G, Liu H, Kim ES, et al. Heparanase promotes tumor infiltration and antitumor activity of CAR-redirected T lymphocytes. *Nat Med* (2015) 21(5):524–9. doi: 10.1038/nm.3833

114. Rodriguez-Garcia A, Lynn RC, Poussin M, Eiva MA, Shaw LC, O'Connor RS, et al. CAR-T cell-mediated depletion of immunosuppressive tumor-associated macrophages promotes endogenous antitumor immunity and augments adoptive immunotherapy. *Nat Commun* (2021) 12(1):877. doi: 10.1038/s41467-021-20893-2

115. Nalawade SA, Shafer P, Bajgain P, McKenna MK, Ali A, Kelly L, et al. Selectively targeting myeloid-derived suppressor cells through TRAIL receptor 2 to enhance the efficacy of CAR T cell therapy for treatment of breast cancer. *J Immunother Cancer* (2021) 9(11):e003237. doi: 10.1136/jitc-2021-003237

116. Condamine T, Kumar V, Ramachandran IR, Youn JI, Celis E, Finnberg N, et al. ER stress regulates myeloid-derived suppressor cell fate through TRAIL-R-mediated apoptosis. *J Clin Invest* (2014) 124(6):2626–39. doi: 10.1172/JCI74056

117. Dominguez GA, Condamine T, Mony S, Hashimoto A, Wang F, Liu Q, et al. Selective targeting of myeloid-derived suppressor cells in cancer patients using DS-8273a, an agonistic TRAIL-R2 antibody. *Clin Cancer Res* (2017) 23(12):2942–50. doi: 10.1158/1078-0432.CCR-16-1784

118. Chandler C, Liu T, Buckanovich R, Coffman LG. The double edge sword of fibrosis in cancer. *Transl Res* (2019) 209:55–67. doi: 10.1016/j.trsl.2019.02.006

119. Levental KR, Yu H, Kass L, Lakins JN, Egeblad M, Erler JT, et al. Matrix crosslinking forces tumor progression by enhancing integrin signaling. *Cell* (2009) 139 (5):891–906. doi: 10.1016/j.cell.2009.10.027

120. Piersma B, Bank RA. Collagen cross-linking mediated by lysyl hydroxylase 2: an enzymatic battlefield to combat fibrosis. *Essays Biochem* (2019) 63(3):377–87. doi: 10.1042/EBC20180051

121. Hosein AN, Brekken RA, Maitra A. Pancreatic cancer stroma: an update on therapeutic targeting strategies. *Nat Rev Gastroenterol Hepatol* (2020) 17(8):487–505. doi: 10.1038/s41575-020-0300-1

122. Sun X, Wu B, Chiang HC, Deng H, Zhang X, Xiong W, et al. Tumour DDR1 promotes collagen fibre alignment to instigate immune exclusion. *Nature* (2021) 599 (7886):673–8. doi: 10.1038/s41586-021-04057-2

123. Murad JP, Tilakawardane D, Park AK, Lopez LS, Young CA, Gibson J, et al. Pre-conditioning modifies the TME to enhance solid tumor CAR T cell efficacy and endogenous protective immunity. *Mol Ther* (2021) 29(7):2335–49. doi: 10.1016/j.ymthe.2021.02.024

124. Kolb M, Kirschner J, Riedel W, Wirtz H, Schmidt M. Cyclophosphamide pulse therapy in idiopathic pulmonary fibrosis. *Eur Respir J* (1998) 12(6):1409–14. doi: 10.1183/09031936.98.12061409

125. Qi C, Gong J, Li J, Liu D, Qin Y, Ge S, et al. Claudin18.2-specific CAR T cells in gastrointestinal cancers: phase 1 trial interim results. *Nat Med* (2022) 28(6):1189–98. doi: 10.1038/s41591-022-01800-8

126. Uslu U, Da T, Assenmacher CA, Scholler J, Young RM, Tchou J, et al. Chimeric antigen receptor T cells as adjuvant therapy for unresectable adenocarcinoma. *Sci Adv* (2023) 9(2):eade2526. doi: 10.1126/sciadv.ade2526

127. Lanitis E, Dangaj D, Irving M, Coukos G. Mechanisms regulating T-cell infiltration and activity in solid tumors. *Ann Oncol* (2017) 28(suppl_12):xii18–32. doi: 10.1093/annonc/mdx238

128. Hawkins ER, D'Souza RR, Klampatsa A. Armored CAR T-cells: the next chapter in T-cell cancer immunotherapy. *Biologics* (2021) 15:95–105. doi: 10.2147/BTT.S291768

129. Chang CH, Qiu J, O'Sullivan D, Buck MD, Noguchi T, Curtis JD, et al. Metabolic competition in the tumor microenvironment is a driver of cancer progression. *Cell* (2015) 162(6):1229–41. doi: 10.1016/j.cell.2015.08.016

130. Peng M, Yin N, Chhangawala S, Xu K, Leslie CS, Li MO. Aerobic glycolysis promotes T helper 1 cell differentiation through an epigenetic mechanism. *Science* (2016) 354(6311):481–4. doi: 10.1126/science.aaf6284

131. Hermans D, Gautam S, Garcia-Canaveras JC, Gromer D, Mitra S, Spolski R, et al. Lactate dehydrogenase inhibition synergizes with IL-21 to promote CD8(+) T cell stemness and antitumor immunity. *Proc Natl Acad Sci U S A* (2020) 117(11):6047–55. doi: 10.1073/pnas.1920413117

132. Papandreou I, Cairns RA, Fontana L, Lim AL, Denko NC. HIF-1 mediates adaptation to hypoxia by actively downregulating mitochondrial oxygen consumption. *Cell Metab* (2006) 3(3):187–97. doi: 10.1016/j.cmet.2006.01.012

133. Seagroves TN, Ryan HE, Lu H, Wouters BG, Knapp M, Thibault P, et al. Transcription factor HIF-1 is a necessary mediator of the pasteur effect in mammalian cells. *Mol Cell Biol* (2001) 21(10):3436–44. doi: 10.1128/MCB.21.10.3436-3444.2001

134. Palazon A, Tyrakis PA, Macias D, Velica P, Rundqvist H, Fitzpatrick S, et al. An HIF-1alpha/VEGF-A axis in cytotoxic T cells regulates tumor progression. *Cancer Cell* (2017) 32(5):669–83.e5. doi: 10.1016/j.ccell.2017.10.003

135. Geiger R, Rieckmann JC, Wolf T, Basso C, Feng Y, Fuhrer T, et al. L-arginine modulates T cell metabolism and enhances survival and anti-tumor activity. *Cell* (2016) 167(3):829–42.e13. doi: 10.1016/j.cell.2016.09.031

136. Cimen Bozkus C, Elzey BD, Crist SA, Ellies LG, Ratliff TL. Expression of cationic amino acid transporter 2 is required for myeloid-derived suppressor cell-mediated control of T cell immunity. *J Immunol* (2015) 195(11):5237–50. doi: 10.4049/jimmunol.1500959

137. Halaby MJ, McGaha TL. Amino acid transport and metabolism in myeloid function. *Front Immunol* (2021) 12:695238. doi: 10.3389/fimmu.2021.695238

138. Zimmermann H. Extracellular metabolism of ATP and other nucleotides. *Naunyn Schmiedebergs Arch Pharmacol* (2000) 362(4-5):299–309. doi: 10.1007/s002100000309

139. Vigano S, Alatzoglou D, Irving M, Menetrier-Caux C, Caux C, Romero P, et al. Targeting adenosine in cancer immunotherapy to enhance T-cell function. *Front Immunol* (2019) 10:925. doi: 10.3389/fimmu.2019.00925

140. Beavis PA, Henderson MA, Giuffrida L, Mills JK, Sek K, Cross RS, et al. Targeting the adenosine 2A receptor enhances chimeric antigen receptor T cell efficacy. *J Clin Invest* (2017) 127(3):929–41. doi: 10.1172/JCI89455

141. Giuffrida L, Sek K, Henderson MA, Lai J, Chen AXY, Meyran D, et al. CRISPR/Cas9 mediated deletion of the adenosine A2A receptor enhances CAR T cell efficacy. *Nat Commun* (2021) 12(1):3236. doi: 10.1038/s41467-021-23331-5

142. Seifert M, Benmebarek M-R, Briukhovetska D, Märkl F, Dörr J, Cadilha BL, et al. Impact of the selective A2AR and A2BR dual antagonist AB928/etrumadenant on CAR T cell function. *Br J Cancer* (2022) 127(12):2175–85. doi: 10.1038/s41416-022-02013-z

143. Deaglio S, Dwyer KM, Gao W, Friedman D, Usheva A, Erat A, et al. Adenosine generation catalyzed by CD39 and CD73 expressed on regulatory T cells mediates immune suppression. *J Exp Med* (2007) 204(6):1257–65. doi: 10.1084/jem.20062512

144. Ohta A, Kini R, Ohta A, Subramanian M, Madasu M, Sitkovsky M. The development and immunosuppressive functions of CD4(+) CD25(+) FoxP3(+) regulatory T cells are under influence of the adenosine-A2A adenosine receptor pathway. *Front Immunol* (2012) 3:190. doi: 10.3389/fimmu.2012.00190

145. Schneider E, Winzer R, Rissiek A, Ricklefs I, Meyer-Schwesinger C, Ricklefs FL, et al. CD73-mediated adenosine production by CD8 T cell-derived extracellular vesicles constitutes an intrinsic mechanism of immune suppression. *Nat Commun* (2021) 12 (1):5911. doi: 10.1038/s41467-021-26134-w

146. Rissiek A, Baumann I, Cuapio A, Mautner A, Kolster M, Arck PC, et al. The expression of CD39 on regulatory T cells is genetically driven and further upregulated at sites of inflammation. *J Autoimmun* (2015) 58:12–20. doi: 10.1016/j.jaut.2014.12.007

147. Mallikarjuna P, Zhou Y, Landstrom M. The synergistic cooperation between TGF-beta and hypoxia in cancer and fibrosis. *Biomolecules* (2022) 12(5):635. doi: 10.3390/biom12050635

148. Alishah K, Birtel M, Masoumi E, Jafarzadeh L, Mirzaee HR, Hadjati J, et al. CRISPR/Cas9-mediated TGFbetaRII disruption enhances anti-tumor efficacy of human chimeric antigen receptor T cells in vitro. *J Transl Med* (2021) 19(1):482. doi: 10.1186/s12967-021-03146-0

149. Bollard CM, Tripic T, Cruz CR, Dotti G, Gottschalk S, Torrano V, et al. Tumor-specific T-cells engineered to overcome tumor immune evasion induce clinical responses in patients with relapsed hodgkin lymphoma. *J Clin Oncol* (2018) 36 (11):1128–39. doi: 10.1200/JCO.2017.74.3179

150. Chu NJ, Overstreet MG, Gilbreth R, Clarke L, Gesse C, Tu E, et al. Abstract 2837: Synthetic TGFb blockade preserves effector function and maintains stemness of GPC3 CAR-T against hepatocellular carcinoma. *Cancer Res* (2022) 82 (12_Supplement):2837. doi: 10.1158/1538-7445.AM2022-2837

151. Kloss CC, Lee J, Zhang A, Chen F, Melenhorst JJ, Lacey SF, et al. Dominant-negative TGF-beta receptor enhances PSMA-targeted human CAR T cell proliferation and augments prostate cancer eradication. *Mol Ther* (2018) 26(7):1855–66. doi: 10.1016/j.ymthe.2018.05.003

152. Li K, Xu J, Wang J, Lu C, Dai Y, Dai Q, et al. Dominant-negative transforming growth factor-beta receptor-armoured mesothelin-targeted chimeric antigen receptor T cells slow tumour growth in a mouse model of ovarian cancer. *Cancer Immunol Immunother* (2023) 72(4):917–28. doi: 10.1007/s00262-022-03290-6

153. Narayan V, Barber-Rotenberg JS, Jung IY, Lacey SF, Rech AJ, Davis MM, et al. PSMA-targeting TGFbeta-insensitive armored CAR T cells in metastatic castration-resistant prostate cancer: a phase 1 trial. *Nat Med* (2022) 28(4):724–34. doi: 10.1038/s41591-022-01726-1

154. Tang N, Cheng C, Zhang X, Qiao M, Li N, Mu W, et al. TGF-beta inhibition *via* CRISPR promotes the long-term efficacy of CAR T cells against solid tumors. *JCI Insight* (2020) 5(4):e133977. doi: 10.1172/jci.insight.133977

155. van Dyk D, Zanvit P, Fazenbaker C, McGlinchey K, Luo W, Pezold J, et al. Abstract LB085: Antitumor activity of AZD0754, a dnTGFbRII armored STEAP2

targeted CAR-T therapy, in preclinical models of prostate cancer. *Cancer Res* (2023) 83 (8_Supplement):LB085–LB. doi: 10.1158/1538-7445.AM2023-LB085

156. Zhang N, Bevan MJ. TGF-beta signaling to T cells inhibits autoimmunity during lymphopenia-driven proliferation. *Nat Immunol* (2012) 13(7):667–73. doi: 10.1038/ni.2319

157. Frangogiannis N. Transforming growth factor-beta in tissue fibrosis. *J Exp Med* (2020) 217(3):e20190103. doi: 10.1084/jem.20190103

158. Cherkassky L, Morello A, Villena-Vargas J, Feng Y, Dimitrov DS, Jones DR, et al. Human CAR T cells with cell-intrinsic PD-1 checkpoint blockade resist tumor-mediated inhibition. *J Clin Invest* (2016) 126(8):3130–44. doi: 10.1172/JCI83092

159. Liu X, Ranganathan R, Jiang S, Fang C, Sun J, Kim S, et al. A chimeric switch-receptor targeting PD1 augments the efficacy of second-generation CAR T cells in advanced solid tumors. *Cancer Res* (2016) 76(6):1578–90. doi: 10.1158/0008-5472.CAN-15-2524

160. Prosser ME, Brown CE, Shami AF, Forman SJ, Jensen MC. Tumor PD-L1 co-stimulates primary human CD8(+) cytotoxic T cells modified to express a PD1:CD28 chimeric receptor. *Mol Immunol* (2012) 51(3-4):263–72. doi: 10.1016/j.molimm.2012.03.023

161. Yamamoto TN, Lee PH, Vodnala SK, Gurusamy D, Kishton RJ, Yu Z, et al. T cells genetically engineered to overcome death signaling enhance adoptive cancer immunotherapy. *J Clin Invest* (2019) 129(4):1551–65. doi: 10.1172/JCI121491

162. Zhang Y, Zhang X, Cheng C, Mu W, Liu X, Li N, et al. CRISPR-Cas9 mediated LAG-3 disruption in CAR-T cells. *Front Med* (2017) 11(4):554–62. doi: 10.1007/s11684-017-0543-6

163. Rowshanravan B, Halliday N, Sansom DM. CTLA-4: a moving target in immunotherapy. *Blood* (2018) 131(1):58–67. doi: 10.1182/blood-2017-06-741033

164. Liu Y, Di S, Shi B, Zhang H, Wang Y, Wu X, et al. Armored inducible expression of IL-12 enhances antitumor activity of glypican-3-targeted chimeric antigen receptor-engineered T cells in hepatocellular carcinoma. *J Immunol* (2019) 203(1):198–207. doi: 10.4049/jimmunol.1800033

165. Yeku OO, Purdon TJ, Koneru M, Spriggs D, Brentjens RJ. Armored CAR T cells enhance antitumor efficacy and overcome the tumor microenvironment. *Sci Rep* (2017) 7(1):10541. doi: 10.1038/s41598-017-10940-8

166. Zhang L, Davies JS, Serna C, Yu Z, Restifo NP, Rosenberg SA, et al. Enhanced efficacy and limited systemic cytokine exposure with membrane-anchored interleukin-12 T-cell therapy in murine tumor models. *J Immunother Cancer* (2020) 8(1):e000210. doi: 10.1136/jitc-2019-000210

167. Rafiq S, Hackett CS, Brentjens RJ. Engineering strategies to overcome the current roadblocks in CAR T cell therapy. *Nat Rev Clin Oncol* (2020) 17(3):147–67. doi: 10.1038/s41571-019-0297-y

168. Hu B, Ren J, Luo Y, Keith B, Young RM, Scholler J, et al. Augmentation of antitumor immunity by human and mouse CAR T cells secreting IL-18. *Cell Rep* (2017) 20(13):3025–33. doi: 10.1016/j.celrep.2017.09.002

169. Avanzi MP G, van Leeuwen D, Li X, Cheung K, Park H, Purdon TJ, et al. IL-18 secreting CAR T cells enhance cell persistence, induce prolonged B cell aplasia and eradicate CD19+ Tumor cells without need for prior conditioning. *Blood* (2016) 128 (22):816–. doi: 10.1182/blood.V128.22.816.816

170. Pegram HJ, Lee JC, Hayman EG, Imperato GH, Tedder TF, Sadelain M, et al. Tumor-targeted T cells modified to secrete IL-12 eradicate systemic tumors without need for prior conditioning. *Blood* (2012) 119(18):4133–41. doi: 10.1182/blood-2011-12-400044

171. Zhou LJ, Smith HM, Waldschmidt TJ, Schwarting R, Daley J, Tedder TF. Tissue-specific expression of the human CD19 gene in transgenic mice inhibits antigen-independent B-lymphocyte development. *Mol Cell Biol* (1994) 14(6):3884–94. doi: 10.1128/MCB.14.6.3884

172. Svoboda J, Landsburg DL, Chong EA, Barta SK, Nasta SD, Ruella M, et al. Fourth generation hucart19-il18 produces durable responses in lymphoma patients previously relapsed/refractory to anti-cd19 car T-cell therapy. *Hematological Oncol* (2023) 41(S2):35–7. doi: 10.1002/hon.3163_6

173. Chen Y, Sun C, Landoni E, Metelitsa L, Dotti G, Savoldo B. Eradication of neuroblastoma by T cells redirected with an optimized GD2-specific chimeric antigen receptor and interleukin-15. *Clin Cancer Res* (2019) 25(9):2915–24. doi: 10.1158/1078-0432.CCR-18-1811

174. Hoyos V, Savoldo B, Quintarelli C, Mahendravada A, Zhang M, Vera J, et al. Engineering CD19-specific T lymphocytes with interleukin-15 and a suicide gene to enhance their anti-lymphoma/leukemia effects and safety. *Leukemia* (2010) 24 (6):1160–70. doi: 10.1038/leu.2010.75

175. Krenciute G, Prinzing BL, Yi Z, Wu MF, Liu H, Dotti G, et al. Transgenic expression of IL15 improves antiglioma activity of IL13Ralpha2-CAR T cells but results in antigen loss variants. *Cancer Immunol Res* (2017) 5(7):571–81. doi: 10.1158/2326-6066.CIR-16-0376

176. Fehniger TA, Suzuki K, Ponnappan A, VanDeusen JB, Cooper MA, Florea SM, et al. Fatal leukemia in interleukin 15 transgenic mice follows early expansions in natural killer and memory phenotype CD8+ T cells. *J Exp Med* (2001) 193(2):219–31. doi: 10.1084/jem.193.2.219

177. Mantovani A, Allavena P, Marchesi F, Garlanda C. Macrophages as tools and targets in cancer therapy. *Nat Rev Drug Discovery* (2022) 21(11):799–820. doi: 10.1038/s41573-022-00520-5

178. Ruella M, Klichinsky M, Kenderian SS, Shestova O, Ziober A, Kraft DO, et al. Overcoming the immunosuppressive tumor microenvironment of hodgkin lymphoma using chimeric antigen receptor T cells. *Cancer Discovery* (2017) 7(10):1154–67. doi: 10.1158/2159-8290.CD-16-0850

179. Dehbashi M, Hojati Z, Motovali-Bashi M, Ganjalikhany MR, Cho WC, Shimosaka A, et al. A novel CAR expressing NK cell targeting CD25 with the prospect of overcoming immune escape mechanism in cancers. *Front Oncol* (2021) 11:649710. doi: 10.3389/fonc.2021.649710

180. Onda M, Kobayashi K, Pastan I. Depletion of regulatory T cells in tumors with an anti-CD25 immunotoxin induces CD8 T cell-mediated systemic antitumor immunity. *Proc Natl Acad Sci U S A* (2019) 116(10):4575–82. doi: 10.1073/pnas.1820388116

181. Melenhorst JJ, Chen GM, Wang M, Porter DL, Chen C, Collins MA, et al. Decade-long leukaemia remissions with persistence of CD4(+) CAR T cells. *Nature* (2022) 602(7897):503–9. doi: 10.1038/s41586-021-04390-6

182. Soerens AG, Kunzli M, Quarnstrom CF, Scott MC, Swanson L, Locquiao JJ, et al. Functional T cells are capable of supernumerary cell division and longevity. *Nature* (2023) 614(7949):762–6. doi: 10.1038/s41586-022-05626-9

183. Yaguchi T, Kobayashi A, Inozume T, Morii K, Nagumo H, Nishio H, et al. Human PBMC-transferred murine MHC class I/II-deficient NOG mice enable long-term evaluation of human immune responses. *Cell Mol Immunol* (2018) 15(11):953–62. doi: 10.1038/cmi.2017.106

184. Brehm MA, Kenney LL, Wiles MV, Low BE, Tisch RM, Burzenski L, et al. Lack of acute xenogeneic graft- versus-host disease, but retention of T-cell function following engraftment of human peripheral blood mononuclear cells in NSG mice deficient in MHC class I and II expression. *FASEB J* (2019) 33(3):3137–51. doi: 10.1096/fj.201800636R

185. Petersdorf EW. Role of major histocompatibility complex variation in graft-versus-host disease after hematopoietic cell transplantation. *F1000Res* (2017) 6:617. doi: 10.12688/f1000research.10990.1

186. Kato D, Yaguchi T, Iwata T, Katoh Y, Morii K, Tsubota K, et al. GPC1 specific CAR-T cells eradicate established solid tumor without adverse effects and synergize with anti-PD-1 Ab. *Elife* (2020) 9:e49392. doi: 10.7554/eLife.49392

187. Kawalekar OU, OC RS, Fraietta JA, Guo L, McGettigan SE, Posey AD Jr., et al. Distinct signaling of coreceptors regulates specific metabolism pathways and impacts memory development in CAR T cells. *Immunity* (2016) 44(3):712. doi: 10.1016/j.immuni.2016.01.021

188. Brentjens RJ, Davila ML, Riviere I, Park J, Wang X, Cowell LG, et al. CD19-targeted T cells rapidly induce molecular remissions in adults with chemotherapy-refractory acute lymphoblastic leukemia. *Sci Transl Med* (2013) 5(177):177ra38. doi: 10.1126/scitranslmed.3005930

189. Lee DW, Kochenderfer JN, Stetler-Stevenson M, Cui YK, Delbrook C, Feldman SA, et al. T cells expressing CD19 chimeric antigen receptors for acute lymphoblastic leukaemia in children and young adults: a phase 1 dose-escalation trial. *Lancet* (2015) 385(9967):517–28. doi: 10.1016/S0140-6736(14)61403-3

190. Porter DL, Hwang WT, Frey NV, Lacey SF, Shaw PA, Loren AW, et al. Chimeric antigen receptor T cells persist and induce sustained remissions in relapsed refractory chronic lymphocytic leukemia. *Sci Transl Med* (2015) 7(303):303ra139. doi: 10.1126/scitranslmed.aac5415

191. Pearce EL, Walsh MC, Cejas PJ, Harms GM, Shen H, Wang LS, et al. Enhancing CD8 T-cell memory by modulating fatty acid metabolism. *Nature* (2009) 460 (7251):103–7. doi: 10.1038/nature08097

192. Sadelain M, Brentjens R, Riviere I. The basic principles of chimeric antigen receptor design. *Cancer Discovery* (2013) 3(4):388–98. doi: 10.1158/2159-8290.CD-12-0548

193. Dotti G, Gottschalk S, Savoldo B, Brenner MK. Design and development of therapies using chimeric antigen receptor-expressing T cells. *Immunol Rev* (2014) 257 (1):107–26. doi: 10.1111/imr.12131

194. Tammana S, Huang X, Wong M, Milone MC, Ma L, Levine BL, et al. 4-1BB and CD28 signaling plays a synergistic role in redirecting umbilical cord blood T cells against B-cell Malignancies. *Hum Gene Ther* (2010) 21(1):75–86. doi: 10.1089/hum.2009.122

195. Guedan S, Posey AD Jr., Shaw C, Wing A, Da T, Patel PR, et al. Enhancing CAR T cell persistence through ICOS and 4-1BB costimulation. *JCI Insight* (2018) 3(1): e96976. doi: 10.1172/jci.insight.96976

196. Enblad G, Karlsson H, Gammelgard G, Wenthe J, Lovgren T, Amini RM, et al. A phase I/IIa trial using CD19-targeted third-generation CAR T cells for lymphoma and leukemia. *Clin Cancer Res* (2018) 24(24):6185–94. doi: 10.1158/1078-0432.CCR-18-0426

197. Zhao X, Yang J, Zhang X, Lu XA, Xiong M, Zhang J, et al. Efficacy and safety of CD28- or 4-1BB-based CD19 CAR-T cells in B cell acute lymphoblastic leukemia. *Mol Ther Oncolytics* (2020) 18:272–81. doi: 10.1016/j.omto.2020.06.016

198. Rosenberg SA. IL-2: the first effective immunotherapy for human cancer. *J Immunol* (2014) 192(12):5451–8. doi: 10.4049/jimmunol.1490019

199. Aspuria PJ, Vivona S, Bauer M, Semana M, Ratti N, McCauley S, et al. An orthogonal IL-2 and IL-2Rbeta system drives persistence and activation of CAR T cells and clearance of bulky lymphoma. *Sci Transl Med* (2021) 13(625):eabg7565. doi: 10.1126/scitranslmed.abg7565

200. Zhang Q, Hresko ME, Picton LK, Su L, Hollander MJ, Nunez-Cruz S, et al. A human orthogonal IL-2 and IL-2Rbeta system enhances CAR T cell expansion and antitumor activity in a murine model of leukemia. *Sci Transl Med* (2021) 13(625): eabg6986. doi: 10.1126/scitranslmed.abg6986

201. Palomba ML, . Mei MG, . Caimi PF, Cortese M, Davila M, Yadnik G, et al. Abstract CT125: A Phase 1 study to evaluate the safety and tolerability of a combination autologous CD19 CAR T cell therapy (SYNCAR-001) and orthogonal IL-2 (STK-009) in subjects with relapsed or refractory CD19 expressing hematologic Malignancies (NCT05665062). *Cancer Res* (2023) 83(CT125):CT125. doi: 10.1158/1538-7445.AM2023-CT125

202. Fraietta JA, Lacey SF, Orlando EJ, Pruteanu-Malinici I, Gohil M, Lundh S, et al. Determinants of response and resistance to CD19 chimeric antigen receptor (CAR) T cell therapy of chronic lymphocytic leukemia. *Nat Med* (2018) 24(5):563–71. doi: 10.1038/s41591-018-0010-1

203. Gattinoni L, Speiser DE, Lichterfeld M, Bonini C. T memory stem cells in health and disease. *Nat Med* (2017) 23(1):18–27. doi: 10.1038/nm.4241

204. Huang J, Khong HT, Dudley ME, El-Gamil M, Li YF, Rosenberg SA, et al. Survival, persistence, and progressive differentiation of adoptively transferred tumor-reactive T cells associated with tumor regression. *J Immunother* (2005) 28(3):258–67. doi: 10.1097/01.cji.0000158855.92792.7a

205. Krishna S, Lowery FJ, Copeland AR, Bahadiroglu E, Mukherjee R, Jia L, et al. Stem-like CD8 T cells mediate response of adoptive cell immunotherapy against human cancer. *Science* (2020) 370(6522):1328–34. doi: 10.1126/science.abb9847

206. Sade-Feldman M, Yizhak K, Bjorgaard SL, Ray JP, de Boer CG, Jenkins RW, et al. Defining T cell states associated with response to checkpoint immunotherapy in melanoma. *Cell* (2019) 176(1-2):404. doi: 10.1016/j.cell.2018.12.034

207. Jafarzadeh L, Masoumi E, Fallah-Mehrjardi K, Mirzaei HR, Hadjati J. Prolonged persistence of chimeric antigen receptor (CAR) T cell in adoptive cancer immunotherapy: challenges and ways forward. *Front Immunol* (2020) 11:702. doi: 10.3389/fimmu.2020.00702

208. Sandau MM, Kohlmeier JE, Woodland DL, Jameson SC. IL-15 regulates both quantitative and qualitative features of the memory CD8 T cell pool. *J Immunol* (2010) 184(1):35–44. doi: 10.4049/jimmunol.0803355

209. Zhang Y, Zhuang Q, Wang F, Zhang C, Xu C, Gu A, et al. Co-expression IL-15 receptor alpha with IL-15 reduces toxicity *via* limiting IL-15 systemic exposure during CAR-T immunotherapy. *J Trans Med* (2022) 20(1):432. doi: 10.1186/s12967-022-03626-x

210. Gust J, Ponce R, Liles WC, Garden GA, Turtle CJ. Cytokines in CAR T cell-associated neurotoxicity. *Front Immunol* (2020) 11:577027. doi: 10.3389/fimmu.2020.577027

211. Hurton LV, Singh H, Najjar AM, Switzer KC, Mi T, Maiti S, et al. Tethered IL-15 augments antitumor activity and promotes a stem-cell memory subset in tumor-specific T cells. *Proc Natl Acad Sci U S A* (2016) 113(48):E7788–E97. doi: 10.1073/pnas.1610544113

212. Jiang Q, Li WQ, Hofmeister RR, Young HA, Hodge DR, Keller JR, et al. Distinct regions of the interleukin-7 receptor regulate different Bcl2 family members. *Mol Cell Biol* (2004) 24(14):6501–13. doi: 10.1128/MCB.24.14.6501-6513.2004

213. Markley JC, Sadelain M. IL-7 and IL-21 are superior to IL-2 and IL-15 in promoting human T cell-mediated rejection of systemic lymphoma in immunodeficient mice. *Blood* (2010) 115(17):3508–19. doi: 10.1182/blood-2009-09-241398

214. Luo H, Su J, Sun R, Sun Y, Wang Y, Dong Y, et al. Coexpression of IL7 and CCL21 increases efficacy of CAR-T cells in solid tumors without requiring preconditioned lymphodepletion. *Clin Cancer Res* (2020) 26(20):5494–505. doi: 10.1158/1078-0432.CCR-20-0777

215. Park JH, Yu Q, Erman B, Appelbaum JS, Montoya-Durango D, Grimes HL, et al. Suppression of IL7Ralpha transcription by IL-7 and other prosurvival cytokines: a novel mechanism for maximizing IL-7-dependent T cell survival. *Immunity* (2004) 21 (2):289–302. doi: 10.1016/j.immuni.2004.07.016

216. Vera JF, Hoyos V, Savoldo B, Quintarelli C, Giordano Attianese GM, Leen AM, et al. Genetic manipulation of tumor-specific cytotoxic T lymphocytes to restore responsiveness to IL-7. *Mol Ther* (2009) 17(5):880–8. doi: 10.1038/mt.2009.34

217. Shum T, Omer B, Tashiro H, Kruse RL, Wagner DL, Parikh K, et al. Constitutive signaling from an engineered IL7 receptor promotes durable tumor elimination by tumor-redirected T cells. *Cancer Discovery* (2017) 7(11):1238–47. doi: 10.1158/2159-8290.CD-17-0538

218. Zeng R, Spolski R, Finkelstein SE, Oh S, Kovanen PE, Hinrichs CS, et al. Synergy of IL-21 and IL-15 in regulating CD8+ T cell expansion and function. *J Exp Med* (2005) 201(1):139–48. doi: 10.1084/jem.20041057

219. Kuchen S, Robbins R, Sims GP, Sheng C, Phillips TM, Lipsky PE, et al. Essential role of IL-21 in B cell activation, expansion, and plasma cell generation during CD4+ T cell-B cell collaboration. *J Immunol* (2007) 179(9):5886–96. doi: 10.4049/jimmunol.179.9.5886

220. Batra SA, Rathi P, Guo L, Courtney AN, Fleurence J, Balzeau J, et al. Glypican-3-specific CAR T cells coexpressing IL15 and IL21 have superior expansion and antitumor activity against hepatocellular carcinoma. *Cancer Immunol Res* (2020) 8 (3):309–20. doi: 10.1158/2326-6066.CIR-19-0293

221. Stach M, Ptackova P, Mucha M, Musil J, Klener P, Otahal P. Inducible secretion of IL-21 augments anti-tumor activity of piggyBac-manufactured chimeric antigen receptor T cells. *Cytotherapy* (2020) 22(12):744–54. doi: 10.1016/j.jcyt.2020.08.005

222. Wang Y, Jiang H, Luo H, Sun Y, Shi B, Sun R, et al. An IL-4/21 inverted cytokine receptor improving CAR-T cell potency in immunosuppressive solid-tumor microenvironment. *Front Immunol* (2019) 10:1691. doi: 10.3389/fimmu.2019.01691

223. Kagoya Y, Tanaka S, Guo T, Anczurowski M, Wang CH, Saso K, et al. A novel chimeric antigen receptor containing a JAK-STAT signaling domain mediates superior antitumor effects. *Nat Med* (2018) 24(3):352–9. doi: 10.1038/nm.4478

224. Cui W, Liu Y, Weinstein JS, Craft J, Kaech SM. An interleukin-21-interleukin-10-STAT3 pathway is critical for functional maturation of memory CD8+ T cells. *Immunity* (2011) 35(5):792–805. doi: 10.1016/j.immuni.2011.09.017

225. Siegel AM, Heimall J, Freeman AF, Hsu AP, Brittain E, Brenchley JM, et al. A critical role for STAT3 transcription factor signaling in the development and maintenance of human T cell memory. *Immunity* (2011) 35(5):806–18. doi: 10.1016/j.immuni.2011.09.016

226. Suarez ER, Chang de K, Sun J, Sui J, Freeman GJ, Signoretti S, et al. Chimeric antigen receptor T cells secreting anti-PD-L1 antibodies more effectively regress renal cell carcinoma in a humanized mouse model. *Oncotarget* (2016) 7(23):34341–55. doi: 10.18632/oncotarget.9114

227. Harrasser M, Gohil SH, Lau H, Della Peruta M, Muczynski V, Patel D, et al. Inducible localized delivery of an anti-PD-1 scFv enhances anti-tumor activity of ROR1 CAR-T cells in TNBC. *Breast Cancer Res* (2022) 24(1):39. doi: 10.1186/s13058-022-01531-1

228. Pan Z, Di S, Shi B, Jiang H, Shi Z, Liu Y, et al. Increased antitumor activities of glypican-3-specific chimeric antigen receptor-modified T cells by coexpression of a soluble PD1-CH3 fusion protein. *Cancer Immunol Immunother* (2018) 67(10):1621–34. doi: 10.1007/s00262-018-2221-1

229. Roberts ZJ, Vezan R, Avanzi MP, Locke FL. Abstract CT055: Phase 1/2 primary analysis of ZUMA-6: Axicabtagene ciloleucel (Axi-Cel) in combination With atezolizumab (Atezo) for the treatment of patients (Pts) with refractory diffuse large B cell lymphoma (DLBCL). *Cancer Res* (2020) 80. doi: 10.18632/oncotarget.9114

230. Hirayama AV, Fiorenza S, Gauthier J, Voutsinas JM, Wu QV, Kimble EL, et al. Timing of PD-L1 blockade with durvalumab may affect outcomes of CD19 CAR-T cell therapy for relapsed/Refractory large B-Cell lymphoma. *Blood* (2022) 140:7447–9. doi: 10.1182/blood-2022-168185

231. Condomines M, Arnason J, Benjamin R, Gunset G, Plotkin J, Sadelain M. Tumor-targeted human T cells expressing CD28-based chimeric antigen receptors circumvent CTLA-4 inhibition. *PloS One* (2015) 10(6):e0130518. doi: 10.1371/journal.pone.0130518

232. Kenderian MD 1 2 SS, Ruella MD 1 M, Shestova PhD 1 O, PharmD 1 MK, Kim MD 1 M, Porter MD 3 DL, et al. Identification of PD1 and TIM3 as checkpoints that limit chimeric antigen receptor T cell efficacy in leukemia. *Biol Blood Marrow Transplantation* (2016) 22(3):S19–21. doi: 10.1158/1538-7445.AM2020-CT055

233. Albelda S. Abstract 3749: Genetic blockade of the protein tyrosine phosphatase SHP1 augments CAR T cell activity against PDL1 expressing solid tumors. *Cancer Res* (2017) 77::3749. doi: 10.1158/1538-7445.AM2017-3749

234. Wiede F, Lu KH, Du X, Liang S, Hochheiser K, Dodd GT, et al. PTPN2 phosphatase deletion in T cells promotes anti-tumour immunity and CAR T-cell efficacy in solid tumours. *EMBO J* (2020) 39(2):e103637. doi: 10.1371/journal.pone.0130518

235. Kumar J, Kumar R, Kumar Singh A, Tsakem EL, Kathania M, Riese MJ, et al. Deletion of Cbl-b inhibits CD8(+) T-cell exhaustion and promotes CAR T-cell function. *J Immunother Cancer* (2021) 9(1). doi: 10.1136/jitc-2020-001688

236. Sutra Del Galy A, Menegatti S, Fuentealba J, Lucibello F, Perrin L, Helft J, et al. *In vivo* genome-wide CRISPR screens identify SOCS1 as intrinsic checkpoint of CD4(+) T(H)1 cell response. *Sci Immunol* (2021) 6(66):eabe8219. doi: 10.1101/2021.04.12.439455

237. Lv J, Qin L, Zhao R, Wu D, Wu Z, Zheng D, et al. Disruption of CISH promotes the antitumor activity of human T cells and decreases PD-1 expression levels. *Mol Ther Oncolytics* (2023) 28:46–58. doi: 10.1016/j.omto.2022.12.003

238. Wiede F, Lu KH, Du X, Zeissig MN, Xu R, Goh PK, et al. PTP1B is an intracellular checkpoint that limits T-cell and CAR T-cell antitumor immunity. *Cancer Discovery* (2022) 12(3):752–73. doi: 10.1158/2159-8290.CD-21-0694

239. Si J, Shi X, Sun S, Zou B, Li Y, An D, et al. Hematopoietic progenitor kinase1 (HPK1) mediates T cell dysfunction and is a druggable target for T cell-based immunotherapies. *Cancer Cell* (2020) 38(4):551–66.e11. doi: 10.1016/j.ccell.2020.08.001

240. Carnevale J, Shifrut E, Kale N, Nyberg WA, Blaeschke F, Chen YY, et al. RASA2 ablation in T cells boosts antigen sensitivity and long-term function. *Nature* (2022) 609 (7925):174–82. doi: 10.1038/s41586-022-05126-w

241. Mai D, Johnson O, Reff J, Fan TJ, Scholler J, Sheppard NC, et al. Combined disruption of T cell inflammatory regulators Regnase-1 and Roquin-1 enhances antitumor activity of engineered human T cells. *Proc Natl Acad Sci U S A* (2023) 120 (12):e2218632120. doi: 10.1073/pnas.2218632120

242. Lee JW, Komar CA, Bengsch F, Graham K, Beatty GL. Genetically engineered mouse models of pancreatic cancer: the KPC model (LSL-kras(G12D/+) ;LSL-trp53 (R172H/+) ;Pdx-1-cre), its variants, and their application in immuno-oncology drug discovery. *Curr Protoc Pharmacol* (2016) 73:14 39 1–14 39 20. doi: 10.1002/cpph.2

243. Liu Y, Wu W, Cai C, Zhang H, Shen H, Han Y. Patient-derived xenograft models in cancer therapy: technologies and applications. *Signal Transduct Target Ther* (2023) 8(1):160. doi: 10.1038/s41392-023-01419-2

244. Alicke B, Totpal K, Schartner JM, Berkley AM, Lehar SM, Capietto AH, et al. Immunization associated with primary tumor growth leads to rejection of commonly used syngeneic tumors upon tumor rechallenge. *J Immunother Cancer* (2020) 8(2). doi: 10.1136/jitc-2020-000532

245. Duncan BB, Dunbar CE, Ishii K. Applying a clinical lens to animal models of CAR-T cell therapies. *Mol Ther Methods Clin Dev* (2022) 27:17–31. doi: 10.1016/j.omtm.2022.08.008

frontiers | Frontiers in Immunology

TYPE Review
PUBLISHED 19 December 2023
DOI 10.3389/fimmu.2023.1291990

Check for updates

OPEN ACCESS

EDITED BY
Silke Paust,
Jackson Laboratory for Genomic Medicine,
United States

REVIEWED BY
Gianluca Matteoli,
KU Leuven, Belgium
Mercedes Lopez-Santalla,
Centro de Investigaciones Energéticas,
Medioambientales y Tecnológicas, Spain

*CORRESPONDENCE
Daniele Corridoni
daniele.corridoni@astrazeneca.com
Tatiana Ort
Tatiana.ort@astrazeneca.com

RECEIVED 10 September 2023
ACCEPTED 29 November 2023
PUBLISHED 19 December 2023

CITATION
Karmele EP, Moldoveanu AL,
Kaymak I, Jugder B-E, Ursin RL,
Bednar KJ, Corridoni D and Ort T (2023)
Single cell RNA-sequencing profiling to
improve the translation between human
IBD and *in vivo* models.
Front. Immunol. 14:1291990.
doi: 10.3389/fimmu.2023.1291990

COPYRIGHT
© 2023 Karmele, Moldoveanu, Kaymak,
Jugder, Ursin, Bednar, Corridoni and Ort.
This is an open-access article distributed
under the terms of the Creative Commons
Attribution License (CC BY). The use,
distribution or reproduction in other
forums is permitted, provided the original
author(s) and the copyright owner(s) are
credited and that the original publication in
this journal is cited, in accordance with
accepted academic practice. No use,
distribution or reproduction is permitted
which does not comply with these terms.

Single cell RNA-sequencing profiling to improve the translation between human IBD and *in vivo* models

Erik P. Karmele[1], Ana Laura Moldoveanu[2], Irem Kaymak[2], Bat-Erdene Jugder[3], Rebecca L. Ursin[3], Kyle J. Bednar[1], Daniele Corridoni[2]* and Tatiana Ort[1]*

[1]Bioscience Immunology, Research and Early Development, Respiratory and Immunology, Biopharmaceuticals R&D, AstraZeneca, Gaithersburg, MD, United States, [2]Bioscience Immunology, Research and Early Development, Respiratory and Immunology, Biopharmaceuticals R&D, AstraZeneca, Cambridge, United Kingdom, [3]Bioscience Immunology, Research and Early Development, Respiratory and Immunology, Biopharmaceuticals R&D, AstraZeneca, Waltham, MA, United States

Inflammatory bowel disease (IBD) is an umbrella term for two conditions (Crohn's Disease and Ulcerative Colitis) that is characterized by chronic inflammation of the gastrointestinal tract. The use of pre-clinical animal models has been invaluable for the understanding of potential disease mechanisms. However, despite promising results of numerous therapeutics in mouse colitis models, many of these therapies did not show clinical benefits in patients with IBD. Single cell RNA-sequencing (scRNA-seq) has recently revolutionized our understanding of complex interactions between the immune system, stromal cells, and epithelial cells by mapping novel cell subpopulations and their remodeling during disease. This technology has not been widely applied to pre-clinical models of IBD. ScRNA-seq profiling of murine models may provide an opportunity to increase the translatability into the clinic, and to choose the most appropriate model to test hypotheses and novel therapeutics. In this review, we have summarized some of the key findings at the single cell transcriptomic level in IBD, how specific signatures have been functionally validated *in vivo*, and highlighted the similarities and differences between scRNA-seq findings in human IBD and experimental mouse models. In each section of this review, we highlight the importance of utilizing this technology to find the most suitable or translational models of IBD based on the cellular therapeutic target.

KEYWORDS

pre-clinical models, Inflammatory bowel disease (IBD), single cell RNA-sequencing (scRNA-seq), epithelial cell, stromal cell, immune cell

Introduction

Inflammatory bowel disease (IBD), consisting of ulcerative colitis (UC) and Crohn's disease (CD), is a chronic relapsing and remitting inflammatory mediated disorder of the lining of the gastrointestinal tract, resulting in clinical symptoms (1). Changes and functional alterations of immune cells and non-hematopoietic cells (including epithelial and stromal cells) are hallmarks of the onset and sustained inflammation associated with IBD (2, 3). Much of what we know about human IBD pathogenesis is attributed to the use of numerous pre-clinical models of IBD. These models include chemically-induced, spontaneous, immune cell-induced, and microbiota-dependent colitis models. These models have been extensively reviewed (4, 5) and the most common pre-clinical IBD models are summarized in Table 1. While numerous pre-clinical models of IBD exist, no single model fully recapitulates the complexity observed in human IBD. Thus, there remains a need to further validate these pre-clinical models of IBD and identify mucosal cell subpopulations with their associated disease-relevant phenotype which may overlay with human IBD. This understanding will potentially increase their translatability into the clinic and help define the best model to test novel therapeutic targets and modalities.

Multimodal single-cell technologies, such as single cell RNA-sequencing (scRNA-seq), have allowed for in-depth analysis and a deeper understanding of tissue architecture and function at individual-cell high-resolution (24). ScRNA-seq has been instrumental to our understanding of immunology and autoimmune diseases, where complex cellular heterogeneity and interactions between immune cells, stromal cells, and epithelial cells are paramount for disease progression. These technologies have enabled an improved understanding of human IBD by identifying novel or rare cell types that were previously undiscovered and how their abundance or function changes during intestinal inflammation may be a driver of disease (25). While scRNA-seq technology has been applied to numerous UC and CD cohorts to better understand the complex biology between immune cells and non-hematopoietic cells, this technology has only begun to be applied to pre-clinical models of IBD for comparative studies with the human condition.

While studies have enriched specific cell populations from pre-clinical models of IBD and characterized these cells by scRNA-seq (26–28), there are gaps in the knowledge of the entire makeup of the inflamed tissue. In this review, we have summarized the key findings from a longitudinal scRNA-seq study that analyzed immune cells, stromal cells, and epithelial cells. Furthermore, we highlight the similarities and differences between scRNA-seq in murine models compared to human IBD. Finally, we emphasize the need for utilizing scRNA-seq technology to find suitable translational models based on the therapeutic target.

A longitudinal scRNA-seq atlas in experimental colitis

While there are other studies utilizing scRNA-seq in enriched cell populations from pre-clinical models, highlighted below is one study that has applied scRNA-seq technology to comprehensively describe the landscape of the epithelial cell, stromal cell, and immune cell populations during the onset and resolution of intestinal inflammation (29). Ho et al. subjected wild-type mice to 1.5% dextran sodium sulfate (DSS) drinking water for 6 days, then placed mice on regular drinking water for the remainder of the study. Colon tissue was collected from mice on days 0, 3, 6, 9, 12, and 15 in biological triplicates. ScRNA-seq was performed on viable cells and 14,624 cells were profiled. ScRNA-seq analysis identified 15 clusters including: mononuclear phagocytes (*Il1b*, *C1qa*, and *C1qb*), epithelial: enteroendocrine cells (*Scgn* and *Pcsk1n*), epithelial: absorptive and secretory cells (*Muc2*, *Spink4*, *Lypd8*, and *Elf3*), endothelial cells (*Pecam1* and *Flt1*), lymphatic cells (*Lyve1*), stromal cells (*Col1a1*, *Pdgfra*, and *Spon2*), two myofibroblast clusters (*Acta2* and *Myh11*), interstitial cells of Cajal (*Ano1* and *Kit*), enteric glial cells (*S100b*), T cells (*Cd3d* and *Cd3g*), plasma cells (*Igha* and *Mzb1*), plasmacytoid dendritic cells (*Siglech* and *Ccr9*), B cells (*Cd19* and *Cd22*), and granulocytes (*Cd14*, *S100a8*, and *S100a9*) (29).

To assess changes in the cellular composition, the numbers of cells in every cluster were counted at each sampling time point. Epithelial cells, stromal cells, myofibroblasts, interstitial cells of Cajal, and enteric glial cells were reduced in number with inflammation and did not repopulate during the resolution phase. In contrast, the numbers of granulocytes and B cells increased with inflammation and did not return to homeostatic numbers measured at steady state. Mononuclear phagocytes peaked in number 6 days after DSS administration and returned to baseline at the end of the study after the removal of DSS drinking water. Lastly, plasma cells decreased at days 6 and 9, but recovered in total numbers by the end of the resolution phase on drinking water at day 12. Furthermore, differentially expressed gene (DEG) analysis demonstrated phenotypic changes in mononuclear phagocytes and stromal cell clusters across all time points. The authors selected 96 "IBD risk genes" to assess how the DEGs identified in their longitudinal scRNA-seq study correlated with human IBD, 79 of the selected 96 human IBD risk genes were expressed at one or more time points and in one or more of the dysregulated cell clusters, suggesting that a dynamic expression pattern is under regulation during intestinal inflammation (29). One example is *Ifng*, which was found to be expressed during the time points associated with inflammation within the T cell cluster (29).

While scRNA-seq has been seldom applied to pre-clinical models of IBD, scRNA-seq has been more readily applied to multiple CD and UC patient cohorts to identify novel cell types, cell-cell interactions, and to generate new hypotheses of IBD pathogenesis. We will discuss in the next section the differences that have been found in human IBD using scRNA-seq in the epithelial cell, stromal cell and immune cell compartments compared to the limited murine studies including but not limited to the study described above.

scRNA-seq in human IBD by cell type and differences observed in murine models

Intestinal epithelial cells

The lining of the gastrointestinal tract (GI) is composed of diverse populations of intestinal epithelial cell lineages with

TABLE 1 Summary of the most commonly used pre-clinical models of IBD.

Classification	Type	Mechanism	Advantages	References
Chemical	Dextran Sodium Sulfate (DSS)	Destruction of colonocytes and dissemination of microbial and dietary contents into the underlying lamina propria	Can induce both acute and chronic inflammation, Can model "flare" and "remission" periods of human disease	(6)
Chemical	Trinitrobenzene sulfonic acid (TNBS)	TNBS serves as a hapten that couples with intestinal antigens that drive immunogenic responses	Drives robust TH1 and TH17 immune responses in the colon tissue	(7, 8)
Chemical	Oxazolone	Oxazalone serves as a haptenizing agent	Model can be used to interrogate type-2 immune responses, specifically IL-13 and the role of NKT cells	(9, 10)
Immune cell-mediated	T cell adoptive transfer model	Naïve $CD4^+$ or $CD8^+$ T cells become activated by the microbiota in the absence of Tregs and secrete IFNγ and IL-17A	Can study T cell subsets, polarization, and migration into the lamina propria, Can study the role of Treg suppression of effector $CD4^+$ T cells	(11, 12)
Genetically Engineered	*Il10*$^{-/-}$	Develop spontaneous colitis characterized by progressive immune cell infiltration	This model has allowed for a better understanding of the impact of the microbiome on intestinal inflammation	(13, 14)
Antibody-induced	Anti-CD40	Agonistic anti-CD40 mAb activates dendritic cells and monocytes to secrete cytokines including IL-12 and IL-23, driving the secretion of IFNγ from NK cells	This model can be used to study the role of innate immune cells in intestinal inflammation	(15)
Spontaneous	TRUC	Spontaneous colitis develops by the production of TNFα and IL-23 in response to the microbiota due to T-bet deficiencies in the innate immune system	Initial model that identified a colitogenic microbiota. Treatment of TRUC mice with anti-TNF alleviates inflammation	(16, 17)
Spontaneous	SAMP1YitFc	Generated by interbreeding of AKR mice. Spontaneous inflammation develops in the terminal ileum and cecum, and is driven by TH1 immune response.	A pre-clinical model that displays inflammation in the terminal ileum and the administration of anti-TNF alleviates inflammation – relevant for Crohn's disease	(18)
Spontaneous	$TNF^{\Delta ARE}$	Ileitis develops spontaneously due to increased stability and production of TNF due to the deletion of the *TNF* AU-rich elements.	Develops patchy inflammation in the ileum and proximal colon – similar to Crohn's disease, Neutralization of TNF alleviates inflammation, 100% penetrance of disease in this strain of mice	(19, 20)
Infectious	*Citrobacter rodentium*	*C. rodentium* attaches to the intestinal epithelial cells driving the cytokine production and activation of both innate and adaptive immune responses	Models human infection with enteropathogenic *Escherichia coli*, Allows the researcher to understand host-pathogen interactions in the context of intestinal inflammation	(21)
Infectious	*Helicobacter hepaticus*	*H. hepaticus* colonizes the colon of mice. In the absence of IL-10 signaling, colitis is characterized by the increased expression of IFNγ and IL-17A	A model for studying the role of IL-10, IL-23, IL-17A, and the innate immune system in the development of intestinal inflammation	(22, 23)

10.3389/fimmu.2023.1291990

specialized functions. These epithelial cells are derived from a common stem-cell precursor, which expresses *LGR5* (30). Intestinal epithelial cells contribute to intestinal homeostasis by maintaining barrier function and secreting mediators in response to the microbiota and underlying immune cells in the lamina propria.

The first scRNA-seq study analyzing human colonic epithelial cells from healthy volunteers or patients with UC, sampled from clinically inflamed and noninflamed mucosa, was published by Parikh et al. in 2019 (31). Visualization of scRNA-seq data identified 10 clusters of intestinal epithelial cells including undifferentiated cells, absorptive colonocytes, goblet cells, and unique enteroendocrine cell populations including L-cells, enterochromaffin cells, and precursor-like cells, and 5 clusters of stem cells. In UC, two additional clusters were identified representing inflammation-associated goblet cells and intraepithelial immune cells. Not only did this analysis provide a comprehensive landscape of the epithelial cells that are present in the healthy colon, but also identified their dysregulation in inflamed UC. One of these subsets were "BEST4/OTOP2" colonocytes. *BEST4* encodes a calcium-sensitive chloride channel, while *OTOP2* encodes a proton-conducting ion channel. These findings highlighted the power of scRNA-seq technology in identifying novel cell populations which could contribute to intestinal homeostasis and/or inflammation. Another prominent cell type linked to disease pathogenesis and barrier function are goblet cells. Goblet cells are mucus-secreting epithelial cells that are critical for the maintenance of barrier function and prevention of bacterial translocation. In IBD both their function and numbers become dysregulated (32). ScRNA-seq analysis of healthy human and UC colonic tissue revealed a distinct cluster of inflammation-associated goblet cells that had decreased expression of *WFDC2* (31), a gene encoding an anti-protease enzyme (33). To explore the significance of the loss of *WFDC2* expression in goblet cells in intestinal homeostasis, *Wfdc2*$^{+/-}$ mice were generated. These mice had abnormalities in colonic epithelial intercellular tight junction proteins, mild-to-modest epithelial cell hyperplasia, immune cell infiltration into the tissue, and proximity of gram-negative and gram-positive bacteria to the colonic epithelium compared to littermate controls (31). Although these mice were not subjected to an induced model of colitis, this study demonstrates how findings from human scRNA-seq samples can be translated in an *in vivo* setting of gastrointestinal tract dysregulation.

These novel populations become critically important in IBD as breakdown in intestinal barrier function is a hallmark phenotype. There has been great interest in underpinning the mechanisms and contributions of epithelial subsets in this loss of barrier function and to target barrier regeneration with novel therapeutics. In other studies, the authors have performed scRNA-seq analysis on healthy and CD or UC cohorts to assess the transcriptomic changes in epithelial cell subsets. One common finding amongst these scRNA-seq analyses is a depletion of BEST4^{+}/OTOP2^{+} colonocytes in UC and CD compared to healthy controls (31, 34, 35). While BEST4-expressing colonocytes are present in the human GI tract, this cell population is absent in the murine gut (36).

The primary function of microfold (M) cells is the transport of antigens from the lumen of the intestine to gut-associated lymphoid tissues such as Peyer's patches (37). ScRNA-seq uncovered an expansion of M cells in UC patients compared to healthy controls (34). Furthermore, these cells expressed elevated levels of *CCL20* and *CCL23*, important chemokines driving immune cell recruitment into the inflamed tissue. The expansion of M cells, detected by immunohistochemistry, held true in a DSS colitis model and treatment with an anti-TNF antibody abrogated the expansion of M cells in the inflamed tissue in mice, suggesting the pro-inflammatory milieu in IBD can impact the differentiation of intestinal epithelial cells during disease (38).

In addition to aiding in our understanding of cell populations in barrier breakdown at the single cell level, scRNA-seq has contributed to identifying novel biological pathways in epithelial cells. Gasdermin-D (GSDM) plays a pivotal role in driving cell death through the pore-forming activity of the protein's N-terminus and has recently been discovered to be required for IL-1β release (39, 40). ScRNA-seq of colonic tissue between healthy and UC patients revealed that secretory and absorptive progenitors, as well as colonocytes, from UC patients express elevated levels of *GSDM* (31, 41). This finding highlights a new mechanism by which GSDM-mediated IL-1β release by intestinal epithelial cells could sustain intestinal inflammation. In yet another example of how scRNA-seq translated into an *in vivo* model, *Gsdmd*$^{+/-}$ mice are protected from DSS-induced colitis as indicated by a decreased infiltration of neutrophils, macrophages, and T cells, and decreased expression of inflammatory cytokines and chemokines (41). This study reiterates the power of scRNA-seq in identifying pathways in previously underappreciated cell populations that are critical for inflammation.

In the longitudinal DSS study described above by Ho et al. (29), upon administration of DSS, enteroendocrine and both absorptive and secretory epithelia cell clusters were reduced. Thus, applying scRNA-seq to additional pre-clinical IBD models would be advantageous to find a suitable model to translate scRNA-seq findings in epithelial cells in human IBD.

Stromal cells

Stromal cells are part of the mesenchymal compartment of the intestine, and represent a distinctive heterogeneous population comprised of non-hematopoietic, non-epithelial cell types (42). Mesenchymal cells regulate homeostasis by promoting extracellular matrix (ECM) turnover through the secretion of ECM factors, such as collagen and glycoproteins, self-renewal of the intestinal epithelial barrier through WNT/β-catenin signaling and colon regeneration through production of prostaglandins (43). However, in the context of inflammation these pathways are subverted into inflammatory processes. During intestinal inflammation, dysregulation of Wnt signaling leads to impaired wound healing characterized by the activation of fibroblasts and myofibroblasts, the accumulation of collagen-rich ECM, culminating in fibrosis. Additionally, TGF-β1 signaling in fibroblasts leads to their transition to an activated phenotype, marked by an increase in ECM production, leading to fibrosis. ScRNA-seq has played a significant role in elucidating the

heterogeneous function of stromal cells and highlighted novel 'cross-talks' with other cells in the intestinal microenvironment. In the first report using unbiased single-cell profiling of over 16,500 human colonic mesenchymal cells from healthy and treatment-naïve UC patients, Kinchen and colleagues have shown how the colonic mesenchyme compartment remodels in the context of IBD (44). Specifically, the authors identified key stromal cell populations involved in immune homeostasis in intestinal inflammation. They identified a distinct cluster found near the epithelial crypts marked by the expression of *SOX6*, *F3* (CD142) and *WTN* genes, which was important in mediating epithelial cell self-renewal in physiological conditions. Interestingly, scRNA-seq of stromal cells from the DSS colitis model revealed similarities between human and mouse stromal cell clusters, with *SOX6* being highly conserved between the two (44).

ScRNA-seq of UC colonic mesenchyme revealed changes in gene expression and cell composition within the stromal compartment (44). Single-cell analysis identified 12 distinct clusters, with a significant expansion of a cluster marked by genes involved in response to TNF and leukocyte migration. Highly ranked markers included lymphocyte trafficking chemokines, such as *CCL19* and *CCL21*; T cell co-stimulatory TNF-superfamily ligand (*TNFSF14*/*LIGHT*) and MHC II invariant chain (CD74); CD24; IL-33 and Lysyl oxidases. In UC, the enrichment of this cluster was associated with a decrease in the *SOX6* expressing cluster in inflamed tissues, further highlighting the heterogeneous nature of the stromal-driven responses. Thus, this study revealed a divergent response in the context of disease, marked by an increase in pro-inflammatory fibroblasts and a reduction in the stromal subsets associated with epithelial self-renewal and resolution of disease. The role of stromal cells in IBD was further validated in the DSS model of colitis (44). ScRNA-seq analysis revealed high expression of *Lox* and *LoxI1* in the mesenchymal populations. Lastly, the authors investigated whether blockade of this pathway could ameliorate DSS. The Lox family of lysyl oxidases generate oxidative stress responses, disturbing the redox balance within the tissues, which in turn mediate recruitment of inflammatory mediators, thus sustaining IBD pathogenicity. Indeed, administration of Lox/LoxI1 inhibitor, β-aminopropionitrile, improved the clinical score of mice receiving DSS drinking water (44).

Kong et al. profiled 720,633 cells from the terminal ileum and colon of CD and non-IBD donors by scRNA-seq (45). The authors identified *CHMP1A, TBX3, and RNF168* as disease-associated genes which are affiliated with myofibroblast activation (45). To validate the roles of these three genes in fibrosis development, the authors generated and pooled siRNA oligos to knockdown *CHMP1A, TBX3, and RNF168* in normal human intestinal fibroblasts. Knockdown of *CHMP1A, TBX3, and RNF168* significantly impaired TGF-β-driven collagen gene expression (45).

To gain a better understanding of the complexity of the fibroblast cellular networks and how they underly stricture formation in CD, Mukherjee and colleagues have generated the first scRNA-seq atlas of strictured bowel from CD patients (46). Specifically, scRNA-seq was performed on CD resections containing non-involved, inflamed non-strictured and strictured segments, as well as non-IBD bowel segments. ScRNA-seq analysis revealed significant differences in the cellular composition between non-inflamed, inflamed and strictured segments. Comparison between non-strictured and strictured segments revealed significant changes in lymphocytes, smooth muscle cells, endothelial cells, fibroblasts and myeloid cells within the epithelial and lamina propria fractions. Additionally, the strictures were highly heterogenous with regards to cell composition, with 19 distinct cell types being identified, further clustered into fibroblasts, smooth muscle and endothelial populations (46).

Further analysis of the fibroblast compartment revealed six fibroblast populations enriched in CD strictures as opposed to non-strictured segments (46). These fibroblasts were characterized by an inflammatory phenotype, marked by the expression of pro-fibrotic markers involved in TGF-β signaling, macrophage differentiation and ECM production. However, the predominant cluster in these strictures were the MMP^+/$WNT5A^+$ fibroblasts, which were previously found to be enriched in the mucosa of patients with UC resistant to anti-TNF therapy (46). Among the populations within the stromal niche, $CXCL14^+$ fibroblasts were the main contributors to transcriptional changes in strictures. These fibroblasts were associated with increased ECM production and CXCL14 displayed pro-fibrotic functions (46).

More importantly, the authors identified Cadherin11 (*CDH11*) as the only cell surface receptor co-expressed in both MMP^+/$WNT5A^+$ and $CXCL14^+$ fibroblasts. Interestingly, *CDH11* expression was shown to increase in CD strictures. The therapeutic potential of targeting CDH11 was shown in a DSS-induced fibrosis model of colitis in *Cdh11* knockout mice (46). In this model, mice are subjected to two cycles of DSS drinking water followed by a recovery period with normal drinking water. Despite no differences in inflammation being observed in *Cdh11* knockout mice compared to wild-type controls, *Cdh11*-knockout mice were protected from fibrosis development. Similarly, administration of an anti-Cdh11 mAb ameliorated DSS-driven fibrosis. In a longitudinal scRNA-seq analysis in the DSS model, Ho et al. observed that stromal cell clusters had strong influences on other clusters, highlighting their potential role in intestinal inflammation (29). Looking closely at these interactions, the authors identified relevant genes during the recovery phase, with the highest expression observed in *Serpina3n*, a serine protease inhibitor. To validate these observations, the authors examined the progression of DSS colitis in a *Serpina3n* knockout mouse. Although the disease progression was similar to wild-type mice, the knockout mice recovered much faster. Furthermore, the authors examined the mechanisms by which Serpina3n ameliorated DSS-induced intestinal inflammation. Using scRNA-seq on colon treated with Serpina3n protein, they observed that genes associated with ECM organization and cytokine mediated signaling pathways were enriched in stromal cells. Additionally, there was a decrease in inflammatory interactions and in the number of neutrophils, warranting the therapeutic potential of Serpina3n to accelerate recovery from intestinal inflammation. Overall, scRNA-seq has been crucial in characterizing the heterogeneity of the stromal population, as well as their interactions with the immune compartment in IBD. Alternatively, applying this technology to preclinical models of IBD could help uncover important

mechanisms underlying resistance to current therapies. To address this, West and colleagues used transcriptomic approaches to uncover relevant genes associated with anti-TNF resistance. Oncostatin M (OSM) is expressed by stromal cells and was identified as a potential biomarker associated with anti-TNF failure (47). This observation was validated in a mouse model of IBD driven by oral *Helicobacter hepaticus* infection and anti-IL-10R blocking antibody, which mirrors the T cell-dependent pathology driving resistance to anti-TNF therapy. Using this model, treatment with an oncostatin receptor-Fc significantly attenuated colitis (47). In a more recent study, bulk and single-cell transcriptomics have been applied to inflamed tissue from three IBD patients' cohorts undergoing surgical resection (48). The authors observed similar gene signatures from therapy non-responders, marked by genes indicating high neutrophil infiltration and activation of fibroblasts at sites of deep ulceration. Further analysis revealed important neutrophil-attractant signatures in fibroblasts, marked by an increase in IL-1R signaling, suggesting that this pathway is important in the inflammatory fibroblast/neutrophil recruitment in patients that are nonresponsive to current therapy (48).

Immune cells

Monocytes/macrophages and dendritic cells

In active IBD, macrophages secrete pro-inflammatory cytokines and react to commensal bacteria, with CD exhibiting aggregates of macrophages and other inflammatory cells (granulomas) associated with higher resection risk (49). IBD susceptibility involves various genetic loci linked to monocyte and macrophage function, including *NOD2*, *ATG16L1*, and *IRGM* (50–52). In 2019, two scRNA-seq studies explored intestinal macrophages in CD and UC. One scRNA-seq analysis of 11 ileal CD patients revealed resident and inflammatory macrophage subtypes. The resident subtype expressed *C1Qs*, *CSF1R*, *MAFB*, and *MRC1*, while inflammatory macrophages showed elevated levels of chemokines (*CXCL2*, *CXCL3*, *CXCL8*) and cytokines (*IL23*, *IL6*, *IL1B*, *IL1A*, *TNF*, *OSM*) Notably, pro-inflammatory interactions between non-epithelial stromal cells and macrophage-derived oncostatin-M (OSM) were found within the inflamed intestine, linked to anti-TNF-resistant CD (53). The second scRNA-seq study conducted on 18 UC patients revealed the presence of an inflammatory monocyte cluster with prominent levels of *OSM* expression that were associated with disease progression and resistance to anti-TNF treatment. A macrophage cluster was also identified that closely interacts with B cells and T cells. This macrophage cluster exhibited an enrichment of genes linked to IBD susceptibility, such as *GPR65*, *ADCY7*, *PTGER4*, *PTPRC*, and *SH2B3* (34). A very recent scRNA-seq study provided a therapeutic map for CD and UC after anti-TNF therapy in a longitudinal manner (54). Importantly, the presence of a granuloma signature, characterized by $C1Q^{high}$ $IL1B^{low}$ resident macrophage cells, was specifically associated with non-responders in CD. Moreover, genes associated with an inflammatory monocyte profile (*S100A9, S100A12, FTH1, IL1RN*) showed higher levels in non-responders but were reduced in responders. The latest study utilizing scRNA-seq and spatial analysis (CosMx Spatial Molecular Imaging) found that resident macrophages were present in both healthy and active IBD patients (55). Notably, inflammatory macrophages displayed patient-specific adaptation, characterized by an alternative activation pattern featuring the expression of EGFR ligands, *NRG1*, *HBEGF*, *CLEC10A*, and *ASGR1*, differing from the conventional M1 signature. The study also suggested a potential role of interactions between M2 or inflammation-dependent associated macrophages (representing the predominant inflammation-dependent macrophage state) and inflammatory fibroblasts in contributing to disease pathophysiology.

Through scRNA-seq studies in mice (56–61), we have gained insights into the diverse inflammatory roles of gut macrophages. In the DSS-induced colitis study, the abundance of $Il1b^{+}$ $C1qa^{+}$ $C1qb^{+}$ macrophages increased in diseased animals, peaking post DSS administration, then returning to baseline during water administration (29). The mouse single-cell findings align with how intestinal cues influence transcription factors shaping macrophage subsets. The recent single-cell investigation using the *Helicobacter hepaticus*-induced colitis model, highlights interferon regulatory factor 5 (IRF5)'s role in mucosal macrophage differentiation. *Irf5* knockout hindered $CD11c^{+}$ mucosal macrophage formation, unveiling IRF5's contribution to pro-inflammatory $CD11c^{+}F4/80^{+}$ macrophages during inflammation, driving colitis development (60). IRF5's link to inflammatory macrophages and genetic risk factors for UC and CD underlines these mouse findings' translational relevance to human IBD (62).

Dendritic cells (DCs) are antigen presenting cells that bridge both innate and adaptive immune responses. In the intestine, DCs continuously sample antigens by extending processes through the epithelial cells and glycocalyx layers into the lumen, or by remaining in the lamina propria or Peyer's patches to process antigens that may have translocated (63). While multiple scRNA-seq studies in humans have begun to showcase the importance of different DC subsets in driving IBD pathogenesis, scRNA-seq studies in mouse models of IBD lag, specifically in the inclusion of diverse DC subsets, such as plasmacytoid DCs (pDCs), conventional DCs (cDCs), and monocyte-derived DCs (moDCs) (34, 45, 53, 54, 64). Corbin et al. used *Helicobacter hepaticus*-induced colitis coupled with an anti-IL-10R mAb in $Irf5^{-/-}$ mice and found the frequencies of DC populations during ongoing inflammation remained unchanged compared to steady-state (60). ScRNA-seq analysis on mononuclear phagocytes taken from the inflamed colonic lamina propria of $CX3CR1^{+}$ wild-type and $Irf5^{-/-}$ mice. Within the four clusters of DCs, all lacked *Cd64* expression, but included *Flt3, Cd11c*, and the DC-specific MHCII genes *H2-DMb2* and *H2-Oa.* DC2-like cells were identified by *Sirpa, Kmo, Cd209a*, and *Cd7* expression. The strong expression profile of *Pu.1* but low *Flt3* expression within these cells from these clusters suggested some may be moDCs. The other two clusters were likely representative of cDC1s (termed "*Xcr1* DC" and expressing $Xcr1^{high}$ $Irf8^{high}$ $Sirpa^{low}$) and a smaller group of $Ccr7^{+}$ migratory DCs. Ho et al. also identified by scRNA-seq that pDCs decrease in number shortly after DSS exposure, however, the numbers stabilize over the resolution phase (29). Overall, this experiment showed that the heterogeneity of DCs could be identified and classified in the

inflamed colonic tissue from these mice using scRNA-seq. The scarcity of murine single-cell studies necessitates further scRNA-seq in IBD models for a better understanding of these cells' pivotal roles.

CD4$^+$ T cells

CD4$^+$ T cell function in the intestine can be broadly categorized as effector (pro-inflammatory) or regulatory (anti-inflammatory). Regulatory T cells (Tregs) are CD4$^+$ T cells that are critical for tolerance and dampening excessive immune responses against dietary and microbial antigens, an integral mechanism for maintaining intestinal homeostasis (65). In IBD, this balance of anti-inflammatory Treg function is lost and exuberant pro-inflammatory T cell responses against the commensal microbes drives and sustains chronic inflammation. In the paragraphs below, we will mainly highlight Treg and TH17 biology (63).

Regulatory T cells

ScRNA-seq studies have been instrumental in advancing our understanding of the complex cellular heterogeneity and gene expression patterns of intestinal Treg cells in UC and CD. ScRNA-seq uncovered previously unidentified FOXP3$^+$ cell subtypes involved in IBD. In a related study, Corridoni et al. (66) utilized multi-modal scRNA-seq to examine colonic CD8$^+$ T cells in healthy individuals and those with UC. Interestingly, they noted an elevated presence of double-positive CD4$^+$ CD8$^+$ FOXP3$^+$ T cells in UC patients. Smillie et al. (34) noted heightened levels of CD8$^+$IL-17$^+$ T cells and Tregs in inflamed UC tissues. They observed a TNF expression shift towards Tregs during inflammation. The study proposed that TNF$^+$ Treg cells could significantly influence IBD progression, potentially causing resistance to TNF antibodies and playing a crucial role in CD8$^+$ T cell adaptability. In healthy tissue, Tregs represented 1% of TNF expression, but this increased to over 14% during inflammation. Interestingly, in another study by Devlin et al. 67) found increased FOXP3$^+$/BATF$^+$ Treg cells in inflamed UC patients. They used scRNA-seq on CD45$^+$ hematopoietic cells from UC patients with and without ileal pouch-anal anastomosis. These Tregs were enriched in inflamed UC and pouchitis samples, suggesting a role for BATF in their recruitment during inflammation. ScRNA-seq conducted by Boland et al. (68) revealed transcriptionally distinct Tregs expressing *ZEB2* in UC. Among Treg gene profiles, 288 genes differed between healthy individuals and UC patients, including *SATB1*, *KLF2*, *MYC*, and *ITGB1*, associated with Treg function. Notably, *ZEB2*, linked to CD8$^+$ T cell function, exhibited high expression in UC-related Treg cells. The reduction of ZEB2 enhanced suppressive function in murine Treg cells.

Huang et al. (69) analyzed initial diagnosis colon biopsies from healthy individuals and CD/UC patients, finding enriched Treg cells (slightly more in CD) and CD8$^+$GZMK$^+$ effector memory T cells in both conditions. Additionally, Jaeger et al. (70) used scRNA-seq and multi-parameter flow cytometry or mass cytometry to examine CD patients' inflamed terminal ileum tissue. Inflammatory tissue IEL showed reduced Tregs, CD8$^+$T, γδT and TFH but elevated TH17 cells. Lamina propria (LP) analysis revealed decreased Tregs and TFH cells, while CD8$^+$T cells and TH17 cells increased. Tregs in LP were enriched in *GPX1* and *GLRX*, associated with oxidative stress protection via FOXP3. *GPX1* expression in LP Tregs hinted at activated anti-oxidative pathways, pertinent to CD due to *GPX1* gene's CD risk connections. Martin et al. (53) examined ileal samples from 13 CD patients at the single-cell level. In their pursuit of unraveling the cellular profile linked to resistance against anti-TNF drug therapy, they observed an abundance of Tregs with elevated IL-10 levels, along with low IL-17A expression within inflamed ileal lesions. Additionally, Treg populations have been detected in CD and UC patients by Mitsialis et al. (71). They observed pro-inflammatory memory-like IL17A$^+$ Treg subsets expanded uniquely in active UC. Among IBD-enriched memory Tregs, one group was FOXP3$^+$, while another was FOXP3^{low} with strong pro-inflammatory cytokine expression (IFNG$^+$TNF$^+$IL17A$^{+/-}$), indicating altered Treg function in IBD. Additionally, they observed an unusual expansion of novel *IL1B*$^+$ Tregs in peripheral active CD compared to inactive CD and active UC. Furthermore, in a recent development by Nie et al., a computational tool called "scIBD" provided an integrated assessment of scRNA-seq data associated with IBD. This platform enabled the recognition of different cell types and IBD-associated genes. The meta-analysis corroborated the greater prevalence of Tregs in both UC and CD compared to healthy tissues, consistent with prior findings (72).

The study by Miragaia et al. (73) conducted single-cell analysis to comparatively investigate human and murine colon Treg populations. In mice, three distinct Treg subpopulations were identified: non-lymphoid tissue (NLT), suppressive, and lymphoid tissue-like (LT). NLT Tregs displayed a GATA3$^+$-subpopulation phenotype, expressing *Gata3*, *Nrp1*, *Areg*, *Il1rl1*, and *Ikzf2*, while suppressive Tregs resembled the peripherally derived RORγt$^+$-subpopulation. LT-like Tregs exhibited LT-associated gene expression (*Sell*, *Ccr7*, *Tcf7*, *Bcl2*) and fewer NLT-associated genes (*Klrg1*, *Cd44*, *Icos*, *Rora*, *Tnfrsf9*, *Itgae*), signifying functional diversity. Notably, 17 human-mouse colon Treg markers overlapped, including *Tnfrsf4*, *Lgals1*, *Srgn*, *Cxcr6*, *Maf*, and *Ikzf3*, indicating conserved roles. Paralogous genes demonstrated inter-organism expression pattern substitutions (e.g., *Pim1-Pim2*), hinting at the evolution of cellular communication pathways. Despite interspecies disparities, the study underscores the conservation of the TNFRSF-NF-κB-pathway between mice and humans (73). Surprisingly, the scRNA-seq study mentioned earlier, which focused on the murine DSS model (29), did not identify Tregs in any of the collected time course samples. However, a very recent preprint (74) took a different approach. Using MERFISH, a method for spatially resolved single-cell transcriptome profiling, they studied spatial and cellular changes during gut inflammation initiation and recovery in a DSS model. In day 9 samples, corresponding to peak inflammation after DSS administration, mucosal remodeling was observed, along with the appearance of diverse cell populations, including Tregs. Thus, the limited investigation of murine Tregs at the single-cell level underscores the need for further scRNA-seq studies on murine IBD models to gain a deeper understanding of the roles played by this essential cell population.

TH17 cells

Naïve CD4$^+$ T cell polarization towards an effector phenotype requires signals from antigen-presentation, co-stimulation, and cytokines in the local tissue environment. *In vitro* polarization of

human CD4$^+$ T cells towards a TH17 phenotype requires TGF-β, IL-1β, IL-6, IL-23 and the expression of RAR-related orphan receptor g (RORγT) (75). Polarized TH17 cells secrete IL-17A, IL-17F, and IL-22 – cytokines which are associated with the development of inflammation. While not required for TH17 differentiation, IL-23 signaling, through the IL-23 receptor complex, promotes RORγT stability and the acquisition of a pathogenic phenotype in these cells. IL-23 is upregulated in numerous autoimmune diseases, including IBD (76). Furthermore, genome-wide association studies have identified *IL23R* as a genetic susceptibility locus for IBD. A key role for IL-23 in IBD pathogenesis has been highlighted by the clinical efficacy of anti-IL-23 biologics (77–79).

Jaeger et al. used scRNA-seq analysis to compare T cells from intra epithelial lymphocytes (IELs) and the lamina propria (LP) found in the terminal ileum of adults with severe CD to measure heterogeneity in T cell lineages and subsets (70). There was a marked increase in pro-inflammatory, activated CD39$^+$CCR6$^+$ and CD39$^+$CD4$^+$ TH17 cells but decreased CD8$^+$T, γδT, TFH and Treg cells in the IEL compartment of CD patients, demonstrating that loss of balance between TH17 and Treg cells plays an important role in disease progression. Within IELs, they identified unique T cell clusters, including one with NKp30$^+$γδT cells expressing RORγt and producing IL-26 upon NKp30 engagement. Some of these T cell subsets expressed TH17 markers including *RORC, IL23R, IL22, CXCR4*, and *IL26*. While these RORγt$^+$ γδ T cells have been shown and described in mouse models (80, 81), Jaeger et al. identified this subset of γδ T cells in the IEL of humans. γδ T cells can constitute as much as 40% of the IELS in the intestine. These cells can have cytotoxic, immunoregulatory, and tissue repair functions within the intestinal mucosa (82). However, the role of human γδ T cells in CD remains to be fully elucidated, with multiple studies showing either a decrease or increase in number in the blood or inflamed tissue (82). Similar analysis in the LP found a biased TH17/Treg ratio in CD. The CD39$^+$ TH17 cells that were found within the IEL may prove to be a double-edged sword, as their expression of *GZMB* and *CCL4* could make them pathogenic and able to recruit other inflammatory cell types to increase epithelial damage (70). Conversely, their production of IL-17 and IL-26 may enhance epithelial barrier integrity and protection (70). Overall, this study showed an altered spatial distribution of T cell subsets between the two cellular compartments, with TH17s in the LP bearing more markers of quiescence (i.e., CXCR4 and CD39) than in the IEL compartment that may correlate with transmural inflammation during IBD pathogenesis (70).

An atlas of over 350,000 cells from the colonic mucosa of patients with and without UC was used to reveal 51 cell subsets, including epithelial, stromal, and immune cells (34). When reviewing T cells, several CD4$^+$ T cell subsets showed increased expression of *IL17A*, showcasing an expansion of TH17 cells with pro-inflammatory phenotypes. However, the CD8$^+$ T cell subsets showed the largest induction on *IL17A*. Using an *in-situ* analysis, the authors found CD8 co-expressed on both CD4$^-$ and CD4$^+$ cells. These CD4$^+$CD8$^+$IL17$^+$ T cells have been largely uncharacterized, however, these cells correlated with activated cytotoxic programs and genetic signatures conducive to TH17 pathogenicity and tissue damage (e.g., *RBPJ* and *IL23R*) that have been reported in mice (83). Kong et al. also showed *IL23R* to be an IBD risk gene in cells taken from the colon and terminal ileum of patients with CD, but they showed the greatest mean expression to be in innate lymphoid cells (ILCs) in both tissue types (45).

A recent study in mice showed that colonic immunopathology driven by Red 40, and IL-23 may not actually depend on these classical TH17 responses; as IL-17A and IL-17F blockade did not prevent colitis development in mice that conditionally expressed *IL23* in CX3CR1-positive myeloid cells (84). Additionally, they sought to define this mechanism further. They used the T cell transfer colitis model, an invaluable model to dissect pathogenic and protective mechanisms of CD4$^+$ T cells (11) and scRNA-seq to identify a new population of IFNγ-secreting CD4$^+$ cytotoxic T lymphocytes that were induced by IL-23 and the food dye Red 40 to promote colitis pathogenesis (27). Without IFNγ, IL-23 and Red 40 did not induce progressive colitis development and prevented colonic epithelial cell death, showcasing perhaps a specialized relationship between IL-23, IL-17, IFNγ, and overall TH17 signaling in the development of IBD in mice (27).

In a longitudinal DSS mouse model, Ho et al. looked at how cell phenotypes changed during inflammation (29). Using a pseudotime analysis, significant changes were observed in T cell subsets (which expressed *Cd3d* and *Cd3g*). The IBD risk gene *Ifng* was expressed over the entire DSS-induced disease time course in the T cell cluster but only at day 6 in stromal cells, indicating subtle dynamic phenotypic changes in different cell types. Capturing these subtle changes over time in a human model is difficult, exemplifying how useful mouse models of IBD can be, especially when paired with scRNA-seq analysis.

CD8$^+$ T cells

CD8$^+$ T cells are a cytotoxic T cell subset that drive cell-death through numerous pathways including perforin and granzyme release and by expressing FAS ligand (85). CD8$^+$ T cells are typically in lower abundance in the intestine at steady state compared to CD4$^+$ T cells (86). Despite numerous evidences that IBD pathology is associated with exuberant CD4$^+$ T cell responses, recent scRNA-seq data revealed that CD8$^+$ T cells also play a role in IBD pathogenesis (25, 66, 68).

T cells sorted from the IELs of healthy donors and CD patients revealed different CD8$^+$ clusters (70). One of these clusters expressed genes associated with an effector phenotype (*KLRG1*, *GZMB*, *GZMK*, and *IFNG*). Whereas, the other CD8$^+$ cluster highly expressed the tissue residency marker *ITGAE*. When these cells were analyzed further using a new clustering strategy, this highlighted the expression of *IL7R*, *IL2* and *TCF7*, genes associated with a memory phenotype. The authors hypothesized

that the resident memory CD8$^+$ T cell cluster might gain cytotoxic and antimicrobial functions via S100A family members during inflammation. In the same study, scRNA-seq of CD8$^+$ T cells in the LP identified three clusters: effector CD8$^+$ T cells (*KLRG1*, *EOMES*, *GZMB*), a second group expressing CD160 and *ITGA1*, and a third group expressing NK cell receptors such as *KLRC1*, *KLRD1*, and *ENTPD1* (70). In summary, similar and unique CD8$^+$ T cell clusters were identified in the IEL and LP compartments of CD patients.

A second scRNA-seq analysis of colonic T cells revealed that CD8$^+$ and γδ T cells both expressed *ENTPD1* (64). This gene codes an ectonucleotidase that converts ATP and ADP to AMP. In colonic CD8$^+$ T cells from pediatric cases of colitis, decreased *ENTPD1* expression was observed in association with a defective cyclic AMP (cAMP) pathway. Mechanistically, the reduction of cAMP is believed to result in platelet aggregation and hyperinflammation. The authors then used DSS-induced acute colitis mouse model to test the effect of dipyrimodole, a phosphodiesterase (PDE) inhibitor. PDE is an enzyme the degrades and inactivates cAMP and cGMP, therefore, inhibiting PDE will increase cAMP levels *in vivo*. Administering mice dipyrimodole increased the colon length, prevented body weight loss, improved barrier function, and crypt structure in the DSS treated mice. As a result, they demonstrated increased expression of *Entpd1* and elevated cAMP levels also influenced platelet aggregation and TNFα production, linking the findings observed in a pre-clinical model of colitis back to human IBD (64).

In yet another study, scRNA-seq of CD8$^+$ T cells from dissociated colonic tissues of UC patients, identified tissue resident (*ITGAE* and *DUSP4*), naïve (*SELL*, *CCR7*, and *TCF7*) double positive CD8$^+$CD4$^+$ (*GZMA*, *RORA*, and *CCR6*) and increased numbers of *IL26* expressing T cells (66). Although *IL26* is not expressed in mice, human IL-26 can signal through the IL-10RB and IL-20RA heterodimeric receptor in mice (87). Deeper analysis of the *IL26*-expressing CD8$^+$ T cells displayed both an ILC3 signature (*RORC*, *CKIT and AHR*), a TH17 signature, and several exhaustion markers (*PDCD1, HAVCR2, and CTLA4*). Interestingly, these *IL26* expressing CD8$^+$ T cells co-expressed *IL23R* and *IL17A*, which has also been shown in a recent longitudinal human single cell therapeutic atlas of IBD (54). To further assess the role of *IL26* in UC, the authors subjected humanized *IL26* transgenic mice to DSS-induced colitis and tested the efficacy of an anti-IL-26 monoclonal antibody. Using these tools, the authors demonstrated that IL-26 has a protective role in the acute model of colitis in mice; however, whether IL-26 has the same protective effect under chronic inflammation conditions remains to be elucidated (66).

While typically associated with protecting the host from infection, a pathogenic role for resident memory CD8$^+$ T cells (Trm) in autoimmune diseases have become appreciated (53, 68, 88). Boland and colleagues identified four CD8$^+$ Trm clusters, expressing high levels of *CD69, ITGAE, CD101, CCR6, ITGA1* and lower levels of *KLF2* and *S1PR1*, with unique clonal expansion of a cluster of CD8$^+$ Trm cells in UC patients compared to healthy controls (68). This cluster also expressed transcripts encoding cytotoxic granules, metabolic regulators, and the transcription factors *ZEB2* and *EOMES*. The authors then used two pre-clinical models of colitis to demonstrate a pathogenic role for CD8$^+$ T cells. First, *Il10* knockout mice fed piroxicam had a marked accumulation of CD8$^+$ T cells in the colon. The administration of an anti-CD8 mAb in these mice reduced weight loss and colon pathology. Secondly, the adoptive transfer of CD8$^+$ T cells transduced with *Eomes* retroviral constructs into Rag1 deficient mice significantly increased weight loss and more colonic inflammation after DSS administration (68).

B cells/plasma cells

Plasma cells are terminally differentiated B cells that secrete immunoglobulin (Ig), including IgM, IgE, IgA, and IgG. While IgA levels are highly abundant in the intestinal tissue and contribute to intestinal homeostasis (89), anti-microbial IgG in the gut is also observed at steady-state (90, 91). The large presence of anti-microbial IgG observed in IBD has renewed interest due to an *FCGR2A* variant associated with disease pathogenesis (92, 93). Thus, the role of IgG in the inflamed mucosa of IBD patients is an area of active investigation.

Huang et al. identified increases in CD138$^+$ plasma cells in pediatric CD subjects by scRNA-seq (64). More specifically, seven B cell clusters including tissue resident B cells (CD44, CD69), CD19$^+$ B cells, CD27^{high} B cells, CD27^{low} B cells, and two CD138$^+$ plasma cell clusters expressing *IGHG1* and *IGHA1* respectively were identified. Interestingly, the tissue resident marker (CD103) was increased in plasmablasts. In addition, they observed the transition from IgA1 to IgG1 in the IBD subjects, in line with the study showing the impact of CXCR4$^+$IgG$^+$ plasma cells to the IBD pathogenesis (94). In another study scRNA-seq study by Boland et al. characterized different subsets of B cells and plasma cells (68). They observed an increase in the IgG1$^+$ plasmablasts in UC whereas IgA2$^+$ plasma cells were elevated in the healthy controls. All together, these scRNA-seq studies highlight the presence of B cells in the inflamed mucosa and bias towards IgG class-switching in plasma cells in human IBD. Uzzan and colleagues identified twenty clusters of B cells isolated from the LP when comparing healthy and UC patients (95). These clusters included naïve B cells (*IGHD*, *FCER2*, and *CD72*), memory B cells (*CD27* and *TNFRSF13B*), atypical memory B cells (*FCRL5*, *FCRL4*, and *DUSP4*), germinal center-like B cells (*AICDA*, *BCL6*, and *FAS*) and plasma cell populations based on the expression of immunoglobulin genes. Additionally, they detected an *IFNG* signature specific to a naive B cell cluster expressing *IGHD*, *FCER2*, and *CD72* suggesting a shift in the systemic humoral response towards a pro-inflammatory IgG B cell phenotype in UC.

Kong et al. collected tissue from CD patients and non-IBD donors from inflamed and non-inflamed regions of the terminal

ileum and the colon and characterized the cellular networks by scRNA-seq (45). B cells were sub-clustered into plasma cells (*SDC1, MZB1, SSR4, XBP1*), B cells (*BANK, MS4A1/CD30, ASDAM28, VPREB3*) and germinal center B cells (*LRMP, GPT2, PAG1*). Plasma cells were a higher percentage of the sample in inflamed CD in the terminal ileum (45). Martin et al. described the GIMATS module, consisting of the presence of IgG-expressing plasma cells, inflammatory mononuclear phagocytes, activated T cells, and stromal cells, is expressed in a subset of ileal CD and is linked to anti-TNF therapy resistance (53).

On the other hand, in the mouse scRNA-seq study Ho et al. described decrease in the IgA producing plasma cell population at most severe time points of intestinal inflammation, whereas IgA plasma cell numbers recovered during the resolution phase (29). While differences in B cell biology have been identified between healthy and human IBD, the role of B cells has begun to be explored in pre-clinical models of IBD. In a separate study by Frede et al, they performed another longitudinal DSS-colitis study where scRNA-seq was performed on enriched B cells from the colonic LP on days 0 and 14 after DSS exposure in mice (26). While no differences in B cell cluster numbers were observed, the authors identified an expansion in an IFN-induced B cell cluster marked by *Serpina3g*, *Serpina3f*, *Stat1*, *Tgtp2*, and *Zpb1* during the mucosal healing stage of disease at day 14. Subsequent experiments where B cells were depleted by administering CD19cre-iDTR^{HET} mice diphtheria toxin during DSS administration enhanced tissue regeneration, suggesting a pathogenic role of B cells in mucosal healing (26).

Conclusions and future perspectives

The advances and application of single cell transcriptomics to human IBD samples have revolutionized our understanding of the complex and dynamic interactions between epithelial cell, stromal cell, and immune cell populations. Additionally, this technology has also been instrumental in identifying novel cell types and rare populations of cells, which were likely not detected previously. While numerous human IBD scRNA-seq studies were highlighted in this review, it is evident that the application of this powerful technology has not been applied enough to pre-clinical models of IBD to translate findings found in human disease. To our knowledge, the only pre-clinical model that applied scRNA-seq to generate a comprehensive landscape of epithelial cells, stromal cells, and immune cells was the longitudinal DSS study by Ho et al. (29). However, this study did not identify all cell types that have been identified by scRNA-seq in human studies (Figure 1). For example, a recent study combining scRNA-seq with spatial analysis (65) uncovered notable diversity within neutrophils in IBD colonic mucosa. Neutrophils were categorized into three distinct states (N1, N2, and N3) based on their unique gene expression profiles.

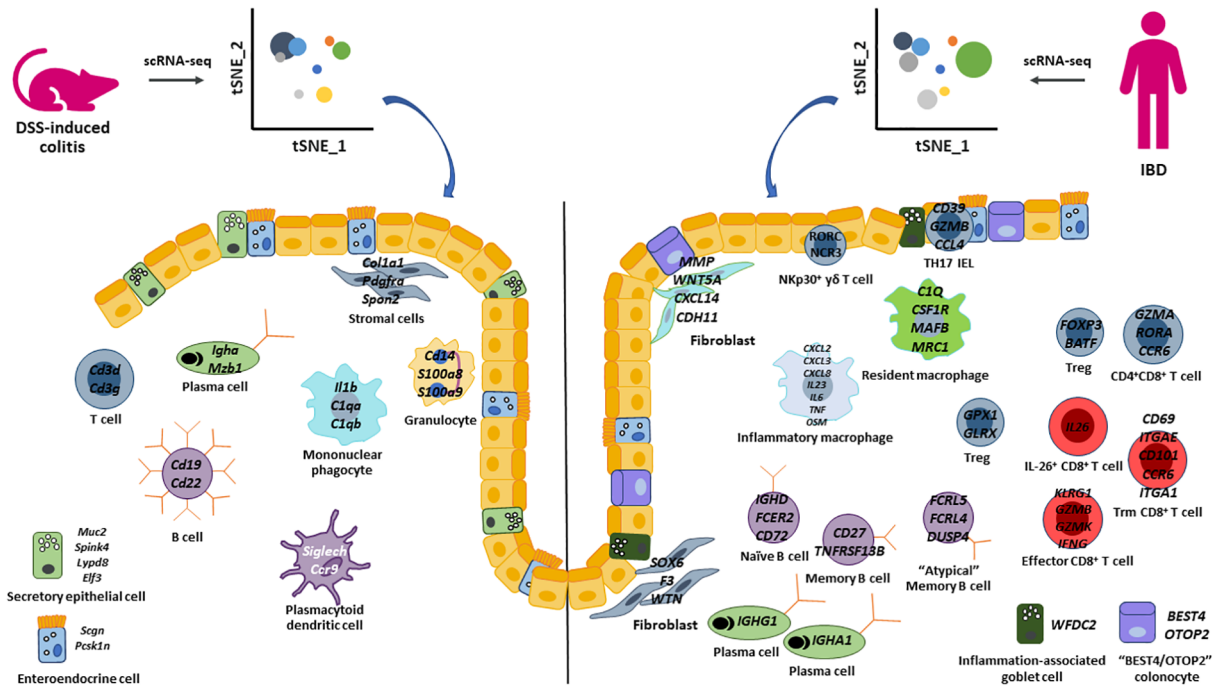

FIGURE 1
Summary of epithelial cell, stromal cell, and immune cell populations identified by scRNA-seq in the DSS-induced colitis model and human IBD. Highlighted key cell populations identified in this review that describe similar and different cell populations between the DSS-colitis pre-clinical model and human IBD.

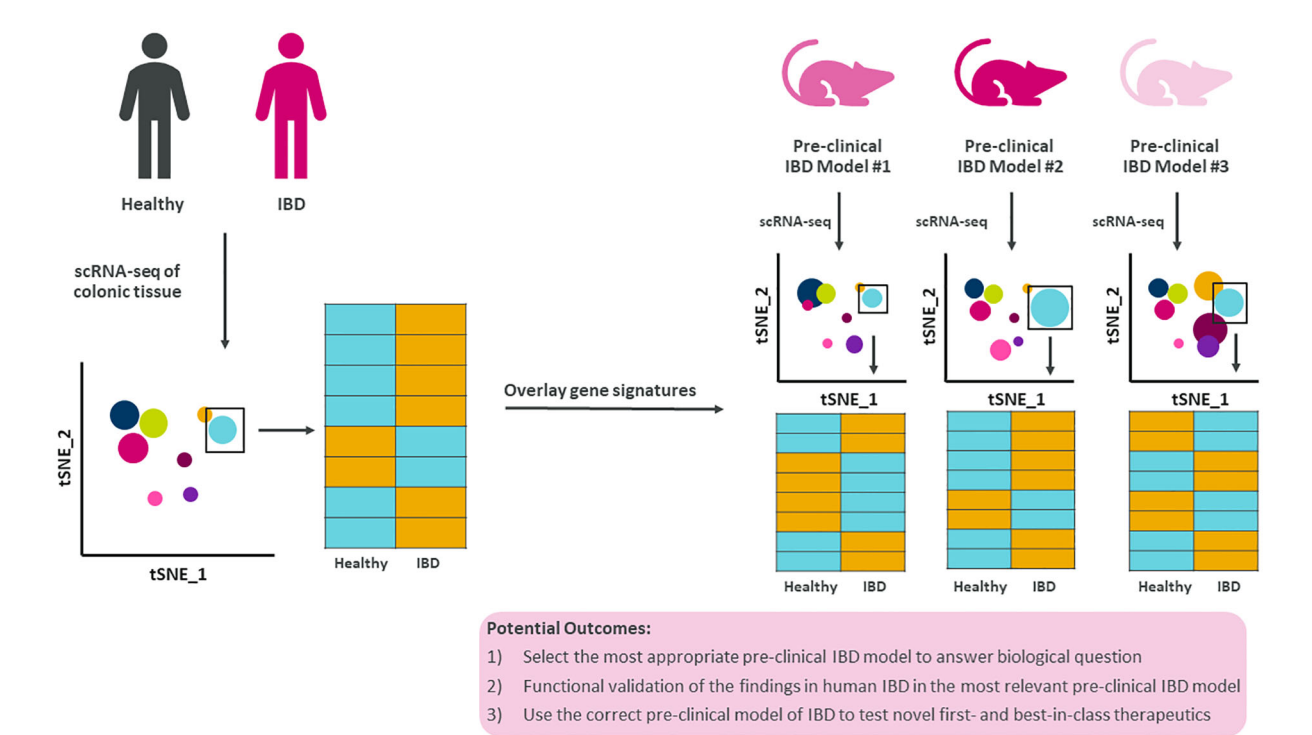

FIGURE 2
Summary figure of how translating single cell findings in human to pre-clinical models improves our understanding of disease. Human IBD gene signatures at the single cell level could be overlayed with single cell gene signatures from multiple pre-clinical models of IBD allowing for data-driven selection of the most appropriate pre-clinical model to test novel biology, questions, and therapeutics.

Furthermore, novel clusters of innate lymphoid cells have been identified and contribute to intestinal inflammation (96, 97). Thus, by expanding the use of scRNA-seq to other pre-clinical models of IBD, we will be better equipped to select the most appropriate model to translate and functionally validate findings from human IBD studies.

Furthermore, by expanding the use of scRNA-seq to all pre-clinical models to generate comprehensive disease atlases with epithelial cells, stromal cells, and immune cells will warrant the opportunity to generate novel hypotheses for therapeutic strategies (Figure 2). Overlaying gene signatures at the single cell level from human IBD and numerous pre-clinical models would significantly increase the likelihood of selecting the most appropriate pre-clinical model to test novel first- and best-in-class therapeutics and modalities to treat and ultimately cure IBD.

Author contributions

EPK: Conceptualization, Writing – original draft, Writing – review & editing. AM: Conceptualization, Writing – original draft, Writing – review & editing. IK: Conceptualization, Writing – original draft, Writing – review & editing. B-EJ: Conceptualization, Writing – original draft, Writing – review & editing. RLU: Conceptualization, Writing – original draft, Writing – review & editing. KJB: Conceptualization, Supervision, Writing – original draft, Writing – review & editing. DC: Conceptualization, Supervision, Writing – original draft, Writing – review & editing. TO: Conceptualization, Supervision, Writing – original draft, Writing – review & editing.

Funding

The author(s) declare that no financial support was received for the research, authorship, and/or publication of this article.

Acknowledgments

We would like to thank Jessica Örnros, Julie Zacharczuk, and Bartosz Poniatowski for assistance with illustrations.

Conflict of interest

EPK, AM, IK, B-EJ, RLU, KJB, DC, TO are employed by the company AstraZeneca.

Publisher's note

All claims expressed in this article are solely those of the authors and do not necessarily represent those of their affiliated organizations, or those of the publisher, the editors and the reviewers. Any product that may be evaluated in this article, or claim that may be made by its manufacturer, is not guaranteed or endorsed by the publisher.

References

1. Singh S, Blanchard A, Walker JR, Graff LA, Miller N, Bernstein CN. Common symptoms and stressors among individuals with inflammatory bowel diseases. *Clin Gastroenterol Hepatol* (2011) 9(9):769–75. doi: 10.1016/j.cgh.2011.05.016

2. Guan Q. A comprehensive review and update on the pathogenesis of inflammatory bowel disease. *J Immunol Res* (2019) 2019:7247238. doi: 10.1155/2019/7247238

3. Barnhoorn MC, Hakuno SK, Bruckner RS, Rogler G, Hawinkels L, Scharl M. Stromal cells in the pathogenesis of inflammatory bowel disease. *J Crohns Colitis* (2020) 14(7):995–1009. doi: 10.1093/ecco-jcc/jjaa009

4. Katsandegwaza B, Horsnell W, Smith K. Inflammatory bowel disease: A review of pre-clinical murine models of human disease. *Int J Mol Sci* (2022) 23(16). doi: 10.3390/ijms23169344

5. Baydi Z, Limami Y, Khalki L, Zaid N, Naya A, Mtairag EM, et al. An update of research animal models of inflammatory bowel disease. *ScientificWorldJournal* (2021) 2021:7479540. doi: 10.1155/2021/7479540

6. Chassaing B, Aitken JD, Malleshappa M, Vijay-Kumar M. Dextran sulfate sodium (Dss)-induced colitis in mice. *Curr Protoc Immunol* (2014) 104:15 25 1–15 25 14. doi: 10.1002/0471142735.im1525s104

7. Antoniou E, Margonis GA, Angelou A, Pikouli A, Argiri P, Karavokyros I, et al. The tnbs-induced colitis animal model: an overview. *Ann Med Surg (Lond)* (2016) 11:9–15. doi: 10.1016/j.amsu.2016.07.019

8. Morris GP, Beck PL, Herridge MS, Depew WT, Szewczuk MR, Wallace JL. Hapten-induced model of chronic inflammation and ulceration in the rat colon. *Gastroenterology* (1989) 96(3):795–803. doi: 10.1016/S0016-5085(89)80079-4

9. Boirivant M, Fuss IJ, Chu A, Strober W. Oxazolone colitis: A murine model of T helper cell type 2 colitis treatable with antibodies to interleukin 4. *J Exp Med* (1998) 188 (10):1929–39. doi: 10.1084/jem.188.10.1929

10. Heller F, Fuss IJ, Nieuwenhuis EE, Blumberg RS, Strober W. Oxazolone colitis, a th2 colitis model resembling ulcerative colitis, is mediated by il-13-producing nk-T cells. *Immunity* (2002) 17(5):629–38. doi: 10.1016/s1074-7613(02)00453-3

11. Mottet C, Uhlig HH, Powrie F. Cutting edge: cure of colitis by cd4+Cd25+ Regulatory T cells. *J Immunol* (2003) 170(8):3939–43. doi: 10.4049/jimmunol.170.8.3939

12. Ostanin DV, Bao J, Koboziev I, Gray L, Robinson-Jackson SA, Kosloski-Davidson M, et al. T cell transfer model of chronic colitis: concepts, considerations, and tricks of the trade. *Am J Physiol Gastrointest Liver Physiol* (2009) 296(2):G135–46. doi: 10.1152/ajpgi.90462.2008

13. Kuhn R, Lohler J, Rennick D, Rajewsky K, Muller W. Interleukin-10-deficient mice develop chronic enterocolitis. *Cell* (1993) 75(2):263–74. doi: 10.1016/0092-8674(93)80068-p

14. Berg DJ, Davidson N, Kuhn R, Muller W, Menon S, Holland G, et al. Enterocolitis and colon cancer in interleukin-10-deficient mice are associated with aberrant cytokine production and cd4(+) th1-like responses. *J Clin Invest* (1996) 98 (4):1010–20. doi: 10.1172/JCI118861

15. Uhlig HH, McKenzie BS, Hue S, Thompson C, Joyce-Shaikh B, Stepankova R, et al. Differential activity of il-12 and il-23 in mucosal and systemic innate immune pathology. *Immunity* (2006) 25(2):309–18. doi: 10.1016/j.immuni.2006.05.017

16. Garrett WS, Lord GM, Punit S, Lugo-Villarino G, Mazmanian SK, Ito S, et al. Communicable ulcerative colitis induced by T-bet deficiency in the innate immune system. *Cell* (2007) 131(1):33–45. doi: 10.1016/j.cell.2007.08.017

17. Garrett WS. Glimcher LH. T-bet-/- rag2-/- ulcerative colitis: the role of T-bet as a peacekeeper of host-commensal relationships. *Cytokine* (2009) 48(1-2):144–7. doi: 10.1016/j.cyto.2009.07.007

18. Pizarro TT, Pastorelli L, Bamias G, Garg RR, Reuter BK, Mercado JR, et al. Samp1/yitfc mouse strain: A spontaneous model of crohn's disease-like ileitis. *Inflammation Bowel Dis* (2011) 17(12):2566–84. doi: 10.1002/ibd.21638

19. Kontoyiannis D, Pasparakis M, Pizarro TT, Cominelli F, Kollias G. Impaired on/off regulation of tnf biosynthesis in mice lacking tnf au-rich elements: implications for joint and gut-associated immunopathologies. *Immunity* (1999) 10(3):387–98. doi: 10.1016/s1074-7613(00)80038-2

20. Kontoyiannis D, Boulougouris G, Manoloukos M, Armaka M, Apostolaki M, Pizarro T, et al. Genetic dissection of the cellular pathways and signaling mechanisms in modeled tumor necrosis factor-induced crohn's-like inflammatory bowel disease. *J Exp Med* (2002) 196(12):1563–74. doi: 10.1084/jem.20020281

21. Higgins LM, Frankel G, Douce G, Dougan G, MacDonald TT. Citrobacter rodentium infection in mice elicits a mucosal th1 cytokine response and lesions similar to those in murine inflammatory bowel disease. *Infect Immun* (1999) 67(6):3031–9. doi: 10.1128/IAI.67.6.3031-3039.1999

22. Kullberg MC, Jankovic D, Feng CG, Hue S, Gorelick PL, McKenzie BS, et al. Il-23 plays a key role in helicobacter hepaticus-induced T cell-dependent colitis. *J Exp Med* (2006) 203(11):2485–94. doi: 10.1084/jem.20061082

23. Fox JG, Ge Z, Whary MT, Erdman SE, Horwitz BH. Helicobacter hepaticus infection in mice: models for understanding lower bowel inflammation and cancer. *Mucosal Immunol* (2011) 4(1):22–30. doi: 10.1038/mi.2010.61

24. Tang F, Barbacioru C, Wang Y, Nordman E, Lee C, Xu N, et al. Mrna-seq whole-transcriptome analysis of a single cell. *Nat Methods* (2009) 6(5):377–82. doi: 10.1038/nmeth.1315

25. Corridoni D, Chapman T, Antanaviciute A, Satsangi J, Simmons A. Inflammatory bowel disease through the lens of single-cell rna-seq technologies. *Inflammation Bowel Dis* (2020) 26(11):1658–68. doi: 10.1093/ibd/izaa089

26. Frede A, Czarnewski P, Monasterio G, Tripathi KP, Bejarano DA, Ramirez Flores RO, et al. B cell expansion hinders the stroma-epithelium regenerative cross talk during mucosal healing. *Immunity* (2022) 55(12):2336–51.e12. doi: 10.1016/j.immuni.2022.11.002

27. Chen L, He Z, Reis BS, Gelles JD, Chipuk JE, Ting AT, et al. Ifn-gamma(+) cytotoxic cd4(+) T lymphocytes are involved in the pathogenesis of colitis induced by il-23 and the food colorant red 40. *Cell Mol Immunol* (2022) 19(7):777–90. doi: 10.1038/s41423-022-00864-3

28. Gurtner A, Borrelli C, Gonzalez-Perez I, Bach K, Acar IE, Nunez NG, et al. Active eosinophils regulate host defence and immune responses in colitis. *Nature* (2023) 615(7950):151–7. doi: 10.1038/s41586-022-05628-7

29. Ho YT, Shimbo T, Wijaya E, Kitayama T, Takaki S, Ikegami K, et al. Longitudinal single-cell transcriptomics reveals a role for serpina3n-mediated resolution of inflammation in a mouse colitis model. *Cell Mol Gastroenterol Hepatol* (2021) 12(2):547–66. doi: 10.1016/j.jcmgh.2021.04.004

30. Barker N, van Es JH, Kuipers J, Kujala P, van den Born M, Cozijnsen M, et al. Identification of stem cells in small intestine and colon by marker gene lgr5. *Nature* (2007) 449(7165):1003–7. doi: 10.1038/nature06196

31. Parikh K, Antanaviciute A, Fawkner-Corbett D, Jagielowicz M, Aulicino A, Lagerholm C, et al. Colonic epithelial cell diversity in health and inflammatory bowel disease. *Nature* (2019) 567(7746):49–55. doi: 10.1038/s41586-019-0992-y

32. Surawicz CM, Haggitt RC, Husseman M, McFarland LV. Mucosal biopsy diagnosis of colitis: acute self-limited colitis and idiopathic inflammatory bowel disease. *Gastroenterology* (1994) 107(3):755–63. doi: 10.1016/0016-5085(94)90124-4

33. Bingle L, Cross SS, High AS, Wallace WA, Rassl D, Yuan G, et al. Wfdc2 (He4): A potential role in the innate immunity of the oral cavity and respiratory tract and the development of adenocarcinomas of the lung. *Respir Res* (2006) 7(1):61. doi: 10.1186/1465-9921-7-61

34. Smillie CS, Biton M, Ordovas-Montanes J, Sullivan KM, Burgin G, Graham DB, et al. Intra- and inter-cellular rewiring of the human colon during ulcerative colitis. *Cell* (2019) 178(3):714–30 e22. doi: 10.1016/j.cell.2019.06.029

35. Maddipatla SC, Kolachala VL, Venkateswaran S, Dodd AF, Pelia RS, Geem D, et al. Assessing cellular and transcriptional diversity of ileal mucosa among treatment-naive and treated crohn's disease. *Inflamm Bowel Dis* (2023) 29(2):274–85. doi: 10.1093/ibd/izac201

36. Burclaff J, Bliton RJ, Breau KA, Ok MT, Gomez-Martinez I, Ranek JS, et al. A proximal-to-distal survey of healthy adult human small intestine and colon epithelium by single-cell transcriptomics. *Cell Mol Gastroenterol Hepatol* (2022) 13(5):1554–89. doi: 10.1016/j.jcmgh.2022.02.007

37. Lelouard H, Fallet M, de Bovis B, Meresse S, Gorvel JP. Peyer's patch dendritic cells sample antigens by extending dendrites through M cell-specific transcellular pores. *Gastroenterology* (2012) 142(3):592–601 e3. doi: 10.1053/j.gastro.2011.11.039

38. Bennett KM, Parnell EA, Sanscartier C, Parks S, Chen G, Nair MG, et al. Induction of colonic M cells during intestinal inflammation. *Am J Pathol* (2016) 186 (5):1166–79. doi: 10.1016/j.ajpath.2015.12.015

39. Ding J, Wang K, Liu W, She Y, Sun Q, Shi J, et al. Pore-forming activity and structural autoinhibition of the gasdermin family. *Nature* (2016) 535(7610):111–6. doi: 10.1038/nature18590

40. Shi J, Zhao Y, Wang K, Shi X, Wang Y, Huang H, et al. Cleavage of gsdmd by inflammatory caspases determines pyroptotic cell death. *Nature* (2015) 526(7575):660–5. doi: 10.1038/nature15514

41. Bulek K, Zhao J, Liao Y, Rana N, Corridoni D, Antanaviciute A, et al. Epithelial-derived gasdermin D mediates nonlytic il-1beta release during experimental colitis. *J Clin Invest* (2020) 130(8):4218–34. doi: 10.1172/JCI138103

42. Nowarski R, Jackson R, Flavell RA. The stromal intervention: regulation of immunity and inflammation at the epithelial-mesenchymal barrier. *Cell* (2017) 168 (3):362–75. doi: 10.1016/j.cell.2016.11.040

43. Bernardo ME, Fibbe WE. Mesenchymal stromal cells: sensors and switchers of inflammation. *Cell Stem Cell* (2013) 13(4):392–402. doi: 10.1016/j.stem.2013.09.006

44. Kinchen J, Chen HH, Parikh K, Antanaviciute A, Jagielowicz M, Fawkner-Corbett D, et al. Structural remodeling of the human colonic mesenchyme in inflammatory bowel disease. *Cell* (2018) 175(2):372–86 e17. doi: 10.1016/j.cell.2018.08.067

45. Kong L, Pokatayev V, Lefkovith A, Carter GT, Creasey EA, Krishna C, et al. The landscape of immune dysregulation in crohn's disease revealed through single-cell transcriptomic profiling in the ileum and colon. *Immunity* (2023) 56(2):444–58.e5. doi: 10.1016/j.immuni.2023.01.002

46. Mukherjee PK, Nguyen QT, Li J, Zhao S, Christensen SM, West GA, et al. Stricturing crohn's disease single-cell rna sequencing reveals fibroblast heterogeneity and intercellular interactions. *Gastroenterology* (2023) 165:1180–96. doi: 10.1053/j.gastro.2023.07.014

47. West NR, Hegazy AN, Owens BMJ, Bullers SJ, Linggi B, Buonocore S, et al. Oncostatin M drives intestinal inflammation and predicts response to tumor necrosis factor-neutralizing therapy in patients with inflammatory bowel disease. *Nat Med* (2017) 23(5):579–89. doi: 10.1038/nm.4307

48. Friedrich M, Pohin M, Jackson MA, Korsunsky I, Bullers SJ, Rue-Albrecht K, et al. Il-1-driven stromal-neutrophil interactions define a subset of patients with inflammatory bowel disease that does not respond to therapies. *Nat Med* (2021) 27 (11):1970–81. doi: 10.1038/s41591-021-01520-5

49. Heresbach D, Alexandre JL, Branger B, Bretagne JF, Cruchant E, Dabadie A, et al. Frequency and significance of granulomas in a cohort of incident cases of crohn's disease. *Gut* (2005) 54(2):215–22. doi: 10.1136/gut.2004.041715

50. Hampe J, Franke A, Rosenstiel P, Till A, Teuber M, Huse K, et al. A genome-wide association scan of nonsynonymous snps identifies a susceptibility variant for crohn disease in atg16l1. *Nat Genet* (2007) 39(2):207–11. doi: 10.1038/ng1954

51. Parkes M, Barrett JC, Prescott NJ, Tremelling M, Anderson CA, Fisher SA, et al. Sequence variants in the autophagy gene irgm and multiple other replicating loci contribute to crohn's disease susceptibility. *Nat Genet* (2007) 39(7):830–2. doi: 10.1038/ng2061

52. Hugot JP, Chamaillard M, Zouali H, Lesage S, Cezard JP, Belaiche J, et al. Association of nod2 leucine-rich repeat variants with susceptibility to crohn's disease. *Nature* (2001) 411(6837):599–603. doi: 10.1038/35079107

53. Martin JC, Chang C, Boschetti G, Ungaro R, Giri M, Grout JA, et al. Single-cell analysis of crohn's disease lesions identifies a pathogenic cellular module associated with resistance to anti-tnf therapy. *Cell* (2019) 178(6):1493–508 e20. doi: 10.1016/j.cell.2019.08.008

54. Thomas T, Rich-Griffin C, Pohin M, Friedrich M, Aschenbrenner D, Pakpoor J, et al. A longitudinal single-cell therapeutic atlas of anti-tumour necrosis factor treatment in inflammatory bowel disease. *BioRvix* (2023). doi: 10.1101/2023.05.05.539635%JbioRxiv

55. Garrido-Trigo A, Corraliza AM, Veny M, Dotti I, Melon-Ardanaz E, Rill A, et al. Macrophage and neutrophil heterogeneity at single-cell spatial resolution in human inflammatory bowel disease. *Nat Commun* (2023) 14(1):4506. doi: 10.1038/s41467-023-40156-6

56. Kang B, Alvarado LJ, Kim T, Lehmann ML, Cho H, He J, et al. Commensal microbiota drive the functional diversification of colon macrophages. *Mucosal Immunol* (2020) 13(2):216–29. doi: 10.1038/s41385-019-0228-3

57. Wuggenig P, Kaya B, Melhem H, Ayata CK, Swiss IBDCI, Hruz P, et al. Loss of the branched-chain amino acid transporter cd98hc alters the development of colonic macrophages in mice. *Commun Biol* (2020) 3(1):130. doi: 10.1038/s42003-020-0842-3

58. Scott CL, T'Jonck W, Martens L, Todorov H, Sichien D, Soen B, et al. The transcription factor zeb2 is required to maintain the tissue-specific identities of macrophages. *Immunity* (2018) 49(2):312–25.e5. doi: 10.1016/j.immuni.2018.07.004

59. Rohm TV, Keller L, Bosch AJT, AlAsfoor S, Baumann Z, Thomas A, et al. Targeting colonic macrophages improves glycemic control in high-fat diet-induced obesity. *Commun Biol* (2022) 5(1):370. doi: 10.1038/s42003-022-03305-z

60. Corbin AL, Gomez-Vazquez M, Berthold DL, Attar M, Arnold IC, Powrie FM, et al. Irf5 guides monocytes toward an inflammatory cd11c(+) macrophage phenotype and promotes intestinal inflammation. *Sci Immunol* (2020) 5(47). doi: 10.1126/sciimmunol.aax6085

61. De Schepper S, Verheijden S, Aguilera-Lizarraga J, Viola MF, Boesmans W, Stakenborg N, et al. Self-maintaining gut macrophages are essential for intestinal homeostasis. *Cell* (2018) 175(2):400–15 e13. doi: 10.1016/j.cell.2018.07.048

62. Krausgruber T, Blazek K, Smallie T, Alzabin S, Lockstone H, Sahgal N, et al. Irf5 promotes inflammatory macrophage polarization and th1-th17 responses. *Nat Immunol* (2011) 12(3):231–8. doi: 10.1038/ni.1990

63. Yan JB, Luo MM, Chen ZY, He BH. The function and role of the th17/treg cell balance in inflammatory bowel disease. *J Immunol Res* (2020) 2020:8813558. doi: 10.1155/2020/8813558

64. Huang B, Chen Z, Geng L, Wang J, Liang H, Cao Y, et al. Mucosal profiling of pediatric-onset colitis and ibd reveals common pathogenics and therapeutic pathways. *Cell* (2019) 179(5):1160–76 e24. doi: 10.1016/j.cell.2019.10.027

65. Ma H, Tao W, Zhu S. T lymphocytes in the intestinal mucosa: defense and tolerance. *Cell Mol Immunol* (2019) 16(3):216–24. doi: 10.1038/s41423-019-0208-2

66. Corridoni D, Antanaviciute A, Gupta T, Fawkner-Corbett D, Aulicino A, Jagielowicz M, et al. Single-cell atlas of colonic cd8(+) T cells in ulcerative colitis. *Nat Med* (2020) 26(9):1480–90. doi: 10.1038/s41591-020-1003-4

67. Devlin JC, Axelrad J, Hine AM, Chang S, Sarkar S, Lin JD, et al. Single-cell transcriptional survey of ileal-anal pouch immune cells from ulcerative colitis patients. *Gastroenterology* (2021) 160(5):1679–93. doi: 10.1053/j.gastro.2020.12.030

68. Boland BS, He Z, Tsai MS, Olvera JG, Omilusik KD, Duong HG, et al. Heterogeneity and clonal relationships of adaptive immune cells in ulcerative colitis revealed by single-cell analyses. *Sci Immunol* (2020) 5(50). doi: 10.1126/sciimmunol.abb4432

69. Huang LJ, Mao XT, Li YY, Liu DD, Fan KQ, Liu RB, et al. Multiomics analyses reveal a critical role of selenium in controlling T cell differentiation in crohn's disease. *Immunity* (2021) 54(8):1728–44 e7. doi: 10.1016/j.immuni.2021.07.004

70. Jaeger N, Gamini R, Cella M, Schettini JL, Bugatti M, Zhao S, et al. Single-cell analyses of crohn's disease tissues reveal intestinal intraepithelial T cells heterogeneity and altered subset distributions. *Nat Commun* (2021) 12(1):1921. doi: 10.1038/s41467-021-22164-6

71. Mitsialis V, Wall S, Liu P, Ordovas-Montanes J, Parmet T, Vukovic M, et al. Single-cell analyses of colon and blood reveal distinct immune cell signatures of ulcerative colitis and crohn's disease. *Gastroenterology* (2020) 159(2):591–608.e10. doi: 10.1053/j.gastro.2020.04.074

72. Nie H, Lin P, Zhang Y, Wan Y, Li J, Yin C, et al. Single-cell meta-analysis of inflammatory bowel disease with scibd. *Nat Comput Sci* (2023) 3(6):522–31. doi: 10.1038/s43588-023-00464-9

73. Miragaia RJ, Gomes T, Chomka A, Jardine L, Riedel A, Hegazy AN, et al. Single-cell transcriptomics of regulatory T cells reveals trajectories of tissue adaptation. *Immunity* (2019) 50(2):493–504 e7. doi: 10.1016/j.immuni.2019.01.001

74. Cadinu P, Sivanathan KN, Misra A, Xu RJ, Mangani D, Yang E, et al. Charting the cellular biogeography in colitis reveals fibroblast trajectories and coordinated spatial remodeling. *bioRxiv* (2023). doi: 10.1101/2023.05.08.539701

75. Bhaumik S, Basu R. Cellular and molecular dynamics of th17 differentiation and its developmental plasticity in the intestinal immune response. *Front Immunol* (2017) 8:254. doi: 10.3389/fimmu.2017.00254

76. Abdo AIK, Tye GJ. Interleukin 23 and autoimmune diseases: current and possible future therapies. *Inflammation Res* (2020) 69(5):463–80. doi: 10.1007/s00011-020-01339-9

77. Feagan BG, Sandborn WJ, D'Haens G, Panes J, Kaser A, Ferrante M, et al. Induction therapy with the selective interleukin-23 inhibitor risankizumab in patients with moderate-to-severe crohn's disease: A randomised, double-blind, placebo-controlled phase 2 study. *Lancet* (2017) 389(10080):1699–709. doi: 10.1016/S0140-6736(17)30570-6

78. Sandborn WJ, Ferrante M, Bhandari BR, Berliba E, Feagan BG, Hibi T, et al. Efficacy and safety of mirikizumab in a randomized phase 2 study of patients with ulcerative colitis. *Gastroenterology* (2020) 158(3):537–49.e10. doi: 10.1053/j.gastro.2019.08.043

79. Sandborn WJ, D'Haens GR, Reinisch W, Panes J, Chan D, Gonzalez S, et al. Guselkumab for the treatment of crohn's disease: induction results from the phase 2 galaxi-1 study. *Gastroenterology* (2022) 162(6):1650–64.e8. doi: 10.1053/j.gastro.2022.01.047

80. Khairallah C, Chu TH, Sheridan BS. Tissue adaptations of memory and tissue-resident gamma delta T cells. *Front Immunol* (2018) 9:2636. doi: 10.3389/fimmu.2018.02636

81. Barros-Martins J, Schmolka N, Fontinha D, Pires de Miranda M, Simas JP, Brok I, et al. Effector gammadelta T cell differentiation relies on master but not auxiliary th cell transcription factors. *J Immunol* (2016) 196(9):3642–52. doi: 10.4049/jimmunol.1501921

82. Catalan-Serra I, Sandvik AK, Bruland T, Andreu-Ballester JC. Gammadelta T cells in crohn's disease: A new player in the disease pathogenesis? *J Crohns Colitis* (2017) 11(9):1135–45. doi: 10.1093/ecco-jcc/jjx039

83. Gaublomme JT, Yosef N, Lee Y, Gertner RS, Yang LV, Wu C, et al. Single-cell genomics unveils critical regulators of th17 cell pathogenicity. *Cell* (2015) 163(6):1400–12. doi: 10.1016/j.cell.2015.11.009

84. He Z, Chen L, Catalan-Dibene J, Bongers G, Faith JJ, Suebsuwong C, et al. Food colorants metabolized by commensal bacteria promote colitis in mice with dysregulated expression of interleukin-23. *Cell Metab* (2021) 33(7):1358–71 e5. doi: 10.1016/j.cmet.2021.04.015

85. Zhang N, Bevan MJ. Cd8(+) T cells: foot soldiers of the immune system. *Immunity* (2011) 35(2):161–8. doi: 10.1016/j.immuni.2011.07.010

86. Shale M, Schiering C, Powrie F. Cd4(+) T-cell subsets in intestinal inflammation. *Immunol Rev* (2013) 252(1):164–82. doi: 10.1111/imr.12039

87. Hor S, Pirzer H, Dumoutier L, Bauer F, Wittmann S, Sticht H, et al. The T-cell lymphokine interleukin-26 targets epithelial cells through the interleukin-20 receptor 1 and interleukin-10 receptor 2 chains. *J Biol Chem* (2004) 279(32):33343–51. doi: 10.1074/jbc.M405000200

88. Thomas MF, Slowikowski K, Manakongtreecheep K, Sen P, Tantivit J, Nasrallah M, et al. Altered interactions between circulating and tissue-resident cd8 T cells with the colonic mucosa define colitis associated with immune checkpoint inhibitors. *BioRvix* (2021). doi: 10.1101/2021.09.17.460868%JbioRxiv

89. Spencer J, Bemark M. Human intestinal B cells in inflammatory diseases. *Nat Rev Gastroenterol Hepatol* (2023) 20(4):254–65. doi: 10.1038/s41575-023-00755-6

90. Kamada N, Sakamoto K, Seo SU, Zeng MY, Kim YG, Cascalho M, et al. Humoral immunity in the gut selectively targets phenotypically virulent attaching-and-effacing bacteria for intraluminal elimination. *Cell Host Microbe* (2015) 17(5):617–27. doi: 10.1016/j.chom.2015.04.001

91. Spencer J, Sollid LM. The human intestinal B-cell response. *Mucosal Immunol* (2016) 9(5):1113–24. doi: 10.1038/mi.2016.59

92. Jostins L, Ripke S, Weersma RK, Duerr RH, McGovern DP, Hui KY, et al. Host-microbe interactions have shaped the genetic architecture of inflammatory bowel disease. *Nature* (2012) 491(7422):119–24. doi: 10.1038/nature11582

93. Castro-Dopico T, Dennison TW, Ferdinand JR, Mathews RJ, Fleming A, Clift D, et al. Anti-commensal igg drives intestinal inflammation and type 17 immunity in ulcerative colitis. *Immunity* (2019) 50(4):1099–114.e10. doi: 10.1016/j.immuni.2019.02.006

94. Buckner CM, Moir S, Kardava L, Ho J, Santich BH, Kim LJ, et al. Cxcr4/igg-expressing plasma cells are associated with human gastrointestinal tissue inflammation. *J Allergy Clin Immunol* (2014) 133(6):1676–85 e5. doi: 10.1016/j.jaci.2013.10.050

95. Uzzan M, Martin JC, Mesin L, Livanos AE, Castro-Dopico T, Huang R, et al. Ulcerative colitis is characterized by a plasmablast-skewed humoral response associated with disease activity. *Nat Med* (2022) 28(4):766–79. doi: 10.1038/s41591-022-01680-y

96. Kokkinou E, Soini T, Pandey RV, van Acker A, Theorell J, Czarnewski P, et al. The single-cell transcriptional landscape of innate and adaptive lymphocytes in pediatric-onset colitis. *Cell Rep Med* (2023) 4(5):101038. doi: 10.1016/j.xcrm.2023.101038

97. Krabbendam L, Heesters BA, Kradolfer CMA, Haverkate NJE, Becker MAJ, Buskens CJ, et al. Cd127+ Cd94+ Innate lymphoid cells expressing granulysin and perforin are expanded in patients with crohn's disease. *Nat Commun* (2021) 12(1):5841. doi: 10.1038/s41467-021-26187-x

frontiers | Frontiers in Immunology

TYPE Original Research
PUBLISHED 04 January 2024
DOI 10.3389/fimmu.2023.1286387

Check for updates

OPEN ACCESS

EDITED BY
Rajan P. Adhikari,
Integrated BioTherapeutics, Inc., United States

REVIEWED BY
Yuichi Maeda,
Osaka University, Japan
Anthony C. Y. Yau,
AliveDx, United Kingdom

*CORRESPONDENCE
Young Sun Suh
tatabox123@hanmail.net
Sang-Il Lee
goldgu@gnu.ac.kr

†These authors have contributed equally to this work

RECEIVED 31 August 2023
ACCEPTED 12 December 2023
PUBLISHED 04 January 2024

CITATION
Kim S, Chun SH, Cheon Y-H, Kim M, Kim H-O, Lee H, Hong S-T, Park S-J, Park MS, Suh YS and Lee S-I (2024) *Peptoniphilus gorbachii* alleviates collagen-induced arthritis in mice by improving intestinal homeostasis and immune regulation.
Front. Immunol. 14:1286387.
doi: 10.3389/fimmu.2023.1286387

COPYRIGHT
© 2024 Kim, Chun, Cheon, Kim, Kim, Lee, Hong, Park, Park, Suh and Lee. This is an open-access article distributed under the terms of the Creative Commons Attribution License (CC BY). The use, distribution or reproduction in other forums is permitted, provided the original author(s) and the copyright owner(s) are credited and that the original publication in this journal is cited, in accordance with accepted academic practice. No use, distribution or reproduction is permitted which does not comply with these terms.

Peptoniphilus gorbachii alleviates collagen-induced arthritis in mice by improving intestinal homeostasis and immune regulation

Suhee Kim[1†], Sung Hak Chun[1†], Yun-Hong Cheon[1], Mingyo Kim[1], Hyun-Ok Kim[1,2], Hanna Lee[1,2], Seong-Tshool Hong[3], Sang-Jun Park[4], Myeong Soo Park[4], Young Sun Suh[1,2*] and Sang-Il Lee[1*]

[1]Department of Internal Medicine and Institute of Health Science, Gyeongsang National University School of Medicine and Hospital, Jinju, Republic of Korea, [2]Department of Internal Medicine, Gyeongsang National University Changwon Hospital, Changwon, Republic of Korea, [3]Department of Biomedical Sciences and Institute for Medical Science, Chonbuk National University Medical School, Jeonju, Republic of Korea, [4]Research Center, BIFIDO Co, Ltd, Hongcheon, Kangwon, Republic of Korea

Introduction: The intricate connection between gut microbiota and rheumatoid arthritis (RA) pathogenesis has gained prominence, although the specific microbial species contributing to RA development remain largely unknown. Recent studies have sought to comprehensively explore alterations in the human microbiome, focusing on identifying disease-related microbial species through blood analysis. Consequently, this study aimed to identify RA-associated microbial species using a serum microbial array system and to investigate the efficacy and underlying mechanisms of potential microbial species for RA treatment.

Methods: Serum immunoglobulin M levels against 384 intestinal microbial species were assessed using a microbial microarray in patients with RA and healthy individuals. We investigated the therapeutic potential of the identified microbial candidate regarding arthritis development, immune responses, gut barrier function, and gut microbiome using a collagen-induced arthritis (CIA) mouse model.

Results: Our findings revealed significant alterations in antibody levels against 36 microbial species in patients with RA compared to healthy individuals. Notably, the antibody levels against *Peptoniphilus gorbachii* (*PG*) were decreased in patients with RA and exhibited an inverse correlation with RA disease activity. *In vitro* experiments demonstrated that *PG* produced acetate and butyrate, while exhibiting anti-inflammatory properties. In CIA mice, *PG* administration suppressed arthritis symptoms, reduced the accumulation of inflammatory monocytes in the mesenteric lymph nodes, and downregulated gene expression of pro-inflammatory cytokines in the ileum. Additionally, *PG* supplementation restored intestinal barrier integrity and partially resolved gut microbial dysbiosis in CIA mice. The fecal

microbiota in *PG*-treated mice corresponded to improved intestinal barrier integrity and reduced inflammatory responses.

Conclusion: This study highlights the potential of serum-based detection of anti-microbial antibodies to identify microbial targets at the species level for RA treatment. Moreover, our findings suggest that *PG*, identified through the microbial microarray analysis, holds therapeutic potential for RA by restoring intestinal barrier integrity and suppressing the immunologic response associated with RA.

KEYWORDS

rheumatoid arthritis, microbiota, *Peptoniphilus gorbachii*, intestinal barrier integrity, inflammatory reaction

1 Introduction

Microbiota has emerged as a crucial factor in human health. Accumulating evidence demonstrates that dysbiosis, defined as imbalanced microbiota composition, is evident in patients with rheumatoid arthritis (RA) (1–5). A balanced microbiota and commensal microbe-derived metabolites are pivotal for maintaining symbiotic relationships within the intestine by reinforcing the epithelial barrier and regulating the mucosal immune response (6). However, microbial dysbiosis can compromise epithelial barrier function, resulting in an influx of bacteria and their metabolites into the bloodstream, leading to increased exposure of immune cells to bacterial antigens and subsequent pro-inflammatory responses (7). Furthermore, the enterotoxin zonulin, secreted by intestinal epithelial cells following microbial stimulation, reduces the expression of intestinal tight junction proteins. This, in turn, induces damage to the gut barrier, T cell-mediated mucosal inflammation, and the transmigration of immune cells from the gut to the joints (8). Therefore, restoring microbiota homeostasis and intestinal barrier function emerges as a promising strategy for preventing or treating RA (9).

Several microorganisms, including *Porphyromonas gingivalis* and *Prevotella copri*, have been implicated in RA pathogenesis. *P. gingivalis* triggers and exacerbates RA by activating Th17 immune responses and encoding peptidyl arginine deiminase, which facilitates the generation of RA-related autoantigen citrullinated peptides (10, 11). *Prevotella copri* has been discovered in both the preclinical stage and in new-onset stages of untreated RA patients and has been shown to contribute to the development of the disease (12, 13). *Lactobacillus salivarius* is consistently enriched in patients with RA, particularly those with highly active RA (14). Conversely, another *Prevotella* species, *Prevotella histicola*, suppresses arthritis via mucosal immune regulation (15). Additionally, *Lactobacillus casei* significantly suppresses the induction of arthritis, restores gut microbiota, and reduces oxidative stress (16, 17). These findings underscore that even within the same genus, distinct species can exert different effects on RA. Therefore, identifying RA-related microorganisms at the species level is pivotal for discovering effective targets for RA treatment.

While 16S rRNA gene sequencing and shotgun metagenomic sequencing of fecal samples are commonly used for identifying RA-associated microorganisms (18), they present limitations. Experimental conditions, such as sequencing errors and genomic repeats, can impact the outcome of these methods (19, 20). Additionally, the fecal microbiome only partially represents the entire gastrointestinal tract microbiota and fails to represent the mouth and lungs microbiota, both implicated in RA pathogenesis (21, 22). Furthermore, the translocation of transient gut microbiota could elicit persistent systemic responses, detectable through a serum microbial antibody array but frequently missed by metagenomic sequencing of fecal samples (23).

As a solution to sequencing limitations, serological testing emerges as a viable alternative for identifying disease-related microorganisms. Clinical practice often employs serological tests to identify causative microorganisms in pneumonia, scrub typhus, and syphilis. Similarly, serological tests have recently been conducted to investigate RA-related microbiota using blood samples. For example, antibodies against *P. gingivalis* were highly observed in patients with RA compared to healthy controls and associated with the presence of anti-cyclic citrullinated peptide antibodies (ACPA) (24–27). Elevated serum antibody levels against *Prevotella copri* were also observed in individuals at risk of or diagnosed with RA (28). Another recent study, using blood samples, demonstrated altered microbial small RNA composition in plasma of patients with RA compared to controls (29). Such blood-based investigations offer the advantage of reflecting changes in microorganisms across various organs, including the mouth, lungs, and intestine, with minimal sample requirements (30).

This study aimed to identify species-level microbial candidates associated with RA through a serum microbial antibody microarray and to demonstrate the therapeutic effects and underlying

mechanisms of these candidate RA-related microbial species in collagen-induced arthritis (CIA) mice.

2 Materials and methods

2.1 Patients

The study included 81 patients with RA and 50 healthy controls (HC) matched for age, sex, and race. Human serum samples were provided by the Gyeongsang National University Hospital (GNUH)-Korea Biobank, sampled in 2017 and 2018. This study was approved by the Institutional Review Board (permit No: GNUH 2017-08-015). RA disease activity was assessed using the Disease Activity Score in 28 joints (DAS28) with measurements of erythrocyte sedimentation rate (ESR) and C-Reactive Protein (CRP) (31, 32). Patient information is summarized in Supplementary Table 1.

2.2 Anti-microbial antibody microarray and analysis

Immunoglobulin M (IgM) antibody levels targeting specific intestinal microbial species were evaluated in serum samples (33, 34). Specifically, 384 species of intestinal microbes obtained from the Gut Microbiota Bank (https://www.gutmicrobiotabank.com) were grown in yeast casitone fatty acid (YCFA) medium (Supplementary Table 2) and homogenized using an automill disruptor (Cosmo Bio, Japan). Microbial lysates were arrayed onto a nylon membrane using a microarray spotter (CapitalBio, China) and fixed by air drying, followed by a subsequent incubation at 80°C for 30 min. The membrane was then blocked in Tris-buffered saline containing 0.1% Tween 20 and 5% nonfat dry milk at 37 °C for 30 min. Patient serum was added to the chips, followed by a 30-min incubation at 37°C. Subsequently, the chips were incubated with Alexa Fluor 647-conjugated goat anti-human IgM secondary antibodies (Thermo Fisher Scientific, Waltham, MA, USA) at 37°C for 30 min. The fluorescence intensity was quantified using a Luxscan (CapitalBio, China). Each experiment involved at least three technical replicates and the average intensities of each sample were normalized using global normalization and Z-transform methods. Microbial richness and evenness were assessed based on species richness and Shannon index (α-diversity of species). Principal coordinate analysis (PCoA) was performed to identify microbial compositional diversity (β-diversity of species). Linear discriminant analysis (LDA) effect size (LEfSe) was performed using the Galaxy framework (https://huttenhower.sph.harvard.edu/galaxy/) to identify bacterial taxa enriched in the serum of healthy individuals and patients with RA ($p < 0.01$, LDA score > 3.0). A heatmap of bacterial species with differential relative abundances was generated ($p < 0.01$, Z-ratio > 1.5). Furthermore, a co-occurrence network was constructed using the Cytoscape v.3.10.0 plugin CoNet ($p < 0.05$ adjusted using the Benjamini-Hochberg correction, correlation coefficient > 0.5 based on four correlation measures including Spearman, Pearson, Bray-Curtis, and Kullback-Leibler).

2.3 Bacterial strains and culture supernatants

Peptoniphilus gorbachii (*PG*) strain WAL 10418 (JBP9-00201) and *P. gingivalis* (JBP11-00401) obtained from the Gut Microbiota Bank were cultured anaerobically at 37°C in YCFA medium. Live *PG* pellets and culture supernatants were prepared by centrifugation of bacterial culture at 12,000 × *g* for 10 min. Additionally, live *PG* pellets were suspended in 10% skim milk in YCFA and freeze-dried. Heat-killed (HK)-*PG* was generated by incubating the bacterial culture at 60°C for 1 h.

2.4 *In-vitro* bacterial competition assay

PG and *P. gingivalis* were grown separately in YCFA medium until reaching an OD_{600} of 0.1. They were then mixed at a 1:1 ratio. Pure cultures of *PG* and *P. gingivalis* were also prepared as controls to assess competition. Co-cultures and single cultures were serially diluted 10-fold eight times after 0, 8, and 16 h of culture. These dilutions were then spread onto agar plates and incubated at 37°C for 48 h. All single colonies visualized on the agar plates were identified by light microscopy following Gram-staining.

2.5 Quantification of short chain fatty acids (SCFAs)

SCFAs in *PG*-cultured supernatants were quantified using gas chromatography/mass spectrometry (GC-2010 Plus, GCMS-TQ 8030, Shimazu, Tokyo, Japan).

2.6 Cell culture and cytokine stimulation

RAW 264.7, a murine macrophage cell line, was maintained in Dulbecco's modified eagle's medium supplemented with 10% fetal bovine serum, 100 U/mL penicillin, and 100 mg/mL streptomycin (GIBCO, Carlsbad, CA, USA). RAW 264.7 cells were seeded in a 24-well plate (1×10^5 cells/well) and cultured for 24 h. Subsequently, cells were exposed to HK-*PG* (1×10^5 cells/well) or *PG* supernatant (0.5%) for 20 h, followed by stimulation with LPS (1 μg/mL; O55:B5, Sigma-Aldrich, St. Louis, MO, USA) for 4 h. Total RNA was extracted from the cells to evaluate pro-inflammatory gene expression.

Mouse small intestinal lamina propria (siLP) cells were isolated as previously described (35). Single-cell suspensions of mesenteric lymph nodes (MLN) were prepared through mechanical grinding and filtering using a nylon mesh. Single-cell suspensions from siLP and MLN were seeded into a 96-well plate (5×10^5 cells/well) and stimulated with monoclonal anti-CD3e (1 μg/mL; clone 145-2C11, BD Biosciences, San Jose, CA, USA) and anti-CD28 (1 μg/mL; clone 37.51, BD Biosciences) antibodies, with or without HK-*PG* (5×10^3 cells/well) or *PG* supernatant (0.5%) for 24 h. Cell culture

supernatants were used for the measurement of IFN-γ and IL-17A levels.

2.7 Animals and arthritis induction

Five-week-old male DBA1/J mice were purchased from Central Laboratory Animal Inc. (Seoul, Korea). All mice were acclimatized for two weeks under specific pathogen-free conditions and fed standard rodent chow and sterile water. Animal experiments were conducted in accordance with the guidelines of Gyeongsang National University (GNU) and approved by the Institutional Animal Care and Use Committee (IACUC approval ID: GNU-200724-M0046) in Korea.

CIA was induced as previously described (36). Briefly, mice were immunized intradermally at the base of the tail with 100 μg bovine type II collagen (CII, Chondrex, Redmond, WA, USA) emulsified with complete Freund's adjuvant (CFA, Sigma-Aldrich) on day 0. Three weeks later (day 21), mice were boosted with CII emulsified with incomplete Freund's adjuvant (IFA, Chondrex). Mice were divided into four groups according to the treatment scheme: (1) naïve mice without treatment and immunization (n = 4), (2) CII-immunized mice without treatment (CIA, n = 8), (3) *PG*-treated CIA mice (CIA/*PG*, n = 9), and (4) antibiotic-treated CIA mice (CIA/AB, n = 8). *PG* treatment was initiated four weeks before the first CII injection and continued for 9 weeks until the end of the experiment (day 35). A total of 1×10^9 colony-forming units (CFUs) of live *PG* suspended in 200 μL of PBS were orally administered to mice three times a week. For antibiotic treatment, ampicillin (1 g/L), vancomycin (0.5 g/L), neomycin (1 g/L), and metronidazole (1 g/L) were administered to mice in the drinking water for a total period of 3 weeks, beginning on day 14 after the first CII injection.

Clinical arthritis scores were evaluated on a scale of 0–4 for each limb three times a week, starting after the second CII injection (day 21), as previously described (36). Mice were sacrificed five weeks post-immunization (day 35) for sample collection.

2.8 Histopathological examination

Ankles were formalin-fixed, decalcified with a decalcifying solution (Sigma-Aldrich), and embedded in paraffin. Ankle joint sections (5 μm) were subjected to hematoxylin and eosin (H&E) and safranin O staining. Slides were imaged using a Nikon microscope imaging system and NIS-Elements software (Nikon Instruments, Tokyo, Japan). The assessment of synovial inflammation, bone erosion, and cartilage damage was conducted as previously described (36).

2.9 CFU assay for *P. gorbachii* colonization in feces

Freshly collected mouse fecal pellets were smashed in 1 mL of YCFA medium, followed by a 10-fold serial dilution six times. One hundred microliters of the serially diluted fecal suspension were spread onto YCFA agar medium, and the agar plates were incubated at 37°C for 16 h in anaerobic conditions. Following visualization of single colonies on the agar plate, approximately 100 single colonies were selected from the plates. The 16S rDNA sequences, encompassing regions V1-V9, were amplified using colony PCR and universal primers (27F 5'-AGAGTTTGATCCTGGCTCAG-3' and 1492R 5'-GGTTACCTTGTTACGACTT-3'). These amplified DNA fragments were sequenced using Sanger sequencing. Full-length 16S rRNA sequences were analyzed in a DNAbaser4.36 analyzer, and contigs of each individual DNA were uploaded to NCBI BLAST for bacterial species identification.

2.10 Quantitative real-time PCR

Total RNA was extracted using TRIzol reagent (Thermo Fisher Scientific) and reverse transcribed using an iScript cDNA synthesis kit (Bio-Rad, Hercules, CA, USA). DNA was subjected to qPCR amplification using a SYBR Green PCR master mix (Thermo Fisher Scientific) on a ViiA 7 Real-time PCR Detection System (Applied Biosystems, Waltham, MA, USA). The expression of target genes relative to glyceraldehyde 3-phosphate dehydrogenase was calculated using the $2^{-\Delta\Delta Ct}$ comparative method. The primer pairs used are listed in Supplementary Table 3.

2.11 Enzyme-linked immunosorbent assay (ELISA)

To measure IFN-γ and IL-17A levels in cell culture supernatants, 96-well plates (Greiner Bio-One GmbH, Frickenhausen, Germany) were coated with IFN-γ (eBioscience, San Diego, CA, USA) or IL-17A monoclonal antibodies (eBioscience) and blocked with BD OptEIA™ Assay diluent (BD Biosciences). Samples were added to the wells and incubated overnight at 4°C. Biotinylated IFN-γ (eBioscience) or IL-17A (eBioscience) antibodies were added, followed by the addition of AKP streptavidin (BD Biosciences). Color was developed by adding 5 mM phosphatase substrate (Sigma-Aldrich), and absorbance was measured at 405 nm using a Versamax microplate reader with SoftMax Pro 6.5.1 software (Molecular Devices, Wokingham, UK).

Serum samples were prepared by centrifuging whole blood collected from mice at 2,000 × g for 10 min at 4°C. Subsequently, the serum samples were subjected to dilutions of 100,000-fold, 4-fold, and 1000-fold for the detection of anti-CII IgG antibody (Chondrex), anti-CCP antibody (MyBioSource Inc., San Diego, CA, USA), and zonulin (MyBioSource Inc.), respectively. The levels of serum autoantibodies and zonulin (MyBioSource Inc.) were measured in accordance with the manufacturer's instructions.

2.12 Flow cytometric analysis

Mouse colonic lamina propria (cLP) cells were isolated as previously described (35), and MLN and ILN cell suspensions

were prepared through mechanical grinding. Cell surface and intracellular cytokine staining were conducted as previously described (35). Cells stained with fluorochrome-conjugated antibodies (Supplementary Table 4) were analyzed using a LSRFortessaTM X-20 flow cytometer (BD Biosciences). Data analysis was carried out using FlowJo (Tree Star Inc., Ashland, OR, USA).

2.13 16S rRNA gene sequencing and analysis

Total bacterial genomic DNA from intracecal samples was extracted using the MagMAX™ Microbiome Ultra Nucleic Acid Isolation Kit on a KingFisher Flex automated DNA/RNA isolation system (Thermo Fisher Scientific), according to the manufacturer's instructions. DNA samples were analyzed using a Nano-300 Micro-spectrophotometer (ALLSHENG, Hangzhou, China) and Qubit 3.0 fluorometer (Thermo Fisher Scientific) to assess concentration and purity of fecal DNA.

Libraries were constructed using the 16S Metagenomic Sequencing Library Preparation guide protocol (Illumina, San Diego, CA, USA). Variable regions 3 and 4 of the bacterial 16S rRNA gene were amplified using Kapa HiFi Hotstart Ready PCR Mix (Kapa Biosystems, Wilmington, MA, USA), with primers targeting MiSeq 341F and 805R. DNA indexing and second PCR were performed using Nextera XT index kits (Illumina). Each PCR product was purified using an Agencourt AMPure XP purification system (Beckman Coulter, Brea, CA, USA). Quantification and size estimation of the library were performed using the QIAxcel Advanced system and QIAxcel DNA High Resolution Kit (Qiagen, Hilden, Germany). Amplicons were pooled for sequencing using an Illumina MiSeq System (2 × 300 bp paired-end reads).

Sequence assembly and quality filtering were processed using QIIME2 software. Raw sequence reads were demultiplexed using the q2-demux plugin, followed by denoising using the DADA2 plugin to eliminate low-quality scores. All amplicon sequence variants (ASVs) were classified using the SILVA 138 99% database. QIIME2's diversity analyses (q2-diversity plugin) and R software were used to present microbial richness, evenness diversity indices, and PCoA. The LEfSe algorithm was implemented using the Galaxy computational tool.

2.14 Statistical analysis

Data visualization and analysis were performed using GraphPad Prism (GraphPad, San Diego, CA, USA) or IBM SPSS (SPSS Inc., Chicago, IL, USA). Statistical significance was evaluated using a t-test or one- or two-way analysis of variance (ANOVA) followed by Fisher's LSD *post hoc* test, or a Mann-Whitney test, Wilcoxon test or Kruskal-Wallis test followed by Dunn's *post hoc* test, depending on the normal distribution of the data. Pearson's correlation was used to assess the correlation between relative bacterial abundances and variables. Permutational multivariate analysis of variance (PERMANOVA) was applied using the QIIME2 plugin to evaluate differences in microbial community structure. Unless otherwise indicated, data are presented as the mean ± standard error of the mean (SEM), and a p value lower than 0.05 was considered significant.

3 Results

3.1 Perturbation of serum anti-microbial antibodies in RA patients

To investigate microbial alterations in patients with RA based on serum antibody profiling, we conducted microbial species-specific IgM microarrays. The α-diversity of serum anti-microbial antibodies revealed a significant decrease in evenness in patients with RA compared to HC, while the richness remained similar between the two groups (Figure 1A). This diversity was further evident in the β-diversity assessment, where PCoA highlighted distinct clustering patterns representing the varying composition of serum anti-microbial antibodies in RA patients and HC (Figure 1B).

We identified discriminative core microbes employing a bacterial taxonomic rank based on the relative abundance of anti-microbial antibodies in the serum from HC and RA patients using an LEfSe analysis (Figure 1C). At the phylum level, Fusobacteria was significantly enriched in HC, whereas Actinobacteria and Bacteroidetes were enriched in patients with RA. At low taxonomic ranks, 6 and 3 classes, 6 and 4 orders, and 8 and 5 families were enriched in HC and patients with RA, respectively. The 9 genera including *Streptococcus*, *Clostridium*, and *Peptoniphilus*, were significantly enriched in HC, whereas 5 genera, including *Corynebacterium*, *Prophyromonas*, and *Bacillus*, were significantly enriched in patients with RA.

The heatmap depicting serum microbial species-specific antibody abundances highlighted significant alterations in antibody abundance against 36 microbial species in patients with RA compared to HC (Figure 1D). Specifically, antibodies against 21 microbial species were decreased, while antibodies against 15 microbial species were increased in patients with RA compared to HC.

3.2 Altered serum anti-microbial antibodies are associated with disease severity in patients with RA

Our study identified significant alterations in 36 anti-microbial antibodies in the comparison of patients with RA and HC (Figure 1D). Correlation analysis was conducted to investigate the association between the abundances of these significant anti-microbial antibodies and RA disease activity, determining associations with disease severity. Notably, anti-microbial antibodies decreased in patients with RA were inversely correlated with disease activity, whereas those elevated in patients were positively correlated with disease activity (Figure 2A).

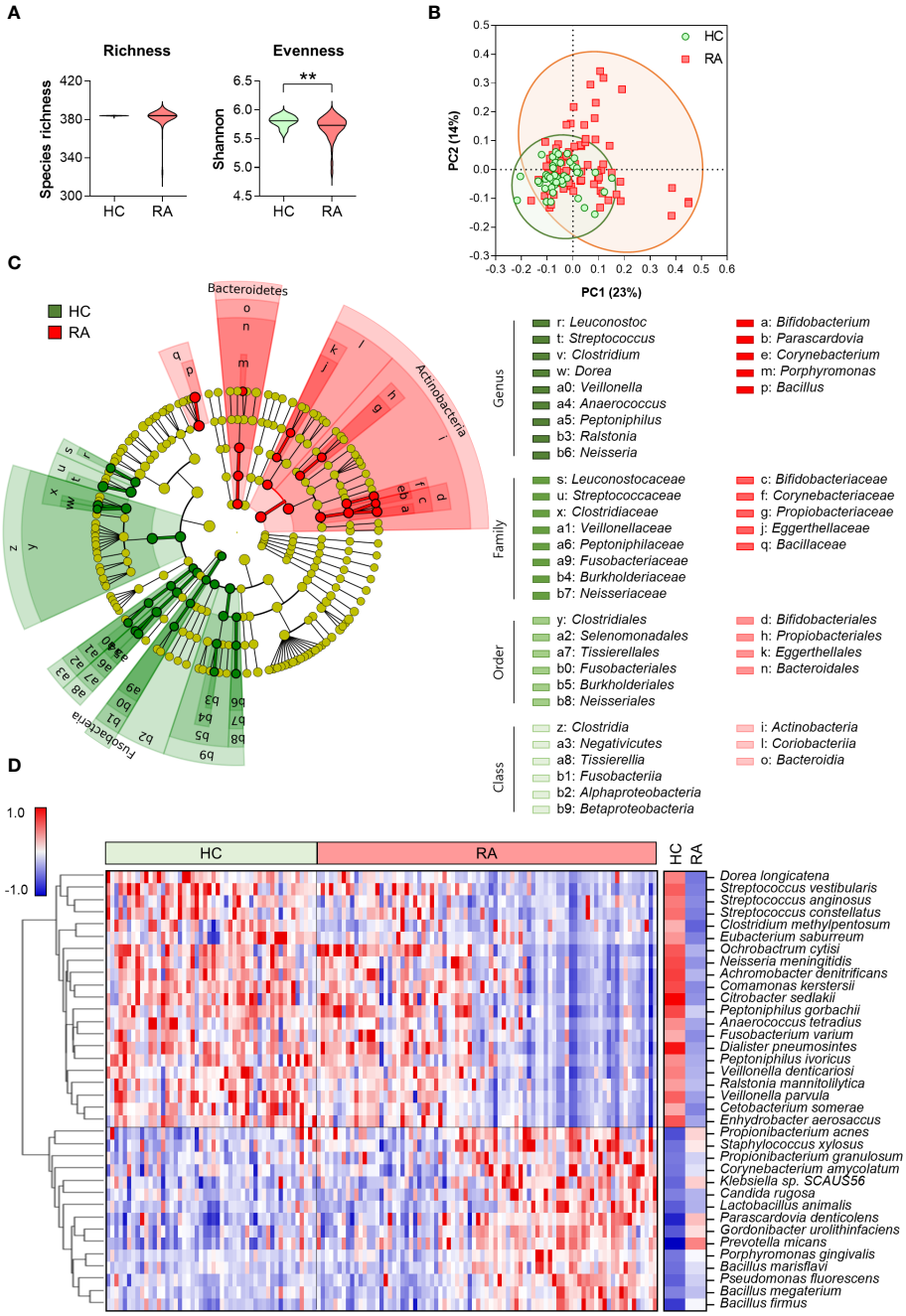

FIGURE 1
Serum anti-microbial antibody profile in healthy control (n = 50) and patients with RA (n = 81). **(A)** α-diversity assessed through microbial species-specific antibody abundance richness and evenness (Mann-Whitney test, $^{**}p < 0.01$). **(B)** β-diversity analyzed using Bray-Curtis PCoA of microbial species-specific antibody communities (PERMANOVA, $p < 0.001$ vs HC). Symbols represent each individual. **(C)** Cladogram generated following a LEfSe analysis at the phylum to genus level (pairwise Wilcoxon test, $p < 0.01$, LDA score > 3.0). Green: taxa enriched in HC, Red: taxa enriched in RA. **(D)** Heatmap depicting differential anti-microbial antibody abundances between HC and patients with RA (t- and z-tests, $p < 0.01$, Z-ratio > 1.5). Blue: low abundance, Red: high abundance. HC: Healthy control, RA: Rheumatoid arthritis, PCoA: Principal coordinates analysis, LDA: Linear discriminant analysis, LEfSe: LDA effect size.

Specifically, the antibodies against *Ochrobactrum cytisi* (*O. cytisi*), *P. gorbachii*, *Dialister pneumosintes* (*D. pneumosintes*), and *Veillonella denticariosi* (*V. denticariosi*) were associated with lower disease severity (Figure 2B). Conversely, antibodies against *Gordonibacter urolithinfaciens* (*G. urolithinfaciens*) and *Pseudomonas fluorescens* (*P. fluorescens*) were associated with higher disease severity, as assessed by DAS28-CRP in patients with RA.

The CoNet approach was employed to infer association patterns among significant 36 anti-microbial antibodies in patients with RA and HC, revealing a higher number of networks in patients with RA compared to HC (Figure 2C), which is suggestive of increased co-occurrences of anti-microbial antibodies in patients with RA. In the RA patient group, most of the networks exhibited direct or indirect connections to one another. Specifically, antibodies against *O. cytisi*,

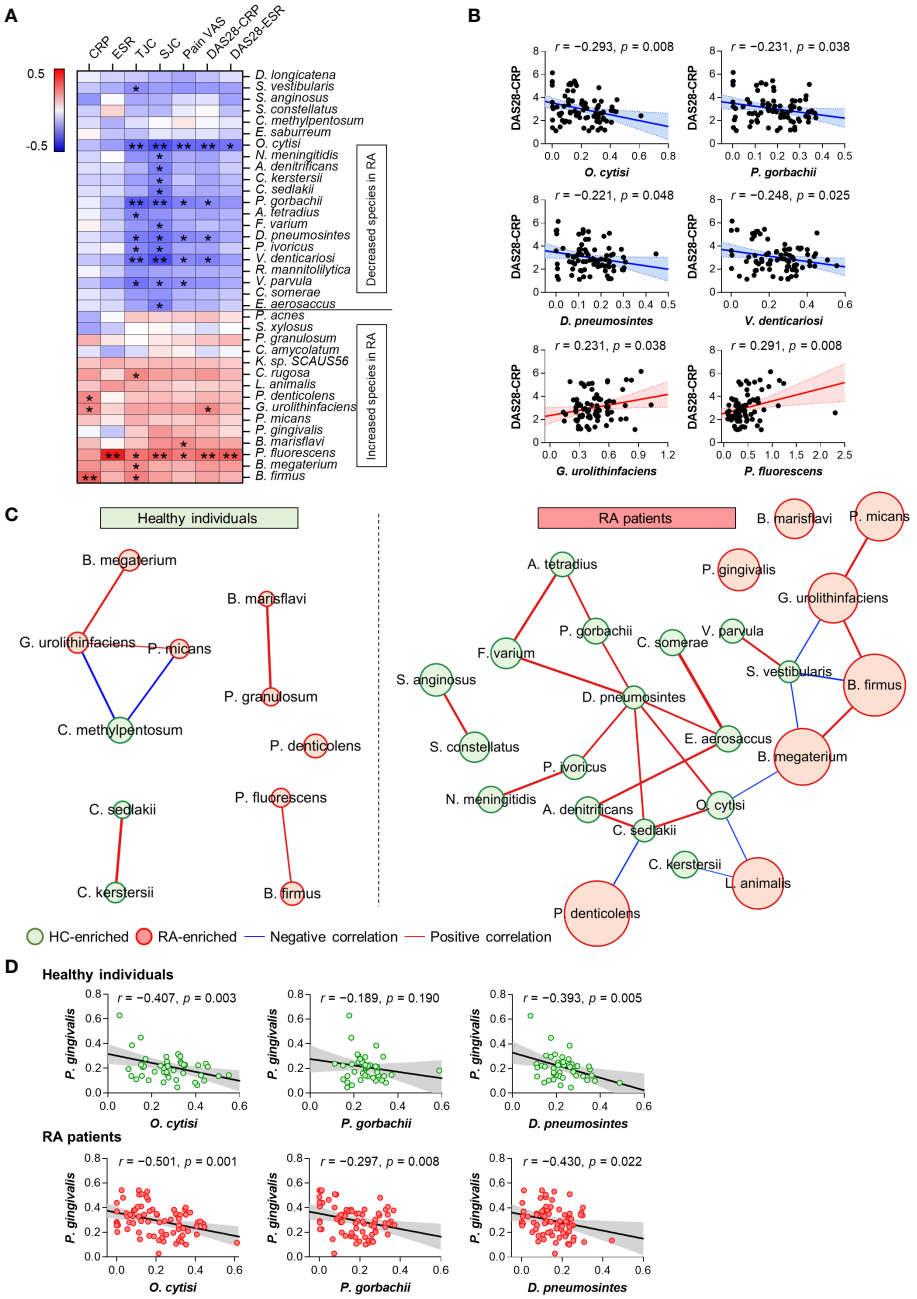

FIGURE 2
Association between altered microbial species-specific antibodies and disease activity in patients with RA (n = 81). **(A)** Correlations between differential anti-microbial antibody abundances and clinical features in patients with RA (Pearson's correlation, *p <0.05, **p < 0.01). Blue: inverse correlation, Red: positive correlation. **(B)** The linear relationships between differential anti-microbial antibody abundances and DAS28 score in patients with RA (Pearson's correlation). Solid lines represent the mean linear regression, while dotted lines indicate 95% confidence intervals. Symbols represent individual RA patients. **(C)** Co-occurrence network of differential anti-microbial antibodies in HC (n = 50) and patients with RA (n = 81). The size of each circle (node) represents the abundance of anti-microbial antibodies enriched in either HC (green node) or RA (red node) patients (Benjamini-Hochberg's correction, p < 0.01). Lines connecting two nodes (edges) indicate the correlation efficiency between anti-microbial antibodies (chosen by Spearman, Pearson, Bray-Curtis, and Kullback-Leibler measures, r > 0.5, p < 0.05). Blue edges: negative correlation, Red edges: positive correlation. **(D)** The linear relationships between antibodies against *P. gingivalis* and disease activity-inversely correlated microbial species in HC and patients with RA (Pearson's correlation). Solid lines represent the mean linear regression, while gray-filled areas indicate 95% confidence intervals. Symbols represent each individual. ESR: Erythrocyte Sedimentation Rate, CRP: C-Reactive Protein, TJC: Tender Joint Count, SJC: Swollen Joint Count, VAS: Visual Analog Scale, DAS: Disease Activity Score.

P. gorbachii, and *D. pneumosintes*, which were enriched in HC and inversely associated with disease activity (Figure 2B), demonstrated positive connections either directly or indirectly within the RA patient network (Figure 2C). Additionally, the anti-*G. urolithinfaciens* antibody, enriched in RA and positively associated with disease activity (Figure 2B), showed positive connections with RA-enriched antibodies such as *P. micans* and *B. firmus*, while displaying an inverse connection with the HC-

enriched *S. vestibularis* antibody. Overall, the altered anti-microbial antibodies exhibited associations with disease severity and interconnected relationships (networks) among themselves in patients with RA.

The analysis of microbial arrays revealed an increased abundance of antibodies targeting *P. gingivalis* in patients with RA, a putative pathogen implicated in RA through protein citrullination (Figure 1D). To further identify specific microbial candidates for RA therapy, we investigated the relationship between antibodies against *P. gingivalis* and three microbial species: *O. cytisi*, *P. gorbachii*, and *D. pneumosintes*. These species were selected based on their association with disease severity and their co-occurrence network (Figures 2B, C). The abundance of anti-*O. cytisi* and anti-*D. pneumosintes* antibodies exhibited an inverse correlation with the abundance of anti-*P. gingivalis* antibody in both patients with RA and HC (Figure 2D). Notably, the abundance of anti-*P. gorbachii* antibody showed an inverse correlation with anti-*P. gingivalis* antibody solely among patients with RA (Figure 2D). Importantly, *P. gorbachii* (*PG*) has been reported to inhibit infection (37) and produce SCFAs which were associated with RA suppression (38). Therefore, based on our bacterial microarray findings and the reported evidence (Supplementary Table 5), we selected *PG* as a potential specific target for RA treatment and further explored its involvement in RA.

3.3 *In-vitro* characteristics of *P. gorbachii*

To investigate the potential mechanisms underlying the therapeutic effects of *PG* in RA, we examined the competitive potential of *PG* against *P. gingivalis*, an RA-associated pathogen. Our *in-vitro* interspecies competition assay revealed an inhibitory impact of *P. gingivalis* on *PG* (Figure 3A). Despite similar growth rates in single cultures of both species, the growth of *PG* was strongly suppressed after 16 h of co-culture with *P. gingivalis*, indicating interference in bacterial growth between the two species.

To validate the ability of *PG* to produce SCFAs, which have therapeutic implications in RA, we performed GC-MS analysis of *PG*-cultured media. *PG* produced SCFAs, including acetate and butyrate (Figure 3B), which have been associated with the alleviation of RA symptoms. Subsequently, we assessed the ability of *PG* to suppress immune responses through evaluation of pro-inflammatory cytokine profiles in RAW 264.7 macrophages, siLP, and MLN cells treated with HK-*PG* or *PG* supernatants under cell-stimulating conditions. Both HK-*PG* and *PG* supernatant downregulated the gene expression of LPS-induced *Il6*, *Il23*, *Il1b*, and *Tnfa* in RAW 264.7 cells (Figure 3C; Supplementary Figure 1). Moreover, HK-*PG* significantly reduced CD3/CD28-induced IFN-γ and IL-17A production in siLP cells, as well as IL-17A production in MLN cells (Figure 3D). However, *PG* supernatant only reduced CD3/CD28-induced IL-17A production in MLN cells (Figure 3E), indicating a specific anti-inflammatory suppression of immune cells. In an additional *in-vitro* experiment involving *P. fluorescens*, *P. gingivalis*, and *P. micans*, bacteria identified as elevated in the serum bacterial microarray analysis of patients with RA, treatment with *P. fluorescens* and *P. gingivalis* independently led to the upregulation of pro-inflammatory cytokine genes in RAW 264.7 cells in the absence of LPS (Supplementary Figure 2A). Meanwhile, the treatment of *P. gingivalis* and *P. micans* did not impact the induction of pro-inflammatory cytokine genes under LPS stimulated condition (Supplementary Figure 2B). Overall, *PG* demonstrated an outstanding effect in inhibiting the upregulation and secretion of pro-inflammatory cytokines associated with activated macrophages and $CD4^+$ T cells. These findings underscore the critical role of *PG* in the modulating both innate and adaptive immune responses, involving key immune cell types such as macrophages and $CD4^+$ T cells, which play a central role in the pathogenesis of RA.

3.4 *P. gorbachii* treatment suppresses arthritis in CIA mice

To determine whether *PG* can prevent RA development *in vivo*, we evaluated the effect of *PG* treatment on arthritis in a CIA mouse model. First, we compared fecal CFUs of *PG* between CIA and *PG*-fed CIA (CIA/*PG*) mice to determine colonization of the intestine following oral administration. The fecal CFUs of *PG* were significantly higher in CIA/*PG* mice than in CIA mice, indicating stable intestinal colonization (Figure 4A).

To clarify the effect of *PG* on arthritis, we treated a group of mice with antibiotics, as a broad spectrum of antibiotics has been reported to reduce arthritis severity in CIA mice (39). Both antibiotic- (CIA/AB) and *PG*-treated (CIA/*PG*) CIA mice exhibited reduced arthritis scores compared to CIA mice (Figure 4B). Furthermore, CIA/*PG* mice showed a clear prevention in arthritis development, with a lower incidence of arthritis than that of CIA mice (Figure 4B). Histopathological analysis using H&E staining revealed decreased inflammatory cell infiltration and bone erosion in CIA/*PG* mice (Figure 4C). Additionally, PG treatment led to the recovery of cartilage thinning in the joints of CIA mice.

To further confirm the suppressive effect of *PG* on arthritis, we investigated the gene expression of pro-inflammatory cytokines and chemokines in the ankles of the experimental groups. CIA/*PG* mice exhibited downregulated gene expression of pro-inflammatory cytokines (*Ifng*, *Il17a*, *Il6*, *Il1b*, and *Il23*) and a chemokine receptor (*Cx3cr1*), which were upregulated in CIA mice (Figure 4D; Supplementary Figure 3A). The gene expression of the anti-inflammatory cytokine *Il10* was also upregulated in the ankles of CIA mice and normalized by *PG* treatment (Figure 4D).

Next, we assessed whether *PG* treatment influenced antigen-specific systemic autoimmunity by measuring serum anti-CII IgG and anti-CCP antibody levels. We observed no significant difference in anti-CII IgG antibody levels between CIA and CIA/*PG* mice; however, CIA/*PG* mice exhibited a trend for lower levels of anti-CII IgG antibody compared to CIA mice (Figure 4E). Furthermore, the elevated serum anti-CCP antibody levels in CIA mice were significantly decreased with *PG* treatment (Figure 4E). These findings suggest that *PG* not only attenuates arthritis severity but also reduces the production of antigen-specific autoantibodies, reflecting its potential therapeutic role in RA.

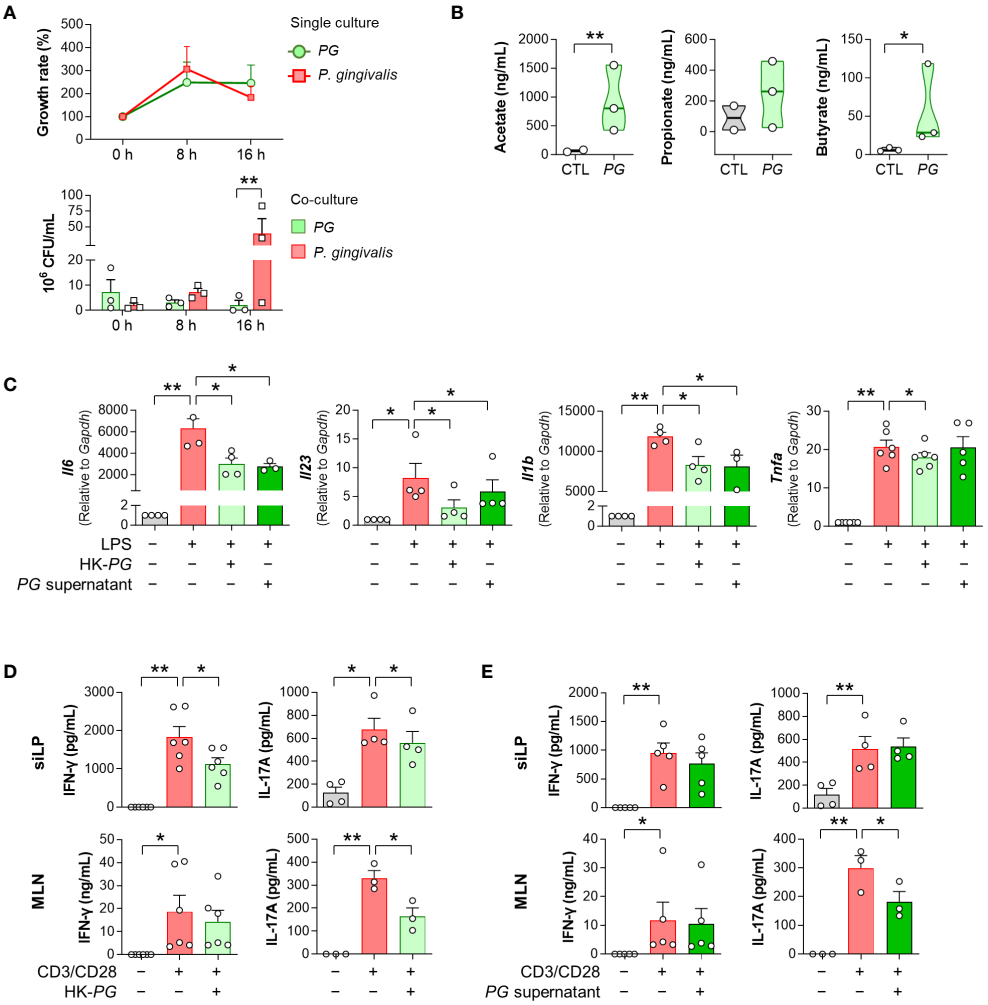

FIGURE 3
In vitro physiological and immunological properties of *P. gorbachii* (*PG*). **(A)** *In vitro* competition assay between *PG* and *P. gingivalis*. *PG* and *P. gingivalis* cultures were prepared each as a control (single culture) and then mixed (co-culture). After 0, 8, and 16 h of single and co-cultures, *PG* and *P. gingivalis* colonies were counted. $n = 3$ for each group and time (Two-way ANOVA, Fisher's LSD *post hoc* test, $^{**}p < 0.01$). **(B)** Measurement of short-chain fatty acids (SCFAs) in *PG*-cultured supernatants. $n = 2–3$ per group (t-test, $^{*}p < 0.05$, $^{**}p < 0.01$). Median and interquartile range (1st – 3rd quartile). **(C)** Pro-inflammatory gene expression of RAW 264.7 cells cultured in the absence or presence of heat-killed (HK)-*PG* or *PG* supernatant under LPS stimulation. $n = 3–6$ per group (One-way ANOVA, Fisher's LSD *post hoc* test, $^{*}p < 0.05$, $^{**}p < 0.01$ vs LPS^{+} control). **(D, E)** IFN-γ and IL-17A concentrations in mouse siLP and MLN cell supernatants cultured in the absence or presence of HK-*PG* **(D)** or *PG* supernatant **(E)** under anti-CD3e and anti-CD28 stimulation. $n = 3–6$ per group (One-way ANOVA, Fisher's LSD *post hoc* test, $^{*}p < 0.05$, $^{**}p < 0.01$ vs $CD3/CD28^{+}$ control). Mean ± SEM. siLP: Small intestinal lamina propria, MLN: Mesenteric lymph node.

3.5 *P. gorbachii* is involved in the suppression of arthritis by improving intestinal inflammation and barrier integrity in CIA mice

In our study, we explored *PG*'s role in regulating immune responses in the gut-joint axis, as prior research has suggested that intestinal inflammation can trigger the onset of RA (40). We conducted an analysis of T cell subsets in the ILN, MLN, and cLP of naïve, CIA, and CIA/*PG* mice using flow cytometry. The detailed gating strategies can be found in Supplementary Figure 4A.

Notably, we observed a significant decrease in the percentage of Th17 ($CD4^{+}IL\text{-}17A^{+}$) cells in the ILN of CIA/*PG* mice compared with that in CIA mice (Figure 5A). Furthermore, *PG* treatment significantly diminished the numbers of Th1 ($CD4^{+}IFN\text{-}\gamma^{+}$) and Th17 cells that had accumulated in the ILN of CIA mice. Interestingly, Treg ($CD4^{+}Foxp3^{+}$) cells, well-known for their immunosuppressive properties, were also increased in CIA mice relative to naïve and CIA/*PG* mice. However, the Th1/Treg and Th17/Treg ratios were higher in CIA mice than in naïve mice, suggesting a preferential differentiation or proliferation toward Th1 and Th17 cells in CIA. Importantly, *PG* treatment effectively restored the Th17/Treg imbalance observed in CIA mice by decreasing the Th17/Treg ratio in CIA/*PG* mice compared to CIA mice.

Although no difference was observed in Th1 and Th17 cells of cLP and MLN between naïve, CIA, and CIA/*PG* mice (Supplementary Figure 4B), *PG* treatment significantly reduced the

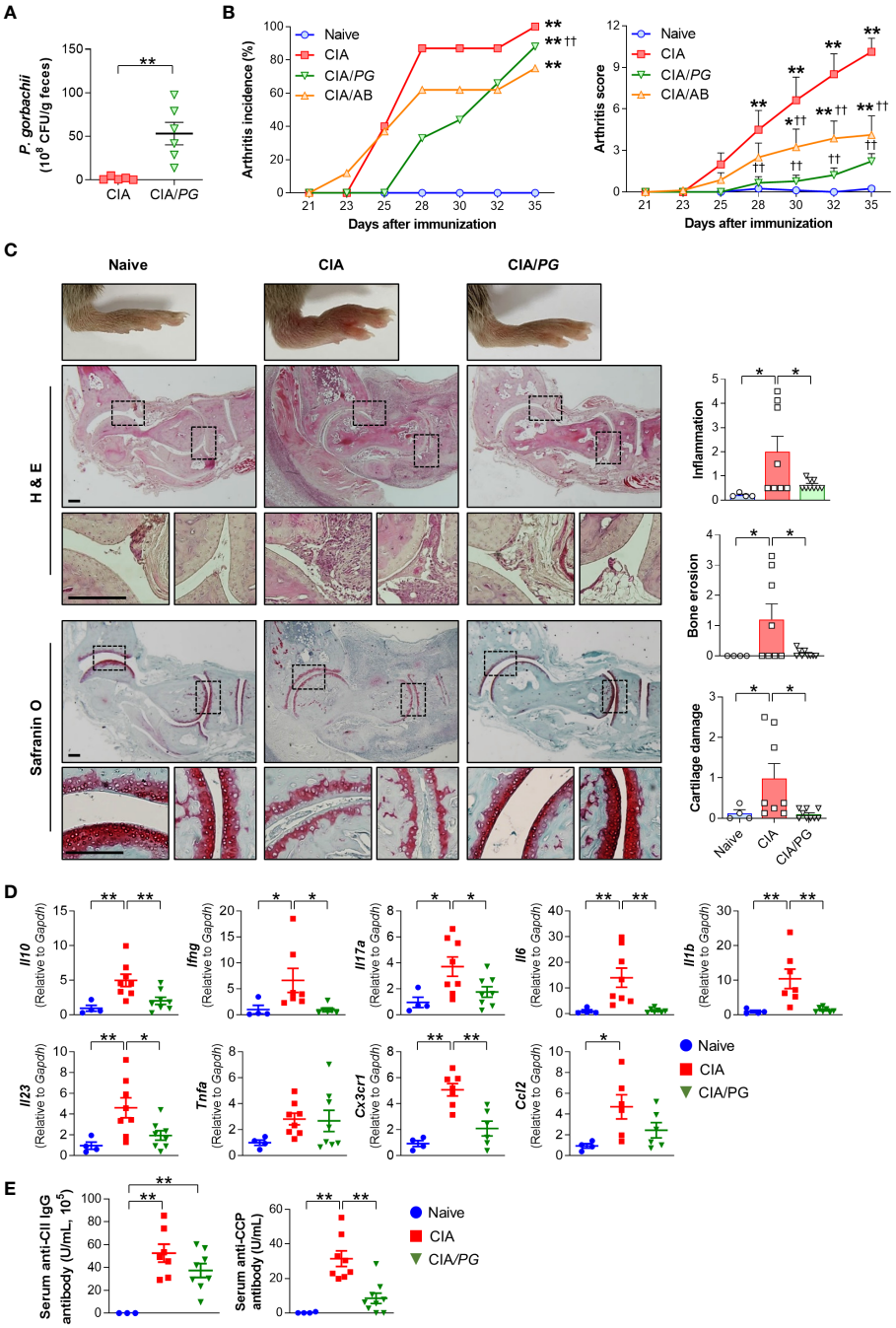

FIGURE 4
Effect of *PG* on arthritis in CIA mice. CIA was induced by intra-dermal injection of CII into mice. *PG* was orally administered for 4 weeks before the first CII injection (day 0) and continued until euthanasia at day 35. Samples were collected from naïve (n = 4), CIA (n = 8), and CIA/*PG* (n = 9) mice at day 35. **(A)** Colonization of *PG* in feces from CIA and CIA/*PG* mice (t-test, $^{**}p < 0.01$). **(B)** Arthritis incidence and scores in the experimental groups (Log-rank test and Two-way ANOVA, Fisher's LSD *post hoc* test, $^{*}p < 0.05$, $^{**}p < 0.01$ vs naïve; $^{\dagger\dagger}p < 0.01$ vs CIA). **(C)** Representative histopathological images and scores of ankle joints stained with H&E and safranin O (One-way ANOVA, Fisher's LSD *post hoc* test, $^{*}p < 0.05$). Scale bar: 200 µm. **(D)** Expression of anti- and pro-inflammatory cytokine genes in ankle samples (One-way ANOVA, Fisher's LSD *post hoc* test, $^{*}p < 0.05$, $^{**}p < 0.01$). **(E)** Serum anti-CII IgG and anti-CCP antibody levels (One-way ANOVA, Fisher's LSD *post hoc* test, $^{**}p < 0.01$). Mean ± SEM.

accumulation of inflammatory monocytes ($CD11b^{+}CX3CR1^{+}Ly6C^{+}$) in the MLN and ILN of CIA mice (Figure 5B). Furthermore, our study encompassed an analysis of conventional dendritic cells (cDCs), with a specific focus on the $CD103^{-}$ cDC2 subset, known for its role in promoting T cell differentiation into Th17 cells. However, our investigation did not reveal significant differences in $CD103^{-}$ cDC2 subset within the cLP and MLN when comparing non-treated CIA and *PG*-treated CIA mouse groups (Supplementary Figure 4C). Although *PG* treatment led to a reduction in both the number and percentage of $CD103^{-}$ cDC2 cells in the ILN of CIA mice, it did not restore normalcy to the population of all cDC subsets within cLP and MLN (Supplementary Figure 4C). Collectively, our

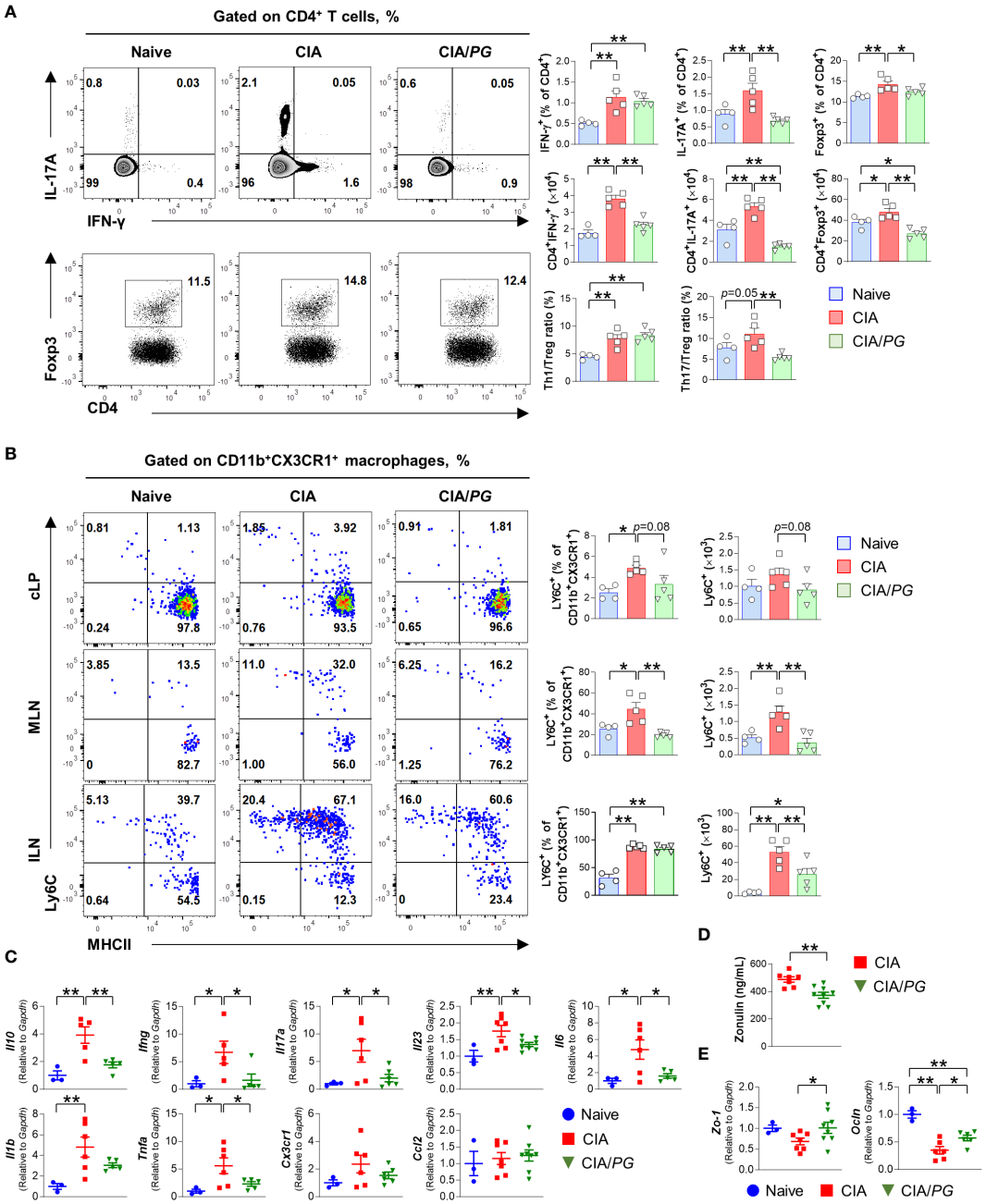

FIGURE 5
Role of *PG* in CIA-characteristic inflammation and intestinal barrier function. Samples were collected from naïve, CIA, and CIA/*PG* mice at 35 days after CII immunization. **(A, B)** Flow cytometry analysis of T cell subsets in the ILN **(A)** and macrophage lineage cells **(B)** from the cLP, MLN, and ILN of naïve (n = 4), CIA (n = 5), and CIA/*PG* (n = 5) mice. **(C–E)** Gene expression of pro-inflammatory cytokines in ileum **(C)**, zonulin levels in serum **(D)**, and gene expression of *Zo-1* and *Ocln* in ileum **(E)** of naïve (n = 3), CIA (n = 6–7), and CIA/*PG* (n = 6–9) mice. Mean ± SEM. One-way ANOVA, Fisher's LSD *post hoc* test **(A–C, E)** and t-test **(D)**, *p < 0.05, **p < 0.01. cLP: Colonic intestinal lamina propria.

findings highlight the potent inhibitory effect of *PG* on Th17 cells in ILN and the marked reduction in the accumulation of inflammatory monocytes in both ILN and gut-associated MLN.

To further understand the intestinal effect of *PG* on RA pathogenesis, we investigated the gene expression of pro-inflammatory cytokines in the ileum of naïve, CIA, and CIA/*PG* mice. The gene expression of *Ifng*, *Il17a*, *Il23*, *Il6*, and *Tnfa* was decreased in the ileal tissues of CIA/*PG* mice compared to those in CIA mice (Figure 5C). Moreover, we evaluated gut barrier integrity using zonulin, which is a protein secreted from gut epithelial cells in response to dietary, gut microbial, or inflammatory stimuli (8). Serum zonulin levels were decreased in CIA/*PG* mice compared to CIA mice, indicating improved gut barrier integrity (Figure 5D). Furthermore, genes encoding tight-junction proteins, *zonula occludens-1* (*Zo-1*) and *occludin* (*Ocln*), were upregulated in the ileum of CIA/*PG* mice compared to those in CIA mice (Figure 5E; Supplementary Figure 3B). These data suggest a protective capacity of *PG* against arthritis through inhibition of CIA intestinal

inflammation, reflected in the prevention of increased gut permeability and the disassembly of tight junctions.

3.6 *P. gorbachii* treatment restores gut microbial alterations in CIA mice

To investigate the effects of *PG* treatment on the gut microbiome, we conducted 16S rRNA gene sequencing analysis of cecal samples from naïve, CIA, and CIA/*PG* mice. Although no significant differences were observed in α-diversity using Chao1 and Shannon indices among cecal microbiota from naïve, CIA, and CIA/*PG* mice (Figure 6A), CIA promoted a change in microbial communities with a clear separation in PCoA plots from the naïve and CIA/*PG* groups (Figure 6B). The cladogram showed discriminative bacterial clades by comparison of different mouse groups, where Bacteroidetes, Patescibacteria, and Firmicutes were the microbial phyla with differential abundances in the cecum of naïve, CIA, and CIA/*PG* mice, respectively (Figure 6C). At lower taxonomic ranks, bacterial taxa enriched in the cecum of naïve mice were *Bacteroidaceae*, *Prevotellaceae*, *Staphylococcaceae*, *Eubacterium coprostanoligenes* (*E. coprostanoligenes*) group, and *Peptococcaceae* families, as well as eight genera including *Bacteroides*, *Alloprevotella*, *Staphylococcus*, *Lachnospiraceae_UCG-006*, *Butyricicoccaceae_UCG-009*, and *E. coprostanoligenes* group. Bacterial taxa enriched in the cecum of CIA mice were the *Saccharimonadaceae* family, as well as the *Desulfovibrio*, *Acetatifactor*, and *Candidatus saccharimonas* genera. Bacterial taxa enriched in the cecum of CIA/*PG* mice were *Lactobacillaceae*, *Streptococcaceae*, *Bacilli_unidentified*, and *Lachnospiraceae* families, as well as six genera including *Lactobacillus*, *Streptococcus*, and *Lachnospriaceae NK4A136* group.

PG treatment restored certain microbial genera and species to levels similar to those of naïve mice (Figures 6D, E). Notably, the relative abundance of the *E. coprostanoligenes* group and *Clostridium leptum* (*C. leptum*) was significantly normalized in the cecum of CIA/*PG* mice. In addition, *PG* treatment also promoted a significant increase in *Blautia_unidentified* and *Streptococcus danieliae* (*S. danieliae*) compared to CIA mice (Figure 6E). Overall, *PG* treatment partially resolved CIA-induced gut microbial dysbiosis, bring the gut microbial profile closer to that of naïve mice. To explore whether these changes in gut microbiota induced by *PG* treatment are linked to the production of SCFAs, we analyzed SCFA levels in cecal samples obtained from naive, CIA, and CIA/*PG* mice. Our analysis revealed a significant reduction in acetate and propionate levels in CIA mice; however, *PG* administration did not restore the decreased levels of acetate and propionate induced by CIA (Supplementary Figure 5). No significant changes in butyrate levels were observed among the three experimental mouse groups.

The correlation analysis between pathobiological molecules and bacterial taxa revealed that significantly abundant bacterial taxa in the cecum of naïve mice tended to be positively correlated with ileal *Ocln* gene expression and negatively correlated with an inflammatory response (Figure 6F). Conversely, significantly abundant bacterial taxa in the cecum of CIA mice showed a tendency for a negative correlation with intestinal epithelial barrier function and a positive correlation with an inflammatory response (Figure 6F). The genus *Streptococcus* and species *S. danieliae* were discriminately enriched in the cecum of CIA/*PG* mice and were associated with improved intestinal barrier integrity, showing a positive correlation with ileal *Zo-1* gene expression and an inverse correlation with serum zonulin level (Figure 6F). Moreover, *Streptococcus* and *S. danieliae* were inversely correlated with the number of MLN Ly6C$^+$ inflammatory monocytes and the gene expression of pro-inflammatory cytokines, such as *Ifng* and *Il17a*. Collectively, these findings demonstrated that the enriched microorganisms in the cecum of CIA/*PG* mice were closely linked to the amelioration of elevated gut permeability and inflammation.

4 Discussion

In this study, we identified altered antibodies against 36 microbial species in patients with RA compared to healthy controls using a serum IgM antibody microarray against 384 microbial species. Among them, *PG* was selected as a candidate microorganism likely to have a therapeutic effect among the bacterial species that were decreased in RA patients and displayed a negative correlation with disease activity. *PG* showed therapeutic potential due to its competitive growth with *P. gingivalis*, its secretion of immunomodulatory SCFAs, and its suppression of inflammatory cytokines associated with macrophage and T cell activation. In a mouse model of CIA, *PG* administration exerted a strong inhibitory effect on Th17 cells in ILN and markedly inhibited inflammatory monocytes in MLN and ILN. Moreover, *PG* improved gut permeability and tight junction disassembly, inhibiting intestinal inflammation in CIA mice.

The most common method currently used for gut microbiota identification is 16S rRNA sequencing of fecal samples. As previously highlighted, some studies have attempted to overcome the limitations of sequencing methods using feces by focusing on serum-based approaches. Continuous exposure to microbes can trigger an antibody response against these microorganisms, offering a potential metric for assessing microbial exposure (41). Although IgA has traditionally been associated with immune responses against gut microbiota, recent research has highlighted the significance of IgM and IgG in host-microbiota interactions (42). A recent study revealed the presence of numerous IgM$^+$ B cells in human intestine, which produce secretory IgM and intestinal IgM reacting to a variety of microbiota (43). IgM, the primary antibody produced by B cells upon antigen exposure before class switching to IgG or IgA (44), is characterized by its large pentameric structure, enabling it to bind to a broader range of bacterial antigens compared to IgG and IgA (45). Consequently, IgM-associated alterations are likely to signify diverse and robust systemic immune responses during the initial stages of disease. This may effectively mirror recent or ongoing shifts in microbiota, serving as a first responder against microbial antigens.

Several studies have explored the potential role of IgM in the immunopathogenesis of various diseases, often mediated through altered gut microbiota. For instance, individuals with obesity have

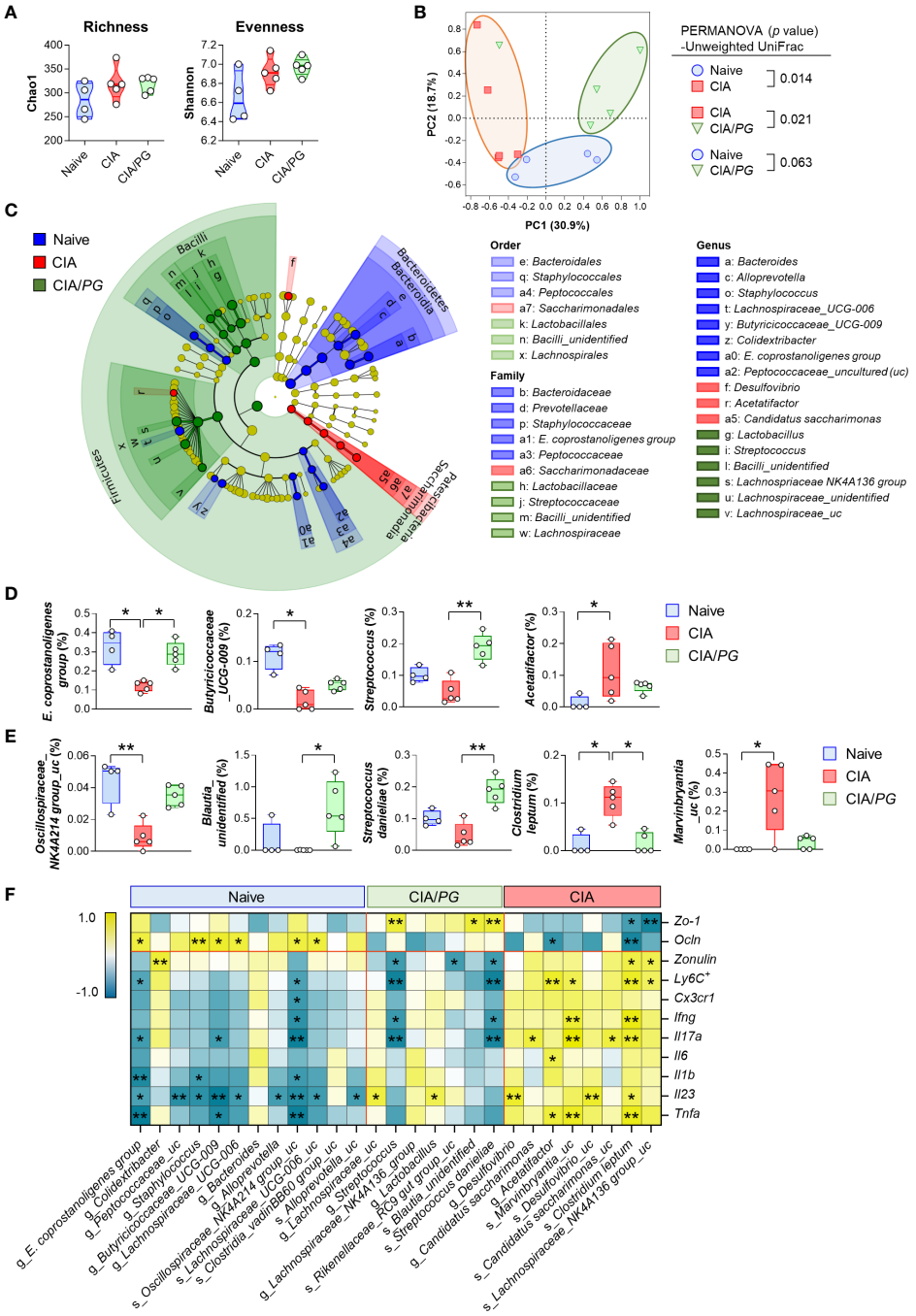

FIGURE 6
Role of *PG* in gut microbiome in CIA. Cecal samples were collected from naïve (n = 4), CIA (n = 5), and CIA/*PG* (n = 5) mice at 35 days after CII immunization and 16S rRNA gene sequencing was conducted. **(A)** α-diversity measured based on the Chao1 and Shannon indices (One-way ANOVA, Fisher's LSD *post hoc* test, $p > 0.05$). Median and interquartile range (1st – 3rd quartile). **(B)** β-diversity assessed using PCoA based on unweighted UniFrac distance matrix. **(C)** Cladogram constructed based on the LEfSe analysis. Colors indicate bacterial taxa discriminately enriched in cecal microbiome of naive (blue), CIA (red), and CIA/*PG* (green) mice (Kruskal-Wallis, pairwise Wilcoxon test, $p < 0.05$, LDA score > 2.0). **(D, E)** Relative abundance of significantly different genera **(D)** and species **(E)** between groups (Kruskal-Wallis, Dunn's *post hoc* test). Median ± min to max. **(F)** Relationship between gut-associated inflammatory profiles and cecal microbial taxa discriminately enriched in each experimental group (Pearson's correlation, $*p < 0.05$, $**p < 0.01$). Colors indicate negative (turquoise) and positive (yellow) correlations.

shown elevated concentrations of plasma IgM (46) along with an increase in IgM-bound gut microbiota (47). Patients with RA exhibited higher IgM and IgA levels compared to control (48), while most patients with poor prognosis displayed elevated levels of IgM antibodies specifically binding to IgG (49). Moreover, RA patients exhibited significantly higher levels of multiple antimicrobial response factors such as EndoCAb IgM and EndoCAb IgA, which are released into circulation in response to microbial exposure when compared to healthy individuals (48). Elevated levels of IgM specific to certain bacterial species were also

observed in RA patients (50). Notably, sera from rheumatoid factor (RF)-positive individuals showed significantly higher levels of IgM antibodies, but not IgG and to a lesser extent IgA, against *Proteus mirabilis*, *Escherichia coli*, and *Klebsiella pneumoniae*, which have been linked with RA (51).

This study was conducted to analyze the microbiota of patients with RA using a serum microbial array designed to detect IgM antibodies against gut microbiota in the serum, building upon the rationale supported by prior research. Our results using this novel method revealed a reduction in the evenness of anti-microbial antibody abundances in patients with RA compared to controls, as well as distinct compositions in these antibody levels between the two groups. Antibodies against a total of 36 microbial species were differentially expressed, with 21 being decreased and 15 being increased in patients with RA compared to HC patients. Notably, we found a significant correlation between the anti-*PG* antibody and RA disease activity, suggesting the potential effectiveness of the RA-specific bacteria, *PG*, as a treatment avenue for RA.

Preliminary data and the literature accentuate the plausibility of employing *PG* for RA treatment. First, *PG* belongs to the microbial taxa associated with disease-suppressive soils (37). Second, *PG* produces butyrate and acetate, immunomodulatory metabolites derived from microbiota (38). Butyrate has been associated with improved proliferation of intestinal epithelial cells, mucin synthesis, and maintenance of mucosal immune homeostasis (52). Acetate is a major SCFA that can be converted to butyrate by gut microbial enzymes (53, 54). Similarly, we showed that *PG* produces butyrate and acetate *in-vitro*, indicating its potential to restore commensal bacterial composition. In addition, the growth of *PG* was inhibited in the presence of *P. gingivalis*, a recognized pathogenic player in RA. Although the specific bacteria involved in competitive interactions with *P. gingivalis* are unknown, *PG* appears to play a role in such interactions. Notably, *PG* administration partially restored certain genera and species, contributing to the partial recovery of gut microbiota homeostasis. This study revealed that *PG* could potentially improve CIA by reinstating eubiosis.

This study has limitations in determining whether *PG* exerts its arthritis-suppressing effects through SCFA production. While our *in-vitro* experiment confirmed *PG*'s capacity to generate SCFAs, we observed no significant differences in cecal SCFA levels between non-treated CIA and *PG*-treated CIA mice. A prior study demonstrated differences in SCFA levels between gut and serum, suggesting the potential systemic transport of SCFAs within the body (55). Their research revealed an increase in serum butyrate levels upon administering *Faeclibacterium prausnitzii*, a representative butyrate-producing bacterium, in CIA mice. However, they reported no distinctions in cecal butyrate levels between non-treated CIA and *F. prausnitzii*-treated CIA mice. Although we were unable to analyze serum SCFAs in our present study, future investigations may be necessary to explore the influence of *PG* on the redistribution of SCFAs between the gut and the circulatory system *in- vivo*.

Pathophysiological immune mechanisms between gut microbiota and RA pathogenesis are potentially multifactorial. Some of these potential interactions might be underlined by the activation of antigen-presenting cells (APCs) via toll-like receptors, enzymatic peptide citrullination induction, antigenic mimicry, control of the host immune system (triggering T cell differentiation), and increased Th17-mediated mucosal inflammation (56). *P gingivalis* contributes to RA pathogenesis by activating Th17 cell-mediated pro-inflammatory responses and encoding peptidyl arginine deiminase, which facilitates the generation of ACPA (10, 11). Additionally, *P. copri* activates APCs through toll-like receptors and stimulates Th17 cell responses and ACPA production by B cells in patients with RA (56). Conversely, *P. histicola* can suppress arthritis development by modulating the immune response (regulation of DCs and generation of Treg cells), resulting in the suppression of Th17 responses and reduction of inflammatory cytokines (15). *PG* suppressed Th17 responses, as well as pro-inflammatory cytokines, inflammatory monocytes, and ACPA production. Our study further elucidates how *PG* contributes to CIA alleviation by curbing Th17 responses and inflammatory monocyte recruitment.

Lymphatic capillaries located within intestinal villi play a vital role in both nutrient absorption and immune cell trafficking to the MLN (57). Gut injuries can result in the release of pro-inflammatory factors that disrupt the integrity of the intestinal barrier (58). Recent evidence underscores the mesenteric lymph as a conduit for gut-derived harmful agents, ultimately contributing to systemic inflammation. These agents, upon absorption into the mesenteric lymphatic duct, possess the potential to activate and transport immune cells including monocytes/macrophages and DCs, thereby propagating systemic inflammation. During tissue injury or infection, monocytes rapidly infiltrate the affected tissues, acquiring pro-inflammatory characteristics, often classified as inflammatory monocytes (59). In inflamed colons, the recruitment of inflammatory monocytes to the LP is facilitated through CCR2, followed by their subsequent migration to the MLN, indicating colon inflammation (60).

In our study, although we did not observe a significant reduction in the population of inflammatory monocytes within the cLP of *PG*-treated CIA mice, we did find compelling evidence of *PG*'s inhibitory effect on the activation/recruitment of inflammatory monocytes within the MLN, implying its potential protective role against gut inflammation and injury. Furthermore, our study demonstrated a down-regulation of pro-inflammatory cytokine genes in the intestines of *PG*-treated CIA mice, accompanied by reduced serum zonulin levels, suggesting that *PG*'s impact on arthritis may be mediated through the modulation of the intestinal microenvironment. We also noted a trend toward reduced CCL2 gene expression in the ankles of *PG*-treated CIA mice, indicating a potential role for *PG* in inhibiting the migration of inflammatory monocytes to the synovium. Monocyte recruitment to the synovium relies on the interaction between chemokine receptors CCR2 and CX3CR1 on the monocyte surface and their ligands CCL2 and CX3CL1, which are produced by fibroblast-like synoviocytes (61). This interaction governs the egress of circulating monocytes and their subsequent recruitment into the RA synovium (62, 63).

Recent studies have highlighted the role of monocytes as APCs capable of activating T cells. In particular, Ly6C$^+$ monocytes play a crucial role in transporting and presenting antigens to cognate T

cells in LNs (59, 64). In RA, cytokines produced by monocytes/macrophages, such as IL-1β, IL-6, and IL-23, are instrumental in driving the polarization of Th17 cells and enhancing IL-17 production in $CD4^+$ T cells (65). Inflammatory monocytes are likely the predominant monocyte subset involved in modulating the Th17 cells response, contributing to the activation and expansion of Th17 cells in inflamed synovial tissue (66, 67). Based on the findings from previous research, it is reasonable to speculate that *PG* contributes to the reduction of inflammatory monocyte recruitment/infiltration in the MLN by mitigating gut inflammation and barrier disruption. Concurrently, *PG* may hinder the trafficking of inflammatory monocytes to the synovium and its draining ILN by regulating CCL2, thereby influencing the induction of Th17 cells in the synovium and preventing the dissemination of systemic inflammation.

Nonetheless, recent studies have unveiled the intricate role of monocytes, including their actions within circulation and migration into tissues and lymphoid organs (59). Monocytes precursors originating from the bone marrow (BM) migrate to diverse organs, including lymphoid tissues like LNs and spleen, as well as nonlymphoid tissues such as the intestines, lung, and skin through blood circulation (68). CCL2 also plays a critical role in the egress of $Ly6C^{hi}$ monocytes from the BM (64). Activated monocytes migrate from the bloodstream into inflamed tissues through chemotaxis mediated CCL2 and CX3CL1, contributing to proinflammatory cytokine production. Monocytes can also traffic to LNs through tissues (69). Hence, it is conceivable that during arthritis, monocytes originating from the BM and circulating in the bloodstream may migrate to inflamed synovium or intestine, subsequently emigrating to their respective draining LNs. In the exploration of *PG*'s mechanisms for mitigating arthritis, unresolved questions remain regarding monocyte migration to tissues and draining LNs, as well as the interactions occurring within this lymphoid network.

Our findings indicate that *PG* influences intestinal permeability, suggesting a potential therapeutic role for *PG* in arthritis by modulating the intestinal environment. Zonulin, a central factor in this process, disrupts intestinal tight-junction proteins, enhances intestinal permeability, and promotes Th1 and Th17 infiltration in the lamina propria before the onset of arthritis (40). A recent study demonstrated that oral treatment with the zonulin antagonist larazotide before the onset of arthritis prevented increased intestinal barrier permeability and attenuated arthritis symptoms in CIA mice (40). ZO-1, an intracellular adaptor protein that binds to numerous transmembrane and cytoplasmic proteins, is required for the assembly of both adherens and tight junctions (70). Our study demonstrated that *PG* supplementation restored intestinal barrier integrity, decreased serum levels of zonulin, and increased gene expression of intestinal tight junction molecules (*Zo-1* and *Ocln*), while also suppressing pro-inflammatory cytokines in the intestine. Thus, *PG* has the potential to ameliorate CIA by restoring intestinal barrier function. However, further mechanistic study is needed to determine which components of *PG*, including its structure or derived metabolites, contribute to the enhancement of intestinal function *in vivo*.

In the current investigation, certain limitations warrant acknowledgment. We did not compare the serum microbial array results with those obtained through fecal 16S RNA sequencing, the most common method for microbiota identification. Furthermore, since the serum microbial arrays examined only 384 microbial strains, the interpretation of the results could be somewhat limited. Lastly, the potential influence of anti-rheumatic drugs on microbiota was not factored into our analysis.

In conclusion, this study reiterates the utility of serum anti-microbial antibody arrays in uncovering therapeutic microbial targets for RA. Furthermore, we demonstrate the therapeutic effect of *PG* in restoring the intestinal barrier integrity and suppressing the immune response against RA. Therefore, *PG* may represent a promising microbiota-targeted therapy for individuals with RA.

Data availability statement

The data presented in the study are deposited in the NCBI Sequence Read Archive (SRA) repository, accession number PRJNA1048658 (https://www.ncbi.nlm.nih.gov/sra/PRJNA1048658).

Ethics statement

The studies involving humans were approved by GNUH Institutional Review Board in Korea (permit No: GNUH 2017-08-015). The studies were conducted in accordance with the local legislation and institutional requirements. The participants provided their written informed consent to participate in this study. The animal study was approved by the Institutional Animal Care and Use Committee of GNU in Korea (IACUC approval ID: GNU-200724-M0046). The study was conducted in accordance with the local legislation and institutional requirements.

Author contributions

SK: Data curation, Formal analysis, Funding acquisition, Methodology, Visualization, Writing – original draft, Writing – review & editing. SC: Data curation, Formal analysis, Methodology, Visualization, Writing – original draft, Writing – review & editing. YC: Writing – review & editing. MK: Writing – review & editing. HK: Writing – review & editing. HL: Data curation, Formal analysis, Writing – review & editing. SH: Data curation, Formal analysis, Methodology, Resources, Writing – original draft, Conceptualization, Writing – review & editing. SP: Methodology, Resources, Writing – review & editing. MP: Methodology, Resources, Writing – review & editing. YS: Data curation, Formal analysis, Funding acquisition, Methodology, Supervision, Writing – original draft, Writing – review & editing, Conceptualization. SL: Data curation, Formal analysis, Funding acquisition, Methodology, Supervision, Writing – original draft, Writing – review & editing, Conceptualization.

Funding

The author(s) declare financial support was received for the research, authorship, and/or publication of this article. This work was supported by the National Research Foundation of Korea (NRF) grants funded by the Korea government (NRF-2018R1D1A1B07046903, NRF-2020R1I1A3071922, NRF-2022R1F1A1071114, http://www.nrf.re.kr/index) and the Biomedical Research Institute Fund (GNUHBRIF-2022-0001) from the Gyeongsang National University Hospital.

Conflict of interest

Authors S-JP and MP are employed by Bifido Co., Ltd.

The remaining authors declare that the research was conducted in the absence of any commercial or financial relationships that could be construed as a potential conflict of interest.

Publisher's note

All claims expressed in this article are solely those of the authors and do not necessarily represent those of their affiliated organizations, or those of the publisher, the editors and the reviewers. Any product that may be evaluated in this article, or claim that may be made by its manufacturer, is not guaranteed or endorsed by the publisher.

Supplementary material

The Supplementary Material for this article can be found online at: https://www.frontiersin.org/articles/10.3389/fimmu.2023.1286387/full#supplementary-material

References

1. Chen J, Chia N, Kalari KR, Yao JZ, Novotna M, Paz Soldan MM, et al. Multiple sclerosis patients have a distinct gut microbiota compared to healthy controls. *Sci Rep* (2016) 6:28484. doi: 10.1038/srep28484

2. Higuchi BS, Rodrigues N, Gonzaga MI, Paiolo JCC, Stefanutto N, Omori WP, et al. Intestinal dysbiosis in autoimmune diabetes is correlated with poor glycemic control and increased interleukin-6: A pilot study. *Front Immunol* (2018) 9:1689. doi: 10.3389/fimmu.2018.01689

3. Kamada N, Seo SU, Chen GY, Nunez G. Role of the gut microbiota in immunity and inflammatory disease. *Nat Rev Immunol* (2013) 13(5):321–35. doi: 10.1038/nri3430

4. Sun Y, Chen Q, Lin P, Xu R, He D, Ji W, et al. Characteristics of gut microbiota in patients with rheumatoid arthritis in shanghai, China. *Front Cell Infect Microbiol* (2019) 9:369. doi: 10.3389/fcimb.2019.00369

5. van der Meulen TA, Harmsen HJM, Vila AV, Kurilshikov A, Liefers SC, Zhernakova A, et al. Shared gut, but distinct oral microbiota composition in primary sjogren's syndrome and systemic lupus erythematosus. *J Autoimmun* (2019) 97:77–87. doi: 10.1016/j.jaut.2018.10.009

6. Kinashi Y. Hase K. Partners in leaky gut syndrome: Intestinal dysbiosis and autoimmunity. *Front Immunol* (2021) 12:673708. doi: 10.3389/fimmu.2021.673708

7. Akuzum B, Lee JY. Context-dependent regulation of type17 immunity by microbiota at the intestinal barrier. *Immune Netw* (2022) 22(6):e46. doi: 10.4110/in.2022.22.e46

8. Barbara G, Barbaro MR, Fuschi D, Palombo M, Falangone F, Cremon C, et al. Inflammatory and microbiota-related regulation of the intestinal epithelial barrier. *Front Nutr* (2021) 8:718356. doi: 10.3389/fnut.2021.718356

9. Rosenbaum JT, Asquith MJ. The microbiome: A revolution in treatment for rheumatic diseases? *Curr Rheumatol Rep* (2016) 18(10):62. doi: 10.1007/s11926-016-0614-8

10. Marchesan JT, Gerow EA, Schaff R, Taut AD, Shin SY, Sugai J, et al. Porphyromonas gingivalis oral infection exacerbates the development and severity of collagen-induced arthritis. *Arthritis Res Ther* (2013) 15(6):R186. doi: 10.1186/ar4376

11. Maresz KJ, Hellvard A, Sroka A, Adamowicz K, Bielecka E, Koziel J, et al. Porphyromonas gingivalis facilitates the development and progression of destructive arthritis through its unique bacterial peptidylarginine deiminase (pad). *PloS Pathog* (2013) 9(9):e1003627. doi: 10.1371/journal.ppat.1003627

12. Alpizar-Rodriguez D, Lesker TR, Gronow A, Gilbert B, Raemy E, Lamacchia C, et al. Prevotella copri in individuals at risk for rheumatoid arthritis. *Ann Rheum Dis* (2019) 78(5):590–3. doi: 10.1136/annrheumdis-2018-214514

13. Scher JU, Sczesnak A, Longman RS, Segata N, Ubeda C, Bielski C, et al. Expansion of intestinal prevotella copri correlates with enhanced susceptibility to arthritis. *Elife* (2013) 2:e01202. doi: 10.7554/eLife.01202

14. Zhang X, Zhang D, Jia H, Feng Q, Wang D, Liang D, et al. The oral and gut microbiomes are perturbed in rheumatoid arthritis and partly normalized after treatment. *Nat Med* (2015) 21(8):895–905. doi: 10.1038/nm.3914

15. Marietta EV, Murray JA, Luckey DH, Jeraldo PR, Lamba A, Patel R, et al. Suppression of inflammatory arthritis by human gut-derived prevotella histicola in humanized mice. *Arthritis Rheumatol* (2016) 68(12):2878–88. doi: 10.1002/art.39785

16. Amdekar S, Singh V, Singh R, Sharma P, Keshav P, Kumar A. Lactobacillus casei reduces the inflammatory joint damage associated with collagen-induced arthritis (cia) by reducing the pro-inflammatory cytokines: Lactobacillus casei: Cox-2 inhibitor. *J Clin Immunol* (2011) 31(2):147–54. doi: 10.1007/s10875-010-9457-7

17. Pan H, Guo R, Ju Y, Wang Q, Zhu J, Xie Y, et al. A single bacterium restores the microbiome dysbiosis to protect bones from destruction in a rat model of rheumatoid arthritis. *Microbiome* (2019) 7(1):107. doi: 10.1186/s40168-019-0719-1

18. Gotschlich EC, Colbert RA, Gill T. Methods in microbiome research: Past, present, and future. *Best Pract Res Clin Rheumatol* (2019) 33(6):101498. doi: 10.1016/j.berh.2020.101498

19. Lindgreen S, Adair KL, Gardner PP. An evaluation of the accuracy and speed of metagenome analysis tools. *Sci Rep* (2016) 6:19233. doi: 10.1038/srep19233

20. Schirmer M, Ijaz UZ, D'Amore R, Hall N, Sloan WT, Quince C. Insight into biases and sequencing errors for amplicon sequencing with the illumina miseq platform. *Nucleic Acids Res* (2015) 43(6):e37. doi: 10.1093/nar/gku1341

21. Lkhagva E, Chung HJ, Hong J, Tang WHW, Lee SI, Hong ST, et al. The regional diversity of gut microbiome along the gi tract of male c57bl/6 mice. *BMC Microbiol* (2021) 21(1):44. doi: 10.1186/s12866-021-02099-0

22. Temoin S, Chakaki A, Askari A, El-Halaby A, Fitzgerald S, Marcus RE, et al. Identification of oral bacterial DNA in synovial fluid of patients with arthritis with native and failed prosthetic joints. *J Clin Rheumatol* (2012) 18(3):117–21. doi: 10.1097/RHU.0b013e3182500c95

23. Vogl T, Klompus S, Leviatan S, Kalka IN, Weinberger A, Wijmenga C, et al. Population-wide diversity and stability of serum antibody epitope repertoires against human microbiota. *Nat Med* (2021) 27(8):1442–50. doi: 10.1038/s41591-021-01409-3

24. Hitchon CA, Chandad F, Ferucci ED, Willemze A, Ioan-Facsinay A, van der Woude D, et al. Antibodies to porphyromonas gingivalis are associated with anticitrullinated protein antibodies in patients with rheumatoid arthritis and their relatives. *J Rheumatol* (2010) 37(6):1105–12. doi: 10.3899/jrheum.091323

25. Mikuls TR, Payne JB, Reinhardt RA, Thiele GM, Maziarz E, Cannella AC, et al. Antibody responses to porphyromonas gingivalis (p. Gingivalis) in subjects with rheumatoid arthritis and periodontitis. *Int Immunopharmacol* (2009) 9(1):38–42. doi: 10.1016/j.intimp.2008.09.008

26. Ogrendik M, Kokino S, Ozdemir F, Bird PS, Hamlet S. Serum antibodies to oral anaerobic bacteria in patients with rheumatoid arthritis. *MedGenMed* (2005) 7(2):2.

27. Okada M, Kobayashi T, Ito S, Yokoyama T, Komatsu Y, Abe A, et al. Antibody responses to periodontopathic bacteria in relation to rheumatoid arthritis in Japanese adults. *J Periodontol* (2011) 82(10):1433–41. doi: 10.1902/jop.2011.110020

28. Seifert JA, Bemis EA, Ramsden K, Lowell C, Polinski K, Feser M, et al. Association of antibodies to prevotella copri in anti-cyclic citrullinated peptide-positive individuals at risk of developing rheumatoid arthritis and in patients with early or established rheumatoid arthritis. *Arthritis Rheumatol* (2023) 75(4):507–16. doi: 10.1002/art.42370

29. Ormseth MJ, Wu Q, Zhao S, Allen RM, Solus J, Sheng Q, et al. Circulating microbial small rnas are altered in patients with rheumatoid arthritis. *Ann Rheum Dis* (2020) 79(12):1557–64. doi: 10.1136/annrheumdis-2020-217589

30. Castillo DJ, Rifkin RF, Cowan DA, Potgieter M. The healthy human blood microbiome: Fact or fiction? *Front Cell Infect Microbiol* (2019) 9:148. doi: 10.3389/fcimb.2019.00148

31. van Riel PL. The development of the disease activity score (das) and the disease activity score using 28 joint counts (das28). *Clin Exp Rheumatol* (2014) 32(5 Suppl 85): S–65-74.

32. van Riel PL, Schumacher HR Jr. How does one assess early rheumatoid arthritis in daily clinical practice? *Best Pract Res Clin Rheumatol* (2001) 15(1):67–76. doi: 10.1053/berh.2000.0126

33. Campanero-Rhodes MA, Lacoma A, Prat C, Garcia E, Solis D. Development and evaluation of a microarray platform for detection of serum antibodies against streptococcus pneumoniae capsular polysaccharides. *Anal Chem* (2020) 92(11):7437–43. doi: 10.1021/acs.analchem.0c01009

34. Li J, Zhai X, Ding C, Liu Y, Dong Q, Xu D, et al. Development of a bacterial macroarray for the rapid screening of targeted antibody-secreted hybridomas. *SLAS Discovery* (2019) 24(2):190–8. doi: 10.1177/2472555218804990

35. Kim M, Galan C, Hill AA, Wu WJ, Fehlner-Peach H, Song HW, et al. Critical role for the microbiota in cx3cr1(+) intestinal mononuclear phagocyte regulation of intestinal t cell responses. *Immunity* (2018) 49(1):151–63 e5. doi: 10.1016/j.immuni.2018.05.009

36. Kim M, Choe Y, Lee H, Jeon MG, Park JH, Noh HS, et al. Blockade of translationally controlled tumor protein attenuated the aggressiveness of fibroblast-like synoviocytes and ameliorated collagen-induced arthritis. *Exp Mol Med* (2021) 53 (1):67–80. doi: 10.1038/s12276-020-00546-y

37. Gomez Exposito R, de Bruijn I, Postma J, Raaijmakers JM. Current insights into the role of rhizosphere bacteria in disease suppressive soils. *Front Microbiol* (2017) 8:2529. doi: 10.3389/fmicb.2017.02529

38. Murphy EC, Frick IM. Gram-positive anaerobic cocci–commensals and opportunistic pathogens. *FEMS Microbiol Rev* (2013) 37(4):520–53. doi: 10.1111/1574-6976.12005

39. Jubair WK, Hendrickson JD, Severs EL, Schulz HM, Adhikari S, Ir D, et al. Modulation of inflammatory arthritis in mice by gut microbiota through mucosal inflammation and autoantibody generation. *Arthritis Rheumatol* (2018) 70(8):1220–33. doi: 10.1002/art.40490

40. Tajik N, Frech M, Schulz O, Schalter F, Lucas S, Azizov V, et al. Targeting zonulin and intestinal epithelial barrier function to prevent onset of arthritis. *Nat Commun* (2020) 11(1):1995. doi: 10.1038/s41467-020-15831-7

41. Zhang P, Minardi LM, Kuenstner JT, Zekan SM, Kruzelock R. Anti-microbial antibodies, host immunity, and autoimmune disease. *Front Med (Lausanne)* (2018) 5:153. doi: 10.3389/fmed.2018.00153

42. Sterlin D, Fadlallah J, Slack E, Gorochov G. The antibody/microbiota interface in health and disease. *Mucosal Immunol* (2020) 13(1):3–11. doi: 10.1038/s41385-019-0192-y

43. Magri G, Comerma L, Pybus M, Sintes J, Llige D, Segura-Garzon D, et al. Human secretory igm emerges from plasma cells clonally related to gut memory b cells and targets highly diverse commensals. *Immunity* (2017) 47(1):118–34 e8. doi: 10.1016/j.immuni.2017.06.013

44. Ouchida R, Mori H, Hase K, Takatsu H, Kurosaki T, Tokuhisa T, et al. Critical role of the igm fc receptor in igm homeostasis, b-cell survival, and humoral immune responses. *Proc Natl Acad Sci U.S.A.* (2012) 109(40):E2699–706. doi: 10.1073/pnas.1210706109

45. Johansen FE, Braathen R, Brandtzaeg P. Role of j chain in secretory immunoglobulin formation. *Scand J Immunol* (2000) 52(3):240–8. doi: 10.1046/j.1365-3083.2000.00790.x

46. Kosaraju R, Guesdon W, Crouch MJ, Teague HL, Sullivan EM, Karlsson EA, et al. B cell activity is impaired in human and mouse obesity and is responsive to an essential fatty acid upon murine influenza infection. *J Immunol* (2017) 198(12):4738–52. doi: 10.4049/jimmunol.1601031

47. Pearson JA, Ding H, Hu C, Peng J, Galuppo B, Wong FS, et al. Igm-associated gut bacteria in obesity and type 2 diabetes in c57bl/6 mice and humans. *Diabetologia* (2022) 65(8):1398–411. doi: 10.1007/s00125-022-05711-8

48. Ayyappan P, Harms RZ, Seifert JA, Bemis EA, Feser ML, Deane KD, et al. Heightened levels of antimicrobial response factors in patients with rheumatoid arthritis. *Front Immunol* (2020) 11:427. doi: 10.3389/fimmu.2020.00427

49. Nicolo A, Amendt T, El Ayoubi O, Young M, Finzel S, Senel M, et al. Rheumatoid factor igm autoantibodies control igg homeostasis. *Front Immunol* (2022) 13:1016263. doi: 10.3389/fimmu.2022.1016263

50. Newkirk MM, Goldbach-Mansky R, Senior BW, Klippel J, Schumacher HR Jr., El-Gabalawy HS. Elevated levels of igm and iga antibodies to proteus mirabilis and igm antibodies to escherichia coli are associated with early rheumatoid factor (rf)-positive rheumatoid arthritis. *Rheumatol (Oxford)* (2005) 44(11):1433–41. doi: 10.1093/rheumatology/kei036

51. Senior BW, McBride PD, Morley KD, Kerr MA. The detection of raised levels of igm to proteus mirabilis in sera from patients with rheumatoid arthritis. *J Med Microbiol* (1995) 43(3):176–84. doi: 10.1099/00222615-43-3-176

52. Chang PV, Hao L, Offermanns S, Medzhitov R. The microbial metabolite butyrate regulates intestinal macrophage function via histone deacetylase inhibition. *Proc Natl Acad Sci U.S.A.* (2014) 111(6):2247–52. doi: 10.1073/pnas.1322269111

53. Herrmann E, Young W, Rosendale D, Reichert-Grimm V, Riedel CU, Conrad R, et al. Rna-based stable isotope probing suggests allobaculum spp. As particularly active glucose assimilators in a complex murine microbiota cultured in *vitro*. *BioMed Res Int* (2017) 2017:1829685. doi: 10.1155/2017/1829685

54. Rios-Covian D, Ruas-Madiedo P, Margolles A, Gueimonde M, de Los Reyes-Gavilan CG, Salazar N. Intestinal short chain fatty acids and their link with diet and human health. *Front Microbiol* (2016) 7:185. doi: 10.3389/fmicb.2016.00185

55. Moon J, Lee AR, Kim H, Jhun J, Lee SY, Choi JW, et al. Faecalibacterium prausnitzii alleviates inflammatory arthritis and regulates il-17 production, short chain fatty acids, and the intestinal microbial flora in experimental mouse model for rheumatoid arthritis. *Arthritis Res Ther* (2023) 25(1):130. doi: 10.1186/s13075-023-03118-3

56. Horta-Baas G, Romero-Figueroa MDS, Montiel-Jarquin AJ, Pizano-Zarate ML, Garcia-Mena J, Ramirez-Duran N. Intestinal dysbiosis and rheumatoid arthritis: A link between gut microbiota and the pathogenesis of rheumatoid arthritis. *J Immunol Res* (2017) 2017:4835189. doi: 10.1155/2017/4835189

57. Kim KW, Song JH. Emerging roles of lymphatic vasculature in immunity. *Immune Netw* (2017) 17(1):68–76. doi: 10.4110/in.2017.17.1.68

58. Ma Y, Yang X, Chatterjee V, Wu MH, Yuan SY. The gut-lung axis in systemic inflammation. Role of mesenteric lymph as a conduit. *Am J Respir Cell Mol Biol* (2021) 64(1):19–28. doi: 10.1165/rcmb.2020-0196TR

59. Jakubzick CV, Randolph GJ, Henson PM. Monocyte differentiation and antigen-presenting functions. *Nat Rev Immunol* (2017) 17(6):349–62. doi: 10.1038/nri.2017.28

60. Zigmond E, Varol C, Farache J, Elmaliah E, Satpathy AT, Friedlander G, et al. Ly6c hi monocytes in the inflamed colon give rise to proinflammatory effector cells and migratory antigen-presenting cells. *Immunity* (2012) 37(6):1076–90. doi: 10.1016/j.immuni.2012.08.026

61. Ancuta P, Liu KY, Misra V, Wacleche VS, Gosselin A, Zhou X, et al. Transcriptional profiling reveals developmental relationship and distinct biological functions of cd16+ and cd16- monocyte subsets. *BMC Genomics* (2009) 10:403. doi: 10.1186/1471-2164-10-403

62. Rana AK, Li Y, Dang Q, Yang F. Monocytes in rheumatoid arthritis: Circulating precursors of macrophages and osteoclasts and, their heterogeneity and plasticity role in ra pathogenesis. *Int Immunopharmacol* (2018) 65:348–59. doi: 10.1016/j.intimp.2018.10.016

63. Sierra-Filardi E, Nieto C, Dominguez-Soto A, Barroso R, Sanchez-Mateos P, Puig-Kroger A, et al. Ccl2 shapes macrophage polarization by gm-csf and m-csf: Identification of ccl2/ccr2-dependent gene expression profile. *J Immunol* (2014) 192 (8):3858–67. doi: 10.4049/jimmunol.1302821

64. Kratofil RM, Kubes P, Deniset JF. Monocyte conversion during inflammation and injury. *Arterioscler Thromb Vasc Biol* (2017) 37(1):35–42. doi: 10.1161/ATVBAHA.116.308198

65. Yoon BR, Yoo SJ, Choi Y, Chung YH, Kim J, Yoo IS, et al. Functional phenotype of synovial monocytes modulating inflammatory t-cell responses in rheumatoid arthritis (ra). *PloS One* (2014) 9(10):e109775. doi: 10.1371/journal.pone.0109775

66. Rossol M, Kraus S, Pierer M, Baerwald C, Wagner U. The cd14(bright) cd16+ monocyte subset is expanded in rheumatoid arthritis and promotes expansion of the th17 cell population. *Arthritis Rheum* (2012) 64(3):671–7. doi: 10.1002/art.33418

67. Winchester R, Giles JT, Nativ S, Downer K, Zhang HZ, Bag-Ozbek A, et al. Association of elevations of specific t cell and monocyte subpopulations in rheumatoid arthritis with subclinical coronary artery atherosclerosis. *Arthritis Rheumatol* (2016) 68 (1):92–102. doi: 10.1002/art.39419

68. Smiljanovic B, Radzikowska A, Kuca-Warnawin E, Kurowska W, Grun JR, Stuhlmuller B, et al. Monocyte alterations in rheumatoid arthritis are dominated by preterm release from bone marrow and prominent triggering in the joint. *Ann Rheum Dis* (2018) 77(2):300–8. doi: 10.1136/annrheumdis-2017-211649

69. Jakubzick C, Gautier EL, Gibbings SL, Sojka DK, Schlitzer A, Johnson TE, et al. Minimal differentiation of classical monocytes as they survey steady-state tissues and transport antigen to lymph nodes. *Immunity* (2013) 39(3):599–610. doi: 10.1016/j.immuni.2013.08.007

70. Van Itallie CM, Fanning AS, Bridges A, Anderson JM. Zo-1 stabilizes the tight junction solute barrier through coupling to the perijunctional cytoskeleton. *Mol Biol Cell* (2009) 20(17):3930–40. doi: 10.1091/mbc.e09-04-0320

Frontiers in Immunology

Explores novel approaches and diagnoses to treat immune disorders.

The official journal of the International Union of Immunological Societies (IUIS) and the most cited in its field, leading the way for research across basic, translational and clinical immunology.

Discover the latest Research Topics

See more →

Frontiers

Avenue du Tribunal-Fédéral 34
1005 Lausanne, Switzerland
frontiersin.org

Contact us

+41 (0)21 510 17 00
frontiersin.org/about/contact